CORROSION CRACKING OF METALLIC MATERIALS

Part I. Summary

Mars G. Fontana

FOREWORD

This report was prepared by the Department of Metallurgical Engineering, The Ohio State University, Columbus, Ohio. The principal investigator for this project was Dr. Mars Fontana, under Contract F33615-69-C-1258. This contract was initiated under Project No. 7312, "Metal Surface Deterioration and Protection," Task No. 731202, "Metal Surface Deterioration," during the period December 15, 1968 through December 31, 1971. This work was administered by the Advanced Metallurgical Studies Branch of the Metals and Ceramics Division, Air Force Materials Laboratory, Wright-Patterson Air Force Base, Ohio, under the direction of Dr. C. T. Lynch and Dr. H. B. Kirkpatrick (AFML/LL).

This report was released by the author in July, 1972.

This technical report has been reviewed and is approved.

C. T. Lynch
Chief, Advanced Metallurgical
Studies Branch
Metals and Ceramics Division
Air Force Materials Laboratory

ABSTRACT

Studies on the stress corrosion cracking of titanium and its alloys involved the initiation and propagation of cracks in aqueous and organic environments, combined effects of stress and potential, corrosion processes within crevices, and alloy composition. Straining electrode studies are reported.

In Ti-6Al-4V specimens, crack initiation was associated with local anodic disintegration at α-β interfaces and at β grains. Crack velocity studies in titanium alloys show that crack velocity was independent of applied potential but directly dependent on stress. Studies within titanium crevices show that the corrosion inside a crevice is accentuated when the IR drop is large; procedures for minimizing this effect are discussed.

Activation energies of 6~7 kcal for stress corrosion cracking were determined for unalloyed titanium and titanium alloys Ti-6Al-4V, Ti-8Al-1V-1Mo, and βIII in $CH_3OH + HCl + H_2O$ and $CH_3OH + Br_2$ solutions, suggesting that either halide ion attack or titanium hydride formation describe the cracking mechanism.

Chemical methods, to reduce the water content of methanol to low levels and to accurately determine these levels, have been developed to examine the effect of these small water concentrations on the stress corrosion cracking behavior of titanium in methanol environments.

Unalloyed titanium failed by stress corrosion cracking in distilled methanol containing chloride as low as 10 ppb. Stress corrosion susceptibility of unalloyed titanium and titanium alloys Ti-8Al-1V-1Mo, Ti-6Al-4V, and βIII increased when CaO was added to absolute methanol to reduce the water content of the methanol from the initial 0.015% level. A further increase in susceptibility was observed in dry methanol vapor. It is believed that the primary reaction of methanol with titanium involves the production of titanium methoxide and hydrogen. Mixtures of carbon tetrachloride and methanol are more reactive to titanium than are either of the pure solvents. Small amounts of bromine added to benzene, carbon tetrachloride, and diethyl ether increased greatly the susceptibility of Ti-8Al-1V-1Mo to cracking. This effect was most pronounced for diethyl ether.

Studies on the effect of grain size of Ti-6Al-4V on stress corrosion cracking in $CH_3OH + H_2O + NaCl$ solution show that increased resistance with decreasing grain size is due primarily to increased crack initiation time.

TABLE OF CONTENTS

TABLE OF CONTENTS (continued)

TABLE OF CONTENTS (continued)

TABLE OF CONTENTS (continued)

TABLE OF CONTENTS (continued)

LIST OF FIGURES

LIST OF FIGURES (Continued)

LIST OF FIGURES (Continued)

LIST OF FIGURES (Continued)

LIST OF FIGURES (Continued)

LIST OF FIGURES (Continued)

LIST OF FIGURES (Continued)

LIST OF FIGURES (Continued)

LIST OF FIGURES (Continued)

LIST OF FIGURES (Continued)

LIST OF FIGURES (Continued)

LIST OF FIGURES (Continued)

LIST OF FIGURES (continued)

LIST OF FIGURES (continued)

LIST OF FIGURES (continued)

LIST OF FIGURES (Continued)

LIST OF FIGURES (continued)

LIST OF FIGURES (continued)

LIST OF FIGURES (Continued)

LIST OF FIGURES (Continued)

LIST OF FIGURES (Continued)

LIST OF FIGURES (Continued)

LIST OF TABLES

LIST OF TABLES (Continued)

LIST OF TABLES (continued)

SECTION I

INTRODUCTION

Stress-corrosion cracking is one of the most important, if not the most important, corrosion problem facing this country. Cracking often occurs prematurely with catastrophic results.

The program was aimed at developing fundamental information concerning the nature and control of stress-corrosion cracking including design of alloys and environmental control. Primary emphasis on titanium alloys and high-strength steels.

Pursuant to the coupling aspects of this program, lectures and seminars were held at AFML by our staff, and a postdoctoral fellow was transferred to AFML and conducted his research there.

Four Master's degrees and six Doctor's degrees were awarded during this period based on this research.

SECTION II

TITANIUM AND TITANIUM-BASE ALLOYS (F. H. Beck)

The objective of this program was to obtain a better understanding of the factors responsible for stress-corrosion cracking in titanium-base alloys. Investigations described below were designed to characterize various titanium-environment stress-cracking systems. The effects of microstructure and state of stress on crack initiation and propagation were important parts of these studies.

Some observations from this work include the following:

In methanol environments crack initiation is highly potential dependent; however, the propagation rate of cracks (SCC) is not greatly influenced by the application of an applied potential (because of the crevice effect) over a considerable range including the corrosion potential. Although it is not known whether halide ions are a necessary, or only a sufficient, condition for cracking, the protective effect of water is known. That is, a stable oxide film will form on titanium when the methanol contains as little as about 0.8% water, even in the presence of halide ions. Methanol will absorb this much water within a short time upon exposure to the ordinary atmosphere. Thus, one would expect stress corrosion cracking to be most serious when precautions were taken to keep the methanol out of contact with air.

In aqueous solutions containing halide ions stress-corrosion cracking susceptibility exists near the corrosion potential. Of particular interest here is the crevice effect, which in precracked specimens, generates a highly sensitive condition for stress-corrosion cracking in water containing chloride ion. This environment, because of its abundance in nature and its known pernicious effects, is of considerable practical importance. The avoidance of "built in" crevices should be a major factor in the prevention of stress-corrosion cracking in this environment. Proper material selection and design can minimize problems in this respect.

More studies are required to define the role of hydrogen in the stress corrosion of titanium materials. Also, studies should emphasize the initiation process with respect to material degradation at these sites.

The following studies on titanium stress corrosion provide evidence in support of most of the cracking mechanisms proposed to date.

A. CREVICE EFFECT DURING POLARIZATION OF Ti-8Al-1Mo-1V ALLOY IN AQUEOUS AND METHANOL ENVIRONMENTS (C. M. Chen)

1. Introduction

If polarization is applied for either anodic[1,2,3,4] or cathodic[5] protection, a crevice effect in some special cases will be important.[6] The same effect should also occur at the apex of cracks or fissures in stress corrosion specimens during polarization and it is clear that a large potential gradient could exist in the crevice. This gradient is caused by the high resistance of the narrow electrolyte path.[6,7] Thus, although a crack exterior is polarized to a certain potential, the crack interior could remain at a different potential. The purpose of the present experiments is to determine the factors influencing this crevice effect at the crack apex when polarization is applied to a stress corrosion specimen.

2. Experimental

Experiments were performed with the apparatus illustrated in Fig. 1. A sheet specimen of Ti-8Al-1Mo-1V alloy measuring 4.5" x 0.025" of the composition given in Table I was secured to one side of the specimen holder through the backup plate by screw, S_1, and the crevice size was adjusted by screw, S_2. After setting the crevice size the crevice assembly was tightly wrapped with Teflon tape up to the position indicated to prevent solution from entering the crevice from the edges. The entire assembly was then immersed into the test solution to the indicated level and the specimen was polarized using a platinum electrode and a Luggin probe located at the crevice exterior. Potentials in the crevice were measured by four Luggin probes inserted in the four probe openings (the Lucite specimen holder) which were located at 3/4" intervals into the crevice. All potentials were measured against saturated calomel electrodes.

Table I - Chemical Compositions of Titanium Alloys (0.025" sheet)

Element	Ti-8Al-1Mo-1V w/o	Ti-6Al-4V (w/o) Alloy #1	Ti-6Al-4V (w/o) Alloy #2
Al	7.85	6.30	6.75
V	1.05	4.10	4.00
Fe	0.13	0.19	0.30
Mo	1.1	--	--
C	0.02	0.03	0.10
N	0.008	0.01	0.05
O	0.08	0.106	0.20
H	102 ppm	60 ppm	150 ppm
Ti	balance	balance	balance

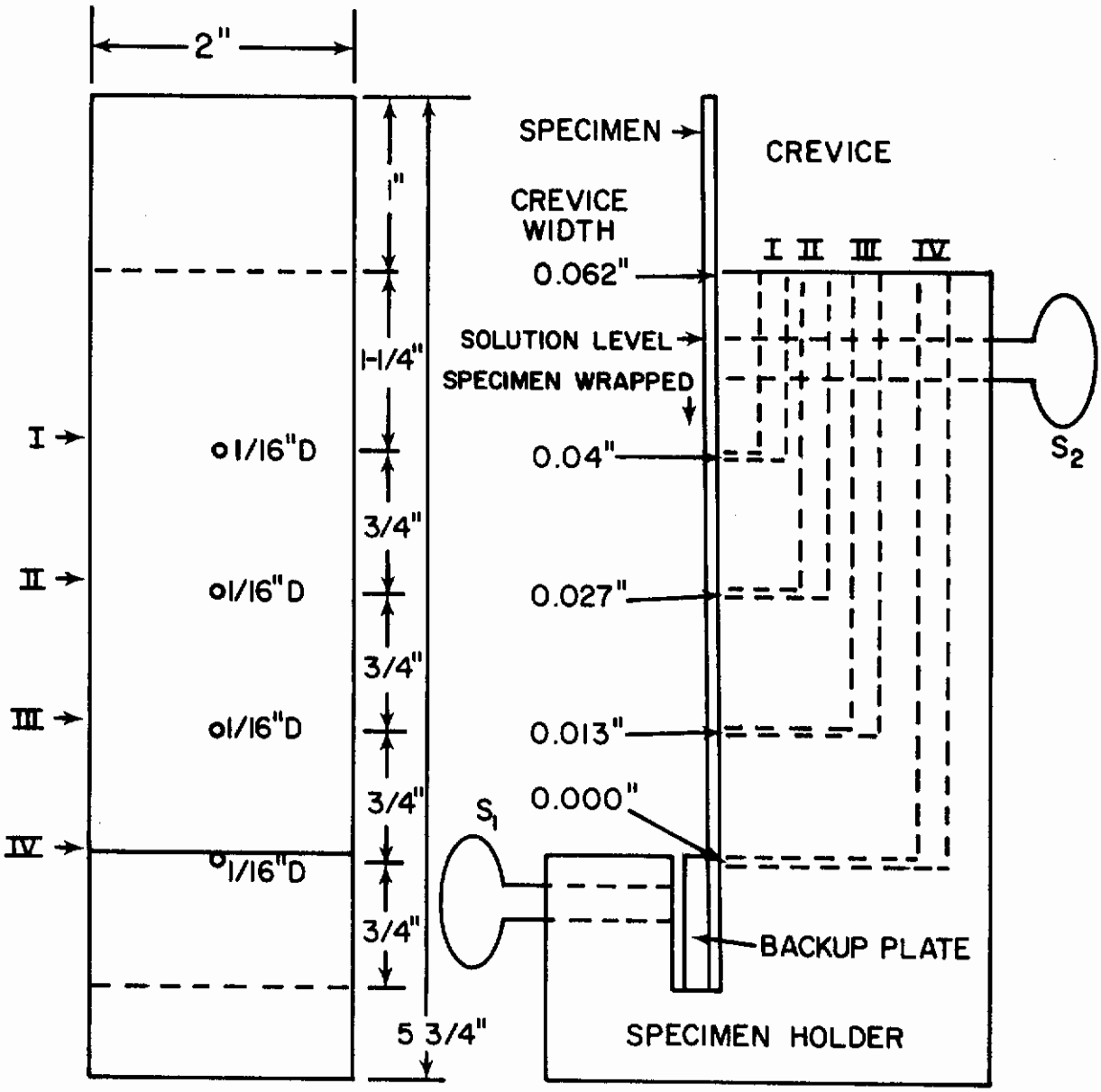

Fig. 1 - Cell for Crevice Effect on Ti-8Al-1Mo-1V Alloy (Specimen holder, back-up plate and screws S_1 and S_2 are lucite)

3. Results

a. Crevice Effect in Sulfuric Acid Solution

Polarization potential at the crevice interior is plotted as the ordinate and polarization potential at the crevice exterior is plotted as the abscissa in the following figures. When the experiment was carried out in 1N H_2SO_4 solution, there was essentially no crevice effect as shown in Fig. 2. Upon increasing the acid in the solution to 10N H_2SO_4, the critical current density for passivation was greatly increased and a crevice effect occurred due to the large anodic dissolution current in the active potential region as shown in Fig. 3. When the crevice exterior became passive, the crevice interior remained active until a certain higher polarization potential was attained. Finally, when the potential at the crevice exterior was high enough, say 1100 mV for crevice I (see Fig. 1), a potential of 1000 mV was observed for crevices (II) and (III) and 200 mV for crevice (IV); in time, the respective crevice regions gradually became passive from exterior to interior and the crevice effect gradually disappeared.

b. Crevice Effect in KBr Solution

As shown in Fig. 4, the anodic current is very small at polarization potentials below that for halogen ion attack and there is no observed crevice effect. When the anodic polarization was increased to approximately 1100 mV (SHE) bromide ion attack occurred and a crevice effect appeared. The potential in the crevice remained constant with a further increase in anodic polarization.

c. Crevice Effect in KI Solution

No crevice effect appeared until the anodic reaction, $2I^- \rightarrow I_2 + 2e$ occurred at approximately 650 mV (SHE) as shown in Fig. 5 and the potential in the crevice remained constant as the polarization potential was raised to about 2050 mV (SHE). When the polarization potential was further increased above 2050 mV (SHE), pitting due to halogen ion attack occurred and the current again increased. Although pitting occurred at the crevice exterior, it did not occur within the crevice and the potential within the crevice remained constant.

d. Crevice Effect in Methanol Solutions

When anodic polarization was applied to the titanium-methanol system in the absence of a passivator, anodic dissolution or halogen ion attack occurred and a crevice effect appeared. Figure 6 is for titanium in methanol + HCl solution and Fig. 7 is for titanium in $CH_3 + H_2SO_4$ solution.

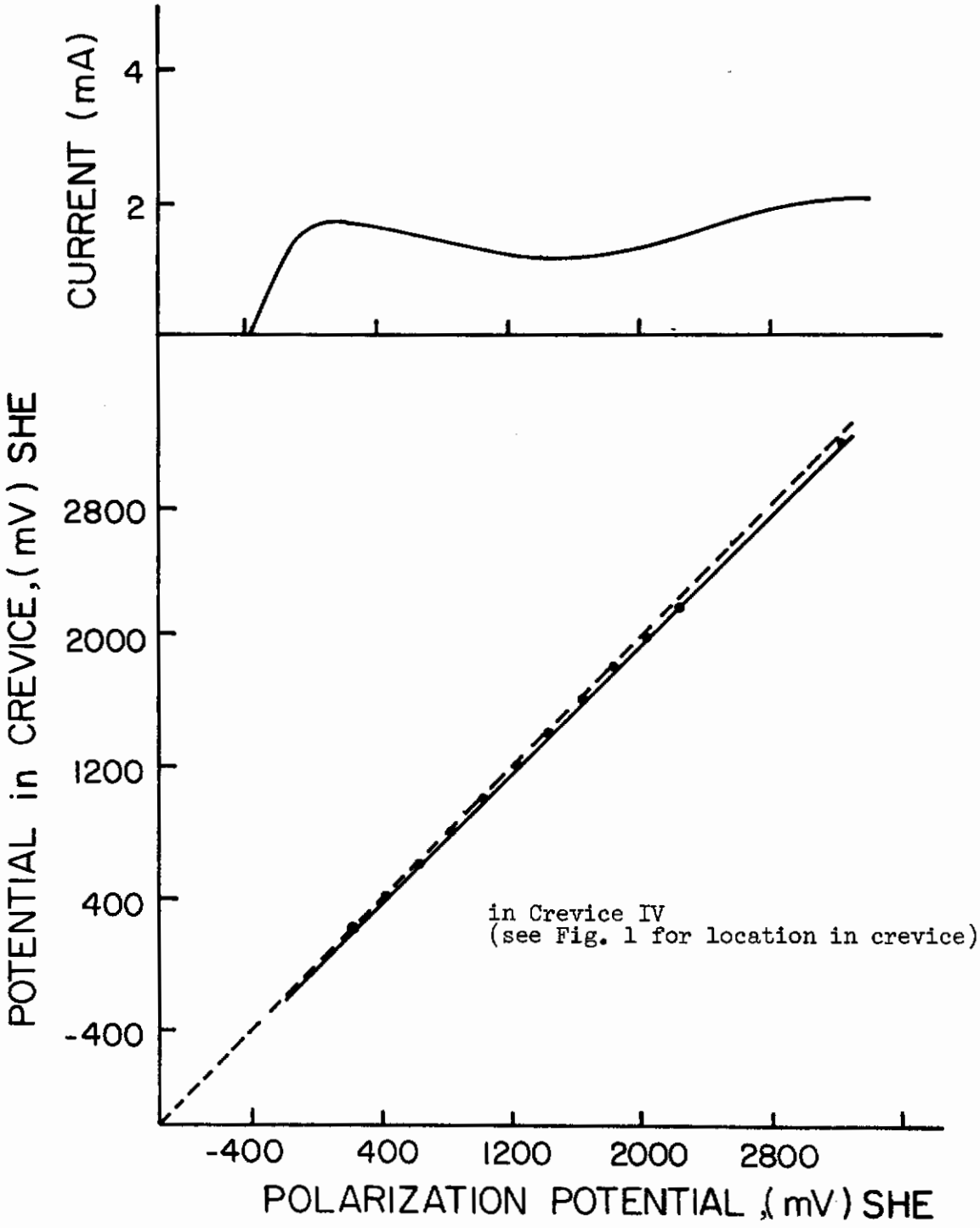

Fig. 2 - Polarization Potential at Crevice Exterior vs. Potential in Crevice (Ti-8Al-1Mo-1V in 1N H_2SO_4)

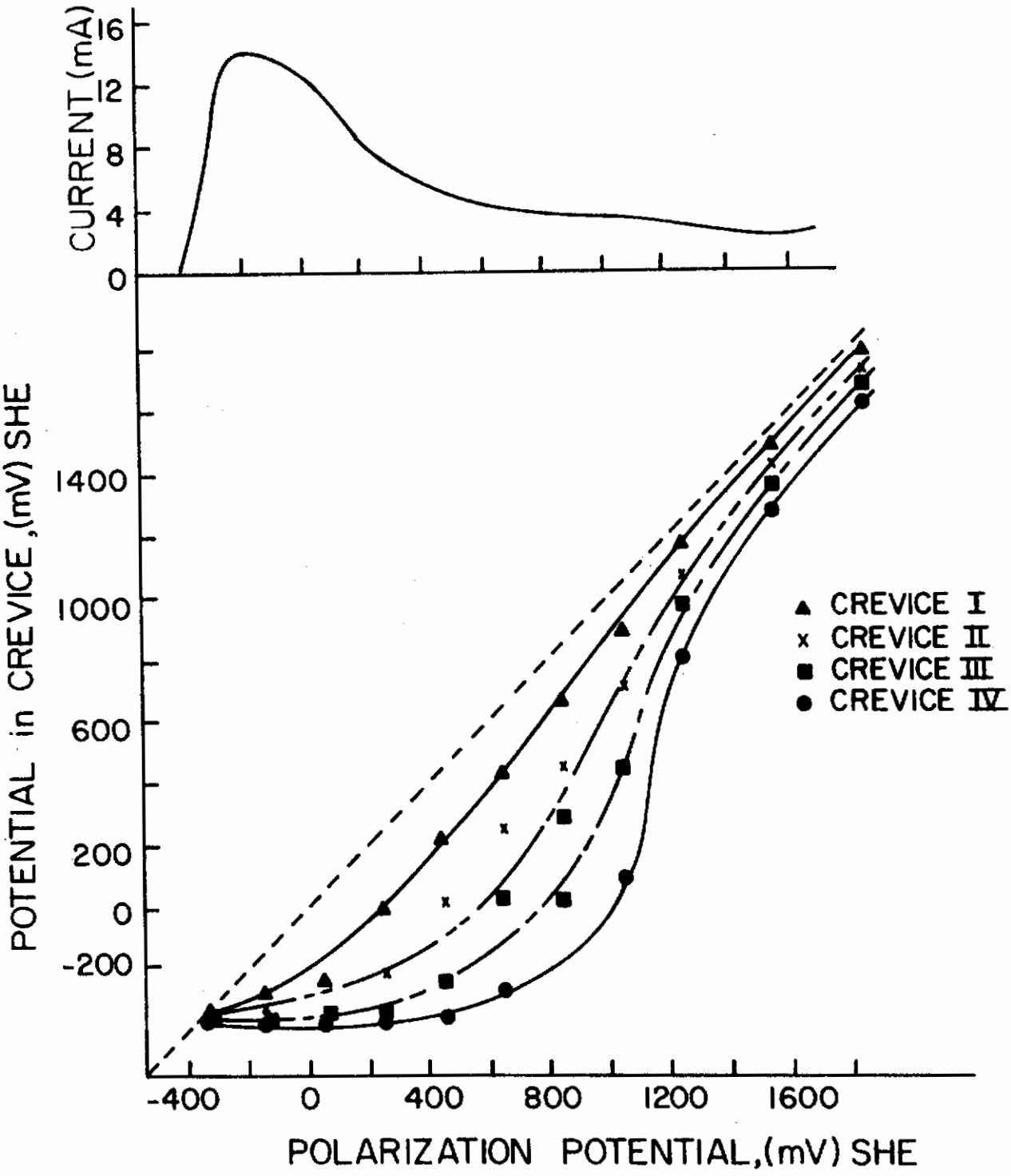

Fig. 3 - Polarization Potential at Crevice Exterior vs. Potential in Crevice (Ti-8Al-1Mo-1V in 10N H_2SO_4)

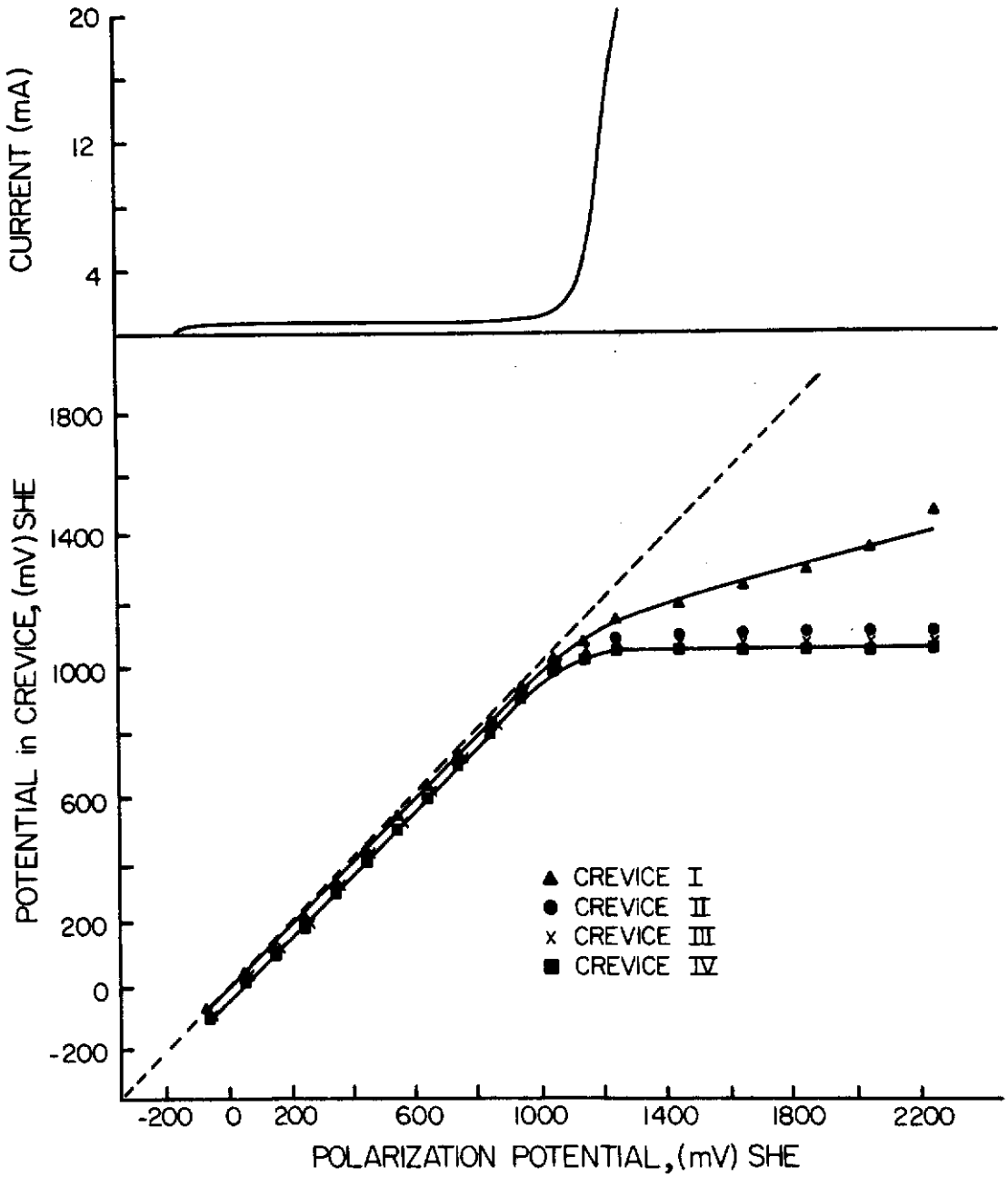

Fig. 4 - Polarization Potential at Crevice Exterior vs. Potential in Crevice (Ti-8Al-1Mo-1V in 0.6N KBr

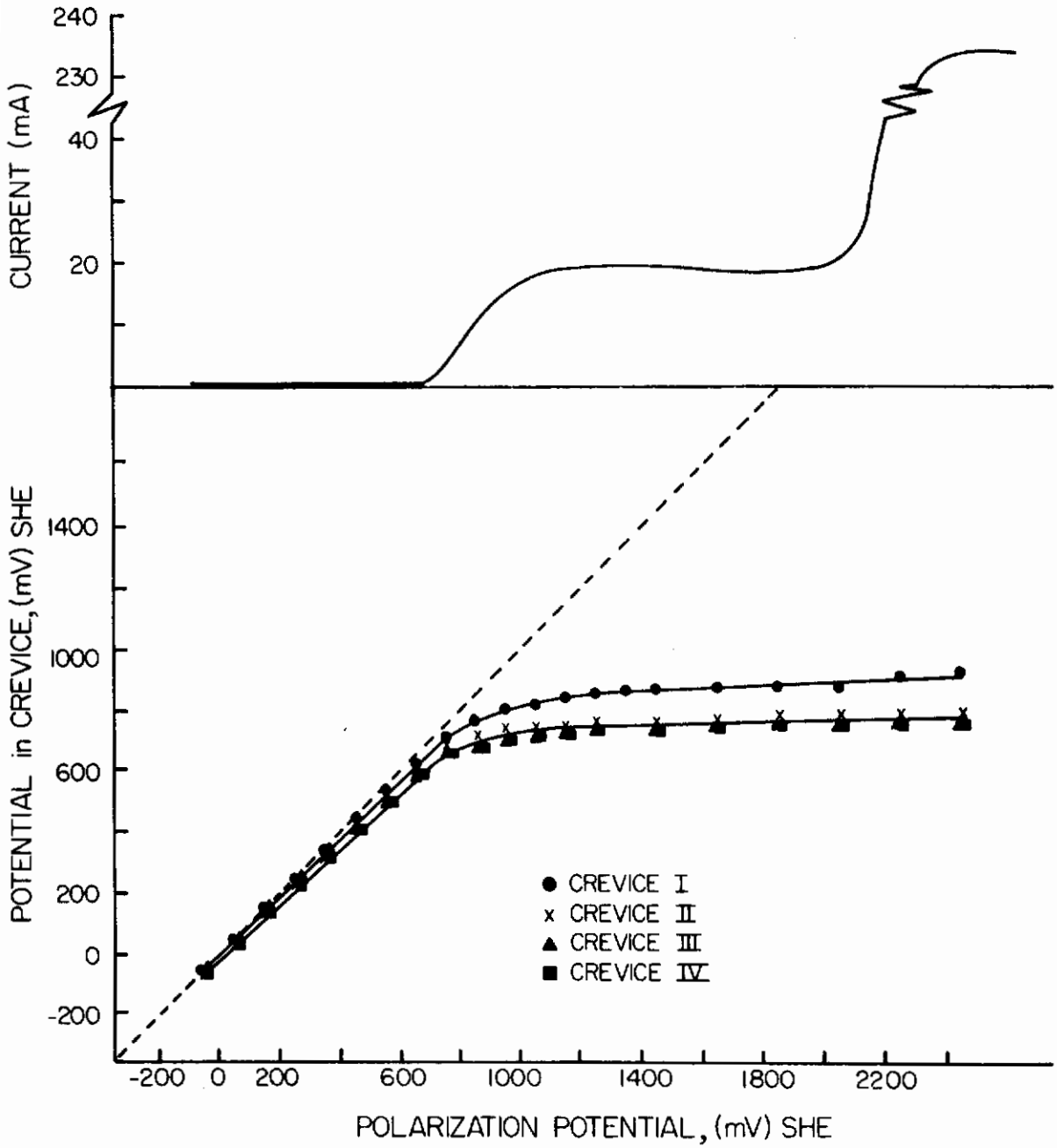

Fig. 5 - Polarization Potential at Crevice Exterior vs. Potential in Crevice (Ti-8Al-1Mo-1V in 0.6N KI)

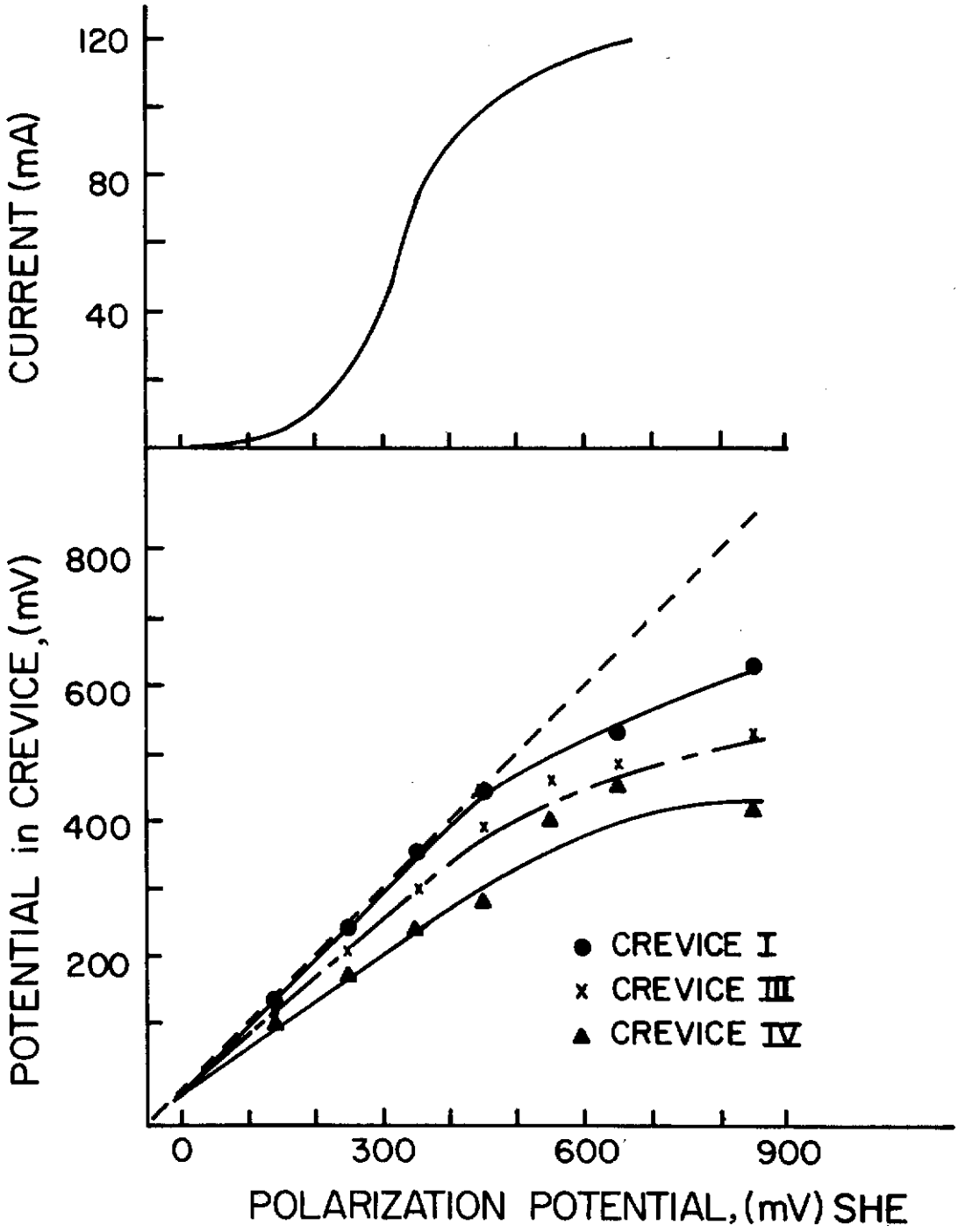

Fig. 6 - Polarization Potential at Crevice Exterior vs. Potential in Crevice (Ti-8Al-1Mo-1V in CH_3OH + 0.37% HCl + 0.63% H_2O)

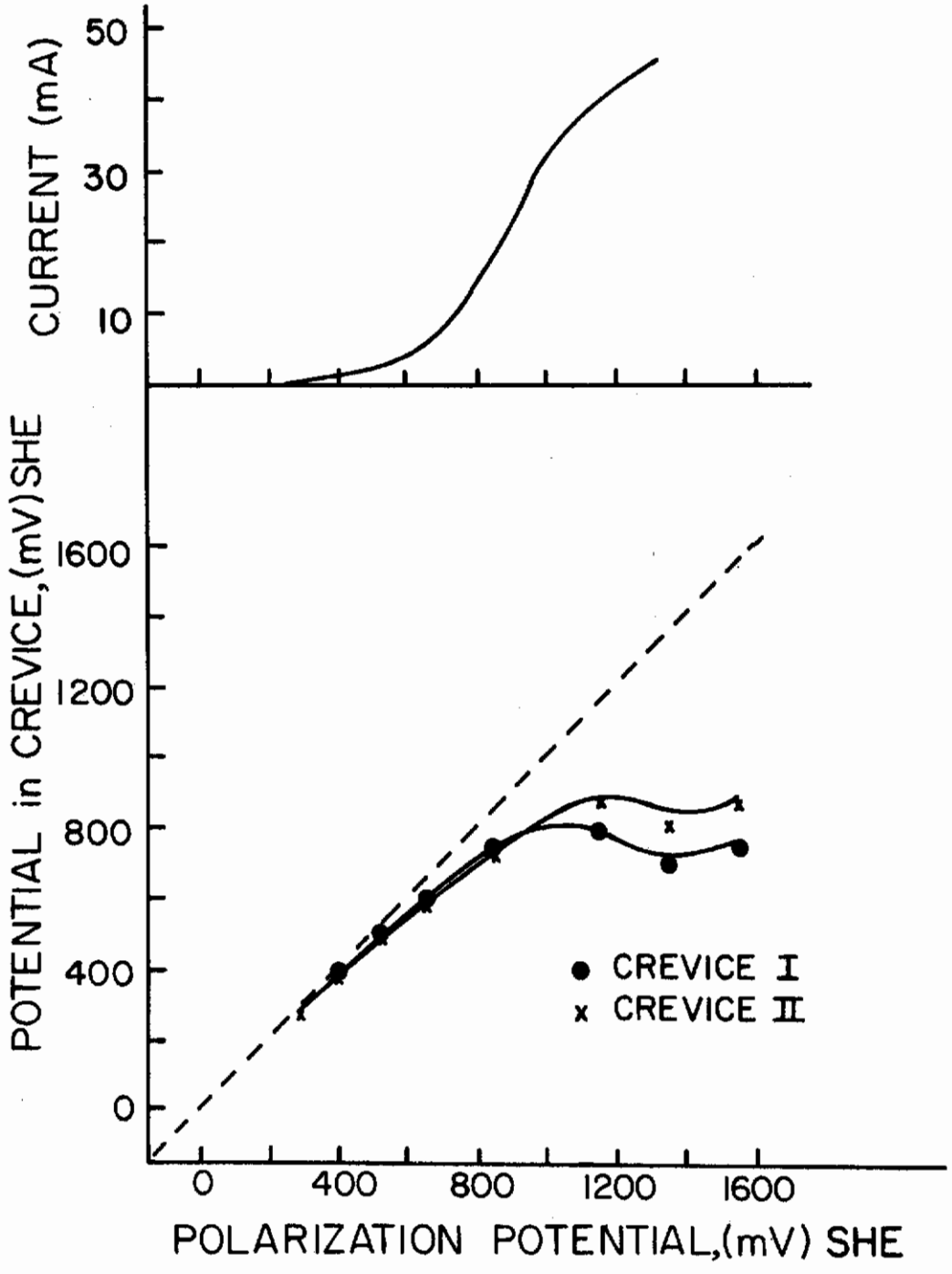

Fig. 7 - Polarization Potential at Crevice Exterior vs. Potential in Crevice (Ti-8Al-1Mo-1V in CH_3OH + 2% H_2SO_4)

e. Crevice Effect during Cathodic Polarization

Figure 8 shows the crevice effect resulting from cathodic polarization of titanium in 0.6M KI solution. When hydrogen gas evolution occurred, the crevice effect appeared. The crevice effect in cathodic polarization results in the crevice potential deviating to the more anodic direction; whereas, in anodic polarization the potential shifts in the more cathodic direction.

4. Discussion

It has been shown[8,9] that the susceptibility of titanium and its alloys to stress-corrosion cracking is potential dependent. Further, it is demonstrated in the present paper that a crevice effect should exist in a crack, and that the polarization potential and the potential at the crack apex can be quite different. This crevice effect occurs from IR drops in the crevice. Therefore, when certain electrochemical reactions occur and, in so doing, cause the polarization current to increase, an IR drop becomes predominant and a crevice effect is observed. When the polarization curve shows an active-passive phenomenon, the critical current density for passivation is the prominent factor influencing the crevice effect. If the current is very large, the crevice exterior becomes passive while the crevice interior remains active; however, when the polarization potential is high enough, passivation occurs inside the crevice and, in time, the crevice effect disappears.

Therefore, the shape of the polarization curve, the pH of the solution and the magnitude of the critical passive current density can have a great influence on the crevice effect. As illustrated in Fig. 9, which considers a system of low solution pH and high critical current density, the potential at the crack tip will remain active at region B although the anodic polarization potential is in the passive region A. In such a system, stress-corrosion cracking at the corrosion potential is likely to result from either anodic dissolution or hydrogen embrittlement. However, when the pH of the solution is high (Fig. 10) and the current density for passivation is small, the potential at the crack apex is readily polarized to the pitting corrosion potential. However, once halogen ion attack occurs, the crevice effect will appear.

In neutral environments, such as aqueous NaCl and KBr solutions, the anodic current is small at applied potentials below that required for halogen ion attack and there is little or no crevice effect. When halogen ion attack occurs, the crevice effect appears simultaneously and thereafter the potential in the crevice interior remains constant. Here it should be noted that in spite of the crevice effect the crevice interior is also polarized to a potential high enough for halogen ion attack. However, in KI solution, the reaction $2I^- \rightarrow I_2 + 2e$ occurs prior to halogen ion attack and the crevice effect appears to be due to this reaction; therefore, the potential in the crevice remains constant. When the potential is further increased, halogen ion attack

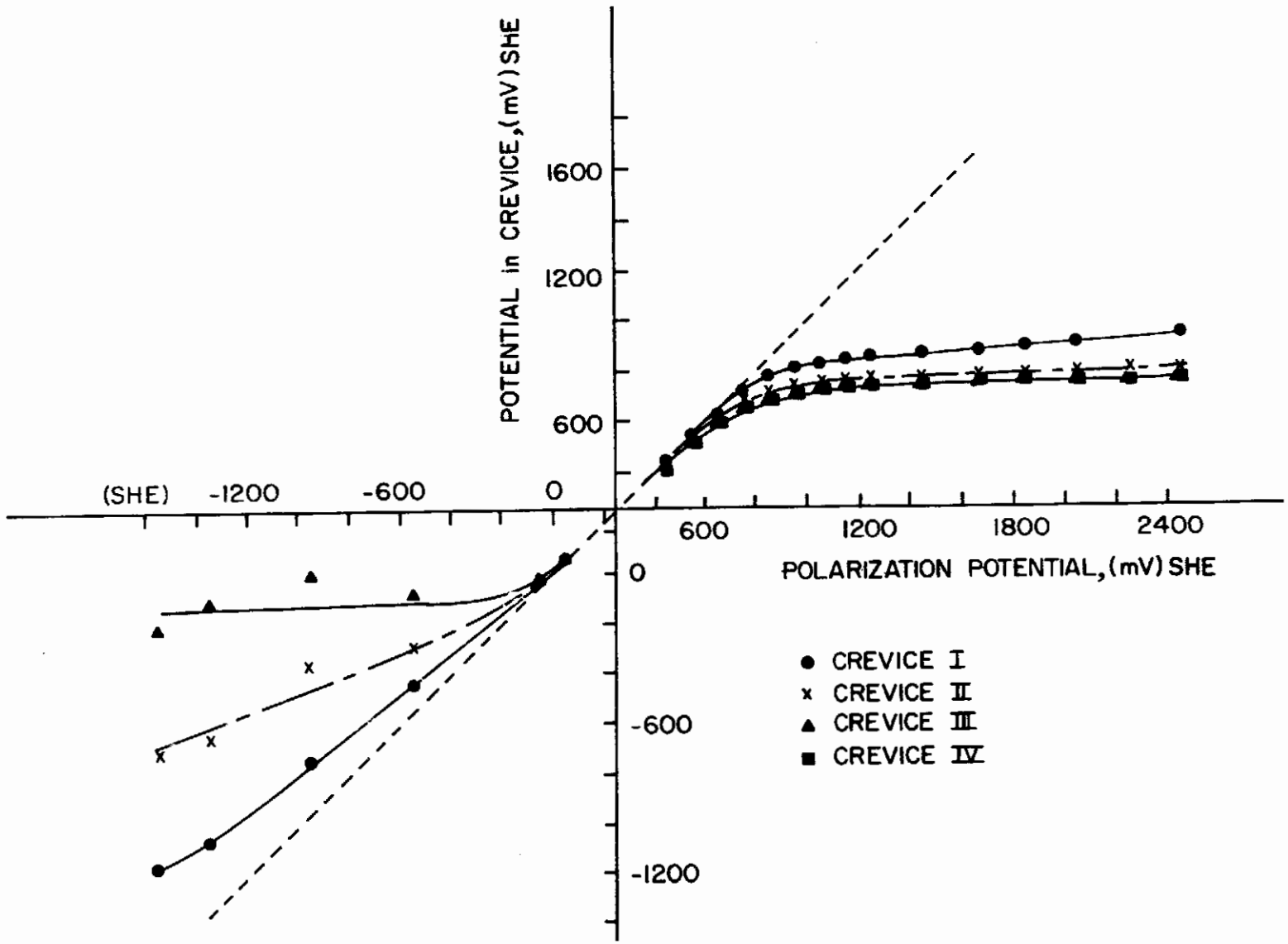

Fig. 8 - Crevice Effect by Anodic and Cathodic Polarization (Ti-8Al-1Mo-1V in 0.6M KI)

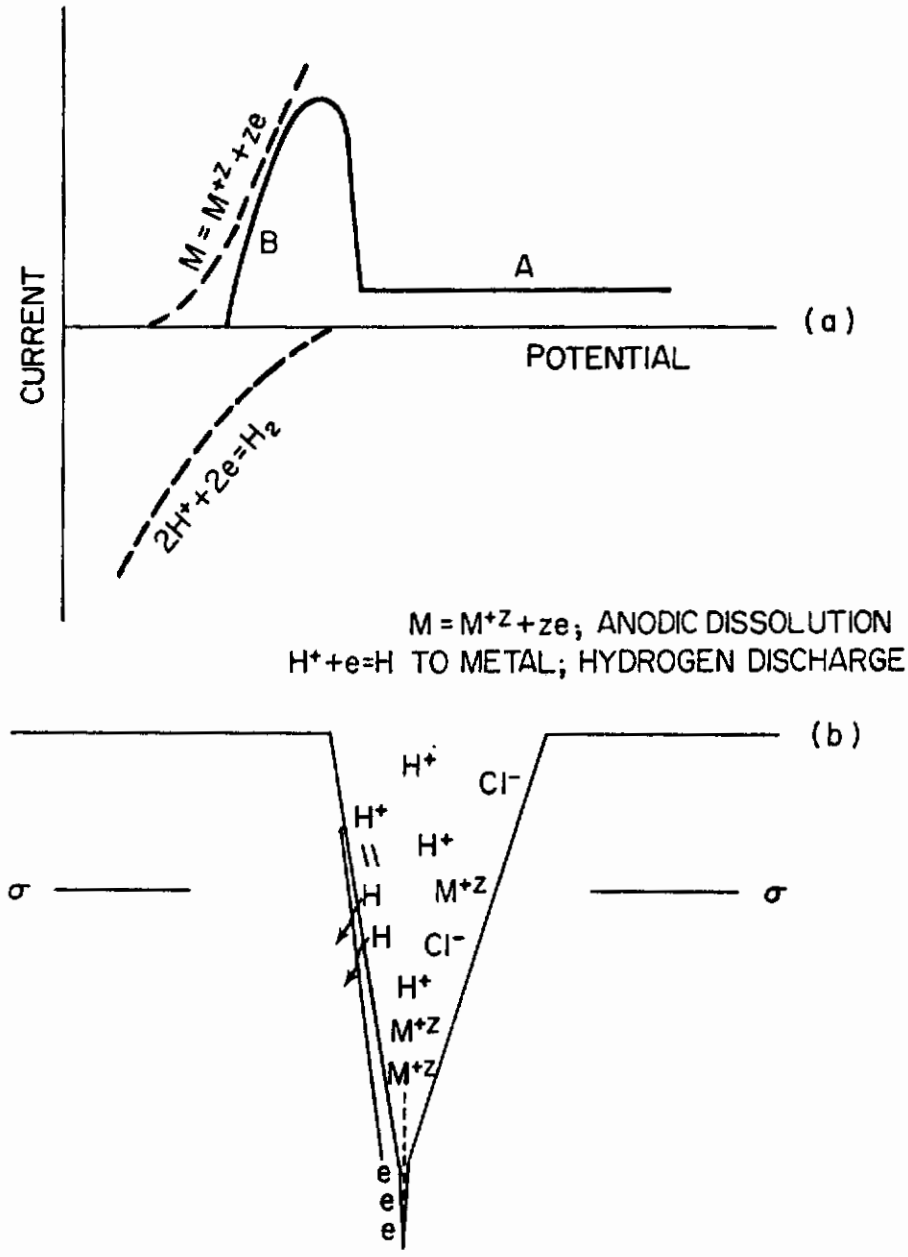

Fig. 9 - Crevice Effect by Low pH and High Passivation Current
(a) Schematic diagram for polarization curve
(b) Schematic picture for a crack at corrosion potential

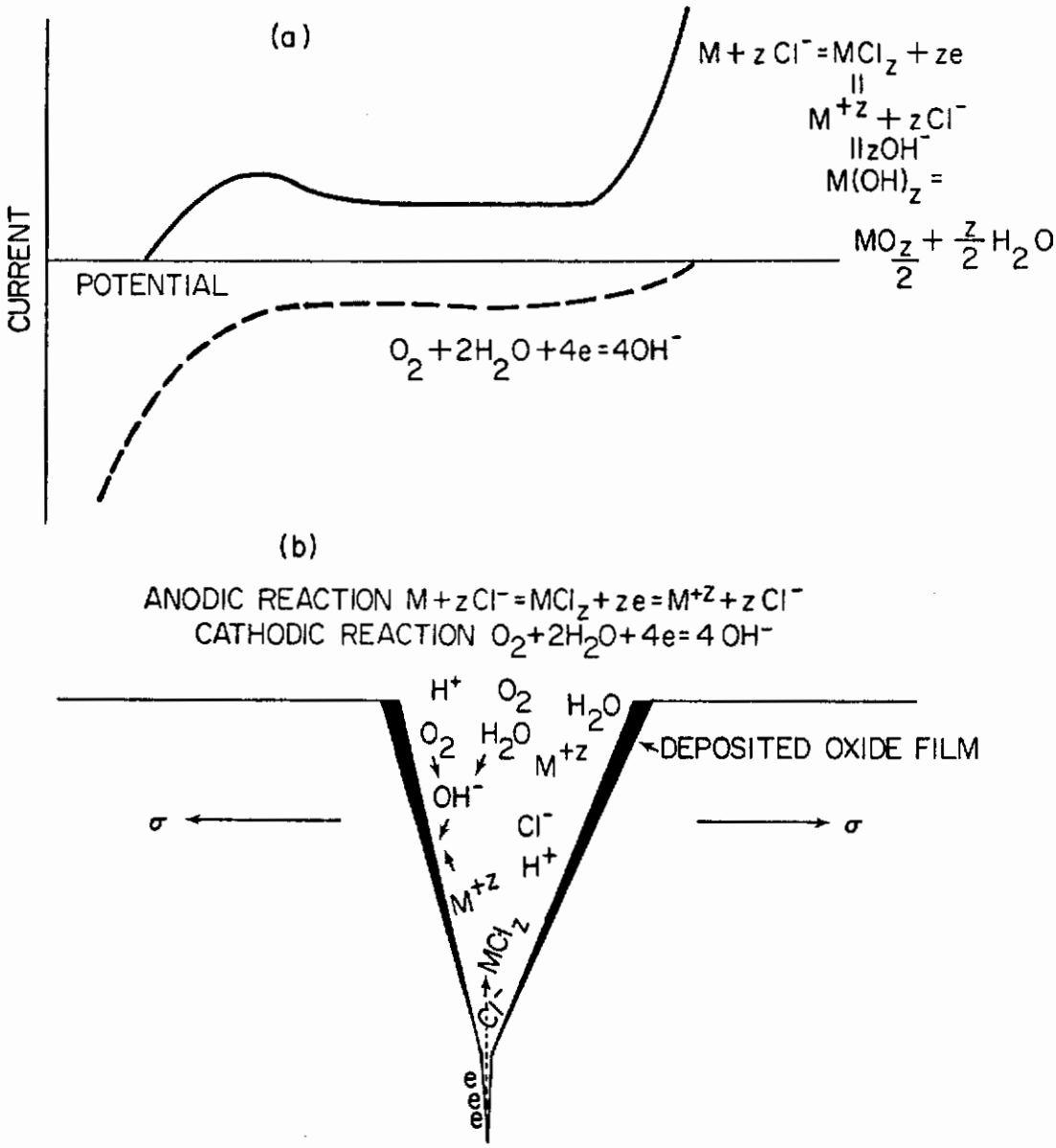

Fig. 10 - Crevice Effect by High pH and Low Passivation Current
(a) Schematic diagram for polarization curve
(b) Schematic picture for a crack of corrosion potential

occurs at the crevice exterior and the current increases rapidly; however, the potential in the crevice interior remains unchanged and so halogen ion attack occurs.

In methanol solutions, in the absence of a passivator, anodic dissolution or halogen ion attack occurs in the very active potential region and the crevice effect appears simultaneously. In this case the potential in the crevice is high enough for the above reactions to occur.

Although the artificial crevice used here is different from a real stress corrosion crack or fissure, the crevice effect in an actual crack can be discussed in a similar manner. Stress-corrosion cracking susceptibility vs. potential data in NaCl and KBr solutions[8,9] show cathodic and anodic protection zones and susceptible zones the latter of which are near the corrosion potential and halogen ion attack regions. From the present results it is reasonable to assume that halogen ion attack occurs at the apex of the crack when the specimen is polarized in the susceptible zone of the halogen ion attack region where the crevice effect occurs. In KI solutions the tendency for susceptibility is different from NaCl and KBr solutions and there is no anodic protection zone as shown in Fig. 11. In this case halogen ion attack occurs at the crack exterior only, and it is not possible for halogen ion attack to occur at the apex due to the occurrence of the $2I^- \rightarrow I_2 + 2e$ reaction; these different tendencies for cracking in the KI and KBr solutions suggest different mechanisms. In methanol solutions it is reasonable to assume that anodic dissolution or halogen ion attack occurs at the crack apex; the susceptibility vs. potential data do not show an anodic protection zone for this environment.

Regardless of the electrochemical reaction in the crevice, whether it be anodic dissolution, halogen ion attack, hydrogen evolution, etc. the crevice effect appears at the crack apex and makes it difficult or impossible to increase polarization within the crack.

This effect is demonstrated in three figures, the first of which (Fig. 12) shows failure time and propagation time vs. polarization potential in the potential region of halogen ion attack in aqueous 0.6M KBr solution. Figure 54 shows failure time and crack initiation time vs. applied potential for Ti6Al-4V in CH_3OH + sat. NaCl + 0.3% H_2O solution, while Fig. 55 illustrates that the crack propagation rate (failure time minus initiation time) is essentially constant over the polarization range studied. From these curves it is evident that the effect of polarization potential on failure time is almost totally accounted for by the initiation time. That is, the applied potential has a pronounced effect on initiation time, but once the crack has started, the polarization potential has little effect on the propagation rate of the crack over wide ranges of applied potential. This implies that once the electrochemical reaction causing the stress-corrosion cracking occurs, the crevice effect will make it difficult to increase polarization at

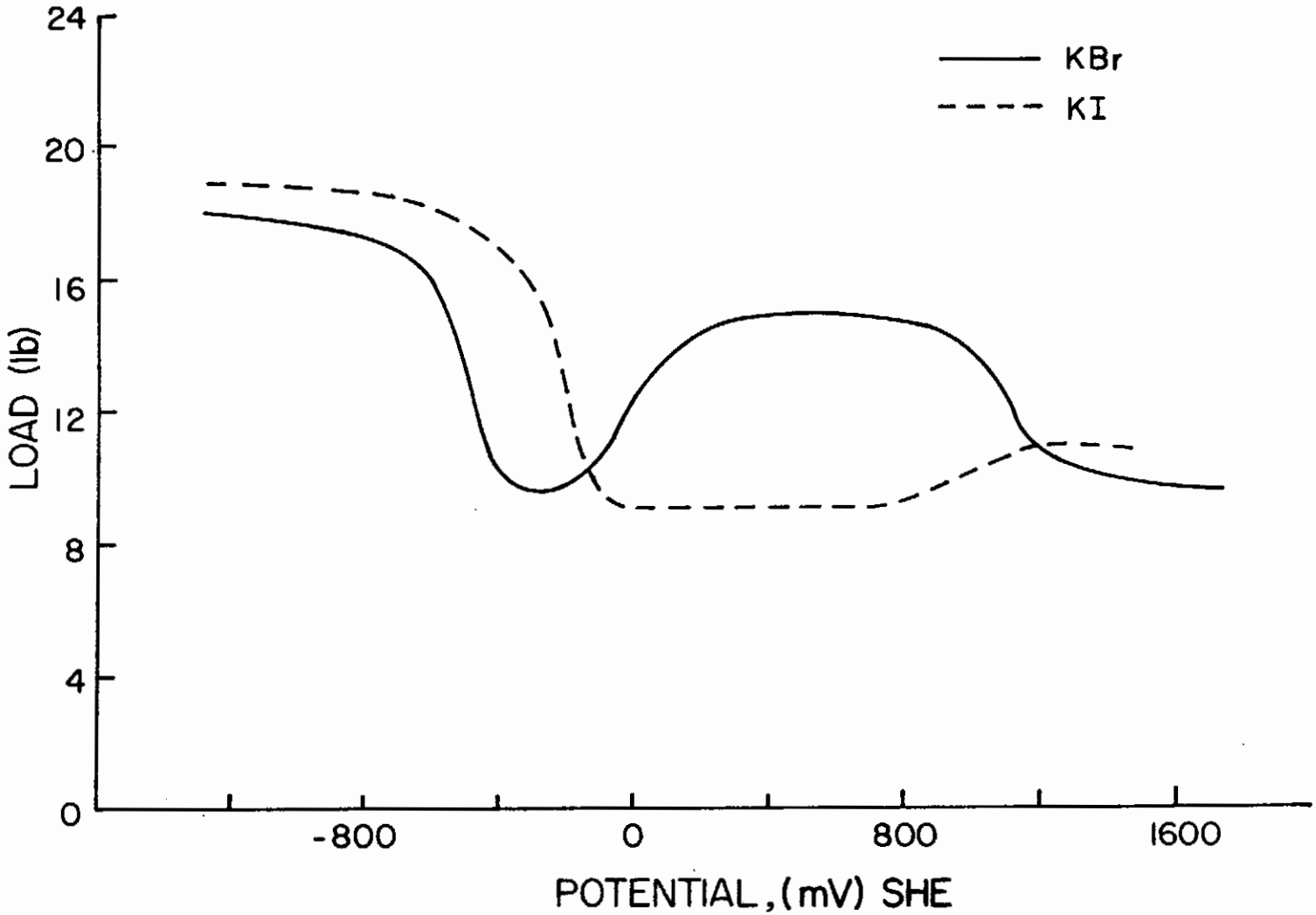

Fig. 11 - Fracture Load vs. Potential (Bend Specimens) (Ti-8Al-1Mo-1V in 0.6M KBr and 0.6M KI Solutions)

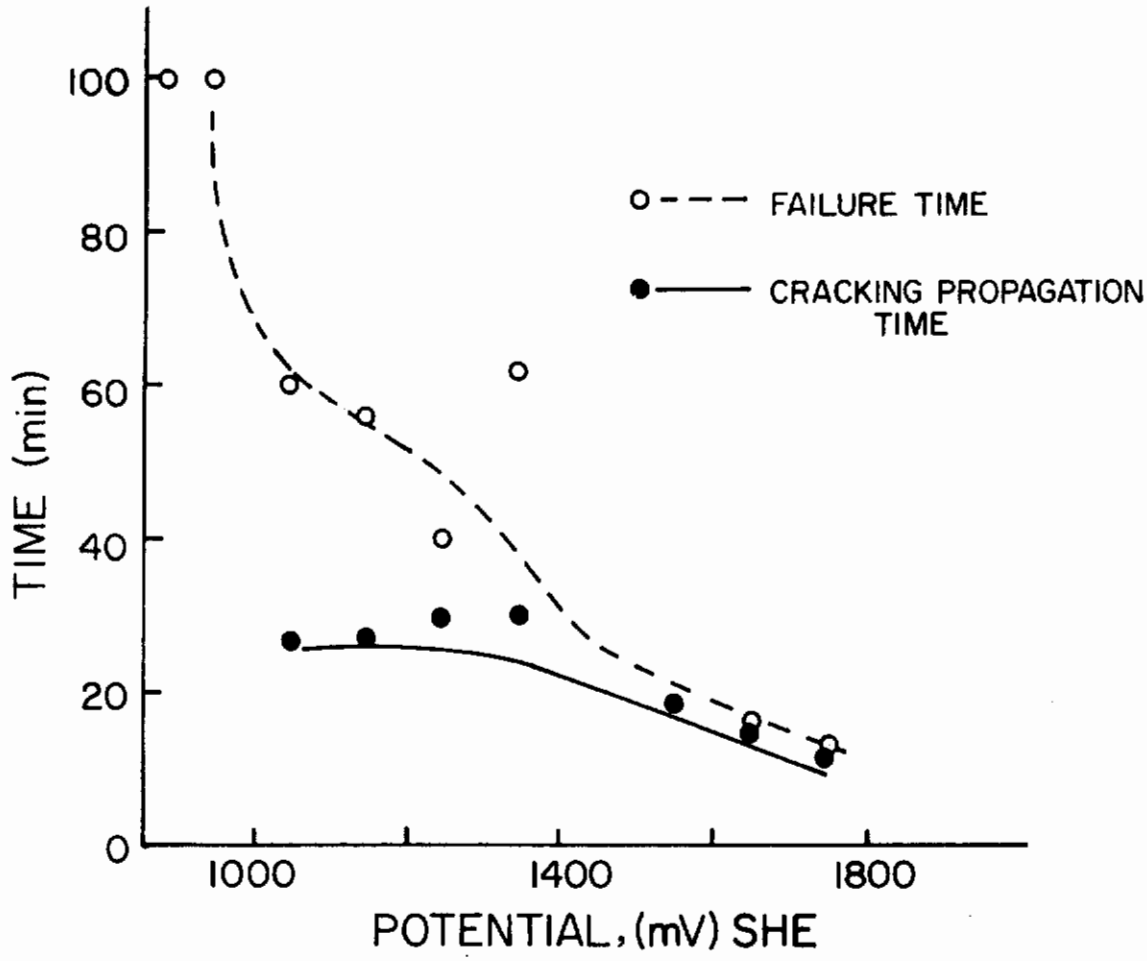

Fig. 12 - Effect of Polarization Potential on Failure Time and Crack Propagation Time for Ti-8Al-1Mo-1V in 0.6M KBr Solution (Notched tensile specimens, load = 80.5 lb, $K_1 = 7.15\sqrt{in.}$)

the crack apex and, therefore, halogen ion attack will cause susceptibility. At the corrosion potential some oxidizing agent such as oxygen is required for stress corrosion cracking susceptibility. If some electrochemical reaction occurs prior to pitting attack, halogen ion attack is not possible at the crack apex as for example in a potassium iodide solution and there will be no susceptibility to cracking in this case.

B. EFFECTS OF STRAIN RATE, WATER CONTENT, AND POLARIZATION POTENTIAL ON THE SUSCEPTIBILITY OF Ti-6Al-4V ALLOY TO STRESS-CORROSION CRACKING BY METHANOL-0.166% HYDROCHLORIC ACID-WATER SOLUTIONS (C. M. Chen)

1. Introduction

Research on the stress-corrosion cracking of Ti-8Al-1Mo-1V alloy in aqueous and methanolic environments emphasized that susceptibility was highly dependent on polarization potential. The research described here includes studies on Ti-6Al-4V alloy in methanol + hydrochloric acid + water solutions. In addition, considerable data were obtained through the use of straining electrodes and the direct observation of crack initiation and propagation.

2. Experimental

Smooth tensile and bend specimens of the dimensions given in Fig. 13 were prepared from rolled Ti-6Al-4V sheet material of composition No. 2, Table I. Specimens were oriented with the long axis either parallel or perpendicular to the rolling direction. The material was used in the annealed condition. Tensile specimens were placed in the test cell illustrated in Fig. 14 and were strained during testing with an Instron machine at strain rates ranging from 0.005 to 0.5 cm/min. Bend specimens were restrained in short lengths of one-inch diameter glass tubing as shown in Fig. 15. Electrical contact to the tensile specimen was made through the specimen grip, while contact with the bend specimen was made by spot welding an insulated wire to one leg of the specimen. Cylindrical platinum counter electrodes surrounded the specimens and Luggin probes were placed in the cells as illustrated. A zooming stereo microscope was used in conjunction with a closed circuit TV camera to observe crack propagation on the bend specimen.

All specimens were polished through 600-grit emery, degreased in acetone, and rinsed in distilled water prior to being placed in the test solution (absolute methanol containing 0.166% hydrochloric acid and from 0.28 to 1.31% distilled water as desired). The external electrical connections were then made through a potentiostat and the test was started.

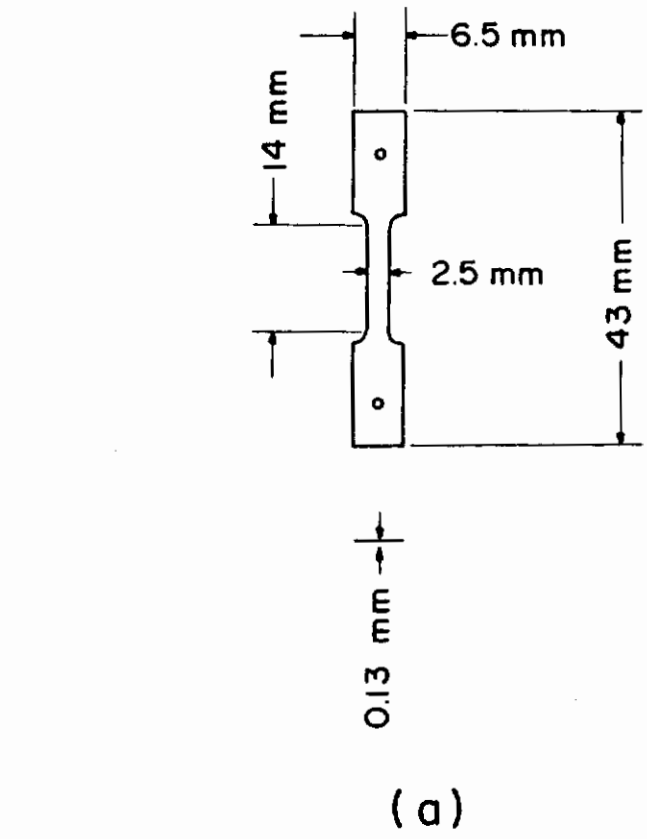

(a)

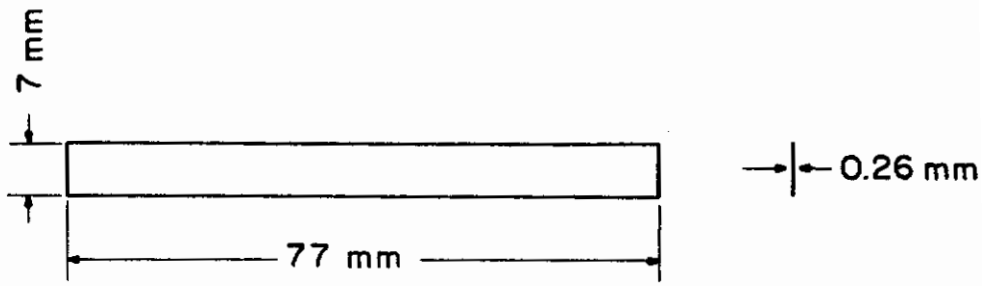

(b)

Fig. 13 - Specimen Configuration: (a) Tensile Specimen for Straining Electrode Tests; (b) Bend Specimen for Static Tests

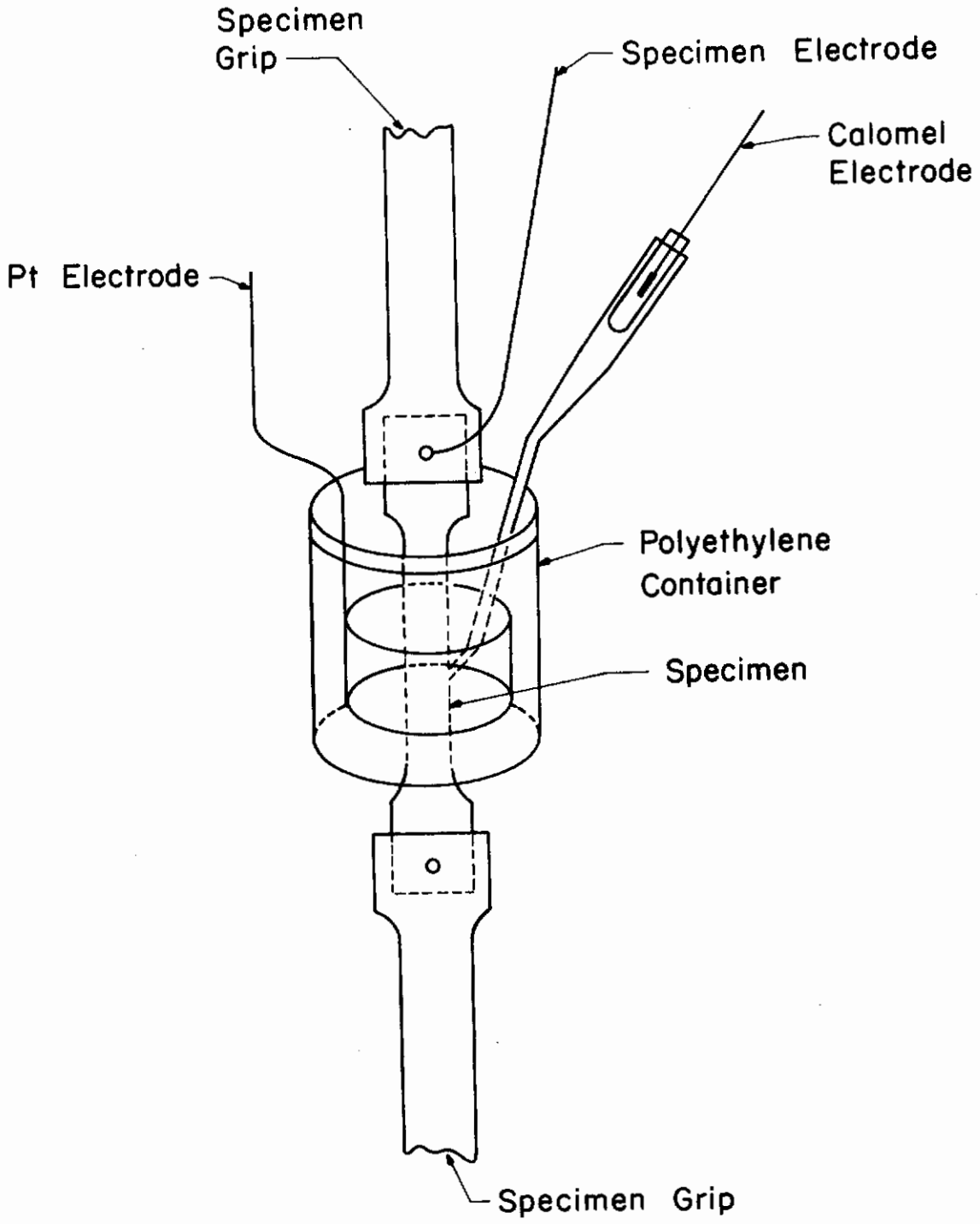

Fig. 14 - Cell for Straining Electrode Tests

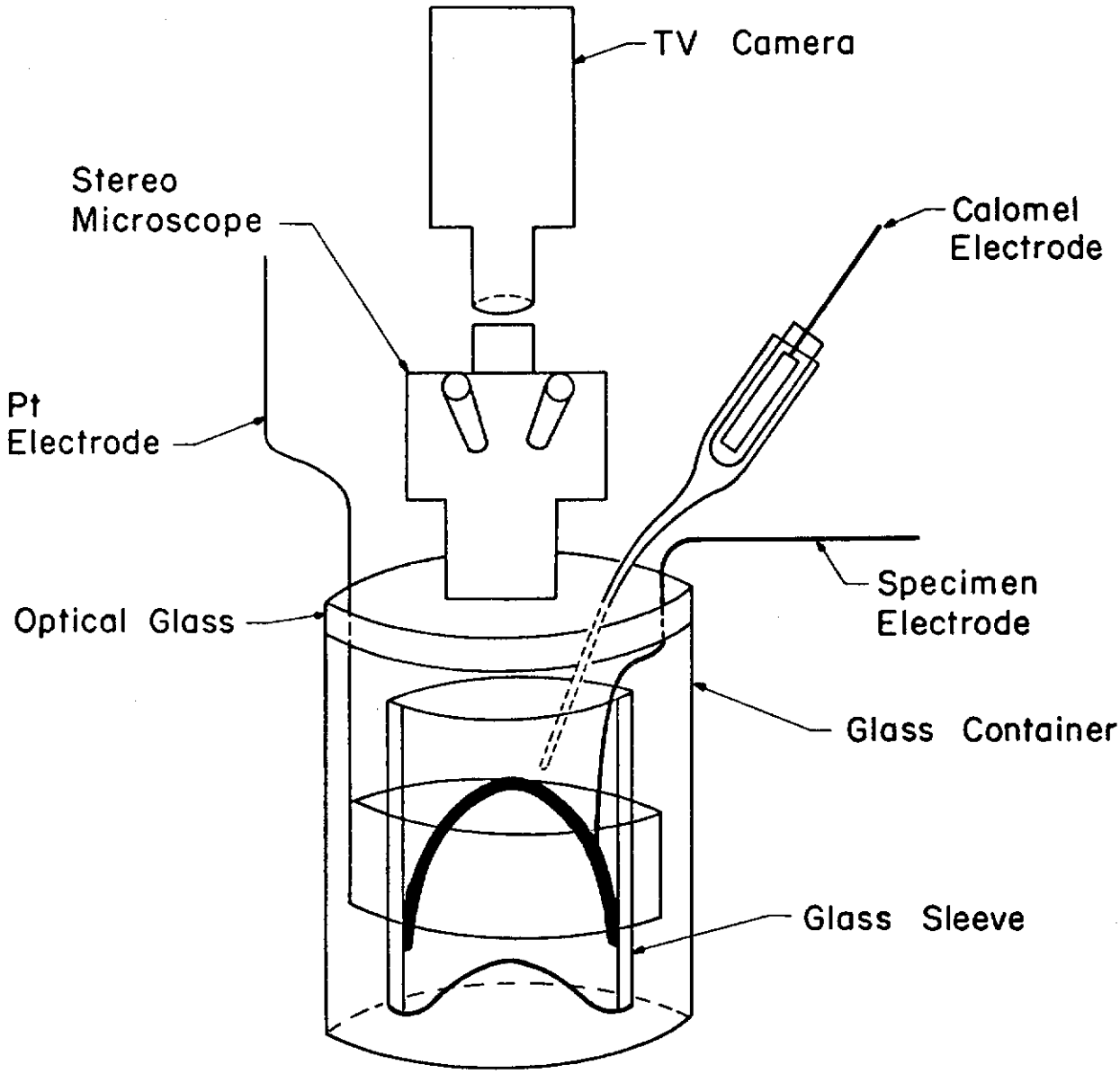

Fig. 15 - Cell for Stress Corrosion Bend Tests

3. Results

a. Effect of Water Content on Elongation of Specimens at Corrosion Potential (strain rate = 0.005 cm/min)

The effect of water concentration in CH_3OH-0.166HCl-H_2O solutions on the elongation of Ti-6Al-4V specimens in which the tensile axis is parallel and perpendicular to the rolling direction is shown in Figs. 16 and 17, respectively. In "pure" methanol solution the specimens with the rolling direction oriented parallel to the tensile axis have an elongation of about 6.4% compared to about 7% in air. This value is reduced to about 3.5 to 4.5% when the CH_3OH-HCl environment contains water in the range of about 0.2 to 0.7%. The elongation increases rapidly to more than 6% when the water is increased from 0.7 to 0.8% as shown in Fig. 16.

Specimens with the rolling direction oriented perpendicular to the tensile axis show the same tendency as for the parallel orientation described above. The curve for the perpendicular orientation is shifted to lower values; i.e., about 3.9% in "pure" methanol, 5% in air, less than 3% in the critical water range (0.2 to 0.7% water), and 4 to 5% at water concentrations of 0.8% and greater. All specimens were strained at a rate of 0.005 cm/min.

b. Effect of Water and Polarization Potential on Elongation

Figure 18 shows that when cathodic polarization is applied to specimens tested in CH_3OH-HCl solutions containing 0.28 to 0.99% H_2O, the elongation is about 7%. Under anodic polarization, the elongation is reduced to about 3.5% when the solution contains 0.7% and less water. The transient potential at which the elongation changes from the higher to the lower value is a function of the water content, as illustrated in Fig. 19 in the low-water-content range (approx. 0.2-0.7%) the transient potentials are located in the corrosion potential range (shaded zone of Fig. 19). The transient potentials are more anodic than the corrosion potential for solutions containing water in excess of 0.7%.

The above data are for specimens having the tensile axis oriented parallel to the rolling direction and tested at a strain rate of 0.005 cm/min.

c. Effect of Water Content on Corrosion Potential of Strained and Nonstrained Electrodes

The effect of water content on the corrosion potential in the absence of an applied strain is shown in Fig. 20-a (readings were taken after the specimens were exposed to the test solution for four minutes). The corrosion potential increases rapidly and linearly in

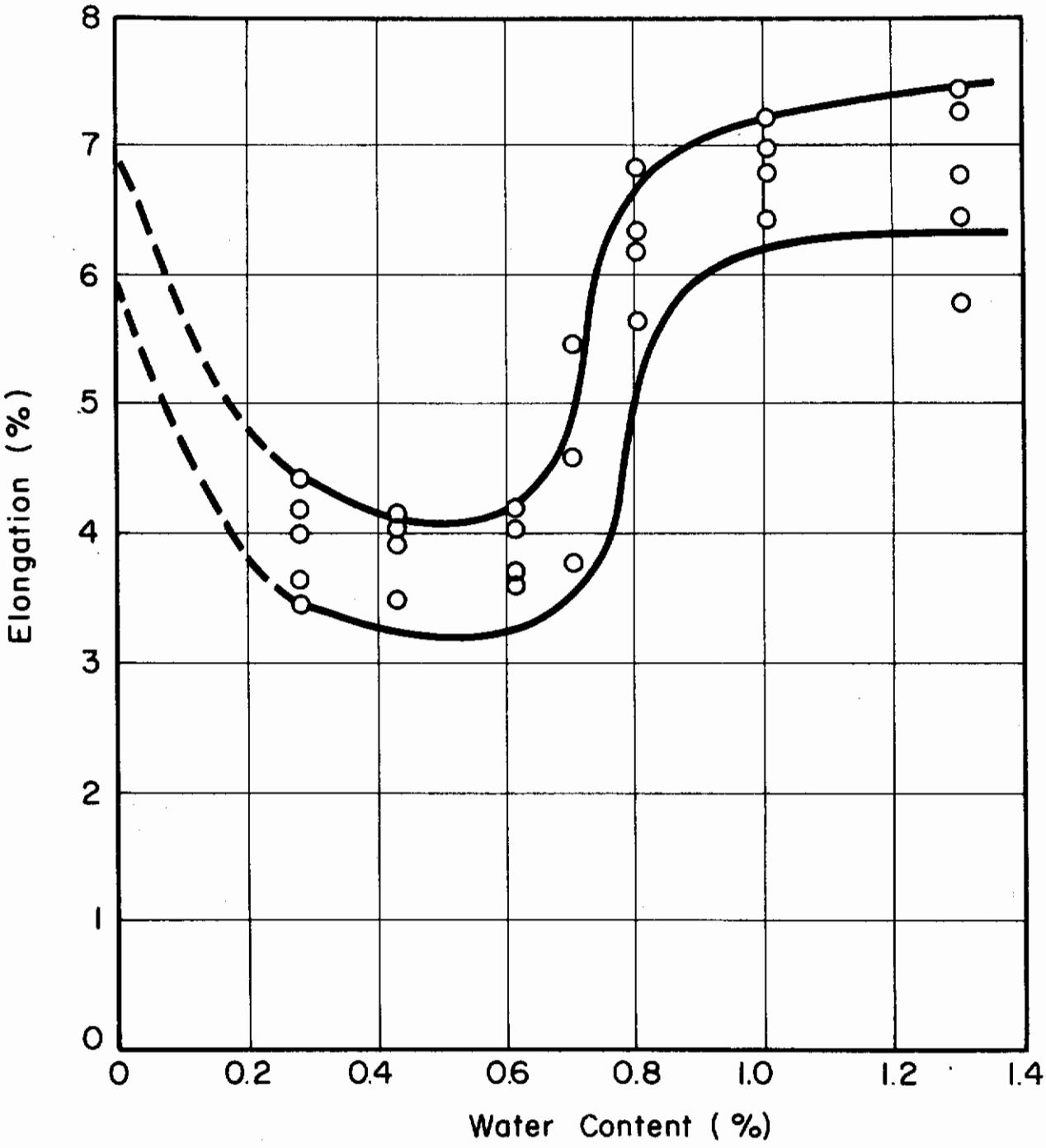

Fig. 16 - Elongation vs. Water Content. CH_3OH + 0.166% HCl + H_2O (Tensile direction parallel to rolling direction; strain rate 0.005 cm/min)

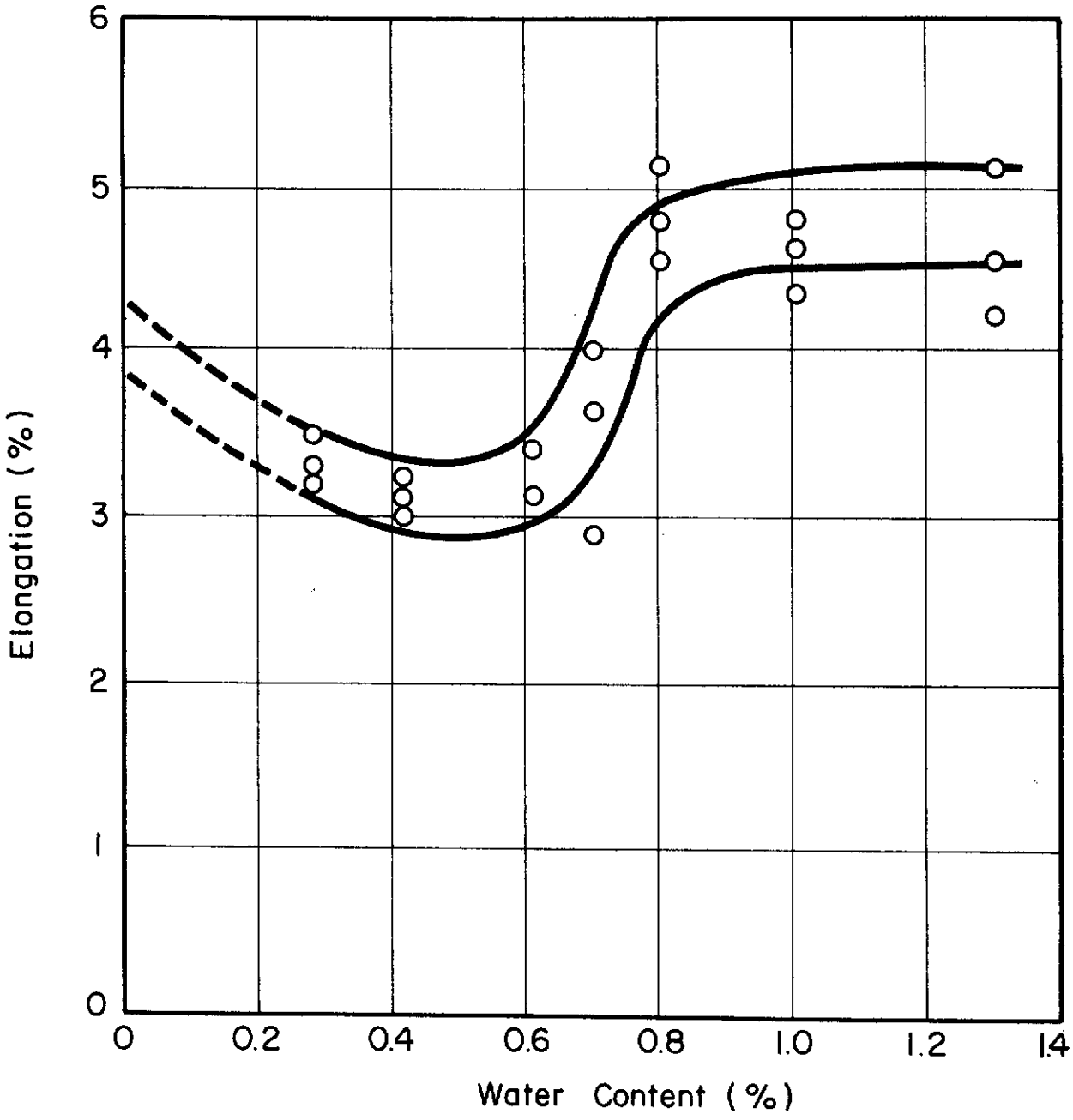

Fig. 17 - Elongation vs. Water Content. CH_3OH + 0.166% HCl + H_2O (Tensile direction perpendicular to rolling direction; strain rate = 0.005 cm/min)

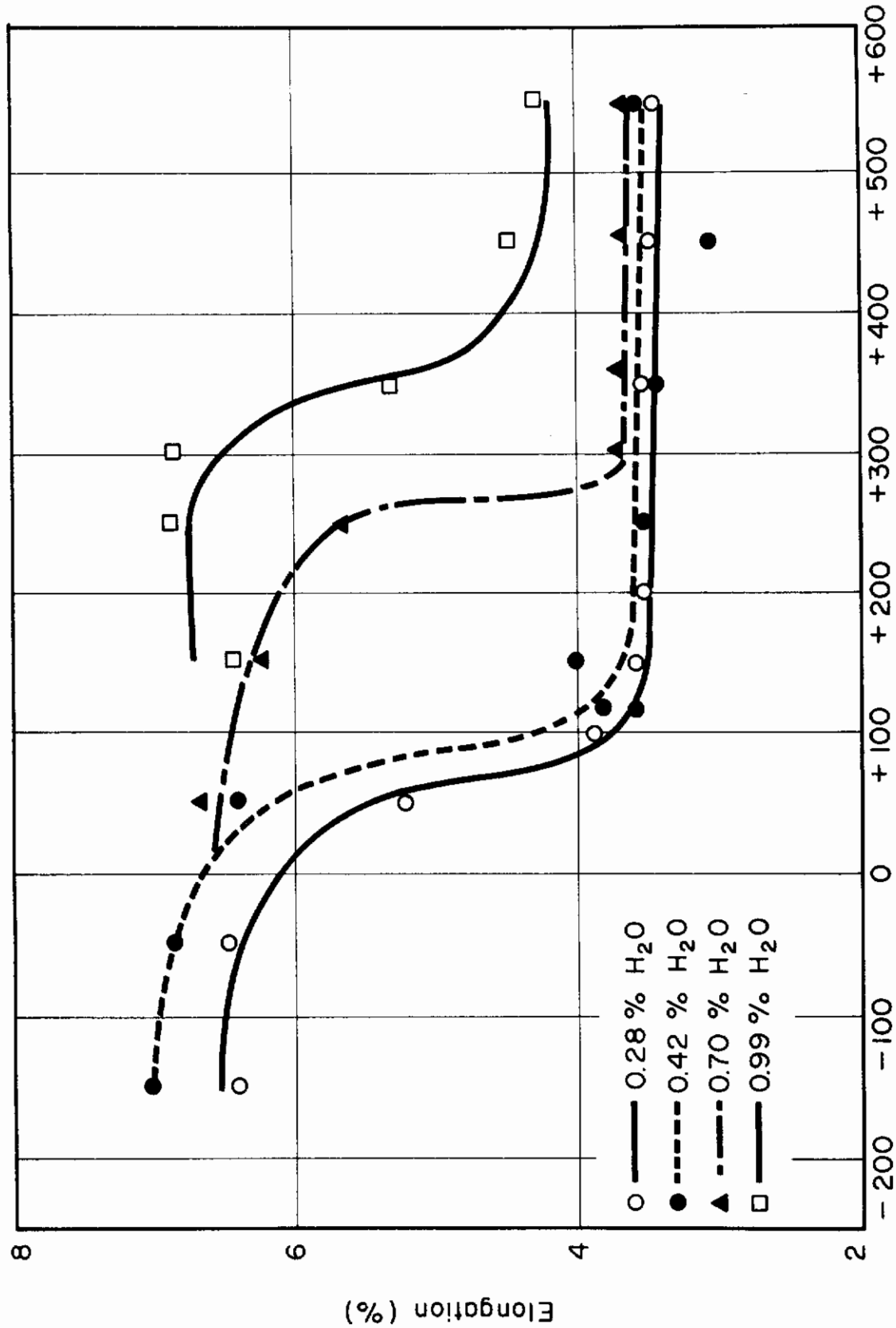

Fig. 18 - Effect of Polarization Potential on Elongation (%)

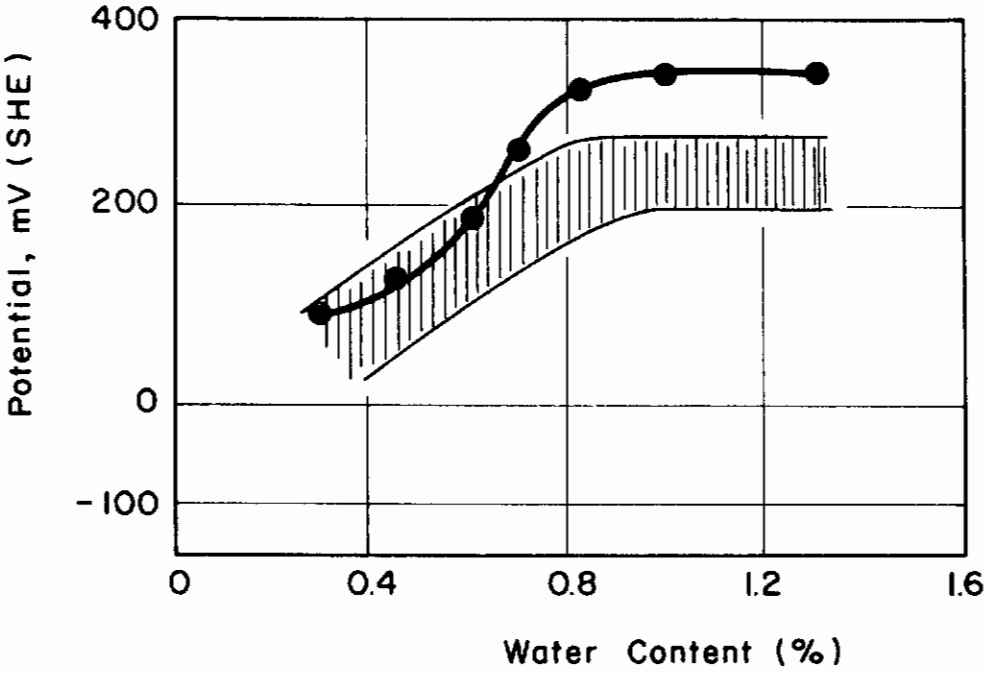

Fig. 19 - Potential vs. Water Content (%)

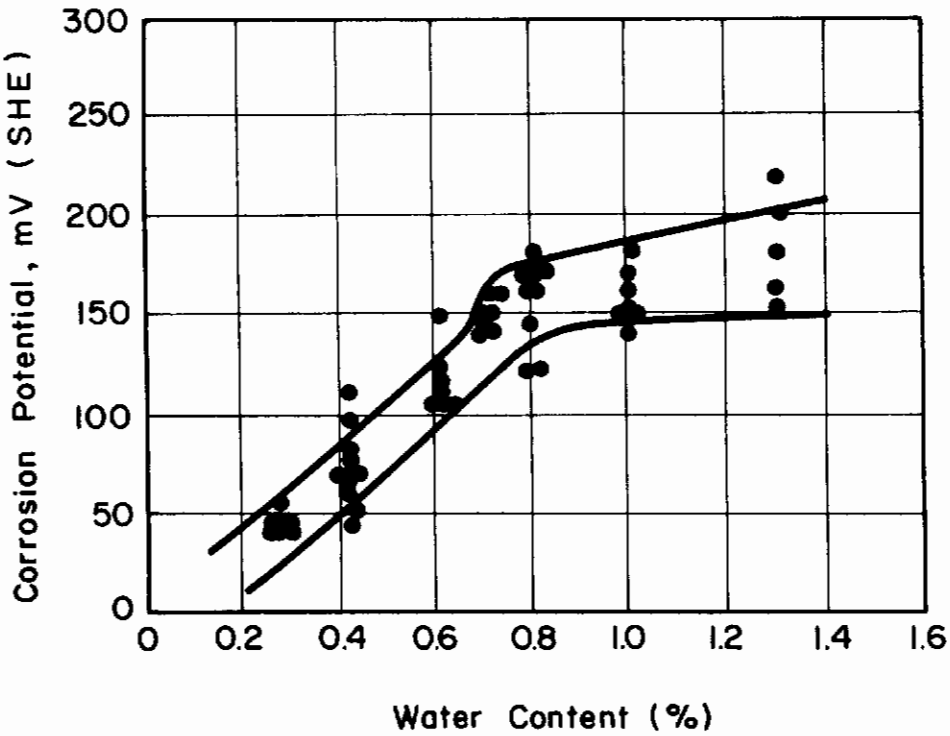

Fig. 20-a - Corrosion Potential vs. Water Content
CH_3OH + 0.166% HCl + H_2O (no applied load)

the anodic direction with water content in the range of about 0.2-0.8%. At 0.8% water and above there is little effect of water on the corrosion potential.

When specimens are strained in solutions containing 0.8% water or less, the corrosion potential increases in the anodic direction when the specimen is going to fail as shown in Fig. 20-b. The corrosion potential then decreases rapidly in the cathodic direction. At water concentrations in excess of 0.8% the corrosion potential was observed to shift gradually in the cathodic direction when the strain was near the yield and finally a rapid cathodic shift was observed at failure. A strain rate of 0.005 cm/min was used.

d. Effect of Water Content on Polarization

Figure 21 shows that water content has little effect on cathodic polarization; however, water has a great effect on the potential at which a rapid anodic current increase is observed; that is, the higher the water content, the more anodic the potential for chloride ion attack.

e. Metallographic Observations

Under anodic polarization, crack formation takes place by a pitting mechanism. In the case of Ti-6Al-4V U-bend specimens in CH_3OH-0.166% HCl-1%H_2O, pits are observed to form at potentials of about +300 mV(SHE), or higher, the number of pits increasing rapidly with potential. Under microscopic observation, cracks are seen to originate at the pits and grow laterally, perpendicular to the direction of tensile stress. Timmer[10] reported that in the case of Ti-6Al-4V alloy in CH_3OH-H_2O-NaCl solutions, the pits originate by selective attack of β grains and along the α-β interface. He also reported observing, by light microscopy, black corrosion product in the pits, and the present author has also observed such material both in the pits and on the fracture surfaces. The corrosion product was identified by electron diffraction as $TiCl_3$.

f. Effect of Strain Rate on Current and Elongation

Figure 22 shows the effect of strain rate on current vs. time for Ti-6Al-4V tested in Ch_3OH + 0.166% HCl + 0.42% H_2O solution at the anodic potential of +350 mV. As the strain rate was increased from 0.005 to 0.5 cm/min, the current increased at a more rapid rate. However, when the current is plotted against strain for the different strain rates, it is observed that the higher rates cause a more gradual increase in current, as illustrated in Fig. 23. Figure 24, elongation vs. strain rate, shows an elongation of about 6% at high strain rates (greater than about 0.03 cm/min) and an elongation of about 3.7% at low strain rates (0.005 cm/min).

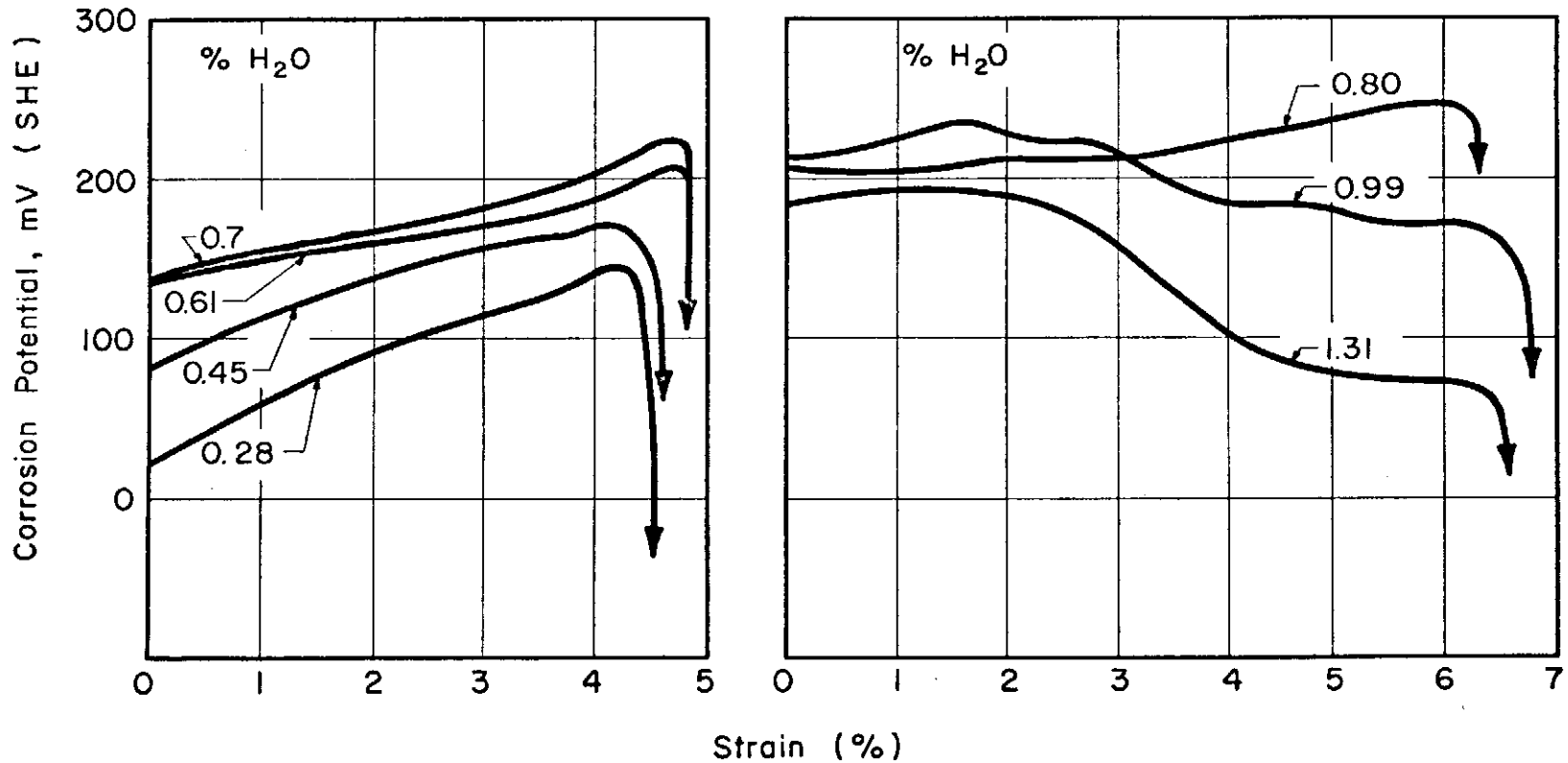

Fig. 20-b - Corrosion Potential vs. Elongation in CH_3OH + 0.166% HCl + H_2O

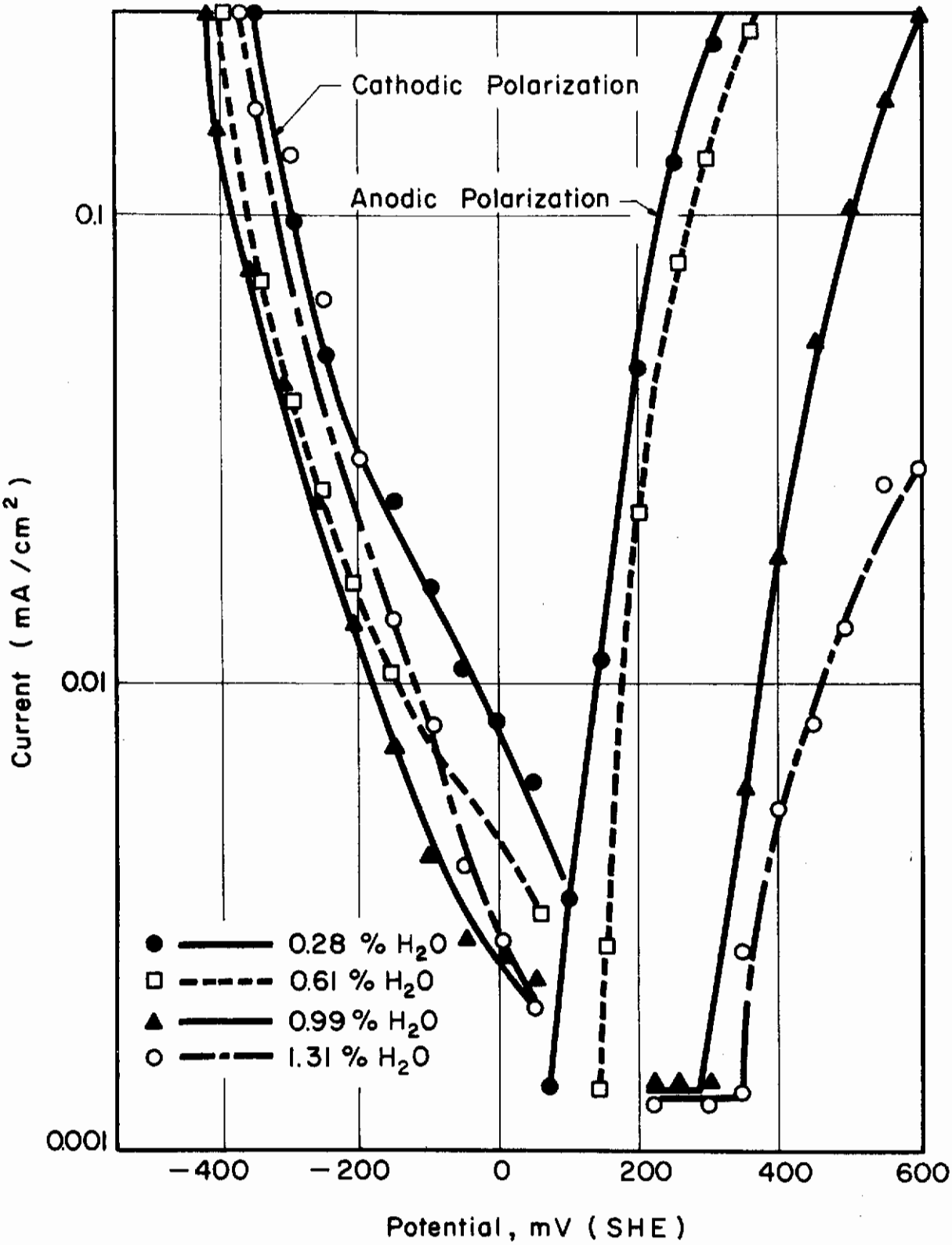

Fig. 21 - Effect of Water Content on the Polarization Curves in CH_3OH + 0.166% HCl + H_2O (scanning rate 25 mV/min)

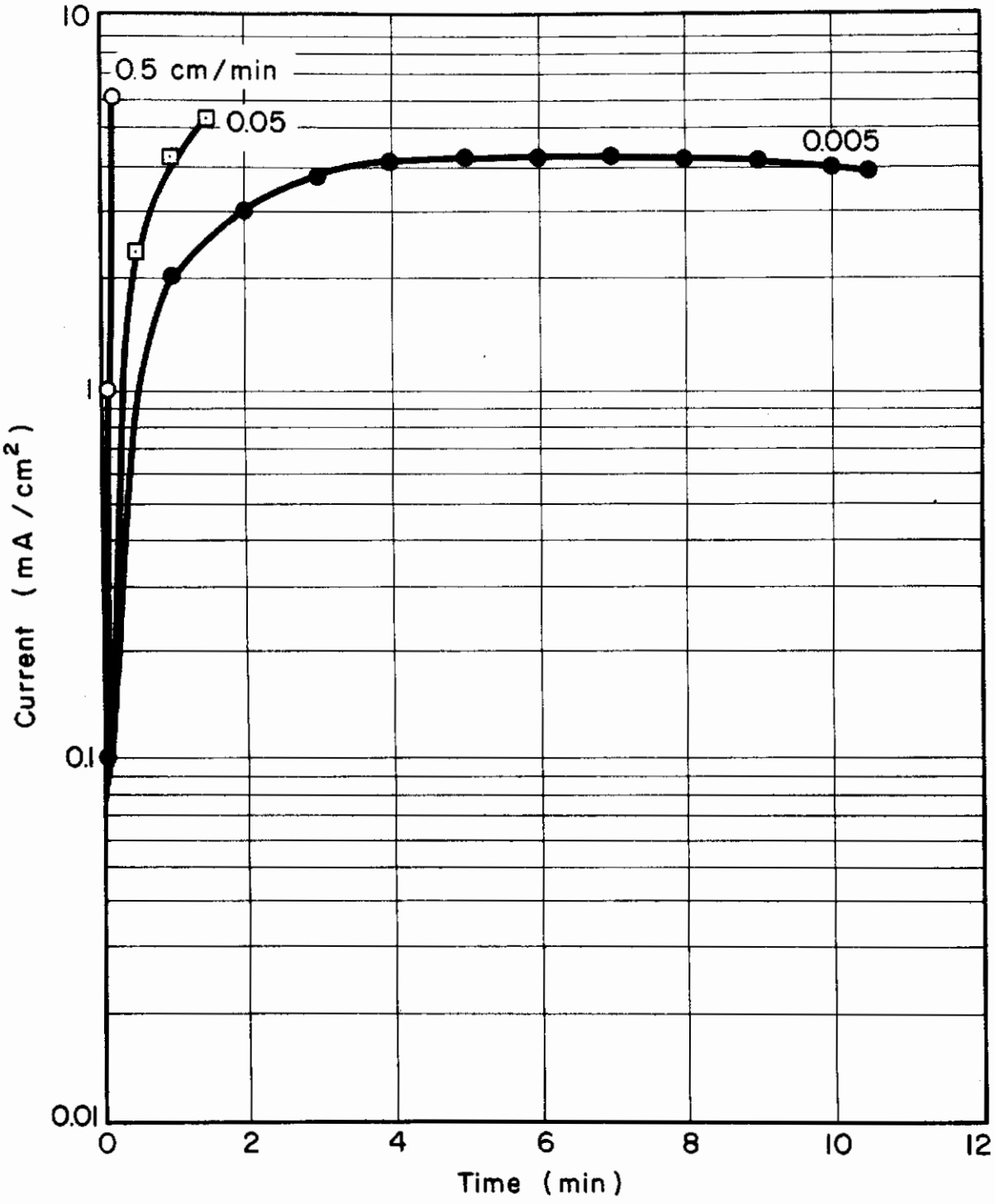

Fig. 22 - Effect of Strain Rate on Current vs. Time in CH_3OH + 0.166% HCl + 0.42% H_2O at +350 mV(SHE)

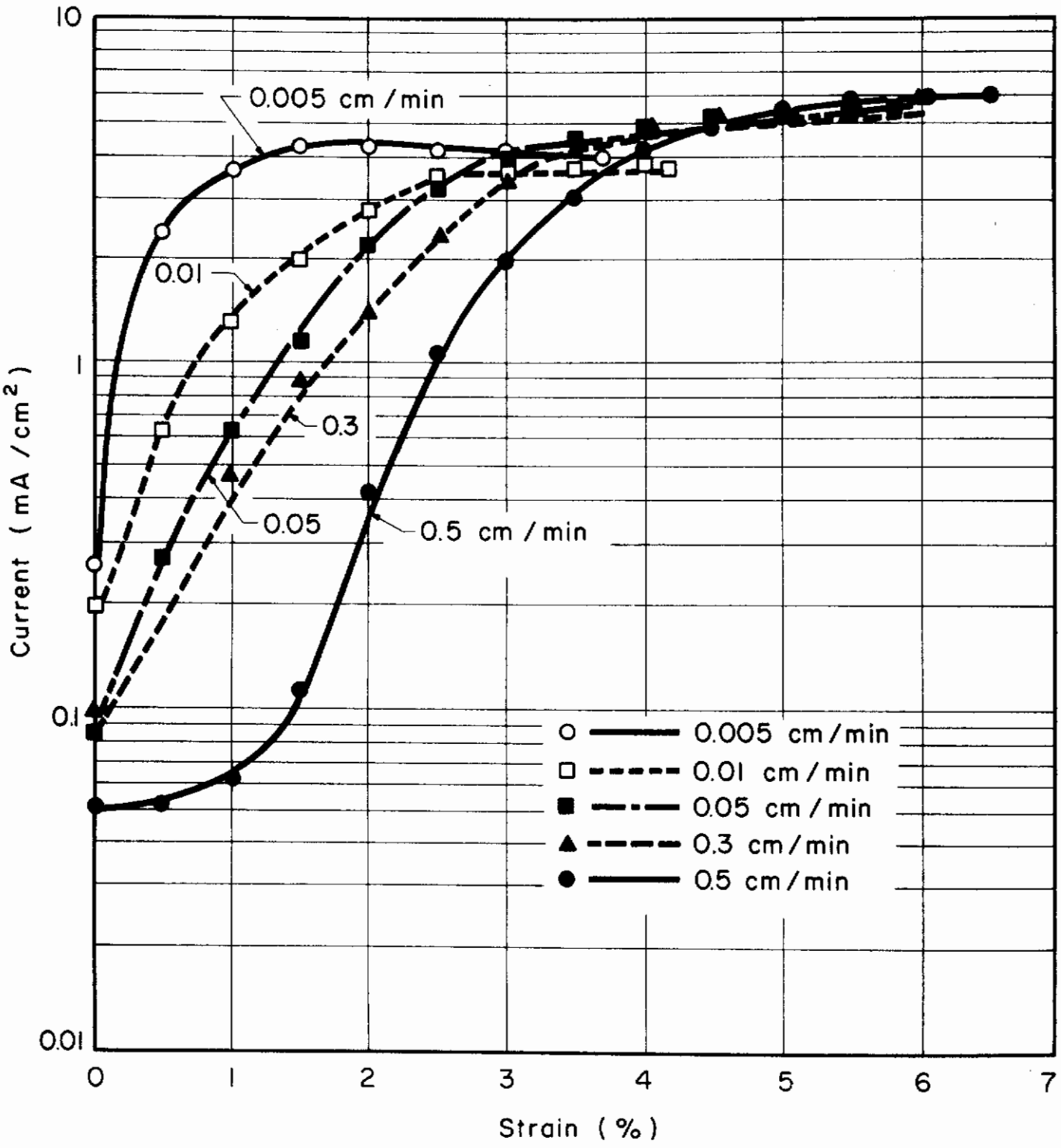

Fig. 23 - Effect of Strain Rate on Current vs. Strain at +350 mV (SHE) in CH_3OH + 0.166% HCl + 0.42% H_2O

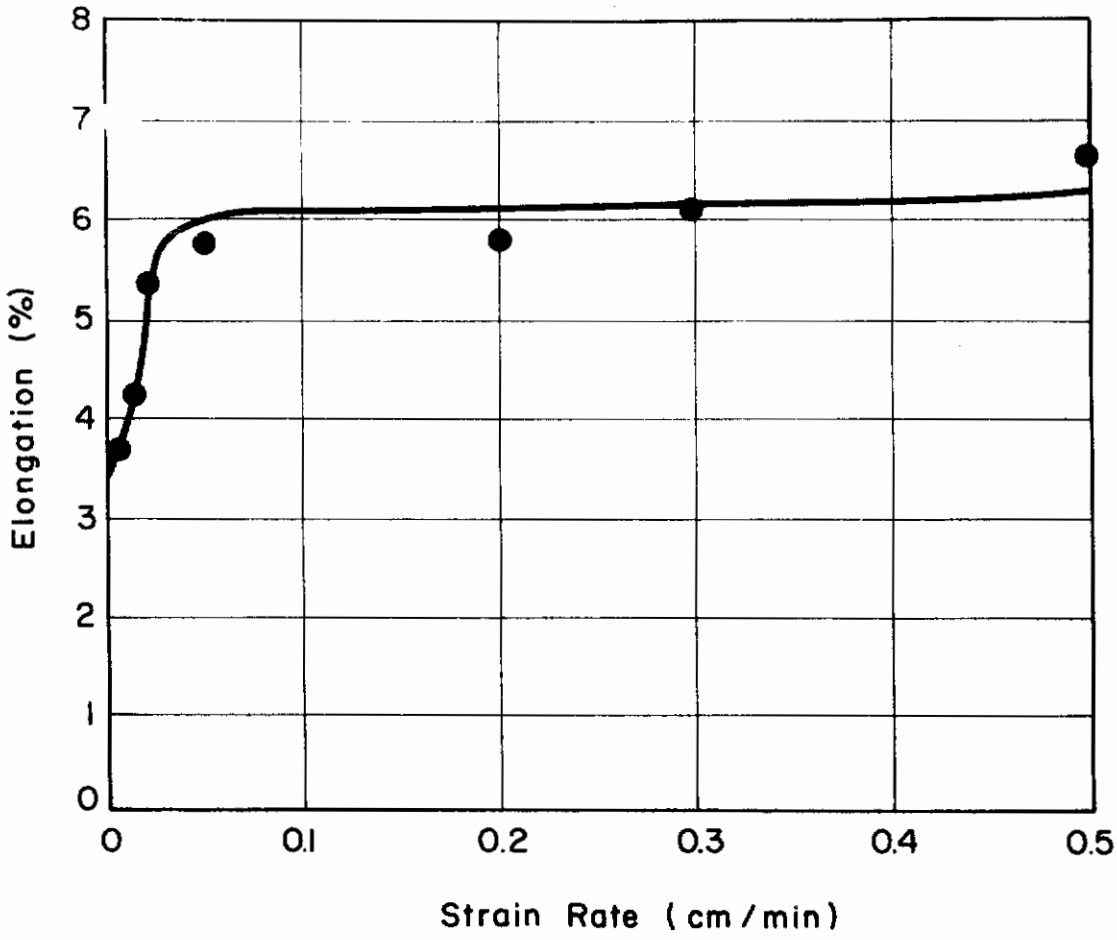

Fig. 24 - Effect of Strain Rate on Specimen Elongation at +350 mV (SHE)

When the specimens are polarized in the anodic region near the corrosion potential (+200 mV) they show the same tendency as described above for the +350 mV tests. Current vs. strain and elongation vs. strain curves are plotted in Figs. 25-a and b, respectively.

When the specimens are polarized in the cathodic region (+50 mV) the behavior is different from the anodically polarized specimens. The higher the strain rate the more rapid the increase of current with time (Fig. 26-a), as was the situation for the anodically polarized specimens; however, the current vs. strain curves in Fig. 26-b show that the current remains almost constant and at a low value until a little more than 3% strain is introduced. Thereafter, the current increases and, the higher the strain rate the more rapidly the current increases with strain. Figure 26-a shows that elongation is constant at about 7% at all strain rates.

Results similar to the above were obtained when the water content of the test solution was increased from 0.42 to 0.8%. The effect of strain rate on current vs. strain is shown in Fig. 27-a, while Fig. 27-b is for elongation vs. strain rate. All specimens were polarized at +550 mV.

g. Effect of Strain Rate on Corrosion Potential

Figures 28-a and b show the effect of strain rate on corrosion potential vs. strain in solutions containing less than 0.8% water. When the strain rate is slow, the corrosion potential increases in the anodic direction; however, at fast strain rates the corrosion potential decreases in the cathodic direction.

At water contents greater than 0.8% the corrosion potential decreases in the cathodic direction regardless of the strain rate as shown in Fig. 28-c. Strain rates in the range 0.005 to 0.5 cm/min were used in the above series of tests.

h. Effect of Water Content on Failure Time of Bend Specimens at Corrosion Potential

Eight specimens were exposed to pure methanol for a period of 200 hours; no failures occurred in this period. In CH_3OH + 0.166% HCl + H_2O solutions the cracking time varies with water content, as illustrated in Fig. 29. Failure times are very short in the range of approximately 0.2 to 0.8% water

i. Effect of Polarization Potential on Failure Time of Bend Specimens

The effect of failure time was determined as a function of polarization potential in CH_3OH + 0.166% HCl + 0.99% H_2O. Results of these experiments are plotted in Fig. 30 which shows short failure times

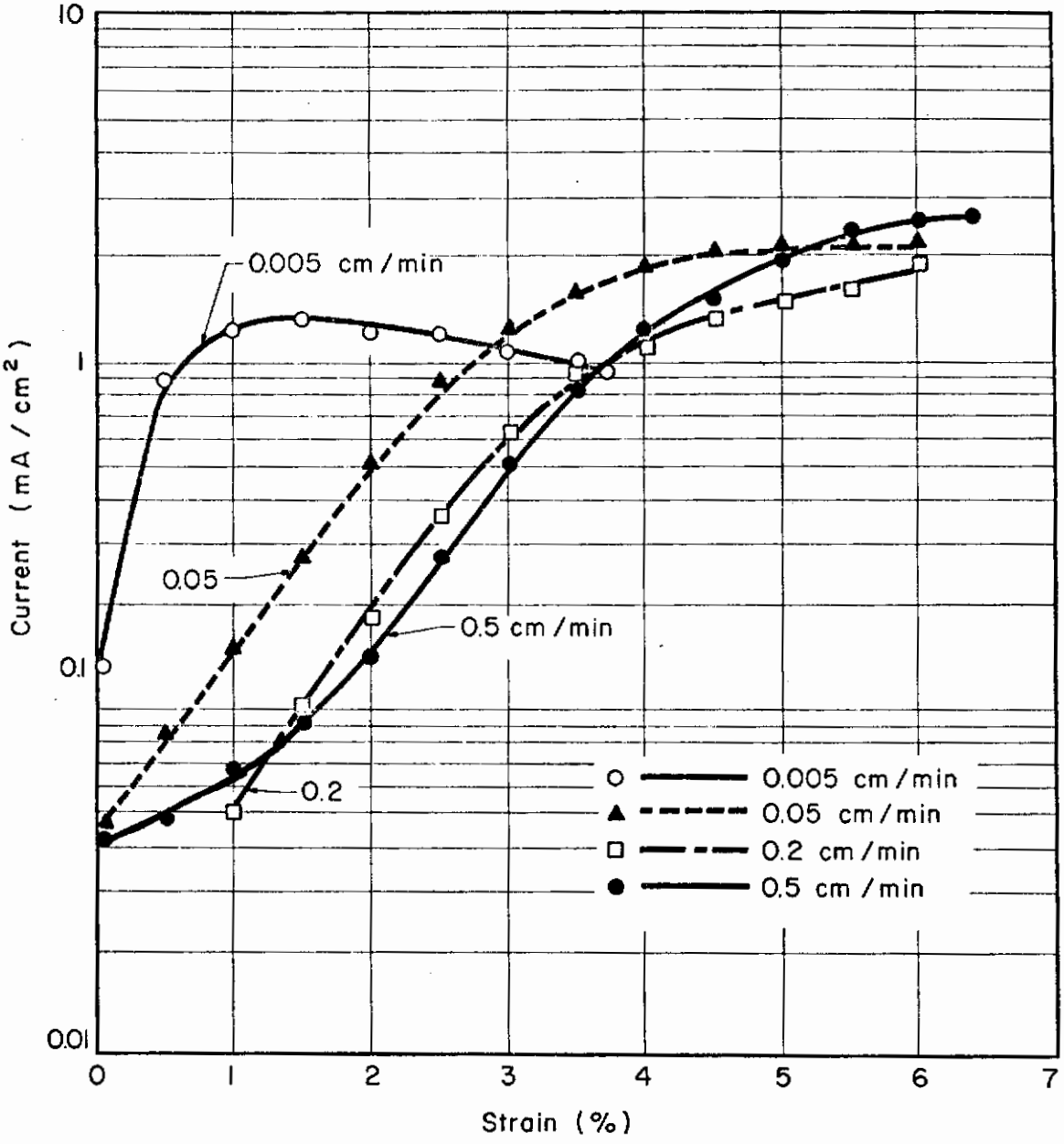

Fig. 25-a - Effect of Strain Rate on Current vs. Strain at +200 mV(SHE) in CH_3OH + 0.166% HCl + 0.42% H_2O

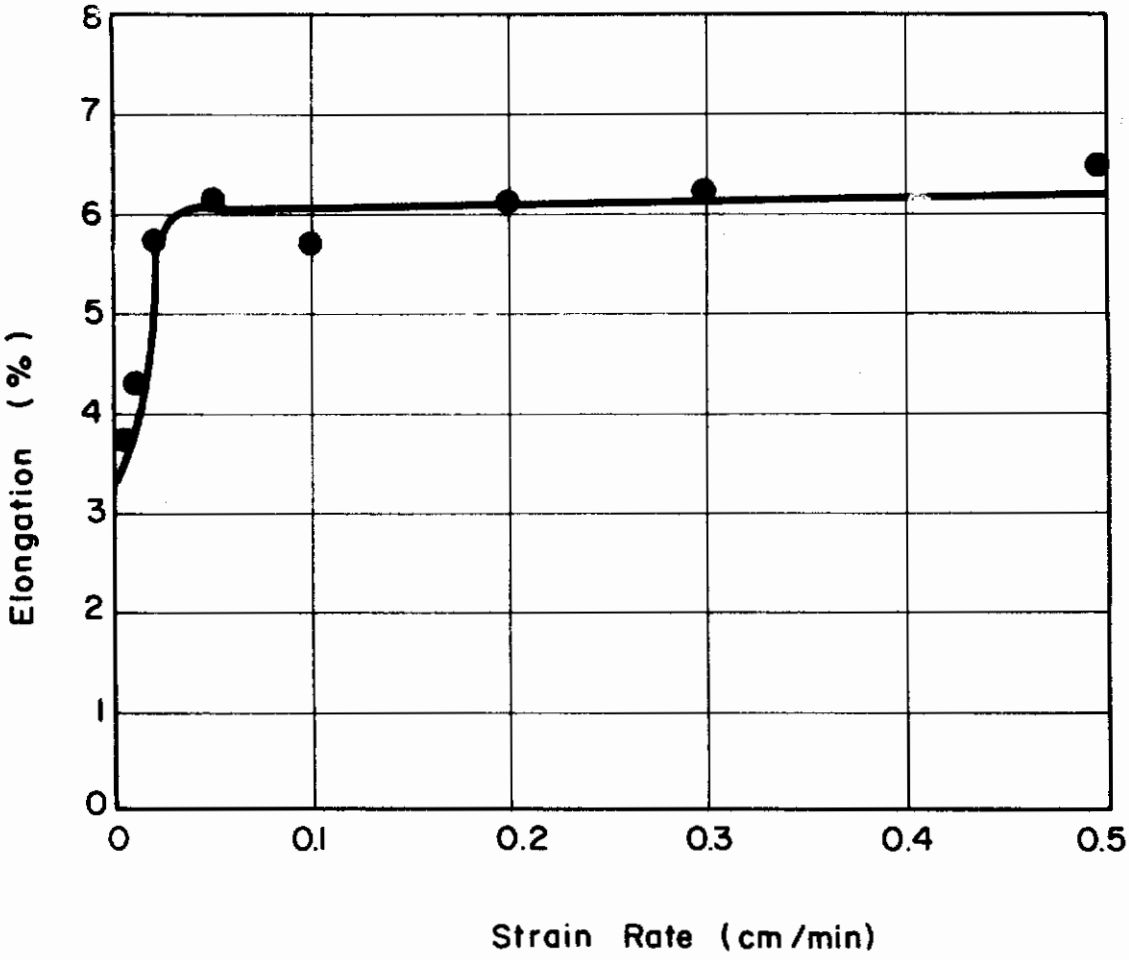

Fig. 25-b - Effect of Strain Rate on Specimen Elongation at +200 mV(SHE) (same environment as Fig. 25-a)

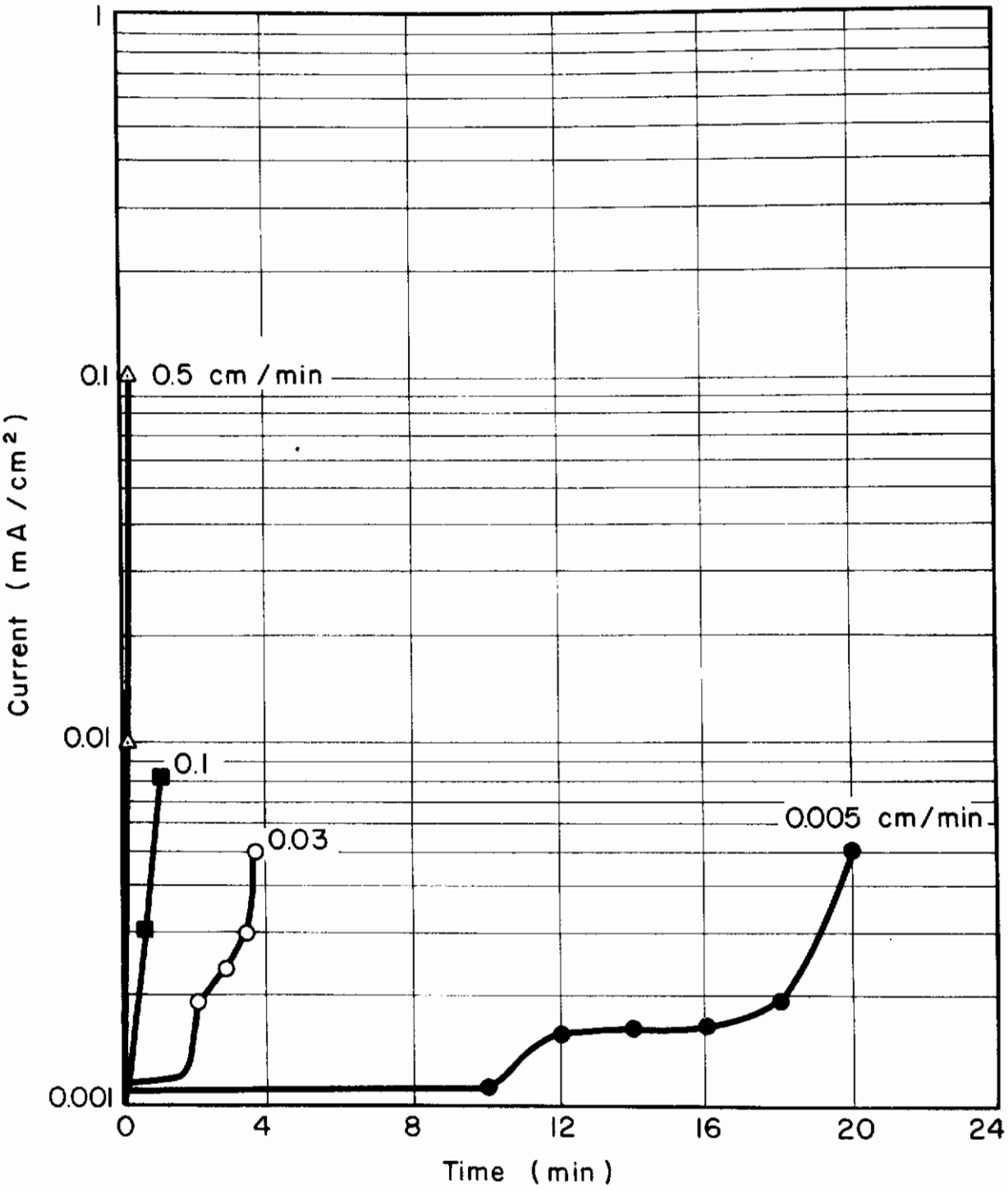

Fig. 26-a - Effect of Strain Rate on Current vs. Time in CH_3OH + 0.166% HCl + 0.42% H_2O at +50 mV(SHE)

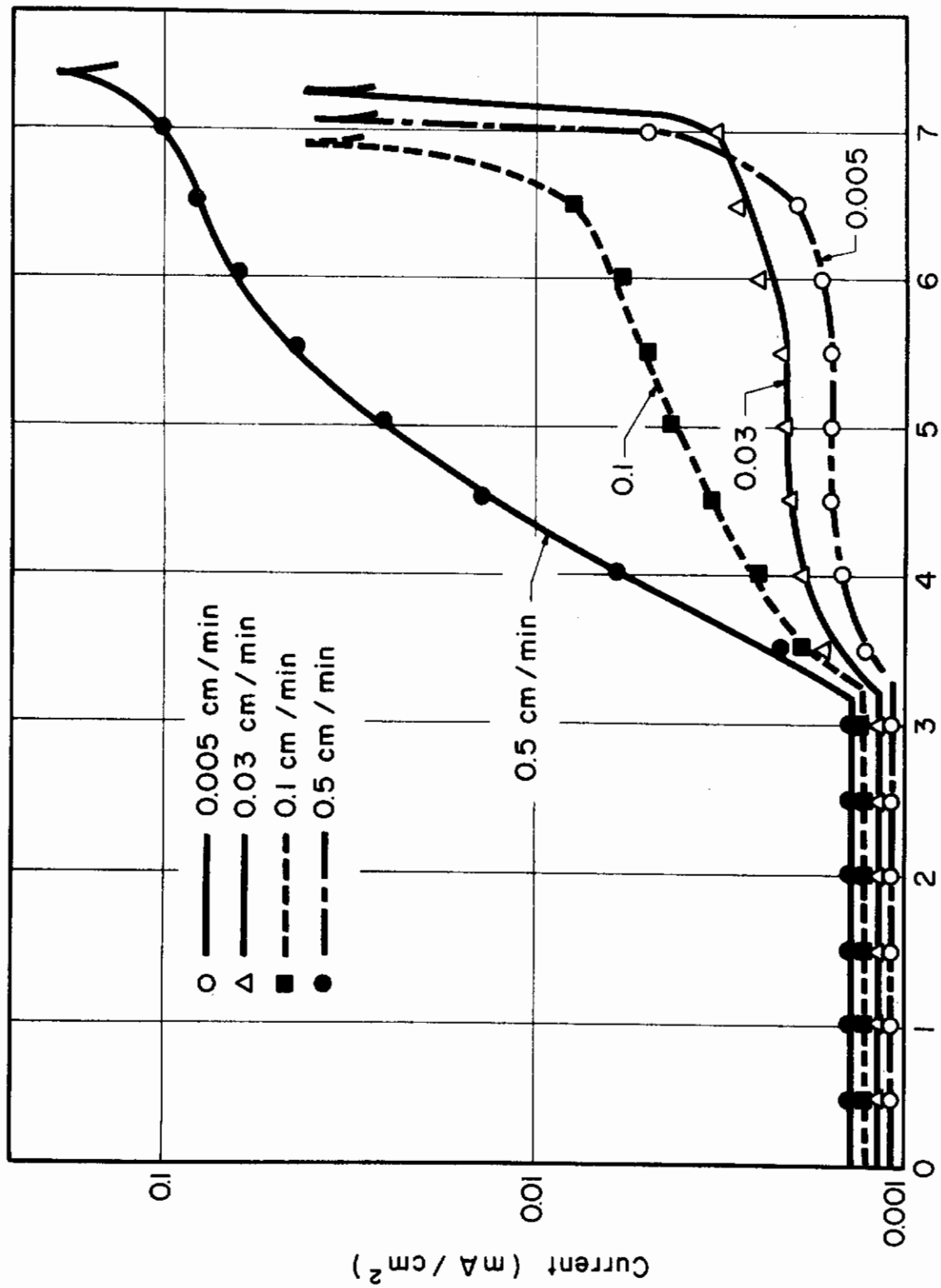

Fig. 26-b - Effect of Strain Rate on Current vs. Strain at +50 mV(SHE) in CH_3OH + 0.166% HCl + 0.42 H_2O

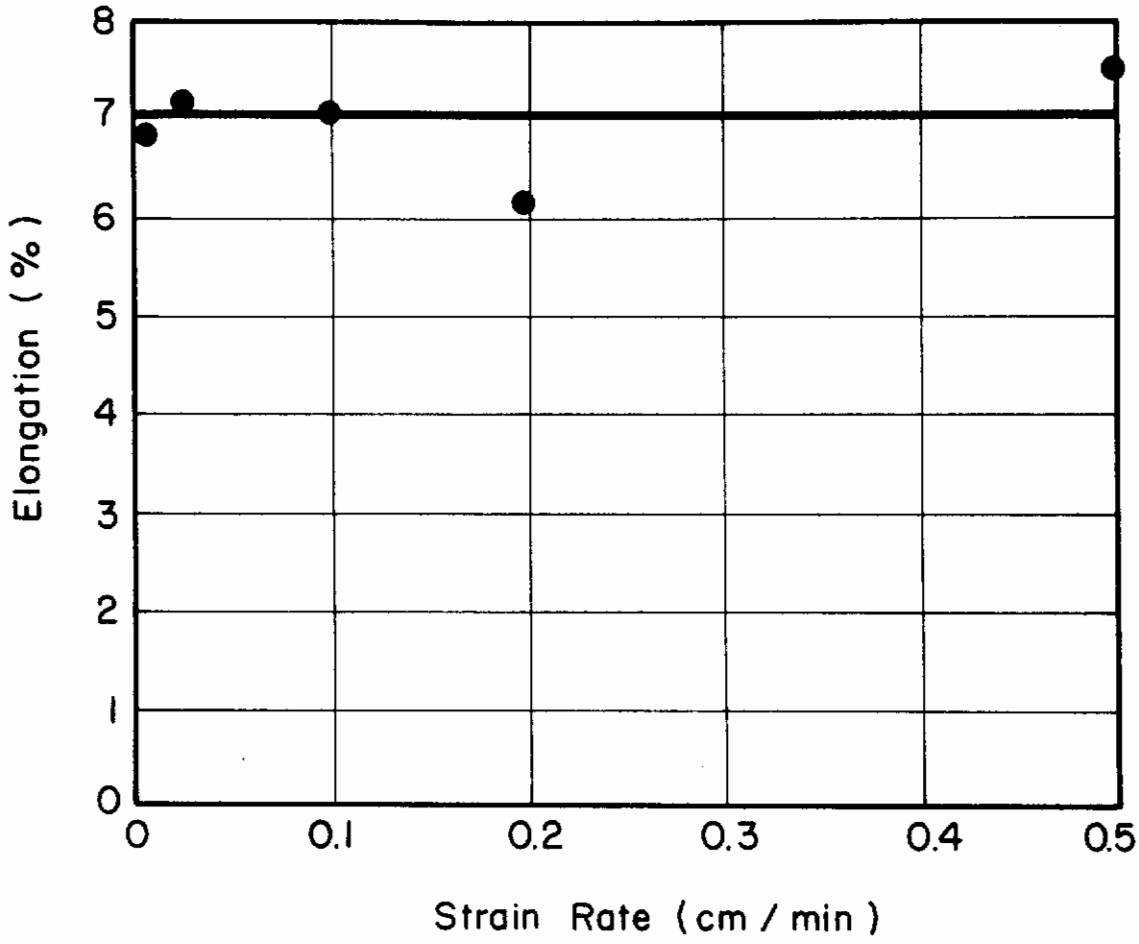

Fig. 26-c - Effect of Strain Rate on Specimen Elongation at +50 mV(SHE)
(same environment as Fig. 26-a and -b)

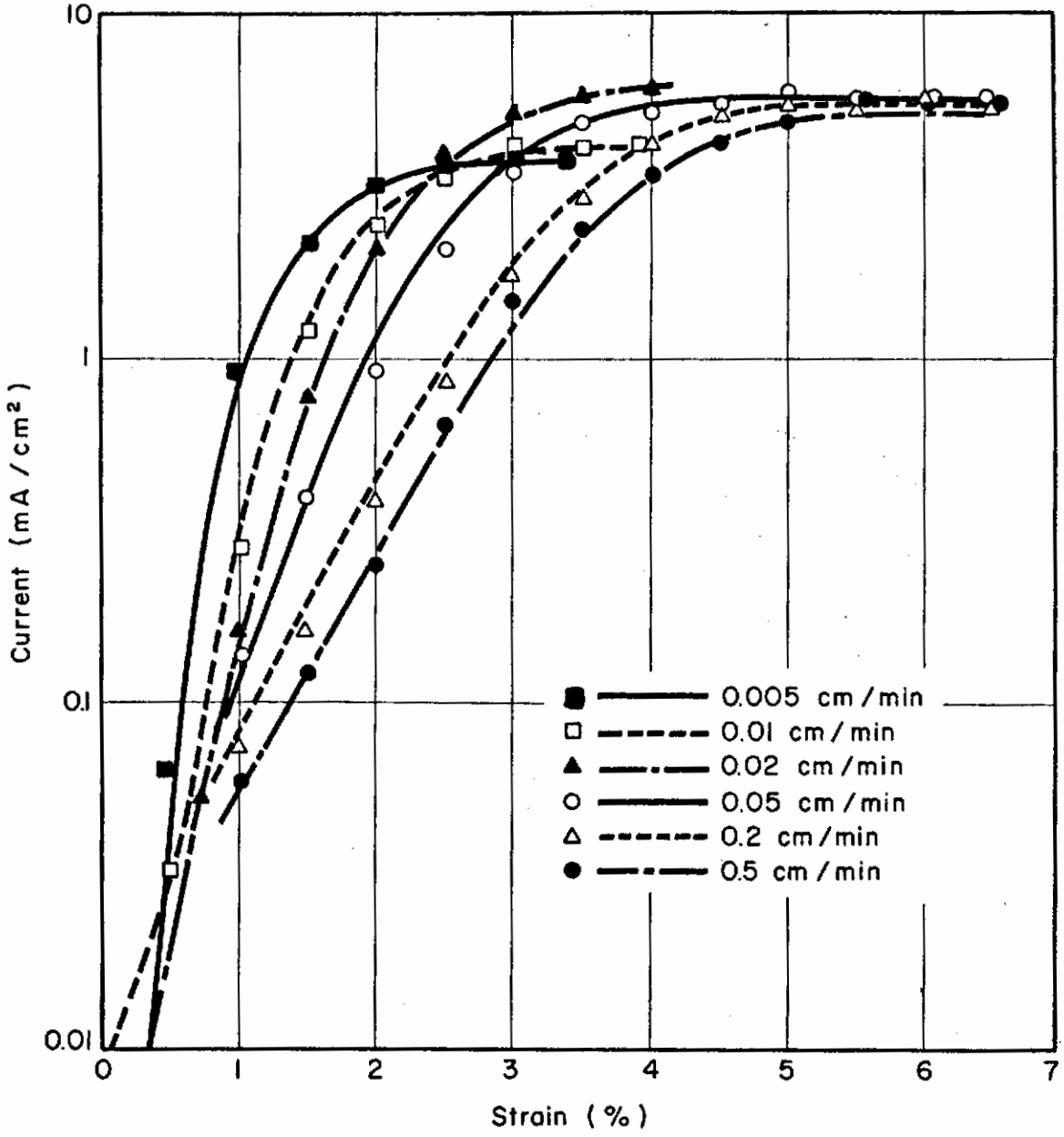

Fig. 27-a - Effect of Strain Rate on Current vs. Strain at +550 mV(SHE) in CH_3OH + 0.166% HCl + 0.80% H_2O

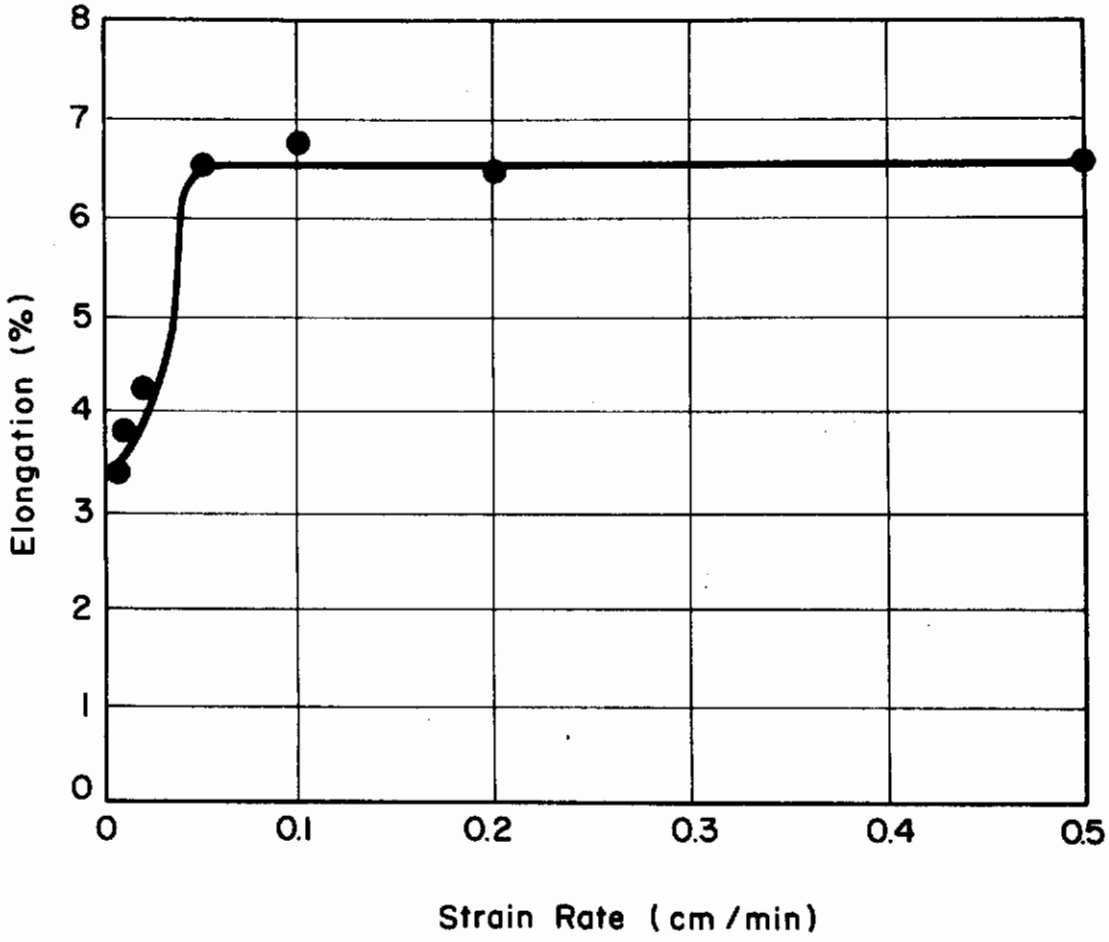

Fig. 27-b - Effect of Strain Rate on Specimen Elongation at +550 mV(SHE) (same environment as Fig. 27-a)

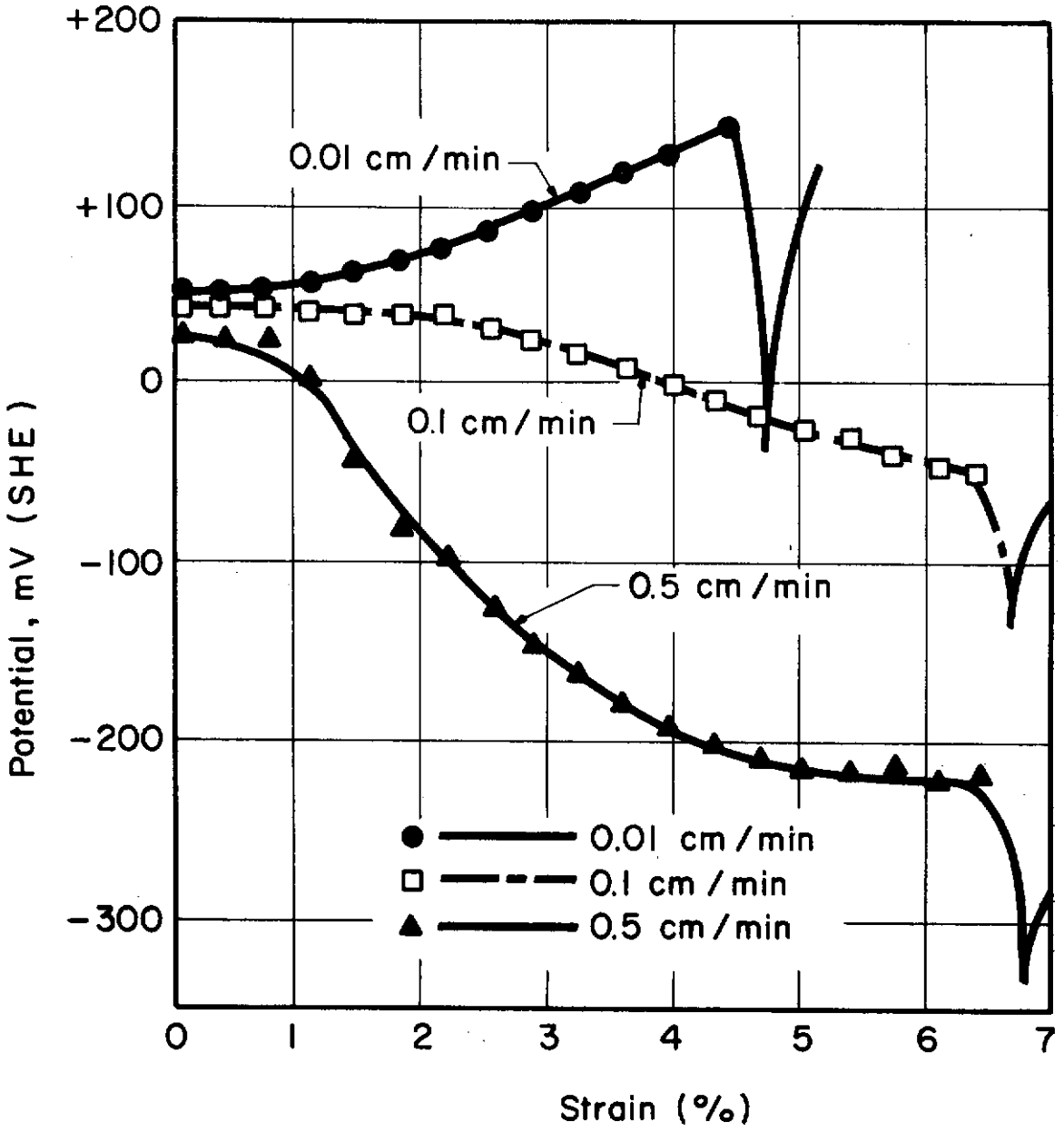

Fig. 28-a - Effect of Strain Rate on Corrosion Potential vs. Strain in CH_3OH + 0.166% HCl + 0.28% H_2O

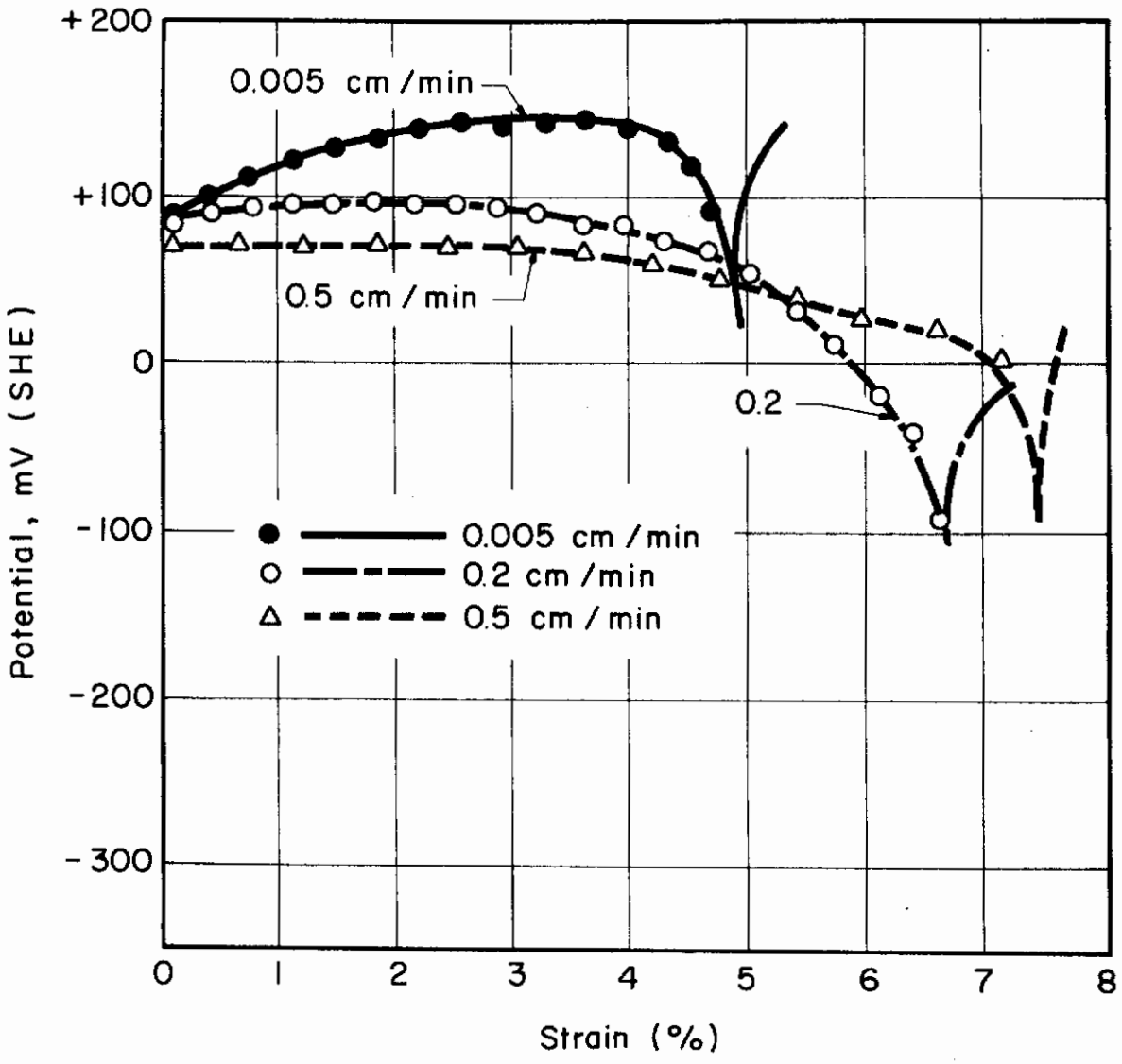

Fig. 28-b - Effect of Strain Rate on Corrosion Potential vs. Strain in CH_3OH + 0.166% HCl + 0.42% H_2O

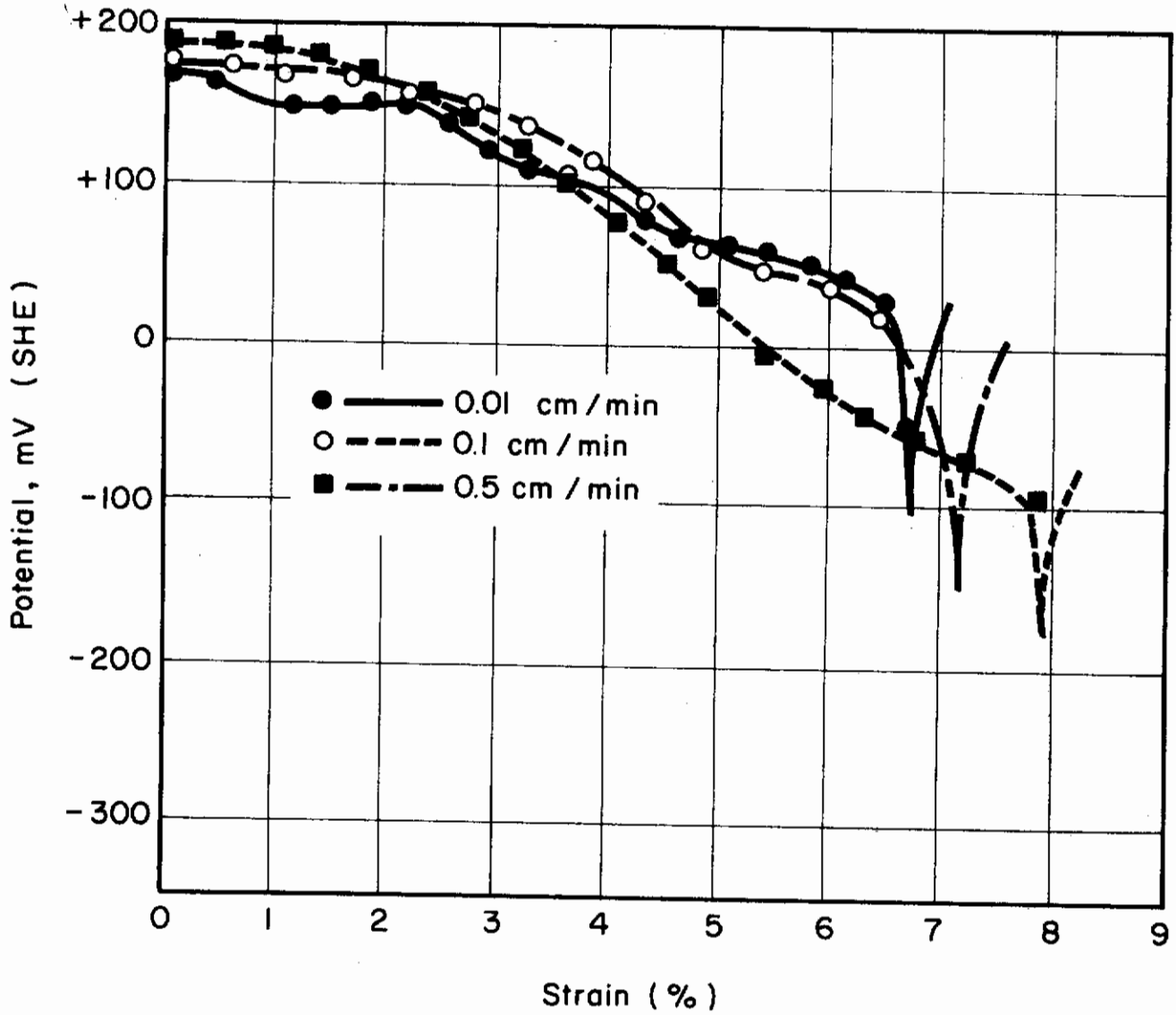

Fig. 28-c - Effect of Strain Rate on Corrosion Potential vs. Strain in CH_3OH + 0.166% HCl + 0.99% H_2O

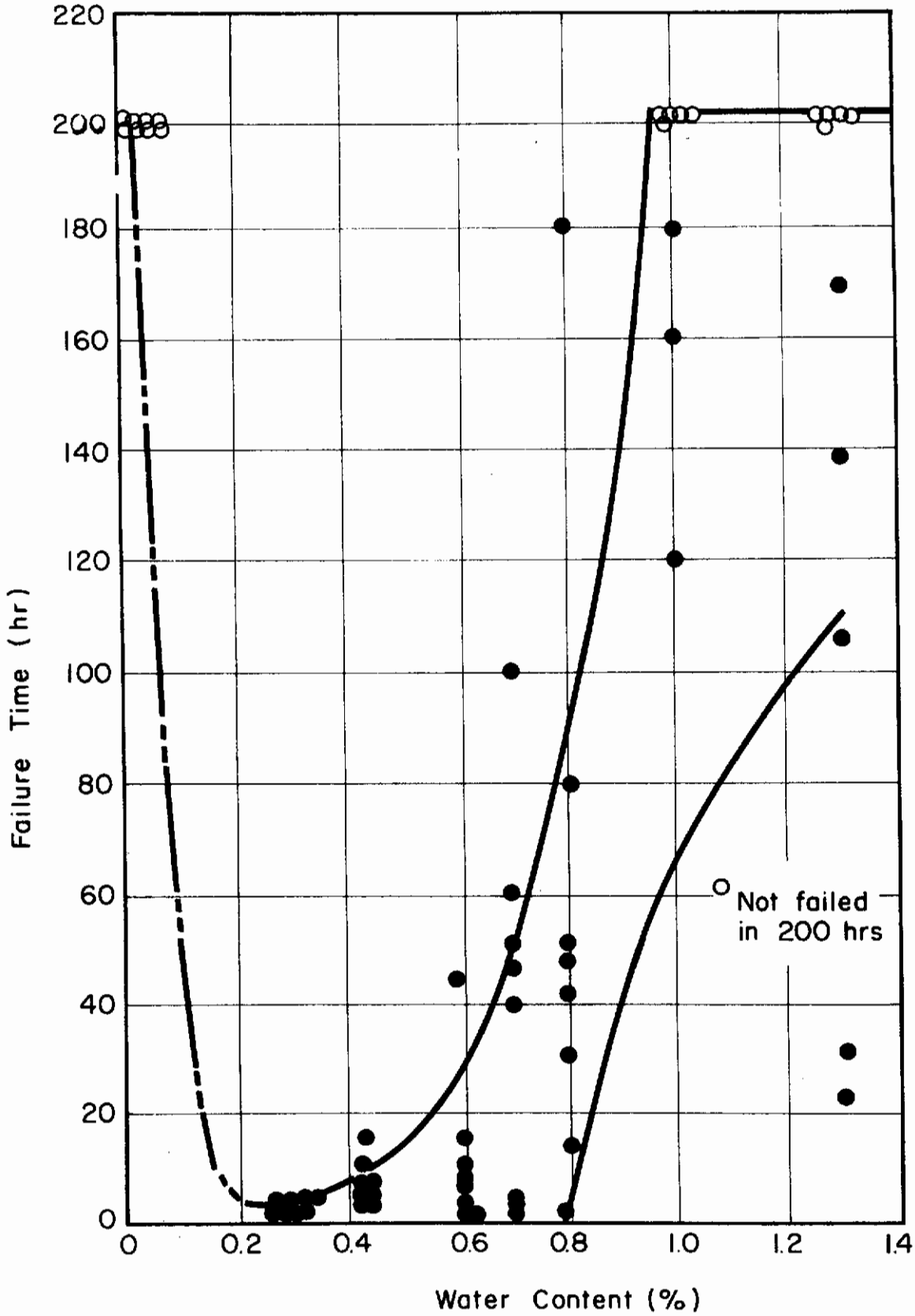

Fig. 29 - Failure Time vs. Water Content at Corrosion Potential

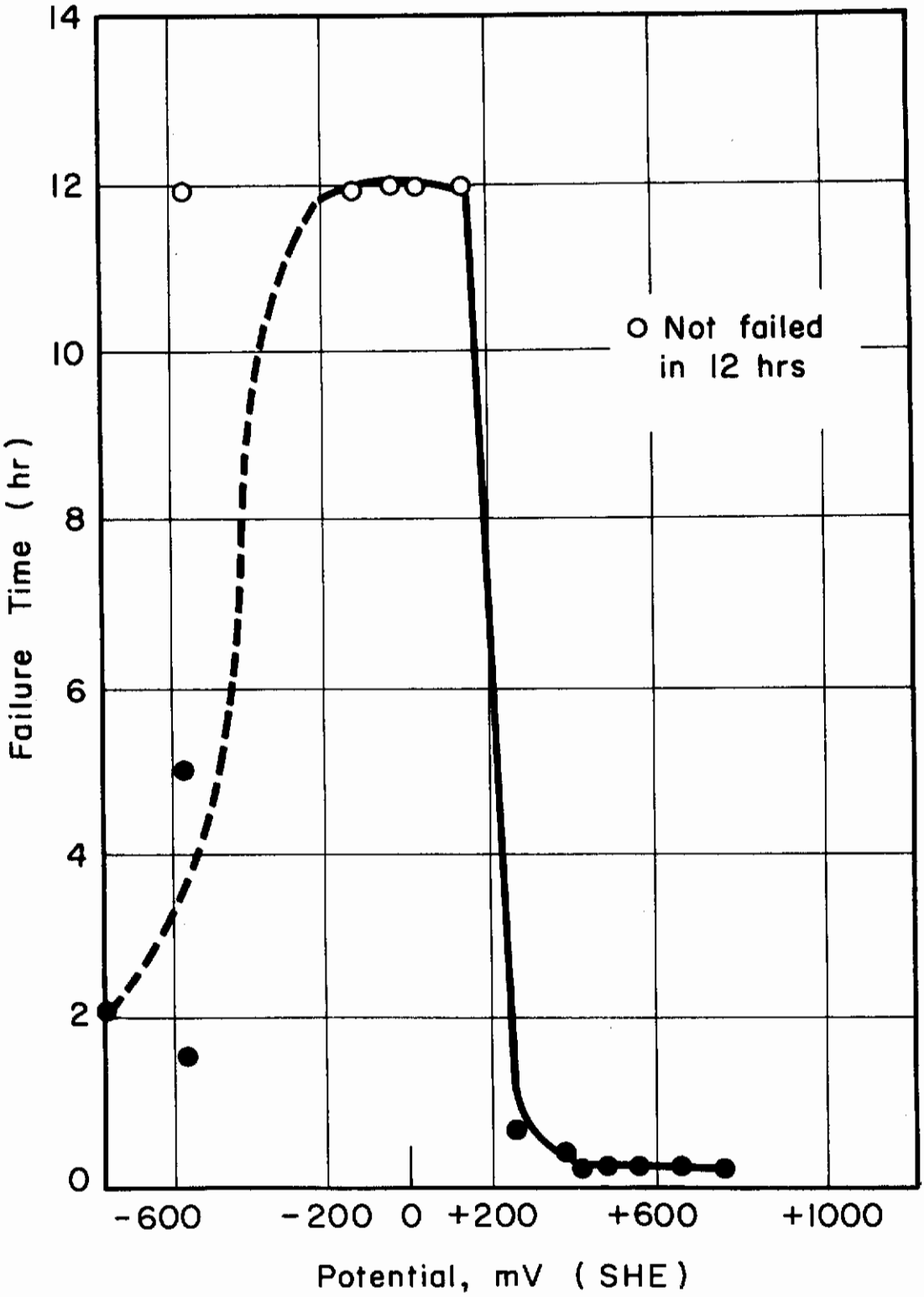

Fig. 30 - Failure Time vs. Polarization Potential in CH_3OH + 0.166% HCl + 0.99% H_2O

(about 15 minutes) in the anodic range of +250 to 800 mV. Specimens cathodically polarized in the approximate range of -500 to +250 mV did not crack during the 12-hour test periods used. At high cathodic potentials (more cathodic than about -500 mV) cracking occurred within a few hours.

4. Discussion

From the results of both dynamic and static tests presented above, it is clear that about 0.8% water in CH_3OH + 0.166 HCl + H_2O solutions is a critical concentration. Electrochemical behavior and cracking susceptibility vary greatly depending on whether the water content is greater or less than this critical concentration. It would appear that the water, when present in concentrations of 0.8% and greater, is sufficient to repair defects which might exist in air-formed oxide films or which are introduced into films during straining. However, less than 0.8% water is insufficient to repair an oxide film. On this basis the following interpretation is made.

When titanium specimens are placed in the methanolic solutions, the portions of the specimen containing the defects described above act as anode areas while the remaining oxide covered surface behaves as a cathode. The anodes will become passivated (oxide film repair) by the presence of water. The number of defects, therefore, decreases with increasing water content and the corrosion potential will shift in the anodic direction, as illustrated in Fig. 20-a. When the water content is high enough (0.8%) all defects will be repaired and the system will approach a steady-state condition.

If a specimen is strained (especially beyond the yield) ruptures will occur in the oxide film causing an increase in active sites, and chloride ion attack will take place in these sites when the solution contains insufficient water for film repair. Under these conditions the corrosion potential will move in the anodic direction. However, when the water content is high enough to repair the film the corrosion potential will move in the cathodic direction, as illustrated in Fig. 20-b, since strain continues to provide new active regions.

Figures 28-a and b show that the corrosion potential becomes more anodic at low strain rates when the environment contains less than the critical amount of water for passivation. This is the result of chloride ion attack. At high strain rates new active regions are provided rapidly enough to prevent chloride ion attack in the newly formed active regions and the increased anodic region causes the potential to move in the cathodic direction. However, when the water content is greater than the critical concentration chloride ion attack does not occur regardless of the strain rate and the corrosion potential will move in the cathodic direction, as illustrated in Fig. 28-c.

When a specimen is strained while at the corrosion potential in a solution containing less than the critical amount of water, the resulting chloride ion attack will cause a substantial decrease in elongation. The application of cathodic polarization or the addition of water to a concentration greater than the critical value prevents chloride ion attack and under either of these conditions no loss in elongation is observed (Figs. 16 - 19). However, if the specimen in the inert environment (critical amount of water added) is polarized in the anodic direction to induce chloride ion attack, the elongation will again be reduced to the low value as in the active environment at the corrosion potential.

The increased current observed during straining under anodic polarization is controlled by the diffusion of chloride ions to the active sites. This current effect is greatest at the low strain rates under conditions promoting the low elongation values described in Figs. 22, 23, 24, 25 and 27. During cathodic polarization the current increase appears to result from anodic dissolution and oxide film formation, and, therefore, the higher the strain rate the more rapid the increase in current with strain. When the strain rate is low some of the newly formed defects will be repaired (oxide film formation) and the increase in current with strain will be more gradual, as shown in Fig. 26.

Failure time of bend specimens was greatly reduced for those stress-corrosion specimens tested in solutions containing less than the critical amount of water. It is suggested that under these conditions, when the water content is insufficient to repair defective regions in the film, some of the active sites will support chloride ion attack. This chloride attack then leads to stress-corrosion failure. When the water content is greater than the critical concentration, longer times will be required for failure to occur (Fig. 29). However, the application of anodic polarization will induce chloride ion attack and cause failure within a short time. In this same environment a low cathodic polarization potential will prevent chloride ion attack and greatly increase failure time. Highly cathodic polarization potentials, however, will reduce failure time. This latter effect probably involves hydrogen embrittlement and, therefore, is different from the mechanism causing failure of specimens polarized in the anodic potential region.

C. STRESS-CORROSION CRACKING OF UNALLOYED TITANIUM IN METHANOL PLUS HCl SOLUTIONS (C. M. Chen)

1. Aims and Significance of Work

This work is concerned with stress corrosion studies of unalloyed titanium (RMI-70) in CH_3OH + 0.17% HCl + X% H_2O solutions. Results show that when the water content of the solution is greater than 1.6% there is no stress corrosion susceptibility, and below this value intergranular failure occurs in about 1.5 hours (Fig. 31). The cracking mechanism is discussed in relation to the activation energy and the effect of grain size on susceptibility. An activation energy of about 5.7 kcal may be

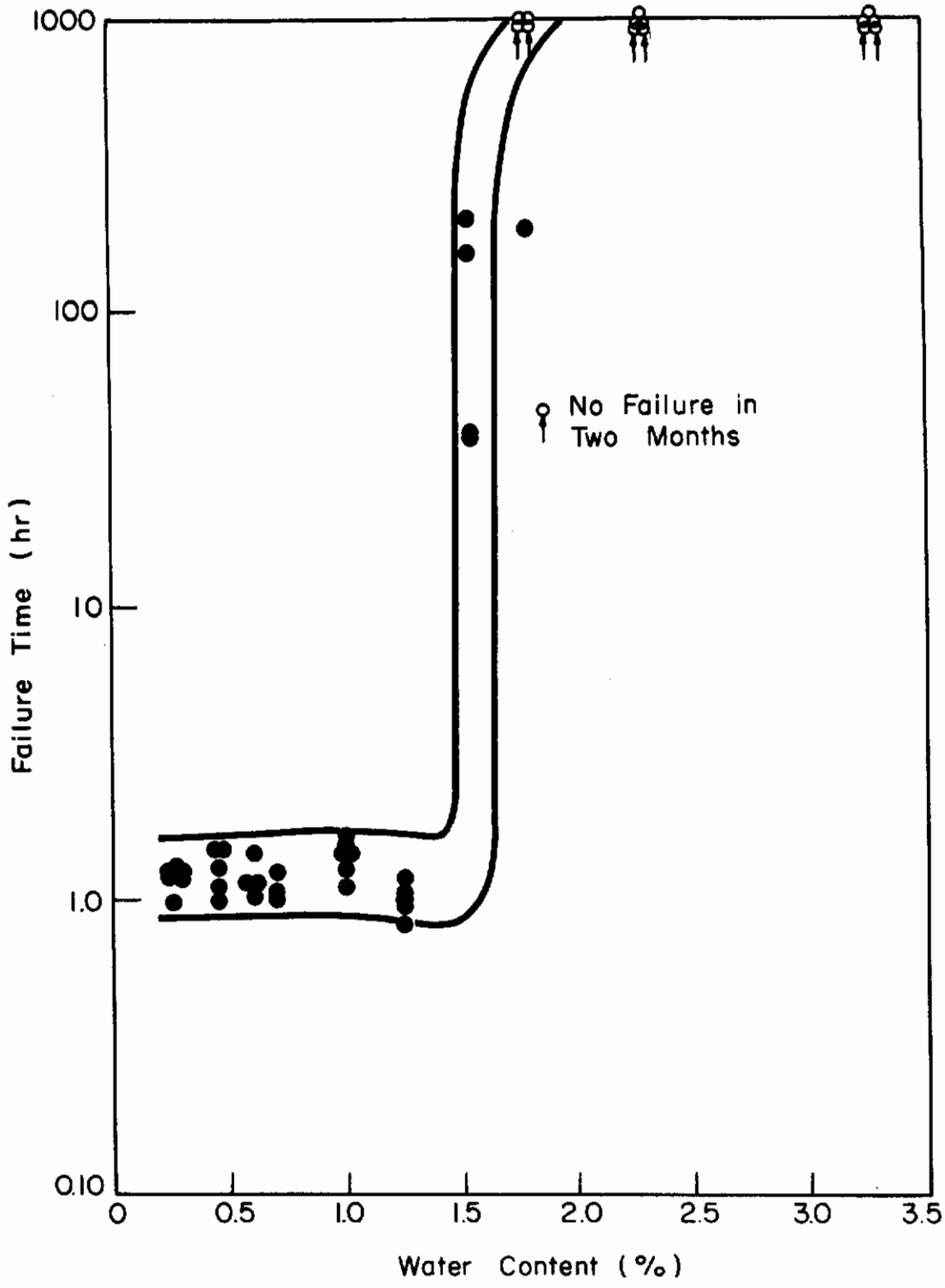

Fig. 31 - Effect of Water Content of CH_3OH + 0.17% HCl Solution on Failure Time of Unalloyed Titanium (tensile axis ⊥ to rolling direction; specimen stressed to yield)

due to the diffusion of the chloride ion in the methanol solution. The linear relation between failure time and $D^{-1/2}$ (where D is the grain size) suggests that dislocation pile-ups, resulting from external loading, cause stress concentrations at the grain boundaries and thereby play an important role in the intergranular cracking susceptibility.

2. Experimental Procedure and Results

The legs of unnotched U-bend specimens (0.6 mm x 7 mm x 77 mm) were placed in short lengths of 25.4 mm glass tubing which served as stressing jigs. These assemblies were placed in the test solution and the temperature was controlled to within ±0.1°C with a thermoelectric temperature regulator. The specimens were oriented with the long axis perpendicular to the rolling direction. Grain size was adjusted by repeated straining (0.3% or 1%) and annealing for various times at 815°C in evacuated vycor capsules. Solutions of CH_3OH + HCl + H_2O were prepared from Baker absolute methanol, Applied Chemical reagent grade HCl, and double-distilled water. The specimens were mechanically polished through 600-grit emery and then rinsed in acetone and methanol prior to stress-corrosion testing. The composition of the unalloyed titanium is stated below.

Table II - Composition of Unalloyed Titanium

Element	% Element
C	0.02
N	0.011
Fe	0.31
O	0.304
H	103 ppm

a. Effect of Water Content at Constant HCl Concentration of CH_3OH Solution on Stress Corrosion Susceptibility

Failure time vs. water content is shown in Fig. 31. When the water content is less than 1.3% the failure time is short--approximately 1.5 hours. When the water content is greater than 1.8%, the specimens did not fail in two months. The critical water content is about 1.6%. Cracking is intergranular, as illustrated in Fig. 32.

b. Apparent Activation Energy of Stress Cracking

As is shown in Fig. 33 the activation energy was determined in the temperature range from 0° to 50°C. When the temperature was increased, the failure time was decreased and there was a linear relationship between the reciprocal temperature and the logarithmic failure

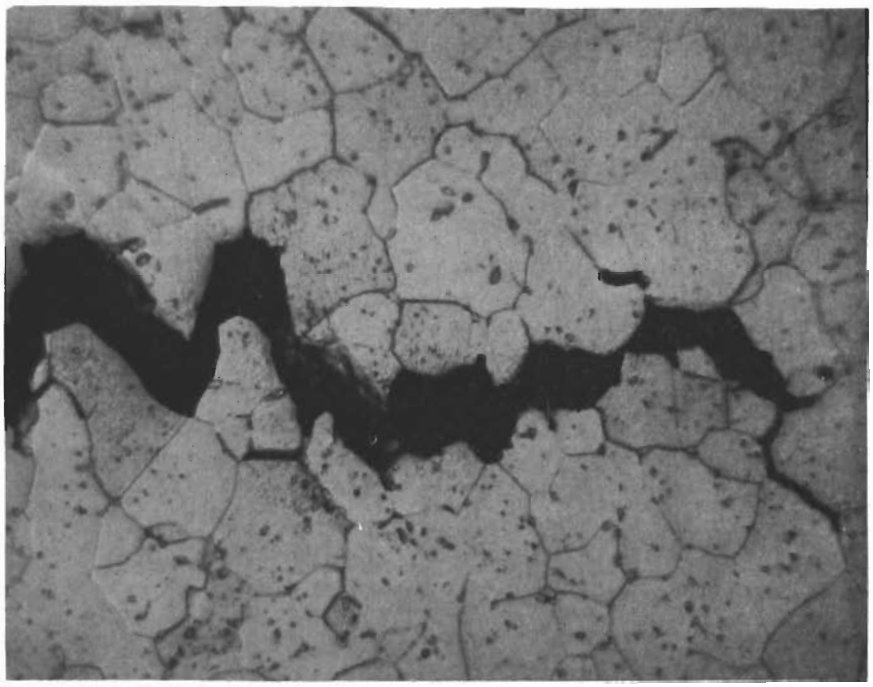

Fig. 32 - Intergranular Crack of Unalloyed Titanium in $CH_3OH + H_2O + HCl$ Solution

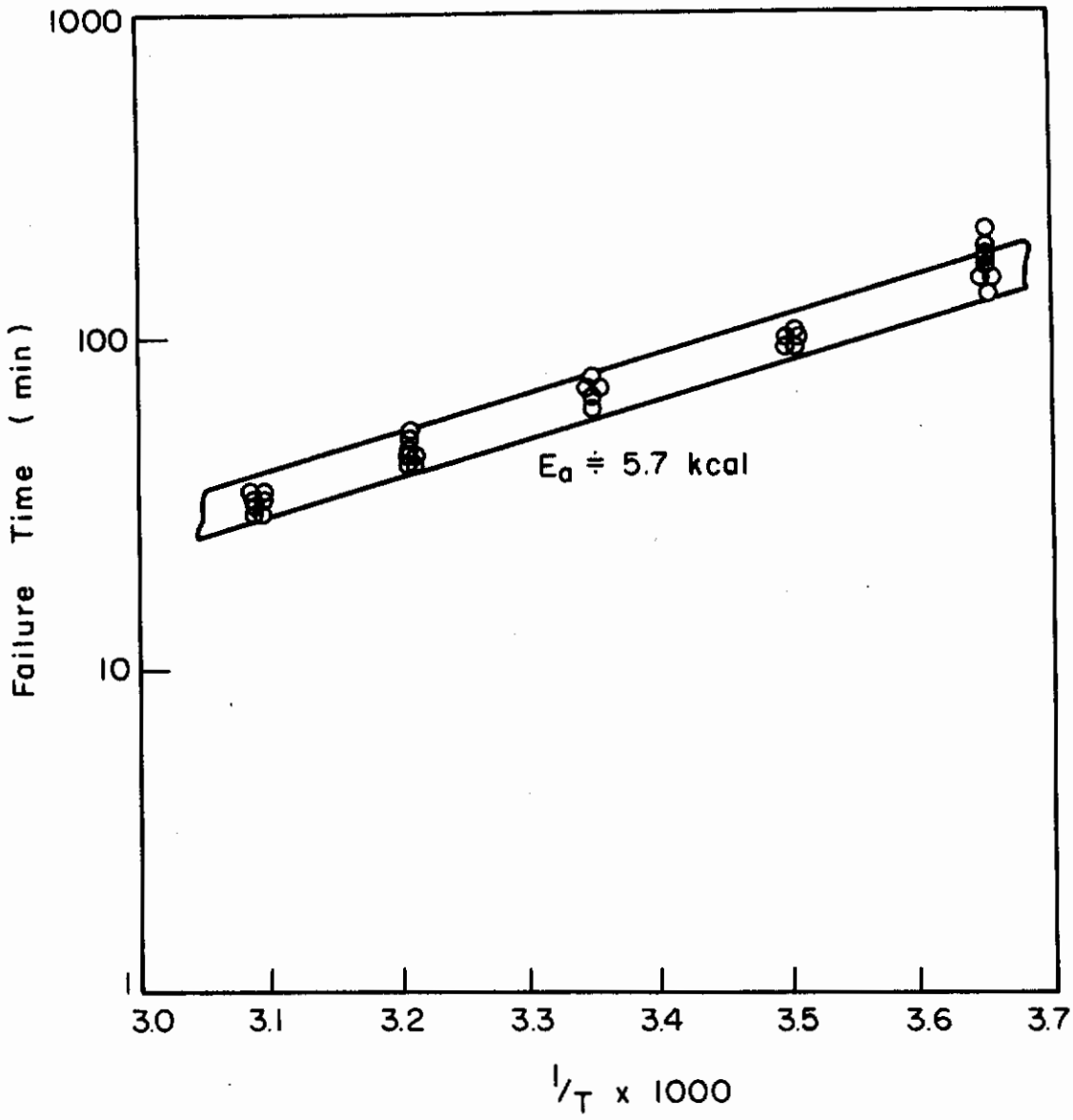

Fig. 33 - Failure Time vs. Reciprocal Temperature for Unalloyed Titanium (tensile axis ⊥ rolling direction; CH_3OH + HCl + H_2O test solution)

time. The activation energy is about 5.7 kcal. This value is almost the same as those determined for Ti-6Al-4V and Ti-8Al-1Mo-1V alloys shown in Fig. 34.

c. Effect of Grain Size on Failure Time

Specimens were stress corrosion tested in CH_3OH + 0.28% H_2O + 0.17% HCl solution at 40°C. Figure 35 shows that as the grain size of the specimen was increased, the failure time was decreased. There is a linear relationship between the failure time and $D^{-1/2}$ where D is the grain diameter.

3. Discussion

The effect of water content in methanol solution on the stress-corrosion cracking of Ti-6Al-4V was discussed in detail in Section II B. When the water content is below 1.6%, the passivator, H_2O, is insufficient to passivate defects in the oxide film for specimens stressed in the solution. These defects are believed to be in the oxide and in the cracking paths located in the grain boundaries. The activation energy for stress-cracking is about 6 - 7 kcal for unalloyed titanium and titanium alloys Ti-6Al-4V or Ti-8Al-1Mo-1V. The stress corrosion mechanism is discussed as due to either titanium hydride formation or to chloride ion attack. Diffusion of hydrogen in β-titanium is much easier than α-titanium, and the diffusion coefficients in these phases obey the following equations[11]:

$$D_\beta = 1.95 \cdot 10^{-3} \exp\left(-\frac{6{,}640 \pm 500}{RT}\right) \text{cm}^2/\text{sec} \qquad (1)$$

$$D_\alpha = 1.8 \cdot 10^{-2} \exp\left(-\frac{12{,}380 \pm 680}{RT}\right) \text{cm}^2/\text{sec} \qquad (2)$$

Although Ti-8Al-1Mo-1V and Ti-6Al-4V alloys are α-alloys, it is possible to have α-phase plus intergranular β-phase by appropriate heat treatments. However, the unalloyed titanium shows only α-phase, and the measured activation energy is only one-half of that of the diffusion of hydrogen in the α-phase. On the other hand, the activation energy of diffusion for the chloride ion in aqueous solution is 4.2 kcal. Therefore, it is not unreasonable to assume that the activation energy for stress cracking is due to the diffusion of chloride ions to the crack apex in the methanol solution in the case of the unalloyed titanium.

In Petch's[12] relation, the fracture stress is proportional to $D^{-1/2}$. According to Eshelby, Frank, and Nabarro,[13] when the dislocation source is located at the center of the grain, the number of dislocations that can be accommodated in the grain is

$$n = \frac{k\pi\tau_s D}{4Gb}, \qquad (3)$$

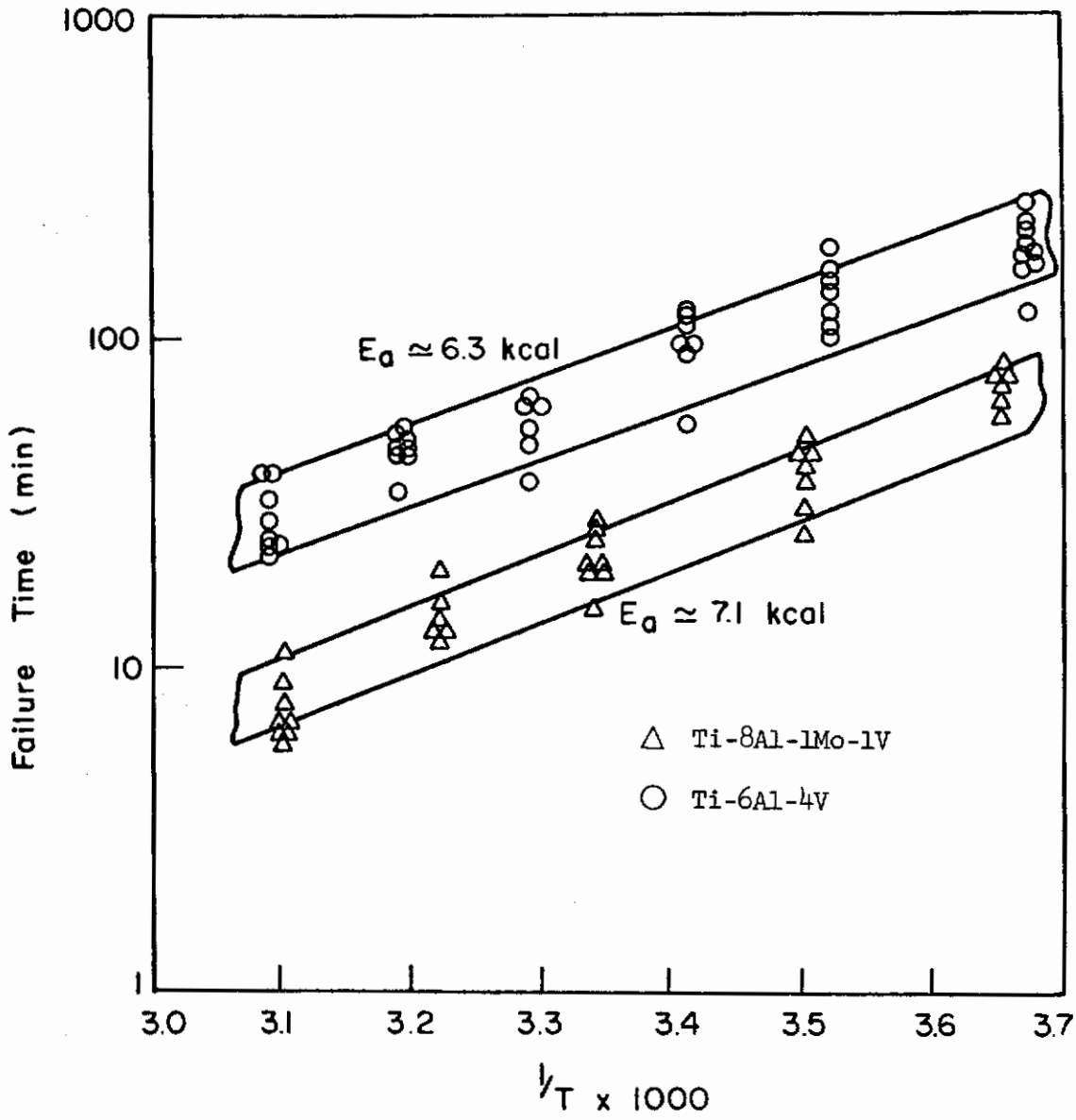

Fig. 34 - Failure Time vs. Reciprocal Temperature Ti-6Al-4V and Ti-8Al-1Mo-1V (tensile axis ⊥ rolling direction; $CH_3OH + HCl + H_2O$ test solution)

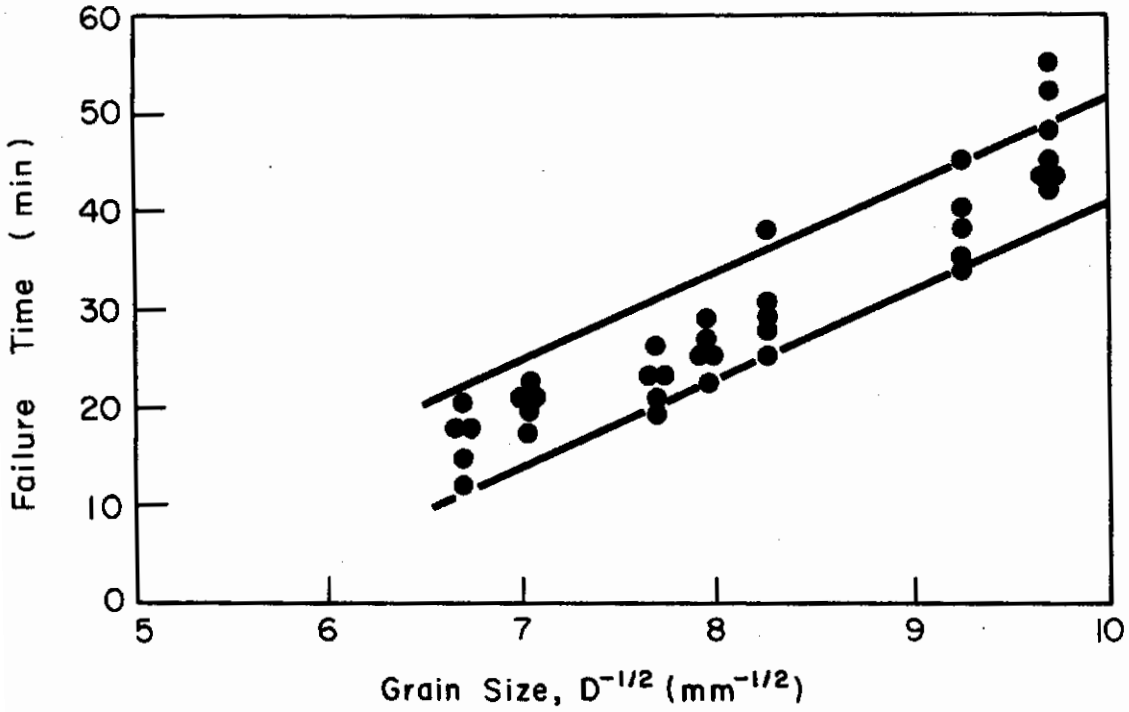

Fig. 35 - Failure Time vs. Grain Size for Unalloyed Titanium (tensile axis ⊥ to rolling direction; CH_3OH + 0.17% HCl + 0.28% H_2O solution)

where D is the grain diameter, and τ_s is the average resolved shear stress which is assumed to be equal to the applied stress τ_a minus the average internal stress τ_i to overcome the resistance to dislocation motion; i.e., $\tau_s = \tau_a - \tau_i$. The stress concentration due to n dislocation pile-ups is n times the average resolved shear stress; i.e.,

$$n\tau_s = \frac{k\pi\tau_s^2 D}{4Gb} . \tag{4}$$

Yielding is assumed to occur when a critical shear stress, τ_c, which is independent of the grain size, is produced at the head of the pile-up. If the shear stresses are converted to uniaxial tensile stresses such that $\tau_a = \sigma_a/2$, $\tau_i = \sigma_i/2$, and $\tau_c = \sigma_c/2$, then, the critical shear stress is given by

$$\frac{\pi k(\sigma_a - \sigma_i)^2 \cdot D}{8Gb} = \sigma_c . \tag{5}$$

Therefore,

$$\sigma_a = \sigma_i + \sqrt{\frac{8Gb\sigma_c}{\pi k} \cdot \frac{1}{D}} = \sigma_i + ky \cdot D^{-1/2} . \tag{6}$$

In addition to this shear stress, $n\tau_s$, there is a field of normal stress at the head of the dislocation pile-up according to Stroh's[14] analysis of the stress distribution. Stroh showed that the tensile stress normal to the line OP in Fig. 36-a is given by

$$\sigma = \frac{3}{4}\left(\frac{D}{\gamma}\right)^{1/2} \tau_s \sin\theta \cos\frac{\theta}{2} . \tag{7}$$

The maximum value of σ occurs at $\cos\theta = 1/3$ or $\theta = 70.5°$; i.e.,

$$\sigma_m = \frac{\tau_s}{\sqrt{3}}\left(\frac{D}{\gamma}\right)^{1/2} . \tag{8}$$

Therefore, when the grain size becomes larger, the normal stress concentration at the grain boundaries becomes larger and is proportional to $D^{1/2}$. Robertson and Tetelman[15] have shown that there are linear relations between failure time and $D^{-1/2}$ in the system of brass in mercury and brass in NH_3 environment. In the unalloyed titanium the failure is intergranular and the linear relation between the failure time and $D^{-1/2}$ suggests that the normal stress concentration caused by the dislocation pile-ups at the grain boundaries is related to the intergranular susceptibility as schematically shown in Fig. 36-b.

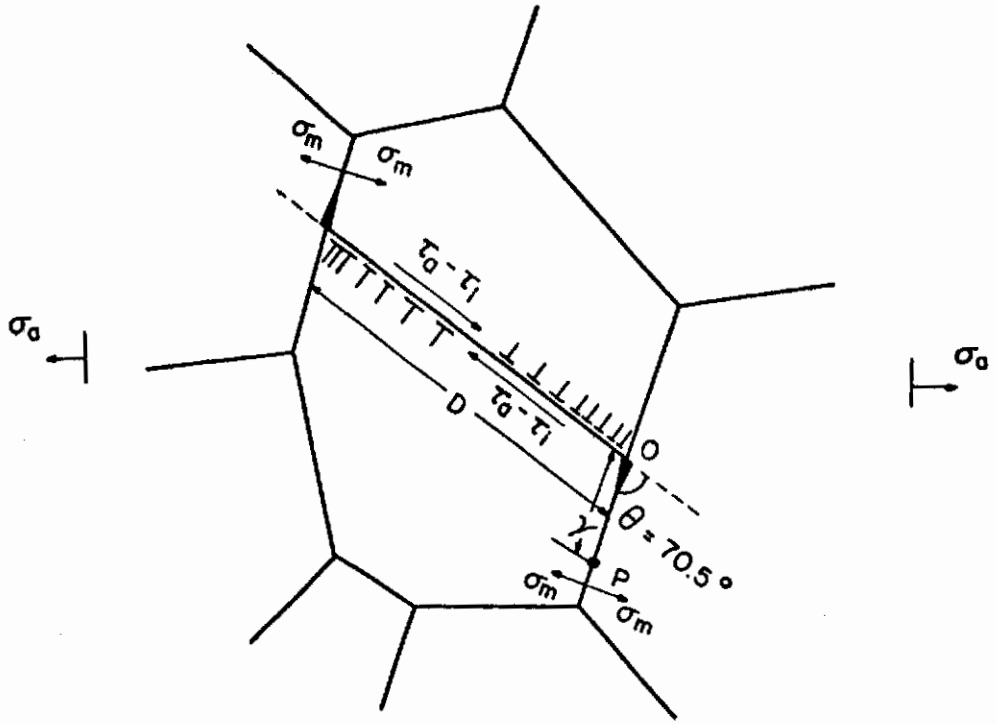

Fig. 36a - Schematic Diagram for Maximum Normal Stress σ_m at the Head of Dislocation Pile-up at the Grain Boundary[14]

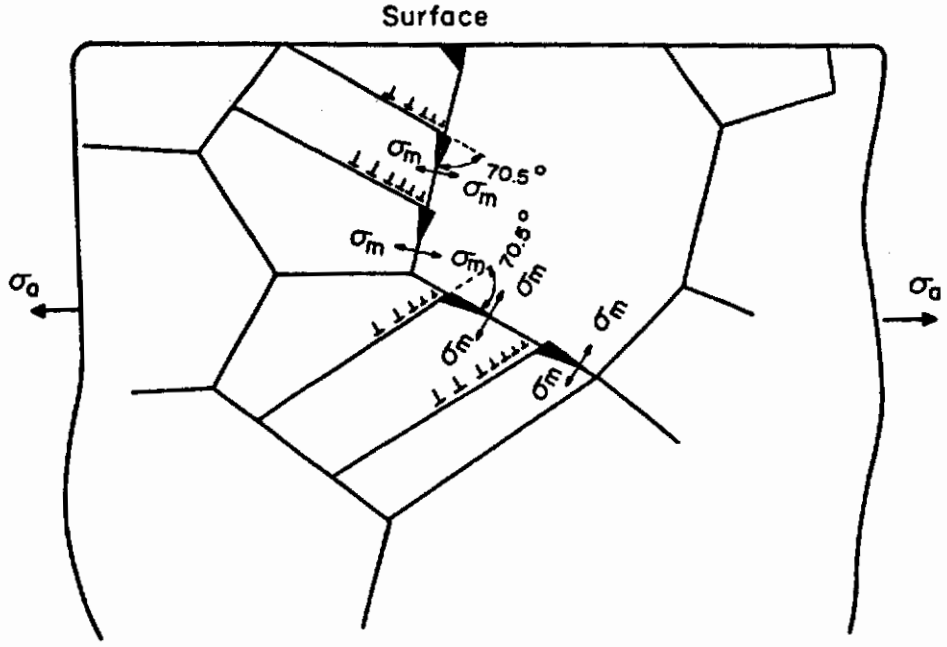

Fig. 36b - Schematic Diagram for Intergranular Cracking Due to the Normal Stress Concentration by Dislocation Pile-up at Grain Boundaries[15]

D. STRESS-CORROSION CRACKING OF α (unalloyed Ti), α + β (Ti-6Al-4V and Ti-8Al-1Mo-1V) and β-III (Ti-11.5Mo-6Zr-4.5Sn) ALLOYS IN METHANOL SOLUTIONS (C. M. Chen)

1. Aims and Significance of Work

This report is concerned with stress corrosion studies of β-III (β-phase alloy) in methanol + HCl + H_2O solutions and unalloyed Ti, Ti-6Al-4V, Ti-8Al-1Mo-1V, and β-III alloys in methanol + Br_2 solutions.

In methanol + 0.17% HCl + X H_2O solutions the water content necessary to prevent cracking of β-III was determined to be greater than 1.5% and the activation energy for cracking in the same environment was about 5.5 kcal; this activation energy is essentially the same as that obtained for unalloyed titanium and the α + β alloys. This suggests that the diffusion of chloride ion in the methanol solution plays an important role in the cracking process.

Tests on unalloyed Ti, Ti-6Al-4V, Ti-8Al-1Mo-1V, and β-III alloys in methanol + Br_2 solutions show that very small amounts of bromine will cause stress corrosion cracking; e.g., with only 5×10^{-4}% Br_2, Ti-8Al-1Mo-1V failed in 2-3 minutes, heat-treated β-III failed in 5-7 minutes, and Ti-6Al-4V failed in 20-50 minutes. When the Br_2 content was less than 5×10^{-5}, all the alloys failed except as-received Ti-8Al-1Mo-1V ⊥ R.D. and the heat-treated β-III alloys.

Metallographic observations showed that when unstressed specimens of unalloyed titanium and β-III alloys are dipped in methanol + Br_2 solution, bromine attacks the grain boundaries, and after extended times these materials become somewhat porous and brittle. X-ray analysis for the unalloyed titanium after long exposure times showed a pattern for titanium only.

2. Experimental Procedure and Results

The legs of unnotched U-bend specimens (77 mm long x 7 mm wide) for unalloyed Ti (0.64 mm thickness), Ti-8Al-1Mo-1V (0.25 mm), Ti-6Al-4V (0.25 mm) were placed in short lengths of 25.4-mm glass tubing which served as stressing jigs; similar type specimens of β-III alloy (0.13 mm x 6 mm x 40 mm) were stressed in short lengths of 17-mm glass tubing. All specimens were oriented with the long axis perpendicular to the rolling direction. β-III specimens were heated at 1700°F for two hours followed by a water quench to assure an all-β microstructure.

All specimens were mechanically polished through 600-grit emery, rinsed in acetone, and dipped in methanol prior to stress-corrosion testing. Specimens for metallographic observation were rough polished with 6 μm diamond compound followed by 0.05 μm alumina, and etched with Kroll's solution.

Test solutions of $CH_3OH + HCl + H_2O$ were prepared from Baker's absolute methanol, Allied Chemical reagent grade HCl and double distilled water. Solutions of $CH_3OH + Br_2$ were prepared from Baker's absolute methanol and purified bromine.

a. Effect of Water Content at Constant HCl Concentration of CH_3OH Solution on Stress Corrosion Susceptibility

Failure time vs. water content is shown in Fig. 37 for the as-received material of Ti-8Al-1Mo-1V alloy. The critical water content is about 0.6% H_2O; specimens failed in 10-1000 minutes below this water content and in 1000-10,000 minutes or more when the water content was increased above 0.6%. Failure time vs. water content is shown in Fig. 38 for as-received material of β-III alloy. The failure time increased from about 20 minutes to about 100 minutes when the water content was increased from 0.28% to 1.3%; however, the failure time was greatly increased when the water content was greater than 1.5%.

b. Apparent Activation Energy of Stress Cracking of β-III Alloy

Figure 39 shows the activation energy for β-III alloy determined in the temperature range from 0° to 50°C. When the temperature was increased, the failure time decreased; the activation energy is about 5.5 kcal. This value is almost the same as those determined for unalloyed Ti (5.7 kcal), Ti-8Al-1Mo-1V (7.1 kcal), and Ti-6Al-4V (6.3 kcal).

c. Stress-Corrosion Cracking in $CH_3OH + Br_2$ Solutions

The effect of bromine concentration in CH_3OH on SCC is shown in Fig. 40-a for Ti-8Al-1Mo-1V, in Fig. 40-b for β-III, in Fig. 40-c for Ti-6Al-4V, and in Fig. 40-d for unalloyed Ti. In all cases these are for as-received materials (either with or without mechanical polishing through 600-grit emery paper). Failure times are plotted against the logarithmic concentration of Br_2. In Ti-8Al-1Mo-1V alloy the curve shows a minimum at about 0.5% Br_2. Alloy Ti-6Al-4V and unalloyed titanium showed similar tendencies except that failure times were longer and minima in the curves were not conspicuous. The minima are probably due to increased corrosion at the higher bromine concentrations. For purposes of comparison, weight loss measurements were made on Ti-8Al-1Mo-1V at 1, 2, 4.5, and 20-hour intervals as a function of bromine concentration in methanol. These results are shown in Fig. 40-c. It is of interest to note that a weight loss of only 10 $\mu g/cm^2$ or less caused failure in five minutes in the methanol + 5×10^{-5}% bromine solution.

The curve for heat-treated β-III alloy is shown in Fig. 41. This curve shows the same tendency as for the Ti-6Al-4V alloy. When the concentration was below 5×10^{-6}% Br_2, the specimen did not fail in 44 hours.

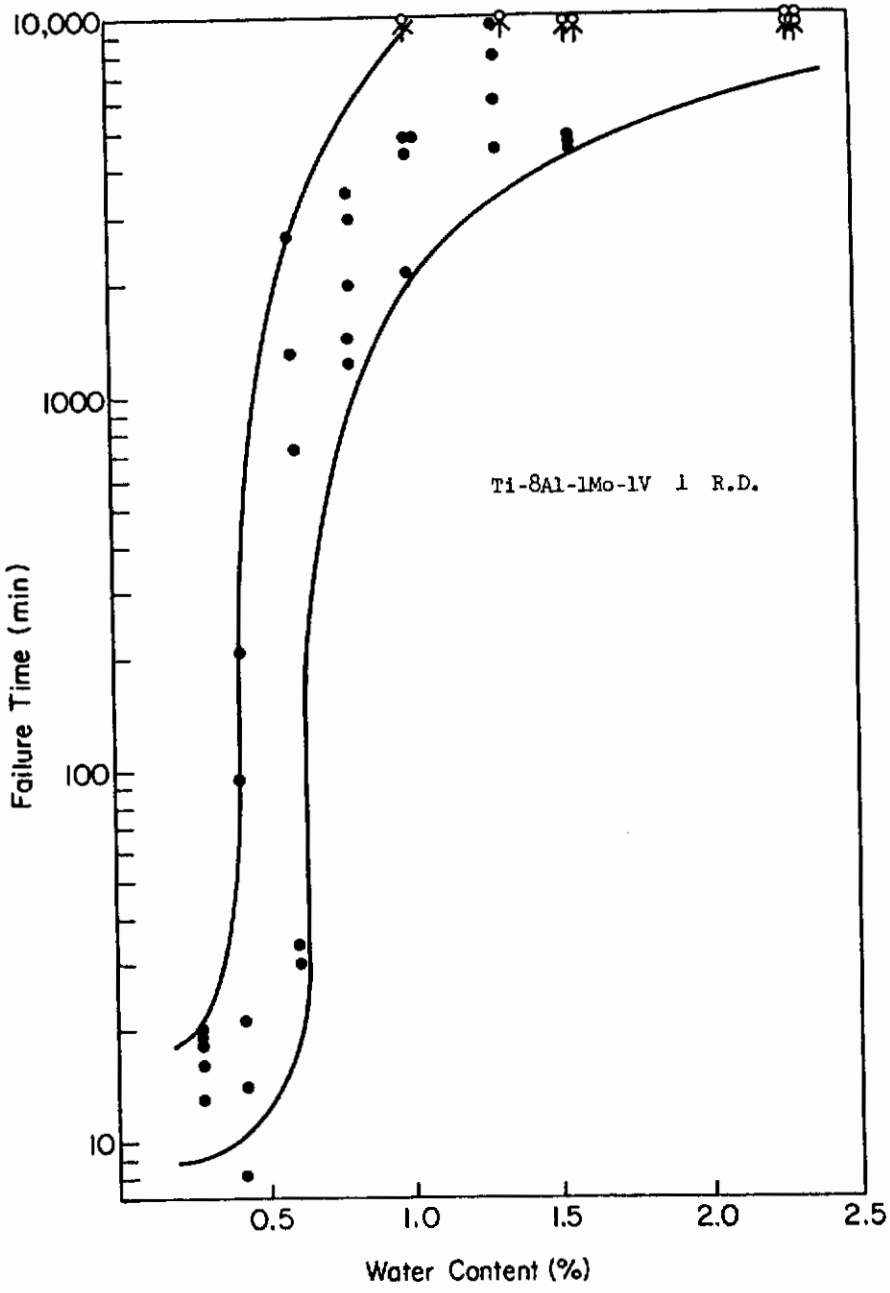

Fig. 37 - Failure Time of Ti-8Al-1Mo-1V vs. Water Content (%) in CH_3OH + 0.17% HCl + X H_2O (tensile axis ⊥ to rolling direction, specimens stressed to yield)

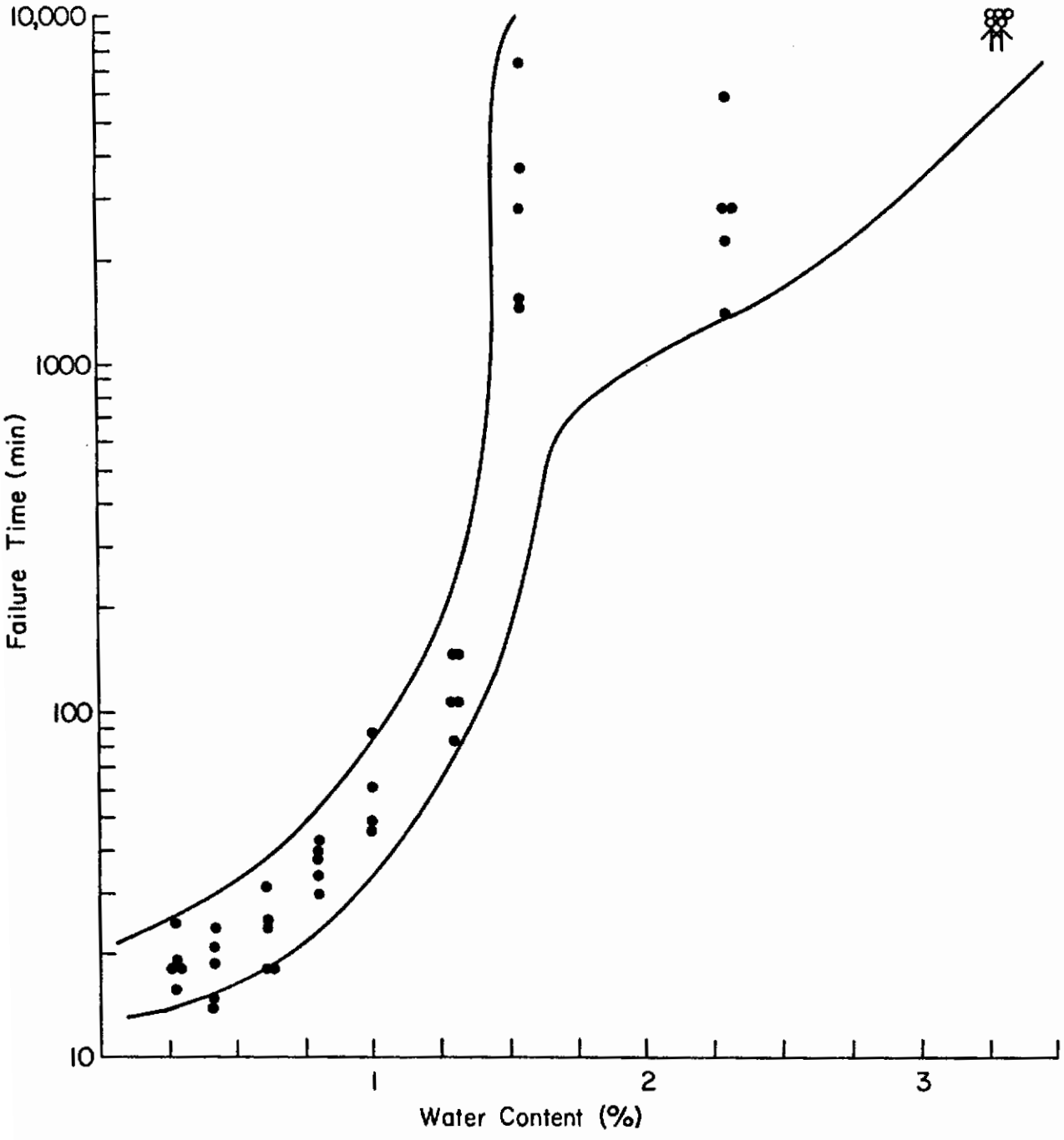

Fig. 38 - Failure Time of β-III Alloy vs. Water Content (%) in CH_3OH + 0.17% HCl + X H_2O (Tensile axis ⊥ to rolling direction, specimen stressed to yield)

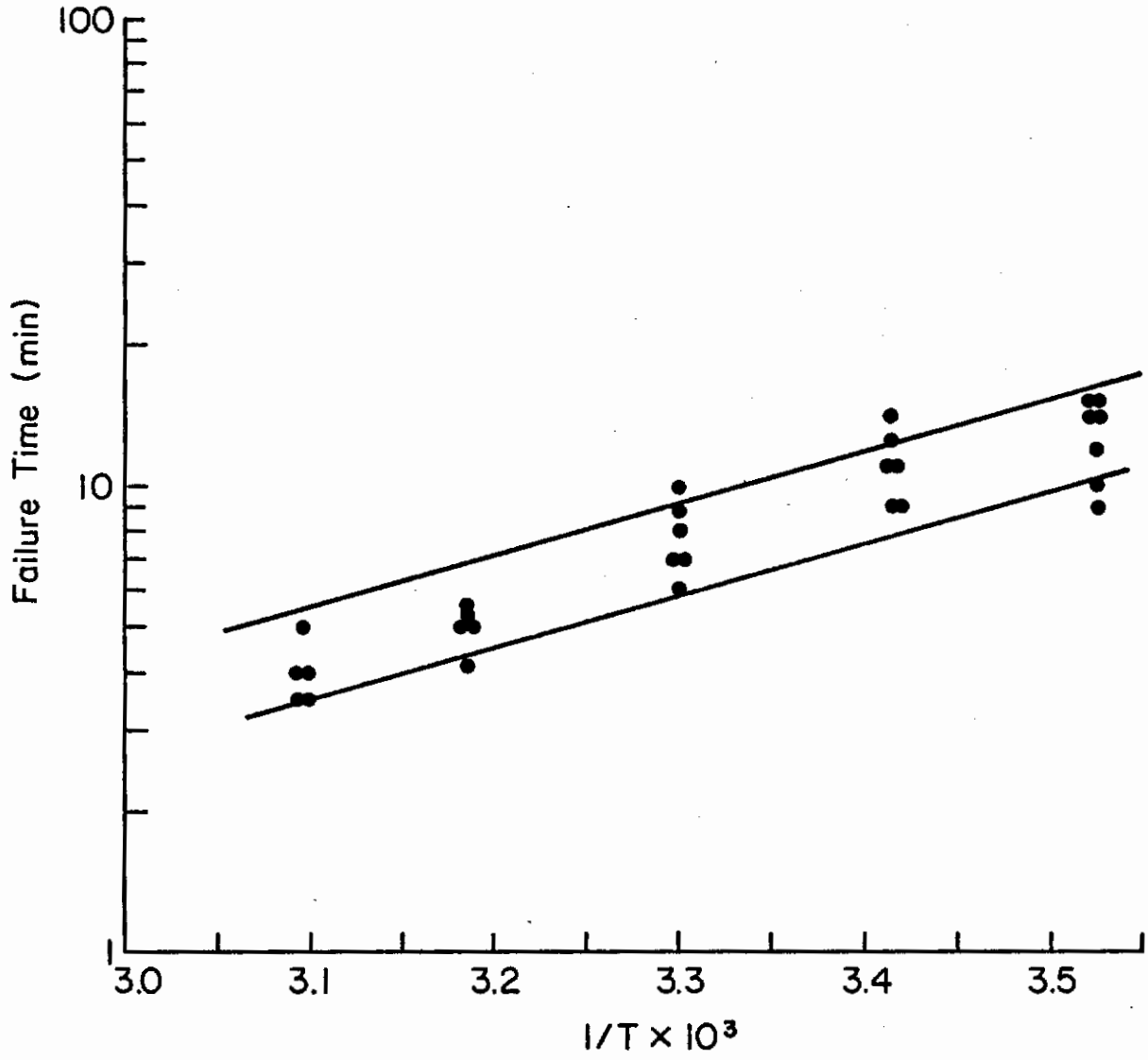

Fig. 39 - Failure Time of β-III Alloy vs. $1/T \times 10^3$ in CH_3OH + 0.17% HCl + 0.28% H_2O (Tensile axis ⊥ to rolling direction, specimen stressed to yield)

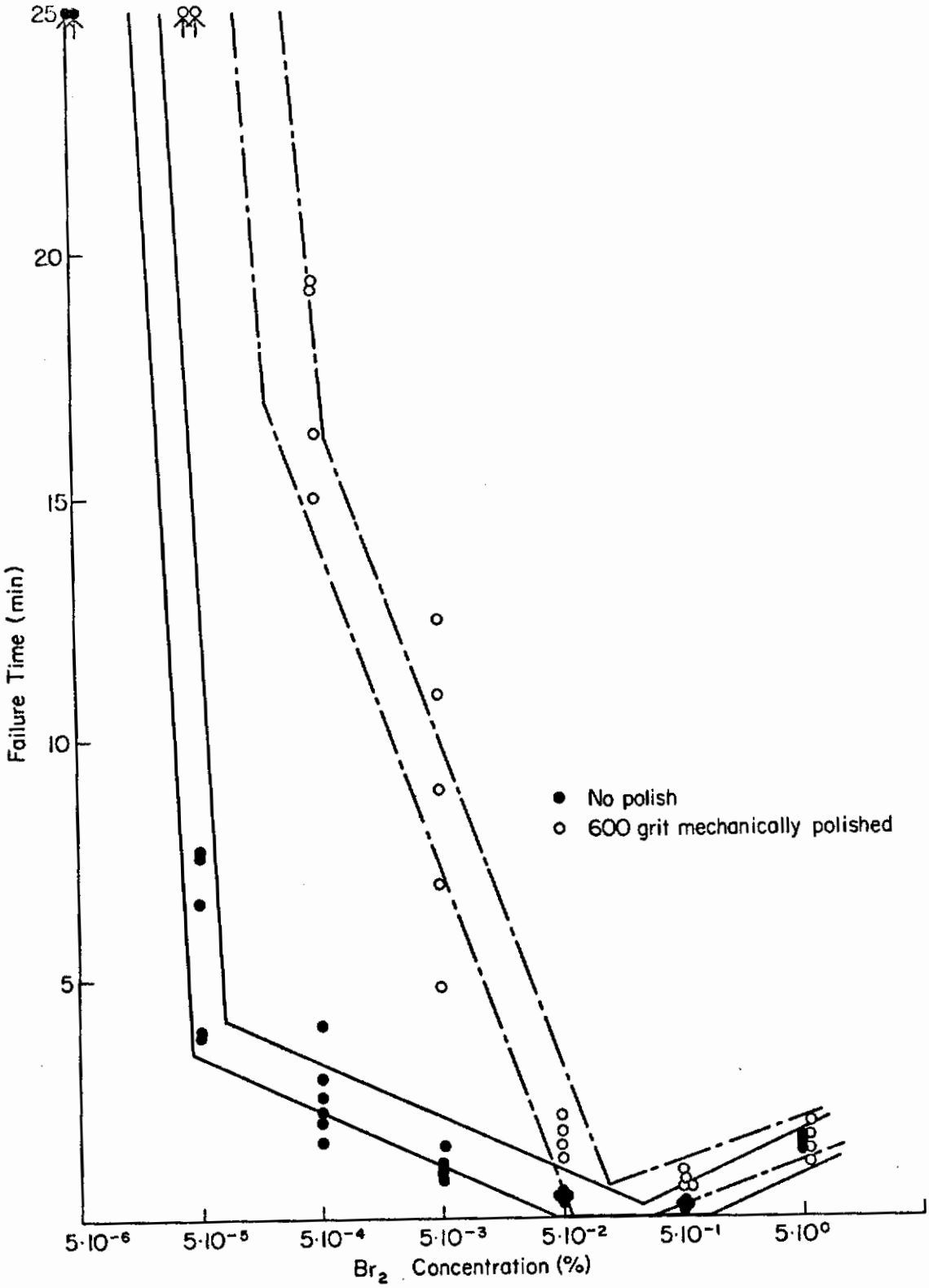

Fig. 40a - Failure Time of Ti-8Al-1Mo-1V vs. Logarithmic Concentration of Br_2 in CH_3OH (tensile axis ⊥ to rolling direction)

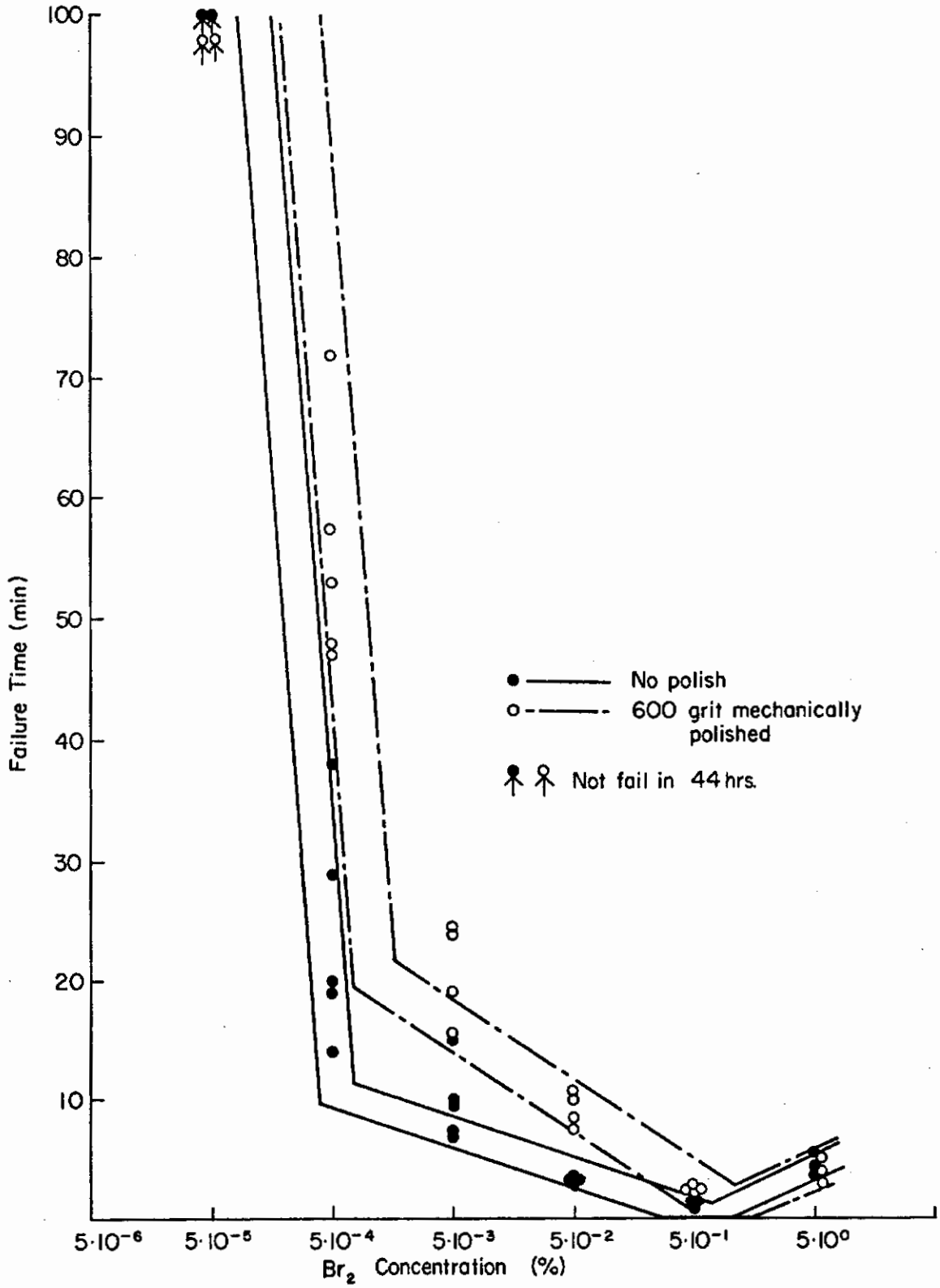

Fig. 40b - Failure Time of β-III Alloy vs. Logarithmic Concentration of Br_2 in CH_3OH (Tensile axis ⊥ to rolling direction)

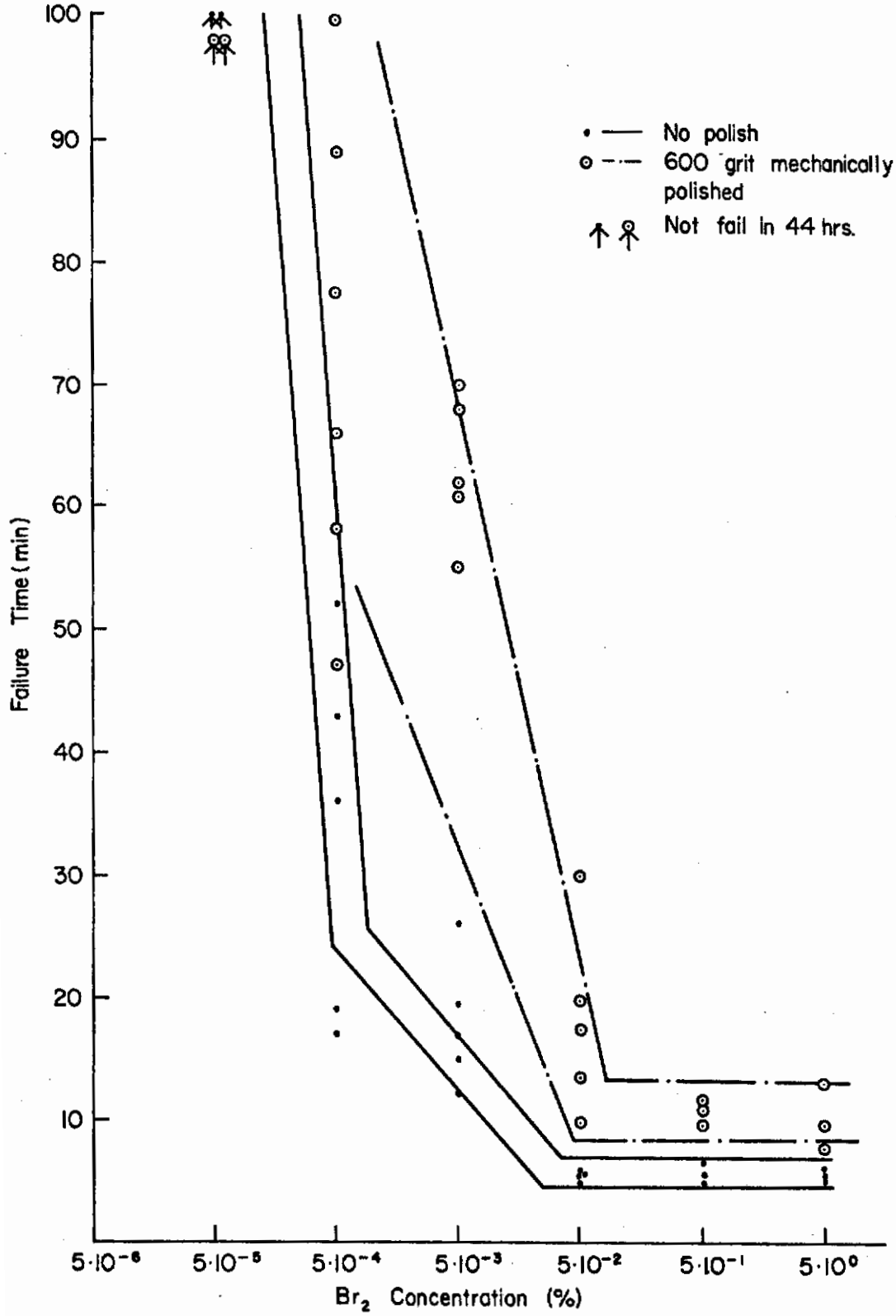

Fig. 40c - Failure Time of Ti-6Al-4V vs. Logarithmic Concentration of Br_2 in CH_3OH (tensile axis ⊥ to rolling direction)

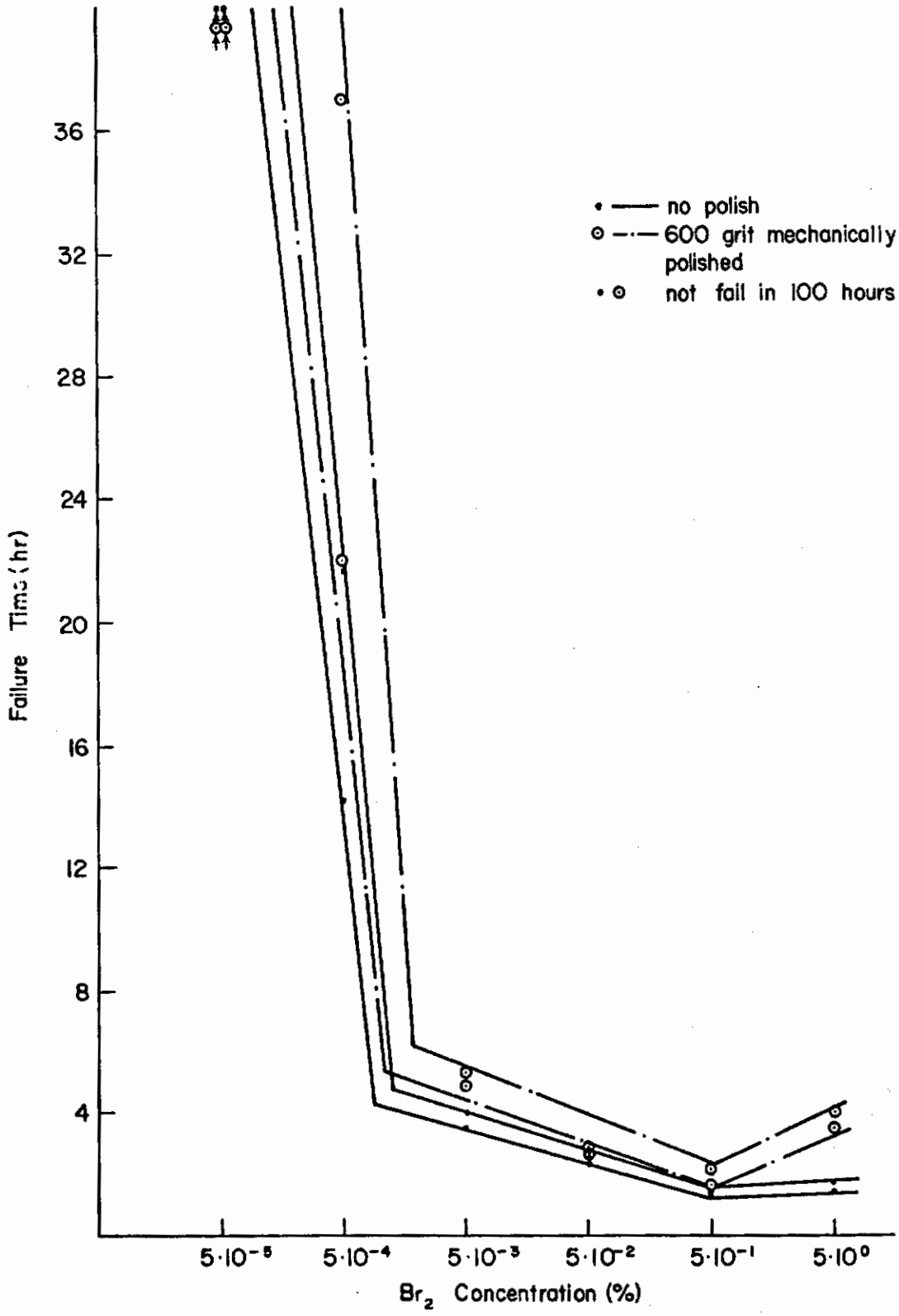

Fig. 40d - Failure Time of Unalloyed Titanium vs. Logarithmic Concentration of Br_2 in CH_3OH (tensile axis ⊥ to rolling direction)

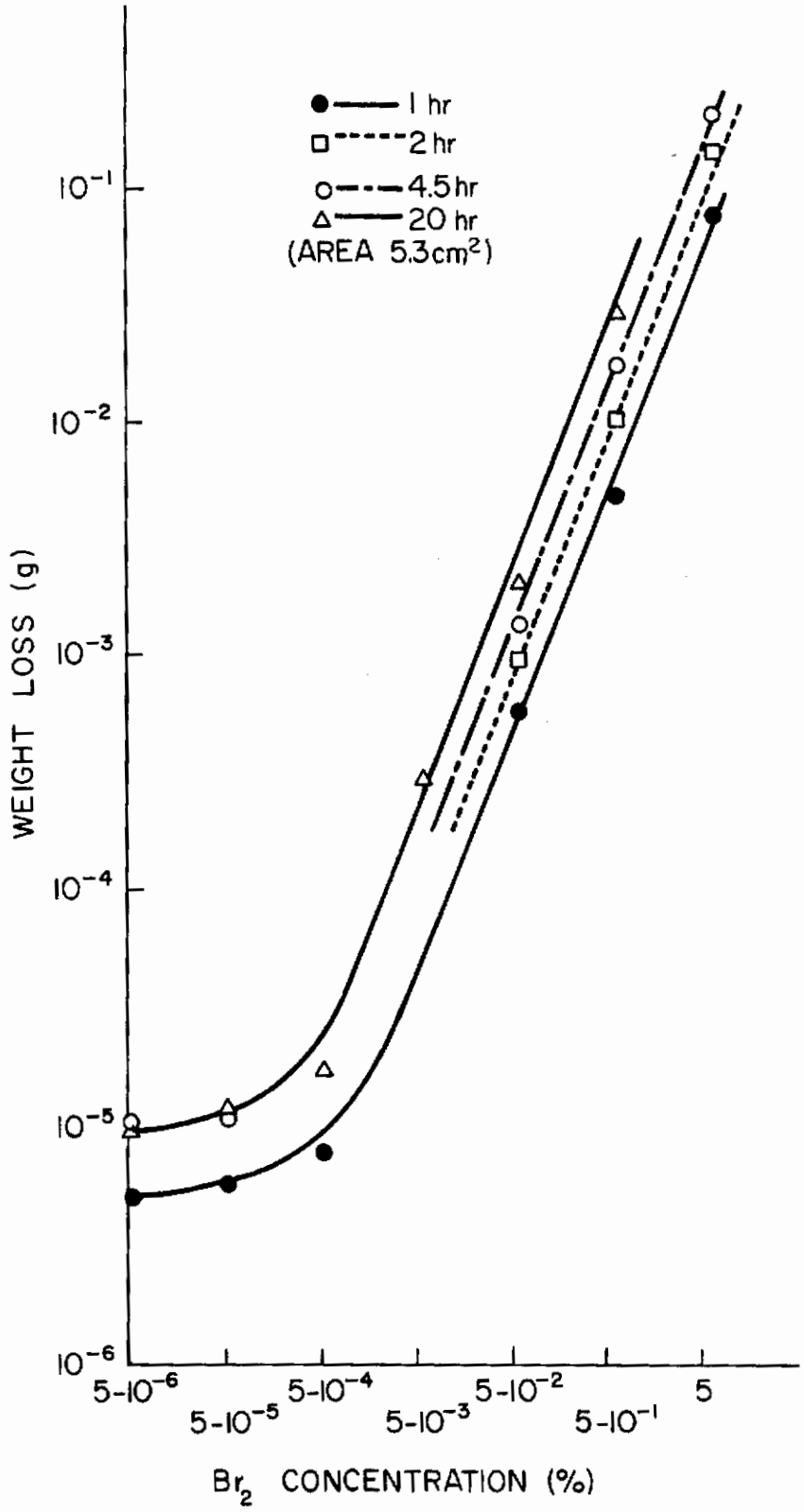

Fig. 40e - Weight Loss of Ti-8Al-1Mo-1V vs. Bromine Concentration in Methanol

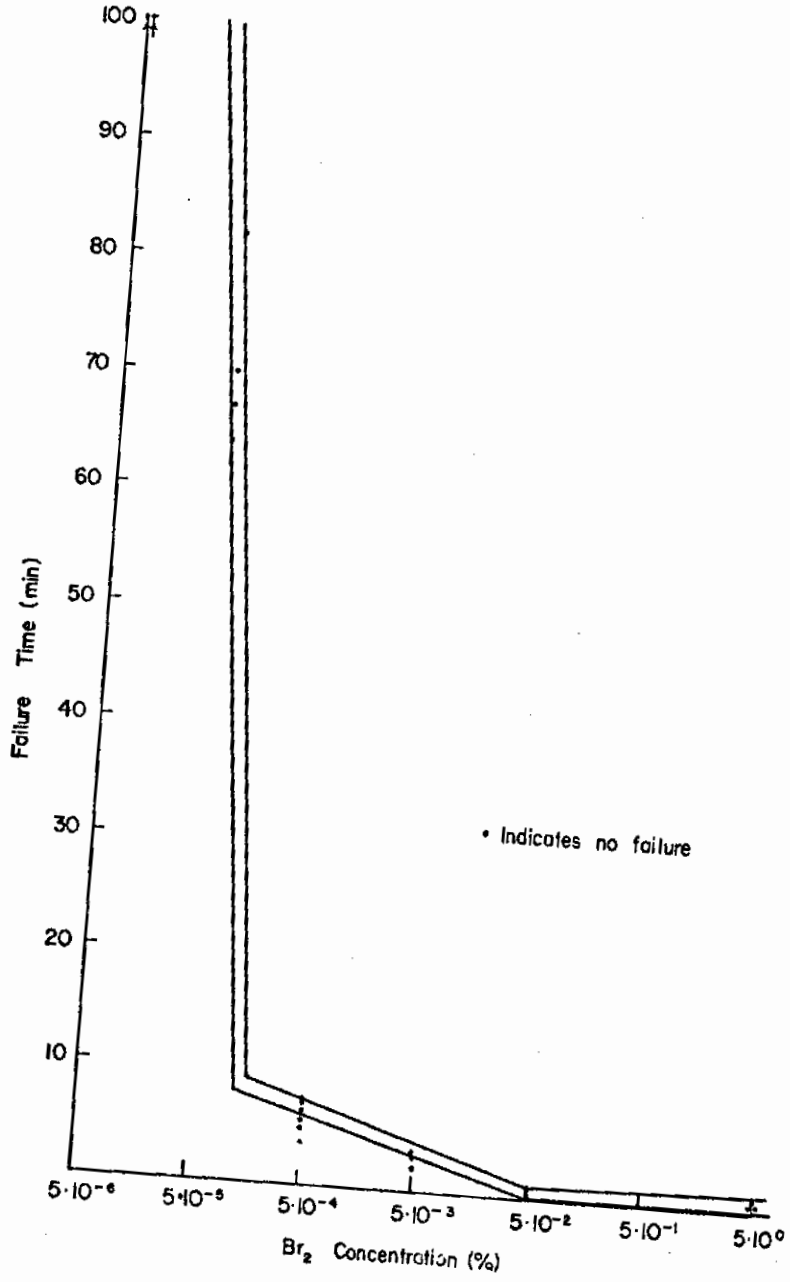

Fig. 41 - Failure Time of β-III Alloy vs. Logarithmic Concentration of Br_2 in CH_3OH (specimen treated at 1700°F for 2 hours and W.Q.)

When the concentration of Br_2 was decreased the failure time increased and there appears to be a linear relationship between the failure time and logarithmic concentration of Br_2. The specimens without mechanical polishing are more susceptible than those with mechanical polishing; the β-III alloy shows the same tendency. Upon decreasing the Br_2 concentration, the failure time decreased at first and then increased linearly with the logarithmic concentration. When the concentration was reduced below $5 \times 10^{-5}\%$ Br_2, the specimen did not fail in 44 hours. Specimens without polishing are more susceptible than those with polishing. The failure time of Ti-6Al-4V was not greatly affected by Br_2 concentration above about 0.05%; reducing the concentration below 0.05% increased the failure time linearly with logarithmic concentration. When the concentration was below $5 \times 10^{-5}\%$ Br_2, the specimen did not fail in 44 hours. Unalloyed titanium specimens without polishing showed the same tendency as Ti-6Al-4V. Specimens with polishing showed minima similar to the Ti-8Al-1Mo-1V and β-III alloys. When the concentration was below $5.10^{-5}\%$ Br_2, the specimens did not fail in 100 hours.

In the case of the Ti-8Al-1Mo-1V alloy, some observations were made of the effect of the relative orientation of the tensile and rolling directions on crack behavior, as illustrated in Figs. 42, 43, and 44. When the tensile direction was perpendicular to the rolling direction, the cracks followed the rolling direction very closely; when the tensile direction was at 45° to that of rolling, the cracks deviated from the rolling direction by about 15°-20°; and when the tensile direction was parallel to the rolling direction, the cracks were oriented both in the rolling direction and at about 15°-20° to it. Fager and Spurr[16] have shown that in the rolled material the (0001) planes are preferentially oriented normal to the plate surface and parallel to the rolling direction. Therefore, orientation of the crack direction at 15°-20° to that of rolling, means that the crack planes approximately follow the $(10\bar{1}7)$ or $(10\bar{1}8)$ cleavage planes.[16,17]

d. Metallographic Observations

(1) When unstressed specimens of unalloyed titanium were dipped in a solution of methanol + 1% Br_2, bromine attacked the grain boundaries; with increased exposure time some of the grains were dissolved out and the material became porous and very brittle. Figure 45 shows the porous material after 68 hours exposure in the solution. This porous material was ground to powder for x-ray analysis to identify the corrosion products. However, it showed a pattern for titanium only.

At moderate tensile stresses, intergranular corrosion and intergranular stress corrosion occur. However, at high stresses, a small amount of transgranular stress corrosion cracking is also observed, as shown in Figure 46.

(2) When the unstressed specimens of heat-treated β-III alloy were exposed to a solution of methanol + 0.05% Br_2, bromine attacked the

Fig. 42 - Stress Corrosion Cracking of Ti-8Al-1Mo-1V in CH_3OH + 0.5% Br_2 X50

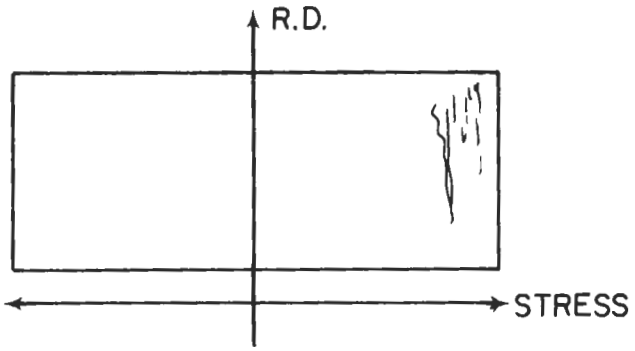

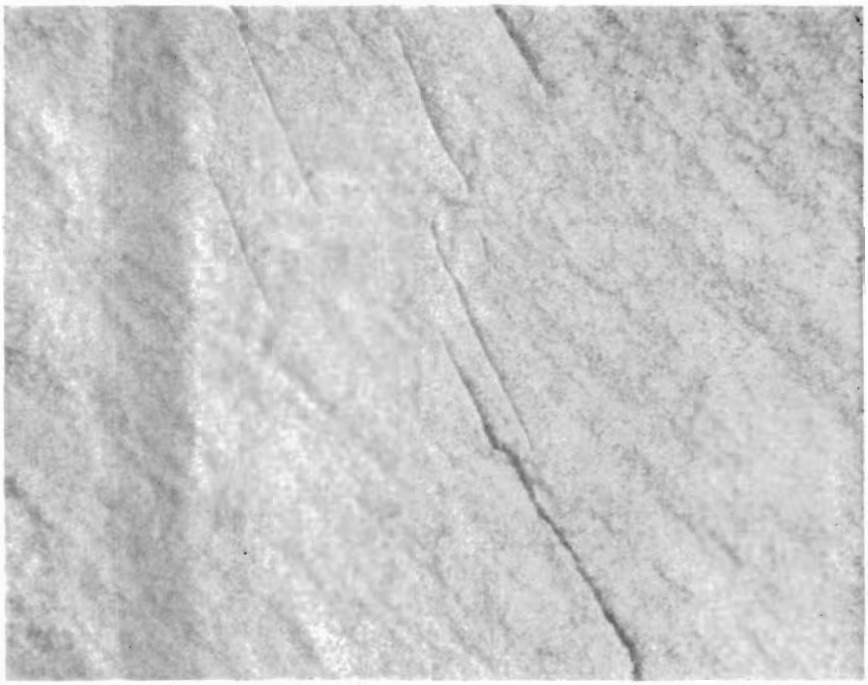

Fig. 43 - Stress Corrosion Cracking of Ti-8Al-1Mo-1V in CH_3OH + 0.5% Br_2 X50

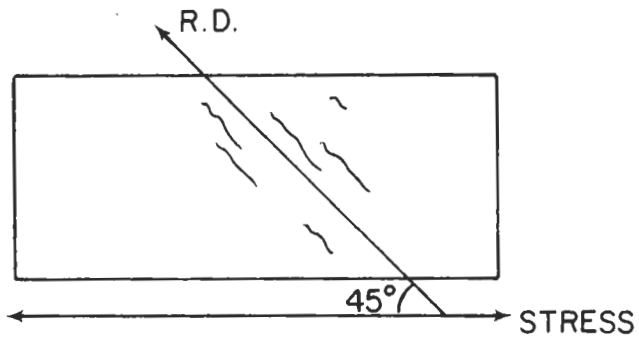

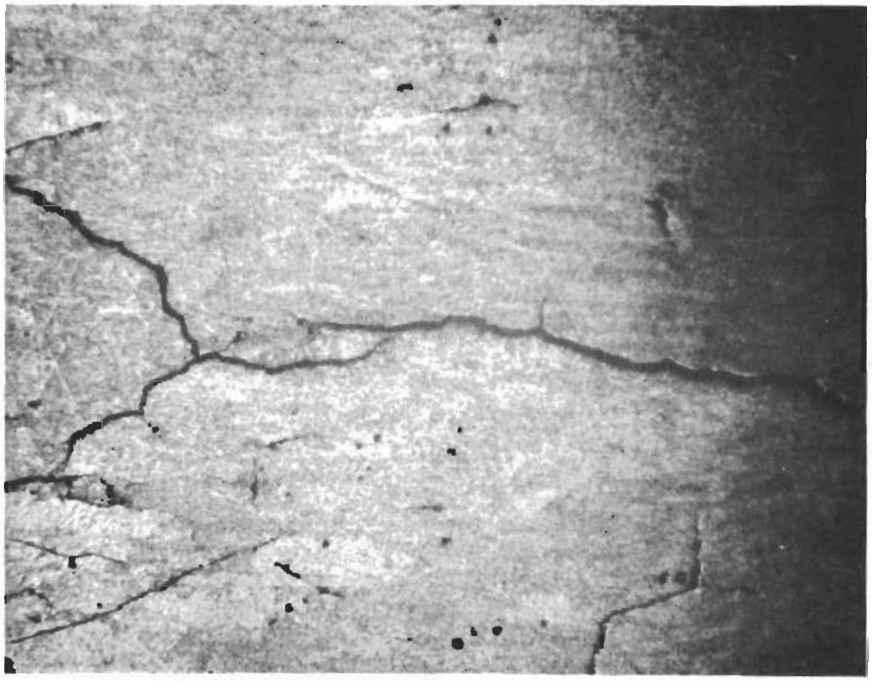

Fig. 44 - Stress Corrosion Cracking of Ti-8Al-1Mo-1V in CH_3OH + 0.5% Br_2 X50

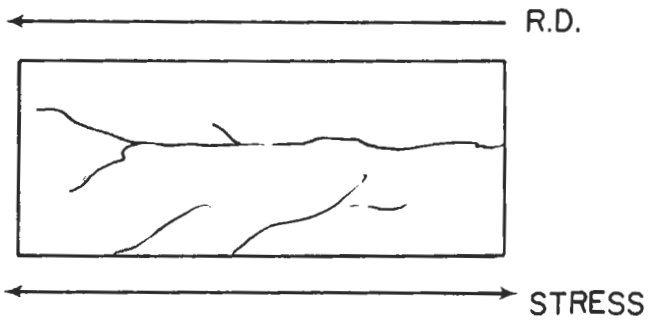

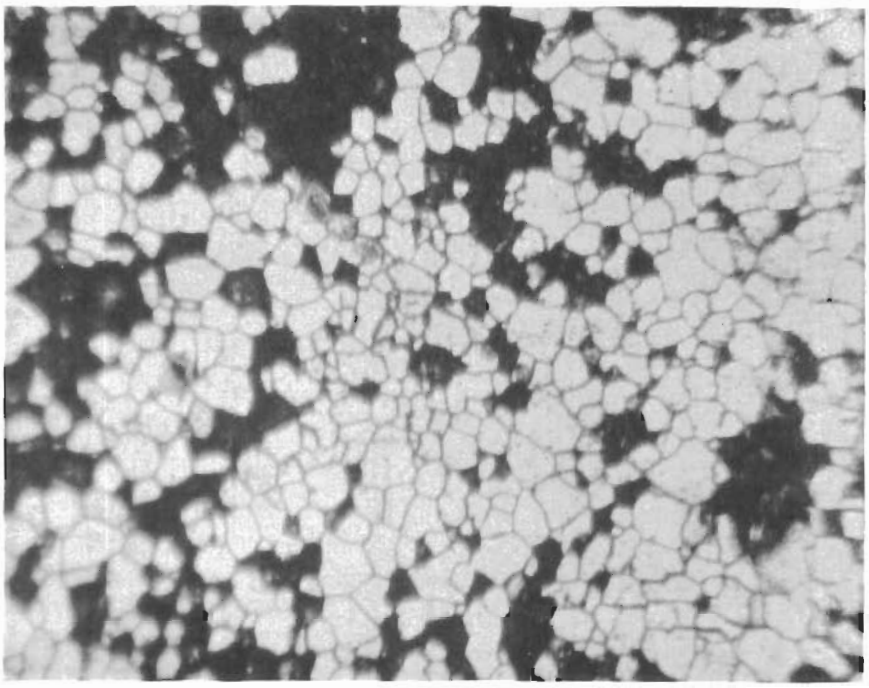

Fig. 45 - Porous Material of Unstressed Unalloyed Titanium Exposed in CH_3OH + 1% Br_2 for 68 Hours (X200)

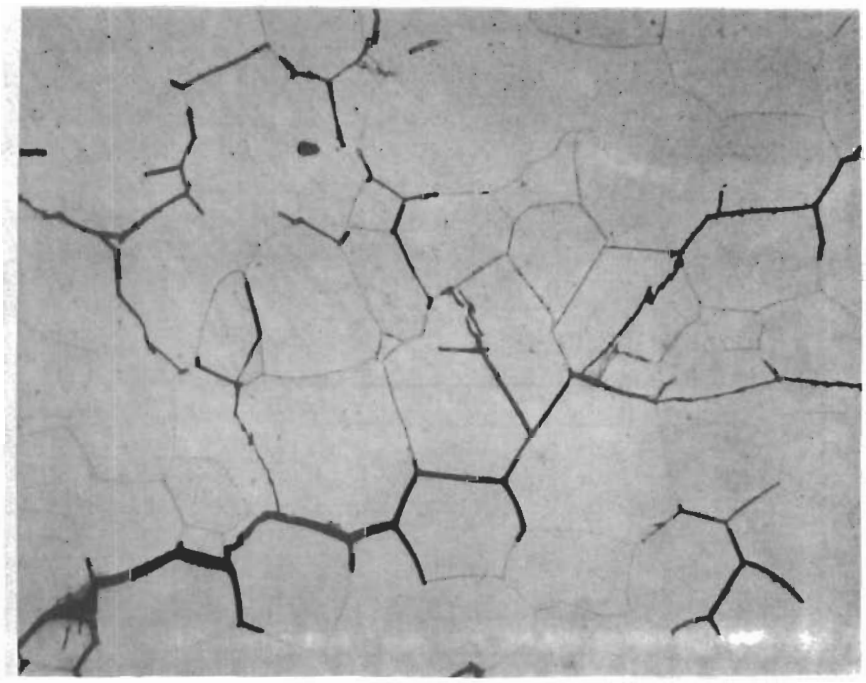

Fig. 46 - Stress Corrosion Cracking of Highly Stressed Unalloyed Titanium (RMI-70) in Methanol + 5% Br_2 Solution (300X)

grain boundaries and the material became very brittle. Figure 47 shows the grain boundary corrosion of β-III exposed in the solution for 164 hours. When external stress was applied transgranular and intergranular SCC occurred as shown in Fig. 48. When the external stress was very high the cracking was almost entirely transgranular and appeared to follow some characteristic crystal plane. The cracks crossed the slip lines (formed by plastic deformation), as shown in Fig. 49.

(3) The heat-treated β-III specimen in methanol + 0.17% HCl + 0.28% H_2O failed by both transgranular and integranular cracking. As shown in Fig. 50 the transgranular cracking follows some characteristic crystallographic direction.

3. Discussion

In CH_3OH + 0.17% HCl + 0.28% H_2O solution, the activation energy of the cracking process for unalloyed Ti, Ti-6Al-4V, Ti8Al-1Mo-1V, and β-III alloys is about 6-7 kcal regardless of the phases present. If stress corrosion susceptibility of these alloys is due to titanium hydride formation by supersaturation of hydrogen in the material, the activation energy for the cracking process should be determined by the hydrogen diffusion process. Therefore, the activation energy should be different: 6.6 kcal in α-phase and 12.4 kcal in β-phase according to Eqs. (1) and (2) for the diffusion coefficients. This may suggest that the diffusion of the chloride ions in the solution plays the important role in the stress cracking process.

In methanol + Br_2 solution there is no doubt about the reaction of bromine with titanium and its alloys to form $TiBr_4$ which is very soluble in the methanol solution. Therefore, it is reasonable to assume that the process in the intergranular stress-corrosion cracking is due to bromine attack as follows:

$$\mathrm{Ti} + 2\mathrm{Br_2} \rightarrow \mathrm{TiBr_4} \downarrow \text{dissolved in methanol} \qquad (9)$$

This reaction occurs at the grain boundary in the absence of an external stress. However, fast transgranular cracking of stressed specimens could result from bromine attack, titanium hydride formation, or stress sorption processes.

E. STRESS-CORROSION CRACKING OF TITANIUM AND ITS ALLOYS IN VARIOUS ENVIRONMENTS (C. H. Chen)

1. Introduction

In addition to the work in the CH_3OH-HCl-H_2O and CH_2OH-Br_2 systems, a number of failure time measurements of U-bend specimens were

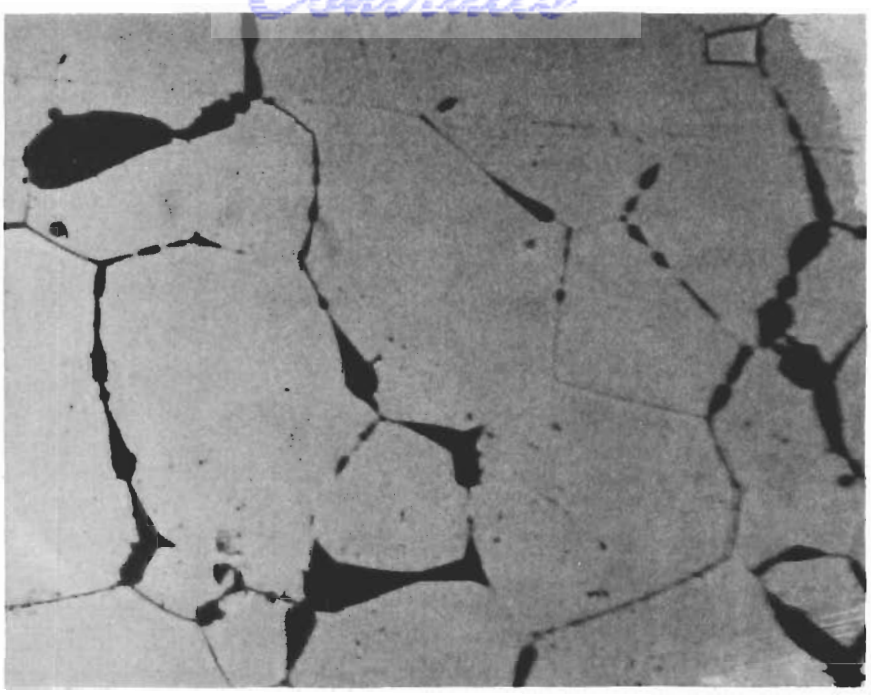

Fig. 47 - Grain Boundary Corrosion of Unstressed β-III Alloy Exposed in CH_3OH + 0.05% Br_2 Solution for 164 Hours (X210)

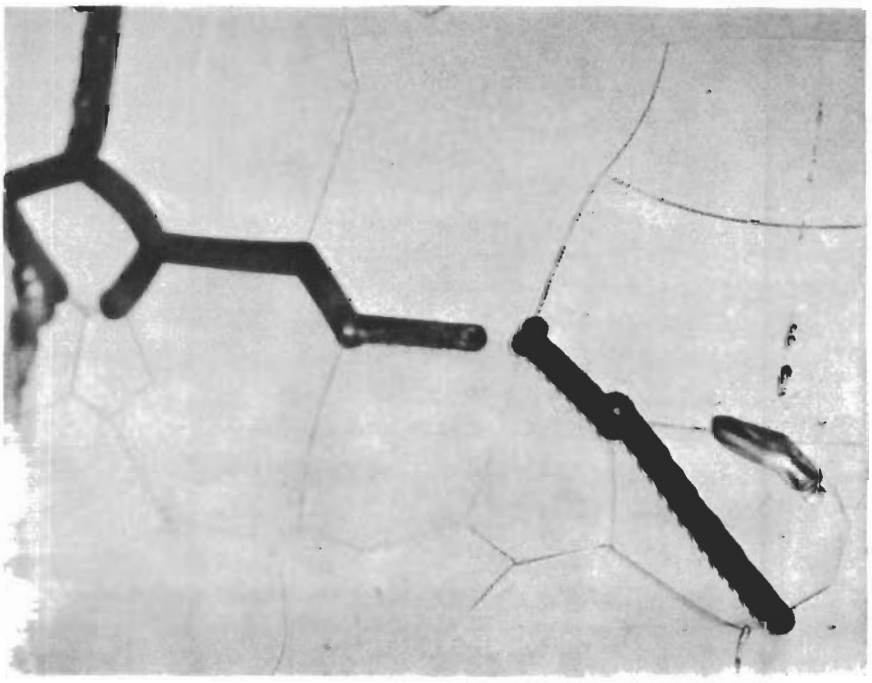

Fig. 48 - Stress Corrosion Cracking of β-III Alloy in CH_3OH + 0.05% Br_2 Solution. (X280)

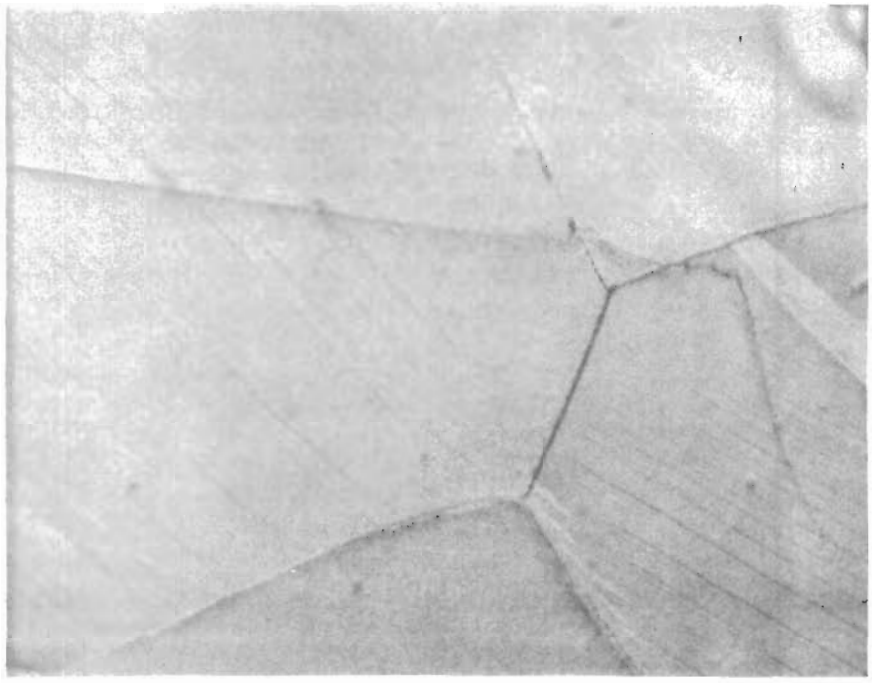

Fig. 49 - Stress Corrosion Cracking of Highly Stressed β-III Alloy in CH_3OH + 0.5% Br_2 Solution; Transgranular Cracking Crosses Slip Lines Formed by Plastic Deformation (X800)

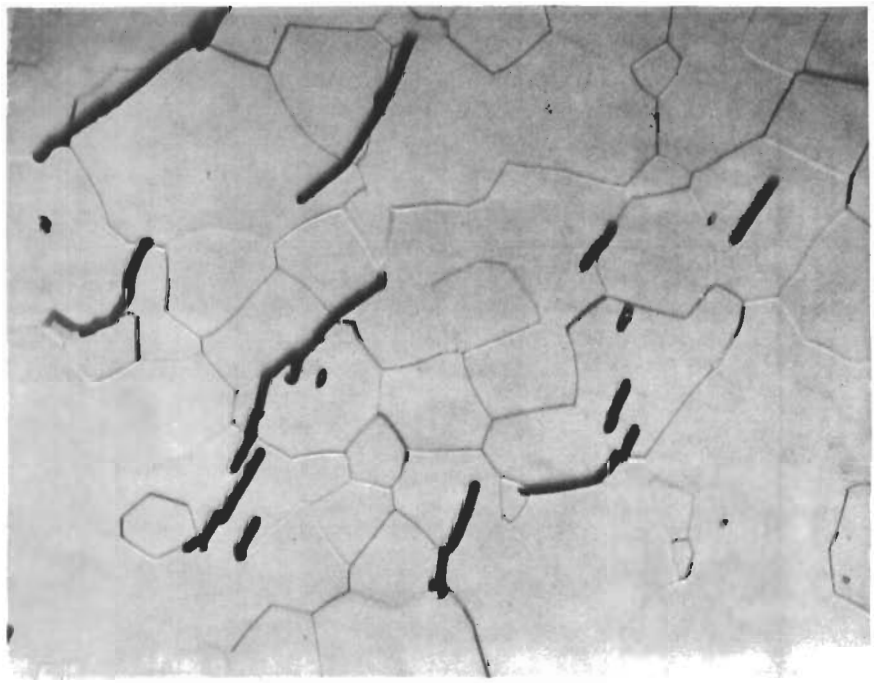

Fig. 50 - Stress Corrosion Cracking of β-III in CH_3OH + 0.17% HCl + 0.28% H_2O Solution (X100)

made in "pure" (as received) solvents and solvents + bromine, in order to note the SCC behavior in the relative absence of water, and effects due to reactions with solvent or the bromine. These results are shown in Table III.

2. Experimental

U-bend stress corrosion specimens of unalloyed titanium (RMI-70) and titanium alloys Ti-6Al-4V, Ti-8Al-1Mo-1V, and Ti-11.5Mo-6Zr-4.5Sn (β-III) were tested in the same manner as previously described. Except for β-III alloy, which was tested in both the as-received and the heat-treated (1700°F for 2 hours and water quenched to provide an all-β phase) conditions, the materials were tested in the as-received condition only.

Test solutions were prepared from reagent grade chemicals. Results and procedures are described in the following section.

3. Results and Discussion

a. Methanol, liquid, absolute, as received

The as-received methanol contains about 0.015% water. In this medium failures were observed in the Ti-8Al-1Mo-1V and β-III alloys after periods of a few hours to several days. The Ti-6Al-4V alloy and the unalloyed RM170 titanium had no failures after 300 hours. For the Ti-6Al-4V alloy, the stress-strain curve in methanol is about the same as in air, having a slightly higher slope and a slightly lowered ultimate elongation. Gegel, Kirkpatrick, and Swinning[18] and Gegel and Fujishiro[19] have reported that when Ti-6-Al-4V was fractured in methanol, TiH_2 was detected on the fracture surfaces by electron diffraction. Whether such hydride formation is causally related to SCC, has yet to be established.

b. Absolute Methanol + CaO Dessicant

Additional measurements were made with methanol containing CaO to lower the water content still further. Under this condition, failures were observed in all the alloys, but not in the unalloyed titanium after 300 hours.

c. Methanol Vapor

Specimens (U-bend) were exposed to methanol vapor by being placed in a dessicator along side a beaker containing liquid CH_3OH over CaO. There was also CaO in the dessicant chamber. Specimen failure occurred in the majority of cases for all three alloys and for the unalloyed metal, and it is interesting that methanol vapor is the only "non-aqueous" medium in which all the metals tested were susceptible. Moreover, the susceptibility to cracking appears to be considerably greater in the vapor than in the as-received liquid absolute alcohol. Except for the unalloyed titanium, the vapor susceptibility is comparable to that in the liquid dried with CaO. Ambrose and Kruger[20] have

Table III - Failure Times for Stress Corrosion Cracking of Titanium and Its Alloys in Organic Solutions

	Ti-8Al-1Mo-IV	Ti-6Al-4V	RMI-70 (Unalloyed Ti)	Ti-11.5Mo-6Zr -4.5Sn (β-III)	β-III (heat treated)
Diethyl Ether	T=1 N.F.=300h	T=1 N.F.=300h	T=1 N.F.=300h	T=1 N.F.=300h	
Diethyl Ether +0.5% Br_2	T=6 F=104m,9m,5m 120m,12m,11m	T=1 F=20h	T=1 N.F.=300h	T=1 F=96h	
Benzene	T=1 N.F.=300h	T=1 N.F.=300h	T=1 N.F.=300h	T=1 N.F.=300h	
Benzene + 0.5% Br_2	T=2 F=65m,100m	T=1 N.F.=300h	T=1 N.F.=300h	T=1 N.F.=300h	
Carbon Tetrachloride	T=3 N.F.=30d	T=3 N.F.=30d	T=3 N.F.=30d	T=3 N.F.=30d	
Carbon Tetrachloride + 0.5% Br_2	T=10 F=3h,10h,20h 23h,30d N.F.=5;30d	T=2 N.F.=300h	T=2 N.F.=300h	T=2 N.F.=300h	T=3 F=1,5h,2h,3h
Methanol	T=8 F=1.5h,3h 101h,20d,20d N.F.=3;30d	T=8 N.F.=300h	T=4 N.F.=300h	T=6 F=44h,60h N.F.=4;200h	
Methanol + CaO	T=4 F=2h,11h,81h N.F.=1;300h	T=4 F=144h,50h 170h,40h	T=2 N.F.=300h	T=6 F=40h,78h,30h 58h,20h,55h	
Methanol Vapor (+CaO)	T=4 F=11h,80h,125h N.F.=1;300h	T=3 F=140h,164h 200h	T=3 F=63h,164h N.F.=1;300h	T=4 F=15h,39h,39h N.F.=1;300h	T=3 F=39h,60h 290h

Failure times of U-bend specimens of as-received titanium and its alloys and heat treated β-III alloy in various media. Tensile stress direction perpendicular to rolling direction. T=total number of specimens tested; F=observed times of failure; N.F.=number not failed after stated time; m=minutes, h=hours; d=days.

reported similar results in the case of unalloyed titanium and Ti-8Al-1Mo-1V and have also reported the detection of formaldehyde in the reaction vessel. On this basis they discussed the possible connection of the stress corrosion cracking with the catalytic dehydrogenation of methanol on the metal surface, according to the reaction

$$CH_3OH = HCHO + H_2 \quad . \tag{10}$$

Since the reaction produces hydrogen, it is tempting to regard the cracking as resulting from hydrogen embrittlement, but on the basis of their results Ambrose and Kruger advance several arguments against this. Reaction (10) is not the only one capable of producing hydrogen. Gegel, Kirkpatrick, and Swinning[18] suggested that titanium might react with anhydrous methanol to form hydrogen and titanium methoxide;

$$Ti + 4CH_3OH = Ti(OCH_3)_4 + 2H_2 \quad . \tag{11}$$

Subsequently, Leith, Hightower, and Harkins[21] demonstrated the occurrence of such a reaction between anhydrous methanol vapor and vacuum-deposited films of titanium, in the temperature range 120°-150°C. The addition of water vapor inhibited the reaction and the addition of hydrogen chloride gas greatly increased the rate of disappearance of the metal film, even at room temperature. The similarity of these effects of water and hydrogen chloride to their effects in the aqueous alcohol solutions, plus the fact that reaction (11) is a "corrosion" reaction involving consumption of the metal, would seem to favor reaction (11) as the one involved in cracking by the methanol vapor, rather than the catalytic reaction (10). On the other hand, given the formaldehyde formation reported by Ambrose and Kruger, it would seem that that reaction (10) actually occurred under their conditions; i.e., U-bend specimens highly strained, probably past their yield point. A dehydrogenation reaction similar to (10) occurs with ethanol in the presence of nickel or copper catalysts, forming acetaldehyde;

$$C_2H_5OH \xrightarrow[Cu]{Ni\ or} CH_3CHO + H_2\uparrow \quad . \tag{12}$$

Kishimoto[22] and Uhara, et al.[23] have shown that the active sites of the catalysis in this reaction are lattice defects; i.e., vacancies or termination points of dislocation lines at the metal surface. Thus, if the U-bend specimens of Ambrose and Kruger were more highly strained than the films of Leith, Hightower, and Harkins, as seems likely, reaction (10) might have been favored over reaction (11). Heterogeneous catalysis processes are known to be sensitive to crystallographic orientation and it may be significant that when heat-treated β-III alloy was exposed to methanol vapor, the transgranular cracks appeared to lie along {001} planes, as shown in Fig. 51.

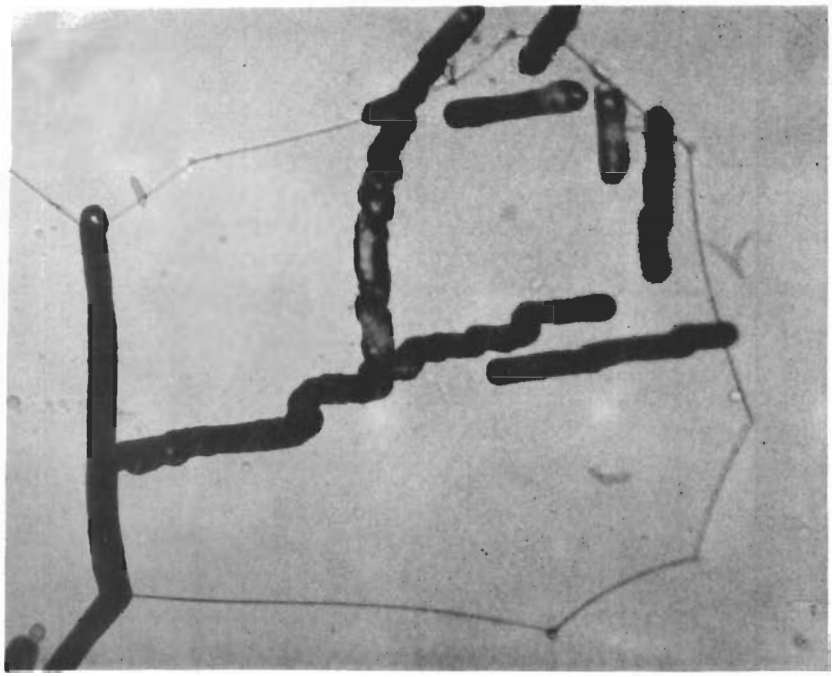

Fig. 51 - Transgranular Stress Corrosion Cracking of Heat-treated β-III Alloy in Methanol Vapor X800

d. "Pure" Solvents

U-bend specimens were exposed to as-received reagent grade benzene, diethyl ether, and carbon tetrachloride. No failures were observed in these environments after 300 hours in the case of benzene and ether, and after 30 days in carbon tetrachloride. However carbon tetrachloride has been reported to accelerate crack growth in notched pre-cracked specimens of Ti-8Al-1Mo-1V.[24,25]

e. Methanol-Carbon Tetrachloride Mixtures

Aluminum alloys containing copper or zinc have been reported to be severely corroded by mixtures of carbon tetrachloride and methanol, more rapidly than by the individual constituents.[26,27] In order to see if there was a similar effect in the stress corrosion of titanium, specimens of unalloyed RM170 titanium were exposed to mixtures of as-received solvents in the range 10-80% by volume CCl_4. In these mixtures, failures occurred after 100-200 hours (Fig. 52), whereas there were no failures after 300 hours in methanol and after 30 days in carbon tetrachloride. Thus there did appear to be some increase of susceptibility. In this case the failures were presumably associated with the reactions

$$CCl_4 + CH_3OH = CHCl_3 + HCHO + HCl \qquad (13)$$

and

$$CHCl_3 + CH_3OH = CH_2Cl_2 + HCHO + HCl \ . \qquad (14)$$

f. Solvents Containing 1/2% Br_2

In order to examine non-aqueous corrosion and the effects of type of solvent on SCC susceptibility, failure time tests were carried out in as-received benzene, ethyl ether, and carbon tetrachloride containing 1/2% dissolved bromine. Results are shown in Table III. In the carbon tetrachloride solution, failures occurred only with part of the Ti-8Al-1Mo-1V specimens and with heat-treated β-III alloy. In the benzene solution, Ti-8Al-1Mo-1V specimens failed fairly rapidly but there were no failures of the other alloys or the unalloyed titanium. In the ether-bromine solution there was a slow failure of as-received β-III and rapid failure of Ti-8Al-1Mo-1V. In the case of the Ti-8Al-1Mo-1V alloy there was noticed a reduction in time to failure as successive specimens were tested in the same ether-bromine solution. Thus, as shown in Table III, the first specimen failed in 104 minutes. After the solution had stood overnight, succeeding specimens failed in nine and five minutes. Upon repeating the test, after the first specimen had failed at 120 minutes, a new specimen was put in immediately and failed in 12 minutes, and the next in 11. This shortening of failure time seems to be due to accumulation of some reaction product in the solution, rather than an aging effect observed by Cocks, et al. in methanol-bromine solutions and attributed to a photochemical reaction between bromine and methanol vapor.[28]

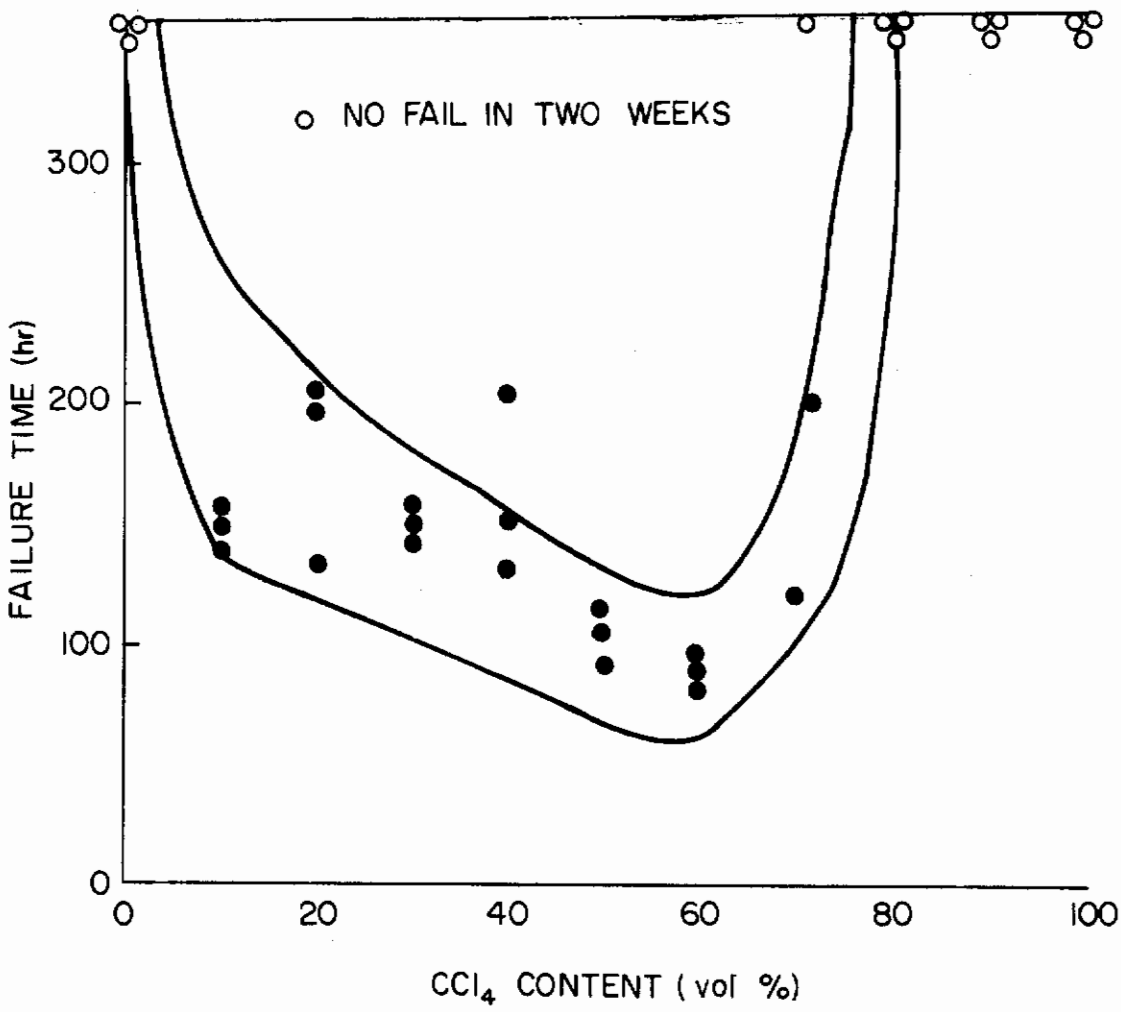

Fig. 52 - Failure Times of Unalloyed RMI-70 Titanium Carbon Tetrachloride Content in CH_3OH + CCl_4 Mixtures

F. EFFECT OF APPLIED POTENTIAL ON CRACK INITIATION AND GROWTH FOR Ti-6Al-4V ALLOY IN METHANOL-WATER-SODIUM CHLORIDE SOLUTIONS (E. J. Timmer)

(This investigation was completed and was the basis of a thesis by E. J. Timmer who received the M.Sc. degree in March, 1969)

1. Introduction

Much experimental work has been reported on the stress-corrosion cracking of titanium alloys in corrosive environments. In most of this literature the stress-corrosion cracking susceptibility was based on the total time-to-failure of the specimens. However, this total time-to-failure can be divided into two stages; i.e., a crack initiation stage and a crack propagation stage. To date, very little work has been performed to separate the mechanisms occurring during these two stages of the stress corrosion process.

The purpose of this investigation was to study the crack initiation stage and the crack growth stage in the Ti-6Al-4V alloy in CH_3OH-H_2O--NaCl solutions and to determine the mechanisms involved. Stress corrosion tests were conducted using smooth bend specimens which were observed at a magnification of 60X during the tests. The effects of applied potential, stress level, and environment upon the crack initiation time, failure time, and crack velocity were investigated. From these results a mechanism for the stress-corrosion cracking of Ti-6Al-4V alloy was proposed.

2. Experimental

A schematic diagram of the apparatus used in this investigation appears in Fig. 53. It consists of a pyrex cell in which the specimen and specimen holder were immersed in the methanol solution, a Luggin probe placed near the sample surface, a saturated calomel reference electrode, a Bausch and Lomb binocular viewer, and a Wenking potentiostat. The Bausch and Lomb viewer provided a magnification of 60X for viewing the stress-corrosion specimen during the test.

The specimen holder, constructed of fused silica, contained a 2-inch long slot to receive the stress corrosion bend specimen. Metal contacts of Ti-6Al-4V at the ends of the slot were used to provide an accurate and constant gage length and to provide an electrical connection from the specimen to the potentiostat. (One of the contacts was of sufficient length to extend above the solution level to an electrical lead. The contacts were painted with micro-stop insulation and covered with Teflon tape to prevent corrosion in these areas during the tests.) The specimens were placed in the holder by inserting a small diameter rubber-coated steel rod under the specimen and then snapping the ends of the specimen into the metal contacts.

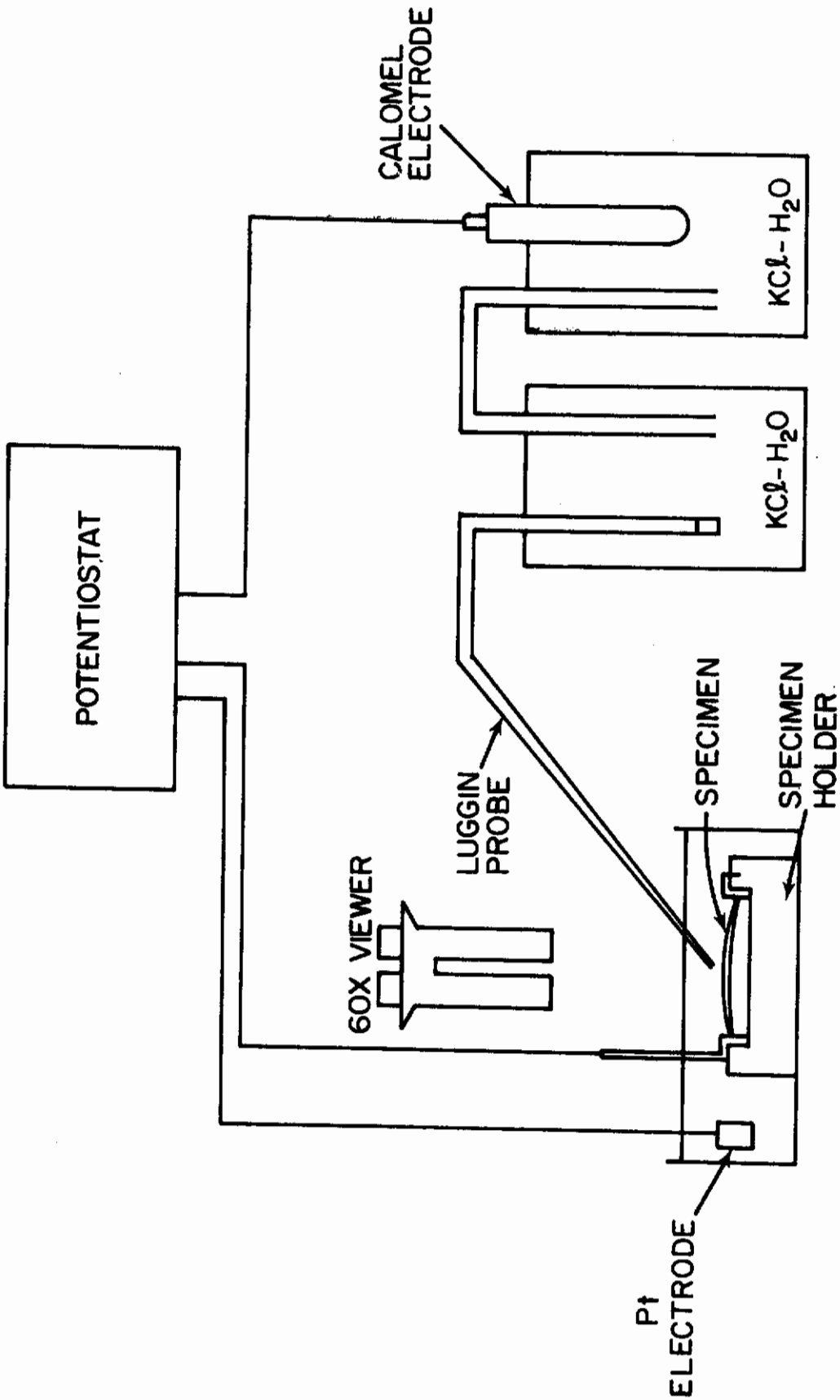

Fig. 53 - Experimental Apparatus

The load applied to the outer fibers of the bend specimens was varied by changing the specimen length, and was calculated from the equation

$$S = \frac{2q^2Et}{Du}, \qquad (15)$$

where

S = maximum tentile stress in the outer fibers,

E = Young's modulus,

t = thickness of the sheet,

D = distance between metal contacts (gage length), and

q and u = parameters that are functions of the ratio of specimen length to D.

Stress corrosion specimens were made from the alloy sheet of the composition given in Table IV. This Ti-6Al-4V sheet was solution heat treated and then aged in a vacuum of 5 x 10^{-5}mm Hg at 1100°F for six hours and furnace cooled. This heat treatment has been reported to give high susceptibility to stress corrosion cracking because of the presence of short-range order in the alloy by formation of Ti_3Al domains. All samples were cut so that the longitudinal direction of the specimen corresponded to the rolling direction of the sheet. Specimens were 0.25" wide X 0.025" thick, and of a length predetermined to give the desired stress level when placed in the holder. The specimens were then lightly cleaned on all surfaces on 280-grit paper to remove excessive oxide; and finally, one of the large surfaces was metallographically polished through number 2 alumina. This polished surface was placed in tension and viewed during the test.

The specimen and holder were then placed into the test cell, electrical connections were made, and the CH_3OH-H_2O-NaCl solution was added. The Luggin probe was then positioned adjacent to the surface of the specimen being examined and the desired potential was applied. When the potential was applied a clock was started and continuous observation of the specimen surface at 60X was begun by scanning the stress-corroding surface for cracks. The time for the first crack to be formed was recorded as the initiation time, and failure time was recorded when the sample was cracked into two parts. Crack velocity was measured on the tension surface of the specimen between cross-hairs as soon as the crack began to propagate from the pit. Current measurements were also recorded for some specimens during the tests.

Table IV - Chemical Compositions of Titanium Alloys (0.025" sheet)

Element	Ti-8Al-1Mo-1V w/o	Ti-6Al-4V w/o
Al	7.85	6.30
V	1.05	4.10
Fe	0.13	0.19
Mo	1.1	
C	0.02	0.03
N	0.008	0.01
O	0.08	0.106
H	102 ppm	60 ppm
Ti	balance	balance

In order to determine the cracking path, the failed specimens were examined with the light microscope in the etched and unetched conditions at magnifications up to 2000X. The specimens were not repolished prior to examination so that the effects of stress-corrosion cracking would not be obliterated. In addition, replicas were made of the fracture surfaces of several specimens to provide electron fractographs. The two-step plastic-carbon replication technique was used.

3. Results

The results of the experimental work appear in Figs. 54 through 69. Figures 54 through 61 present the effects of applied potential, stress, percent water, and sodium chloride concentration upon the crack initiation time, failure time, and crack velocity. Figures 62 through 68 show the results of the metallographic examinations.

a. Effect of Potential

The effect of applied potential on crack initiation time, total failure time, and crack velocity is shown in Figs. 54 and 55. In these tests, the bend specimens were stressed to 80% of the yield stress in the outer fibers, and were immersed in a CH_3OH-0.3% H_2O-saturated NaCl solution. This solution was shown by several investigators[29,30,31] to be the most effective in causing stress-corrosion cracking of titaium alloys. From Fig. 54, the Ti-6Al-4V alloy was susceptible to stress-corrosion cracking over a wide range of applied potentials, from approximately -650 mV to +500mV (SHE). The crack initiation time and total failure time decreased significantly in this range with increasing anodic potential, and were minimum near +150mV (SHE). Crack velocity measured on the tension surface, however, increased only slightly with increasing potential, and was approximately 0.003 mm/sec in the susceptible potential

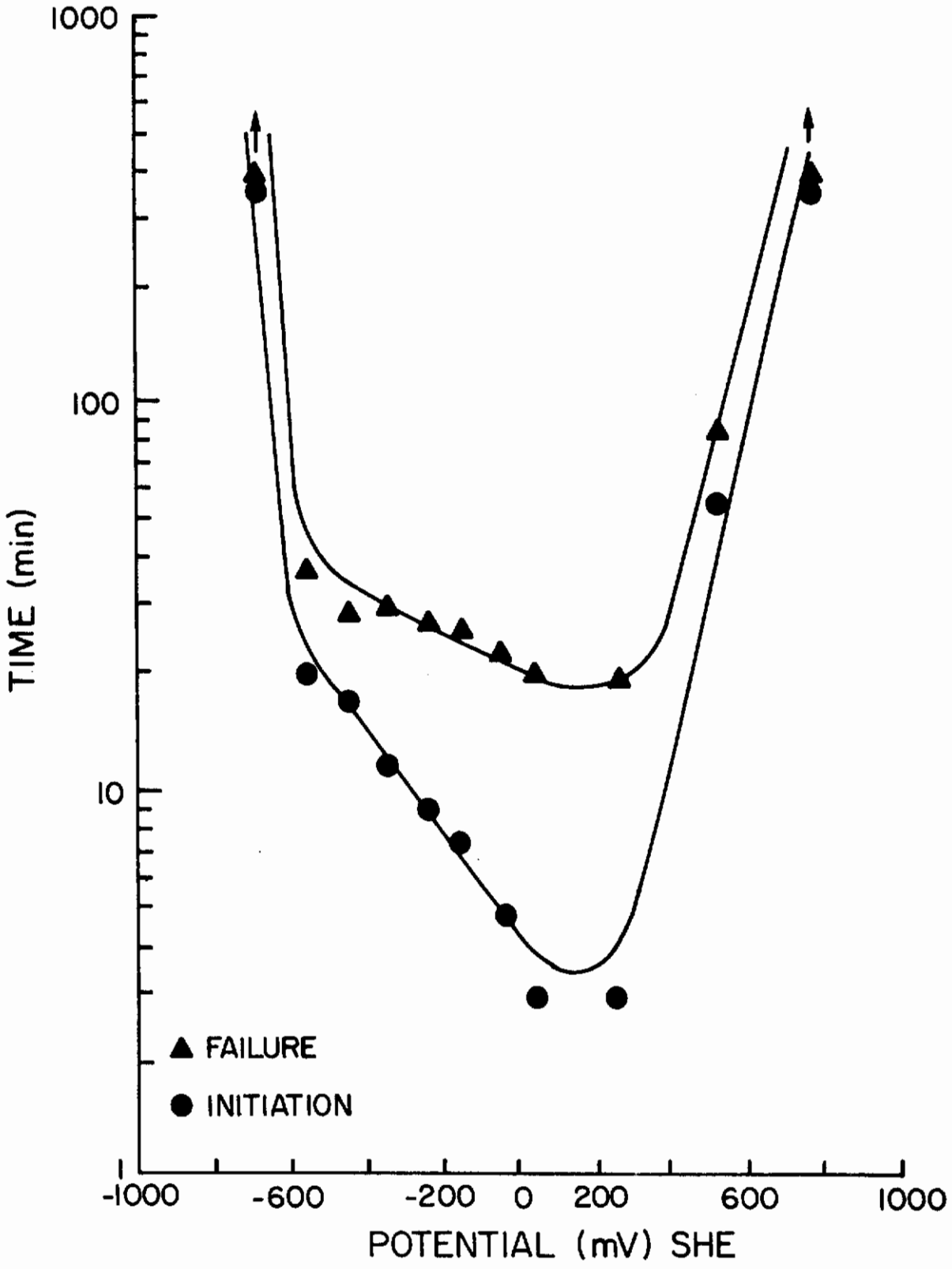

Fig. 54 - The Effect of Applied Potential upon Crack Initiation Time and Failure Time in Methanol-0.3% Water and Saturated NaCl (specimens stressed to 80% of yield stress)

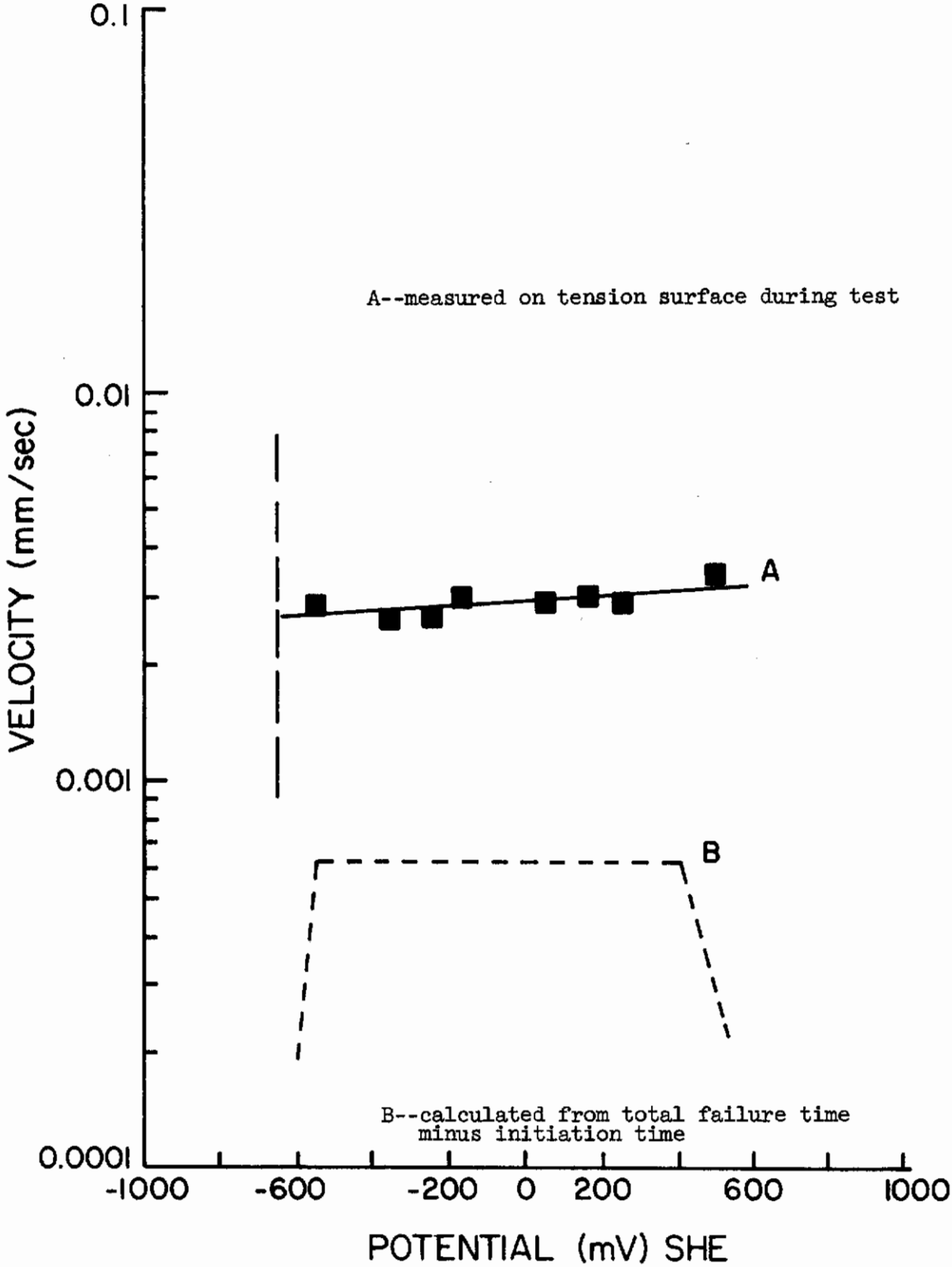

Fig. 55 - The Effect of Applied Potential upon Crack Velocity in Methanol-0.3% Water and Saturated NaCl (specimens stressed to 80% of yield stress)

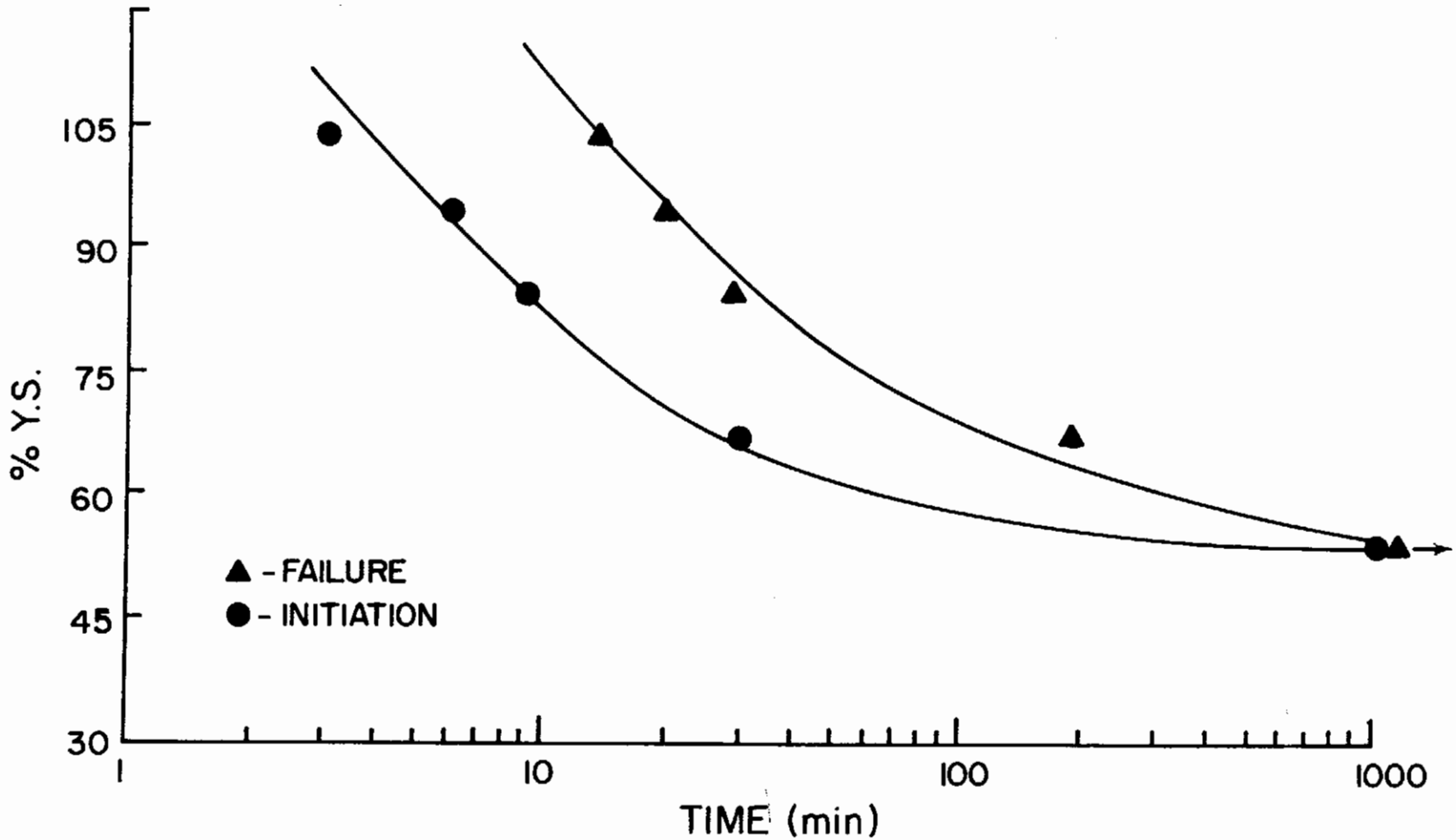

Fig. 56 - The Effect of Stress Level upon Crack Initiation Time and Failure Time in Methanol-0.3% Water and Saturated NaCl at 0 mV

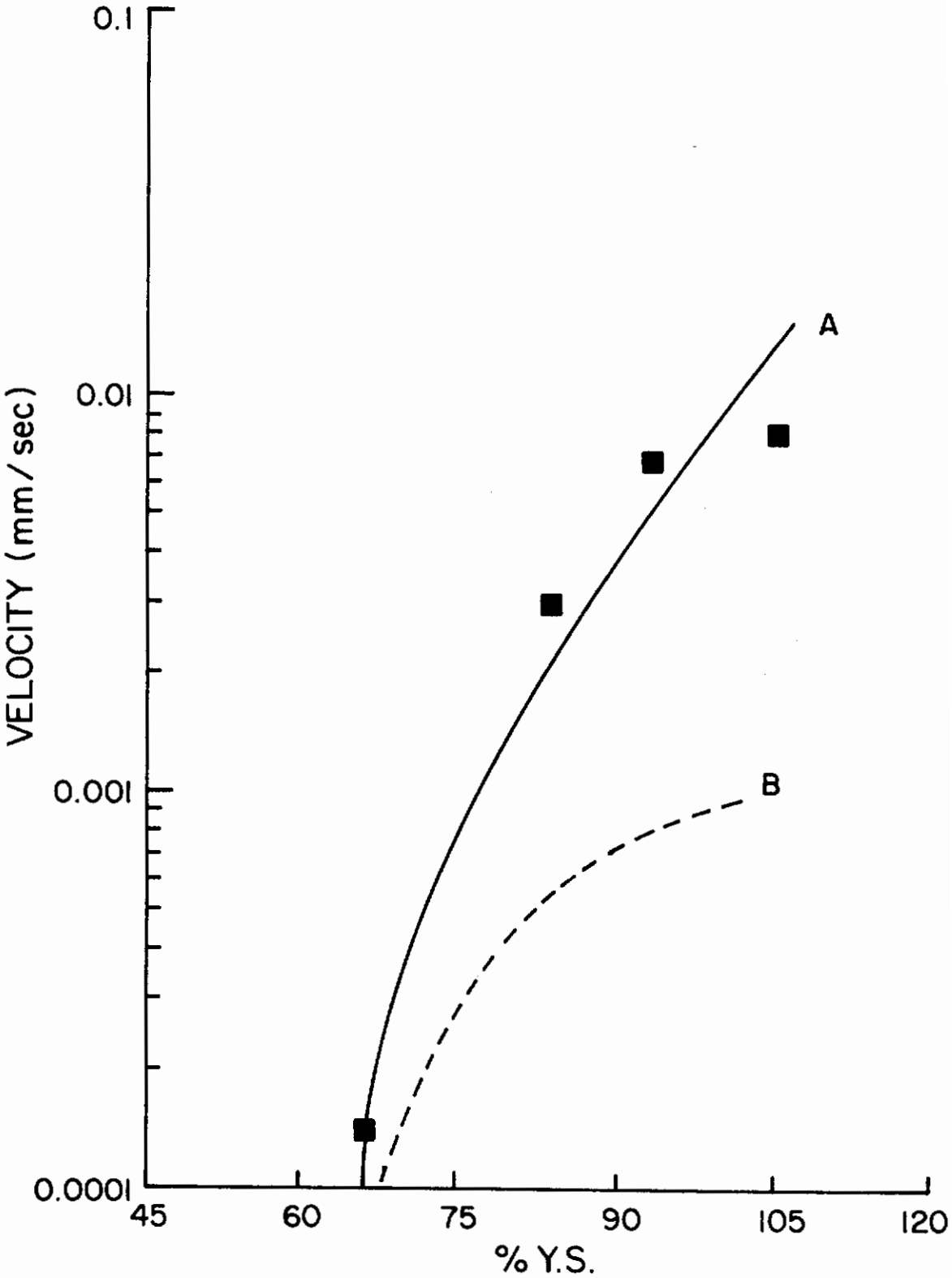

Fig. 57 - The Effect of Stress Level upon Crack Velocity; Specimen Polarized at 0 mV in Methanol-0.3% Water Saturated NaCl
A--measured on tension surface during test
B--calculated from total failure time minus initiation time

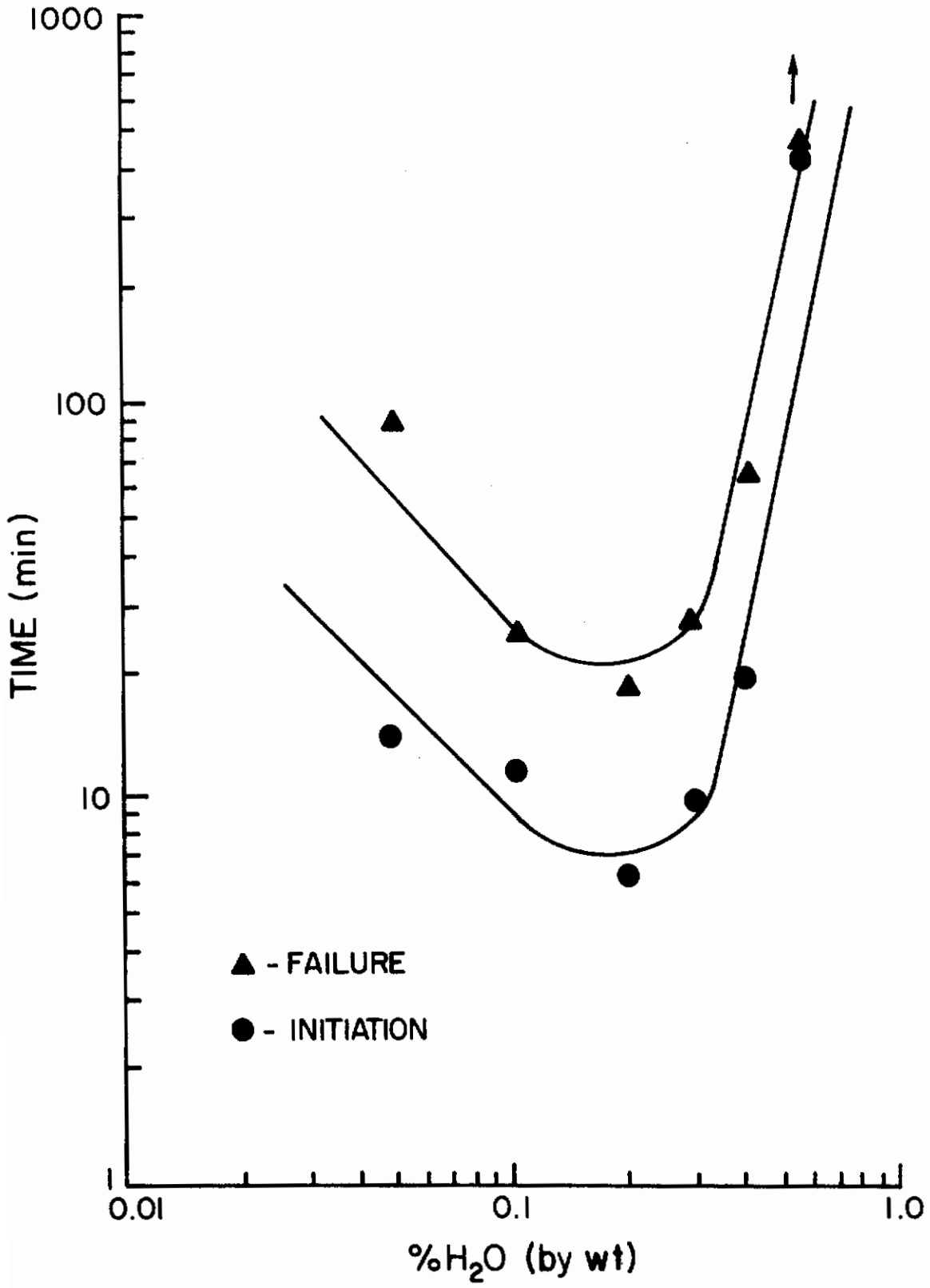

Fig. 58 - The Effect of Water Content upon Crack Initiation Time and Failure Time. Specimens Polarized at 0 mV and Stressed to 80% of the Yield Strength in Methanol-Saturated NaCl

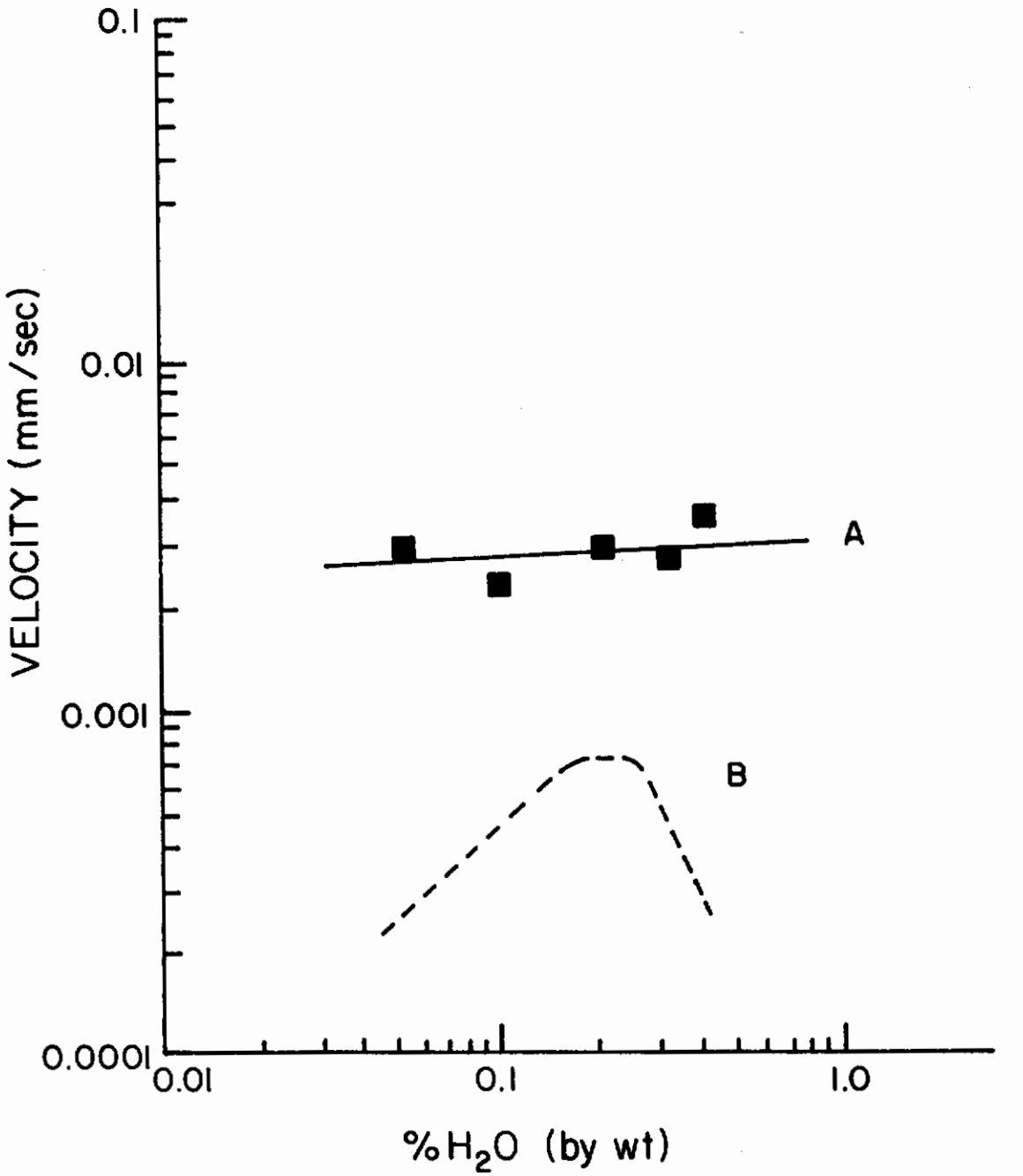

Fig. 59 - The Effect of Water Content upon Crack Velocity. Specimen Polarized at 0 mV and Stressed to 80% of the Yield Strength in Methanol-Saturated NaCl
A--measured on tension surface during test
B--calculated from total failure time minus initiation time

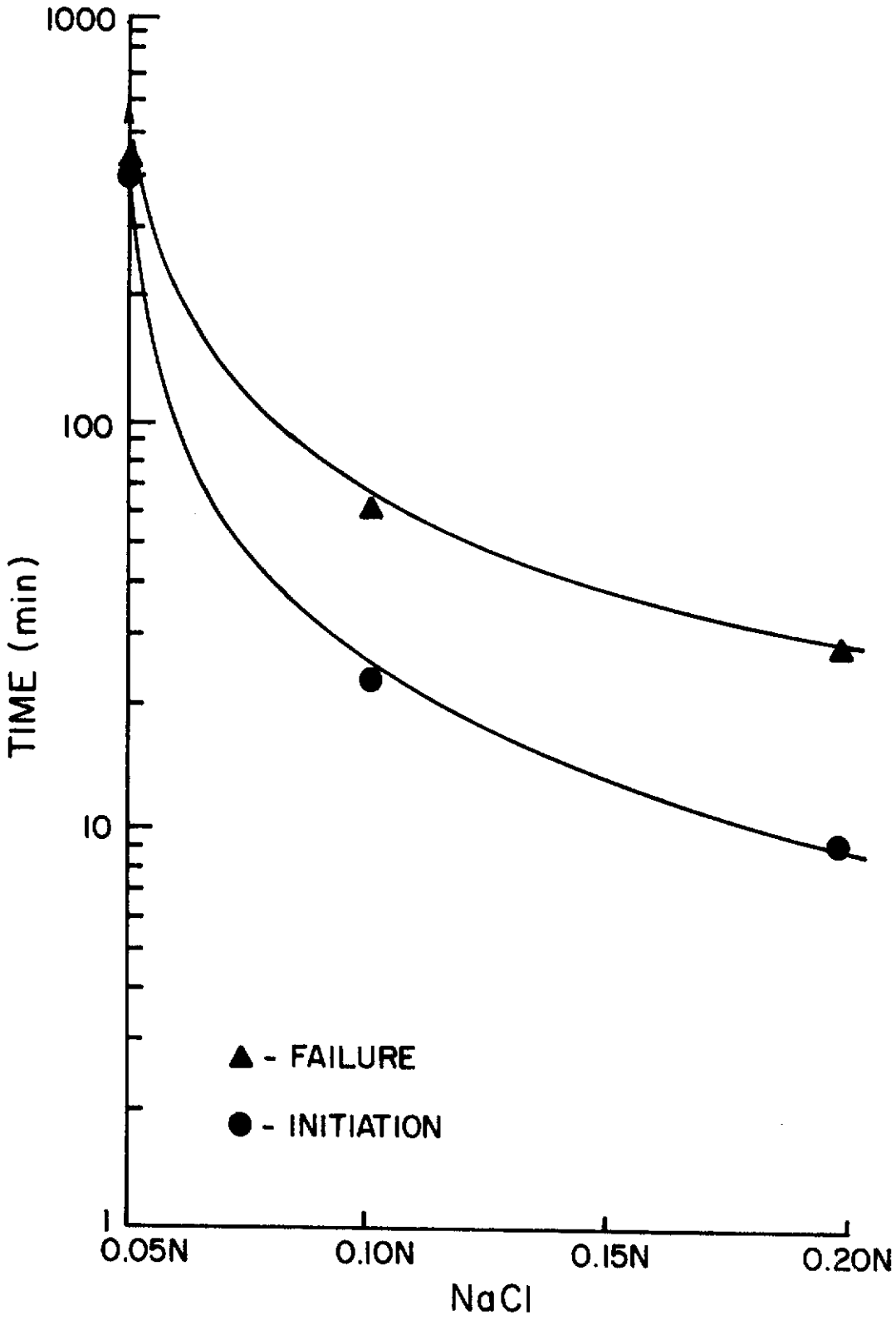

Fig. 60 - The Effect of NaCl Content upon Crack Initiation and Failure Times. Specimens Polarized at 0 mV and Stressed to 80% of the Yield Strength in Methanol-0.3% Water

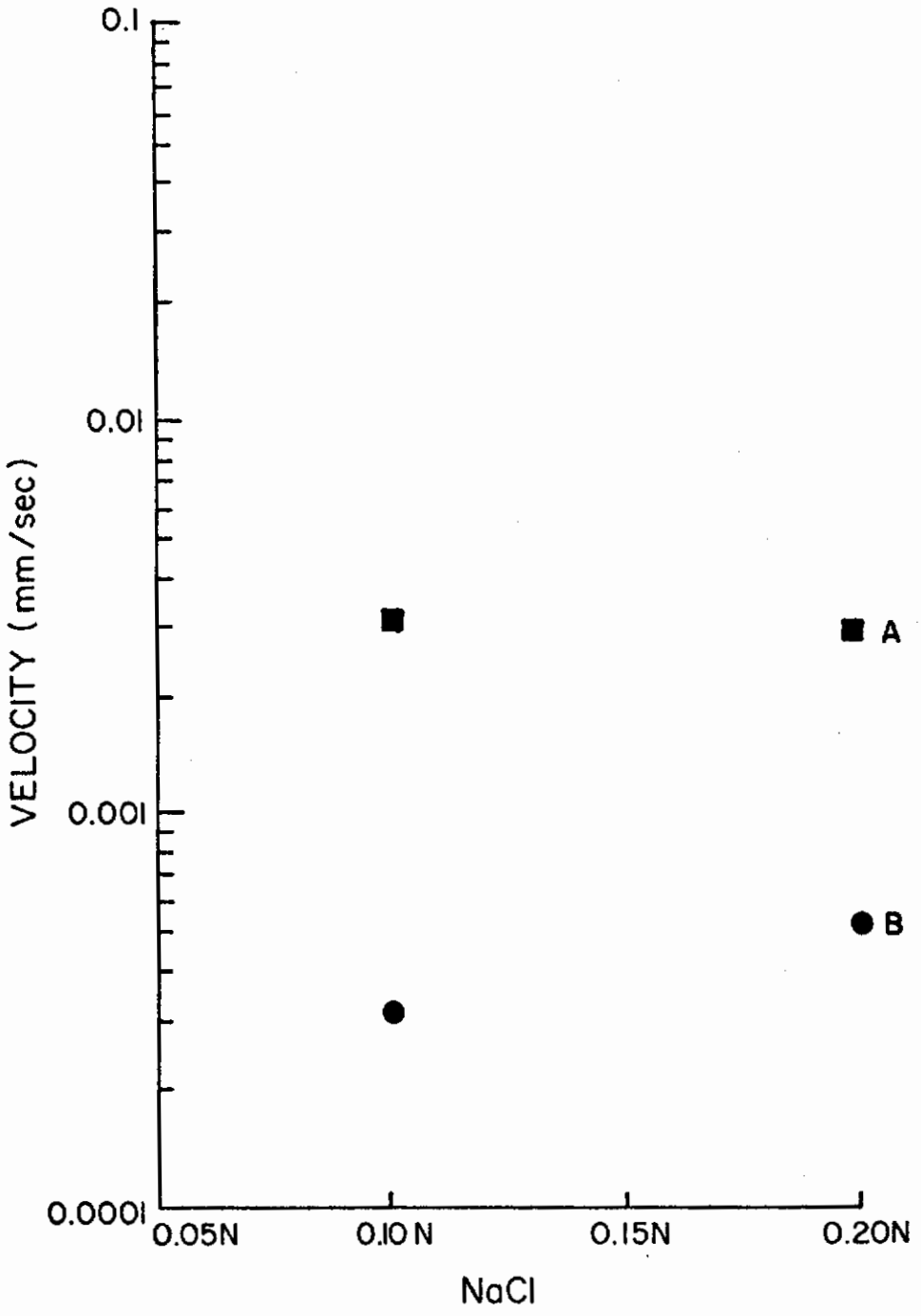

Fig. 61 - The Effect of NaCl Content upon Crack Velocity. Specimens Polarized at 0 mV and Stressed to 80% of Yield Strength in Methanol-0.3% Water
A--measured on tension surface during test
B--calculated from total failure time minus initiation time

Fig. 62 - Crack Propagation from a Pit
X250

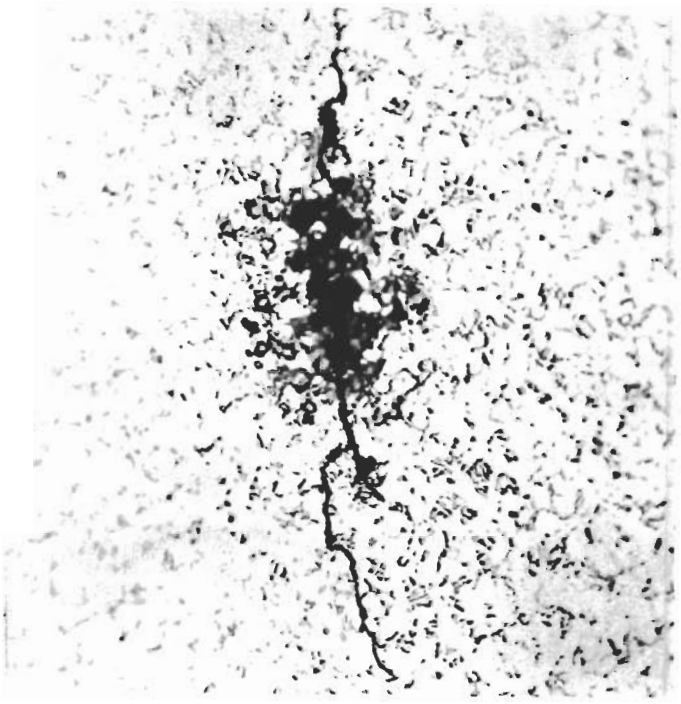

Fig. 63 - Crack Propagation from a Pit
Kroll's Etch X500

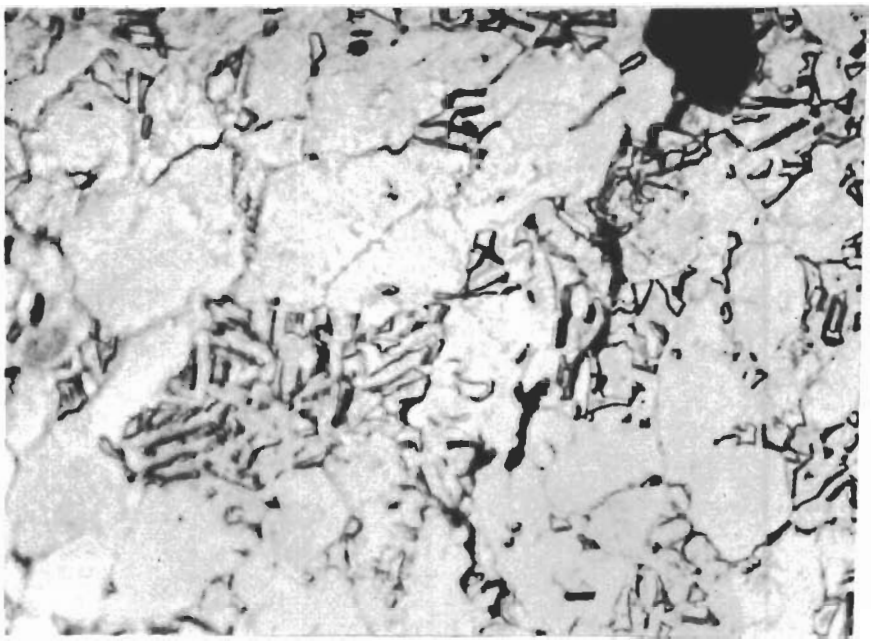

Fig. 64 - Preferential Corrosion at the α-β Interface and β Phase in Ti-6Al-4V (note: pit at top of picture)
Kroll's Etch X2000

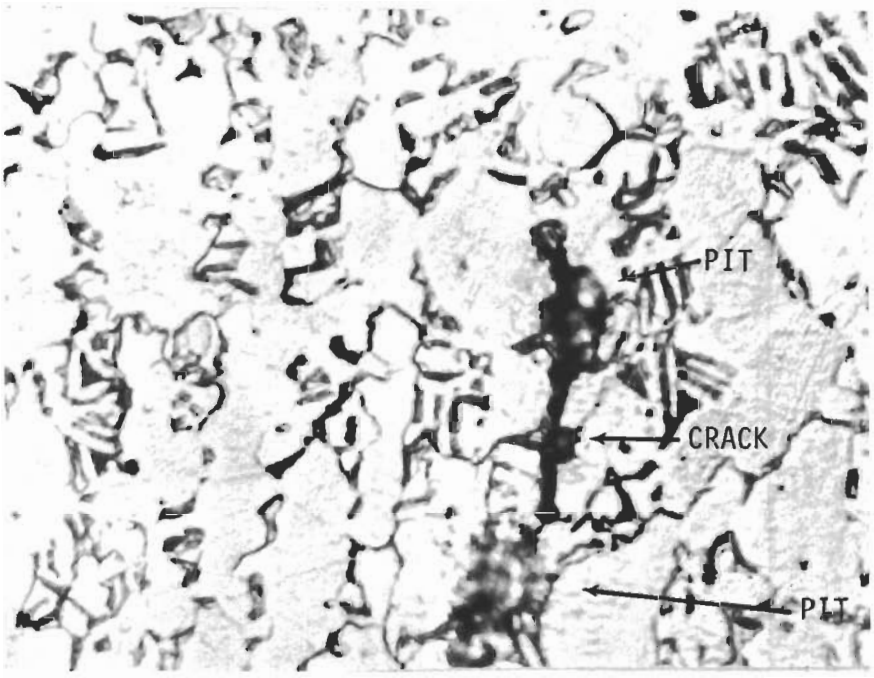

Fig. 65 - Preferential Corrosion at the α-β Interface and β Phase in Ti-6Al-4V (note: micro-crack between two small pits)
Kroll's Etch X2000

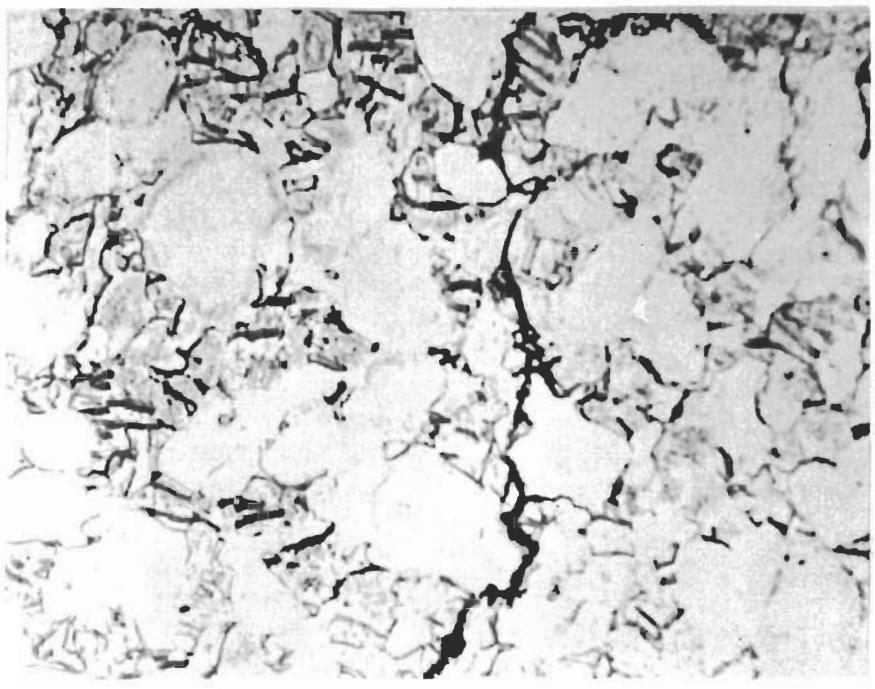

Fig. 66 - Cracks in a Failed Ti-6Al-4V Specimen (note: black areas associated with preferential α-β interface corrosion) Kroll's Etch X2000

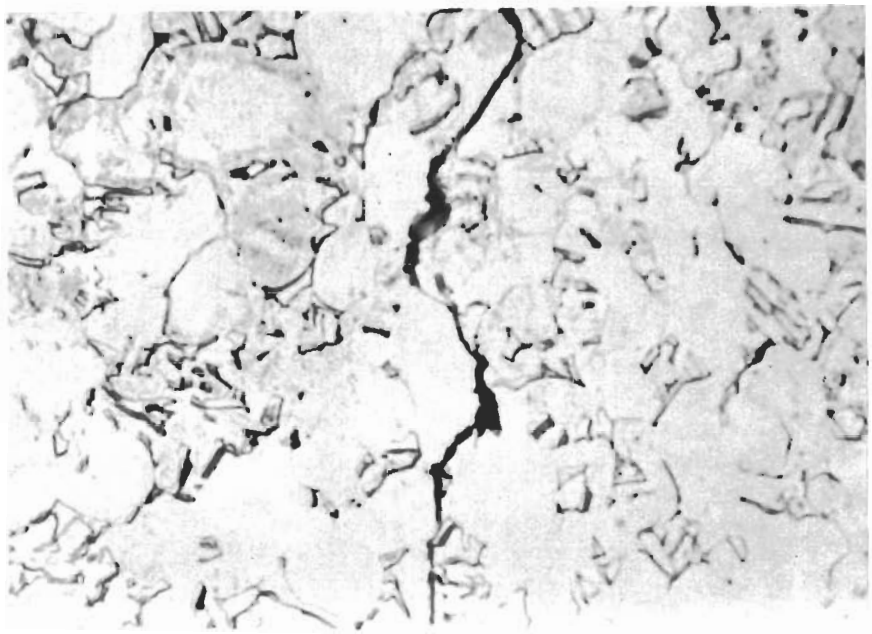

Fig. 67 - Cracks in a Failed Ti-6Al-4V Specimen Kroll's Etch X2000

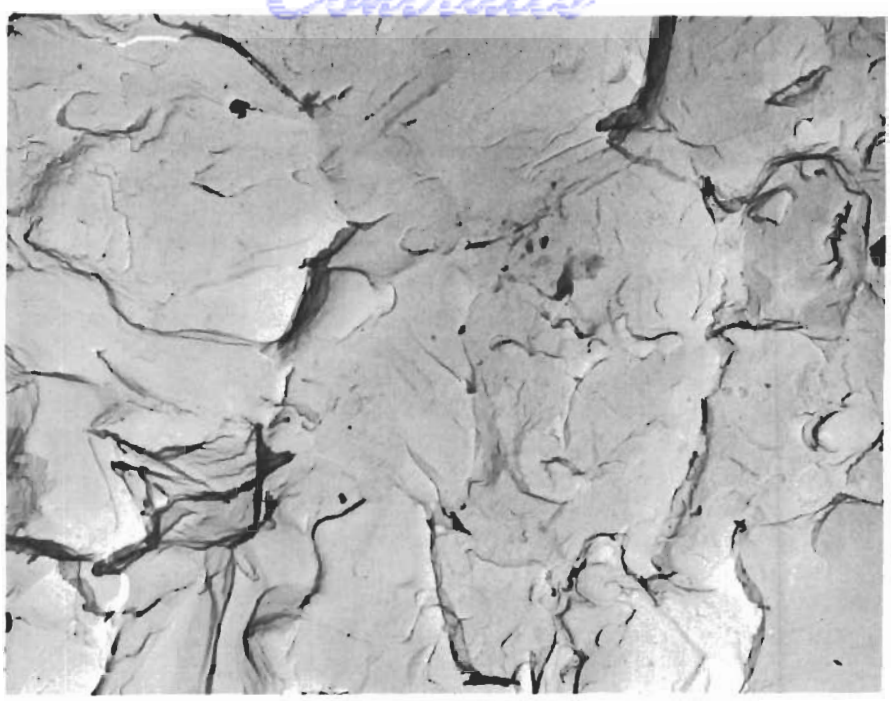

Fig. 68 - Electron Micrograph of Fracture Surface of Ti-6Al-4V Specimen (note: cleavage fracture) X7000

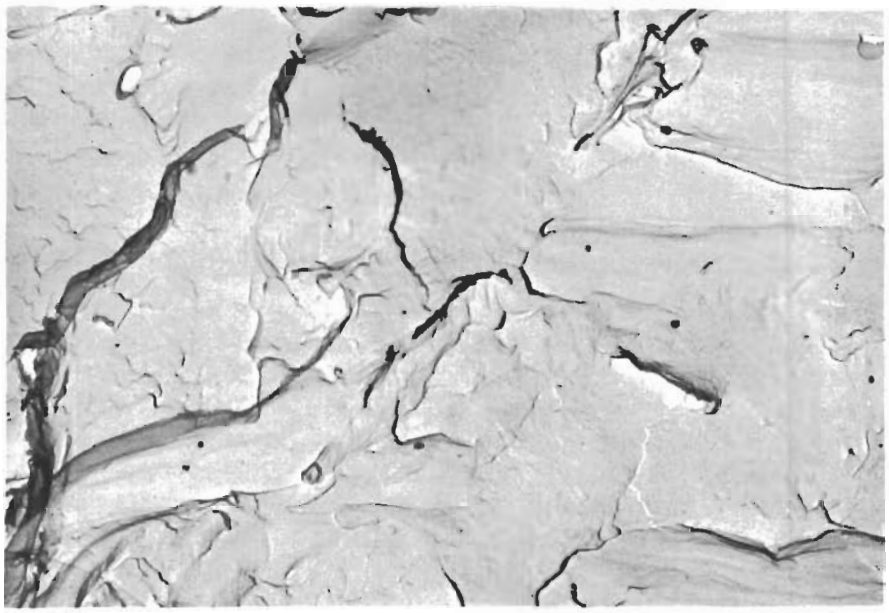

Fig. 69 - Electron Micrograph of Fracture Surface of Ti-6Al-4V Specimen (note: intergranular fracture and quasicleavage fracture) X7000

range (curve A of Fig. 55). Curve B of Fig. 55 shows the crack velocity obtained by subtracting the crack initiation time from the total failure time. Although the crack velocity obtained by the latter method is somewhat lower than that measured on the tension surface, the crack velocity is still constant over a significant part of the susceptible potential range. At the extremes of the potential range investigated the alloy is much more resistant to stress corrosion as indicated by the sharp increase in both crack initiation and total failure times (Fig. 54). Curve B of Fig. 55 shows that crack velocity decreases rapidly with increases in cathodic and anodic potentials in these highly cathodic and highly anodic potential ranges. It appears that the crack initiation time has the predominant effect on the total time-to-failure in the highly susceptible potential region.

In all of the figures presented, each data point on the graph represents an average of between three and five test results. The data scatter for the crack initiation times and failure times in the various tests was small and was approximately 0.5-1.0 minute for crack initiation times and 2-3 minutes for failure times. The main cause of scatter for the failure times was probably due to judging when the sample was broken into two parts. Cocks et al.[32] showed that aging the test solution, methanol-bromine, had a considerable effect on the times-to-failure of Ti-6Al-4V alloy specimens and concluded that this was the cause of data scatter in many reports. Therefore, in all of the tests conducted during this investigation, the CH_3OH-H_2O-NaCl solutions were allowed to age for five hours before the tests. In addition, it has been shown[33] that a mechanically polished surface on a stress corrosion cracking specimen produced the least data scatter of any surface preparation; therefore, this technique was also used.

b. Effect of Stress

Figures 56 and 57 show the relation of stress to crack initiation time, failure time, and crack velocity. As reported in the literature, increasing the stress was found to decrease total failure time and to increase crack velocity. In addition, it was found that crack initiation time decreased with increasing stress. A threshold stress of about 60% of the yield stress appears to be necessary to cause stress corrosion crack initiation and propagation. A potential of 0 mV was applied to the specimens during these tests in order to shorten the testing time. CH_3OH-0.30% H_2O-saturated NaCl solution was used.

c. Effect of Solution Composition

The effects of sodium chloride and water concentrations were determined by holding either the water at 0.3% or the sodium chloride at saturation. The effect of water content on initiation time, failure time, and crack velocity appears in Figs. 58 and 59. When water concentration is varied both crack initiation time and failure time show a minimum at approximately 0.2% water. From Fig. 59, velocity measured on the tension surface was found to be independent of water content (curve A),

and to show a maximum at about 0.2% (curve B, total failure time minus initiation time).

Figures 60 and 61 show the results of varying the sodium chloride concentration. It can be seen that crack initiation time and failure time decrease with increasing sodium chloride concentration and that the minimum times occur in a saturated sodium chloride solution; i.e., at 0.195N NaCl. Only two points exist for the change in crack velocity with sodium chloride concentration; it appears that velocity was relatively independent of the chloride content, curve A, and increased slightly with NaCl conc., curve B. The most aggressive environment for causing stress corrosion cracking of Ti-6Al-4V alloy appears to be CH_3OH containing 0.2% water and saturated with NaCl.

d. Visual and Metallographic Results

The sequence of crack initiation and propagation on smooth specimens of Ti-6Al-4V alloy in CH_3OH-H_2O-NaCl solutions was observed at 60X. After the potential was applied, black spots (surface pits) began to appear on the surface. During the incubation time, these pits would grow in diameter and in depth until much black corrosion product was evident around the pits. Abruptly, cracks were seen propagating from the pits in a direction perpendicular to the applied tensile stress. The individual cracks would then proceed to grow until another crack from another pit was encountered. The total failure of the specimen resulted from cracks being formed at various pits on the surface and interconnecting with one another across the specimen width. At the cathodic potentials, little general surface dissolution occurred; however, as the potential was increased, the surface dissolution was increased until at approximately +500 mV (SHE), the entire sample was covered with a black corrosion product, and no pits were seen.

Photomicrographs of cracks that propagated from surface pits appear in Figs. 62 and 63 and emphasize how localized disintegration has occurred around the pits. Figures 64 and 65 show the selective attack of the α-β interface and β particle during pit formation and disintegration. Stress corrosion cracks in failed specimens are shown in Figs. 66 and 67. These figures show that cracking was intergranular along α-β interfaces and also transgranular through some α grains. Again, it can be seen from these photomicrographs that the α-β interfaces were the sites of preferential corrosion. Figures 68 and 69 are electron fractographs from failed specimens and show that failure was associated with intergranular fracture, cleavage fracture, and ductile fracture. Figure 69 also shows quasi-cleavage fracture.

4. Discussion

The results presented in Figs. 54 through 69 support the observations of Sedriks et al.[29] that the stress-corrosion cracking of smooth specimens of Ti-6Al-4V alloy in CH_3OH-H_2O-NaCl solutions can be separated into a crack initiation stage that is associated with anodic dissolution,

and a crack growth stage that is associated with predominantly mechanical failure probably resulting from hydrogen embrittlement. During the crack initiation stage, preferential corrosion was observed at the α-β interfaces and intergranular β particles and resulted in localized anode disintegration and pit formation. The crack growth stage was associated with intergranular cracking and transgranular cleavage cracking. The crack velocity on the tension surface was found to be independent of applied potential but very dependent upon stress level.

Significantly, the crack initiation stage was shown in Figs. 54 and 55 to have the predominant influence upon the total time-to-failure of the specimens since crack velocity was essentially constant at all potentials. This result is in agreement with the work of Green and Myers[34] who found that crack propagation in Type 302 stainless steel in boiling $MgCl_2$ did not appear to have an appreciable effect upon the total time-to-failure. The variation in failure times of the specimens was attributed to the variation in crack incubation time. Thus, if the crack initiation time was long, the total failure was long, and vice versa. Therefore, by controlling the crack initiation time, the total failure time of the specimen can be controlled, and stress-corrosion cracking of this alloy eliminated providing there are no prior cracks existing for other reasons.

Figure 54 showed the variation of crack initiation time with applied potential in CH_3OH-0.3% H_2O saturated NaCl solution. From this, and from visual and metallographic results, it was apparent that the crack incubation stage of the stress corrosion process in smooth specimens of Ti-6Al-4V alloy consisted of localized anodic dissolution of the metal at α=β interfaces, β particles, and some grain boundaries resulting in disintegration and eventual pit formation at localized areas. The presence of a black corrosion product at the pits has been identified by others.[35] The preferential attack at the α-β interfaces and β particles was probably caused by the unprotective oxide formed in these areas as a result of the high vanadium content of the base metal. When the potential was applied, breakdown of the oxide layer at some of the α-β interfaces probably occurred and preferential attack took place. Localized corrosion continued to occur at these sites until a pit of sufficient depth to cause crack growth was formed. At the base of the pit, short intergranular cracks were probably also formed and enhanced the onset of crack growth due to the notch effect and other factors to be discussed. A pit at this state of development probably appears as in Fig. 70.

As the potential was increased in the anodic direction past the open-circuit corrosion potential of the specimens (-550 mV), significant localized anodic dissolution could occur on the surface, and a few scattered pits would form after some time. Continuing to increase the potential in the anodic direction in the susceptible range resulted in more pits being formed on the surface and in an increased current density at these pits. Menzies and Averill[35] observed that anodic disintegration

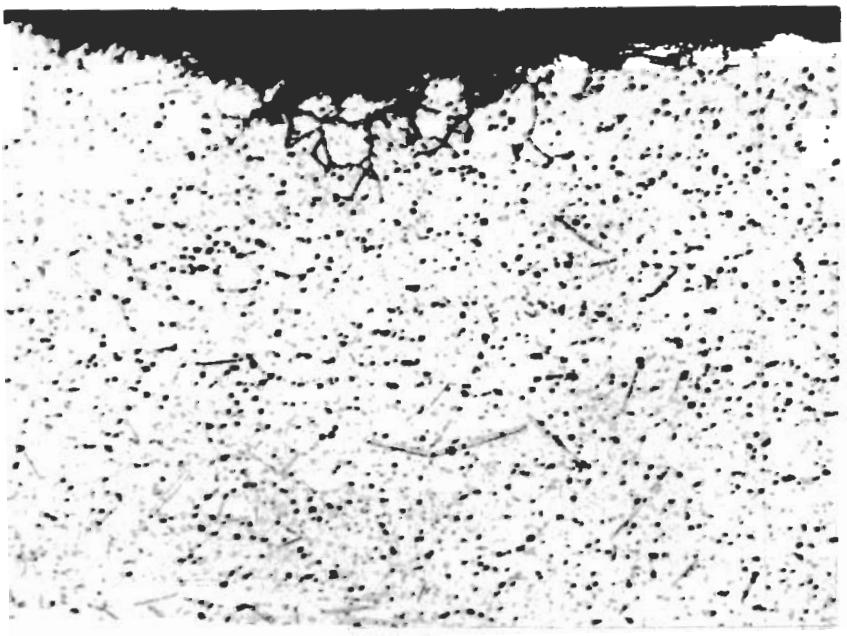

Fig. 70 - Cross Section of Corrosion Pit with Intergranular Cracks at the Base (Ref. 36)

of titanium metal surfaces in CH_3OH-HCl solutions began at localized areas on the surface and progressed over the entire surface as the current density was increased. This effect explains why the number of corrosion pits on the surface of the Ti-6Al-4V alloy was increased with increasing potential in the susceptible range and why the crack initiation time was decreased with increasing potential in this range. Thus more pits would occur on the surface of the specimen as the applied potential is increased; this effect was observed visually. At the lowest potential in the susceptible range where crack initiation and crack growth occurred (approximately -640 mV), a certain number of coulombs was required to cause pit growth to a sufficient depth to bring about cracking, and this minimum number of coulombs for cracking was a constant, no matter what potential was applied to the specimen. The reduction in crack initiation time with increasing potential in the susceptible range was attributed to the fact that at the more anodic potentials, the current density at the pits was higher, and therefore, the critical number of coulombs needed to cause cracking was achieved in a shorter time.

In the susceptible potential range up to approximately +150 mV, the corrosion of the specimen was confined to the pits and adjacent areas, since no evidence of black corrosion product was observed at other places on the surface (Figs. 62 and 63). However, as the potential was increased past +150 mV, the black corrosion product began to appear over more and more of the surface until at a potential of +500 mV the entire surface was covered. Thus, the localized anodic disintegration and pitting in the susceptible range changed to general disintegration over the entire surface as the potential was increased above +150 mV. This effect was observed also by Menzies and Averill. Therefore, although the corrosion rate was more rapid at the higher potentials, the anodic disintegration occurred uniformly over the surface so that no deep pits could form. This effect explains the surprising result that the Ti-6Al-4V specimens appeared to become more resistant to stress corrosion cracking at the higher anodic potentials ($>$ +150 mV).

The resistance of the Ti-6Al-4V specimens to crack initiation at cathodic potentials below -650 mV was related to the small extent to which the localized anodic reactions were occurring. In fact, after exposure at -630 mV for 300 minutes, the Ti-6Al-4V specimens exhibited no evidence of corrosion; i.e., black corrosion product.

As predicted, Fig. 56 shows that increasing the stress level decreased the incubation time for cracking and was associated with exposing more of the alloy surface at the active sites to the solution. Thus, the pits could form at a faster rate at the higher stresses, and, in turn, could reduce the crack initiation time.

The data in Figs. 58 and 59 that show the effect of water concentration upon crack initiation time, failure time, and crack velocity, concur with those of Haney et al.[30] and can be explained in a similar manner. It was shown that the crack initiation stage was associated with localized attack at the α-β interfaces and β particles and that these

features were located at the grain boundaries. Haney et al. concluded that the minimum in the failure time versus water concentration curve occurred when the grain boundaries were barely passivated. As more water was added to the methanol solutions, at constant potential, the quality of passivity on the bulk grain surface improved and the current densities at the active α-β interfaces and the β particles were increased so that less time was required for the pits to grow to the critical depth. The critical water content, 0.2% H_2O, was associated with the α-β interfaces and intergranular β particles being barely passivated. At water contents above 1 wt%, the entire alloy surface was passivated and no corrosion occurred.

The effect of the sodium chloride concentration upon the crack initiation time as shown in Fig. 60 was explained by considering the results of Alyward and Whitener[37] who concluded that the surface of a zirconium specimen in CH_3OH-HCl solution was uniformly covered with chloride ions. Therefore, as the corrosion pits formed on the surface of the Ti-6Al-4V alloy in CH_3OH-H_2O-NaCl solution, chloride ions probably had to diffuse from other areas on the surface or from the solution to the pits in order to continue the anodic disintegration associated with the crack initiation stage. At low sodium chloride concentrations much migration of the chloride ions would have to occur to continue pitting attack; and, therefore, the time taken for this build-up of chloride ion concentration could account for the increased incubation period. This effect would be more pronounced the lower the sodium chloride concentration.

From the results of Figs. 55 and 57 it was apparent that crack velocity was independent of applied potential and dependent only upon stress level. T. R. Beck[38] has shown that in aqueous NaCl solutions the crack velocity in Ti-8Al-1Mo-1V increased with increasing chloride concentration and increasing anodic potential, and concluded that crack velocity was dependent upon electrochemistry. He qualified this conclusion by stating that it was applicable only to those titanium alloys without α_2 dispersion strengthening and, therefore, of low yield strength. However, for titanium alloys that have been heat treated to give a dispersion of α_2 (Ti_3Al) in the matrix, and to have a high yield strength, Beck concluded that the crack velocity was given by the expression

$$V = V_o + V_m \ , \qquad (16)$$

where

V = total crack velocity,

V_o = electrochemical term, and

V_m = mechanical term .

V_o increases with increasing sodium chloride concentration, applied potential, and increasing stress level while V_m increases with increasing stress level.

Since the Ti-6Al-4V alloy in the present study was heat-treated at a temperature to precipitate α_2 in the matrix and, thus, have a high yield stress, the equation for total crack velocity was valid in this work. From Figs. 55 and 57, V_o, the electrochemical velocity, was found to be negligible, and, therefore, the crack velocity in CH_3OH-H_2O-NaCl solutions was associated with V_m only, the mechanical failure velocity. Since cleavage markings were observed on the specimen fracture surface, Figs. 68 and 69, it was concluded that hydrogen embrittlement was the probable cause of failure of the sample and determined the value of V_m, the mechanical failure velocity. Much evidence exists for this kind of failure, but many investigators have eliminated this mode of failure because they do not feel that this mechanism could occur at high anodic potentials where hydrogen evolution seems unlikely.

Greene[6] has observed a potential drop of approximately one volt down a stainless steel crevice specimen in aqueous sodium chloride solutions; and recently, Chen[39] has shown the same effect for a Ti-8Al-1Mo-1V alloy crevice specimen immersed in CH_3OH-0.63% H_2O-37% HCl solution. A potential drop of approximately 150 mV was observed and increased with decreasing crevice width. Therefore, although the potential applied on the surface of a stress-corroding specimen may be anodic, the potential at some depth below the surface in a pit or a crack might be low enough to cause hydrogen evolution. This could account for the observation[36] that hydrogen evolution occurred on stressed 18Cr-8Ni steels in boiling $MgCl_2$ solutions particularly when they were anodically polarized, and which increased the crack density and depth. Therefore, hydrogen evolution at the base of a pit or crack in Ti-6Al-4V could occur in methanol solution due to the crevice effect since the methanol solutions have a low conductivity. The crack initiation time observed for all the samples could be associated with the time needed for the pit to reach the critical depth where hydrogen evolution could occur and embrittle the alloy. In any case, it appears probable that hydrogen evolution can occur because of the crevice effect.

Another source of hydrogen for embrittlement that has not been considered and that may be significant, is the hydrogen content of the α-β interfaces and the β phase as heat treated. It has been shown[40] that hydrogen segregates to the α-β interfaces and the β phase and that these may contain many times the hydrogen content of the α phase. Therefore, since corrosion during the crack initiation stage was localized at these areas, the hydrogen contained there could be liberated during this stage and could easily diffuse into the metal either along the α-β interfaces or into the α grains along slip plane. The higher the rate of dissolution on the surface (i.e., the higher the potential) the more important this contribution would become, because the cathodic reduction reaction would be decreasing while the hydrogen liberation from the α-β interfaces and β phase would not. Therefore, the two sources mentioned

would seem to be able to provide sufficient hydrogen for embrittlement at all potentials. Evidence for this was shown by the observation that titanium hydride films were forming on the specimen at anodic potentials.

To account for the cleavage fracture observed on the fracture surfaces, hydrogen embrittlement was concluded to be the mechanism for crack growth. More specifically, the formation of titanium hydride ($Ti\text{-}H_{1.9}$) could be associated with crack propagation from the intergranular cracks at the base of the pits. Menzies and Averill[35] observed black films forming on the surfaces of titanium metal dissolving in CH_3OH-HCl solutions and identified these as titanium hydride films. Since black films were also observed to form on the surface of the Ti-6Al-4V specimen in CH_3OH-H_2O-NaCl solution, it was concluded that titanium hydride could have formed in these tests. Berger et al.[41] and Robinson et al.[42] have shown that hydride precipitates at α-β interfaces during straining in air, while Scully[43] has shown hydride precipitation along slip planes in the α grain. In addition, Robinson et. al.[42] have shown that the nucleation of titanium hydride was stress dependent; i.e., a critical stress was needed to nucleate the phase. This explains the results obtained in Fig. 56 where it was found that a critical threshold stress level was needed in order to cause crack initiation and propagation. No cracking occurred unless the stress level in the alloy was greater than about 60% of the yield strength. As the corrosion pit grew in depth in the surface and the short intergranular cracks were formed, the stress intensity at the tips of the intergranular cracks was increased, and a triaxial state of stress was formed which could lead to nucleation of the titanium hydride phase when the critical stress level was reached. The place of nucleation of the hydride would depend upon stress level, state of stress, and grain orientation and could occur either along the α-β interfaces or in the α grains. The formation of short range order by Ti_3Al precipitation reduces the propensity for cross-slip and produces wider slip steps in the α phase, both of which promote hydride formation in this phase.

Scully[43] has observed cleavage initiated at a grain boundary and progressing into an α grain in Ti-5Al-2.5Sn after immersion in a CH_3OH-HCl solution and pulled in air. Therefore, it appears that the hydrogen generated during pit formation in the crack initiation stage diffuses into the alloy, either along α-β interfaces or into the α grains, to form brittle titanium hydride plates when the crack tip stress level reaches the critical value and cleavage failure results.

The way in which titanium hydride causes failure in titanium alloys is not understood. There is evidence that the fracture of a hydride precipitate favors cleavage propagation in the plastic zone immediately ahead of it. Formation of a few layers of hydride structure on the slip plane will provide substantial barriers to dislocation movement, particularly since in the Ti-6Al-4V alloy, heat treated for the present study, cross-slip is not easy. Therefore, in the Ti-6Al-4V alloy that exhibits short-range order, fracture could occur by hydride

initiating bursts of brittle crack propagation that could move through the alloy from purely metallurgical reasons. It appears, therefore, that the intergranular and transgranular stress corrosion cracking of the Ti-6Al-4V alloy in CH_3OH-H_2O-NaCl solutions can be attributed to a form of slow strain rate embrittlement.

G. EFFECT OF GRAIN SIZE ON STRESS-CORROSION CRACKING OF Ti-6Al-4V ALLOY IN METHANOL H_2O NaCl SOLUTION (I. J. Loomba)

(This investigation was completed and was the basis of a thesis by I. J. Loomba who received the M.Sc. degree in December, 1970)

1. Aim and Significance of the Work

The aim of this investigation was to determine the effect of grain size on crack initiation and crack propagation times, crack initiation and propagation paths, and the effect of stress on crack initiation and propagation times.

Previous experiments on titanium demonstrated that stress-corrosion cracks in titanium alloys exposed to methanol-hydrochloric acid-water solutions originate from pits which, in turn, are associated with β phase and α-β interfaces. Also, a strong tendency exists for the pits to be elongated in the rolling direction and for stress-corrosion cracks to propagate parallel to the rolling direction.

Crack initiation and propagation studies are being conducted on Ti-6Al-4V alloy in the above environment. Large-grained specimens, prepared by strain annealing, are being used in this work. It is hoped that strain annealing will provide large enough grains to permit studies of selected crystals of known crystallographic orientation.

2. Experimental Procedure

a. Materials

The experimental work was carried out on 0.025-inch thick Ti-6Al-4V alloy sheet obtained from Reactive Metals, Inc. The composition of the alloy and physical properties of the as-received material are given in Table V. Strips were sheared from the alloy sheet with rolling direction parallel to the length of the strip.

Rolling was used as the straining method, 5% and 30% reductions in thickness were made. Subsequent to rolling, all specimens were encapsulated in quartz tubes with 10^{-5} mm Hg pressure of argon gas and annealed for various times at 925°C.

Specimens with 5% reduction were solution-treated at 925°C for 1, 5, 10, 20, and 30 days, while specimens with 30% reduction were

solution-treated at 925°C for 1, 2, 4, 8, and 12 days. Solution treatment was followed by water quenching. Structures showed an increased amount (>50%) of β and/or α' phases[44] in all cases. Specimens with 5% reduction and 10 days solution treatment and with 30% reduction and four days solution treatment had attained about the maximum grain growth and both were of equivalent size. Little additional grain growth was observed for specimens with longer solution treatments.

Table V - Composition and Properties of Ti-6Al-4V Alloy

Composition	
Element	% Weight
C	0.03
N	0.012
Fe	0.13
Al	6.4
V	4.3
O	0.108
H	58 ppm
Physical Properties	
Ultimate tensile strength	134.8/139.1 ksi
Yield stress (0.2% offset)(transverse)	127.0/132.9 ksi

Above composition and properties were provided by the supplier.

Since the increased amount of β and α' phases was not desired in the final structure, the following procedure was employed. Specimens were rolled to 5, 10, 20, and 30% reduction, encapsulated as before, and annealed at 925°C for one and two days. The amount of β phase was almost the same as in the initial structure. Grain growth for specimens with 5% reduction and annealed for two days at 925°C was almost the same as obtained for specimens with 30% reduction and annealed at 925°C for one day. Similar results were obtained for specimens with 10 and 20% reduction.

On the basis of the above observations, stress corrosion specimens are being annealed, after 10% reduction, at 925°C for 1, 2, 4, 8, 16, 32, and 64 hours. Annealing is being done in a vacuum furnace at a pressure of 10^{-6} mmHg.

Tensile testing was done on an Instron testing machine. Three specimens (0.222" x 0.25" x 1.5" gauge length) were tested for each heat treatment. Table VI contains the average value of yield strength and Young's modulus. The long axis was used as the rolling direction.

Table VI - Properties of Alloy Ti-6Al-4V Subsequent to 10% Cold Rolling and Annealing at 918°C

Yield stress (0.2% offset) (transverse) (average)	127.5 ksi
Young's modulus (average)	6.335×10^6 psi

After heat treatment all the specimens were polished on 600-grit silicon carbide paper. Specimens for metallographic work were final polished on 6-μm diamond polishing compound followed by 0.05 μm gamma alumina powder. Etching was done with the solution of following compositions: HF, 2%; HNO_3, 6%; H_2O, 92%.

The test solution used throughout the investigation was methanol + 0.3% water saturated with NaCl. Sodium chloride and methanol were reagent grade (water content of methanol varied from 0.02% to 0.04%). Double distilled water, containing less than 1 ppm of impurities expressed in terms of NaCl, was used. Freshly prepared solution was used in each experiment.

b. Experimental Apparatus

Three-point loaded, unnotched bend specimens were used. A Ti-6Al-4V alloy wire was used to connect the specimen to an Anotrol potential controller. A Luggin probe placed near the sample surface was connected to the calomel reference electrode through KCl solution. A platinum electrode was used as the counter electrode. An optical microscope was used to observe crack initiation and propagation at 100X. The objective lens was coated with silicone lubricant to protect it from the methanol solution.

The deflection of the specimen is related to the stress by the following formula:

$$d = \frac{SL^2}{6Et}, \qquad (17)$$

where

d = the maximum deflection in inches,

S = the maximum stress in psi,

L = the length between supports of specimen holder in inches,

E = the Young's modulus of the material in psi,

and

t = the thickness of the specimen in inches.

The deflection was measured with a deflectometer to 0.0001-inch accuracy. After the specimen was stressed to the desired extent, the specimen and holder were placed in the test cell. The counter electrode was placed near the specimen and the glass dish was covered with a plexiglass sheet containing holes for receiving the microscope objective and Luggin probe (the cover was used to keep moisture pickup by methanol from the atmosphere to a minimum). The glass dish and Luggin probe were then filled with 600 ml of freshly prepared methanol + 0.3% water and NaCl (saturated) solution. A potential of 0 mV (SHE) was applied in all cases. The time was recorded from the time the potential was applied. Cracks were observed to initiate from pits. The initiation of the crack was recorded as that time when any of the pits transformed to a crack. Failure time was taken as that time when the material had failed completely.

3. Results

Examples of grain sizes obtained by strain annealing are shown in Figs. 71-77. Table VII shows the grain size variation with change in annealing time.

Table VII - Average Grain Diameter of Ti-6Al-4V Subsequent to 10% Cold Reduction (rolling) and Annealing for Various Times at 918°C

Annealing Time (hr)	Average Grain Diameter (inch)
1	0.0044
2	0.0057
4	0.0064
8	0.0072
16	0.0095
32	0.0110
64	0.0130

The grain diameter was calculated by counting the number of grains in a 4-inch^2 area of the photographs taken at 1000X.

a. Stress-Corrosion Cracking

In all stress corrosion tests, when the potential was applied, corrosion started at once as localized corrosion in the form of pits elongated in a direction normal to the tensile axis (at 100X). Figure 78 shows some of these elongated pits. Cracks started inside the elongated pits in all the tests performed in this investigation. The crack appears as a dark black line against the dull black background of the pit.

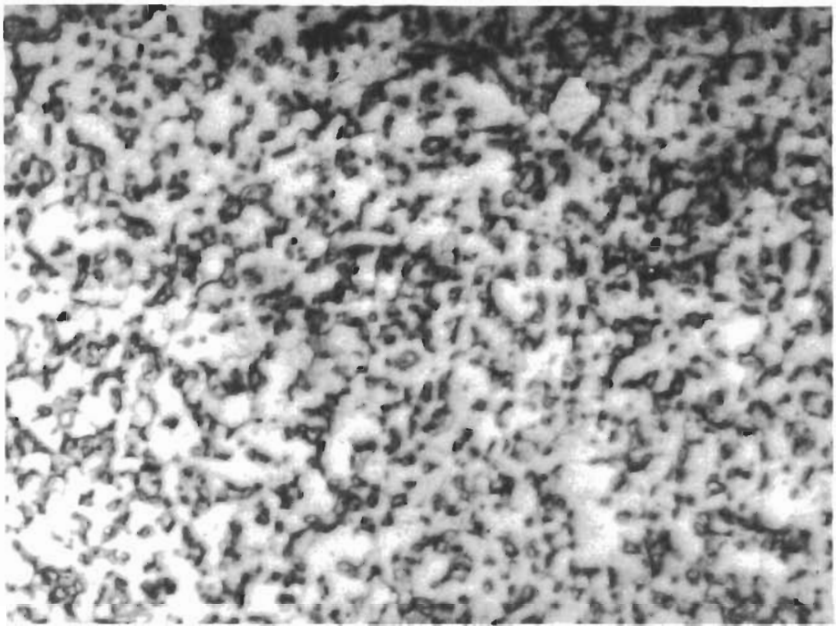

Fig. 71 - Grain Size of 10% Rolled and 1 Hour Annealed Specimen at 918°C; Average Grain Diameter 0.0044 Inch (1000X)

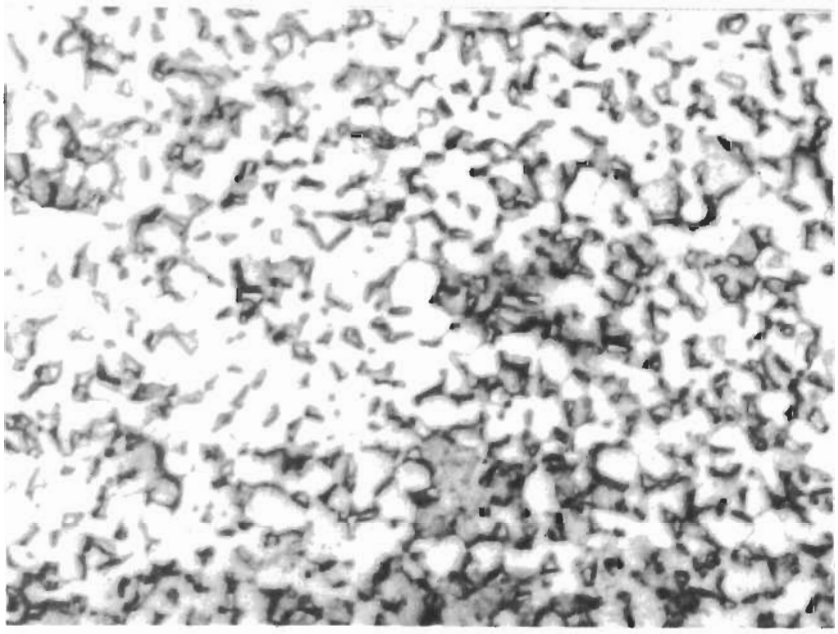

Fig. 72 - Grain Size of 10% Rolled and 2 Hour Annealed Specimen at 918°C; Average Grain Diameter 0.0057 Inch (1000X)

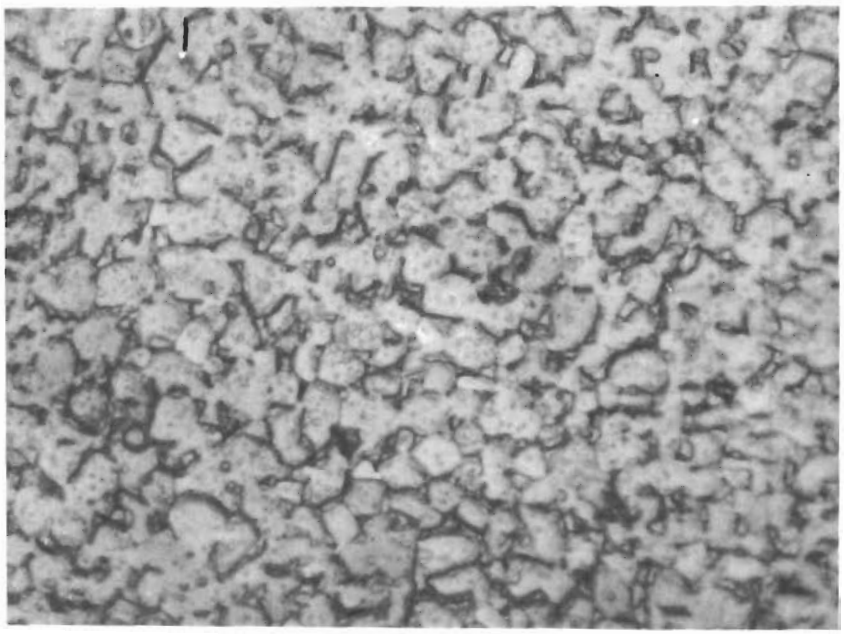

Fig. 73 - Grain Size of 10% Rolled and 4 Hour Annealed Specimen at 918°C; Average Grain Diameter 0.0064 Inch (1000X)

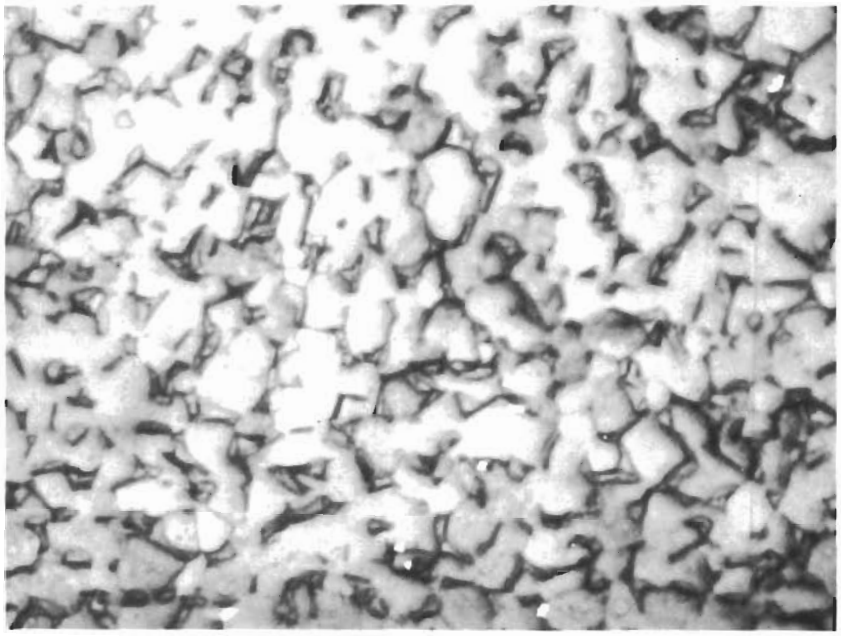

Fig. 74 - Grain Size of 10% Rolled and 8 Hour Annealed Specimen at 918°C; Average Grain Diameter 0.0072 Inch (1000X)

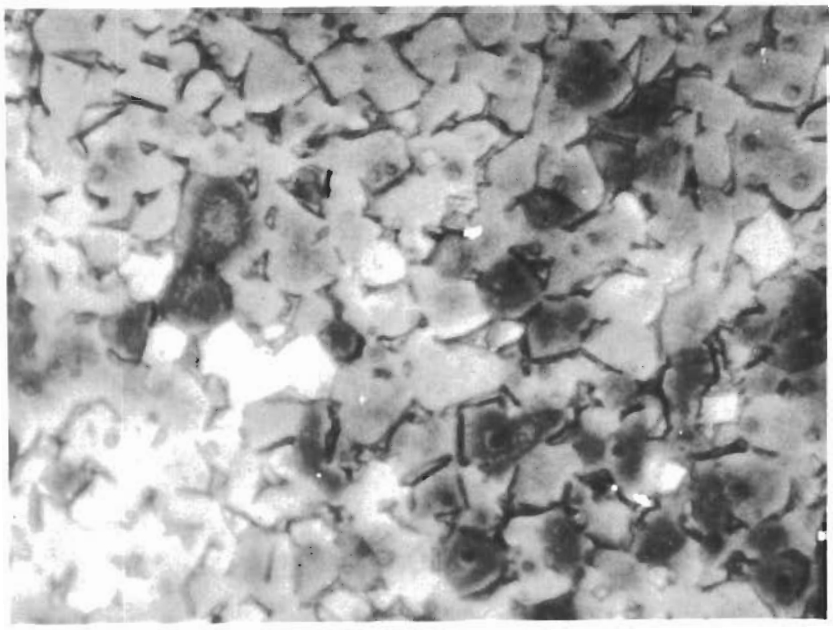

Fig. 75 - Grain Size of 10% Rolled and 16 Hour Annealed Specimen at 918° C; Average Grain Diameter 0.0095 Inch (1000X)

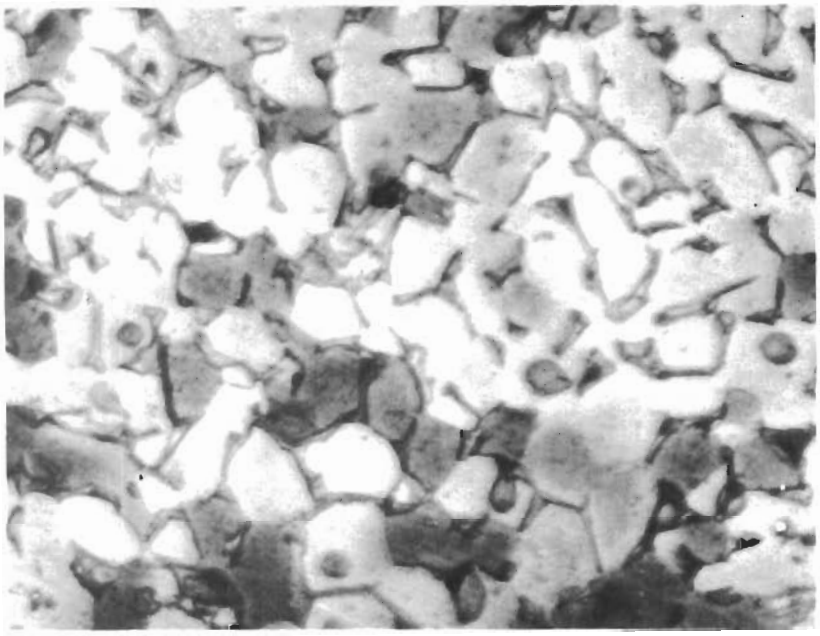

Fig. 76 - Grain Size of 10% Rolled and 32 Hour Annealed Specimen at 918° C; Average Grain Diameter 0.0110 Inch (1000X)

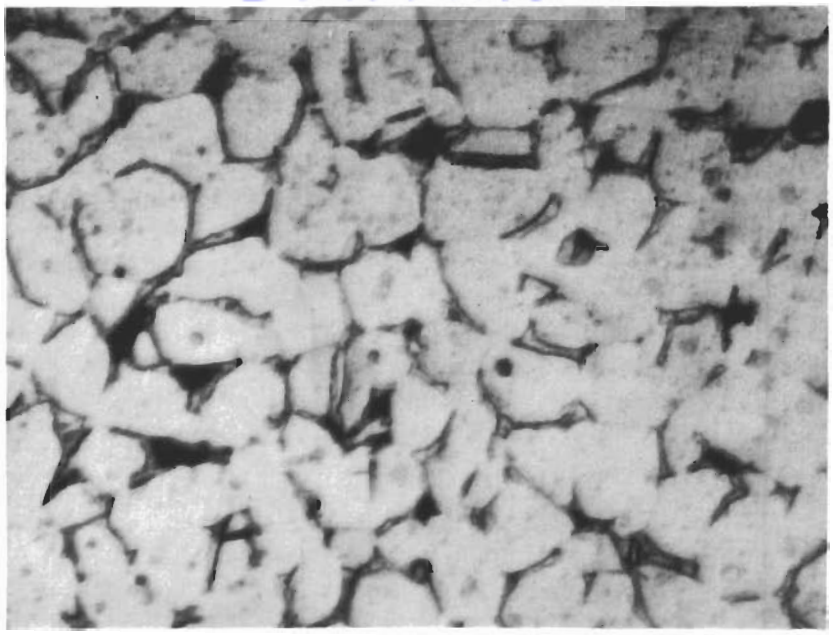

Fig. 77 - Grain Size of 10% Rolled and 64 Hour Annealed Specimen at 918°C; Average Grain Diameter 0.0130 Inch (100X)

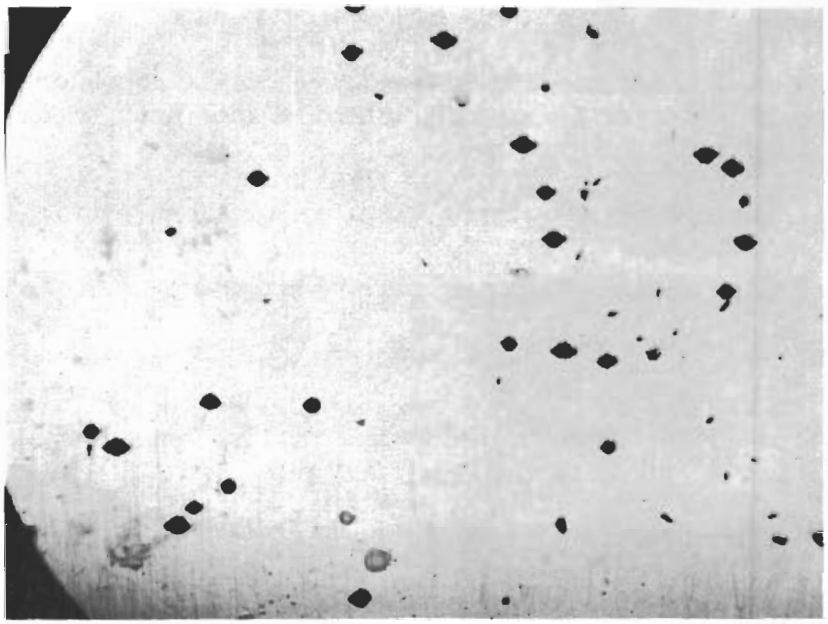

Fig. 78 - Pitting and Crack Initiation; Crack Initiation Occurred in 9 Minutes after Potential Was Applied. (100X)

Almost every pit gave rise to a crack, as shown in Fig. 79. Almost every elongated pit shown in Fig. 78 contains a crack. In all cases the crack started from the middle of the specimen and not from the edges. These cracks were observed to propagate in a direction perpendicular to the applied stress. The cracks would then proceed to grow until encountering another crack, as shown in Fig. 80. Crack propagation rate was slow in the beginning but increased as the size of the crack increased. The crack size shown in Fig. 79 was obtained 18 minutes after initiation (Fig. 78). It took only eight minutes for the crack in Fig. 79 to grow across the width of the specimen.

b. Effect of Stress

Figures 81 and 82 show the relation of stress to initiation time, propagation time, failure time, and rate of crack propagation. As apparent from Fig. 81 the initiation time, propagation time, and failure time decreased with increasing stress level. As the stress level was increased from 50% of the yield stress (0.2% offset) to 110% of the yield stress the propagation time decreased from 139 minutes to 19 minutes. Table VIII shows the applied stress, initiation time, propagation time, and failure time for these experiments.

c. Effect of Grain Size

Pit density and crack density increased with increasing grain size at a constant stress level. It was also observed that the pit had to grow larger in small grain size specimens to give rise to a crack as compared to larger grain size specimens.

Figure 83 shows that crack initiation (pitting) occurs at the α-β grain boundary. Cracks propagating from the pits are both transgranular and intergranular in nature. Figures 84-87 show the crack paths in different grain size specimens. The crack path is mixed (i.e., both intergranular and transgranular) in all the cases.

Figures 88-89 show the relation between $D^{-1/2}$ (D is grain diameter) to crack initiation time and failure time, respectively. The crack initiation time and failure time give straight lines when plotted against $D^{-1/2}$. The initiation time of the smallest grain size specimen is about 300% longer than that of the largest grain size specimen investigated. Also, the propagation time of the smallest grain size specimen (failure time less initiation time, Fig. 90) is about 21% longer than that of the largest grain. Thus, the decrease in failure time with increasing grain size is mainly attributed to the crack initiation time.

4. Discussion

Stress corrosion failure of Ti-6Al-4V in methanol + NaCl + water solution is made up of two parts; i.e., (a) initiation time and (b) propagation time.

Fig. 79 - Crack Propagation from the Pit; Shape of the Crack 18 Minutes after the Initiation (100X)

Fig. 80 - Linking of Propagating Cracks; Shape of the Crack 18 Minutes after the Initiation (100X)

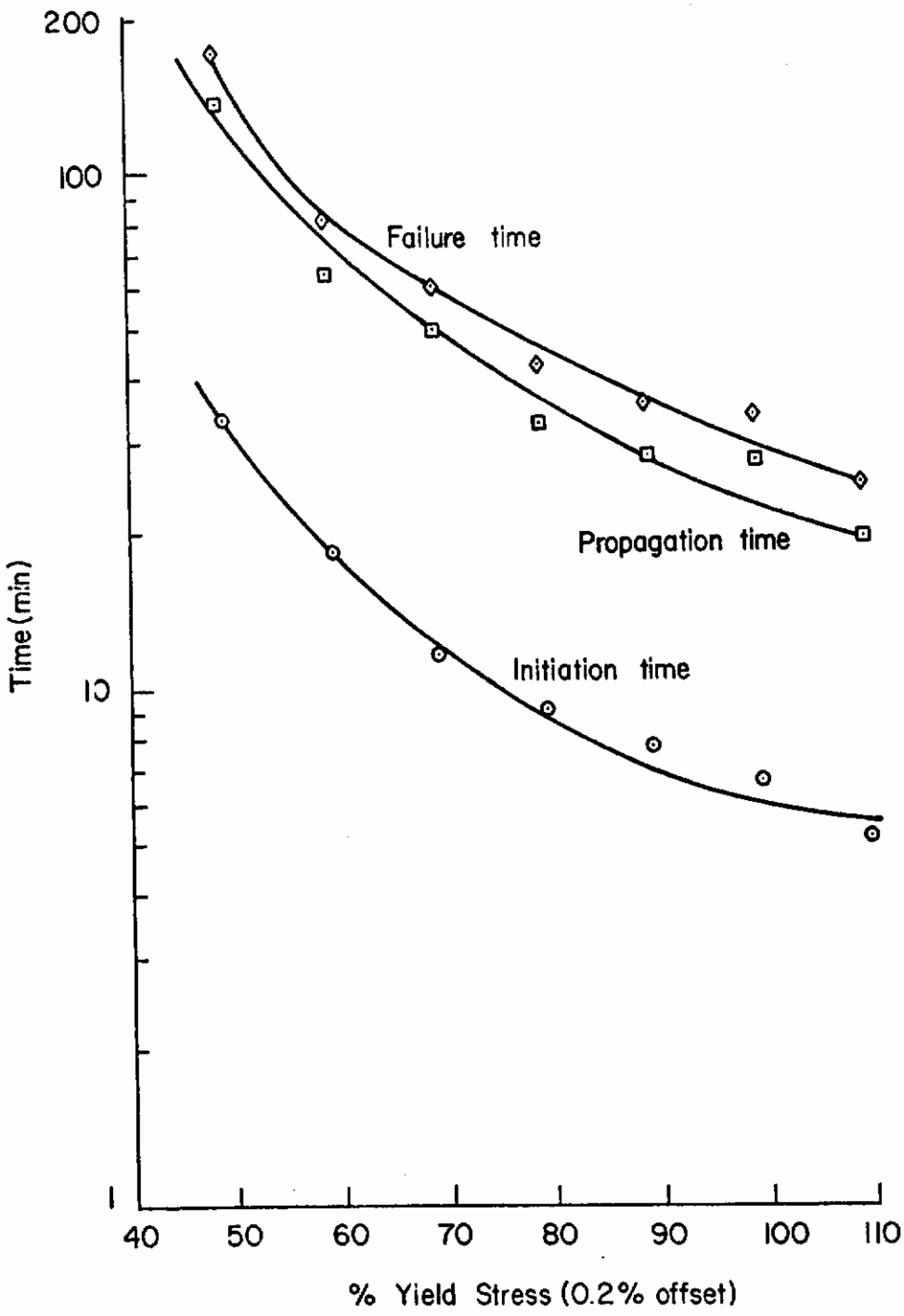

Fig. 81 - The Effect of Applied Stress on Crack Initiation, Crack Propagation and Failure Times

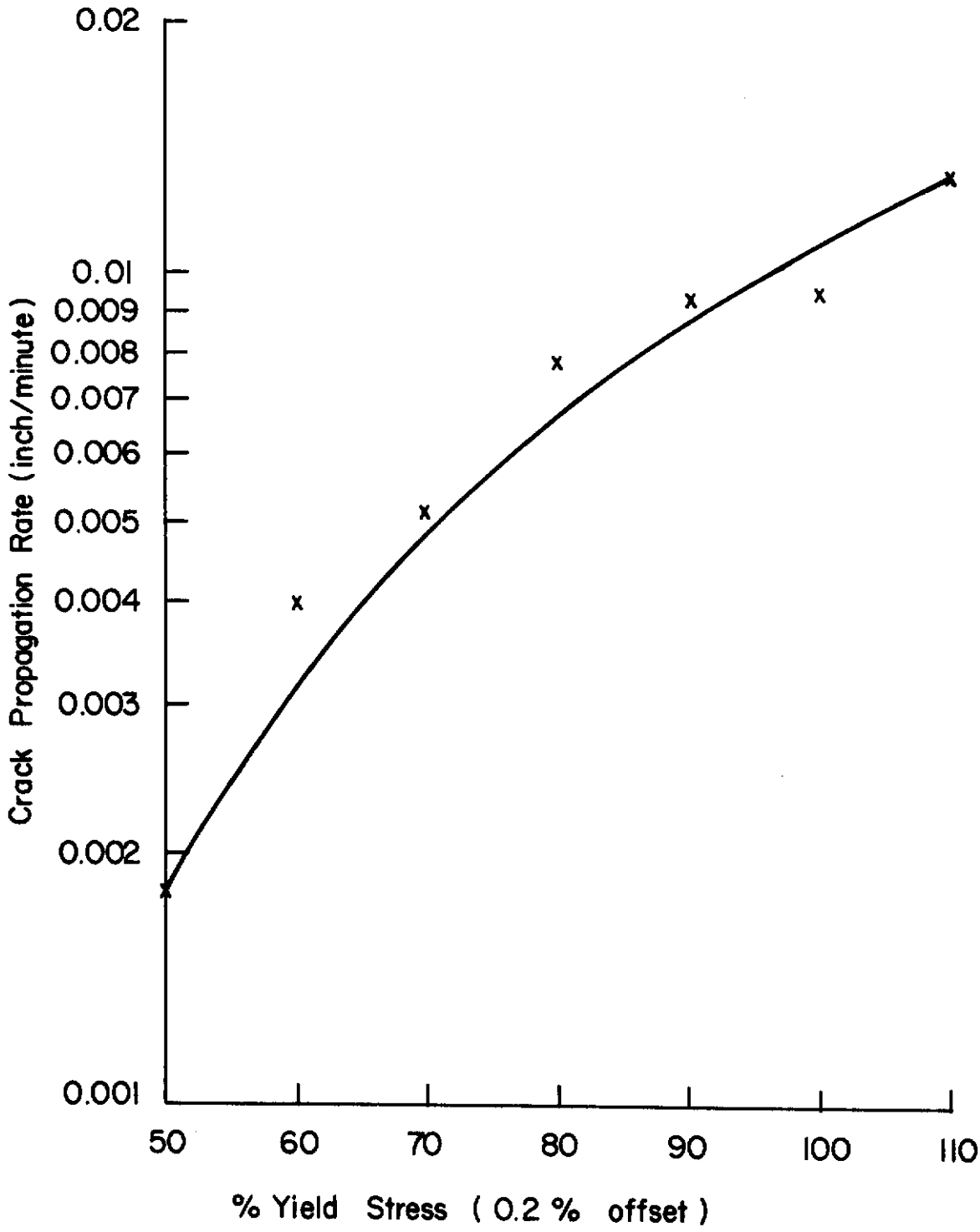

Fig. 82 - The Effect of Applied Stress on Crack Propagation Rate

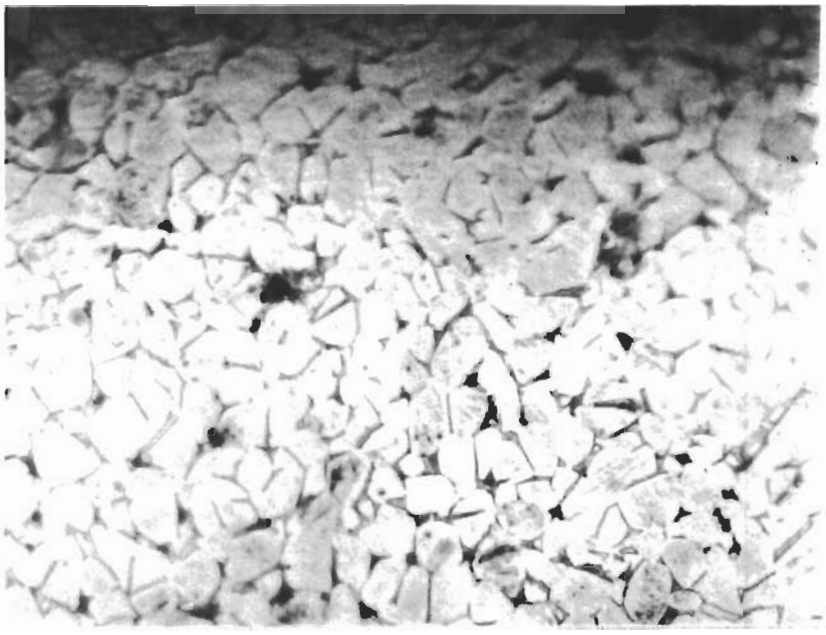

Fig. 83 - Pitting Occurs at the Grain Boundary (600X)

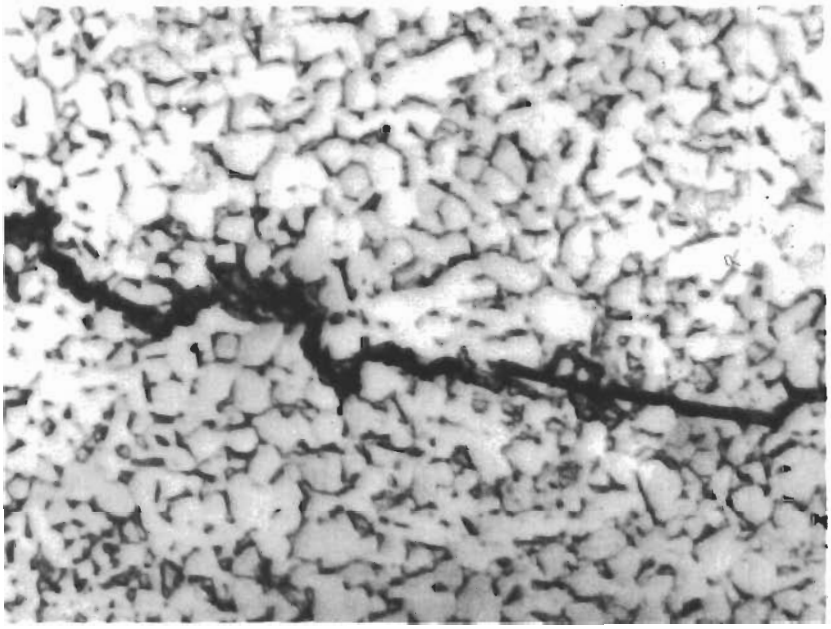

Fig. 84 - Mixed Mode of Failure in 10% Rolled and 2 Hour Annealed Specimen at 918° C (1000X)

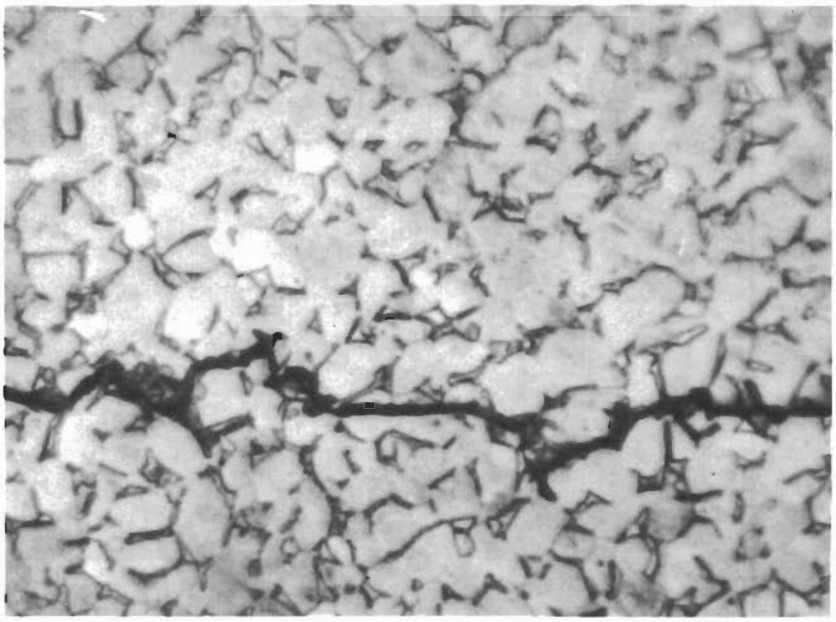

Fig. 85 - Mixed Mode of Failure in 10% Rolled and 8 Hour Annealed Specimen at 918°C (1000X)

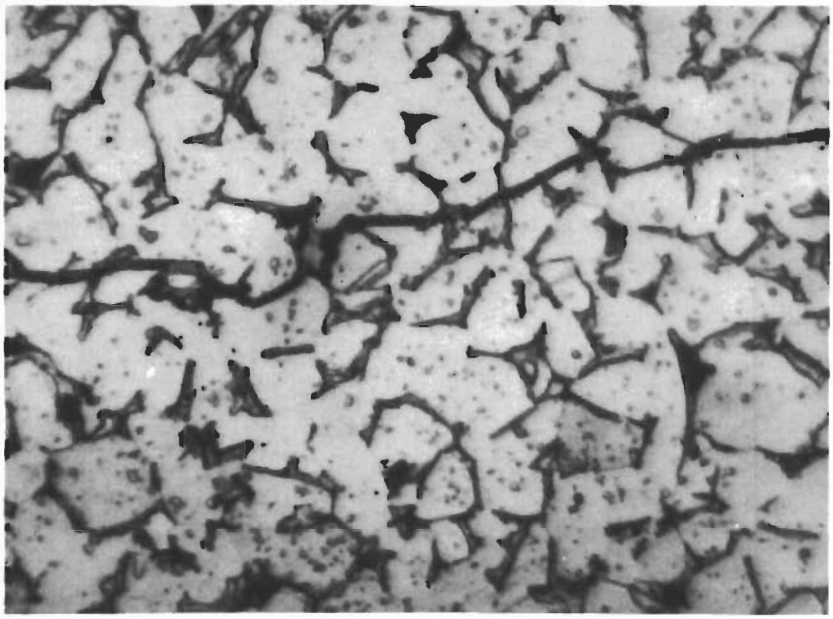

Fig. 86 - Mixed Mode of Failure in 10% Rolled and 32 Hour Annealed Specimen at 918°C (1000X)

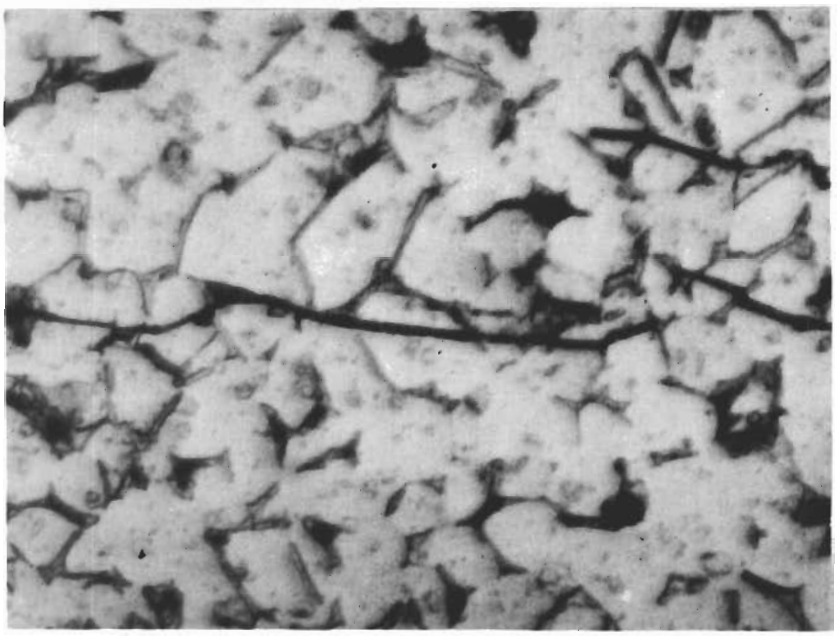

Fig. 87 - Mixed Mode of Failure in 10% Rolled and 64 Hour Annealed Specimen (1000X)

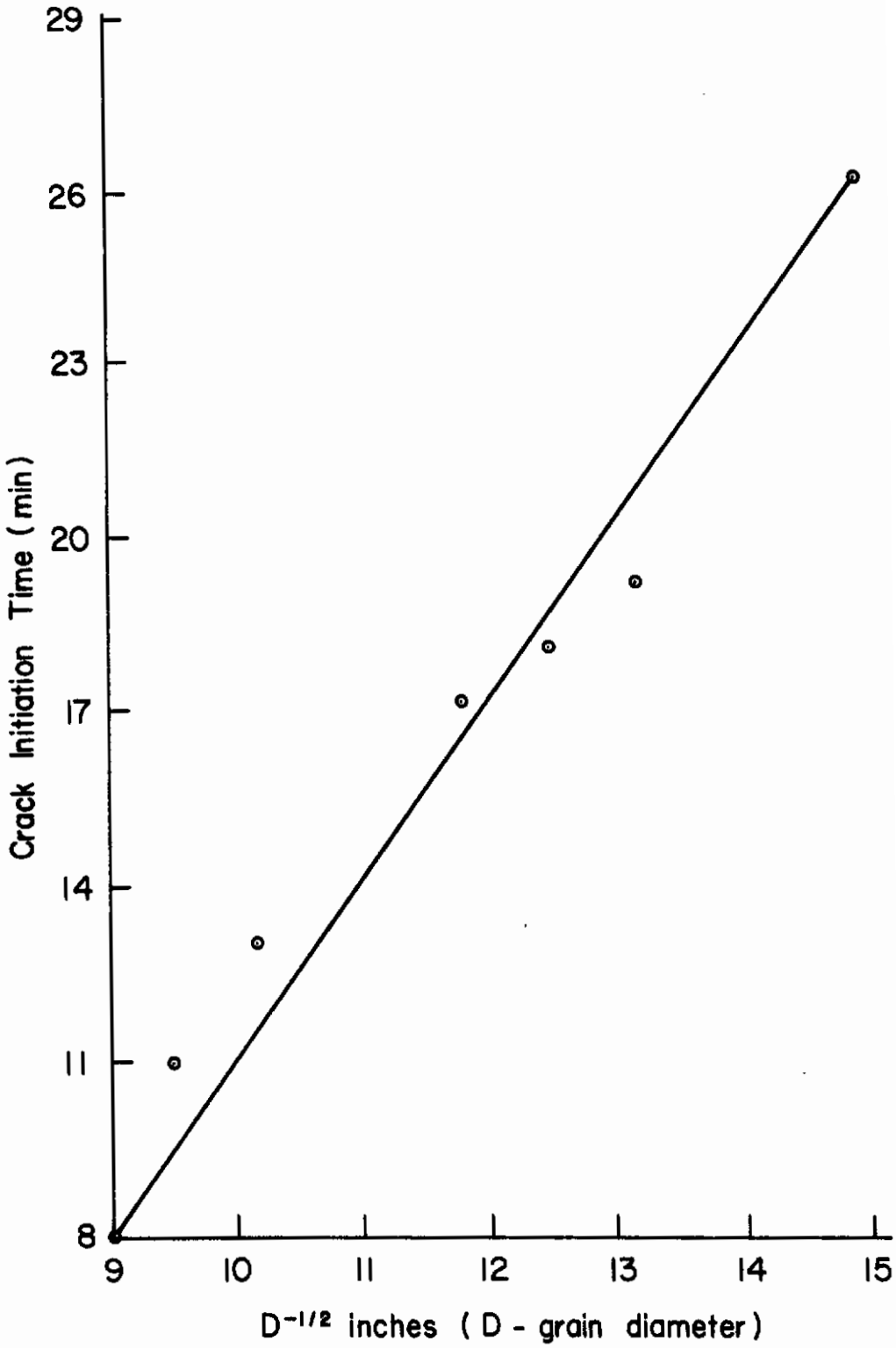

Fig. 88 - Effect of Grain Size upon Crack Initiation Time

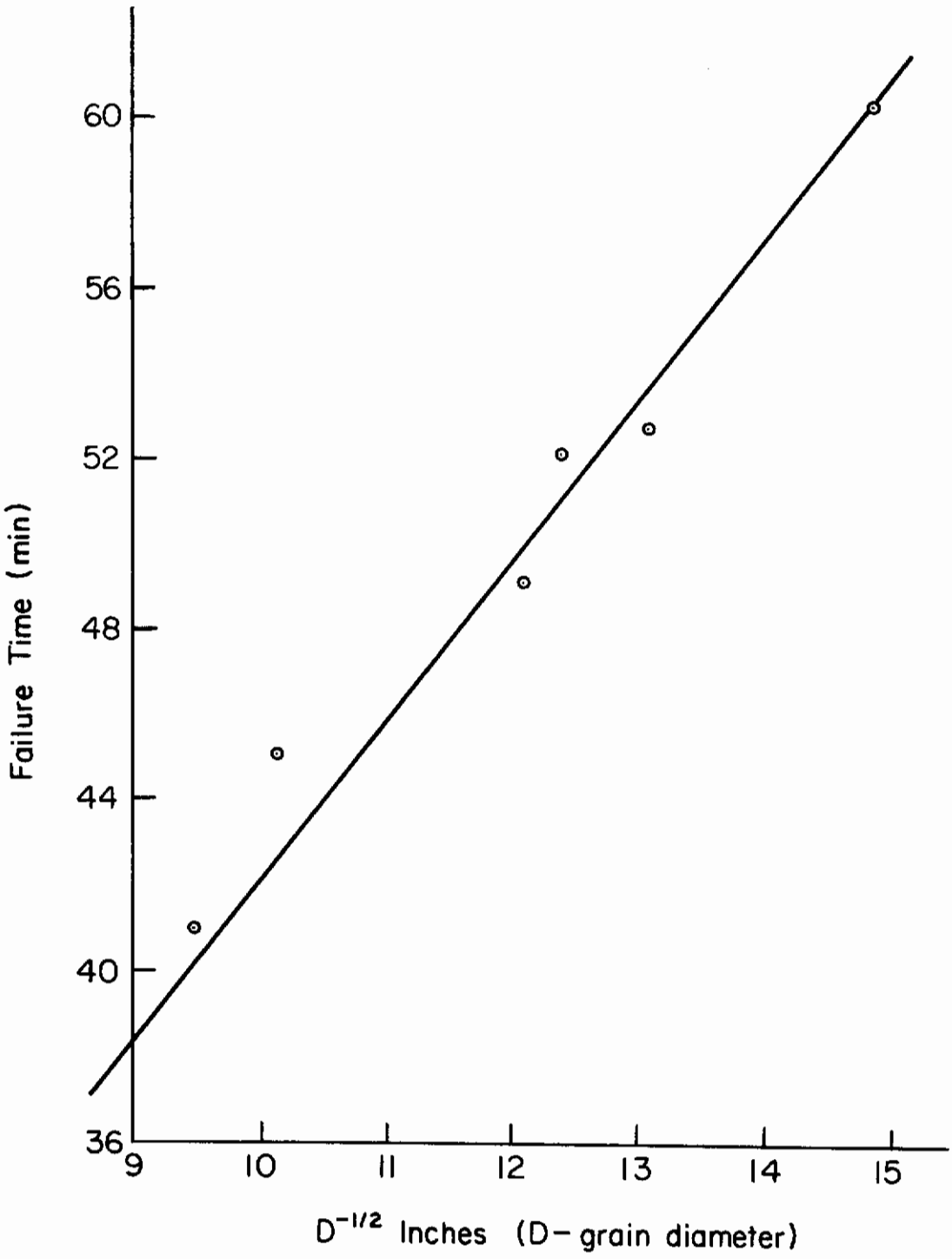

Fig. 89 - Effect of Varying Grain Size upon Failure Time

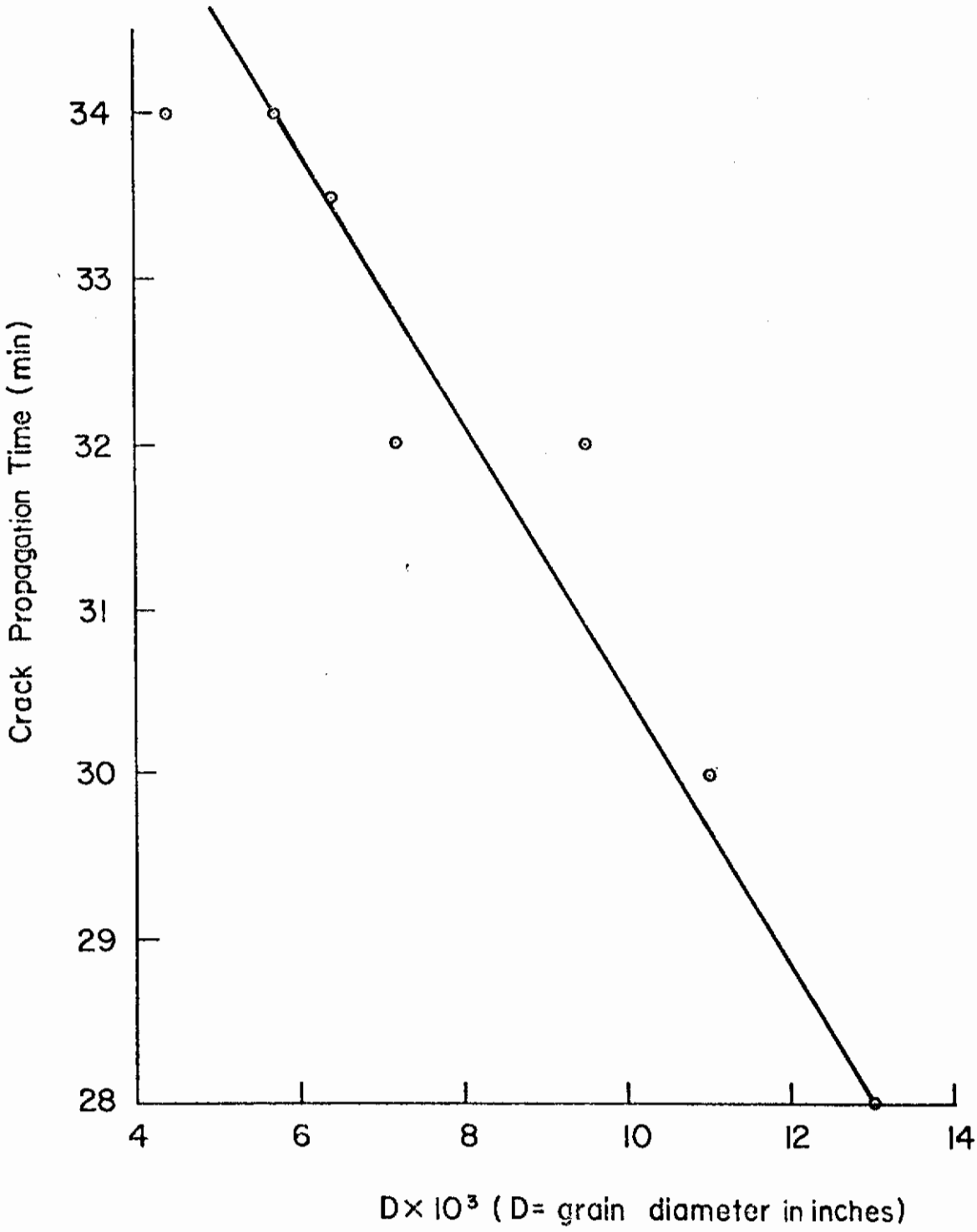

Fig. 90 - Effect of Grain Size upon Crack Propagation Time

Table VIII - Effect of Applied Stress on Crack Initiation, Crack Propagation, and Failure Times

% Yield Stress (0.2% offset)	Average Initiation Time (min)	Average Propagation Time (min)	Propagation Rate (inch/min)	Average Failure Time (min)
110	5	19	0.0132	24
100	6.5	27	0.0093	33
90	7.5	27.5	0.0092	35
80	9	32	0.0078	41
70	11.5	49	0.0051	60.5
60	18.5	63.5	0.0040	82
50	33.5	138.5	0.0018	172
40	No initiation even after 48 hours of exposure			

Average value was obtained from minimum of three tests. There was maximum variation of 3 minutes in initiation time and 5 minutes in failure time for specimens stressed to more than 60% of yield stress. The variation was about 15 minutes in failure time for specimens stressed to 50% of yield stress.

a. Initiation Time

The resistance of titanium alloys to stress-corrosion cracking is attributed to a stable passive film. Many investigators believe that crack initiation occurs when this passive oxide film is penetrated by the halide ions.[45-47,15,29] Film destruction may also be assisted by an applied stress. In this study, anodic dissolution occurred at local areas at α-β grain boundaries resulting in pits, as shown in Figs. 79 and 80. Localized attack at the grain boundary is reasonable since anodic dissolution is favorable at high-energy sites.

According to Petch[12] more dislocation pileups will occur at the surface in a large-grain size material than in a finer-grain size material at the same stress level. These dislocation pileups create high energy sites for incubation of stress corrosion cracks. This has been found to be true in the case of stress-corrosion cracking of Ti-6Al-4V alloy. Figure 88 shows that as the grain size increases the incubation time decreases in accordance with the Petch equation. An increase in applied stress also decreases the initiation time, as shown in Fig. 81, by creating high-energy sites. Barnwell, Myers and Saxer[48] also think that this dislocation pileup model accounts for lower crack initiation times in Type 302 steel.

Some authors,[49,50] believe that crack initiation in α-Ti alloys in methanol + hydrochloric acid solutions occurs by some form of hydrogen embrittlement. The free corrosion potentials in methanol + iodine and methanol + bromine solutions are positive with respect to standard hydrogen electrode.[45,51,52] Thus, in methanol + bromine solutions the reduction of bromine to bromide is a more likely cathodic reaction[51] than the evolution of hydrogen. Similar arguments may apply in the case of methanol + iodine solutions.[52] In the case of Ti-5 wt% Al-2.5 wt% Sn alloy in methanol + 0.6 wt% HCl + 1.0 wt% water, the free corrosion potential is -10 mV(SHE) and the application of small cathodic currents should favor the evolution of hydrogen and result in a decrease in initiation time if hydrogen embrittlement is responsible for the crack initiation. On the other hand, if anodic dissolution is responsible for crack initiation, the application of small anodic currents would be expected to reduce times-to-failure. Such behavior, which is similar to that observed in methanol + iodine solutions,[52] indicates that the crack initiation involves anodic dissolution. This evidence supports the theory that crack initiation in Ti-6Al-4V in methanol + NaCl + water solution is most probably due to anodic dissolution.

The pits formed by the anodic dissolution of Ti-6Al-4V alloy, shown in Fig. 78, act as notches, which serve as stress raisers. Also, increased stress results from dislocation pileups at the head of the notch. A stress raiser has been shown to be necessary for transgranular stress-corrosion cracking.[53,54] The presence of a notch, attendant dislocation pileups, and chloride ions all seem to have a part in the crack initiation process.

The decrease in stress corrosion failure time of Ti-6Al-4V in methanol + NaCl + water solution is mainly due to a decrease in initiation time with increasing grain size. The greater proportion of the failure time is accounted for by the initiation time as the grain size of the alloy decreases. Similar results were obtained by Green and Myers[34] for Type 302 austenitic stainless steel exposed to boiling 42 wt% magnesium chloride solution.

b. Crack Propagation

The crack propagation of Ti-6Al-4V in methanol + NaCl + water solution is of a mixed mode (i.e., intergranular and transgranular), as shown in Figs. 84-87. Other investigators[55] have also found that Ti-6Al-4V fails in both intergranular and transgranular manners. The intergranular part of the crack is believed to result from the anodic dissolution. This is supported by the observation of intergranular cracking along with cleavage failure of Ti-5Al-2.5 Sn in methanol + HCl + water solution.[47] Powell and Scully[47] also observed that increasing the potential in the anodic direction increases intergranular stress-corrosion cracking of the alloy and at very high positive potentials the alloy fails entirely by the intergranular mode.

The transgranular part of the crack observed in Ti-6Al-4V in this investigation is due to cleavage. This is supported by many investigators.[47,53,56,57] Transgranular failure occurs in alloys which show reduced propensity for cross slip.[29,53,56,58] The function of aluminum is important in this respect since it inhibits cross slip in the titanium lattice.[59] Sedriks, Green, and Slattery[29] showed that the path of cracking was influenced by the aluminum content. The stress-corrosion cracking path in pure titanium and Ti-2.09 wt% Al alloy was intergranular. Ti-5.1 wt% Al alloy gave a mixed type of fracture (i.e., both intergranular and transgranular) and entirely transgranular fracture was obtained in the Ti-7.76 wt% Al alloy. Beck et al.[60] observed that increasing the aluminum content changes the dislocation structure from the tangled networks of the metal to the co-planar arrays, the formation of which results in reduced propensity for cross slip. The slip steps gradually become broader and the alloys become increasingly more difficult to passivate and, therefore, to repassivate.[19] This type of mechanism is suggested to be operating in stress-corrosion cracking of Ti-6Al-4V in methanol + NaCl + water solution.

After the crack has initiated, a current of chloride ions flows into the tip zone, according to Beck.[61] These chloride ions are responsible for stress corrosion cracking of Ti-6Al-4V either through chemical or surface processes. According to the electrochemical mass transport kinetic model of Beck[61] only a mass-transport limited current of halide ions goes to the crack tip. The magnitude of this current is approximately equal to the current required for the formation of a monolayer of chloride ions or the formation of titanium halide at the crack tip zone. According to Pourbaix, titanium of valence 2 is thermodynamically stable at the suspected negative potential of the crack tip. The

activation energy of 3.5 kcal obtained by Beck[61] is consistent with mass-transport limited current of halide ions.

Chloride ions at the crack tip zone probably reduce the surface energy of Ti-6Al-4V alloy and transgranular stress-corrosion cracking (cleavage failure) occurs at lower stresses than the yield strength of the alloy. Coleman, Weinstein and Rostoker[46] experimentally found that mild steel with adsorbed hydrogen has about 500 erg/cm^2 of surface energy while the accepted value for iron with respect to its vapor is about 1600 erg/cm^2. The interfacial energy of solid iron with respect to liquid lithium is about 730 erg/cm^2. Solid 70/30 brass has an interfacial energy with respect to mercury of 280 erg/cm^2 and the accepted value of surface energy of 70/30 brass with respect to its own vapor is about 1500 erg/cm^2. Thus, it is not unreasonable to assume that the surface energy of Ti-6Al-4V decreases in the presence of chloride ions.

Increasing the stress level decreases the propagation time as shown in Fig. 81. This is in accordance with the literature.[29,60,31]

Figure 90 demonstrates that crack propagation time increases linearly with decreasing grain size; however, this effect of grain size on crack propagation is small over the range of grain size studied. This suggests that the improved resistance of fine-grained Ti-6Al-4V alloy to stress-corrosion cracking is due primarily to the increased crack initiation time.

5. Conclusions

a. An increase in stress decreases the crack initiation and crack propagation times.

b. Crack initiation time decreases as the grain size increases for tests conducted at the same stress level according to the Petch equation.

c. Although the crack propagation time decreases with increasing grain size, this difference is not very significant when compared to crack initiation time.

d. Crack initiation starts at the grain boundary and occurs by an anodic dissolution process.

e. Cracks propagate by both intergranular and transgranular manners. Chloride ions are a significant factor in the initiation and propagation of stress corrosion cracks.

H. AN INVESTIGATION OF THE CHEMICAL FACTORS AFFECTING THE STRESS CORROSION CRACKING OF TITANIUM IN METHANOL ENVIRONMENTS

(J. F. Gloz)

1. Introduction

The use of titanium as an engineering material in critical applications has been seriously hampered by its susceptibility to stress corrosion cracking and catastrophic failure. While a great deal of empirical information exists about the conditions known to induce susceptibility, the nature of the cracking process itself is not well understood. This investigation was intended to explore several fundamental aspects of the stress corrosion phenomenon. One aspect involves the role of halide ions, particularly chloride, in the cracking process. There is considerable disagreement over whether halide ions are a necessary or only a sufficient condition for cracking to occur. Contradictory evidence has been reported in the literature. Mazza,[62] using bend specimens of commercially sure titanium, found intergranular cracking in 10^{-5}M NaCl-methanol solutions (0.1% H_2O). Cracking was even observed in halide-free solutions at very low water contents (130 ppm H_2O), although only after 700 hours. On the other hand, Haney and Wearmouth[63] tested pure titanium foils exposed to methanol-HCl solutions and found no failures at concentrations less than 10^{-5}N HCl for exposure times up to 3000 hours. There is no question, however, that chlorides can markedly reduce failure times. In the latter experiments, specimens exposed to 10^{-2}N HCl-methanol solutions failed in 2 to 3 hours. To clarify the role of chloride ions in the cracking process, stress corrosion experiments were conducted in purified methanol.

Another important factor in characterizing stress corrosion is understanding the effect of solution composition. The solution composition is a critical factor in determining the stability of the passive film on titanium. Since stress corrosion involves penetration of the passive film and prevention or retardation of repassivation of exposed metal surfaces, it is desirable to know how the stability of the passive film is affected by changing the solution composition. To investigate this question, anodic polarization experiments were carried out in a series of methanol-hydrochloric acid solutions.

2. Experimental

The material used in all parts of this study was commercially pure titanium (RMI 30) supplied by Reactive Metals Inc. The nominal composition is listed in Table IX.

Table IX - Composition of the Commercially Pure Titanium Used in This Investigation (RMI-30)

Iron	0.05%
Oxygen	0.08%
Carbon	0.02%
Nitrogen	< 0.01%
Aluminum	trace
Vanadium	trace
Manganese	trace
Chlorine	non-detectible
Titanium	balance

a. Stress Corrosion Cracking Tests

(1) Moisture Contamination Problems--A serious problem in obtaining meaningful stress corrosion data in methanol solutions is contamination by moisture. The passivating properties of water are well known and even the presence of very small amounts can markedly affect cracking behavior. This problem is aggravated by the fact that methanol is very hygroscopic and readily absorbs moisture from the atmosphere. The magnitude of this problem is illustrated in Fig. 91 where the water content of a methanol solution is plotted as a function of atmospheric exposure time. It can be seen that the water content of the solution increased by two orders of magnitude in about five hours. This points out the absolute necessity of isolating methanol test solutions with low water contents from the atmosphere. The erratic results reported by some investigators[64] have been attributed to variations in the water content of their test solutions. To avoid the problems associated with moisture contamination, methods were developed to dry and purify the methanol and to measure its water content.

(2) Methanol Drying and Purification Technique--Several methods were considered for reducing the moisture content of the methanol to a reproducibly low level. Water removal by passing the alcohol over molecular sieves (Linde 5Å) was tried but found to be unsatisfactory. A method originally proposed by Lund and Bjerrum[65] for the dehydration of ethanol was found to give better results. This method involves the refluxing of boiling methanol over magnesum chips. The magnesium reacts with the methanol to form magnesium methylate according to the reaction,

$$Mg + 2CH_3OH \rightarrow Mg(OCH_3)_2 + H_2 \ . \qquad (18)$$

The magnesium methylate then reacts with any water present to form magnesium hydroxide as follows:

$$Mg(OCH_3)_2 + 2H_2O \rightarrow Mg(OH)_2 + 2CH_3OH \ . \qquad (19)$$

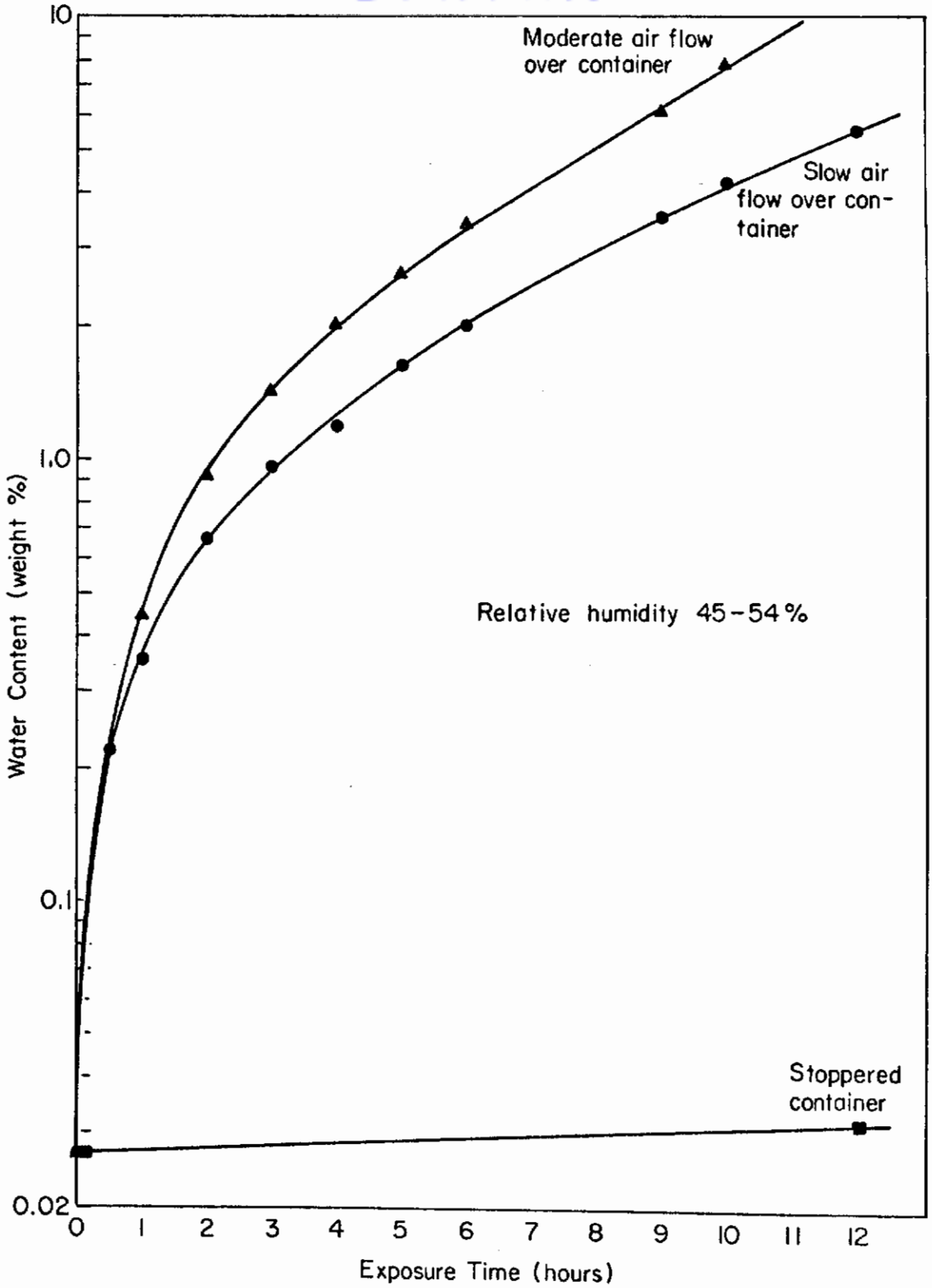

Fig. 91 - Moisture Pickup by Methanol vs. Atmospheric Exposure Time

Magnesium hydroxide is very insoluble and precipitates out of solution. The resultant solution is distilled to give pure, dry methanol. To maintain the purity of the distillate, an enclosed system for storing and transferring it was deemed necessary. A schematic diagram of the drying apparatus and the test cell is shown in Fig. 92. Pure, dry nitrogen is used to pump the solution through the system.

(3) Water Determination Technique--To determine low water concentrations, a method proposed by Karl Fischer[66] was adopted. This method consists of titrating the unknown sample with Karl Fischer reagent and comparing the results to a standard sample. The reagent is composed of dioxane, pyridine, iodine, and methanol as a solvent. While a visual end-point determination is possible in colorless solutions, electrometric techniques give more precise results. A direct titration, "dead stop" method[67] was employed in this study. In this method, a potential is applied across two platinum electrodes and the current is monitored by a galvanometer or microammeter. During titration, as long as water is present, the anode is depolarized but the cathode is polarized. At the endpoint, there is no free water to react with the iodine in the Karl Fischer reagent and the excess iodine depolarizes the cathode resulting in a current surge. Determinations down to 10-100 ppm water are possible with this technique.

(4) Chloride Ion Determination Techniques--Accurate determinations of very low levels of chloride ions were considered to be essential in this experiment since the presence or absence of these ions was the critical question. A specific ion electrode using a solid membrane was found to give satisfactory results. In principle, a solid membrane electrode uses a thin crystal of a slightly soluble salt of the ion to be determined as a sensor. In this case, the sensor was a crystal of silver chloride. A potential difference develops across the crystal membrane when it is placed in a solution containing the specific ion to be determined. This potential difference depends upon the concentration of the ion, in this case the chloride ion, at the membrane surface. The concentration of the ion is thus related to the electrode potential measured against a suitable reference electrode. The limit of detection of such ion-sensitive electrodes depends upon the solubility product of the sensing crystal in the given solution. In aqueous solutions, the limit of detection of a chloride ion electrode is about 0.5 ppm Cl^- (1.4×10^{-5} M) at 25°C. However, the solubility product of silver chloride is much lower in methanol than in water.[68] The theoretical lower limit of detection of chloride ions is about 0.015 ppm Cl^- (3×10^{-7} M). Kinetic factors, however, permit somewhat lower levels to be measured.

(5) Test Procedure--The stress corrosion test specimens were unnotched tensile specimens. The dimensions of the specimens are shown in Fig. 93. After machining, the samples were vacuum annealed for 30 minutes at 1300°F(705°C). The average yield stress was 32,300 lb/in.^{2}. The test cell was designed to be airtight to prevent

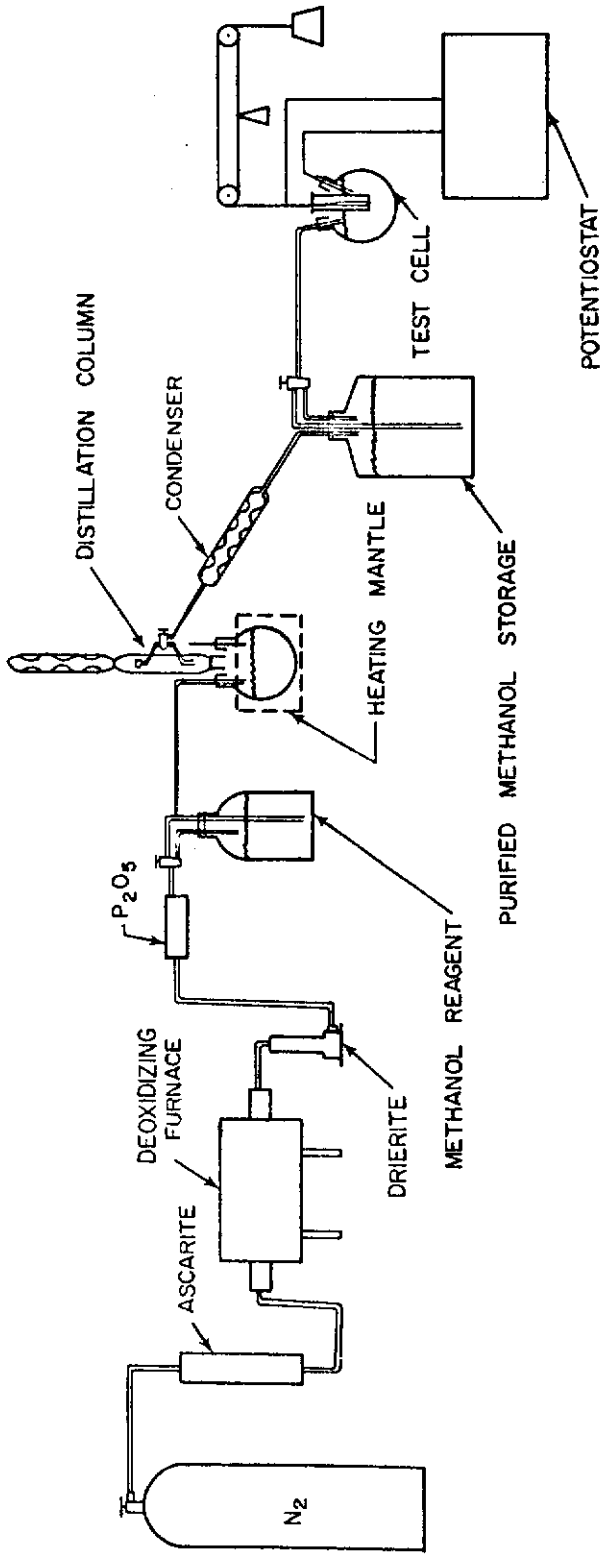

Fig. 92 - Schematic Diagram of Methanol Drying Apparatus and Test Cell

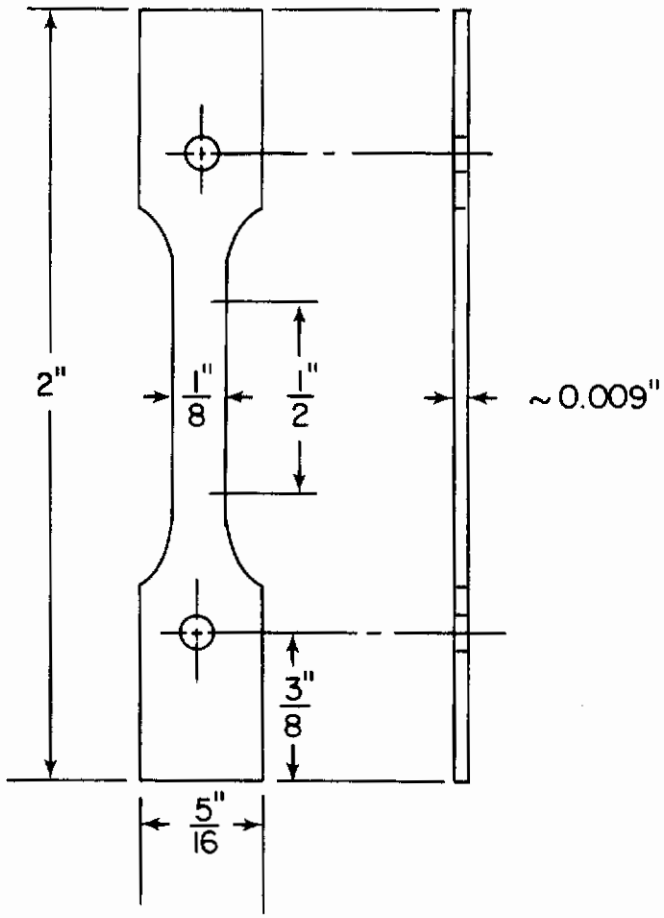

Fig. 93 - Dimensions of Tensile Specimens Used in Stress Corrosion Tests

moisture pickup from the atmosphere. Before being inserted in the cell, the specimens were polished through 600-grit paper, rinsed with acetone and dried. The system was purged with dry nitrogen for several hours before the methanol was introduced. After the test solution was introduced. The specimen was loaded to 90% of the yield stress and the time to failure was recorded. The methanol had been purified by the process described above. Conductivity measurements were made with a Beckman "Solu-bridge" conductivity bridge. The measurement of the chloride ion concentration in the methanol was carried out with an Orion Specific Ion Electrode used in conjunction with an Orion Double Junction Reference Electrode. Methanol saturated with potassium nitrate was used as the outer filling solution in the reference electrode. A calibration curve for methanol was plotted using a series of methanol standards with known chloride ion concentrations. Measurements were made at 25 ± 1°C.

b. Polarization Tests

To study the polarization behavior of titanium in methanol-hydrochloric acid solutions, commercially pure titanium sheet 0.025 in. thick was cut into squares approximately 1 cm^2 in area. The squares were mounted in a Teflon electrode holder with Quickmount mounting material. Electrical contact was achieved by attaching a copper wire to the rear surface of the specimen. The electrode holder is similar to one previously described by Myers[89] but modified so that the surface of the specimen is flush with the mount surface. This prevents gas or air bubbles from becoming trapped and covering part of the specimen surface. Before being introduced into the polarization cell, the exposed titanium surface was polished through 600 grit paper and dipped in a 33% nitric acid - 1.6% hydrofluoric acid pickling solution for 45 seconds. After insertion in the cell, the specimen was allowed to remain in the solution with no potential applied for five minutes. This procedure removed any air-formed surface film and hopefully resulted in the formation of a film more typical of one that might be formed if the passive film were ruptured by mechanical means (such as straining or bending) and the underlying metal had to equilibrate with the bulk solution.

The test solutions were prepared from reagent grade methanol and hydrochloric acid. The composition of the solutions used are listed in Table X.

Table X - Composition of Solutions Used in the Polarization Experiments (Values expressed in weight percent)

Solution	HCl, %	H_2O, %	Balance
A	15	25	CH_3OH
B	10	16.7	CH_3OH
C	5	8.4	CH_3OH
D	1	1.8	CH_3OH
E	0.1	0.19	CH_3OH
F	0.01	0.05	CH_3OH

A test was run in aqueous 5N HCl as a reference. During the upward anodic scan, the potential was shifted from the corrosion potential to +2000 mV at approximately 110 mV/min. For the reverse scan experiments, the specimens were polished and pickled as before. However, after the specimen was placed in the cell, the potential was immediately shifted to +2000 mV and then scanned down at -110 mV/min to -800 mV. The electrode potential was referred to a saturated calomel reference electrode via a Luggen probe and a salt bridge. The potentiostat was an Anatrol Model 4100 with a 10 V DC voltage capacity. A Wenking PVR 63 potentiometer was used to monitor the potential.

3. Results

a. Stress Corrosion Test in Pure Methanol

Results for the stress-corrosion cracking of commercially pure titanium are shown in Table XI.

Table XI - Test Results for (RMI-30) Titanium in Pure Methanol

Test	Load (% of yield stress)	Water Content (%)	Chloride Ion Content (%)	Time To Failure (hr)
1	90	0.04	< 0.010	No Failure after 100 hours (test terminated)
2	90	0.05	< 0.010	248
3	90	0.05	< 0.010	242

Examination of the fracture surface indicated a brittle type fracture with no localized yielding. The exterior surface appeared bright with no evidence of corrosive attack. However, one complicating factor was that cracking would occur at the liquid vapor interface on a specimen which was not completely submerged. This would occur even if the liquid vapor interface was in a region considerably wider and presumably less highly stressed than the gage length region.

The purified methanol used in these experiments had chloride ion levels below the limit of detection of the specific ion electrode technique. This can be seen from the typical calibration curve shown in Fig. 94. Further evidence that the purified methanol was indeed pure was obtained from conductivity measurements on the methanol. The measured conductivity was 0.4-0.6 micromho/cm (approximately half the value for reagent grade methanol). Such a low conductivity indicates that the purified methanol has a very low concentration of ions of any type.

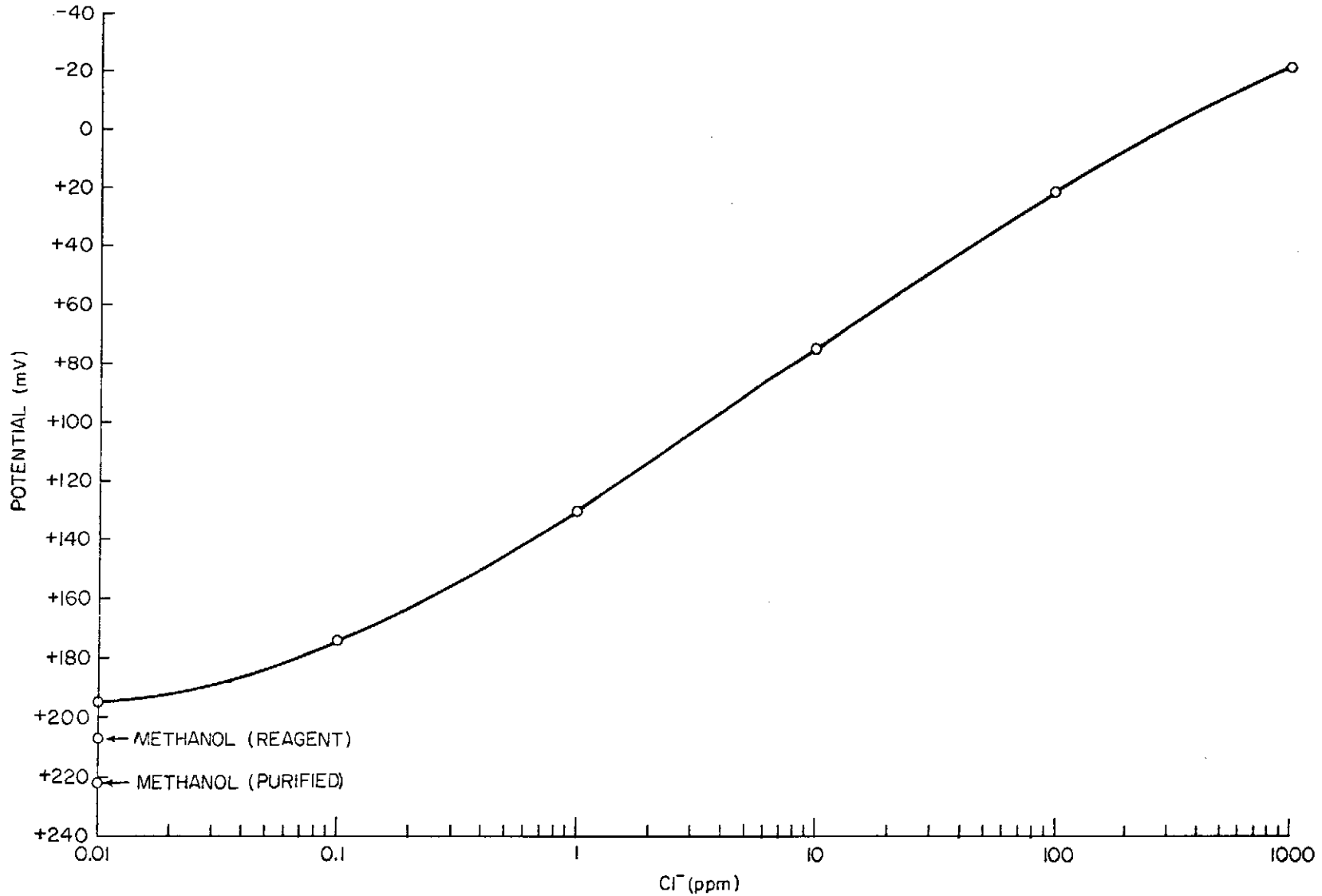

Fig. 94 - Calibration Curve for Cl^- Ion Electrode with Methanol LiCl Standards (T = 25 ± 0.3°C)

b. Polarization Experiments in CH_3OH-HCl-H_2O Solutions

The results of the polarization experiments are shown in Figs. 95 and 96. Figure 95 shows the upward anodic scan in various solutions. Curves for solutions A, B, and C show low currents over the entire potential region. However, in solution D, which contains 1% HCl and 1.8% H_2O, the current begins to oscillate above +100 mV and then climbs rapidly. Thus it is apparent that passivity breaks down at higher anodic potentials. In solutions E and F, which have very low water content, no passive region is observed and current densities may become two or three orders of magnitude higher than those encountered under passive conditions. The tests were terminated whenever the DC cell voltage reached 10 V, the limit of the potentiostat. Figure 96 shows the results for the reverse scans. The starting potential was +2000 mV and the potential was scanned in a negative direction. In this case, the curves for solutions A and B exhibit passive behavior over the entire anodic range. The anodic-cathodic transition occurs at a potential several hundred mV positive. For tests in the other solutions, C, D, E, and F, the anodic-cathodic transition occurred at about -300 mV.

Visual inspection of the specimen surface during the course of polarization in solutions A and B showed no perceptible changes. However, during the reverse scan in solution C, a clear viscous liquid was observed to flow off the specimen. The liquid apparently had a higher specific gravity than the test solution and flowed to the bottom of the cell. As this liquid was being generated, the surface of the specimen darkened perceptibly. This darkening was found to be due to a porous, black, non-adherent layer on the surface of the sample that apparently grew by advancing into the titanium. It was noted that the longer a specimen was held in the potential region where this product formed, the greater was the distance that this layer had penetrated into the specimen. This material could be scraped off easily and became powdery when dry. Metallographic examination of the surface of this layer showed small bright regions of unattacked metal completely surrounded by black regions where the metal had been dissolved away. The dissolved regions appeared to coincide with grain boundaries. X-ray analysis of the powder indicated that it was pure titanium. This layer was found to occur in some other solutions when the potential was shifted immediately to a high anodic value. In those cases where the specimen was allowed to stand at the corrosion potential before polarization was begun, pitting rather than intergranular attack was the predominant type of corrosion. The change in the surface condition of the samples after polarization in the given solutions is shown in Table XII. It should be pointed out that some specimens were in the anodic potential range longer than others because the tests in which the voltage limit of the potentiostat was reached were terminated at that point. The specimens in solutions with low HCl-H_2O contents were thus in the anodic region the shortest times.

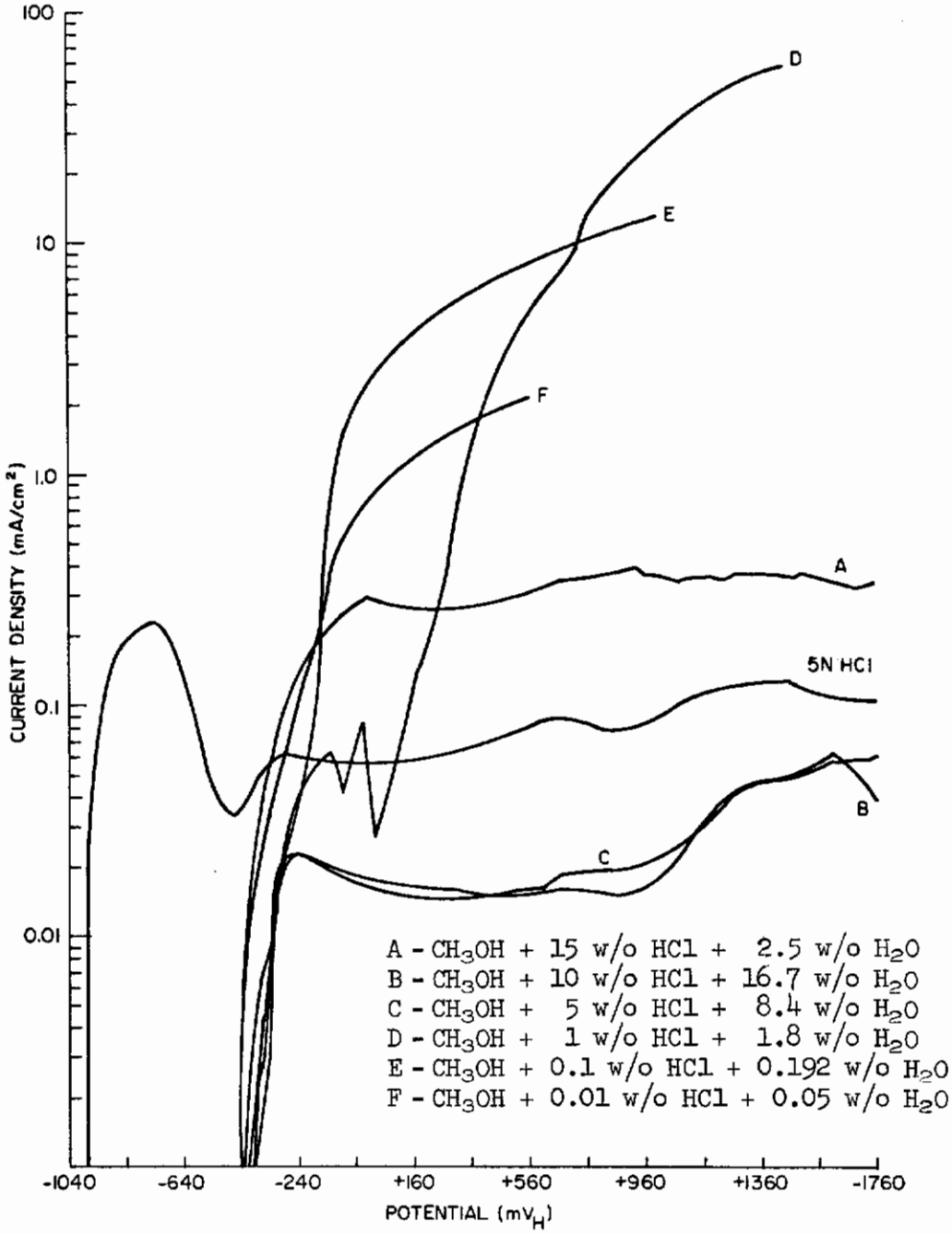

Fig. 95 - Anodic Polarization Curves for Commercially Pure Titanium in Methanol, HCl, Water Solutions

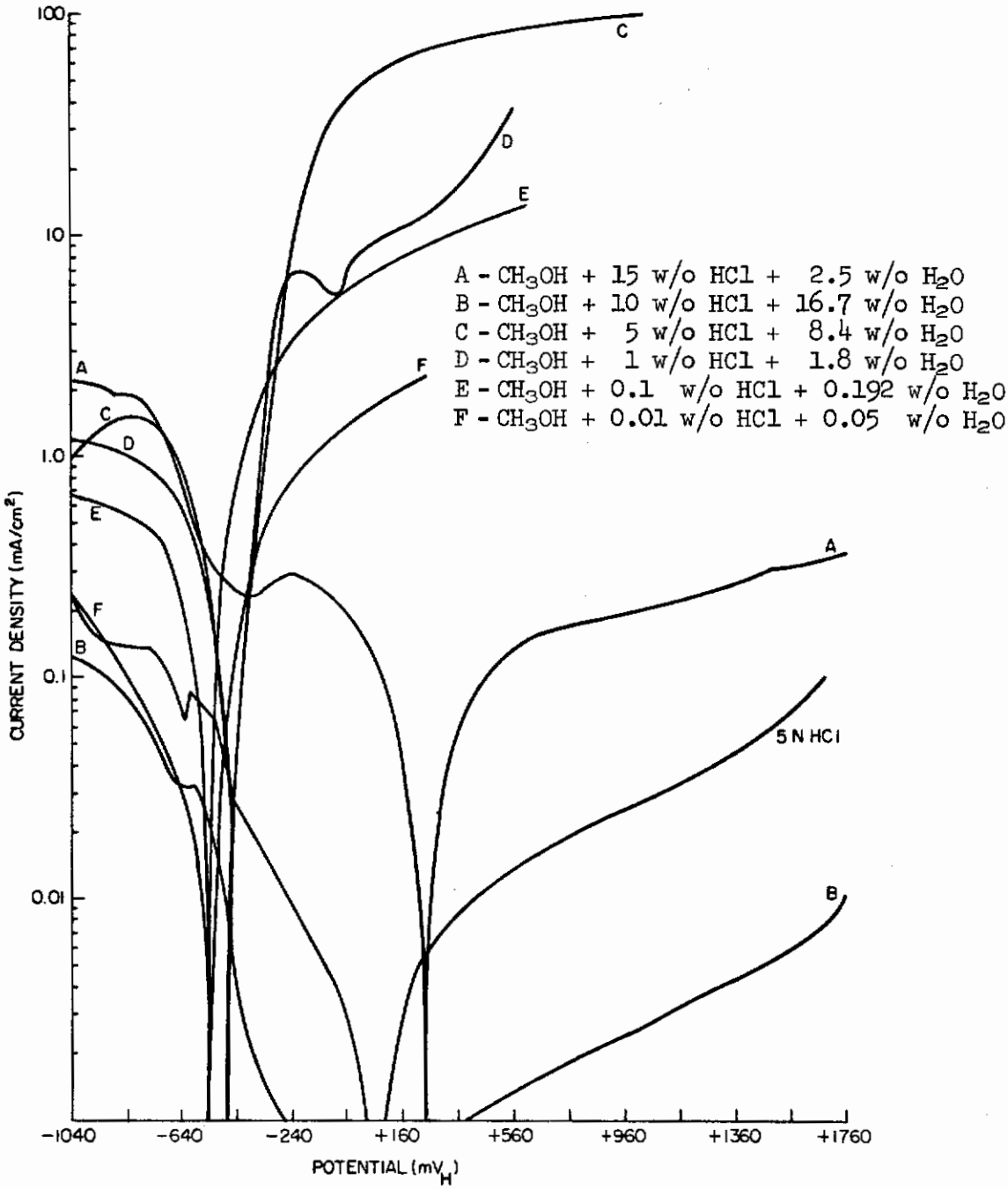

Fig. 96 - Anodic Polarization Curves for Commercially Pure Titanium in Methanol, HCl, H_2O Solutions (Reverse Scan)

Table XII - Change in Surface Condition of Titanium After Polarization in Various Methanol - HCl-H_2O Solutions

Solution	Surface Condition	
	Upward Scan	Reverse Scan
A	No significant change	No significant change
B	No significant change	No significant change
C	No significant change	Rapid formation of dark layer over entire specimen surface
D	Random pitting consisting of a small number of rather large pits	Severe attack, entire surface covered by dark layer
E	Pitting but pits are small, surface still bright	Slight darkening of surface accompanied by some pitting, pit density greater than in upward scan
F	Slight pitting	Some very small pits apparent, surface relatively bright

The amount of the clear liquid flowing off the specimen seemed to be directly proportional to the amount of corrosion or pitting occurring on the surface. When a solution containing this liquid was allowed to stand for a day it took on a clear, bright yellow color which was stable. While the liquid has not been identified as yet, it is presently believed to be a titanium chloride or some titanium complex which gradually hydrolyzes to a yellow compound when allowed to stand in contact with a water-containing solution.

4. Discussion

The results of the stress corrosion cracking tests show that titanium is susceptible to cracking in the absence of chloride ions. The analytical technique used to assay the purity of the methanol in the stress corrosion experiments showed that the chloride ion concentration was less than ten parts per billion. It is difficult to conceive how any concentration this low could participate in the cracking process in a significant way. Therefore, it is clear that in methanol, stress corrosion cracking of titanium can occur by a mechanism other than chloride ion attack. This does not mean that chloride ions may not accelerate or enhance cracking but only that their presence is not necessary for cracking to occur.

The main alternatives to a mechanism based upon halide ion attack are embrittlement due to hydrogen or titanium hydride or local anodic dissolution leading to crack growth. The polarization experiments performed in this investigation were intended to provide more information about the electrochemical behavior of titanium in methanol-hydrochloric acid solutions. In particular, it was hoped to learn more about the effect of these solutions on passivity. For dissolution to occur, the passive film on titanium must be penetrated or removed. The presence of a passivator, such as water, is important in this regard. Above a certain water content, any break in the passive film is immediately repassivated even though there may be a high level of aggressive ions in the solution. This is stable passivity as indicated in the curves for solutions A and B in Figs. 95 and 96. If a passive film is stable once formed but will not repair itself spontaneously, then metastable passivity exists and any breakdown of the film leads to attack. This type of behavior is shown in the curve for solution C in Figs 95 and 96. During the upward scan, the specimen exhibits completely passive behavior. However, if the passive film is chemically disrupted and the specimen is held at an anodic potential, a passive film does not form and attack occurs very rapidly. Curve D indicates behavior close to the border line between metastable passivity and nonpassivity. The passive film begins to break down during the upward scan and apparently there is not enough water present to repassivate the surface. The reverse scan shows completely active behavior as do the curves for solutions E and F which contain still lower water contents; in these solutions, there is no passive region. The critical water content for maintaining passivity in CH_3OH-HCl-H_2O solutions is close to 1.8% based upon the curves in

Fig. 95. This agrees well with the value of 1.6% found by Chen (Section IIC) for stress-corrosion cracking experiments with titanium U-bend specimens (see Fig. 31). Note that below approximately 1.6% water, the specimens failed in about one hour but above 1.6% there were no failures after 1000 hours. This last observation suggests that reverse scan polarization tests may be of practical significance in evaluating susceptibility to stress corrosion cracking without conventional long-term stress corrosion tests. If a specimen has its air-formed surface film removed and a reverse scan anodic polarization is run, completely passive behavior indicates that the material would spontaneously repassivate even if the passive film were ruptured. On the other hand, if active behavior or borderline passivity is observed during the reverse scan, any break in the passive film may result in rapid attack and stress corrosion cracking. In this case, regular stress corrosion tests should be conducted to evaluate the degree of susceptibility. More work must be done to determine just how general the validity of this evaluation technique is. In particular, it should be tested in other environments.

The high current densities encountered in some solutions, together with the layer of pure titanium found on the specimen surface and evidence of dissolution at the grain boundaries, suggest that intergranular attack occurs at a very high rate. The powdery titanium layer on the surface of the specimens after polarization is probably a layer of relatively loose titanium grains left behind after the grain boundaries have been dissolved away. This leads to the question of whether intergranular attack and stress corrosion are related. While the fact that titanium is susceptible to intergranular attack in methanol solutions containing chloride ions is well-known, there has not been much information published about the rate of intergranular attack and whether it is compatible with observed stress corrosion cracking rates. A rough calculation based upon the currents observed on corroding specimens indicates that the rate of intergranular attack is theoretically compatible with observed crack propagation rates. For example, if it is assumed that only 10% of the surface of the specimen consists of grain boundary area and that only this area is being attacked, then the effective current density at the grain boundaries may be 1 A/cm^2 based upon a 0.1 A current on a 1 cm^2 surface. If this value is substituted into a Faraday type equation relating current to weight loss, it is possible to estimate the rate of intergranular attack. The penetration rate is given by the following equation:

$$P = \frac{JM}{nF\rho} = \frac{\omega}{\rho At} , \qquad (20)$$

where

P - penetration rate,
J - current density at the grain boundaries,
M - atomic weight of titanium,
n - number of electrons involved in the dissolution reaction,
F - Faraday's constant,
ρ - density of titanium,

ω - weight of titanium dissolved,
A - effective area of the grain boundaries on the surface, and
t - time of exposure.

If the following values are substituted into the above equation:

$J = 0.10$ A/cm^2; $M = 47.9$ g/mole; $n = 2$; $F = 96{,}500$ coul./equivalent; and $\rho = 4.5$ g/cm^3;

then a value of 5.5×10^{-4} cm/s is obtained for the penetration rate. This is the same order of magnitude as the crack propagation rates measured by other investigators[10,70] in this project on Ti-6Al-4V alloys. Thus while intergranular attack may or may not be the controlling factor in the stress corrosion cracking of titanium in CH_3OH-HCl solutions, there is evidence that a dissolution mechanism is plausible.

4. Conclusions

a. While chloride ions enhance the susceptibility of titanium to stress-corrosion cracking in methanol, they are not absolutely necessary for cracking to occur.

b. The water content of the solution is the most important factor in determining the stability of the passive film on titanium in CH_3OH-HCl solutions.

c. Intergranular corrosion is the dominant mode of attack of commercially pure titanium in CH_3OH-HCl solutions and the rate of attack is theoretically compatable with observed stress-corrosion cracking rates.

I. STRESS-CORROSION CRACKING OF TITANIUM IN 12N HCl and 10N H_2SO_4 SOLUTIONS (C. M. Chen)

1. Introduction

Titanium is a very active element which would corrode rapidly if it were not for the oxide film that forms in oxygen- or water-containing environments.[71] The electrochemical behavior of titanium has been widely investigated,[9,72-88] particularly in relation to stress corrosion cracking. However, the nature of the Pourbaix diagram,[82,88,89] the dissolution mechanisms,[71,72,76,79,80] and the stress corrosion cracking mechanism[8,18,20,47,59,63,90-94] are still not quite certain. In particular, the role of TiH_2 is not understood. Thermodynamically, the existence of TiH_2 in aqueous solutions was anticipated by many investigators. Otsuka,[77,78,94] and Sukhotin and Tungusova[76] found TiH_2 on titanium surfaces and found it to be a protective film on the metal. A. J. E. Pourbaix, Marek, and Hochman[83] found TiH_2 was formed in the cathodic region in 12N HCl solution; however, it was not protective. The Pourbaix diagram was derived by Schmets and M. Pourbaix[88] using the standard potential of Ti^{+++}/Ti^{++} couple as -0.37 V.[95] However, Olver

and Ross[87] evaluated the potential to be about -2.0 V; therefore, the existence of Ti^{++} is dubious and titanium seems to be oxidized directly to Ti^{+++} without any solution-soluble intermediates.[80,83,96] Armstrong et al.[80] assumed the dissolution of titanium to be H^+ catalyzed, in contrast to Fe [97] and Ni[98] which are OH^- catalyzed. Sukhotin et al., however, assumed the anodic dissolution was due to the oxidation of TiH_2 to Ti^{+++}. Pourbaix et al.[83] and our laboratory found large anodic dissolution in the cathodic region in 12N HCl solution; this would suggest another anodic dissolution mechanism. This report is concerned with the stress corrosion cracking and anodic dissolution mechanisms in aqueous solutions.

2. Experimental

The electrolytes were Mallinchrodt's Analytical Reagent, Hydrochloric Acid (≃ 37%) and B and A A.C.S. Reagent, Sulfuric Acid (≃ 96%). The stress corrosion cracking test was carried out in a closed cell which allows He gas, oxygen, or air to be bubbled through the solution (Fig. 97). The specimen was bent to the yield stress in a steel-stressing jig which was completely coated with Boehler's Plastic Epoxide except for the metal contact parts. The bent specimen was covered with Dekhotinsky cement and then microstop except for about 0.5 cm^2 area on the tensile side exposed in the solution. An erosion-corrosion technique was used in this experiment to obtain fresh surfaces. The ring-shape specimen was attached to a rotating shaft against which a graphite brush was pushed providing electrical connection. The specimen was rotated in an abrasive of Al_2O_3 powder at speeds up to about 10,000 rpm. Platinum wire was used as a counter electrode and was located in a fritted glass tube to isolate it from the abrasive and avoid diffusion of the evolved Cl_2 into the specimen compartment. An Anotrol potentiostat was used for polarization and a Honeywell Electronik 19 recorder was used for current.

3. Results

a. Figure 98-a shows the polarization curve of unalloyed titanium in 12N HCl solution. The potential was applied stepwise at a rate of 40 mV/3min. In the cathodic region, current had a tendency to decrease slightly after the potential was applied in region A, however in region B (from about -715 mV, SHE) the current increased significantly with time. Thomas and Nobe[81] found that a deviation from Tafel behavior occurred in sulfuric acid (pH = 0.25 to 2.25) at -755 mV (SHE) and the current density was greater than the value obtained by extrapolation of the Tafel line. An example of current vs. time at -725 mV in 12N HCl solution is shown in Fig. 98-b. After an incubation period, the current increases steadily; however, after a certain time the current begins to decrease and suddenly drops to a certain value. This represents the onset of some anodic process. Figure 99 shows high purity titanium polarized at -755 mV for 4 hr; (a) is as-received high-purity Ti -- definite pitting looking like localized corrosion can be observed, and (b) is the picture for zone-refined iodide titanium. The material grows

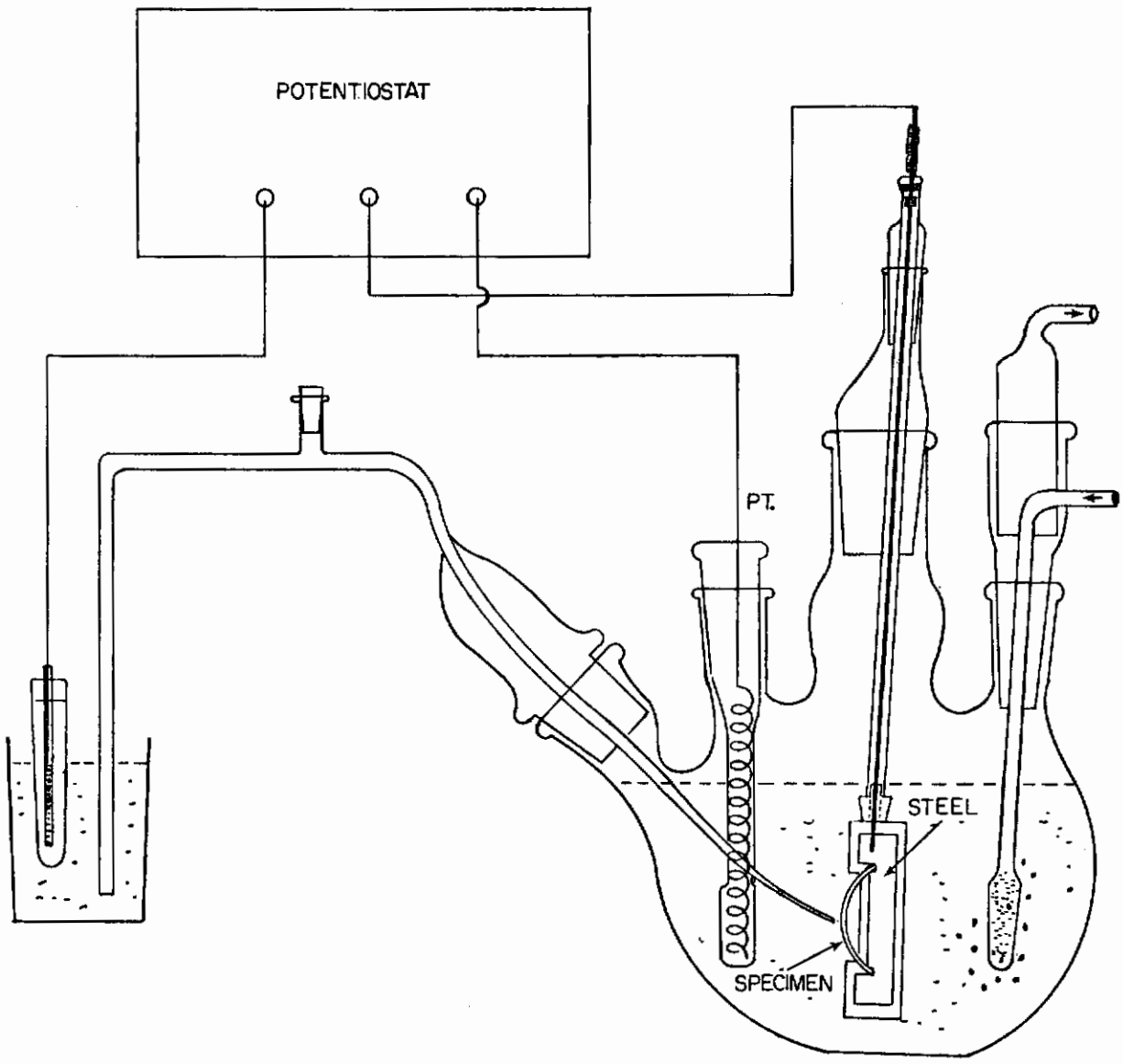

Fig. 97 - Apparatus for Stress Corrosion Test in 10N H_2SO_4 and 12N HCl

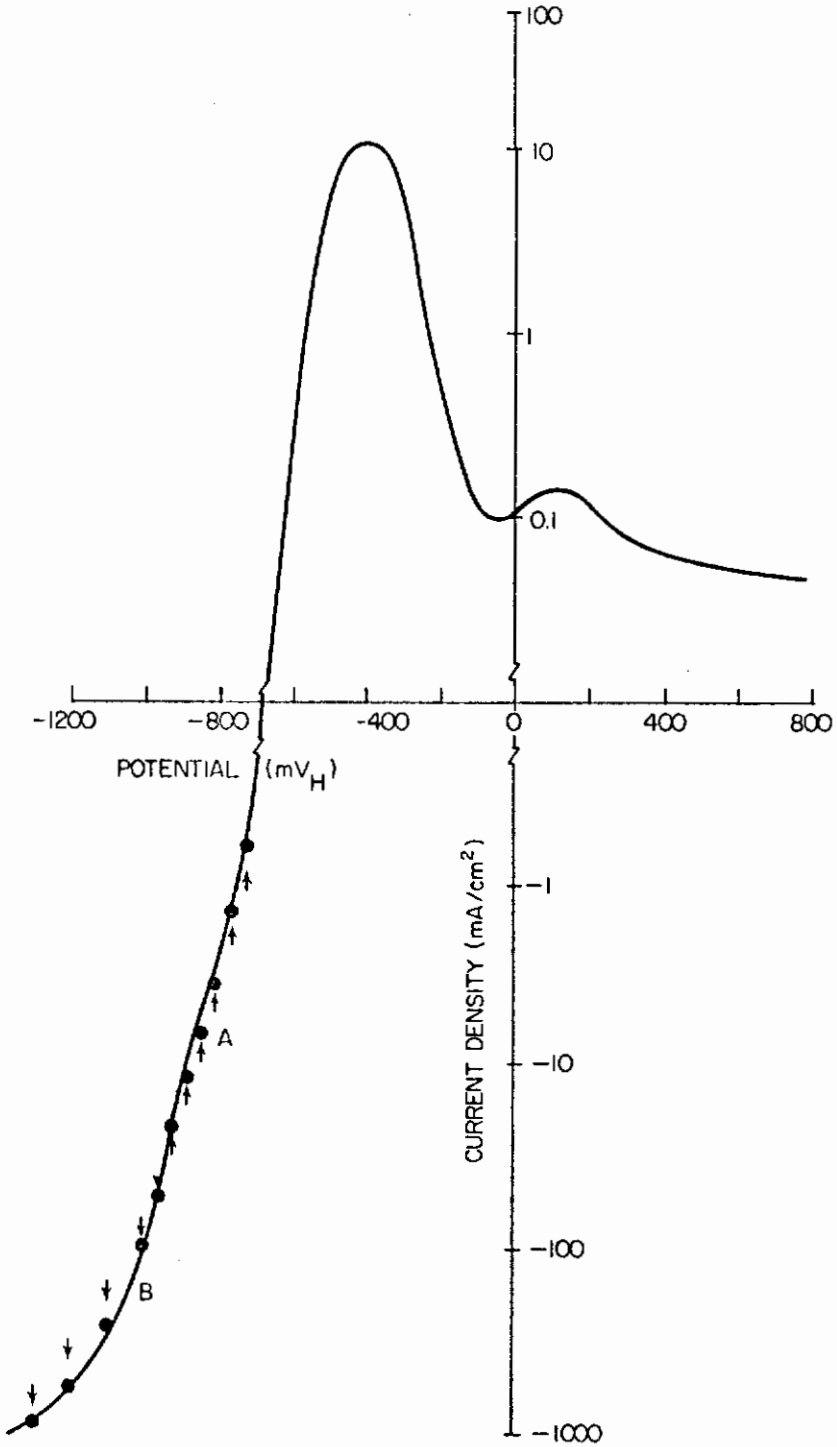

Fig. 98-a - Polarization Curve of Unalloyed Titanium in 12N HCl Solution He Bubbles

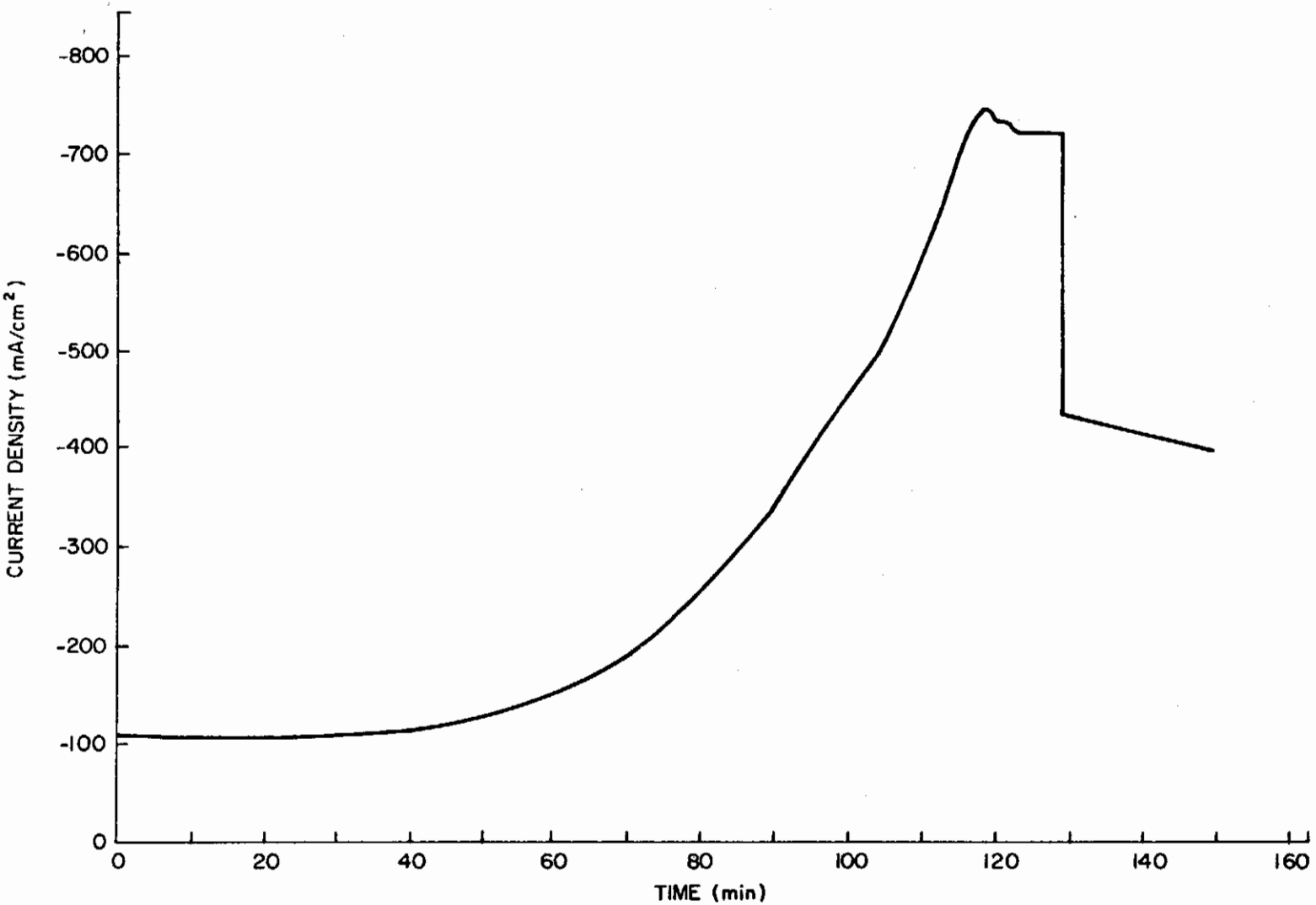

Fig. 98-b - Current vs. Time for Unalloyed Titanium Polarized at -755 mV (SHE) in 12N HCl Solution

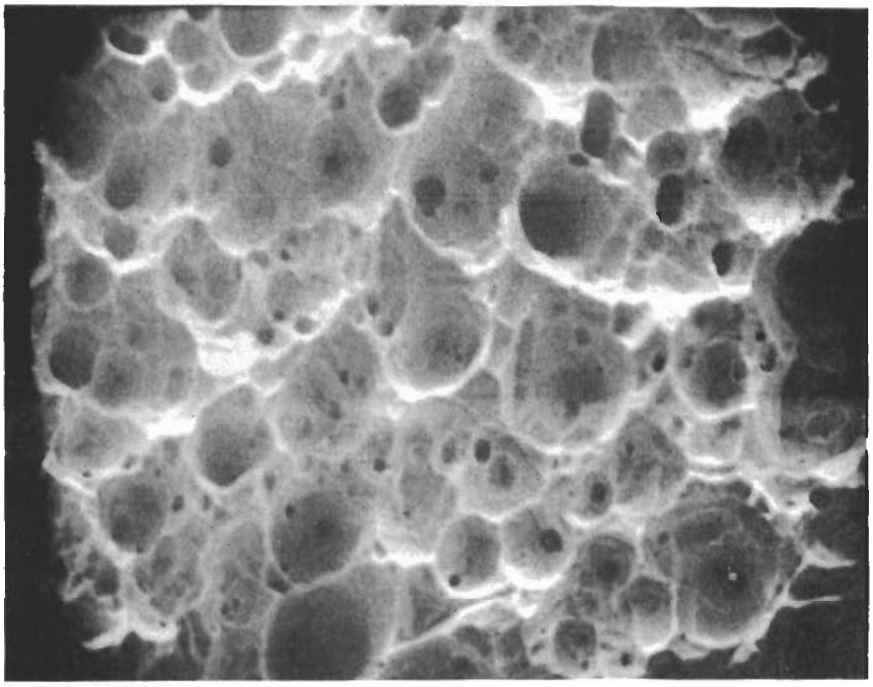

(a) X500

(b) X20

Fig. 99 - Microphotograph of Pure Titanium Surface Polarized at -755 mV for 4 hours
(a) as-received high purity Ti
(b) zone-refined iodide Ti

to big crystals and the corrosion seems to be general; however, the specimen also has the characteristics of localized corrosion in the grain. Pourbaix et al. observed a similar phenomenon and reported a change in polarity of the current, however, we failed to detect it. In the anodic region, a second hump appeared which seems to be similar to that found by Otsuka[78] in 4N H_2SO_4 solution.

b. In 10N sulfuric acid solution without abrasive, the polarization behavior was almost non-affected by the rotational speed, as shown by the solid lines in Fig. 100. However, when the specimen was rotated in the solution containing 20 vol % Al_2O_3 abrasive, the cathodic current was greatly reduced, indicating some anodic process was occurring (dotted lines in Fig. 100). In 12N HCl solution without Al_2O_3 abrasive, the polarization curve of the specimen under static conditions shows almost the same behavior as that in the sulfuric acid solution (solid line in Fig. 101). However, when the specimen was rotated, the cathodic current was greatly reduced, as shown in Fig. 101 by a solid line. When the specimen was rotated in 12N HCl with 20 vol % Al_2O_3 abrasive, the polarization curve shows the same tendency as in the 10N H_2SO_4 solution with abrasive except that the current fluctuation is larger in the former cases and the average current is smaller. Obviously, when a titanium specimen is rotated in a solution containing abrasive, the surface film is destroyed allowing some anodic process to occur; therefore, the external current (i.e. = $\Sigma ic - \Sigma ia$) is reduced. It is interesting that 10N H_2SO_4 needs abrasive for this reduction, however, the concentrated HCl achieves it just by rotation of the specimen without abrasive.

c. Stress-corrosion cracking behavior, as influenced by polarization in 10N H_2SO_4 solution, is shown in Fig. 102. Definitely, no susceptibility can be found in the potential range from -955 mV to +2,245 mV (SHE) in 72 hr; however, in 12N HCl solution, the tendency is quite different, as shown in Fig. 103. In the cathodic region at -955 mV, the unalloyed titanium failed in 4 to 20 hours. The solution bubbled with oxygen gas or air seems to be a little more susceptible than the solution bubbled with He gas. This susceptibility seems to increase in the anodic direction. The maximum susceptibility seems to correspond to the potential of the maximum anodic current; i.e., about -155 mV (SHE). There is no susceptibility in the passivation region up to +2,245 mV (SHE). Observation of stress corrosion cracked specimens both in cathodic and anodic susceptibility regions reveals the same surface characteristics of localized corrosion as shown in Fig. 99, which is without applied stress. The differing behavior between 10N H_2SO_4 and 12N HCl solutions indicates the degree of chloride ion influence on the susceptibility of titanium and its alloys, whether it is due to anodic dissolution or hydrogen embrittlement. If we assume that anodic dissolution occurred in both solutions (10N H_2SO_4 and 12N HCl) at the active anodic potential region, the characteristics of localized corrosion by chloride ion seem very important.

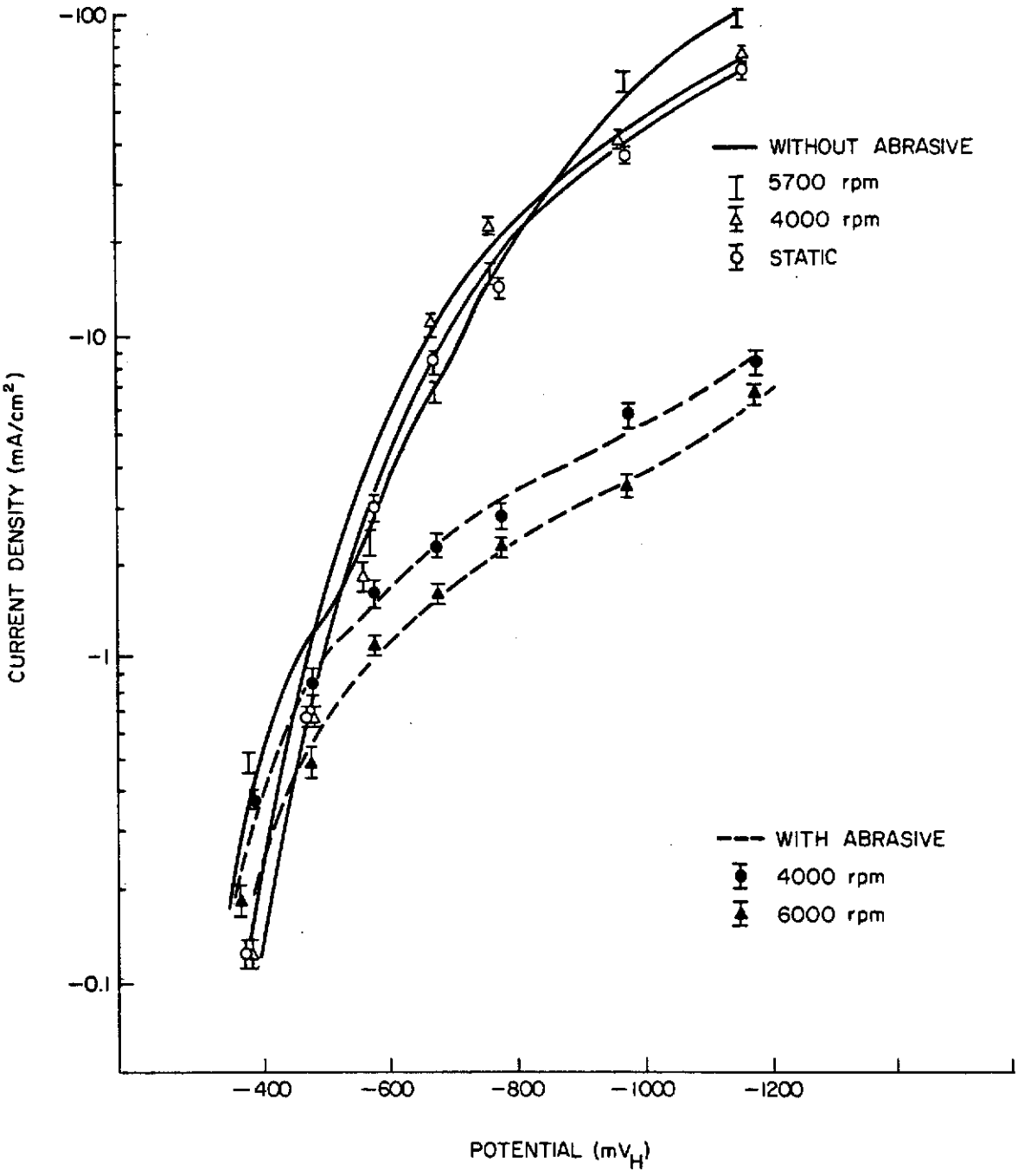

Fig. 100 - Polarization Curves of the Rotating Titanium Specimen in 10N H_2SO_4 Solution

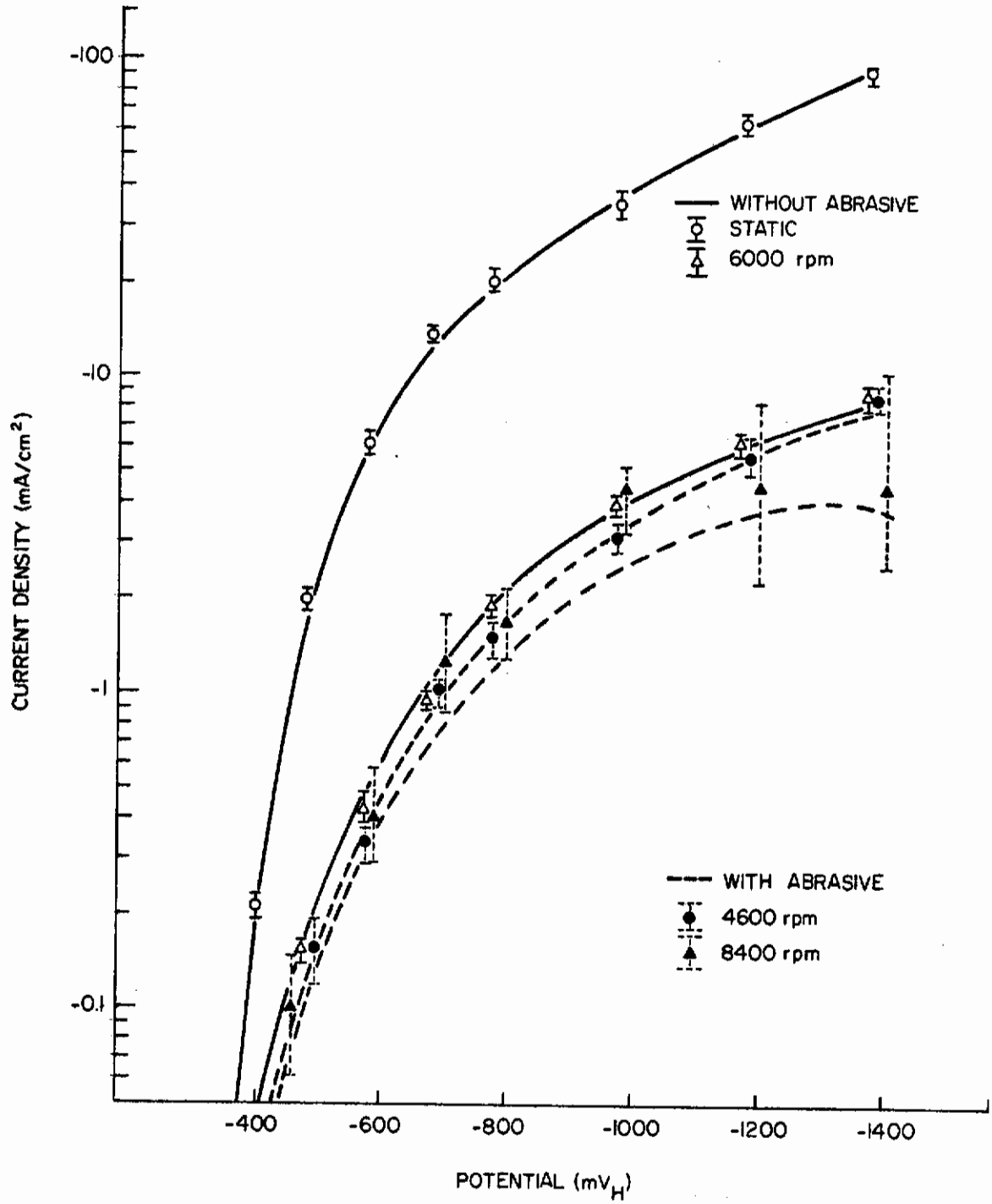

Fig. 101 - Polarization Curves of the Rotating Titanium Specimen in 12N HCl Solution

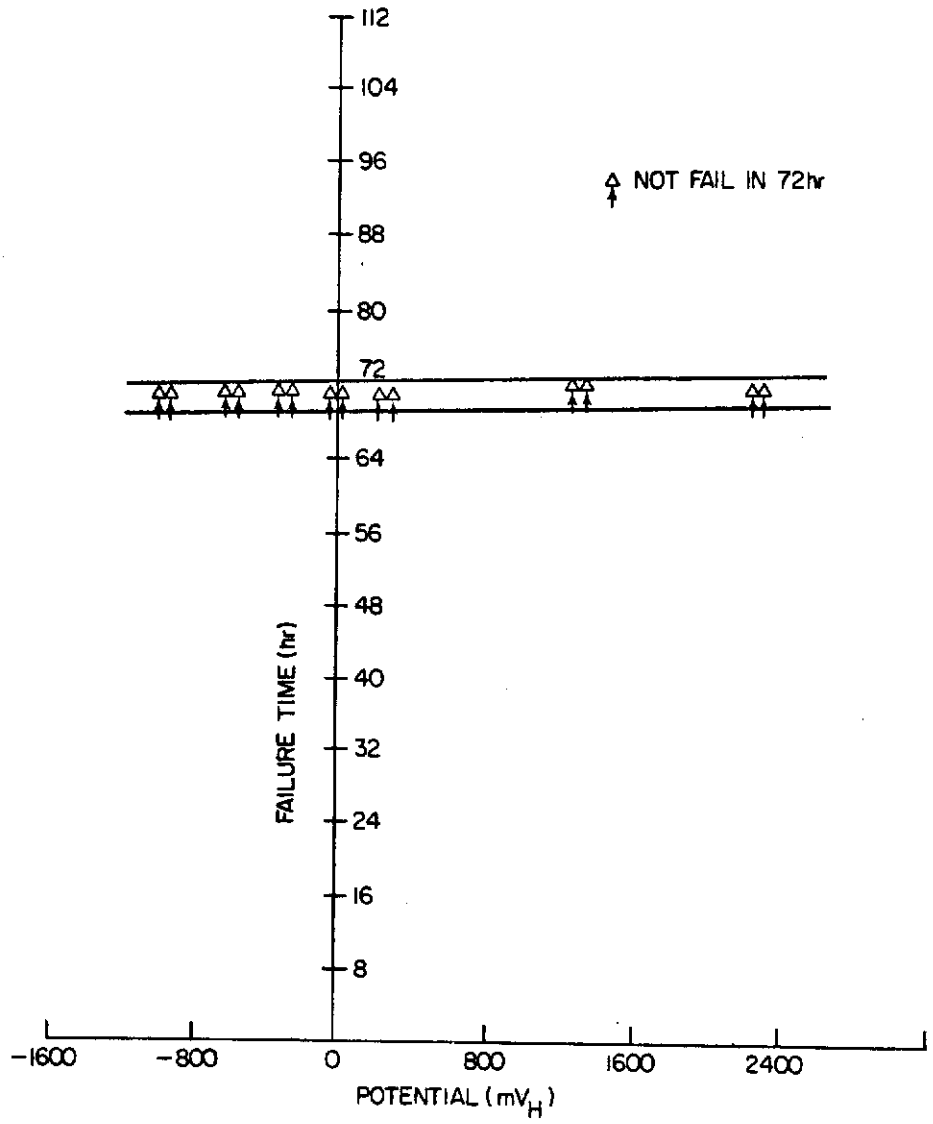

Fig. 102 - Failure Time vs. Potential for Unalloyed Titanium in 10N H_2SO_4 Solution

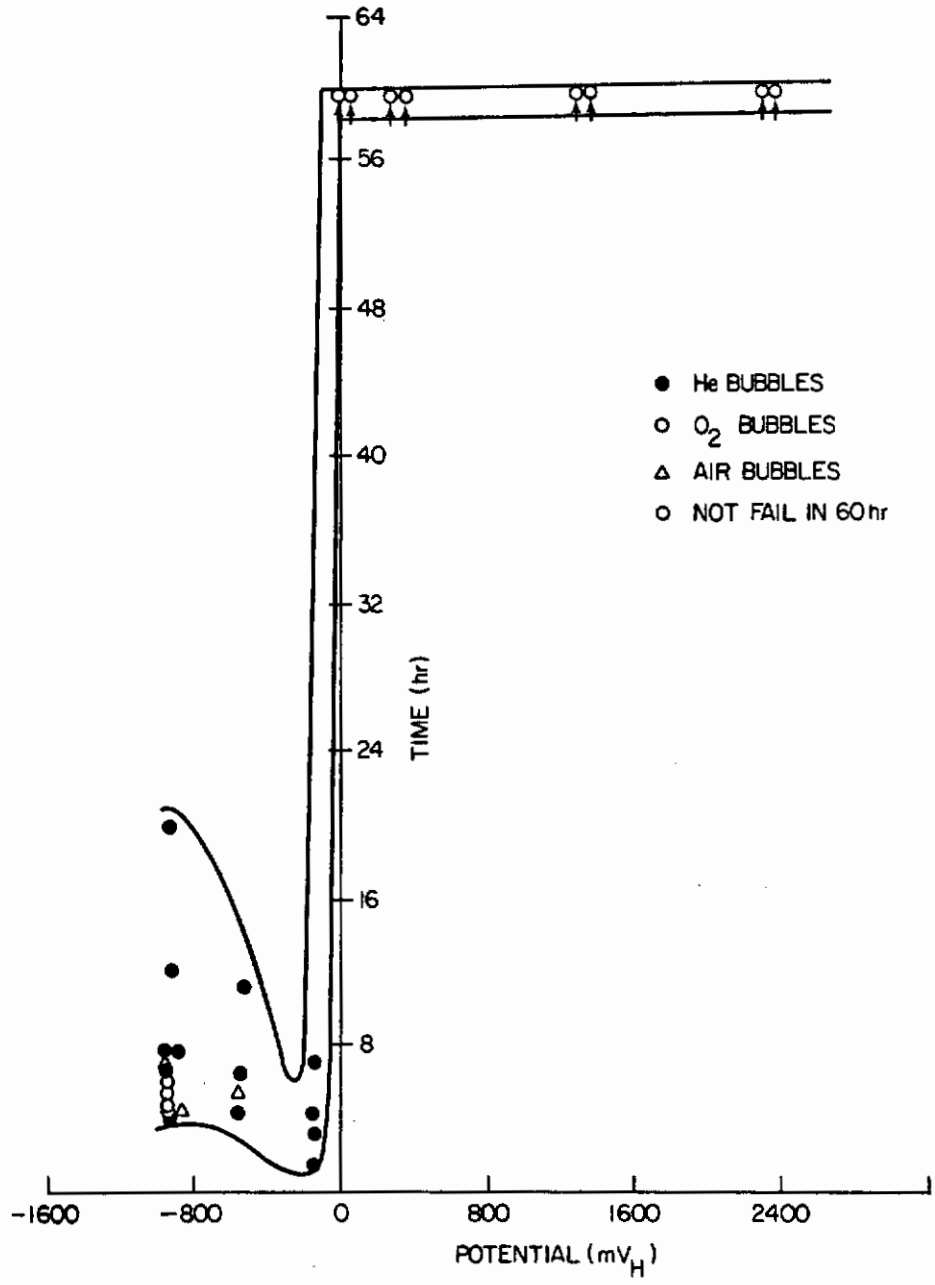

Fig. 103 - Failure Time vs. Potential for Unalloyed Titanium in 12N HCl Solution

When U-bend Ti-8Al-1Mo-1V was immersed in 2N HCl solution for about two months, considerable general corrosion occurred; however, there was no stress corrosion cracking. Sufficient hydrogen was adsorbed into the specimen that the material became so embrittled it could be broken easily with finger pressure. An X-ray analysis was made and the diffraction pattern was somewhat different from the pattern reported by Otsuka[94] and Jaffee,[99] Table XII E, F. When unalloyed titanium coupons were dipped in 12N HCl solution for several days (A for 4 days, B for 5 days, and C for 6 days), the diffraction patterns can be reasonably identified as Ti and TiH_2, although the pattern is more similar to that reported by Jaffee[99] than that by Otsuka.[94] If peaks at $2\theta = 35.40°$ and 41.10° (i.e., d = 2.536 and 2.248, respectively) corresponds to the two greatest intensity lines of TiH_2, then the trace of titanium hydride on the surface would be roughly at the ratio of A/4 = B/5 = C/10; i.e., the trace would be increased as time goes on (Table XIII A, B, C).

4. Discussion

Titanium is not a noble metal. The metal generally exhibits a high potential because a thin film of oxide is formed on its surface and protects the metal; e.g.,

Ti/TiO	: $Ti + H_2O = TiO + 2H^+ + 2e$	$E = -1.31 - 0.059$ PH, (21)
Ti/Ti_2O_3	: $2Ti + 3H_2O = Ti_2O_3 + 6H^+ + 6e$	$E = -1.25 - 0.059$ PH, (22)
Ti/Ti_3O_5	: $3Ti + 5H_2O = Ti_3O_5 + 10H^+ + 10e$	$E = -1.16 - 0.059$ PH, (23)
Ti/TiO_2	: $Ti + 4H_2O = TiO_2 + 4H^+ + 4e$	$E = -1.07 - 0.059$ PH, (24)
Ti/Ti_2O_3	: $TiO + H_2O = \frac{1}{2}Ti_2O_3 + 2H^+ + 2e$	$E = -1.15 - 0.059$ PH, (25)
Ti_2O_3/Ti_3O_5	: $3Ti_2O_3 + H_2O = 2Ti_3O_5 + 2H^+ + 2e$	$E = -0.33 - 0.059$ PH, (26)
Ti_2O_3/TiO_2	: $\frac{1}{2}Ti_2O_3 + \frac{1}{2}H_2O = TiO_2 + H^+ + e$	$E = -0.33 - 0.059$ PH, and (27)
Ti_3O_5/TiO_2	: $Ti_3O_5 + H_2O = 3TiO_2 + 2H^+ + 2e$	$E = -0.33 - 0.059$ PH. (28)

The corrosion potential of Ti in acid solution is located at about -455 mV (SHE); therefore, lower valency oxides such as TiO or Ti_2O_3 could exist. However, since these oxides are soluble in the acid solution, they do not protect titanium perfectly from active dissolution. When an anodic polarization potential is applied, the anodic current will be increased (Fig. 104-a);[79] and at the passivation potential, some porous Ti_3O_5 oxide film[79] or an adsorbed film,[74] will be formed. When the polarization potential reaches the complete passivation potential which may correspond to the second hump in the passive region in Fig. 98-a, an oxide film of TiO_2 (rutile) is formed and protects Ti completely from dissolution (Fig. 104-b).[78] However, as pointed out by Otsuka,[78] in 4M H_2SO_4 solution, this hump may be due to the oxidation of hydrogen gas adsorbed in the material. Pourbaix[89] modified his old diagram,[88] taking into account TiH_2 formation. Olver and Ross[87] estimated the standard potential of Ti^{++}/Ti^{+++} couple as about -2.1 V instead of Forbes and Hall's -0.37 V.[95] This large negative potential for this couple would require that Ti be oxidized directly to Ti^{+++} in the aqueous solution. Sukhotin and Tungusova[76] found titanium hydride film formed on the surface of titanium and that it affects the

Table XIII - X-ray Analysis Data

From Literature						Unalloyed Experiment								Ti-8Al-1Mo-1V Experiment			
Ti		TiH_2 (Ref.99)		TiH_2 (Ref.94)		D--As received material		A--12N HCl 4 days		B--12N HCl 5 days		C--12N HCl 6 days		E--U-bend in 2N HCl 2 mos.		F--Grounded powder from E	
d	I/I_o	d	I/I_o	d	I/I_o	d	I/I_o	d	I/I_o	d	I/I_o	d	I/I_o	d	I/I_o	d	I/I_o
2.557	30					2.557	5										
		2.50	50	2.569	100			2.536	20	2.536	25	2.539	45	2.481	100	2.465	100
2.342	26					2.344	100	2.338	100	2.338	100	2.341	100	2.362	20	2.356	45
								2.276	2	2.276	2						
2.244	100					2.243	35	2.249	15	2.243	25	2.243	15				
		2.20	100	2.224	25			2.248	4	2.249	5	2.248	10				
		2.10	10?													2.149	30
1.726	19					1.726	16	1.725	15	1.726	18	1.726	20			1.797	6
		1.55	30	1.573	35			1.552	2	1.552	5	1.552	7	1.518	67	1.687	6
1.475	17					1.475	5	1.472	6	1.474	4	1.474	4	1.465	33	1.514	18
1.332	16					1.333	33	1.332	30	1.331	55	1.333	30	1.361	27	1.363	12
		1.33	35	1.3418	25					1.330	5	1.326	5	1.328	33		
1.276	2													1.296	46	1.296	6
		1.27	8	1.2851	8					1.270	2	1.271	1				
1.247	16					1.248	5	1.247	4	1.248	8	1.248	5	1.245	20		
1.233	13					1.231	3	1.232	2	1.232	5						
1.1708	2					1.1717	13	1.1717	20	1.1717	10	1.1717	10				
1.1220	2					1.1216	2										
1.0652	3					1.0654	5	1.0645	8	1.0650	10	1.0650	7				
		1.01	10					1.0070	1	1.0096	2						
0.9895	6					0.9897	2	0.9883	1	0.9890	6	0.9883	5				
0.9458	11					0.9455	2	0.9455	1	0.9455	2	0.9452	4				
0.9175	10					0.9176	10	0.9171	10	0.9176	7	0.9176	5				
0.8927	4																
0.8796	4					0.8802	11	0.8800	16	0.8802	20	0.8802	10				
0.8634	2																

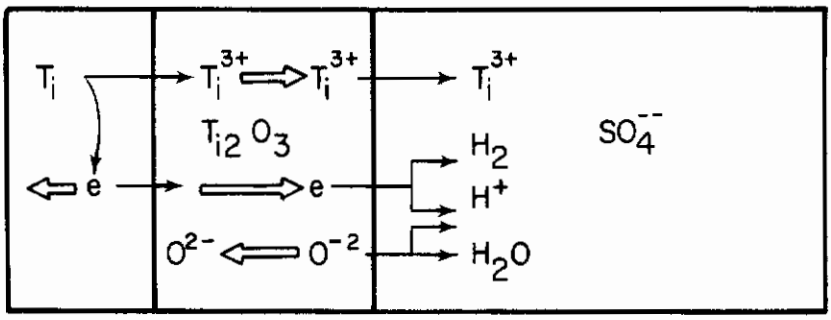

(a)

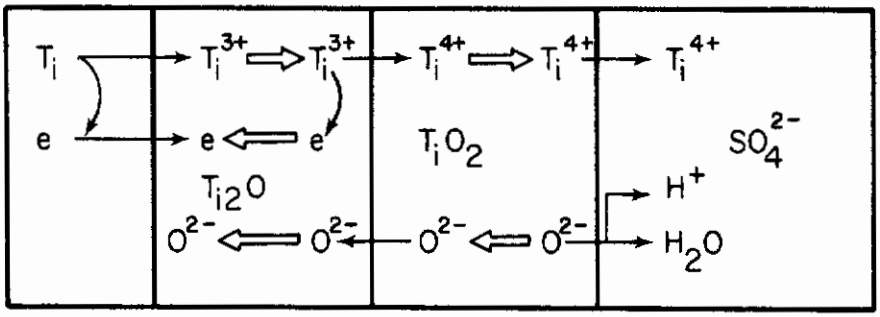

(b)

Fig. 104 - Schematic Diagram for Anodic Dissolution - (a) and Passivation - (b) of Titanium in H_2SO_4 Solution

anodic dissolution. Their calculation of thermodynamic potentials of TiH and TiH_2 formation (-15.0 and -20.9 kcal/mole, respectively) was from thermodynamic data of Stalinski and Buganski;[100] i.e.,

$$Ti + H^+ + e = TiH \qquad E_o = 0.65\ V \tag{29}$$

and

$$Ti + 2H^+ + 2e = TiH_2 \qquad E_o = 0.45\ V \tag{30}$$

They postulate that with the cathodic potential more than 0.45 - 0.65 V, the surface of titanium is always covered by a hydride layer and, therefore, the characteristic of anodic behavior, including activation and passivation, is governed by the electrochemical properties of this layer; e.g., the anodic dissolution is due to the electrochemical reaction,

$$TiH_2 = Ti^{+++} + 2H^+ + 5e \tag{31}$$

and passivation of Ti is due to the appearance of passivating oxide formed on the surface of the hydride layers.

Armstrong et al.[80] recently reported that the anodic dissolution of Ti in sulfuric acid is an H^+ catalyzed process and, that it dissolves directly to Ti^{+++}, without any solution-soluble intermediates as follows:

$$Ti \leftrightharpoons Tiads^{2+} + 2e \tag{32}$$
$$Tiads^{2+} + H^+ \rightarrow Ti^{3+} Hads \tag{33}$$
$$Hads \leftrightharpoons H^+ + e \tag{34}$$

This mechanism is in contrast to Fe and Ni which are OH^- catalyzed proposed by Bochris et al. as follows:

$$Ni + OH^- \leftrightharpoons NiOHads + e \tag{35}$$
$$NiOHads \leftrightharpoons NiOH^+(sol.) + e \tag{36}$$
$$NiOH^+ + OH^- \leftrightharpoons Ni(OH)_2\downarrow \tag{37}$$

and

$$Fe + OH^- \leftrightharpoons FeOHads + e \tag{38}$$
$$FeOHads \leftrightharpoons FeOH^+(sol.) + e \tag{39}$$
$$FeOH^+ \leftrightharpoons Fe^{++} + OH^- \tag{40}$$

In the cathodic region, the kinetics of hydrogen evolution reaction were interpreted by a dual barrier model of Thomas and Nobe.[81] They explain that their kinetic data are dependent on the potential across the oxide film and the potential across the double layer in the electrolyte. In a high cathodic region at approximately -755 mV (SHE), they found deviations from Tafel behavior commencing with an analogous increase in the cathodic current. A possible explanation of this phenomenon suggested by them is the complete reduction of the incipient oxide film at this potential and the subsequent hydrogen ion discharge on the oxide-free titanium. This interpretation seems to be in accord with the results of Beck[101] who reported that the rate of hydrogen evolution reaction on an

oxide-free surface in 12N HCl was greater than on an oxide-covered surface. A second feasible explanation suggested by Nobe et al.[81] is the possible titanium hydride formation from oxide Ti_2O_3 or TiO_2 at -755 mV (SHE). From Stalinski et al.[100] thermodynamic data,

$$Ti_2O_3/TiH_2;\ Ti_2O_3 + 10H^+ + 10e = 2TiH_2 + 3H_2O;\ E = -1.000 - 0.059\ pH \quad (41)$$
$$TiO_2/TiH_2\ ;\ TiO_2 + 6H^+ + 6e = TiH_2 + 2H_2O\ ;\ E = -0.937 - 0.059\ pH \quad (42)$$

and thus the titanium hydride reduces the overvoltage of the hydrogen evolution reaction.[80,83]

In our experiment with polarization at -755 mV (SHE) in 12N HCl solution (Fig. 98-b), after the incubation period, the cathodic current begins to increase steadily. This probably indicates that the thickness of the oxide film has decreased, and therefore the overvoltage of the hydrogen evolution reaction has been reduced. When the oxide film is completely reduced, some anodic process should occur besides the cathodic hydrogen evolution. The possible reaction in 12N HCl solution will be

$$Ti + XCl^- \leftrightharpoons TiCl_x^x + Ti^{+++} \leftrightharpoons XCl^- + 3e, \quad (43)$$
$$Ti + 2H^+ \leftrightharpoons Ti + H_2, \text{ or} \quad (44)$$
$$Ti + 2H^+ + 2e \leftrightharpoons TiH_2, \text{ etc} \quad (45)$$

As the anodic reaction starts to occur, a rapid change in the external current should appear, as shown in Fig. 98-b. The specimen surface appears as that in Fig. 99-a,b; clearly the anodic process that occurred had the characteristics of localized corrosion by chloride ion in 12N HCl solution.

In the rotating electrode experiments, when the titanium surface film was depleted by Al_2O_3 abrasive, the anodic process occurred; the cathodic external current was therefore reduced (Fig. 100, 101). As to stress-corrosion cracking behavior, there is no susceptibility in 10N H_2SO_4 solution. However, in 12N HCl solution, both in the cathodic and active anodic regions, stress corrosion cracking occurred, no susceptibility was found in the passive region up to 2,250 mV (SHE). Thermodynamically titanium hydride will be formed on the titanium surface[76] or on the titanium oxide surface[81] both in 10N H_2SO_4 and 12N HCl solution. Also in the active anodic region, anodic dissolution occurs in both solutions. Comparing the results in these two solutions suggests that the existence of chloride ion greatly contributes to the susceptibility. Whether these chloride ions assist formation of titanium hydride, hydrogen adsorption in the material, or accelerate anodic dissolution is not clear. Following Beck's model,[83] the characteristic localized corrosion by chloride ion seems to be the most influential aspect in the susceptibility. This characteristic corrosion was found on the titanium specimen, both with and without applied stress in the cathodic and active anodic regions in 12N HCl solution. The same characteristic could not be found in 10N H_2SO_4 solution.

As a summary of this work, titanium dissolves in the solution through a non-protective oxide film as is shown in Fig. 104-a[79] and anodic passivation occurred by the formation of a protective film of TiO_2 (Fig. 104-b).[79] As to the cathodic region, a hydrogen evolution reaction occurs on titanium oxide film (Ti_2O_3) in the Tafel-behavior region (A in Fig. 98-a). In region B, the overvoltage of the hydrogen evolution reaction is decreased with time; this might mean that the oxide film on the surface is being reduced, becoming thinner and thinner. When the surface oxide film is completely reduced, some anodic process with the oxide-free titanium should occur and, therefore the cathodic external current drops rapidly. In stress corrosion cracking behavior, the function of the localized corrosion by chloride ion seems to be the most important aspect.

SECTION III

PHENOMENOLOGICAL ASPECTS OF CHEMICAL CRACKING
(J. W. Spretnak and F. H. Beck)

This research was designed to study the effect of the macroscopic state of stress on the susceptibility to stress corrosion cracking.

A. EFFECT OF STATE OF STRESS ON THE SUSCEPTIBILITY OF TITANIUM BASE ALLOYS TO STRESS CORROSION CRACKING (S. Mahmound)

1. Aims and Significance of Work

The mechanisms by which mechanical and metallurgical variables influence the stress corrosion cracking behavior of titanium-base alloys are not clearly understood at the present time. This lack of understanding is due, in part, to an incomplete appreciation of the state of stress, deformation behavior of the alloy, surface characteristics, stress gradient, and the composite role of such variables upon susceptibility to stress corrosion cracking. This work is designed to review some of the principal known facts governing mechanical and metallurgical behavior in the absence of stress corrosion environments, and then to determine the manner in which such behavior may be influenced by stress corrosion cracking environments.

Two complementary avenues of approach are being used to investigate the phenomenon of stress corrosion cracking in two titanium-base alloys. In the first, or micro-mechanical method, the effects of various factors such as heat treatment, texture, and grain size are being studied. In the second, or phenomenological method, the general macroscopic laws for fracture are being studied. Eventually, the two investigations will be correlated to provide a single self-consistent approach to stress corrosion cracking problems.

The state of stress in a homogeneous isotropic metal is completely defined by the three principal stresses. Therefore, the stress state at fracture can be represented by a stress in three-dimensional Cartesian coordinate stress space. The specific influence of the state of stress on susceptibility to stress corrosion cracking has not been studied in detail nor well defined.

Laboratory work is being undertaken to study chemical cracking as a function of state of stress. It is planned to survey the first two stress quadrants which contain tensile stress

$$\sigma_x = + \ , \quad \sigma_z = + \ ; \tag{46}$$

$$\sigma_x = - \ , \quad \sigma_z = + \ . \tag{47}$$

It is hoped that the initiation and the propagation stages can be defined by monitoring the pitting stage by electrochemical techniques and establishing a suitable criterion for the onset of the propagation stage.

2. Material and Experimental Analysis

Ti-6Al-4V and Ti-8Al-1Mo-1V sheets, 0.025-inch and 0.050-inch thick, are being used for the bending and tensile studies. The same alloys, in the form of a 0.25-inch diameter rod, are being used for the torsion-bending testing. The heat treatments of the two alloys are as follows:

(a) Ti-6Al-4V

(1) Annealed for one-half hour at 1700/1725°F in an argon atmosphere followed by a water quench.

(2) Aged for four hours at 1250°F followed by an air quench.

(b) Ti-8Al-1Mo-1V

Reheated mill-annealed material at 1450°F for 15 minutes in an argon atmosphere followed by an air quench.

In his research various states of stress are being used. The following is a brief summary of each method:

Uniaxial tension: Un-notched specimens.

Biaxial tension: Bending of flat specimens having various ratios of width-to-thickness, w/t, will provide two states of stress. Narrow specimens (small ratio of w/t) provide a state of plane stress; wide specimens (large ratio of w/t) provide a state of plane strain.

Combined bending-torsion: Figure 105 illustrates the apparatus to obtain various ratios of maximum normal stress to maximum shear stress. Load (P/2) is put on the specimen (1) lying on the supports (2) through the arms (3). The specimen undergoes torsion and bending. Here the relationship of maximum normal stress to the maximum shear stress remains constant during testing. The relationship is

$$\frac{\sigma_{max}}{\tau_{max}} \quad 1 + \quad \frac{1}{\sqrt{1 + (a/k)^2}} \quad . \tag{48}$$

Parameters a and k are defined in the figure.

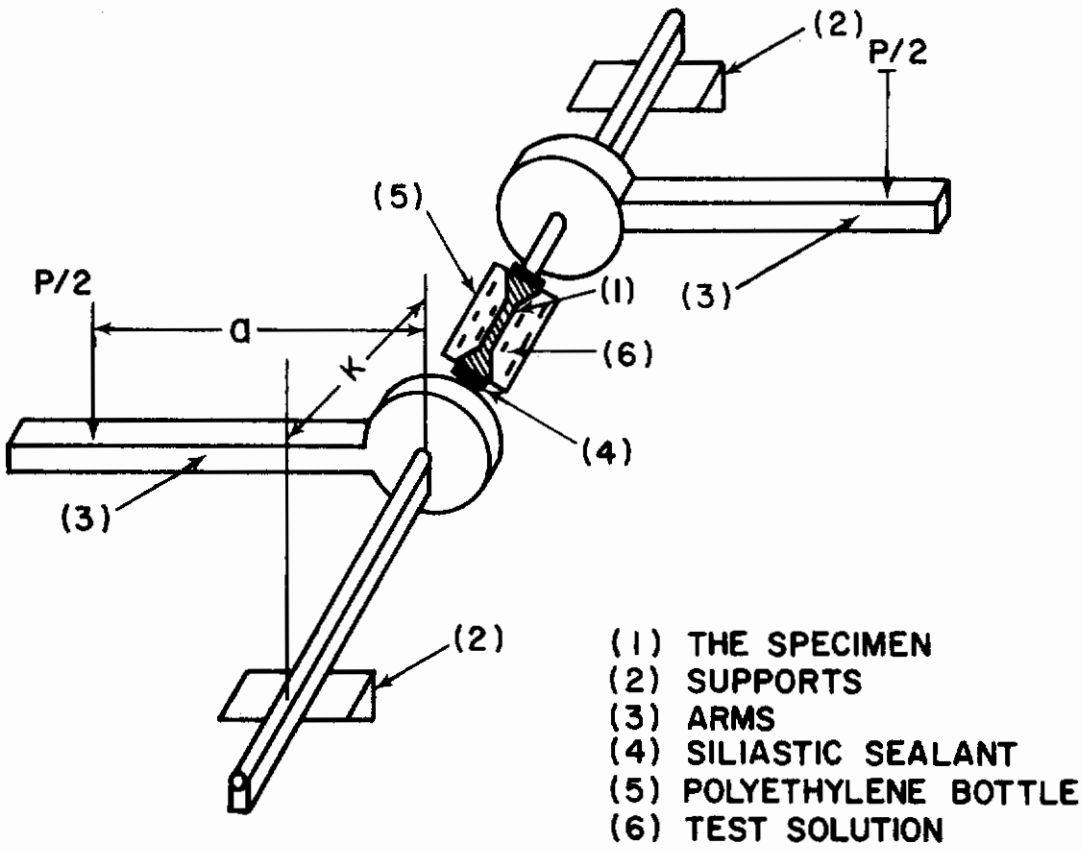

Fig. 105 - Schematic Diagram of Combined Bending-Torsion Apparatus (1) specimen, (2) supports, (3) arms, (4) siliastic sealant, (5) polyethylene bottle, (6) test solution

The apparatus is designed to provide stress conditions over a range of $1 \leq (\sigma/\tau) \leq 2$. Furthermore, the angle between the maximum normal stress plane and the plane perpendicular to the specimen axis is given by

$$\sin 2\varphi = \frac{1}{\sqrt{1 + (k/a)^2}} \quad . \tag{49}$$

From Eq. (48) it is evident, that while modifying the ratio a/k, one is able to change the state of stress from simple bending to torsion.

Notched bend specimens: Experiments to define the state of stress in the vicinity of a notch are in progress. Twenty specimens of the design illustrated in Fig. 106 were prepared from Ti-6Al-4V alloy in the duplex-annealed condition. These specimens will be used to investigate the role of notch plasticity on crack initiation and propagation in various environments, including CH_3OH-HCl-H_2O solutions.

Using a scaled-up Bakelite model and with the assistance of Dr. L. J. Segerlind (Department of Engineering Mechanics, OSU) the stress analysis for the above geometry was determined. Experimental data and the stress distribution agreed very closely with the theoretical treatment. (A completely elastic solution to this problem was obtained by G. A. Griffis[104] and J. W. Spretnak[105] using the finite differences method.) The theoretically and experimentally obtained values of the elastic stress concentration factor for the specimen considered are 2.06 and 2.10, respectively. The proposed boundary conditions in the theoretical analysis were verified experimentally and it was found that (1) a parabolic shear stress distribution, (2) a linear bending stress distribution, and (3) no shift in the neutral axis exist for measurements made 10 mm to the right and left of the centerline of the specimen.

This section is concerned with the following studies.

a. Definition of the crack initiation process in terms of point of origin and path of propagation.

b. Separation of the total fracture energy into crack initiation and crack propagation components.

c. Evaluation of a maximum strain criterion for crack initiation.

d. Investigation of the sequence of events in the plastic zone at the crack tip.

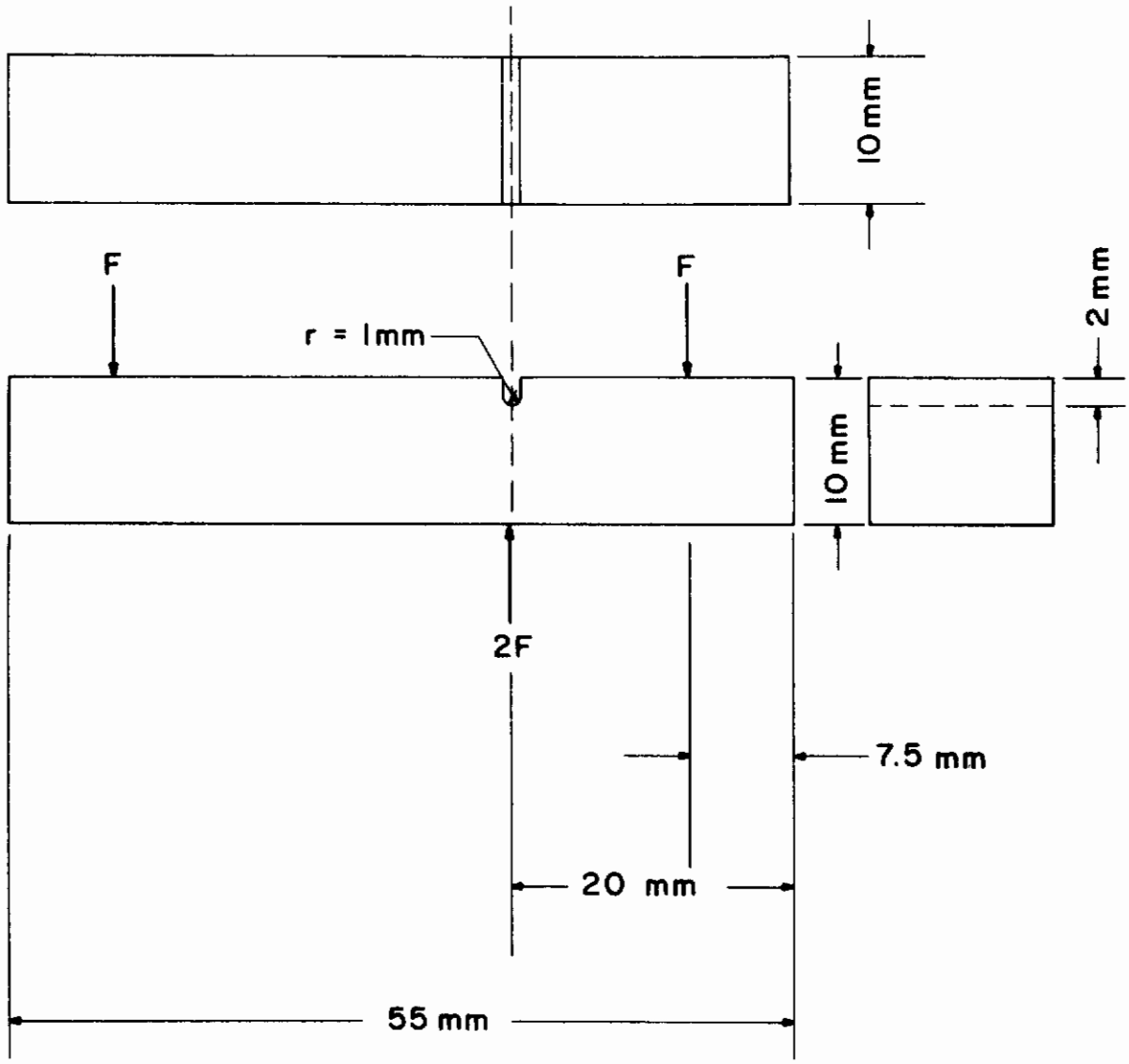

Fig. 106 - Notched Bend Specimen

3. Preliminary Results

a. Stress Analysis

The theoretical stress analysis is given in Ref. 102. Experimental stress analysis consisted of determining the elastic stress concentration factor, K_e, which was found to be 2.06. Using the scaled-up bakelite model, the distribution of the bending stress is shown in Fig. 107. The strain field or the fringe pattern is shown in Fig. 108.

b. Load-Deflection Curves

Generation of a load-deflection diagram during a notched bar test provides one way for determining crack initiation and crack propagation energies. Such a curve further enables the two components of toughness (i.e., strength and ductility) to be assessed. Measurements of the diagram were made in air and in the CH_3OH + 0.37% HCl + 0.63% H_2O test environment. Figure 109 shows the experimental set-up while representative curves are shown in Fig. 110. Somewhere between the start of loading and the maximum load, a crack forms at the notch root close to the mid-longitudinal section of the bar. The exact location, on the load-deflection diagram, of the point of initiation has proved difficult to determine with precision. The area under the curve to this point represents the crack initiation energy. The total area minus that for crack initiation represents the crack propagation energy.

The most common method of discerning between elastic and plastic deformation has been by etch pitting techniques. This etch serves to reveal areas which have been deformed beyond the yield. Several trials, none of which proved entirely successful, were attempted to discern plastically deformed regions. Figure 111 is a photograph of these plastic zones. Further work is in progress to reveal the size of the plastic zone using microhardness techniques. This technique is used for several purposes; i.e.,

(1) compare the size of the plastic zone measured experimentally to that predicted theoretically,

(2) obtain a qualitative description of the development of the plastic zone, and

(3) determine the volume of the deformed metal in the fractured bars. This quantity will be obtained for both halves of the fractured bars on their surface and mid-thickness sections.

c. Critical Strain Measurements

It was found that the plastic zone at the tip of the notch or a crack expands on loading until a critical strain at the notch root is attained. At this strain, the material undergoes a rheological

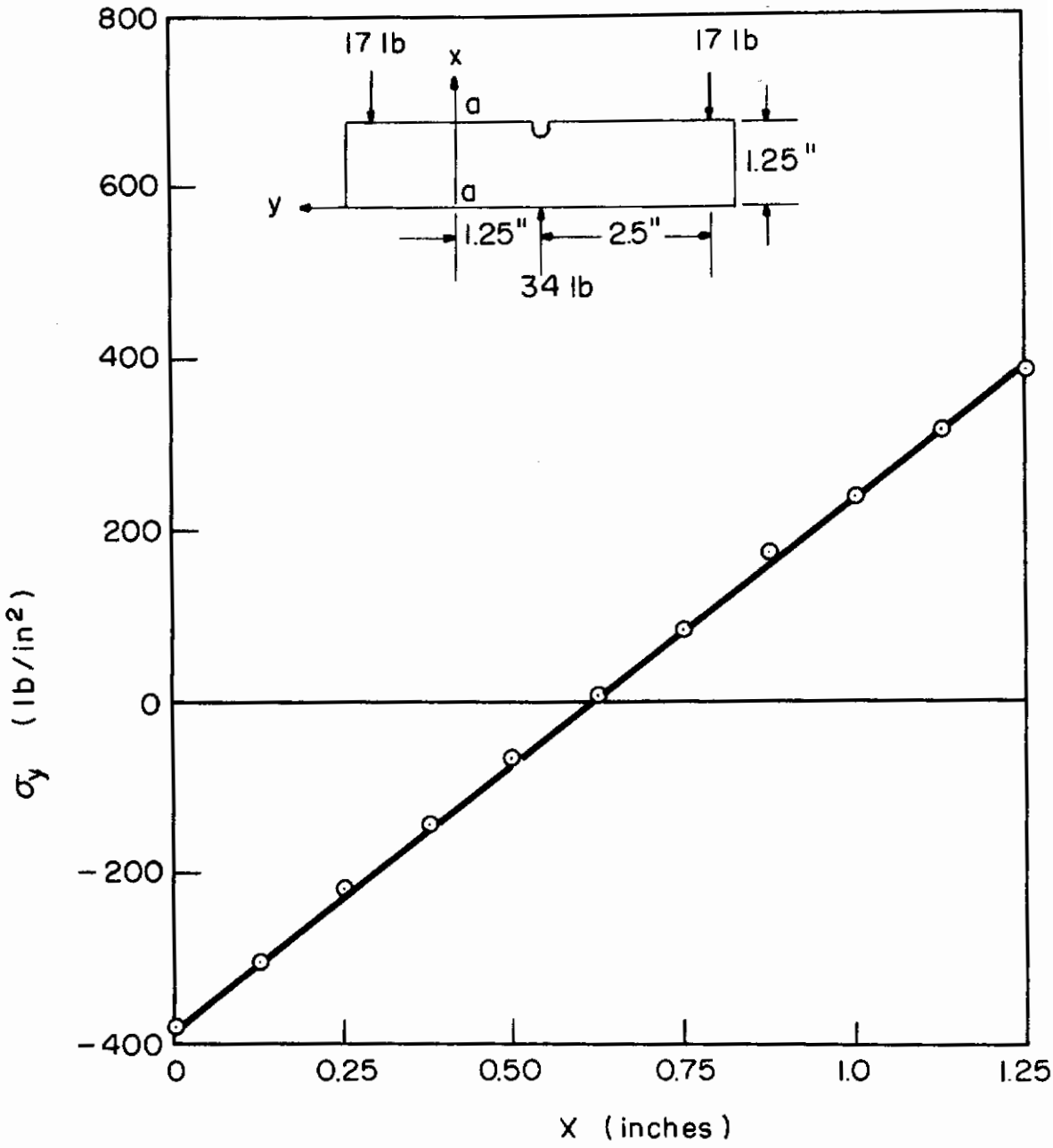

Fig. 107 - Normal Stress Distribution Across Section a-a
(Photoelastic Material, PSM-5)

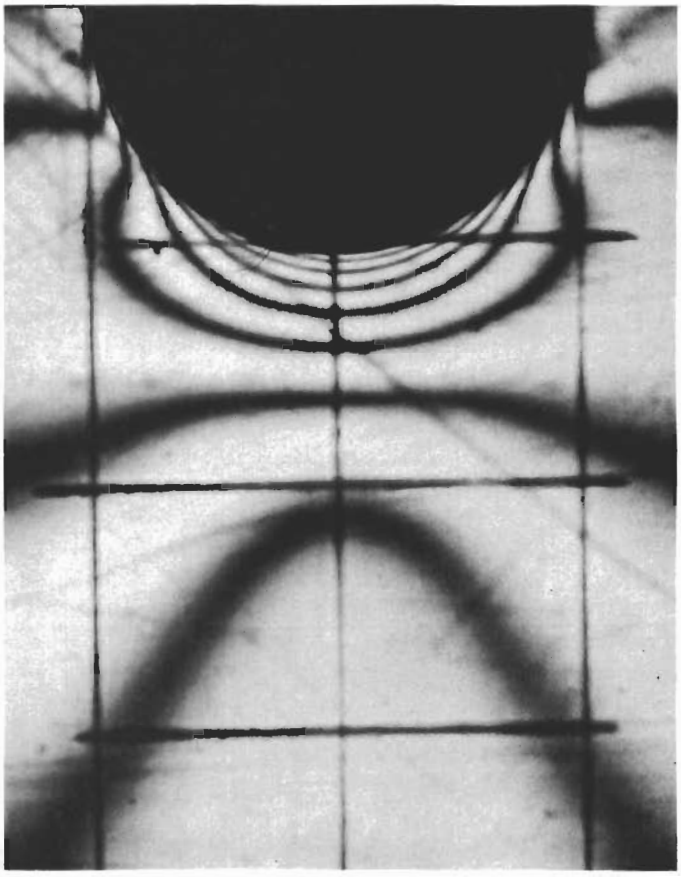

Fig. 108 - Fringe Pattern Under Notch
(7 fringes are showing)

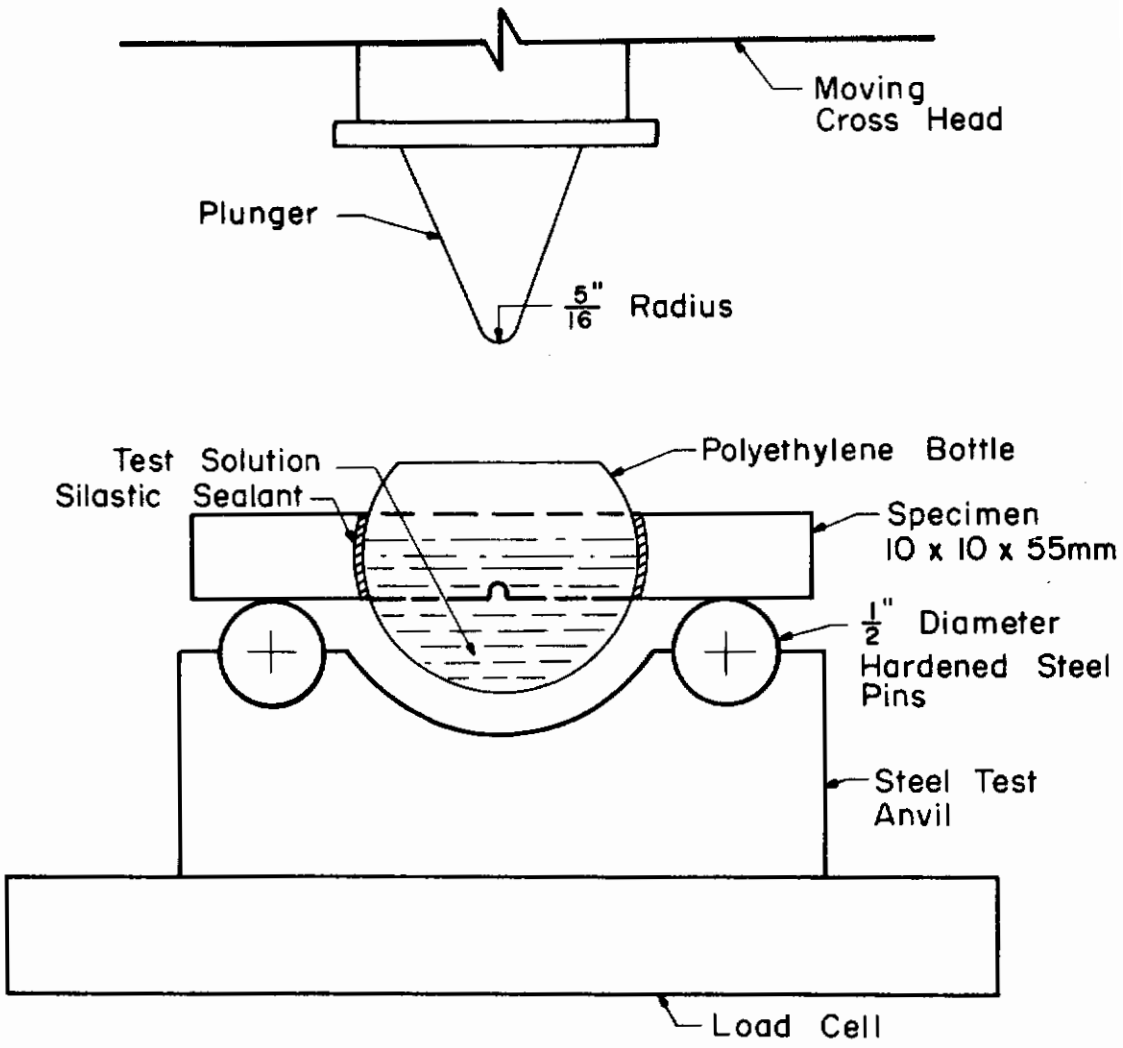

Fig. 109 - Schematic Diagram of Test Apparatus

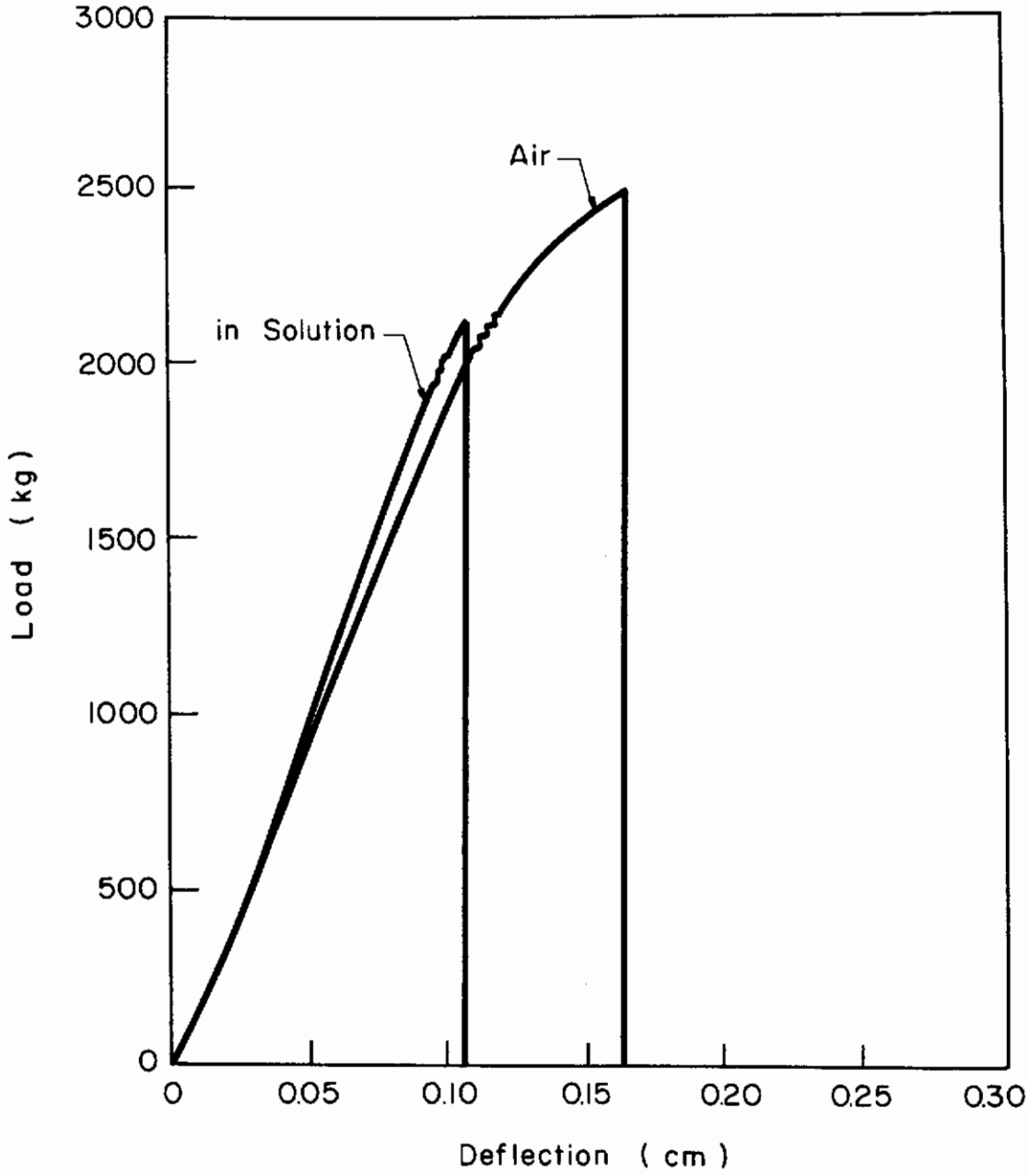

Fig. 110 - Load-Deflection Diagram for Ti-6-4 in Air and in CH_3OH + HCl + H_2O Solution (Cross-head speed = 0.05 cm/min)

Fig. 111 - Tested Specimens Showing Plastic Zone Under Notch

transformation into fluid-like flow, in which it is susceptible to localization of flow along "characteristics" (slip lines in slip line fields), which are directions of critical maximum shear stress and also directions of pure shear. Plastic instabilities may be mounted along these directions: "Weak instabilities lead to stable slow crack propagation; strong instabilities lead to unstable fast propagation (brittle fracture)."[105] Measurements were made for some of the specimens to estimate the strain at the root of the notch. These measurements consisted of measuring the contraction in the transverse directions before and after loading. The following are typical values:

No. of Specimens	Thickness before Testing	Thickness after Testing
8 (in CH_3OH + HCl + H_2O solution)	0.394"	0.377" - 0.388"
2 (in air)	0.394"	0.383" - 0.387"

More specimens will be tested to define this quantity precisely.

d. Angle of Bend

Bend angle measurements are in progress. A correlation between the bend angle and the conventional strain will be made by the following methods:

(1) determinations from the load-deflection curves,

(2) photographically by measuring the radius of curvature, and

(3) measurements from scaled-up model.

e. Fractographic Studies

Limited fractographic analysis was performed. Scanning electron fractographs were made from specimens tested in air and in the CH_3OH-HCl-H_2O environments. No evidence was found for "hard particle"-induced dimple formation.

SECTION IV

STRESS CORROSION CRACKING OF STEELS (R. W. Staehle)

The aim of this program is to identify and quantify processes which are fundamental to the initiation and propagation of stress corrosion cracks. The individual efforts described herein are considered to be key factors from which an effective quantitative basis for stress corrosion cracking can be developed.

The ultimate aim of the work is to provide a quantitative basis for designing high-strength alloys and heat treatments which are resistant to catastrophic stress corrosion cracking.

SIGNIFICANT ACCOMPLISHMENTS

The significant factors considered to affect the stress corrosion cracking of high-strength steels include the following: structure, alloy chemistry, hydrogen entry, hydrogen structure interaction, alloy strength, nature of the protective film, reactivity of second phases, acoustical pulses, relative effects of various environmental species and phases. We envision the proper approach to resolving the problem of stress corrosion cracking as identifying the unit processes involved and quantifying them. While extensive direct stress corrosion cracking experiments were conducted in this program, more emphasis was placed upon quantifying the unit processes. Significant in this regard are the following:

1. The hydrogen trapped in the lattice was shown clearly to be related to the interfacial area of incoherent boundaries.

2. The passive film thickness on Fe base alloys containing Ni and Cr was shown to vary linearly with pH and potential for pH 4 to 12 in the passive region. The range of thickness varied from 10 to 70 A in these ranges.

3. The sonic emission rate (emissions/unit length) from advancing cracks depends greatly on the strength level of the alloy and also upon the type of environment used (aqueous or hydrogen gas). These emissions may be useful as an NDT method or a diagnostic tool.

4. The chemical reactivity of metal carbides (important constituents of high-strength steels) was found to depend greatly upon the pH, potential, and solution species. Under certain cases the carbide is more reactive than the metal, and under other cases the reverse is true.

5. Detailed processes associated with hydrogen entry on metal surfaces were defined for the case associated with arsenic

(AsO_2) in solution. It was found that arsenic in its metallic (AsO) condition was the critical form for accelerating hydrogen entry. This means that arsenic in the metallic form in the alloy would equally promote hydrogen entry. Thus, if arsenic segregates to the grain boundary, then hydrogen would preferably enter the grain boundary.

6. Experiments to assess the effects of structure on stress corrosion cracking behavior were conducted at constant yield stress. Experiments were conducted using heat treatments designed to produce coherent and noncoherent interfaces in Type 4340 and 250 maraging steel. The alloy with noncoherent interfaces were found to greatly inhibit both the propagation of cracks and to delay K_{Ic}. This may be the basis for significantly improved alloys.

7. Experiments to compare the relative effects of water in gaseous hydrogen show that the detailed aspects of crack propagation in a single material (4340) are quite different. A complete comparison of stress corrosion cracking behavior in gaseous and aqueous environments was performed.

A. CONTROLLED PHENOMENOLOGICAL STUDY OF CRACK PROPAGATION (G. E. Kerns)

1. Objectives and Background

The objective of this investigation is to obtain a set of reliable phenomenological information on the propagation of stress corrosion cracks in several high-strength steels exposed to well-controlled gaseous and aqueous environments. The specific quantities being measured are crack velocity as a function of stress intensity, fractographic features, and sonic emission activity. Important features of the environments being controlled are partial pressure of gas, concentration of impurities added to gas, buffered pH of solutions, and electrochemical potential.

2. Measurement of Crack Length

Preliminary testing was conducted to determine the relationship between crack length and deflection under constant load. Cantilever beam specimens were fatigue-cracked to various depths. A cracked specimen would be loaded, in 12-pound increments, allowed to equilibrate, and the beam deflection was then measured.

All specimens tested were AISI 4335 steel, heat treated as follows: 1550°F for one hour, oil quench, and a temper of 400°F for one hour, air cool. Specimen dimensions, as well as the relationship for stress intensity factor, are given in Fig. 112. All specimens were tested under plane strain conditions, using cantilever beam type loading. The data reported herein were obtained using gaseous H_2/Ar mixtures.

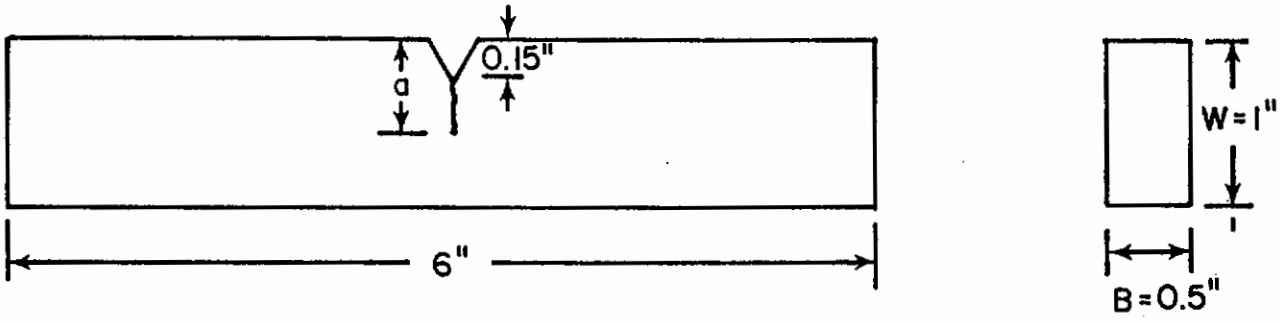

$$K_I \text{ (plane strain conditions)}$$

$$K_I \text{ (psi-in.}^{1/2}\text{)} = \frac{4.12(\Sigma M)\sqrt{1/\alpha^3 - \alpha^3}}{BW^{3/2}}$$

$$\alpha = 1 - a/W$$

ΣM = sum of moments (in.-lbs.) about the fixed end of the specimen

Fig. 112 - Specimen Size and Relationship Governing Stress Intensity Factor

The impurity levels of the as-received gases were below 100 ppm. Figure 113 shows the purifying apparatus for the gaseous mixtures.

Figure 114 shows the cantilever beam testing arrangement. The deflections were measured using a Daytronic Model DS1000 transducer, mounted normal to the beam in series with a Daytronic Model 201B transducer exciter-demodulator. This reading, in millivolts, was recorded on an Esterline Angus strip chart recorder.

This resultant data, shown in Fig. 115 were then used to predict crack length as a function of load and deflection. It was noted that crack growth in hydrogen gas gives a macroscopically dark fracture surface, while catastrophic failure or propagation in air leaves a bright surface. Therefore, the end of the hydrogen-induced growth zone could be discerned from the color transition on the fracture surface.

The curves described above were used to predict the crack length at which a specimen underwent catastrophic failure at constant load. This fracture stage is characterized by an extremely rapid change in crack growth and acoustic emission rates. The observed crack length at the end of the hydrogen propagation zone was compared to that predicted

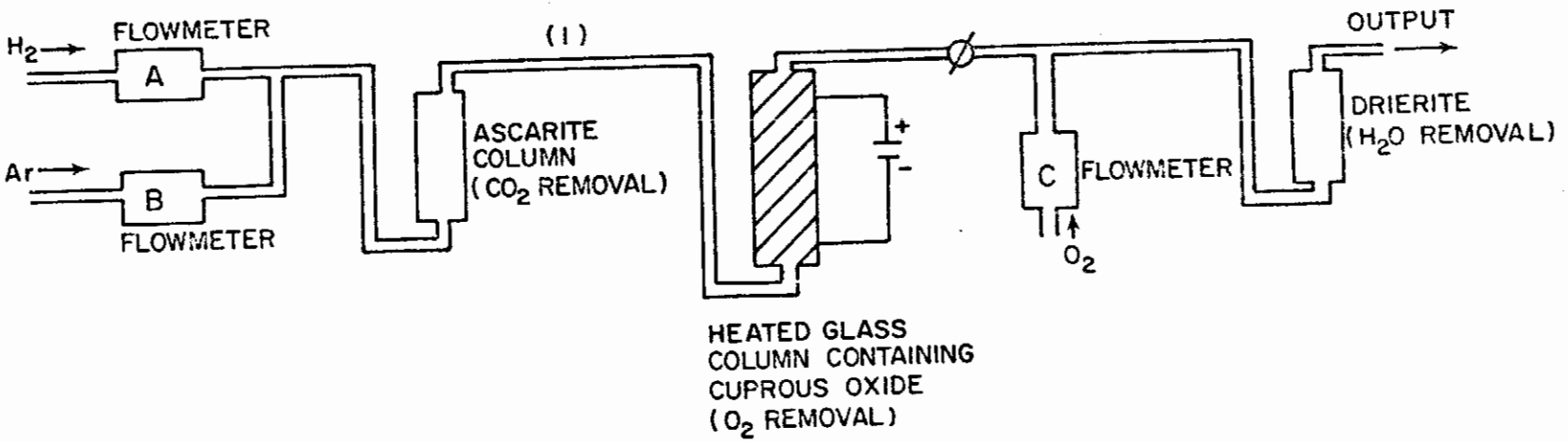

Flowmeters A and C are of the multi-range monometer type, while meter B is a single range monometer.

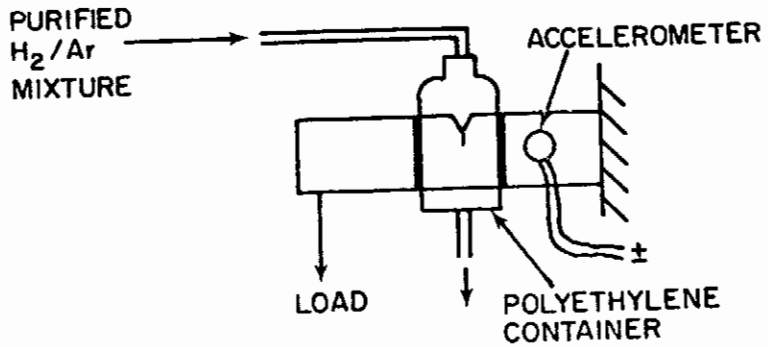

(1) Copper and glass tubing was used throughout the system to avoid oxygen pickup

Fig. 113 - Gas Purification System Being Used for Crack Propagation Studies

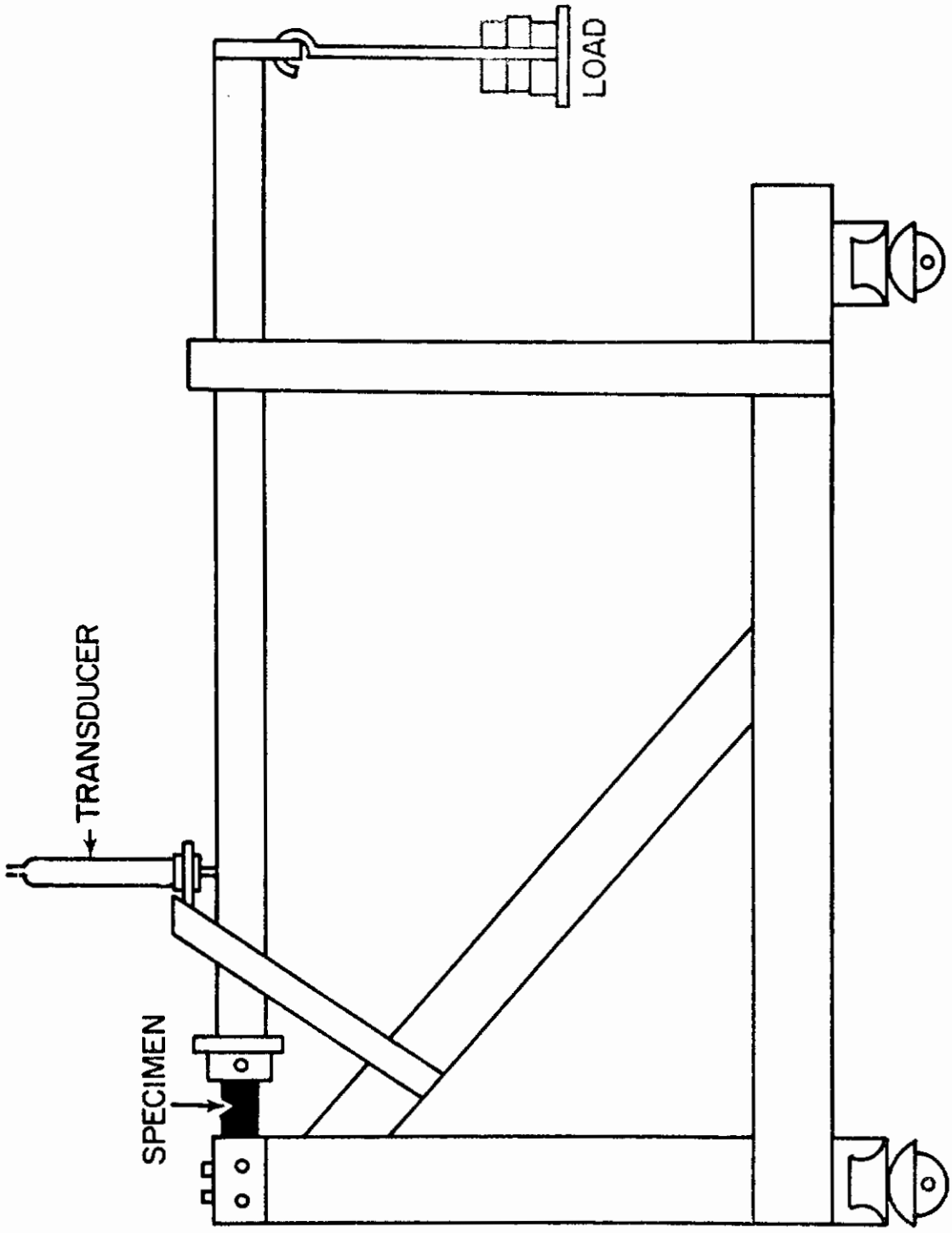

Fig. 114 - Cantilever Beam Apparatus

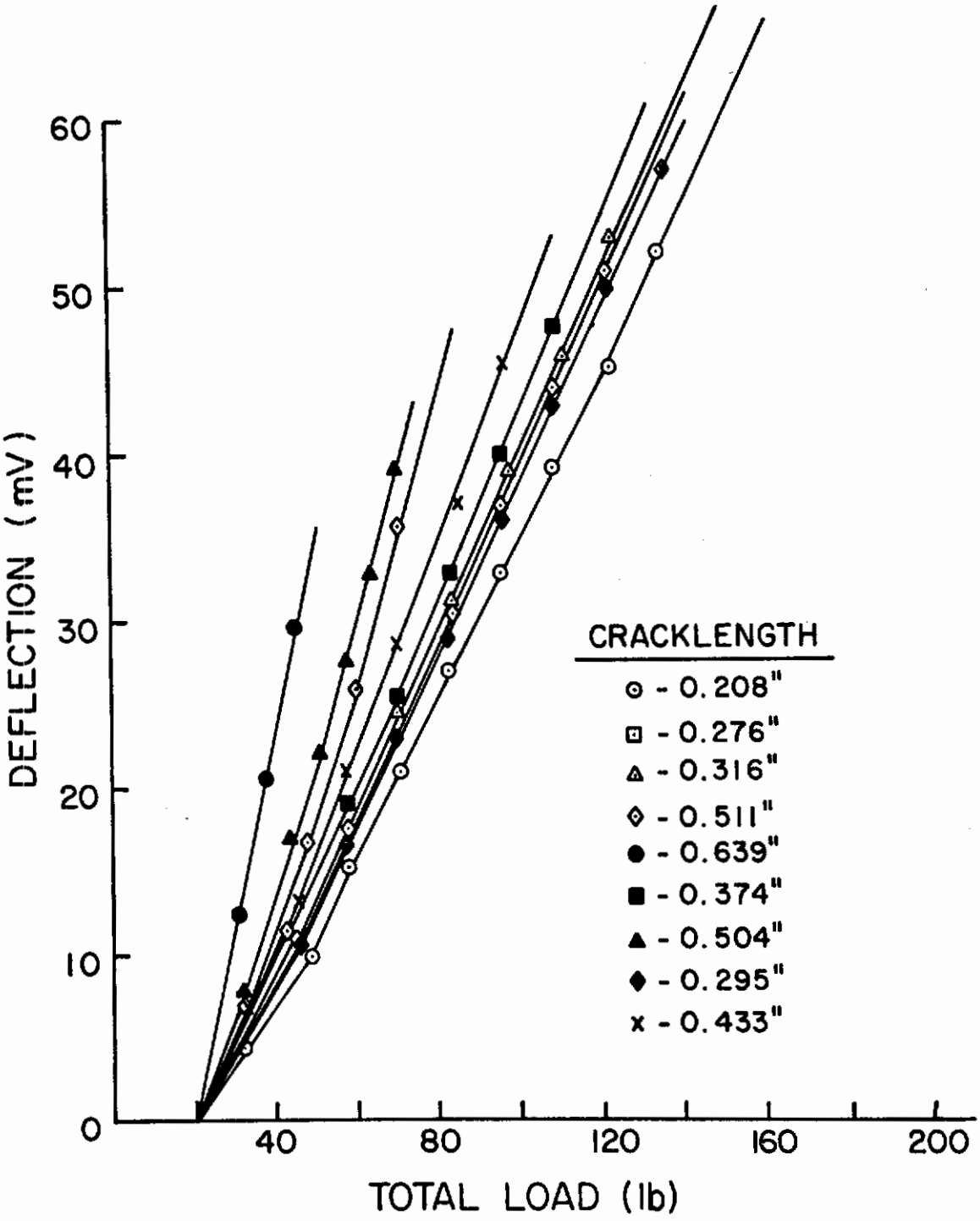

Fig. 115 - Relationship Between Crack Length, Load, and Deflection as Determined in Argon Atmosphere for 4335 Steel

by the calibration curves, since the deflection and load at the onset of catastrophic failure were known. Errors up to 20% were observed.

In order to obtain a compliance curve which accounted for the crack front geometry, 14 specimens were fatigue-cracked giving initial crack lengths of approximately 0.350 inch. The specimens were then loaded to a starting K_1 value of 35-40 ksi-inch$^{1/2}$. After equilibration in an argon atmosphere, hydrogen gas was introduced, giving rise to slow crack growth. Oxygen gas was then introduced to halt crack growth at a desired value of deflection. While in an oxygen environment, the specimen was rapidly loaded to failure. As shown in Brown and Srawley's text[104] on plane strain fracture toughness testing, the parameters E, ν, B/P, and a/W are the significant variables for a calibration curve of this type, where

E = Young's modulus (psi),
ν = compliance change (in.),
B = specimen thickness (in.),
P = load (lb.)
a = crack length (in.), and
W = specimen width (in.).

Such a calibration curve is independent of stress intensity factor and is based on the assumption of no plastic deformation.[105]

For the purpose of this investigation, the elastic compliance, ν, is determined by the conversion of the beam deflection (mV) and the transducer calibration curve in Fig. 116; i.e., 0.005 inch/mV. Since the deflection is due to a change in crack length, the crack length, a, is replaced by $(a_f - a_c)$, where

a_f = crack length at end of hydrogen propagation

and

a_c = initial center crack length.

Because E and P (static load) are constant, and ν is a linear function of deflection (δ) in millivolts, the data are plotted in Fig. 117 as δB (millivolt-inches) vs. $(a_f - a_c)/W$ (unitless). The 95% confidence limits on the least squares plot in Fig. 117 are also shown.

3. General Description of Acoustic Emission Technique

As the crack propagates, a fraction of the stored elastic energy at the crack tip is released with each increment of crack growth. This energy translated through the lattice as stress waves may be detected by a piezoelectric crystal fastened to the surface of the specimen. As the accelerometer is accelerated by the stress wave, crystal resonance and a sinusoidal charge difference across the crystal are produced. Treating the accelerometer as a single-degree-of-freedom spring mass system results

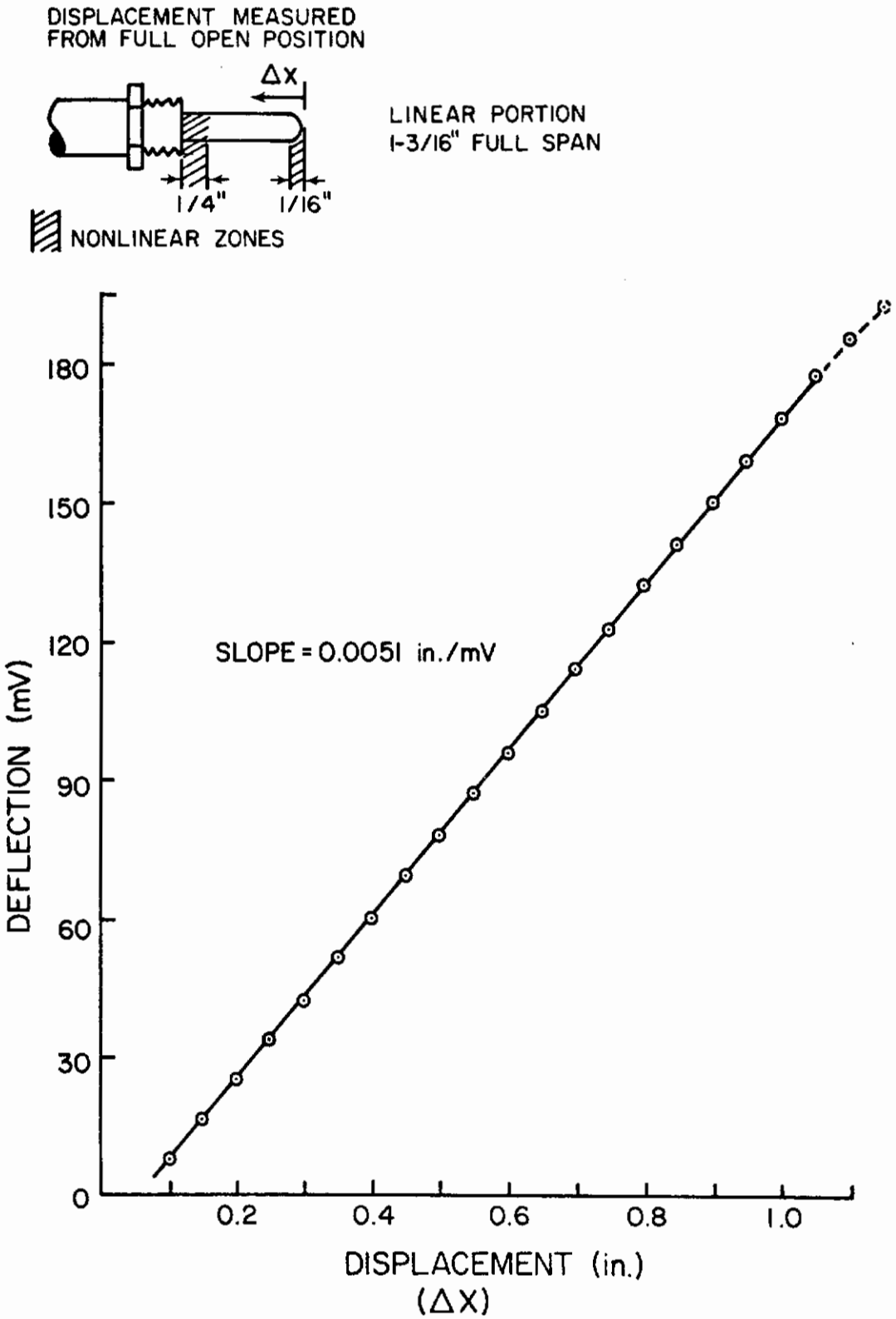

Fig. 116 - Deflection of Beam vs. Displacement for Cantilever Beam Specimen

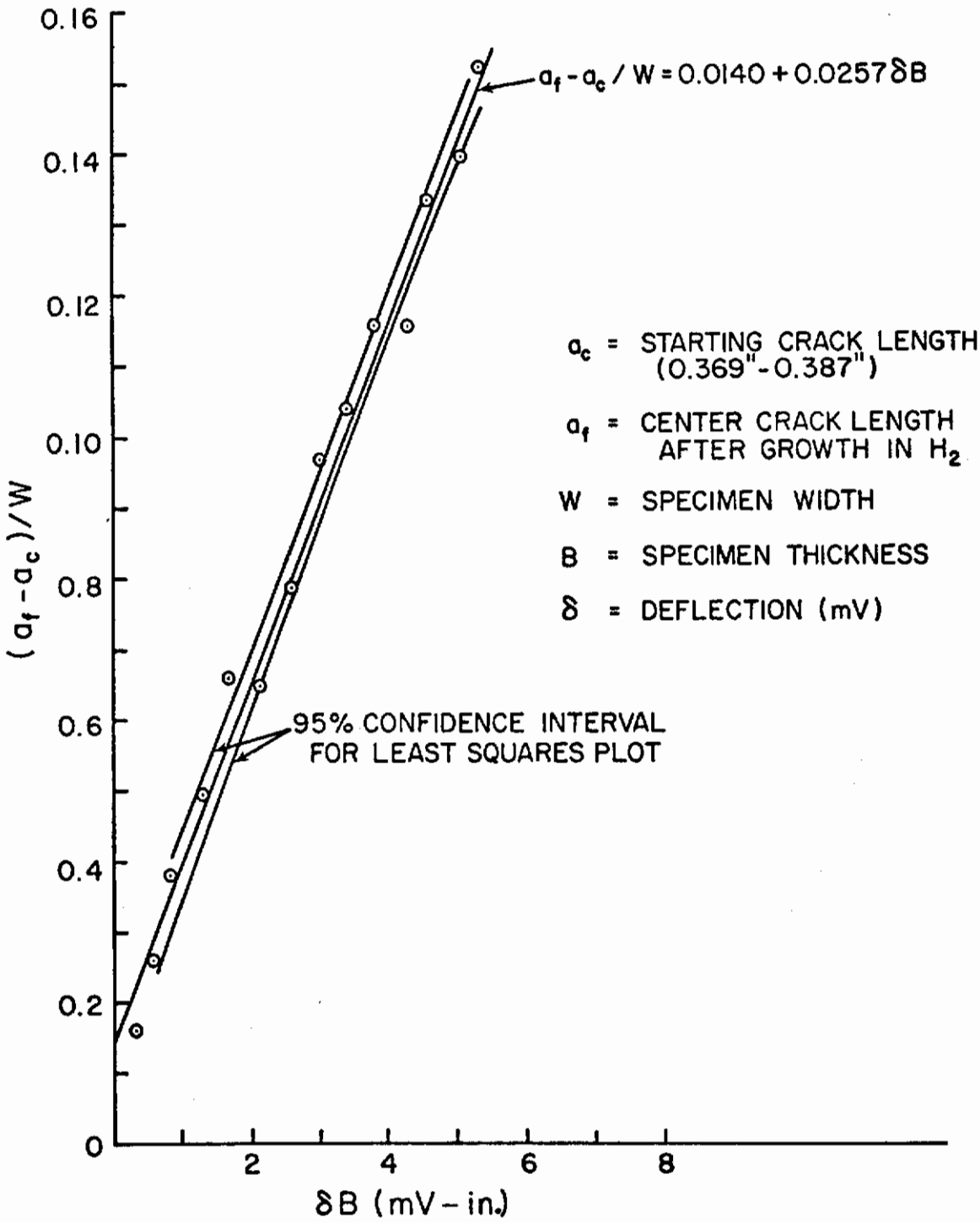

Fig. 117 - Calibration Curve for Pre-Cracked 4335 Cantilever Beam Specimens

in various solutions for the displacement of the crystal with respect to time as different forcing functions are used.

If the crystal is subjected to a spike pulse (large force for a very short time), mathematical solutions such as those found in Kinsler and Frey[106] show that the displacement, acceleration, and charge differential of a piezoelectric crystal are of a damped sinusoidal form. Therefore, when a stress wave is emitted from a growing crack and strikes the accelerometer, the output voltage of the accelerometer is of a sine wave nature, but decaying with time. The response of the accelerometer is maximum at its natural resonance frequency. By filtering the various frequencies emitted by the crystal using a pass band filter, the resonance frequency component for each emission can be examined. The size and number of resonance peaks associated with each output of the crystal can be taken as a relative measure of the size of the initial phonon or energy release from the crack tip.

The advantages of an accelerometer are that the resonance frequency is quite independent of mounting techniques and the voltage across the accelerometer can be converted into an absolute acceleration or force. It must be noted here that the output of the crystal is a strong function of frequency above 1/5 of the natural resonance frequency, so that the use of an accelerometer at its natural resonance frequency allows it to be used as a comparative tool only. The acceleration values obtained at this frequency will always be higher than the true values. However, the increased response of the crystal in this frequency range enables it to be a more sensitive tool.

In this investigation the number of resonance peaks above a certain voltage value will be used as a relative measure of the size of the emission. A larger energy release from the crack tip will resonate the crystal with a larger amplitude or for a longer time, or both. The number of resonance peaks associated with the emission above a certain voltage level will be larger.

4. Specific Description of Acoustic Detection System

The overall arrangement of the system for detecting acoustical emissions is shown in Fig. 118. The acoustic emission is detected by an Endevco Model 2272 accelerometer (natural resonance frequency of 37 kHz), and amplified, using an Endevco Model 2711B charge amplifier. The output of the amplifier is 5V/g. The amplifier output is sent into a Daytronic Model 724 filter, operating in a 15 kHz double-high pass mode. The gain of the filter for a 33.3 kHz signal is 0.204. For viewing purposes the output of the filter is fed into a Hewlett-Packard Model 132A dual beam oscilloscope. The output of the oscilloscope was fed into a Hickok Model DMS 3200P mainframe, containing a DP-150 1 MC counter plug-in unit. The events counted by the plug-in unit were recorded, using a four-digit Hickok PR 4900 printer. This system was used in conjunction with an Electro Instruments Model A20B-34 amplifier in series with a Honeywell

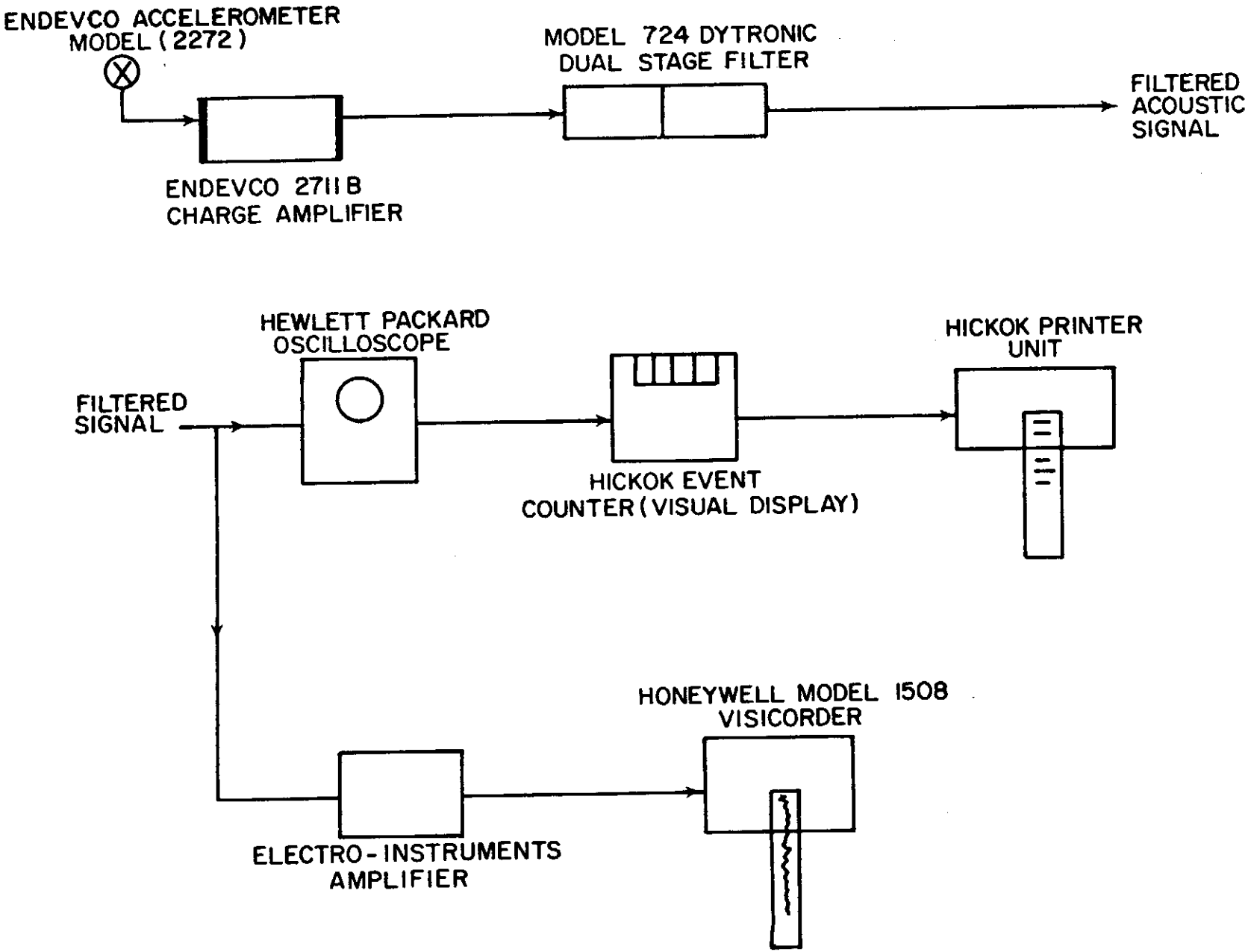

Fig. 118 - Electronic System for Detection of Acoustic Emissions

Model 1508 visicorder. The two electronic systems allow three measurements to be made :

a. The Hickok event counter permits the counting of the number of resonance peaks associated with each acoustic emission. The output is the number of resonance peaks recorded during the print cycle. This parameter is used as a relative measure of the energy release from the crack tip, and therefore, the amount of crack growth.

b. A Hewlett-Packard Model 197A oscilloscope camera is used with the oscilloscope. The oscilloscope is triggered by the slope of any incoming signal, thereby allowing the emissions to be successfully photographed without over-exposure due to the intensity of the base line on the oscilloscope over a long period of time. In this manner the amplitude and period of the signals can be recorded.

c. The Honeywell visicorder, with a frequency response of only 13 kHz, allows individual emissions to be recorded without resolving the number of resonance peaks contained in a given emission.

The instrumentation allows the use of acoustic emission detection as a quantitative technique in monitoring hydrogen-induced slow crack growth.

5. Trigger Level for Detecting Acoustical Emissions

The trigger level for the Hickok event counter was adjusted to record all resonance peaks above 0.01 g (as determined by the voltage-acceleration constant for the accelerometer). Because of the resonance of the crystal, the real acceleration value required for triggering the counter is much less than 0.01 g; however, the correction factor is constant and can be neglected, but only in a comparative study. The effect of stress intensity factor on crack growth rate and emission rate are given for four specimens of AISI 4335 steel at low hydrogen partial pressures in Tables XIV-XVII. Photographs of acoustic emission signals obtained from specimens during crack growth are shown in Fig. 119.

Examination of the emission data shows a sporadic pattern while the crack growth rate showed a relatively steady increase with increasing stress intensity factor. During the testing of the specimens, it was noticed that ultra-high frequency interference was present which occurred in bursts. After consultation with the manufacturer of the Model 724 filter, it was learned that operation of the filter in a bandpass (30 kHz to 40 kHz) mode eliminated the interference. This interference may explain, in part, the sporadic emission data.

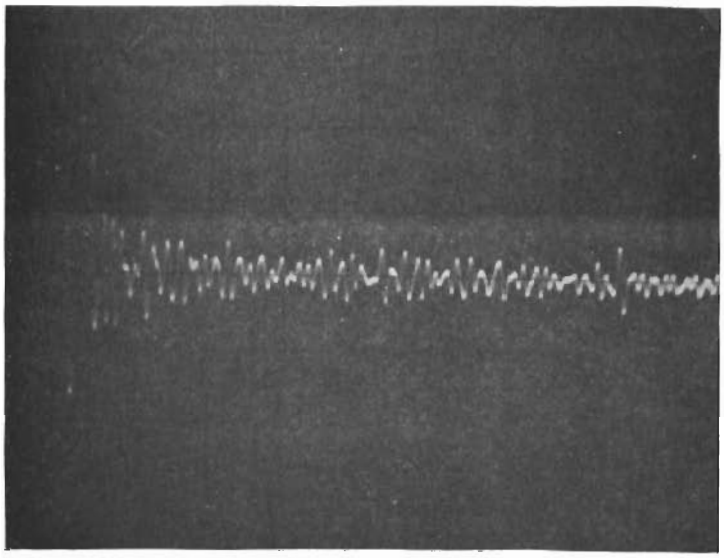

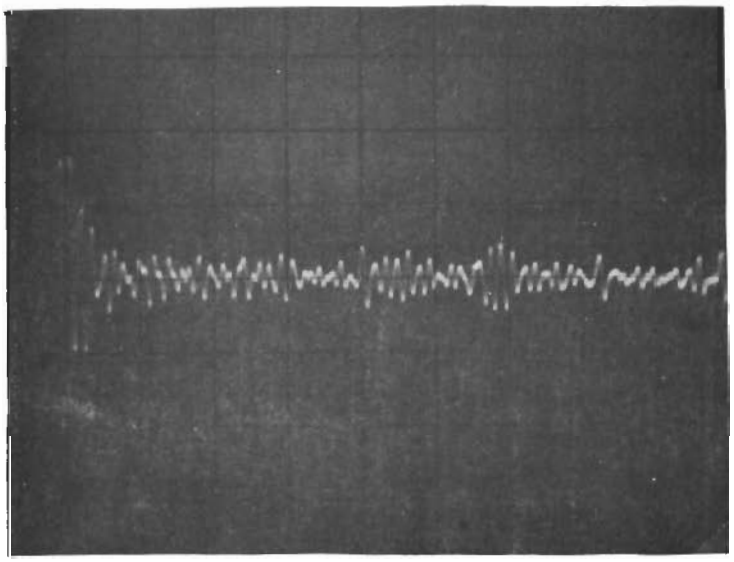

Fig. 119 - Photographs of Oscillographic Trace Produced by Acoustic Emission During Crack Propagation in 4335 Steel
Vertical Scale - 0.02 g/cm; horizontal scale - 0.2 msec/cm

Table XIV - Stress Intensity Factors, Crack Growth Rates, and Emission Rates for a Hydrogen Level of 3.3%

Stress Intensity Factor** (ksi-in.$^{1/2}$)	Crack Growth Rate (in./min)	Resonance Peaks Counted* per Minute
55.1	.0009	10.5
56.1	.0009	23.0
57.2	.0010	10.0
58.4	.0008	38.0
59.3	.0010	9.0
61.3	.0011	23.0
62.8	.0013	26.0
64.8	.0010	50.5
66.9	.0013	36.0
69.2	.0017	52.5
72.4	.0020	120.0
77.2	.0035	401.0

Initial stress intensity - 51.5 ksi-in.$^{1/2}$

* Trigger level set at 0.0085 g using square wave generator

** K_1 values based on maximum cracked length for parabolic crack front

Investigation of the trigger level adjustment for the Hickok counter showed conclusively that the trigger level must be set using a sinusoidal wave form of the same frequency as that for accelerometer resonance. Square wave generators and low-frequency sine wave generators were found to be unsatisfactory.

In order to determine the optimum trigger level for detecting the maximum number of emissions, while eliminating extraneous background noise, a third investigation was conducted. The accelerometer was mounted on a loaded 4335 steel specimen exposed to air. The trigger level of the counting system was lowered until background noise was detected. The results of this test are shown in Fig. 120. A trigger level of at least 0.013 g was required to avoid extraneous background noise.

Table XV - Stress Intensity Factors, Crack Growth Rates, and Emission Rates for a Hydrogen Level of 6.9%

Stress Intensity Factor** (ksi-in.$^{1/2}$)	Crack Growth Rate (in./min)	Resonance Peaks Counted* per Minute
55.2	.0014	5.0
56.1	.0014	22.0
57.1	.0018	83.0
58.2	.0018	16.0
59.2	.0018	16.0
60.5	.0020	56.0
62.0	.0023	116.0
63.7	.0024	24.0
65.6	.0027	32.0
67.8	.0027	18.0
70.3	.0031	61.0
73.2	.0038	128.0
77.4	.0051	249.0

Initial stress intensity - 50.4 ksi-in.$^{1/2}$

* Trigger level set at 0.01 g using a square wave generator

** K_1 values based on maximum crack length for parabolic crack front

Table XVI - Stress Intensity Factors, Crack Growth Rates, and Emission Rates for a Hydrogen Level of 7.1%

Stress Intensity Factor** (ksi-in.$^{1/2}$)	Crack Growth Rate (in./min)	Resonance Peaks Counted* per Minute
51.8	.0019	30.0
52.5	.0024	10.0
53.1	.0024	32.0
54.0	.0027	23.0
54.8	.0034	132.0
56.0	.0037	140.0
57.2	.0047	144.0
58.6	.0044	219.0
60.2	.0056	307.0

Initial stress intensity - 48.0 ksi-in.$^{1/2}$

* Trigger level set at 0.01 g using a square wave generator

** K_1 values based on maximum crack length for parabolic crack front

Table XVII - Stress Intensity Factors, Crack Growth Rates, and Emission Rates for a Hydrogen Level of 7.7%

Stress Intensity Factor** (ksi-in.$^{1/2}$	Crack Growth Rate (in./min)	Resonance Peaks Counted* per Minute
53.8	.0027	38.0
55.1	.0027	29.0
56.5	.0034	257.0
58.1	.0034	43.0
59.9	.0034	67.0
62.0	.0045	56.0
64.5	.0047	114.0
69.1	.0075	365.0

Initial stress intensity - 48.6 ksi-in.$^{1/2}$

* Trigger level set at 0.01 g using a square wave generator

** K_1 values based on maximum crack length for parabolic crack front

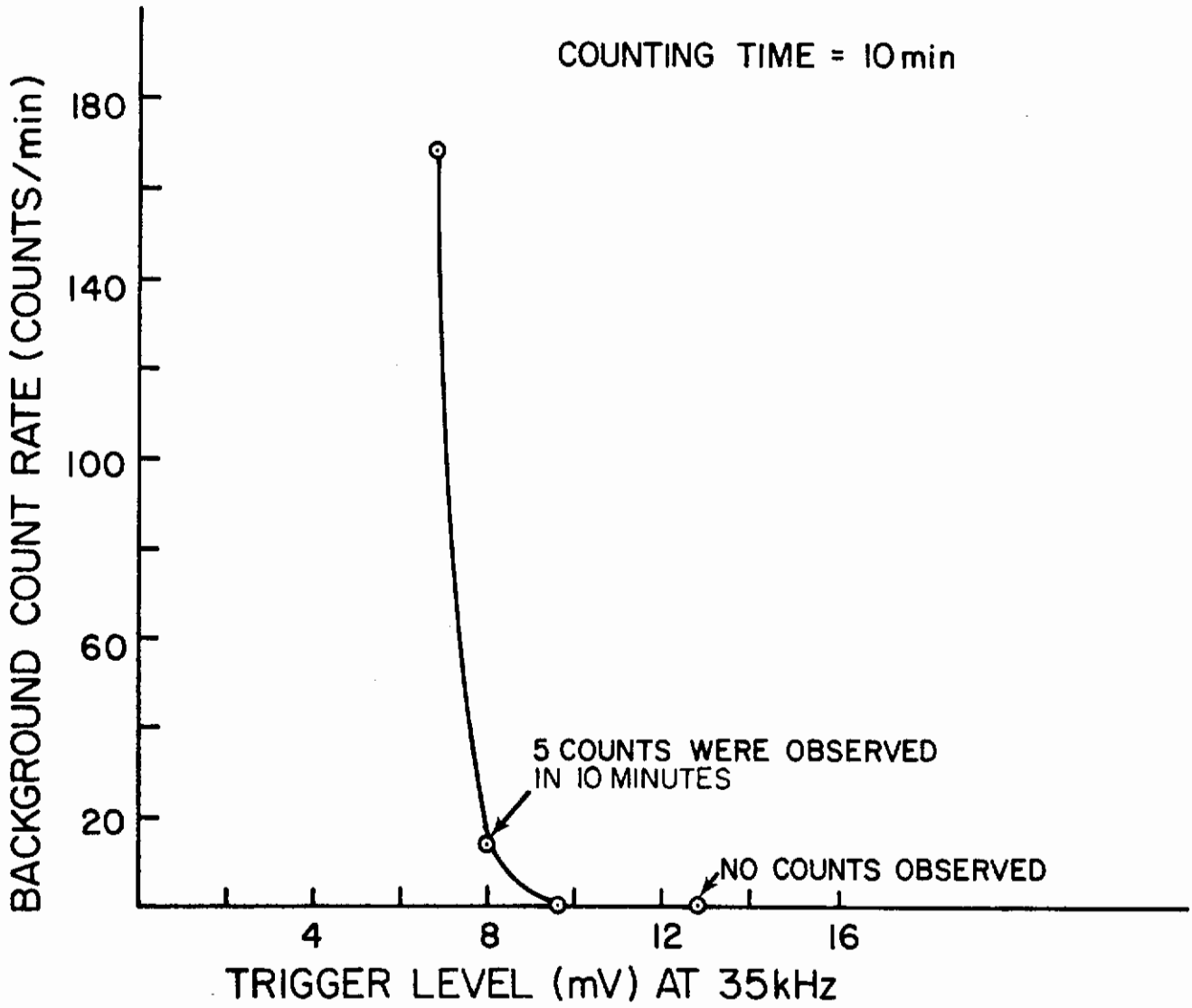

Fig. 120 - Background Count Rate vs. Trigger Level Setting (mV) of Peak Computer for a Specimen of 4335 Steel Loaded but Undergoing no Crack Growth

6. Nature of the Acoustical Pulse and its Detection

Experimental results to date have given no information as to the amplitude or frequency content of the actual signal. Effects such as reflection (and mode conversion), material attenuation, and the piezoelectric properties of the detector must be evaluated in order to obtain information regarding the initial signal. Attenuation will depend on the geometry of the wave (planar, spherical), as well as other wave properties. Therefore, knowledge as to reflection phenomena and detector response must first be obtained in order to know the properties of the acoustic signal leaving a crack.

Two avenues of approach are available to determine these effects; i.e., (1) to experimentally determine the response characteristics of the piezoelectric detector and to determine what reflections have occurred before the signal reaches the piezoelectric device, or (2) to alter the physical dimensions of transmitting medium, as well as the response characteristics of the transducer such that reflections and transducer resonance are minimal.

a. Investigation of the Response Characteristics of Endevco 2272 Accelerometer

(1) Test Procedure--The first investigation was that of determining how the Endevco accelerometer used in past studies responds to stress waves of various frequencies while mechanically loaded by coupling to steel. Using an elliptical PZT-4 ceramic disc ($\frac{1}{2}$"x1"x0.049") as a driving transducer, stress waves of various frequencies were transmitted to the accelerometer directly, and through two thicknesses of AISI 4335 steel, as shown in Fig. 121. Dow Corning ignition sealing compound DC-4 was used as the couplant. The stress wave was generated by a sinusoidal voltage (4.0 V peak-to-peak) applied across the driving transducer. This voltage was held constant, and the output of the accelerometer (after amplification and filtering) was monitored as a function of oscillator frequency. The sine wave was generated by a Hewlett-Packard 200 CD test oscillator. The value of 4.0 V for the voltage across the driving ceramic was chosen because it produced measureable accelerometer outputs at all frequencies up to the radial mode resonance frequency of the driving element (164 kHz).

(2) Results and Discussion--The accelerometer response curves and the electrical circuit are shown in Figs. 122-124. The presence of a radial mode resonance in the driving transducer at 164 kHz produced an explainable response peak for the accelerometer at that frequency. The response curves of the accelerometer show that the use of an accelerometer to detect frequency components in a stress wave above that of its own resonance frequency (37 kHz) is impractical, even in the case of a simple specimen geometry and a periodic, continuous stress wave. The response of the accelerometer appears to be a function of source-to-detector distance, and is undoubtedly affected by mechanical oscillation of the

DIRECT COUPLING

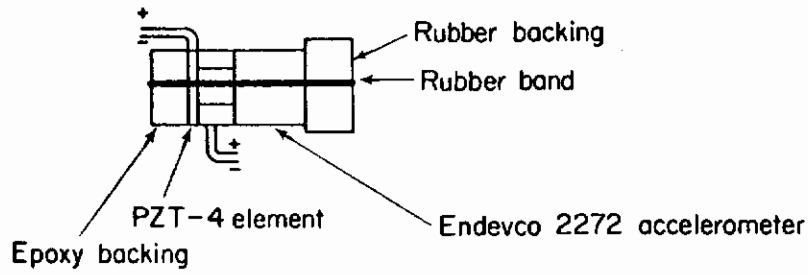

COUPLING THROUGH 1/2" DIMENSION OF STEEL SECTION*

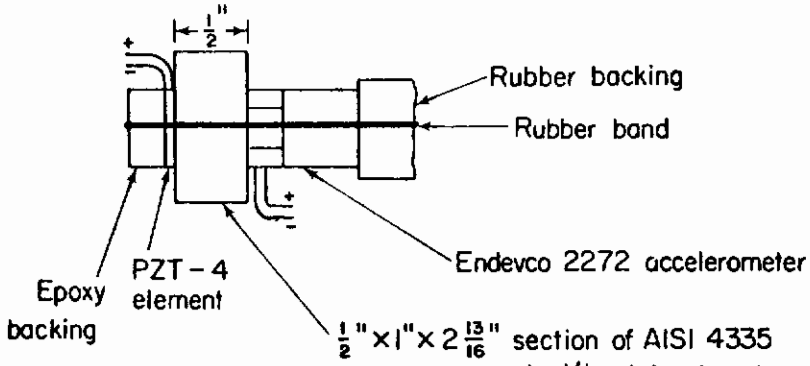

COUPLING THROUGH 1" DIMENSION OF STEEL SECTION*

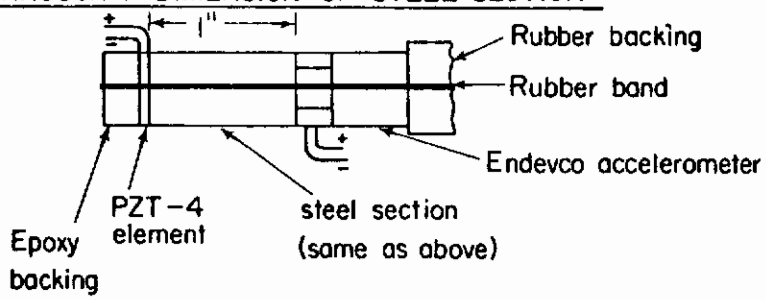

*In both cases transducer and accelerometer were located midway along the length of the steel section

Fig. 121 - Methods of Coupling PZT-4 Disc to Endevco Accelerometer

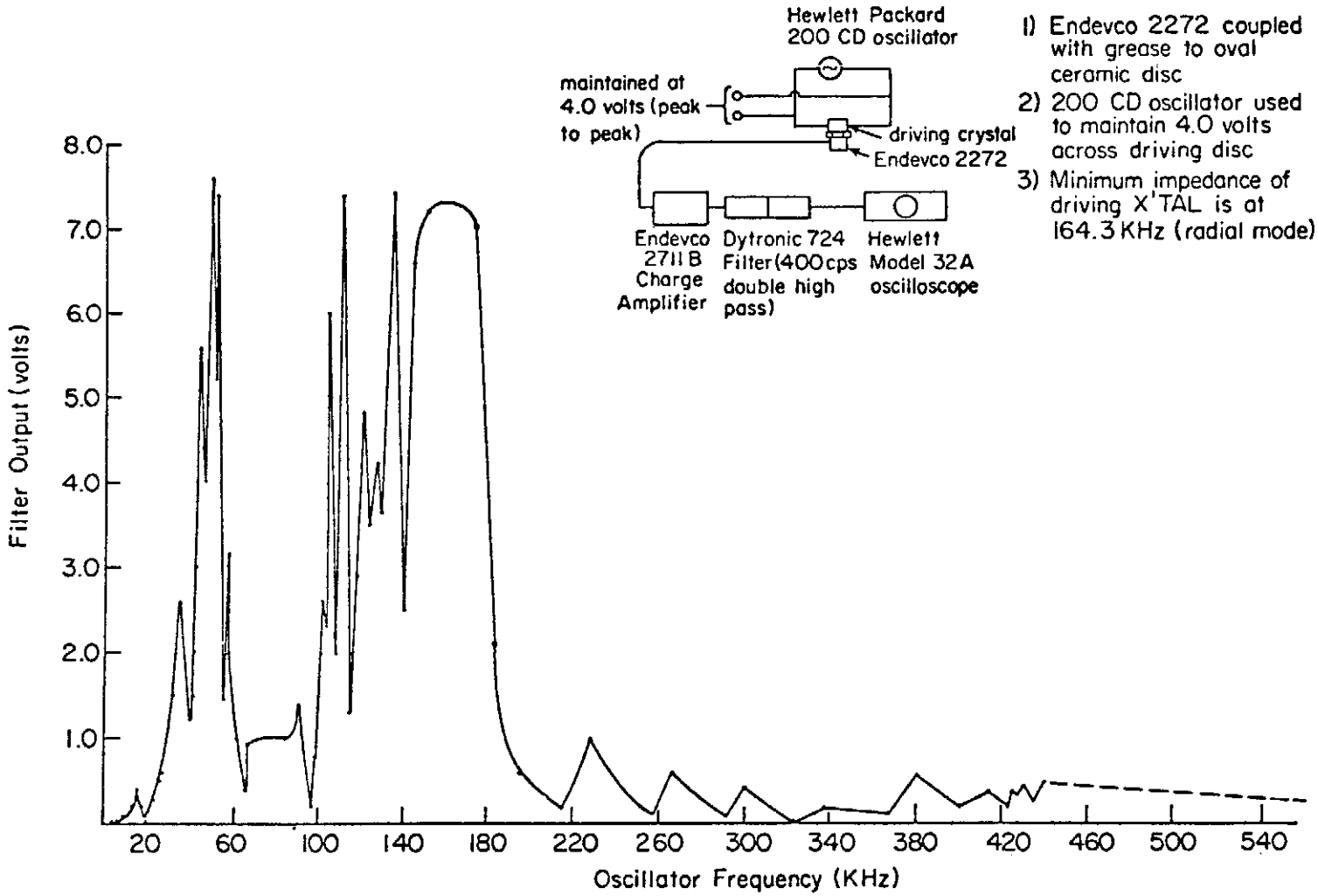

Fig. 122 - Response Curve of Endevco 2272 Accelerometer When Coupled Directly to PZT-4 Crystal

*Electrical circuit was the same as shown in Fig. 116

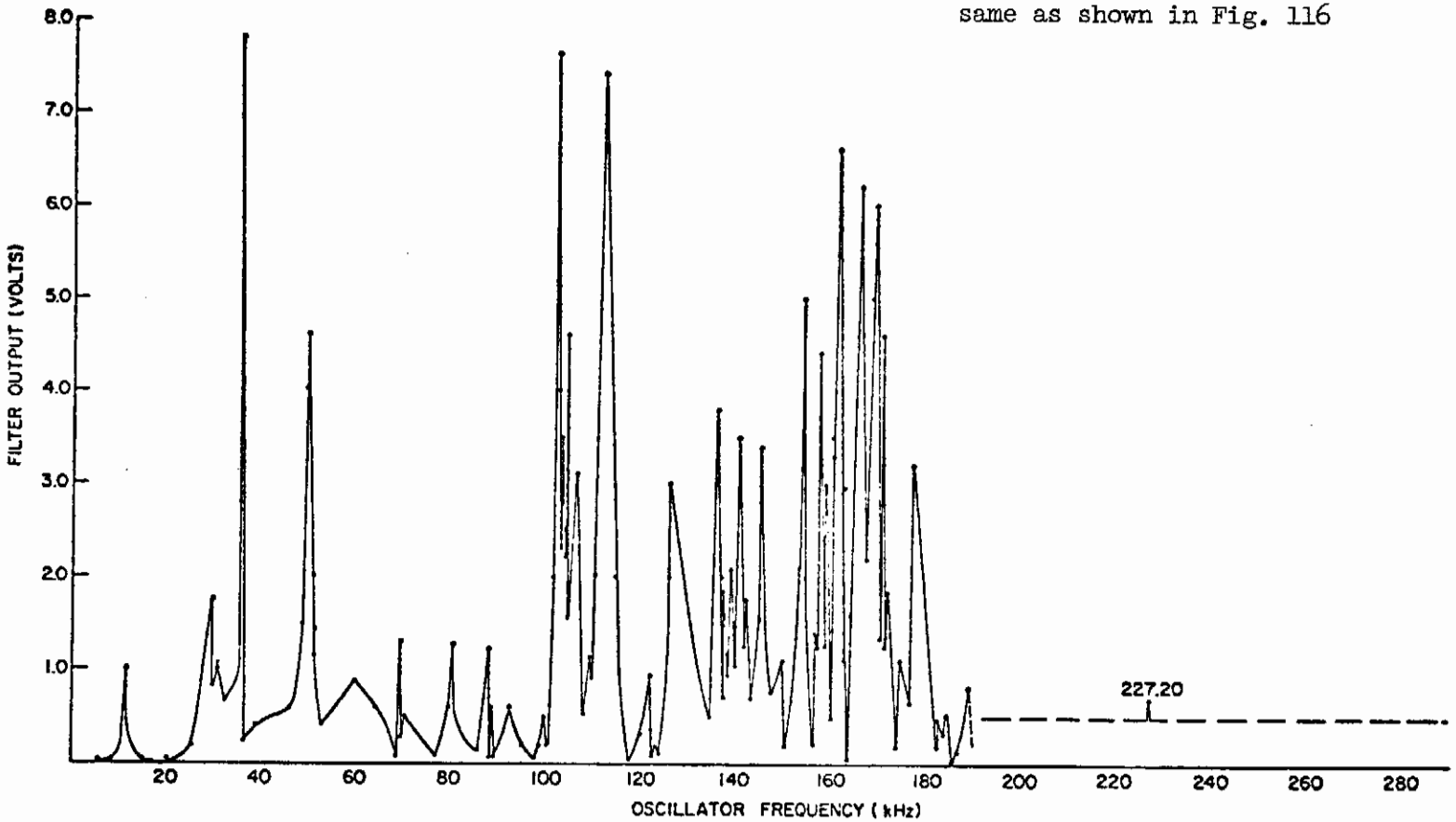

Fig. 123 - Response Curve of Endevco 2272 Accelerometer When Coupled to PZT-4 Crystal Through $\frac{1}{2}$ Inch Dimension of Steel Section*

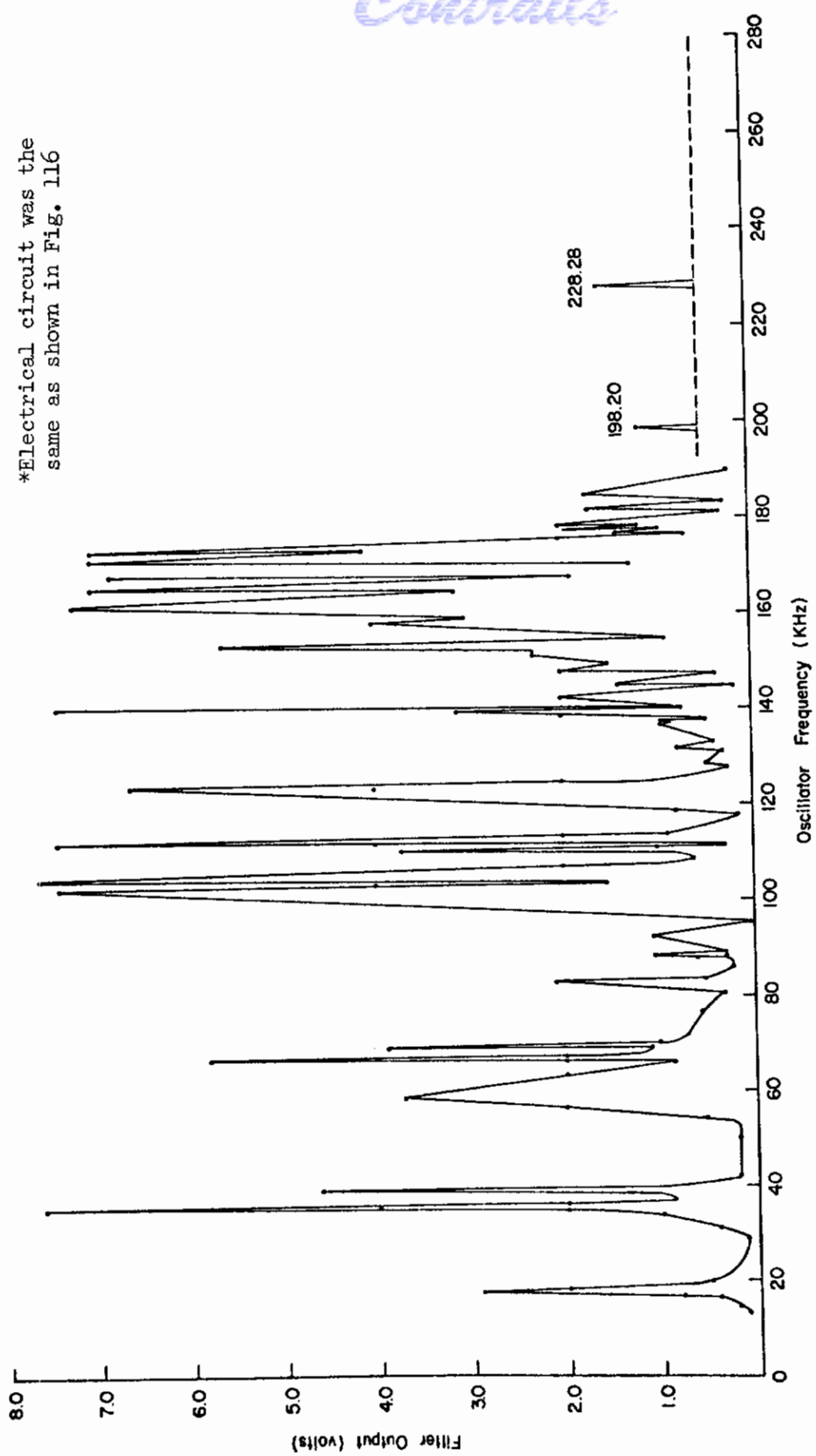

Fig. 124 - Response Curve of Endevco 2272 Accelerometer When Coupled to PZT-4 Crystal Through 1 Inch Dimension of Steel Section*

specimen. In Fig. 124, for example, the response peaks at approximately 100 kHz may be explained by standing waves in the 1-inch dimension of the steel section. Taking the volocity of a longitudinal wave in Armco iron as 23.5×10^4 inch/s,[107] and calculating the frequency for standing waves in the 1-inch dimension, it is seen that mechanical resonance of the specimen can occur at 117.5 kHz. All of the response peaks, however, cannot be explained by simple harmonic modes of vibration of the steel section. Therefore, the response of an accelerometer is quite complex when mechanically loaded and excited by frequencies above its resonance frequency.

b. Experimentation Using a 16-MHz Branson Transducer

(1) Test Procedure--In order to avoid transducer resonance, a Branson Z-103-B transducer (16 MHz resonance frequency) was used to detect acoustic emissions from stress corrosion cracks growing in various environments. The specimens were of the single cantilever beam type used in prior studies (Tech. Reps. AFML-69-16, 70-2). The material was AISI 4335 steel, heat-treated as follows: 1500°F/1 hr, O.Q. + 400°F/1 hr A.C. The cantilever loading assembly was the same as that used in the prior work cited above.

A sinusoidal voltage was applied across the transducer using a Hewlett-Packard 651 B test oscillator. The frequency was varied to a maximum (test oscillator limit) of 10 MHz. The voltage across the transducer was monitored, and no resonance occurred below 10 MHz. The transducer was mounted on the test specimens as shown in Fig. 125. Seven tests were performed by allowing a fatigue crack to grow in gaseous and aqueous environments, while the acoustic signals were recorded photographically. Random photographs were taken during each test. The applied stress intensity factors and environments are given in Table XVIII. The electrical system is shown in Fig. 125. The gas-purifying system and aqueous corrosion apparatus were the same as described in Technical Report AFML-69-16.

(2) Results and Discussion--Figures 126-130 show five random photographs of the transducer output for each test. The results show considerable variation in pulse shape for each environment. Also the presence of periodic signals (Figs. 126, 127) appear to indicate reflection phenomena with frequency components well below the natural resonance frequency of the transducer. On a comparative basis, there appears to be little effect of environment on signal shape using this experimental technique.

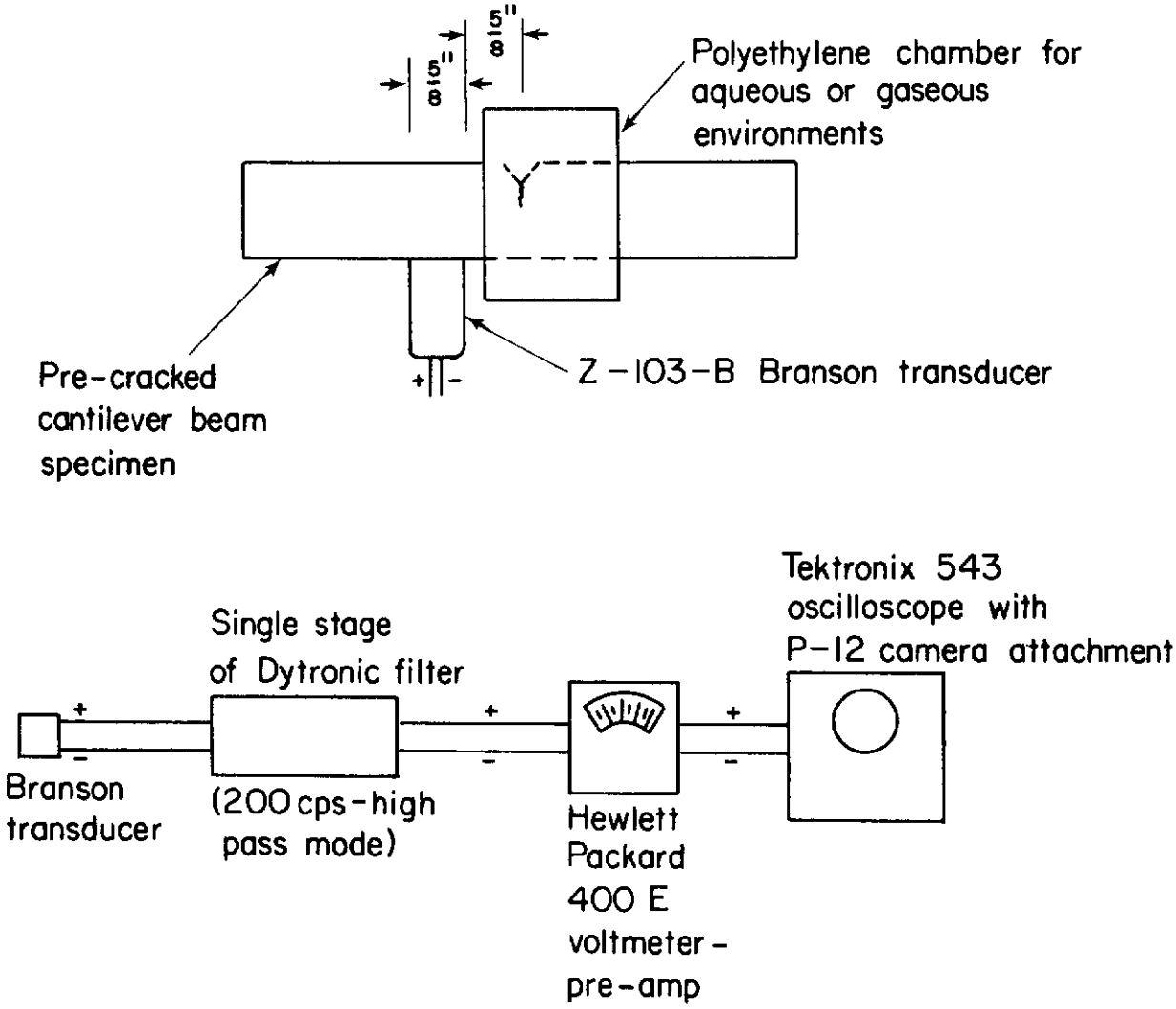

Fig. 125 - Test Apparatus for Experiments with Branson Transducer

Table XVIII - Test Conditions for Cantilever Beam Specimens

Specimen	Initial Stress Intensity Factor (ksi-in.$^{1/2}$)	Environment*	Applied Potential**
CDG-78	38.04	23.1% H_2	--
CDG-79	40.30	23.1% H_2	--
CDG-80	42.82	23.1% H_2	--
CDG-81	38.56	100% H_2	--
CDG-82	41.39	1N HCl	-1.0 V
CDG-83	46.23	1N HCl	+1.0 V
CDG-84	49.42	$3\frac{1}{2}$% NaCl adj. to pH = 13 with NaOH	+1.5 V

*Total flow rate of gaseous mixtures and pure H_2 was 6.5 cc/minute
**Potential controlled by Magna Research potentiostat Model 4700M, and all potentials are WRT (SCE)

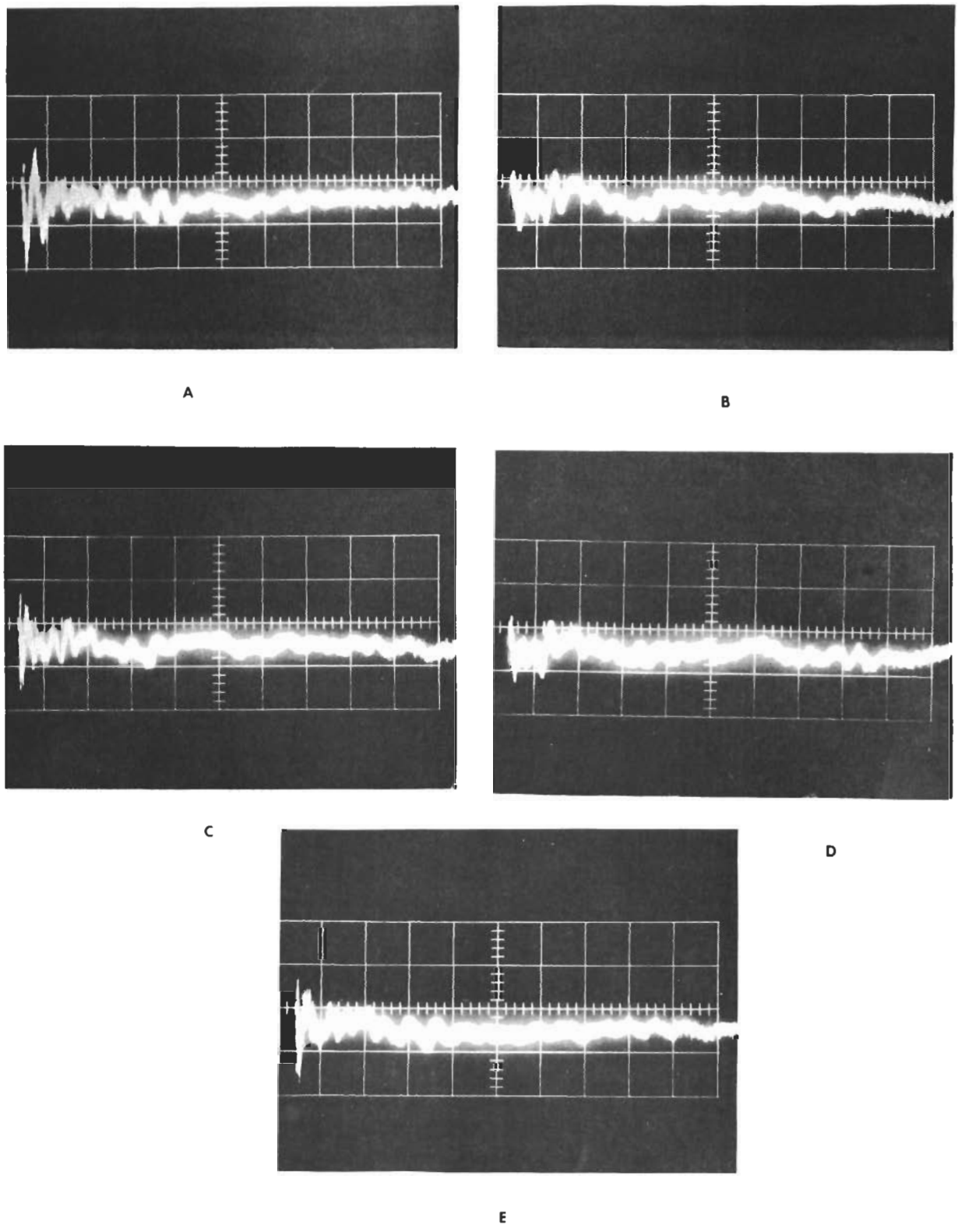

Fig. 126 - Photographs of Acoustic Emissions in 23.1% H_2 (Spec. CDG-78); horizontal scale - 500 μsec/cm vertical scale - 5 mV/cm

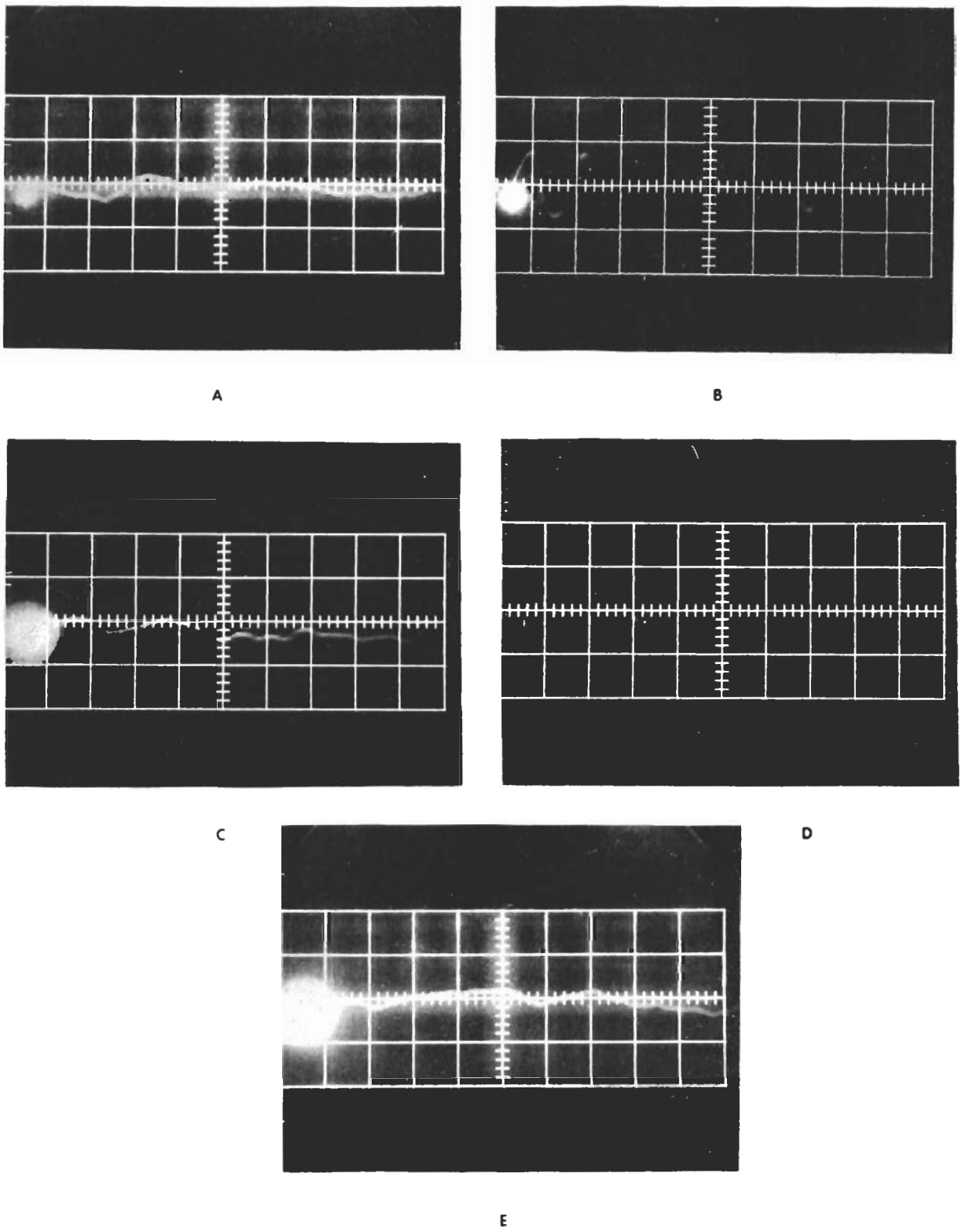

Fig. 127 - Photographs of Acoustic Emissions in 23.1% H_2 (Spec. CDG-79); horizontal scale - 1 μsec/cm
vertical scale - 10 mV/cm

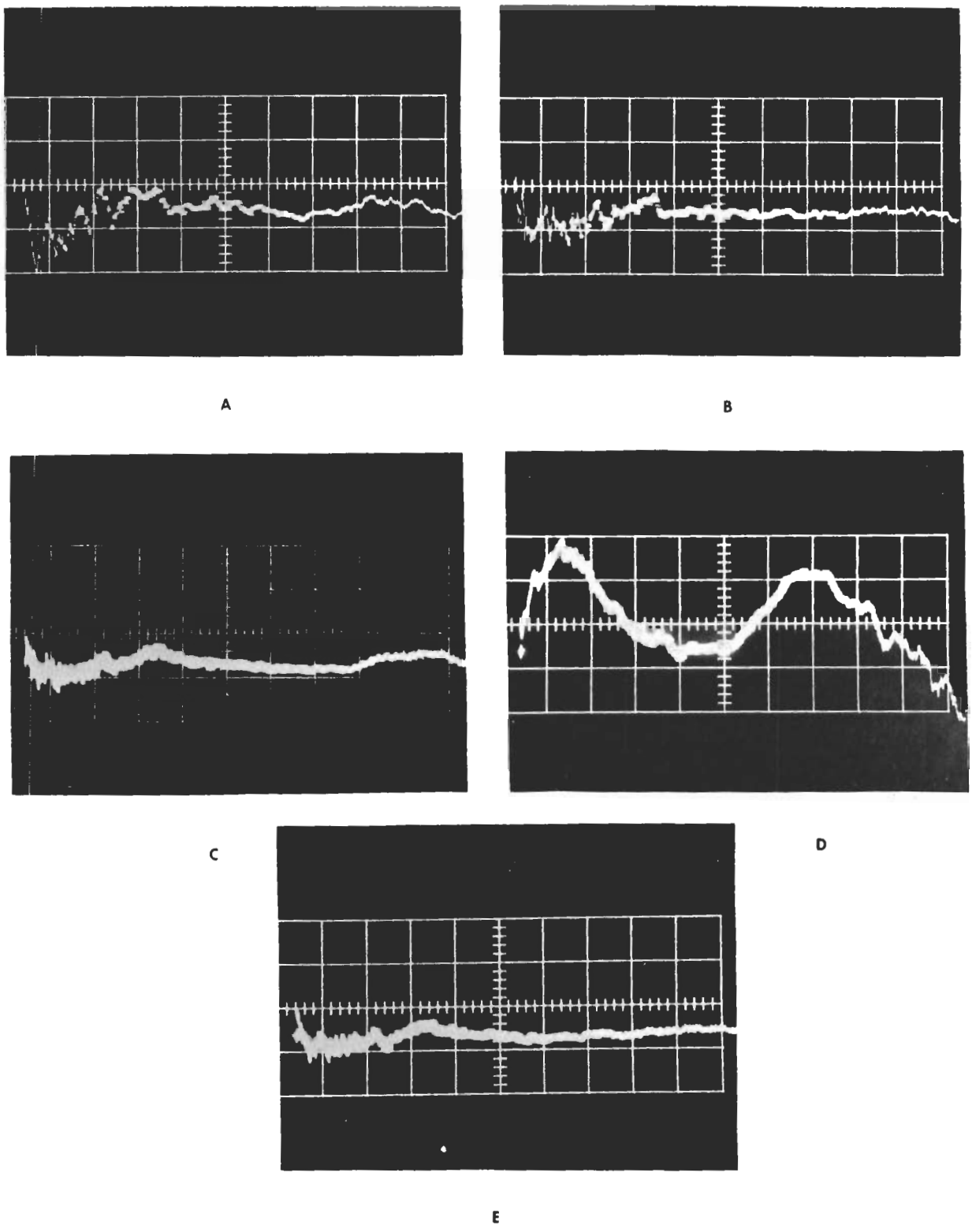

Fig. 128 - Photographs of Acoustic Emissions in 1N HCl at -1500 mV WRT (SCE) (Spec. CDG-82); horizontal scale - 50 μsec/cm vertical scale - 10 mV/cm

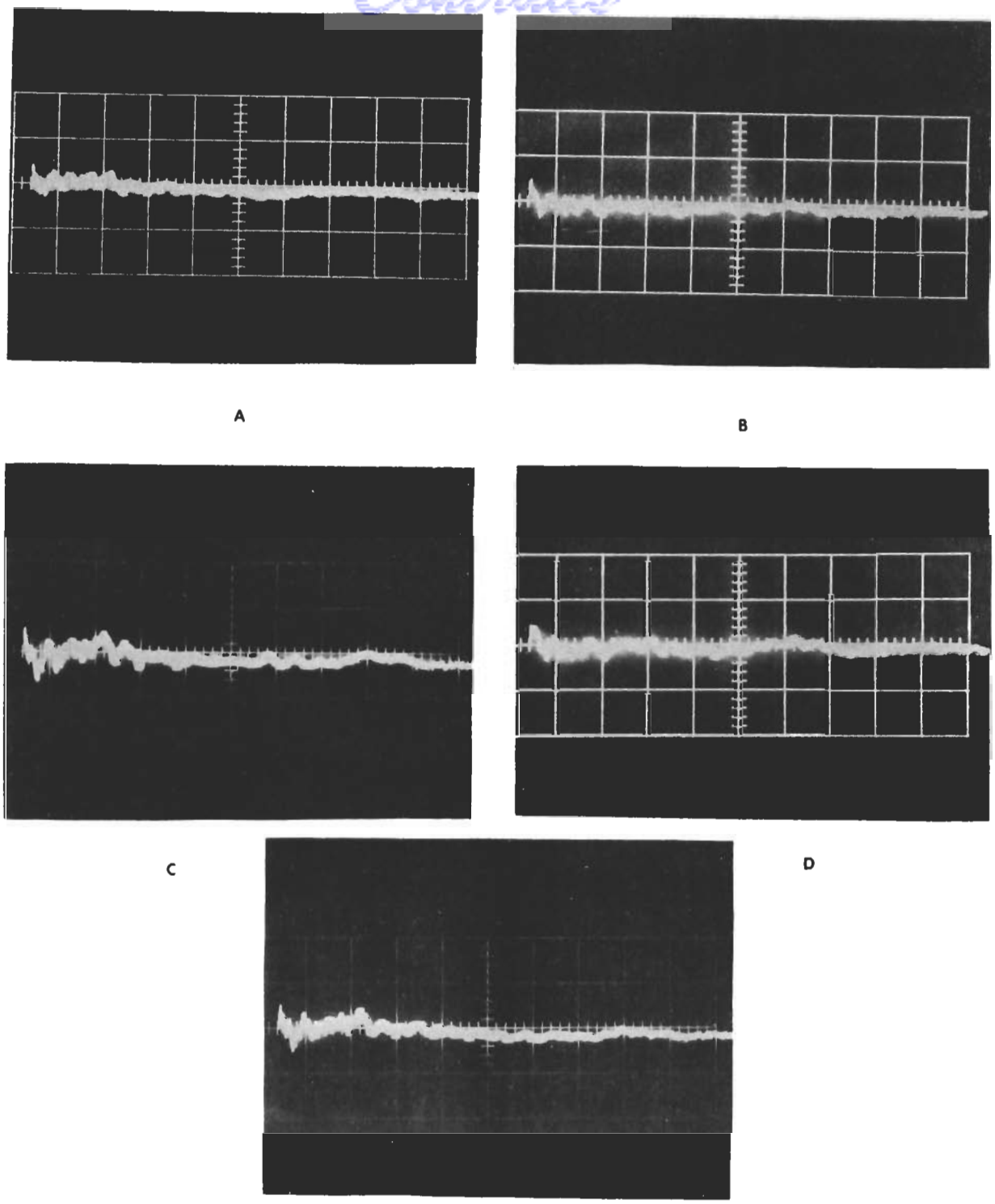

Fig. 129 - Photographs of Acoustic Emissions in 1N HCl at +1200 mV WRT (SCE) (Spec. CDG-83); horizontal scale - 50 μsec/cm vertical scale - 10 mV/cm

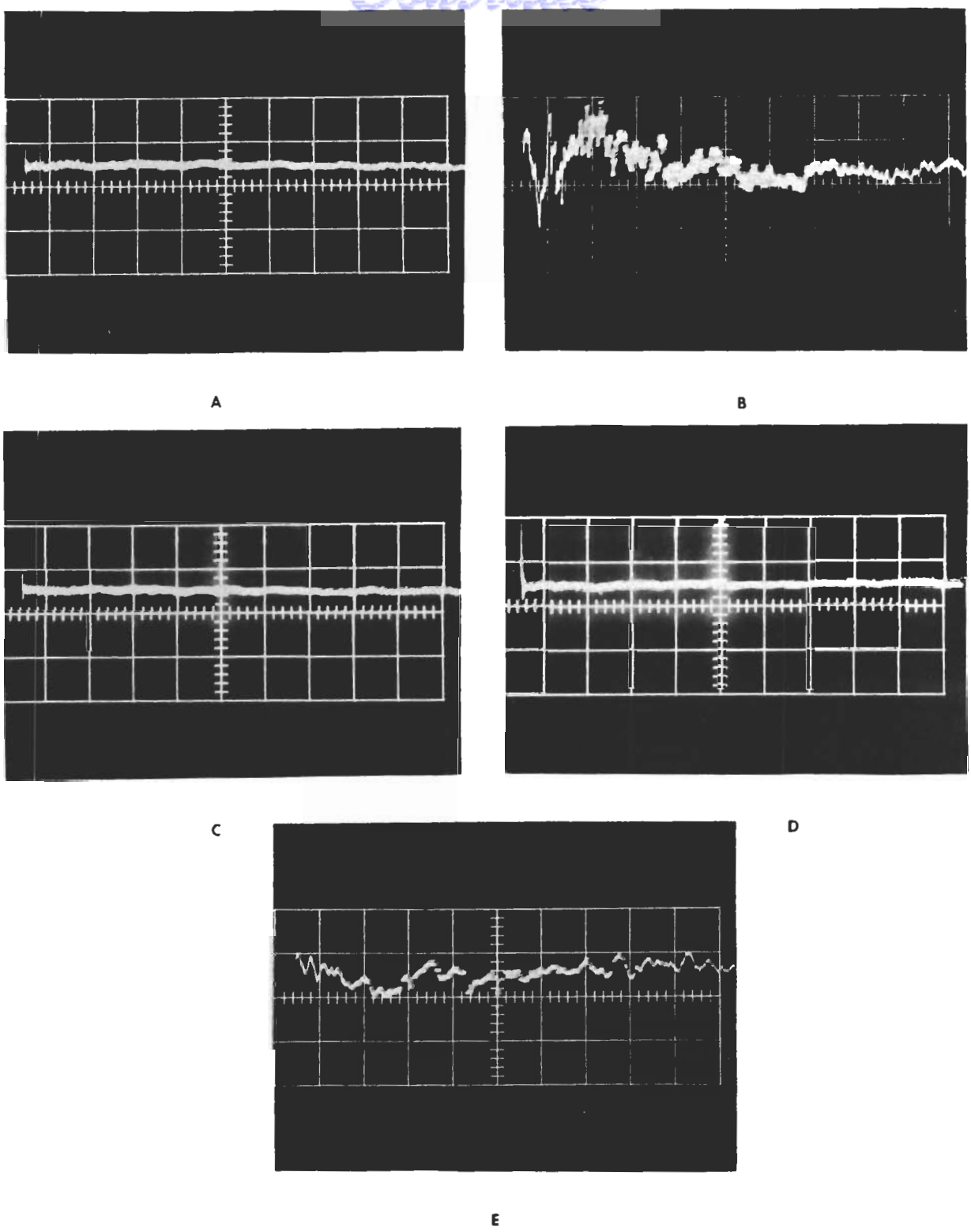

Fig. 130 - Photographs of Acoustic Emissions in $3\frac{1}{2}\%$ NaCl (adjusted to pH = 13.0 with NaOH) at +1500 mV WRT (SCE) (Spec. CDG-84; horizontal scale - 50 μsec/cm
vertical scale - 10 mV/cm

c. Experimentation Using PZT-4 Ceramic Element and Sections of Steel on Sides of Specimens

(1) Experimental Procedure--The effect of reflections in the transmitting medium can be determined by (a) providing an acoustic medium adjacent to the specimen such that portions of the wave which would normally reflect from free surfaces are attenuated, preventing their superposition on the wave portion which travels directly to the detector; or (2) to provide a medium (which is acoustically matched to the specimen material) into which the wave may pass and undergo reflection at a much later time.

Condition (b) is easily met by coupling sections of 4335 steel to the sides of the test specimen, as shown in Fig. 131. If the prefatigue crack length is large, and the piezoelectric detector is placed below the crack, the source-to-detector distance can be made quite small as shown in Fig. 132. If the detecting element is 0.235 inch from the crack and we assume a longitudinal wave of velocity 23.5×10^4 inch/s generated at the mid-thickness of the specimen, the time to reach the detector is 1 μs. The minimum distance for the wave to travel if it reflected from the free surface of the specimen (with steel sections on the sides) is 1.5 inch. The time required for this portion of the wave to reflect and then strike the detector is at least 6 μs. The shortest time would be 5.3 μs (source is at specimen-side plate interface). Therefore, by examining only the first 5 μs of the signal, the effect of superimposed reflections should be minimal.

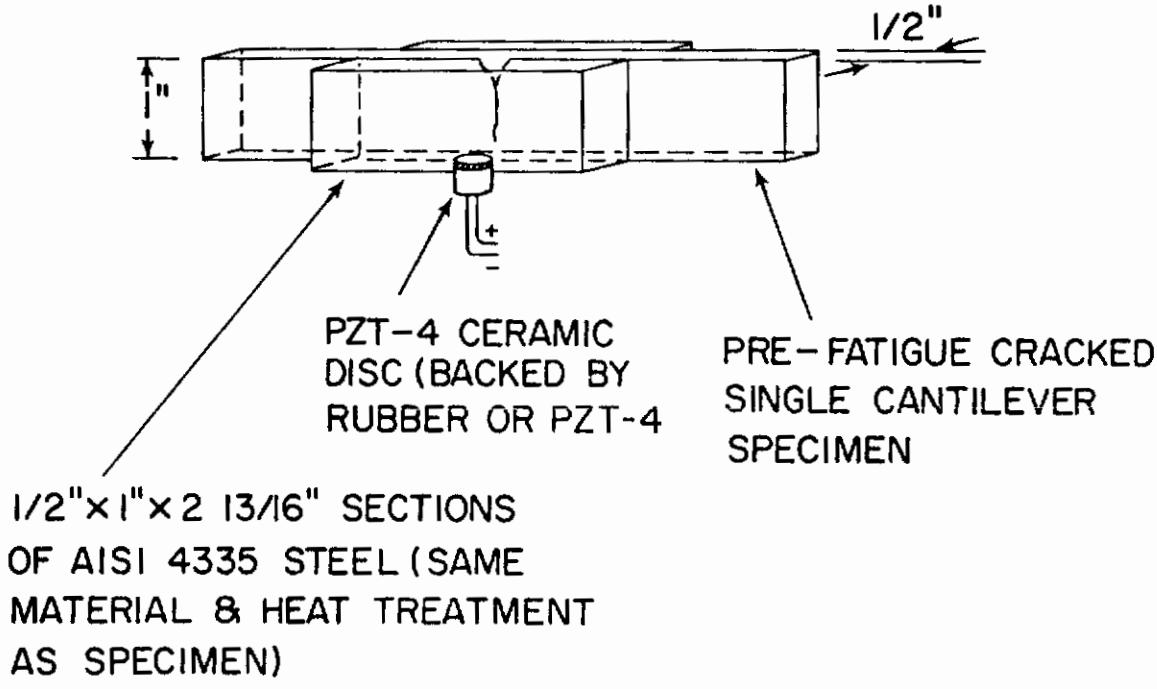

Fig. 131 - Test Apparatus for Experiments with PZT-4 Ceramic Disk

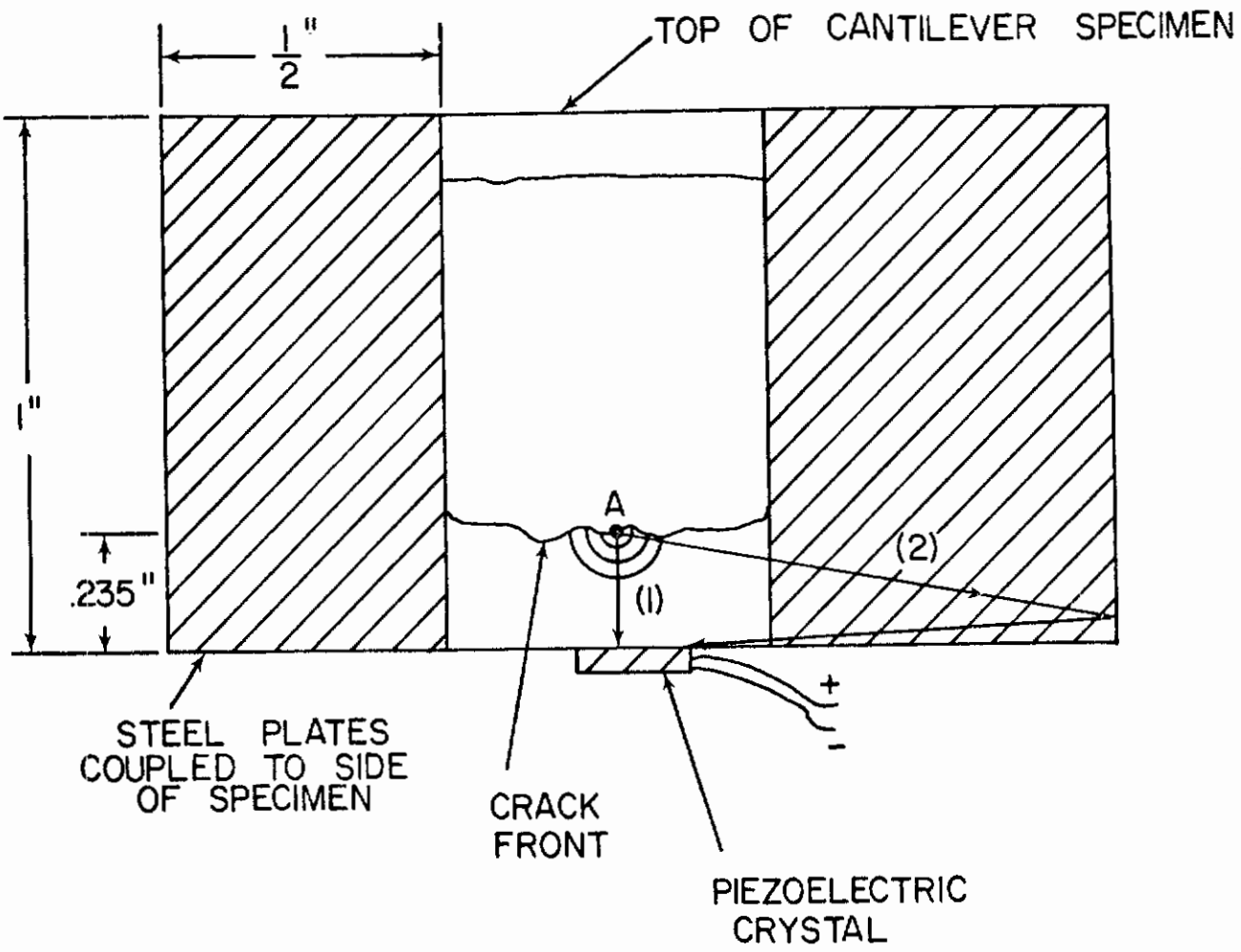

Path (1) - Direct Wave Strikes Crystal in 1 μs
Path (2) - Reflected Portion of Wave Strikes Crystal in 5 μs (or longer)
Point A - Wave Source

Fig. 132 - Cross-Sectional View of Cantilever Specimen Showing Wave Paths to Crystal

Two tests were performed using the technique described above. The prefatigue crack was extended to within 0.25 inch of the detecting element. To detect the emissions, a portion of the PZT-4 disc (described in this report) having a maximum dimension of 0.50 inch was used. The electronic system was the same as that used with the Branson transducer. In the first test the PZT-4 ceramic was backed by a rubber stopper. In the second test a 1/2 inch cube of PZT-4 (with the polarization direction parallel to the plane of the detecting disc) was used. The environment was 0.1N HCl applied to the crack tip from a beaker. This procedure was used so as (1) to allow access to the transducer, and (2) to prevent uncoupling of the transducer from the specimen while inserting the specimen into an environment chamber.

A second series of tests was performed with two detecting elements (PZT-4) and a Tektronix Type 555 dual beam oscilloscope. Signals from the crystals were photographed by allowing one of the crystal output signals to trigger the oscilloscope sweep. The cracks were propagated in a dry H_2 (pure) environment. Both detecting crystals were backed by PZT-4. The oscilloscope and pre-amplifiers were adjusted to give the same gain for both crystals.

(2) Results and Discussion--Figure 133 shows five randomly photographed signals for the case where the single PZT-4 disc was backed by a rubber stopper. The photographs show two resonance modes of the detecting disc to be present. These frequencies (2.0 to 2.5 MHz and 250 kHz) are in fair agreement with the predicted[108] values for a 0.050-inch disc, 0-350-inch diameter (1.5 MHz and 250 kHz). The disc was irregularly shaped to avoid the lower frequency radial mode. Its average width was approximately 0.350-inch, however, indicating that the radial resonance mode still occurred. The backing of the detecting disc by the PZT-4 cube in the second test gave a medium of the same acoustic impedance as the detecting crystal. This removed the free surface condition for reflection and satisfied the conditions for minimum acoustic impedance mismatch described by Mason.[109] The results are shown by the three photographs in Fig. 134. No apparent resonance effects were present.

Figure 135 shows five random photographs obtained when two piezoelectric discs were used. The oscilloscope sweep was triggered by the upper beam signal. The applied initial stress intensity factor was 45.80 ksi-in.$^{1/2}$.

Additional signal photographs, obtained using two backed detector discs, show occasional resonance phenomena in Figs. 136 and 137.

By further experimentation it was found that pulses of microsecond duration, such as those in Figs. 133-135 could be produced by electrical light switches in the laboratory. Also ultrahigh frequency signals (several megahertz), as seen in Fig. 135 were found to be noise signals from the Hewlett-Packard voltmeter pre-amlifiers. In many cases, however, signals such as in Fig. 133(e) and in Figs. 135(a) and (b), show crystal resonance. It is, therefore, very possible that the acoustic signal is of microsecond duration, since it is unlikely that power line noise (switches, etc.) could excite mechanical resonance of the transducer. In general, the pulse shapes observed during cracking were varied and similar to that shown in Fig. 133(c). The electrical noise signals observed were rather similar in that they were either of very short duration, with no obvious periodicity, or of very high frequency content (well above any natural first harmonic frequency of the crystal).

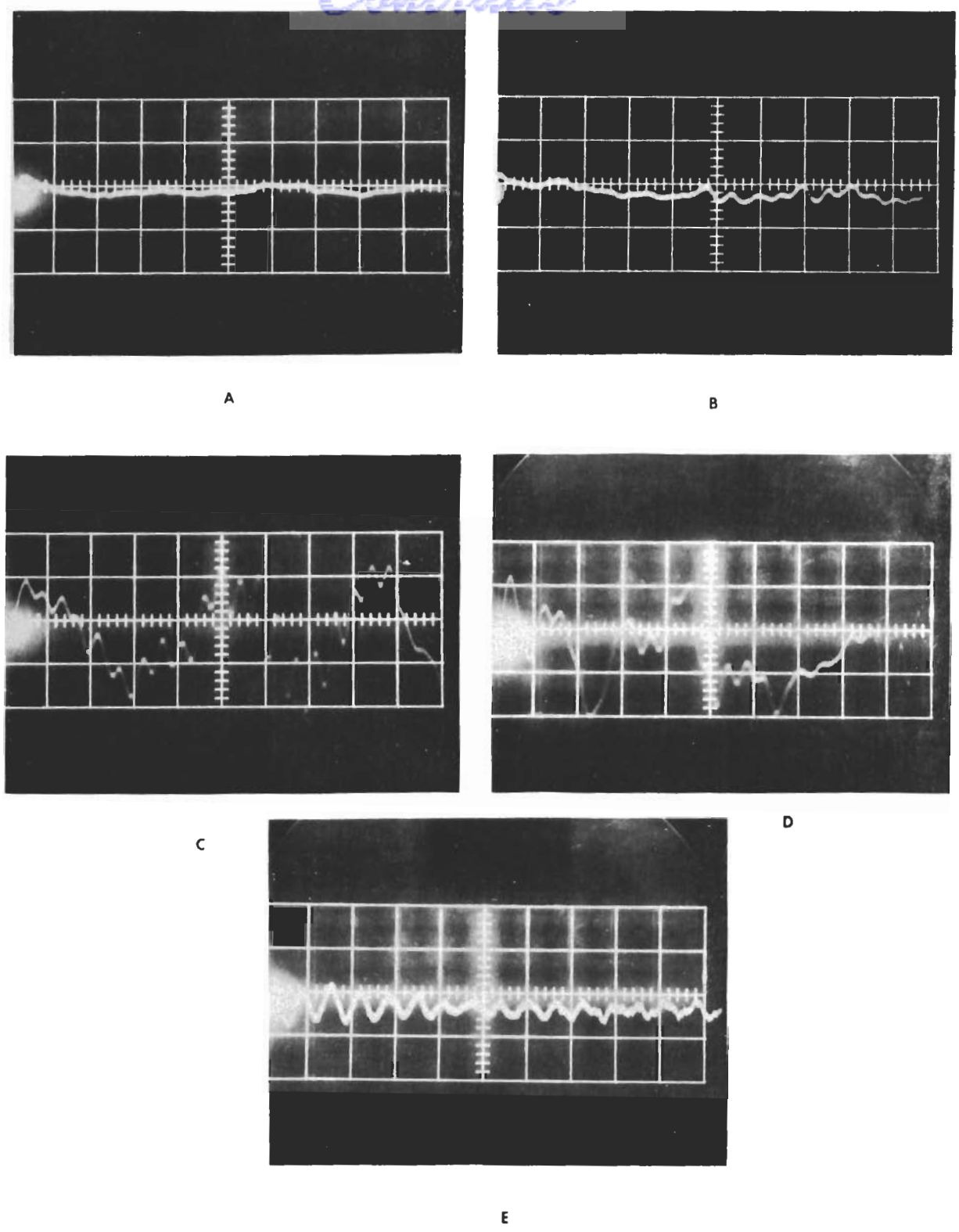

Fig. 133 - Photographs of Acoustic Emissions in 0.1N HCl (Spec. CDG-85); horizontal scale - 1 μs/cm (photos 1-4), 5μs/cm (photo 5)
vertical scale - 4 mV/cm

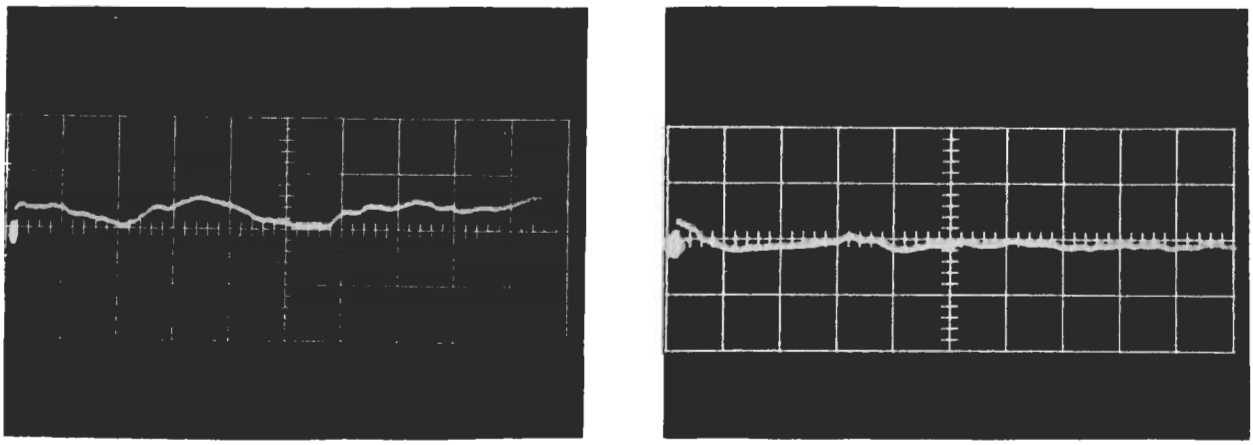

A

B

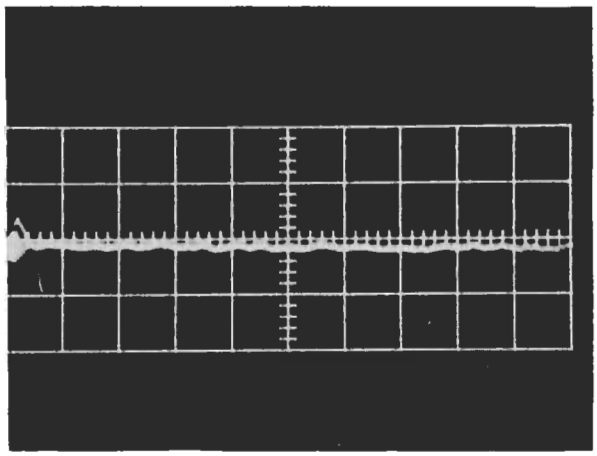

C

Fig. 134 - Photographs of Acoustic Emissions in 0.1N HCl (Spec. CDG-86); horizontal scale - 1 μs/cm
vertical scale - 5 mV/cm

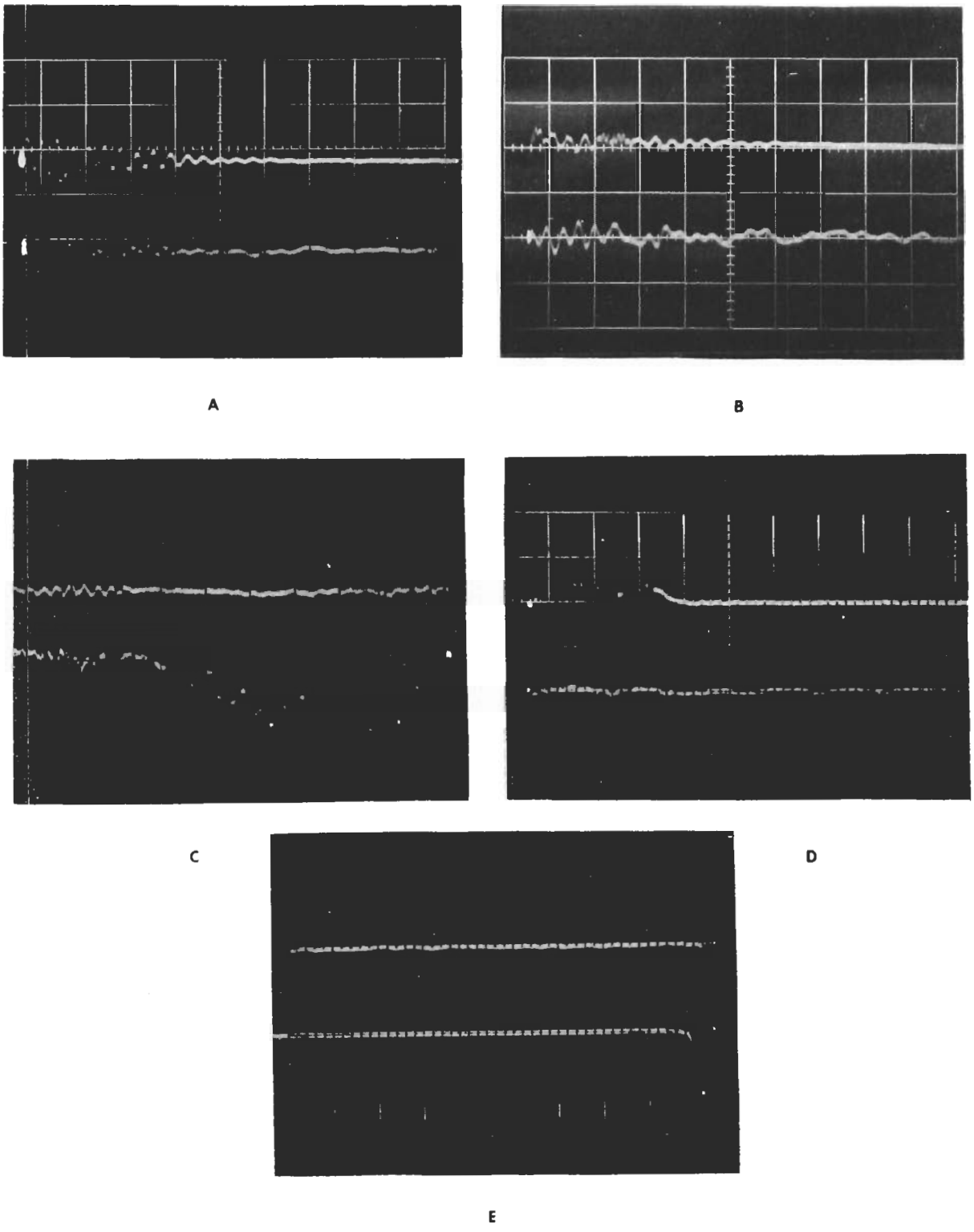

Fig. 135 - Photographs of Acoustic Emissions in Pure H_2 (Spec. CDG-88); horizontal scale - 1 μs/cm

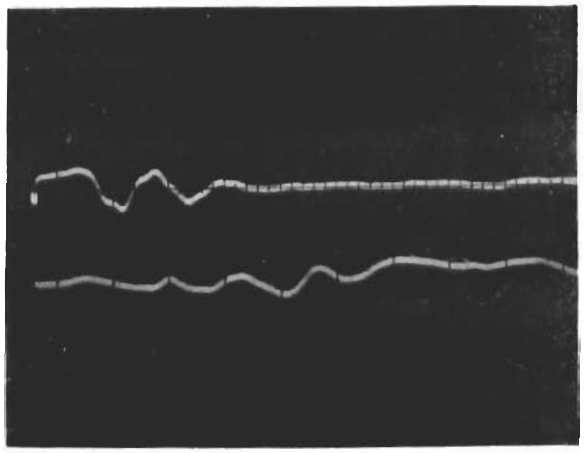

A

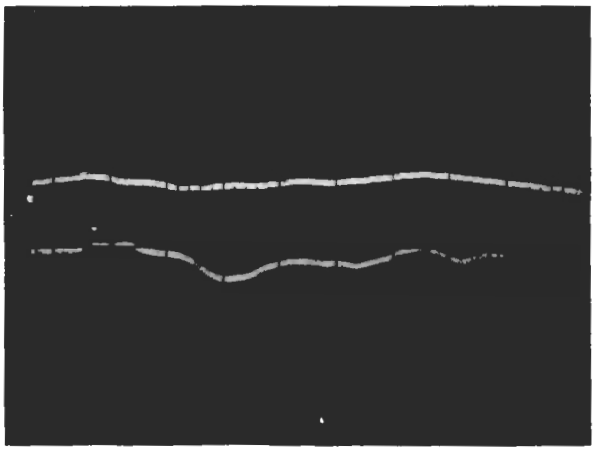

B

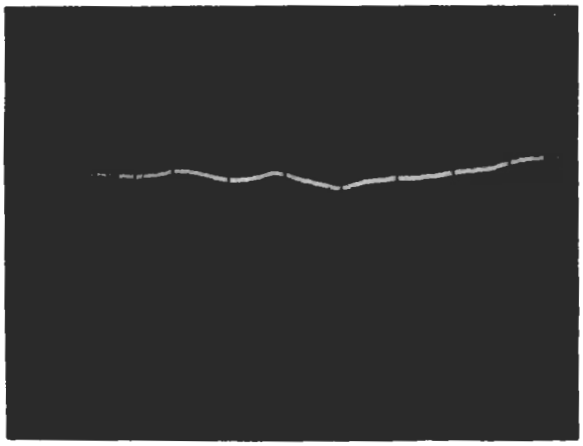

C

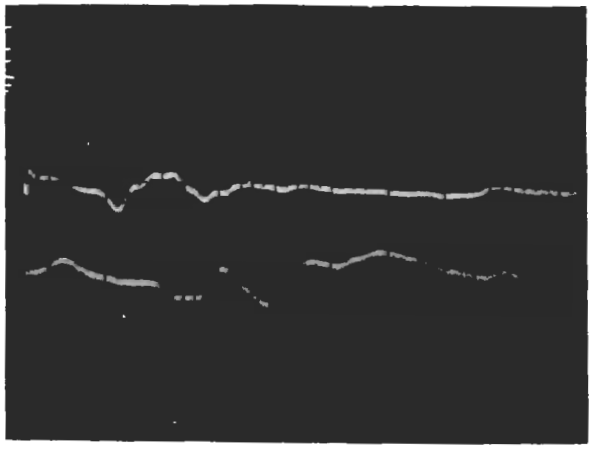

D

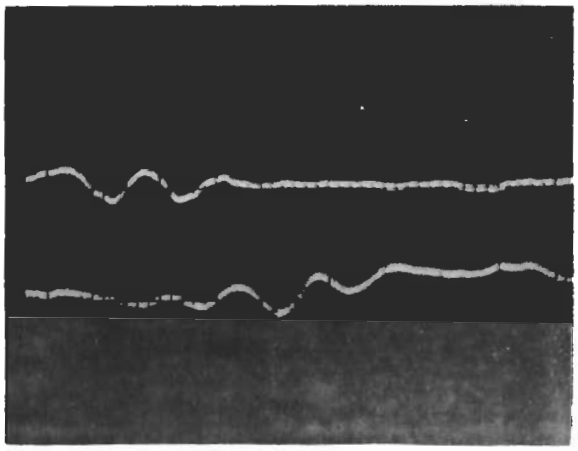

E

Fig. 136 - Photographs of Acoustic Emissions in Pure H_2;
Specimen - AISI 4335 Steel, Tempered at 400°F;
horizontal scale - 1 μs/cm

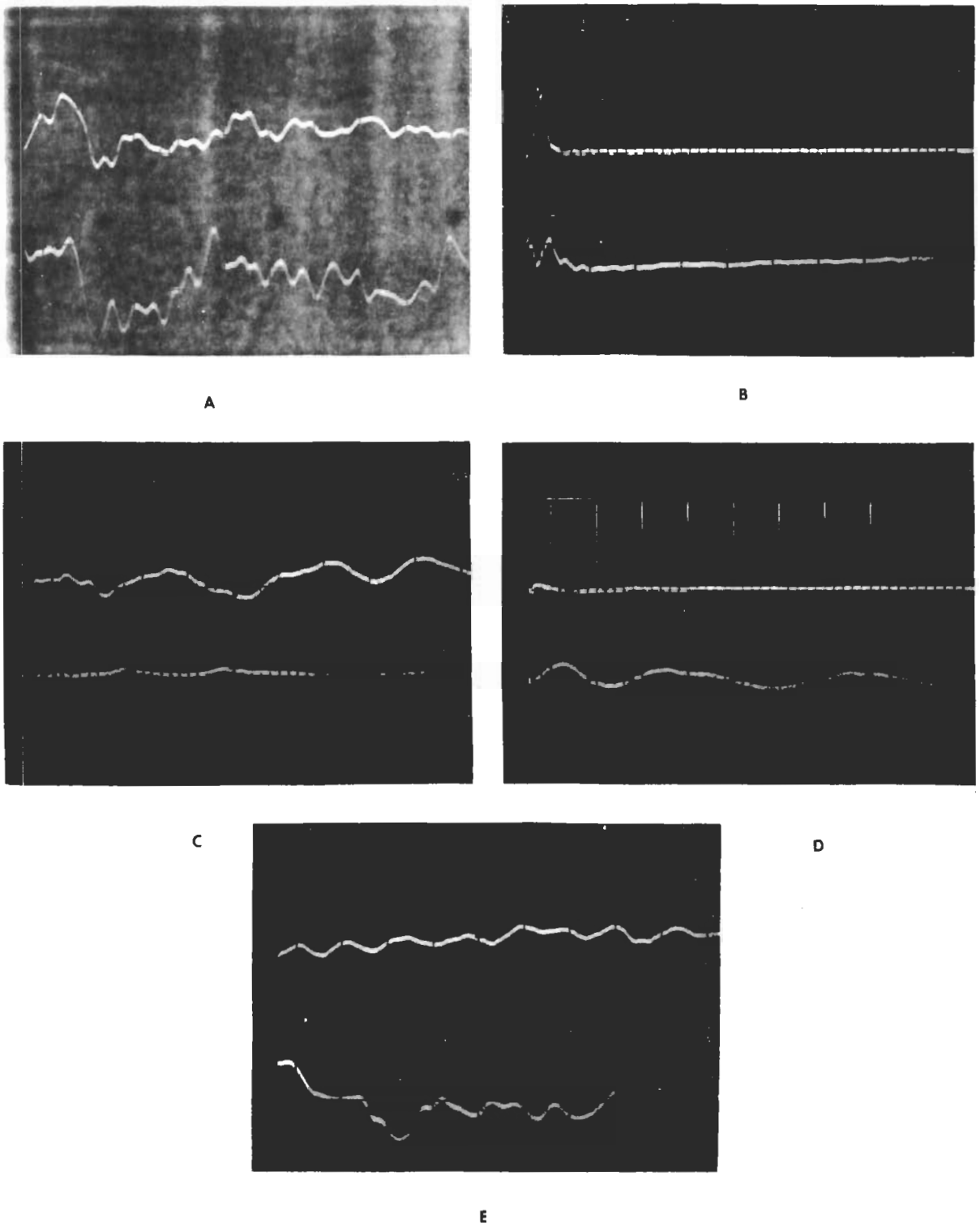

Fig. 137 - Photographs of Acoustic Emissions in Pure H_2;
Specimen - AISI 4335 Steel, Tempered at 400°F;
horizontal scale - 1 μs/cm

d. Conclusions

The experimental results have shown that:

(1) Removing conditions for reflection in the transducer and in the transmitting medium greatly alters the signal produced by a piezoelectric detector when stress waves are produced.

(2) Eliminating reflection phenomena by altering detector and specimen geometry provides a simpler approach to stress wave analysis than the attempt to determine the distortion of the wave due to reflections.

7. Comparison of Acoustical Activity in Dry H_2 and Aqueous Environments

These measurements were performed to compare the nature of the acoustical activity in dry H_2 and aqueous environments. Both environments cause SCC in high-strength steels. A single alloy was used in two heat-treated conditions.

a. Specimen Preparation

The material used in this investigation was AISI Type 4335 steel. The nominal chemical composition is shown in Table XIX. Seven specimens of the single cantilever type used previously were machined and heat-treated to different strength levels. The heat treatment and approximate tensile strength (estimated from R_C scale hardness measurements) are given in Table XX. Four hardness measurements were made on each specimen approximately 3/16" from the fracture surface. The average value was used to approximate the tensile strength.

Table XIX - Nominal Chemical Analyses of AISI Type 4335 Steel

C	0.38 - 0.43%
Mn	0.60 - 0.80%
Si	0.20 - 0.35%
Ni	1.65 - 2.0%
Cr	0.70 - 0.90%
Mo	0.20 - 0.30%
P	0.4% Max
S	0.04% Max

Table XX - Heat Treatments, Tensile Strengths, Test Environments, and Initial Stress Intensity Factors for Single Cantilever Beam Specimens

Specimen No.	Test Environment	Austenitizing* Temp.(°F)	Tempering** Temp.(°F)	Approx. Tensile Strength (ksi)	Initial Stress Intensity Factor (ksi-in.$^{1/2}$)
90	3.5% NaCl	1500	400	237	43.81
92	Dry H_2	1500	400	224	~ 49.6
93	Dry H_2	1600	400	227	43.47
94	Dry H_2	1600	400	229	41.15
95	Dry H_2	1600	800	194	41.21
98	3½% NaCl	1600	800	188	43.80
99	Dry H_2	1600	400	240	39.74

* Austenitizing in all cases was for 1 hour, followed by oil quench.
** Tempering in all cases was for 1 hour, followed by air cool.

Following heat treatment, the specimens were ground to a 120-grit finish and pre-cracked by fatiguing. Two specimens were tested in 3.5% NaCl solution at a potential of -1.0 volt (SCE). The remaining five specimens were tested in a H_2-Ar gas mixture containing 9.1 vol% H_2 at slightly over atmospheric pressure. Initial stress intensity factors, along with the test environments, are given in Table XX.

b. Acoustic Detection

Acoustic emission signals were detected using an Endevco 2272 accelerometer (resonance frequency of 37 kHz), coupled with an Endevco 2711B charge amplifier. The output of the amplifier was fed into a Dytronic 724 filter (operated in a 30 - 40 kHz band pass mode), and subsequently into a Hickok DP150 counter. Before filtering, the signals were also stored on magnetic tape, using a Sony TC 105 tape recorder; the electronic apparatus is shown in Fig. 138. The accelerometer was fastened to the specimens using a 10/32 cap screw with a milled head (.015" thick) and Metalset A-4 epoxy resin cement (see Fig. 139).

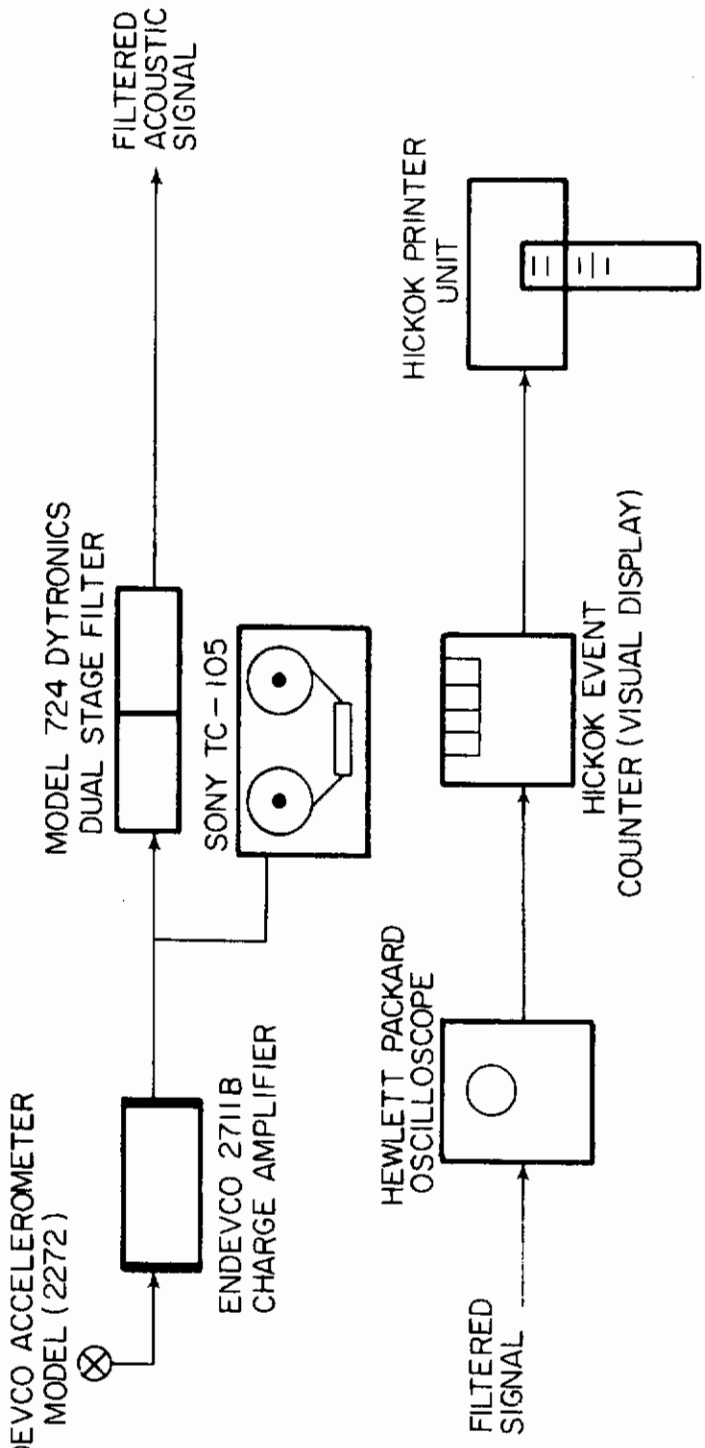

Fig. 138 - Electronic System for Detection of Acoustic Emissions

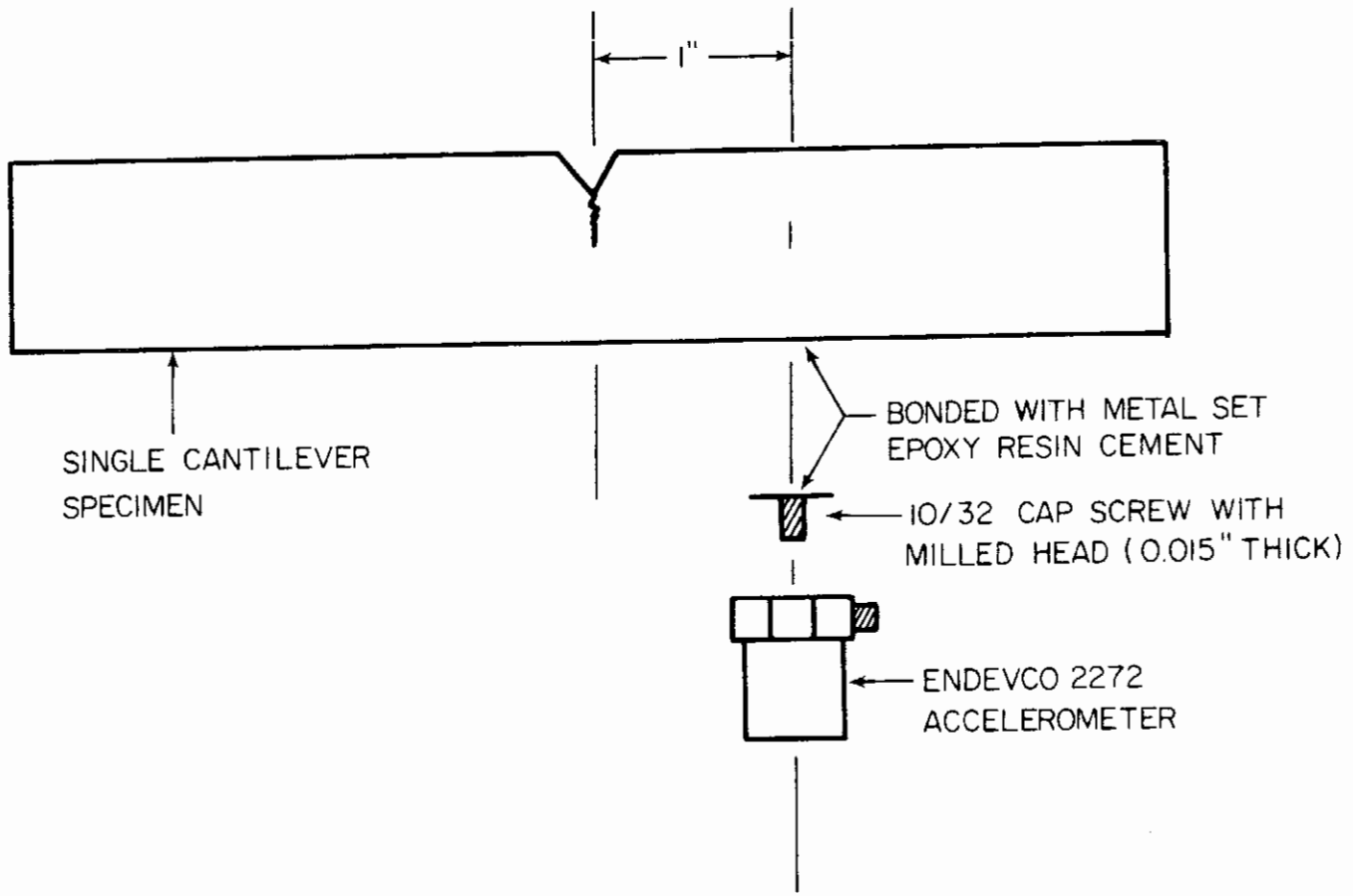

Fig. 139 - Diagram Illustrating Bonding of Accelerometer to Specimen

In determining whether a particular increment of crack extension is associated with a single emission, it is necessary to record emissions, rather than resonance peak counts. The latter technique is affected by both the number and size of emissions, but cannot discriminate between a small number of large emissions or vice versa. In order to determine the number of emissions and their relative size, the acoustic pattern obtained from the 227 ksi specimen (No. 93) was replayed from the tape recorder into an oscilloscope. The oscilloscope triggering level was adjusted such that a 2 ms sweep occurred when the oscilloscope was triggered by signals on the tape. One sweep would occur for a signal of a chosen signal-to-noise ratio. Values of 4, 6, 8, and 10 were chosen. At lower signal-to-noise ratios, it was found that periodic noise from the Hickok printer unit (one print-out every 10 s) triggered the oscilloscope. In all instances resolvable signals were found to produce only one oscilloscope sweep. The gate output of the oscilloscope was then fed into a Hickok DP150 1 MHz counter, and one count was observed for each oscilloscope sweep (hence, each emission). The electronic system is shown in Fig. 140.

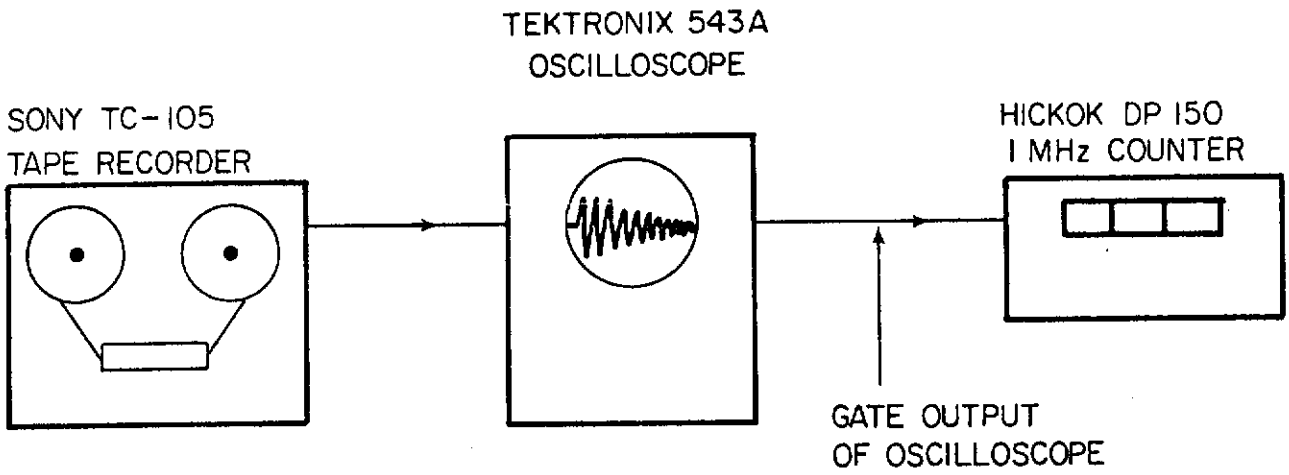

Fig. 140 - Electronic System for Counting Acoustic Emissions

c. Testing Procedure

The single cantilever specimens were tested under constant load conditions, as previously described. Beam deflection was monitored using a Daytronic Model DS-1000 transducer, and has been found to be proportional to crack length change under constant load conditions. To determine the effect of strength level on acoustic behavior, resonance peak counts were recorded as a function of beam deflection.

d. Results

The data on counts vs. deflection for the gaseous tests is shown in Fig. 141. Similar results for the two aqueous tests are shown in Fig. 142. Figure 143 shows the number of emissions as a function of signal-to-noise ratio for the 227 ksi dry H_2 specimen showing the maximum acoustic activity. By monitoring the tape recording for the specimen used in the crack profile study it was found that 39 large emissions had occurred. Figure 144 shows typical etched microstructures in a dry H_2 cracked region, as well as the microstructure in the as-annealed and condition.

The emission activity during cracking in dry H_2 gas is seen to be significantly greater than that observed with specimens of the same strength level in the NaCl solution. The data for the 1600°F specimens tested in dry H_2 show that the higher-strength-level specimen tested at 41.2 ksi-in$^{1/2}$ gave more counts than the lower-strength specimen for the same amount of deflection. Also, increasing the stress intensity factor produces more acoustic activity at the 227-229 ksi strength level. The effect of strength level is also seen in the aqueous tests.

The dry H_2 test data for the specimens austenitized at 1500°F showed more emission activity in the lower-strength-level specimen; however, the initial stress intensity factor was 25% greater. In general, the number of counts per unit deflection (hence, per unit crack extension) is increased by both stress intensity factor and strength level.

Examination of the fracture surfaces of the 227 ksi and 194 ksi specimens from the dry H_2 tests by plastic-carbon replica techniques showed that regions of quasi-cleavage, intergranular fracture, and equiaxed, dimpled fracture were present on both fracture surfaces. However, quasi-cleavage and intergranular fracture appeared to be the primary fracture modes in the specimen showing the higher acoustic activity; photomicrographs are not available at this time. Dunegan and Green,[110] however, observed that greater acoustic activity is associated with cleavage-type fractures and higher strength levels. Both inter- and transgranular fracture modes appear to be present in the sectioned specimen, as seen in Fig. 144. Attempts to etch prior austenite grain bounaries by the Haruff and Underwood technique[111] have been unsuccessful with such specimens austenitized below 1600°F.

e. Conclusions

The acoustic emission studies have shown that

(1) acoustic activity is increased by higher stress intensity factors or higher strength levels; and

(2) more emission activity is observed when dry H_2 cracking occurs, as opposed to aqueous cracking with cathodic polarization.

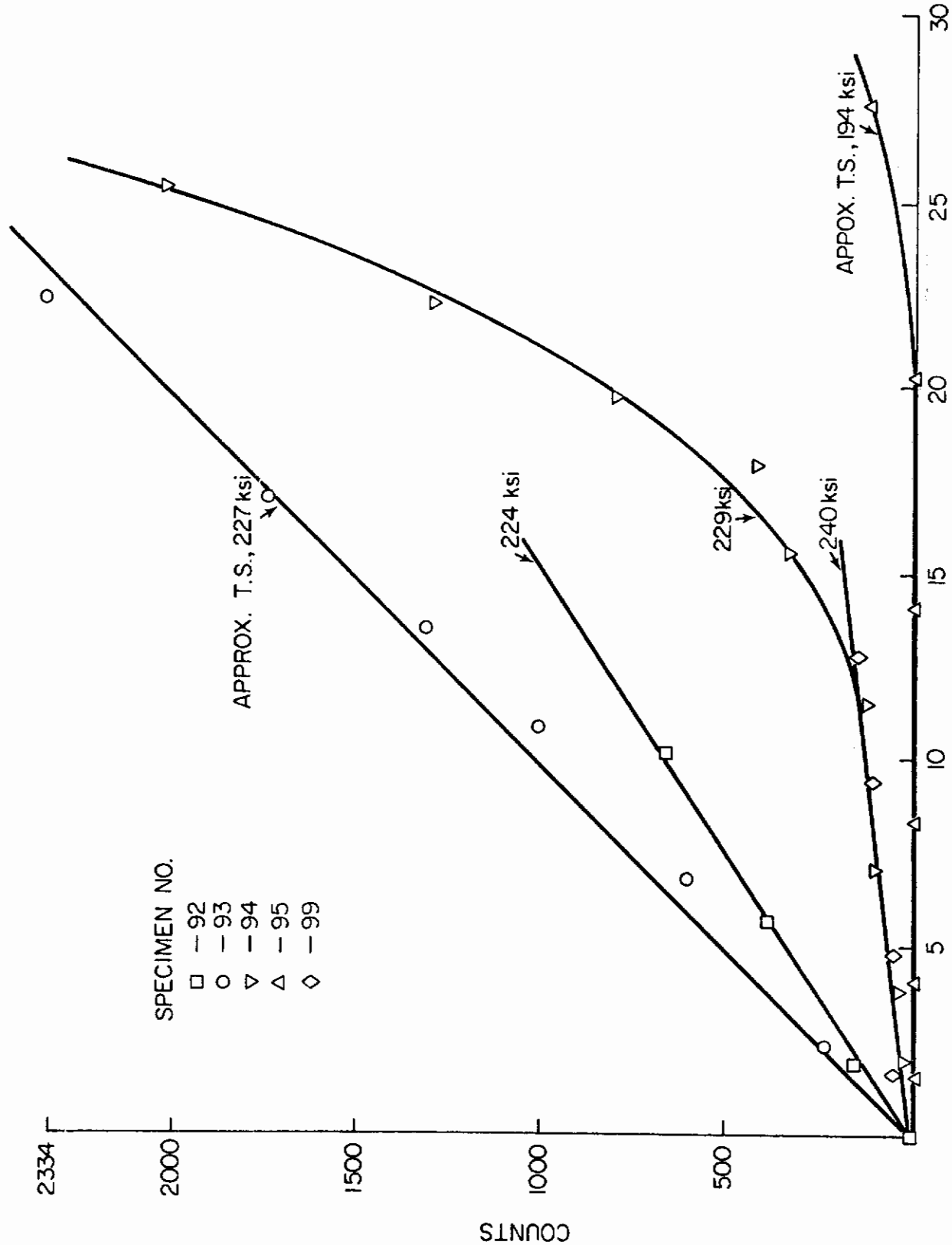

Fig. 141 - Counts vs. Deflection for Specimens Tested in H_2/Ar Mixture (9.1 vol% H_2)

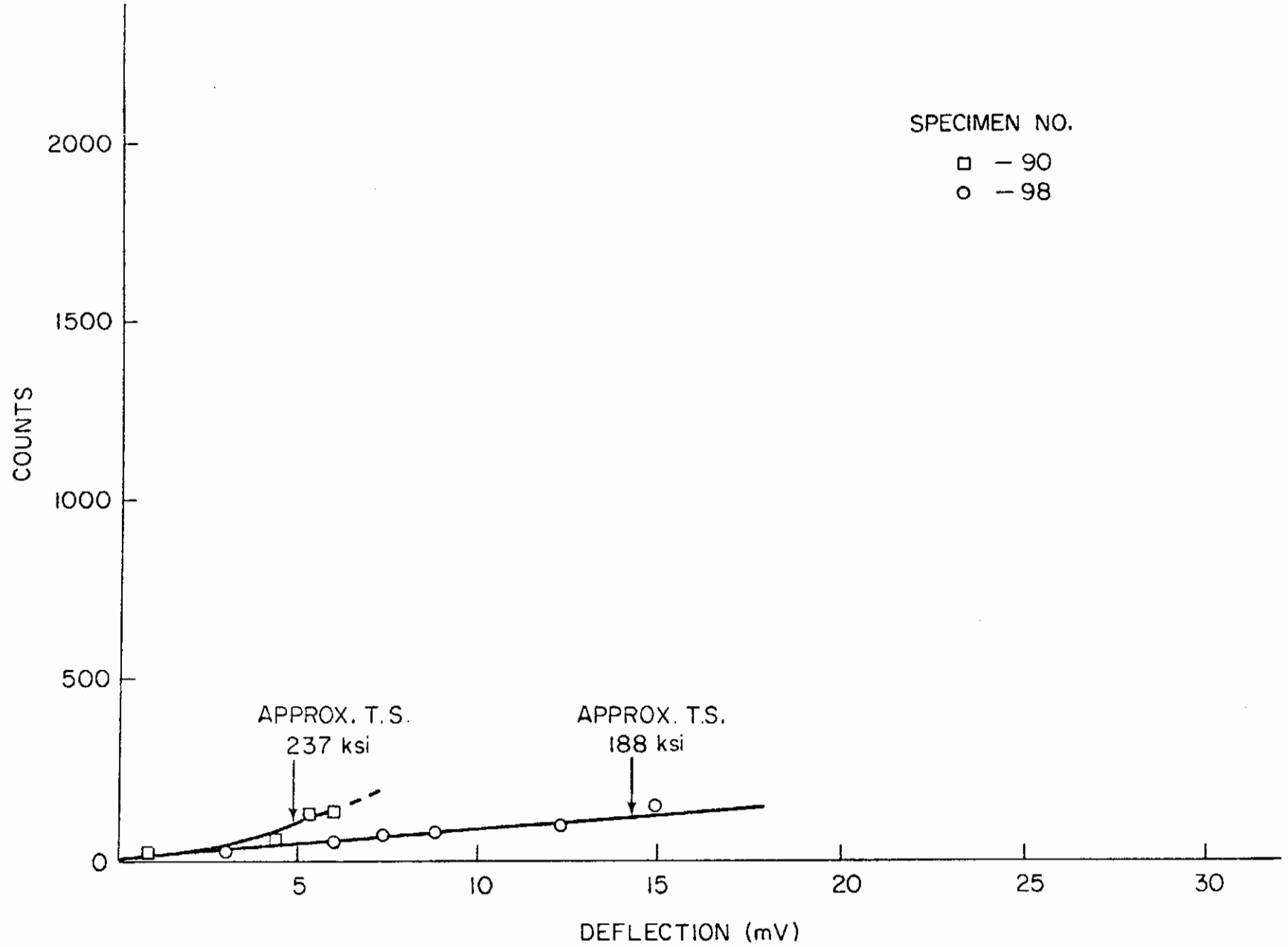

Fig. 142 - Counts vs. Deflection for Specimens Tested in $3\frac{1}{2}\%$ NaCl at -1.0 V (SCE)

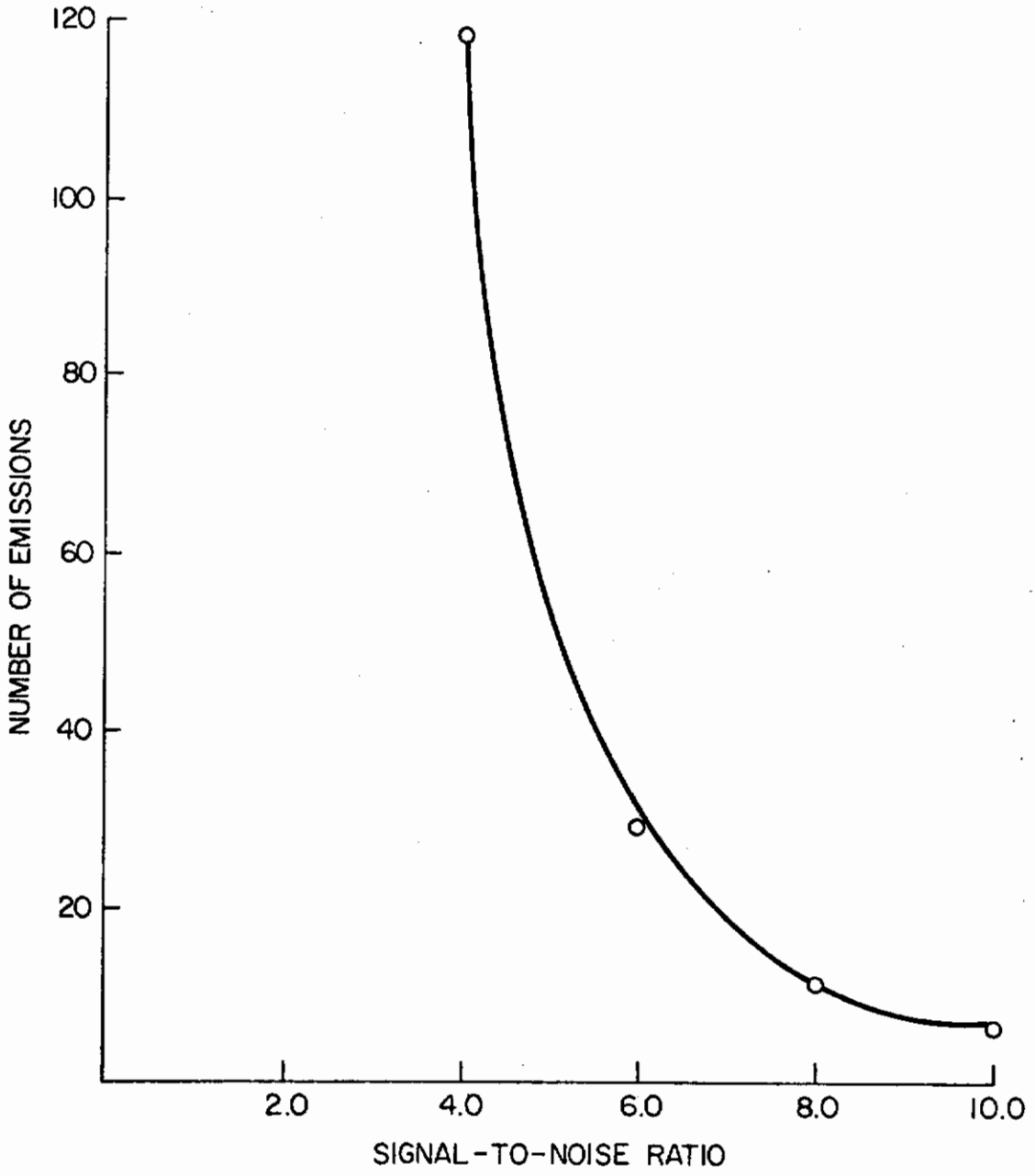

Fig. 143 - Size Distribution of Emissions During Cracking of 227 ksi Specimen in Dry H_2

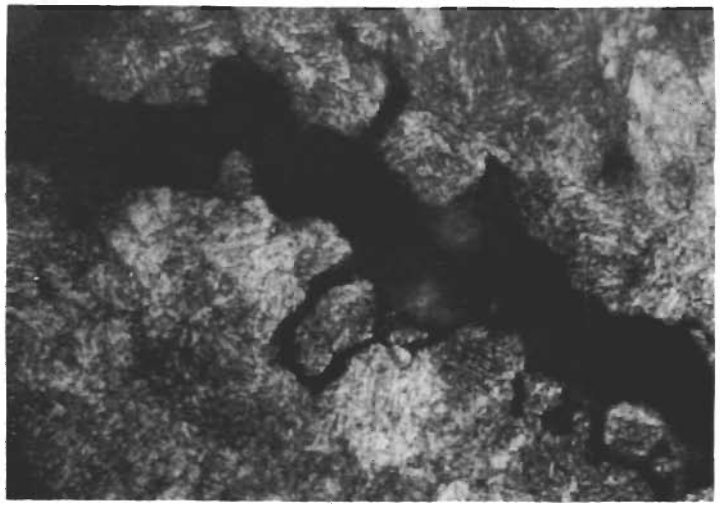

Crack Region - Etched Electrolytically at 10 A in 10% Chromic Acid

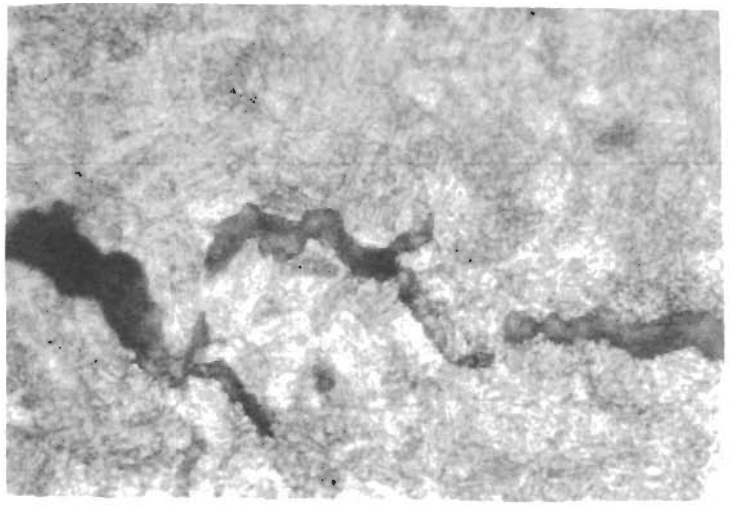

Crack Region - Etched Electrolytically at 10 A in 10% Chromic Acid

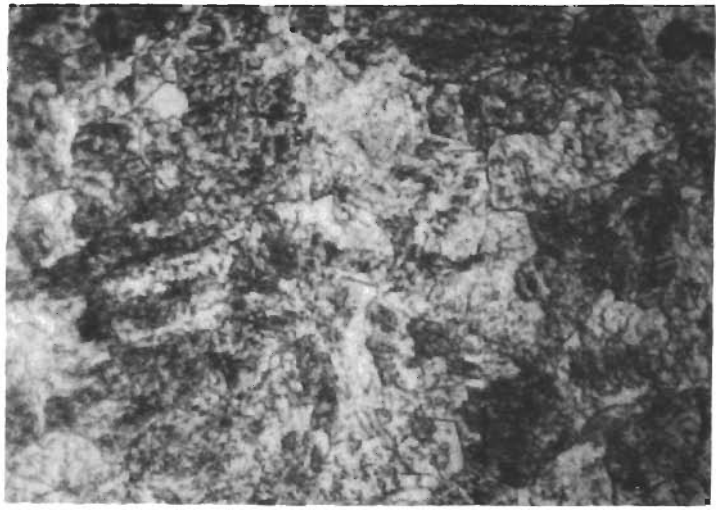

Annealed Structure - Etched with Vilella's Reagent

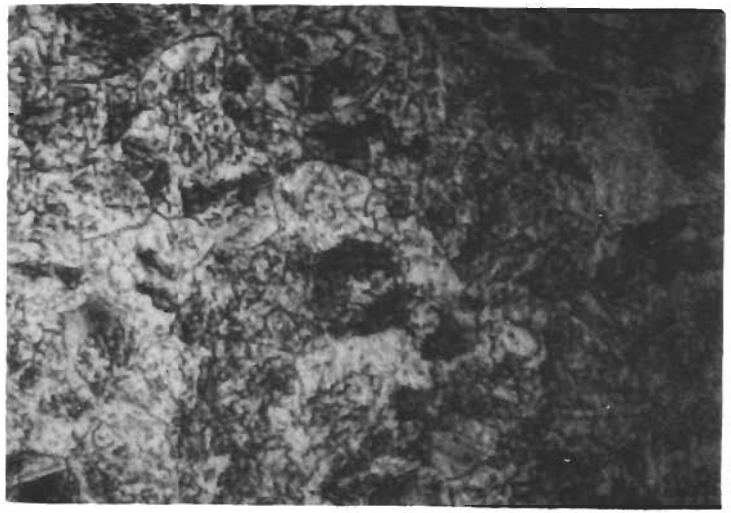

Annealed Structure - Etched with Vilella's Reagent

Fig. 144 - Photomicrographs of Crack Region in 224 ksi Specimen and of Microstructure After 1575°F Anneal

8. Crack Profile Study

Dry hydrogen cracking was induced in one specimen (No. 92) until approximately 0.170" crack growth had occurred. The cracking was then stopped by purging the environmental chamber with pure argon. The specimen was then sectioned such that the region containing the crack was removed. The surface normal to the crack plane and parallel to the crack growth direction (shown in Fig. 145) was ground and polished several times to show the crack profile through the thickness of the specimen. This was done to determine if a discrete increment of crack growth, corresponding to one emission, could be observed. Successive polishing using 0.3 and 0.05 μm alumina) and re-examination at one stage of the sectioning was done to determine how the crack profile changed through the specimen thickness. Results of the examination are shown in Figs. 146-150.

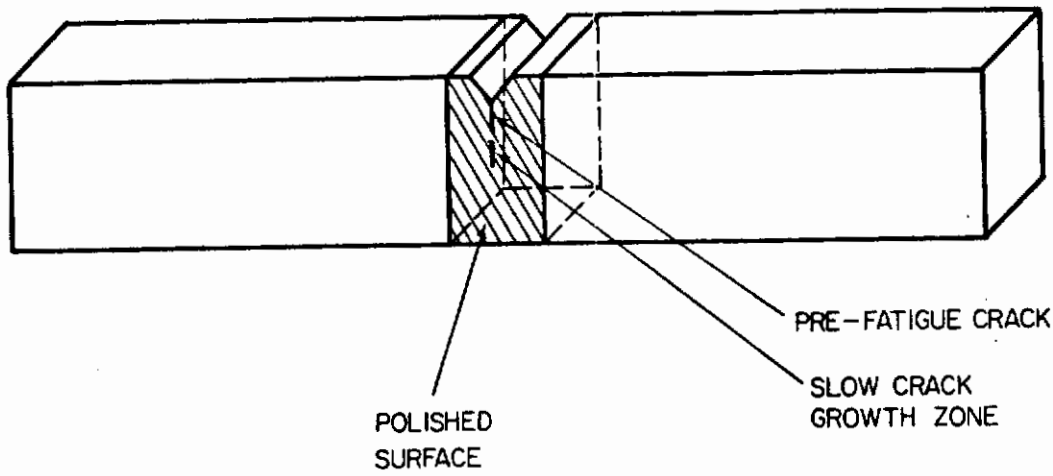

Fig. 145 - Sectioning of Dry H_2 Cracked Test Specimen

The photomicrographs of the crack profile in the 224 ksi specimen show that the cracking is discontinuous, with unbroken regions of material behind the main crack front. The effect of such regions on the acoustic behavior is not understood at this time. However, it is apparent that the correlation of acoustic emissions with a one-dimensional model for crack extension would be an over-simplification. Comparison of the length of the slow growth zone (approx. 0.170") with the 39 large emissions observed during crackingyields a value of 0.004"-0.005" for one increment of crack growth (hence, one emission). Examination of the slow-growth zone shows that the crack profile is indeed step-like in regions, with an apparent growth increment of the predicted order of

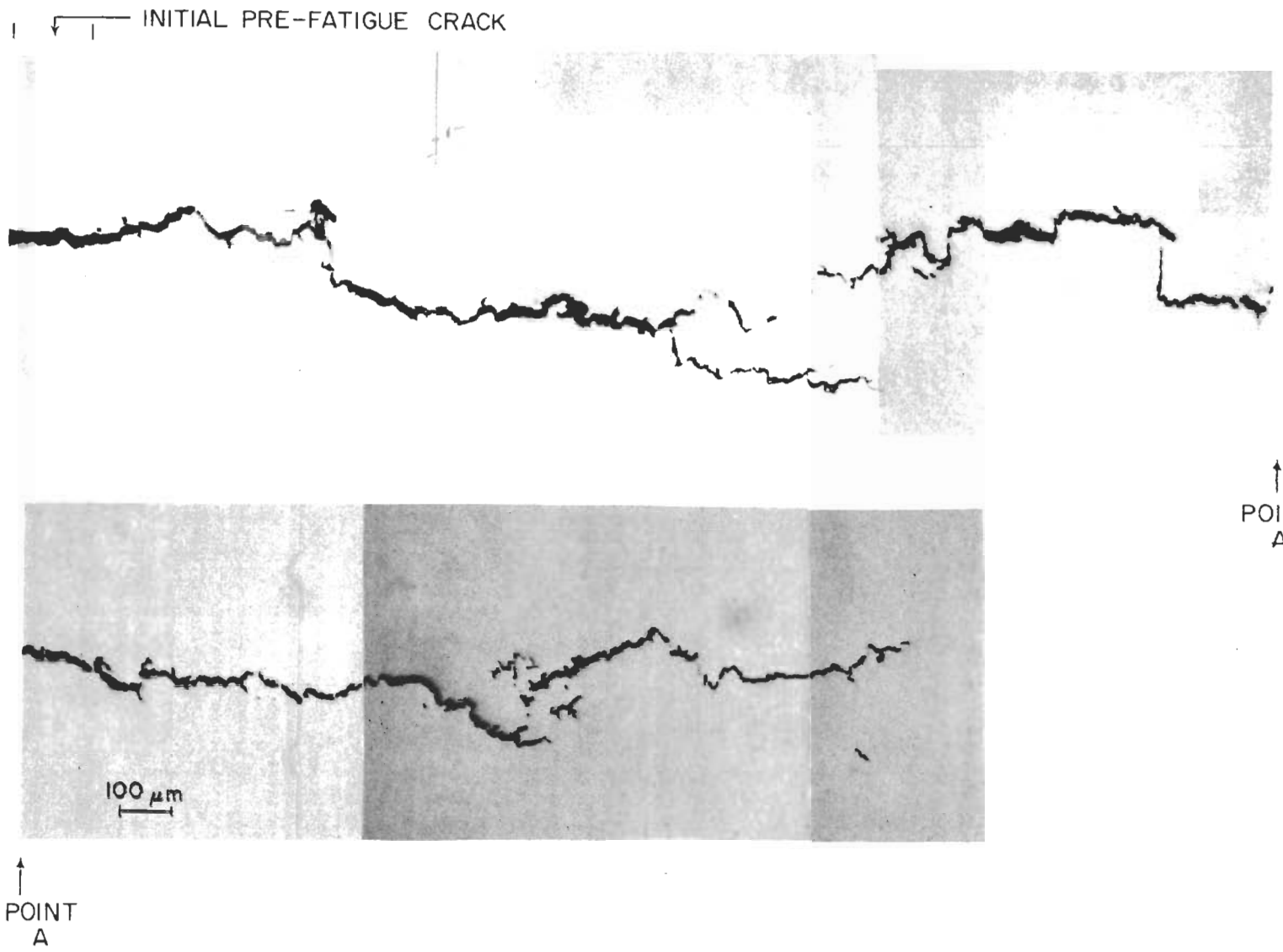

Fig. 146 - Photomicrographs Showing Crack Profile 0.102 Inch Below Surface of 224 ksi Specimen

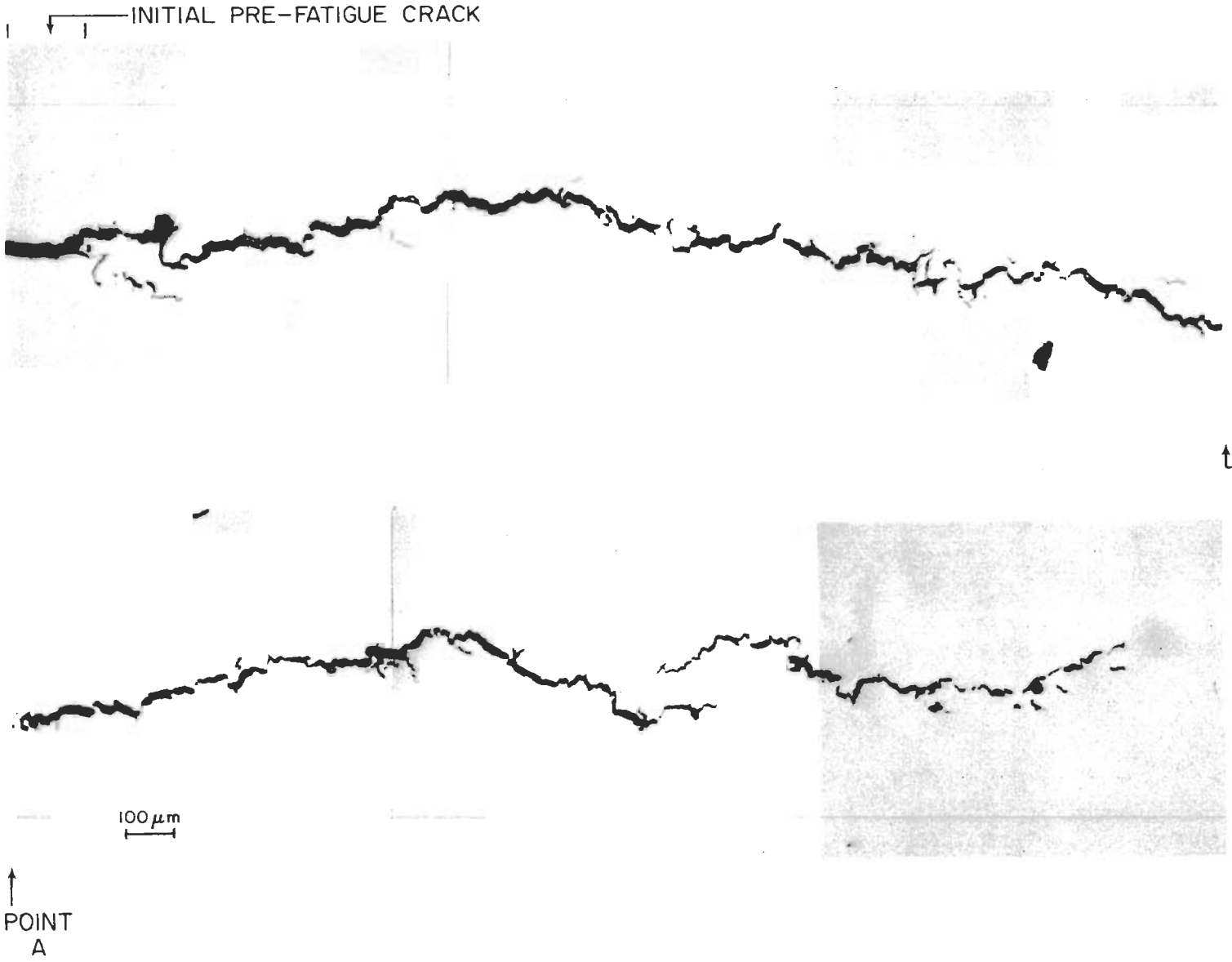

Fig. 147 - Photomicrographs Showing Crack Profile 0.176 Inch Below Surface of 224 ksi Specimen

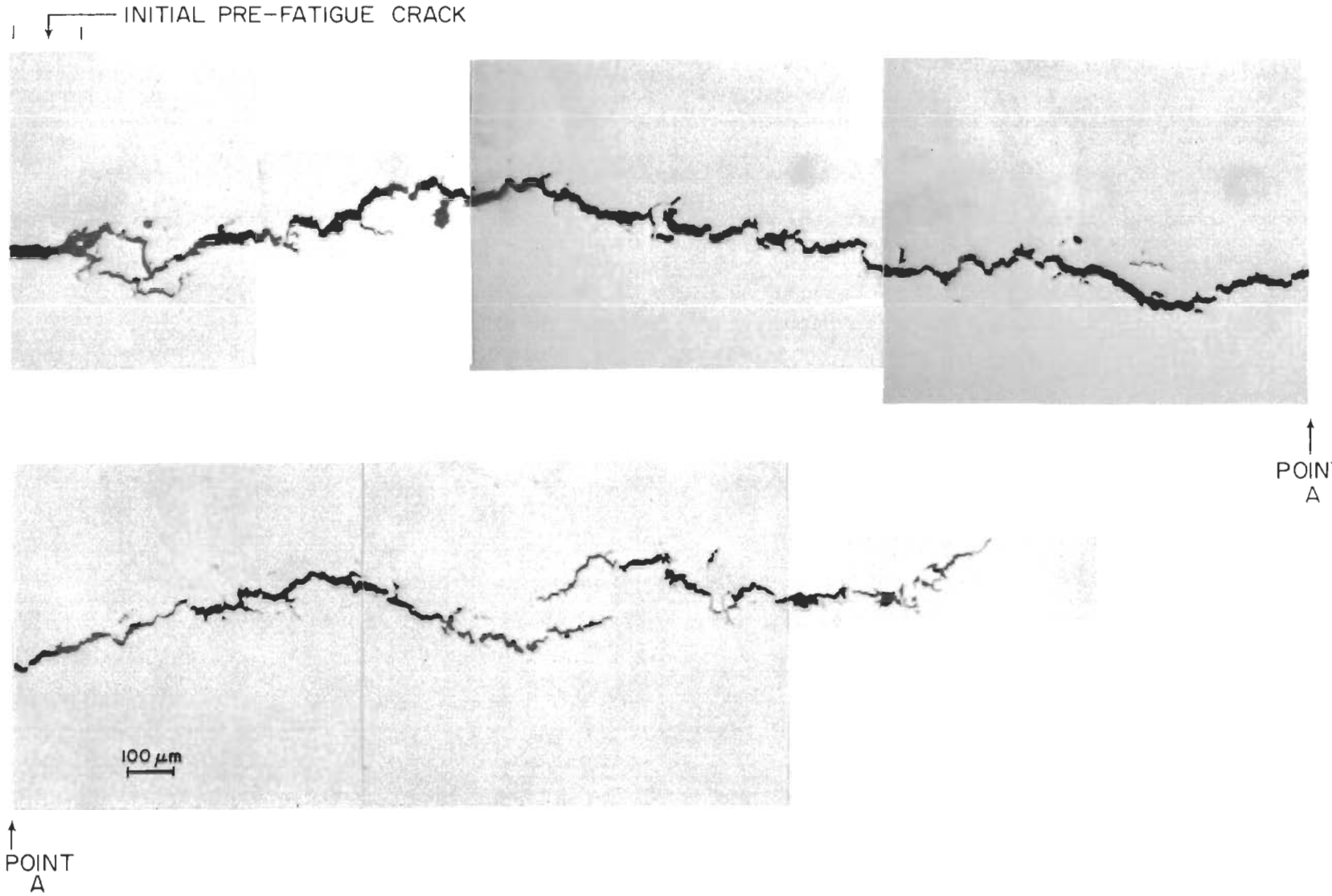

Fig. 148 - Photomicrographs Showing Crack Profile 0.177 Inch Below Surface of 224 ksi Specimen

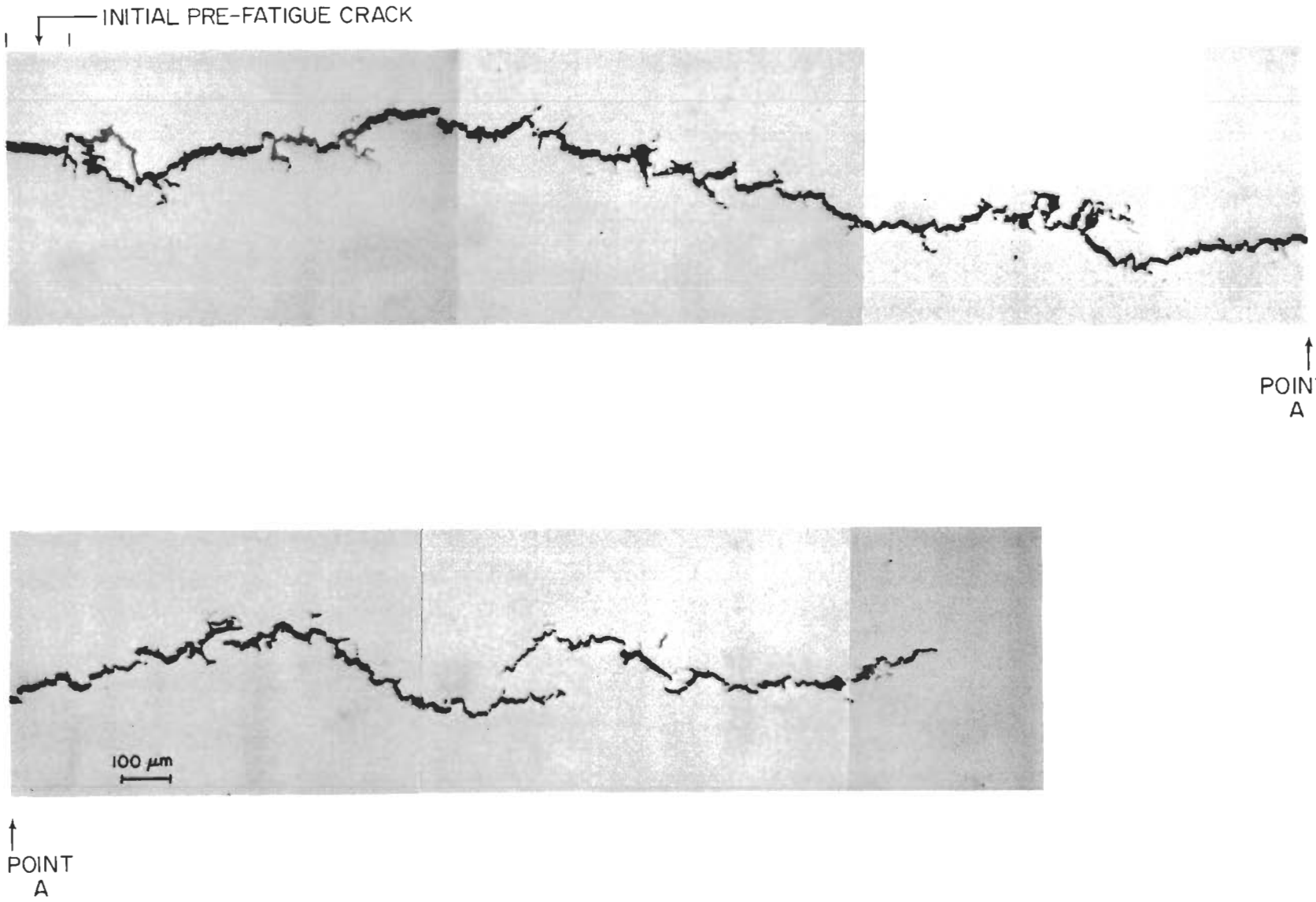

Fig. 149 - Photomicrographs Showing Same Region as Fig. 148 After Repolishing With 0.3 μm and 0.05 μm Alumina (less than 0.001 inch removed)

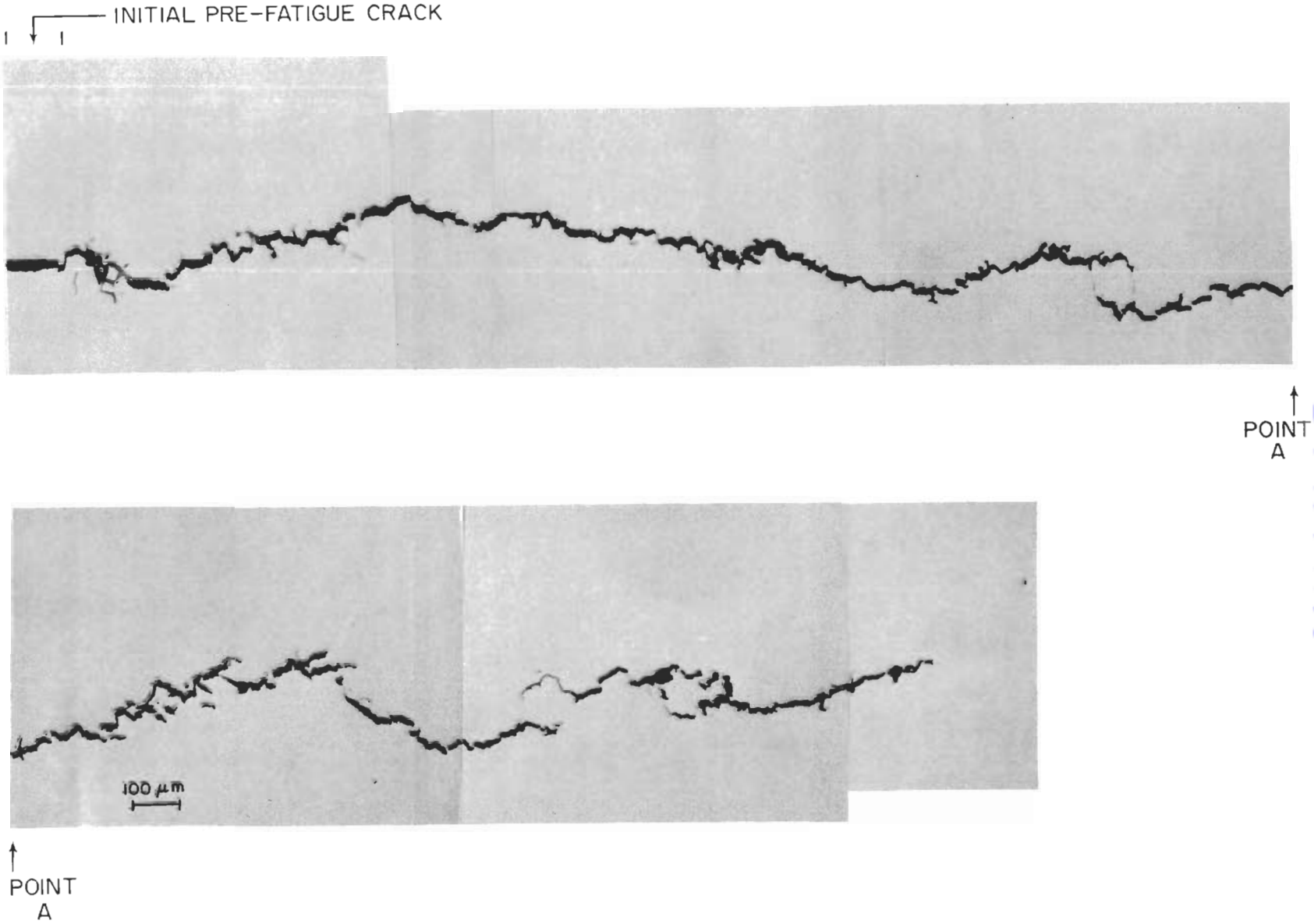

Fig. 150 - Photomicrographs Showing Same Region as Fig. 149 After Repolishing with 0.3 μm and 0.05 μm Alumina (less than 0.001 inch removed)

magnitude. This is particularly evident in Fig. 151; however, the incremental geometry of the crack is apparent only in certain regions. Also, the obvious changes in crack profile in the specimen thickness direction suggest that more significant information regarding emission sources might be obtained by examining the fracture surface by techniques such as scanning electron microscopy.

Examination of the crack profile in Fig. 146 showed bifurcation of the crack. Macroscopic examination prior to sectioning also showed apparent bifurcation. However, examination of regions closer to the mid-thickness of the specimen shows that such bifurcation is absent. Hence, crack branching may indeed be a function of stress state (i.e., plane strain vs. plane stress).

9. Crack Velocity Measurements

a. Background

The primary objective of this program is to compare the crack growth kinetics and acoustic emission behavior of high-strength steel in both gaseous and aqueous environments. Experimental variables include prior austenite grain size, strength level, stress intensity factor, gas pressure, temperature, and state of stress (plane strain vs. plane stress).

Recent work in dry H_2 environments has shown that molecular hydrogen promotes stress corrosion cracking of high-strength steel. Although there is considerable disagreement as to the mechanistic aspects of SCC in hydrogen environments,[112,114] there is agreement as to the pressure and temperature dependence of crack velocity in H_2 gas.[112,114,115] However, the effects of strength level, grain size, or other material parameters have not been studied. Also, stress corrosion studies in gaseous species containing both hydrogen and atoms cathodic poisons, such as arsine (AsH_3), phosphene (PH_3), hydrogen sulfide (H_2S), or ammonia (NH_3) could not be found in the literature. Since such poisons enhance hydrogen permeation through steel,[116] their presence as a gas phase hydrogen compound may clarify the mechanism in gaseous hydrogen cracking.

b. Experimental Procedure

The loading and vacuum systems used in the gaseous studies are shown in Fig. 152. Crack opening displacement is measured using a Schaevitz Engr. PCD-121-125 DC linear variable differential transformer. The specimen (double cantilever beam geometry) is shown in Fig. 153. The aqueous testing was conducted using a Satec Model D creep test machine and a Daytronic LVDT system, shown in Fig. 154. Typical output voltage vs. displacement plots for both LVDT's are shown in Figs. 155 and 156.

In both environments, deflection - time data was obtained until 0.001"-0.002" deflection occurred. The data were then treated by

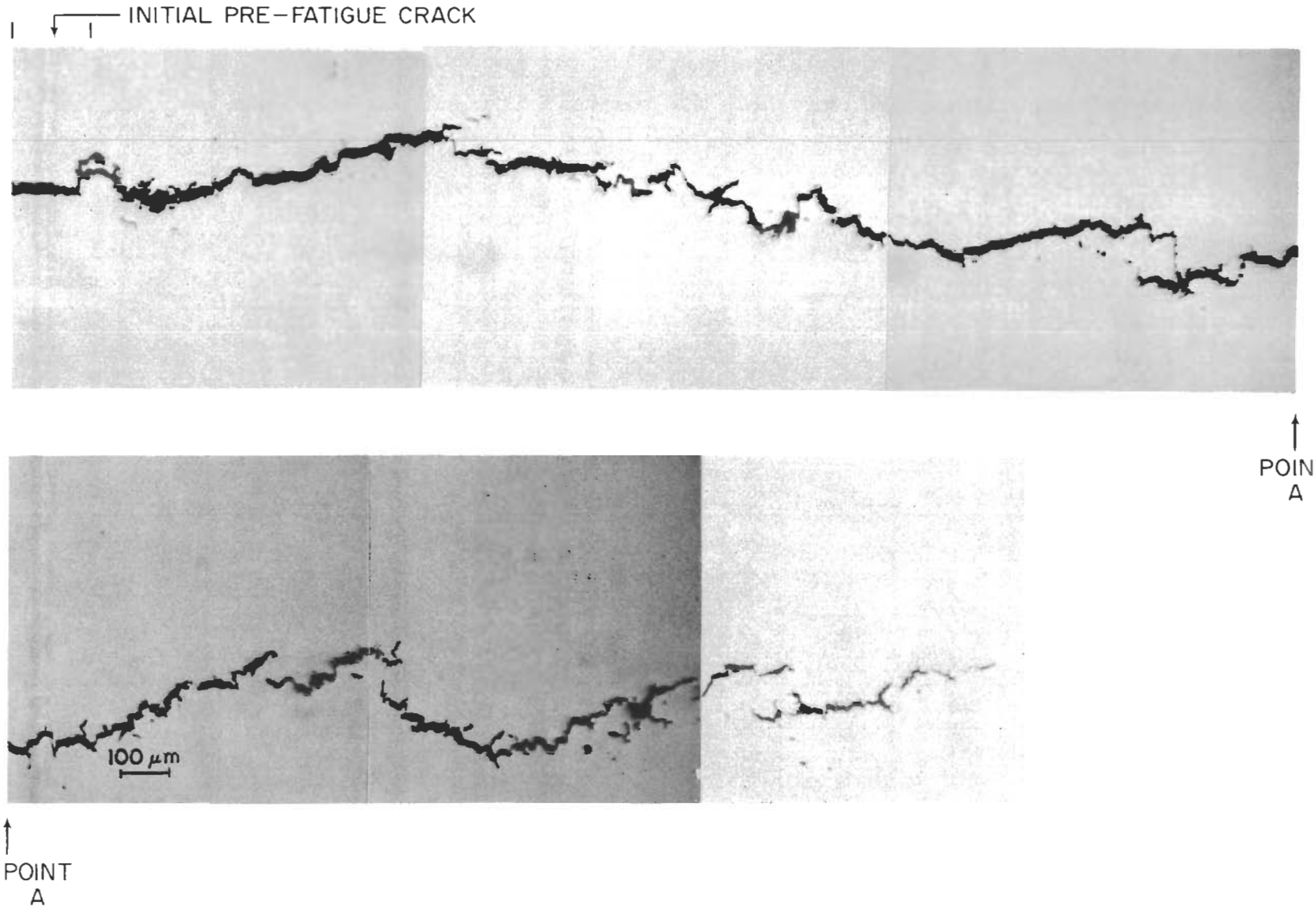

Fig. 151 - Photomicrographs Showing Crack Profile 0.178 Inch Below Surface of 224 ksi Specimen

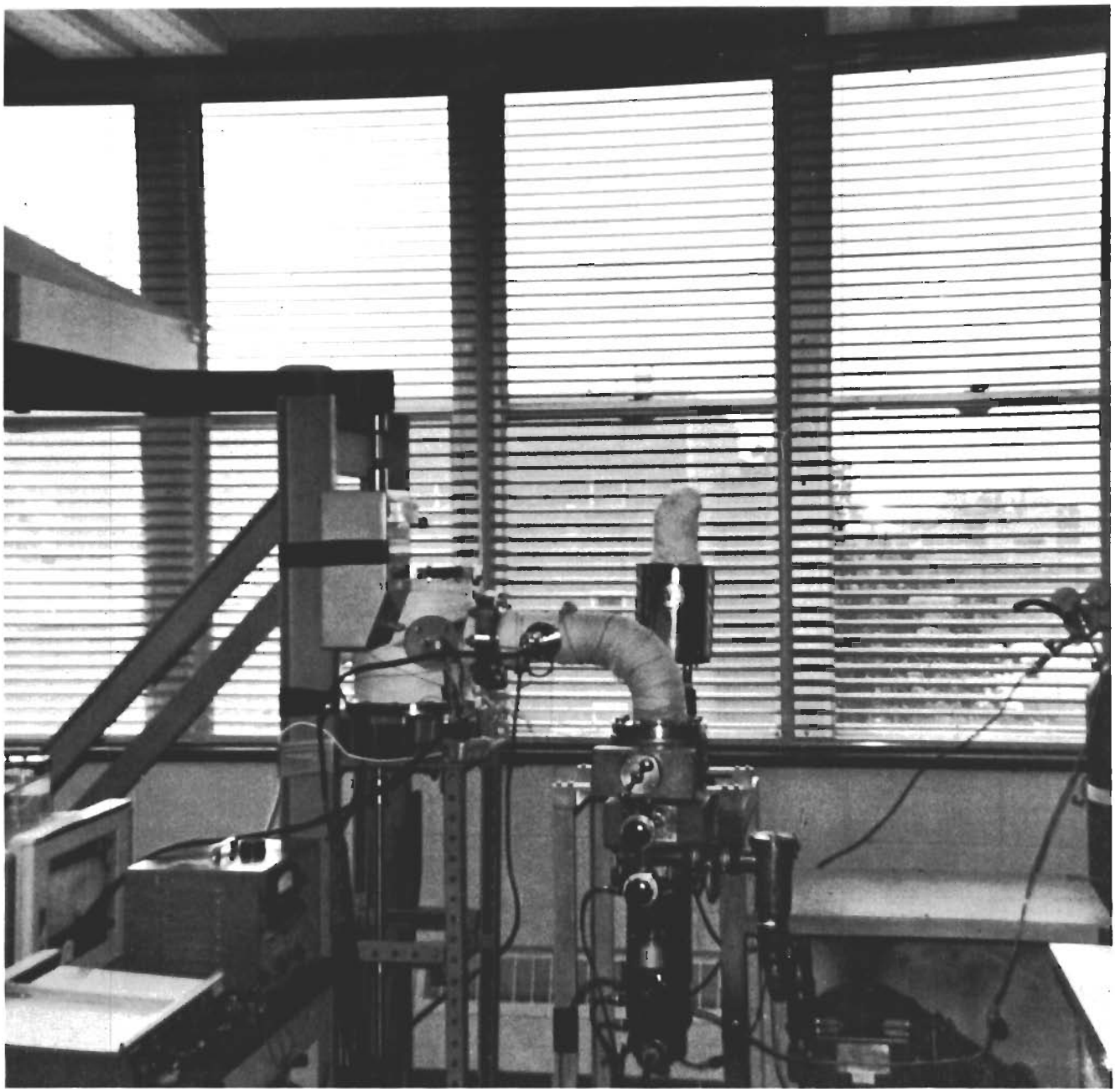

Fig. 152 - Vacuum Loading System for Gaseous Hydrogen Testing

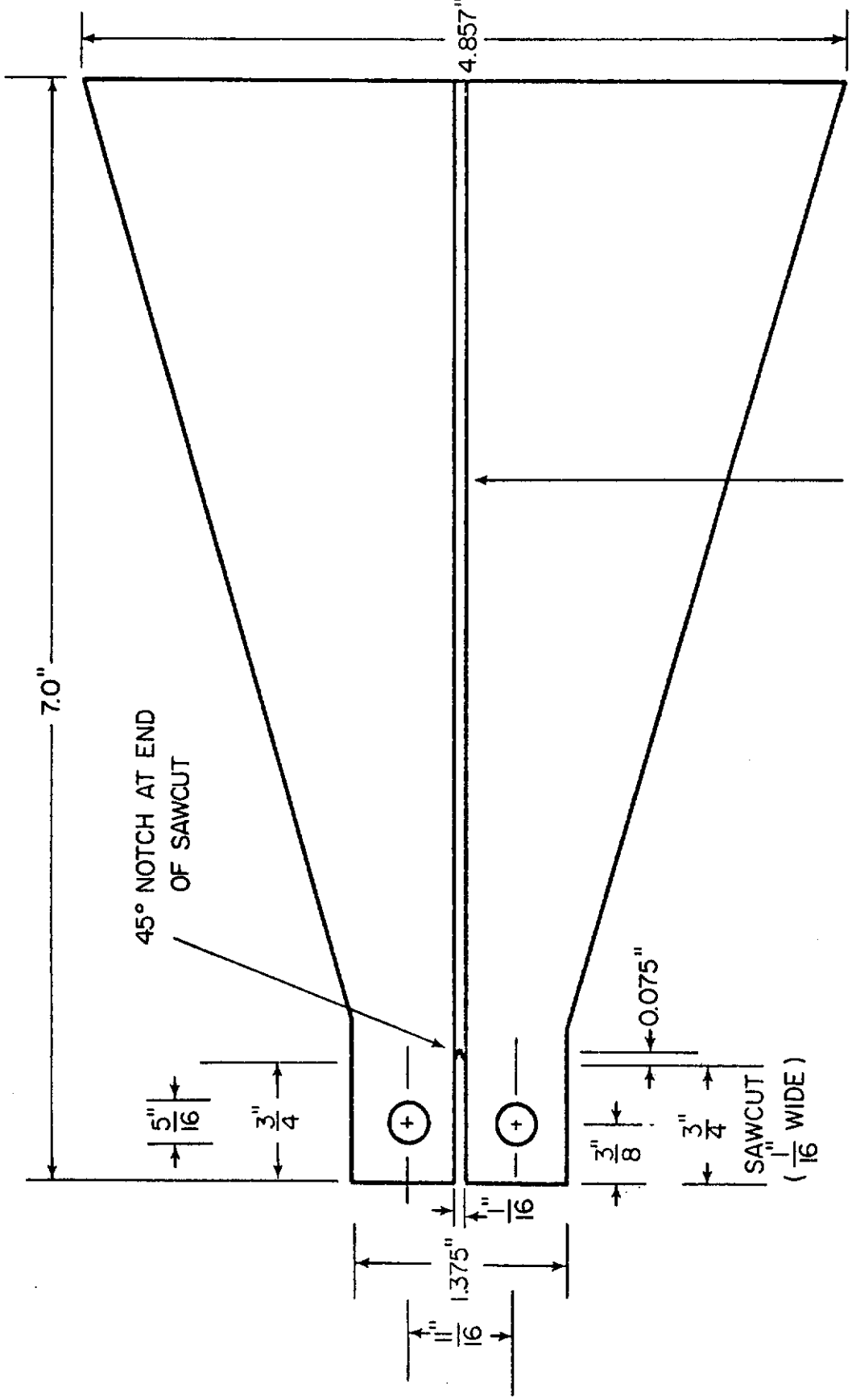

Fig. 153 - Double Cantilever Beam Specimen (distance between tips of side grooves is 0.293" for plane strain specimens, 0.125" for plane stress specimens)

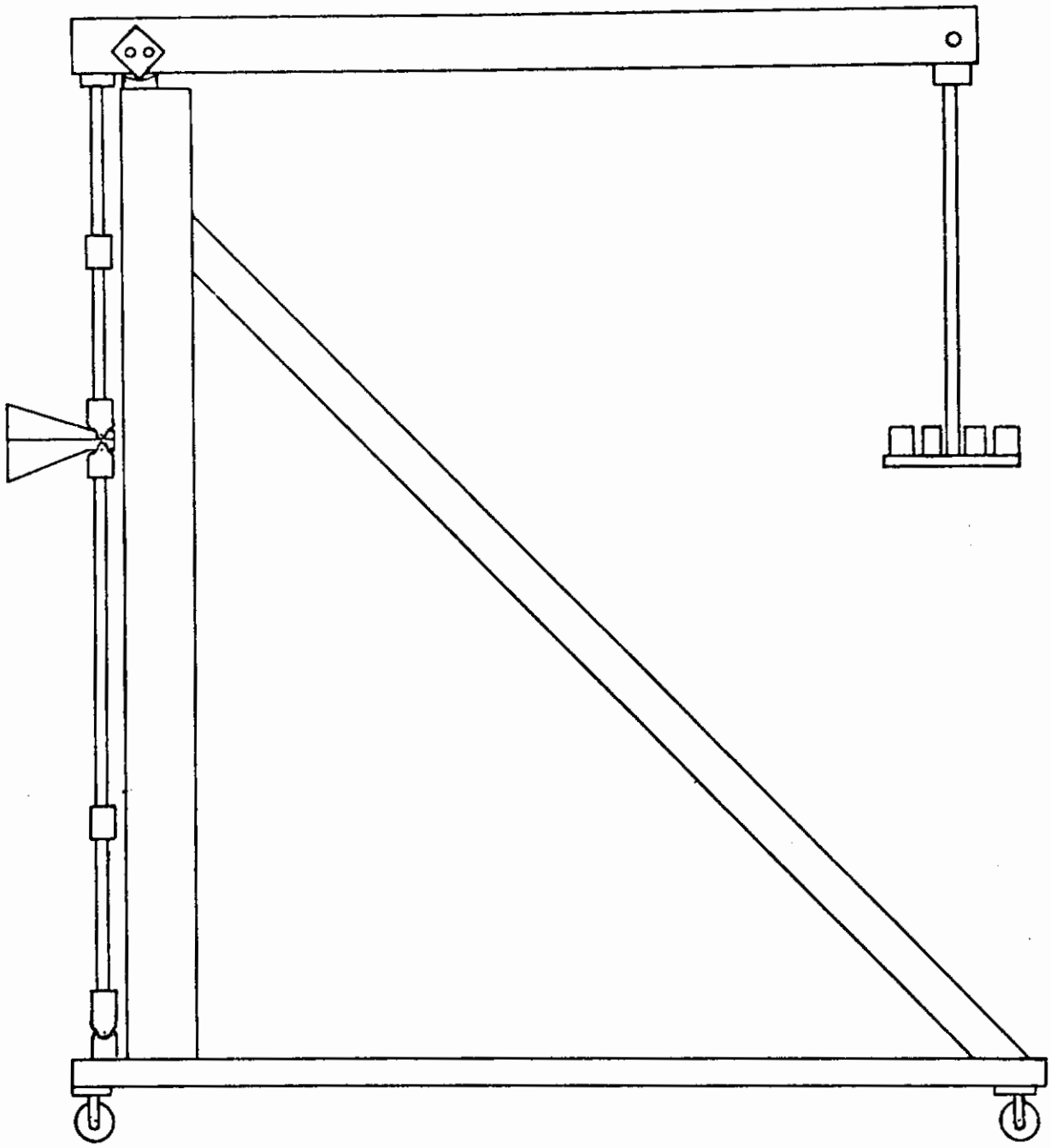

Fig. 154 - Loading Frame for Double Cantilever Beam Specimens

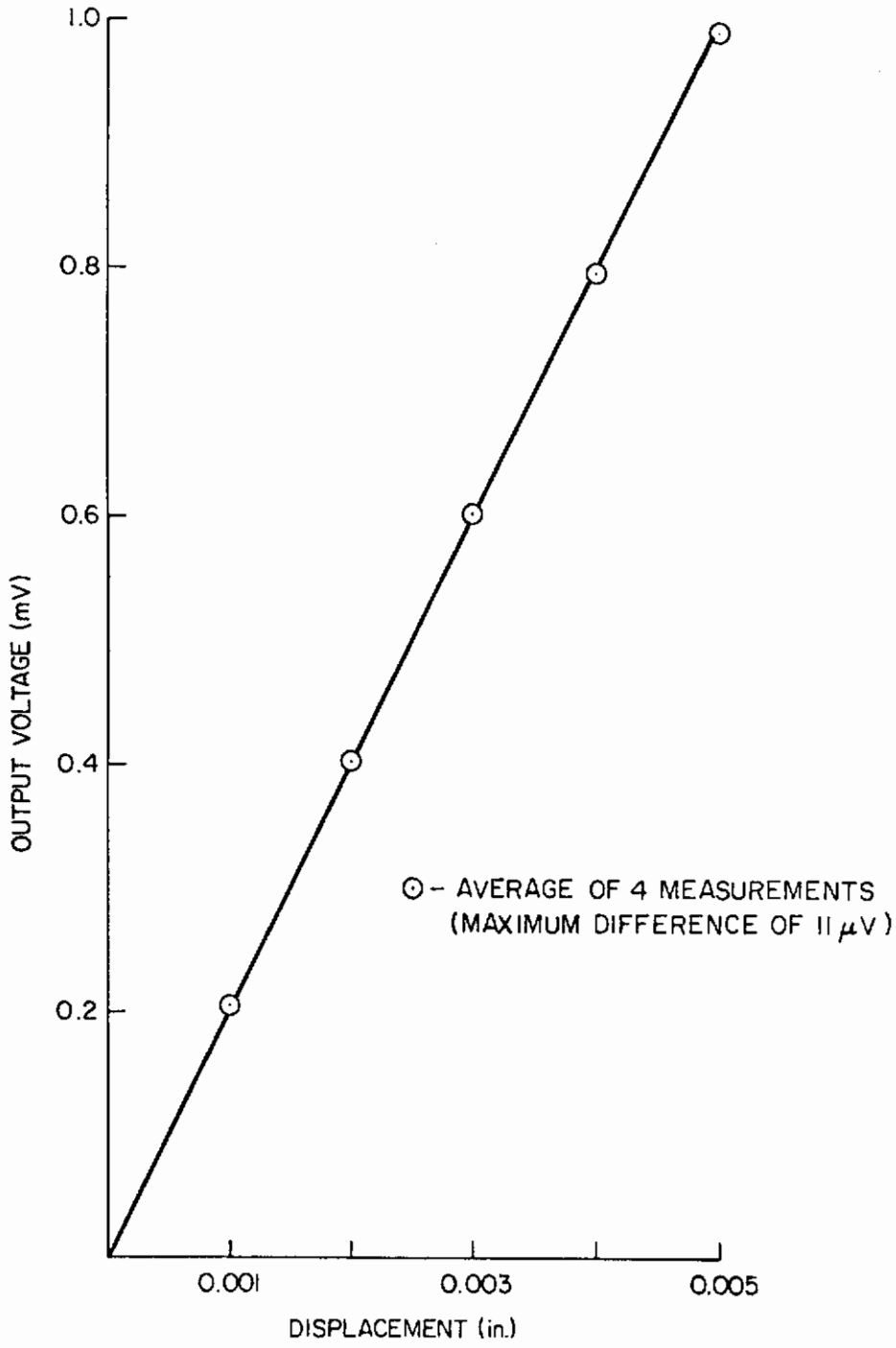

Fig. 155 - Output Voltage vs. Displacement for Daytronic DS100 Linear Displacement Transducer

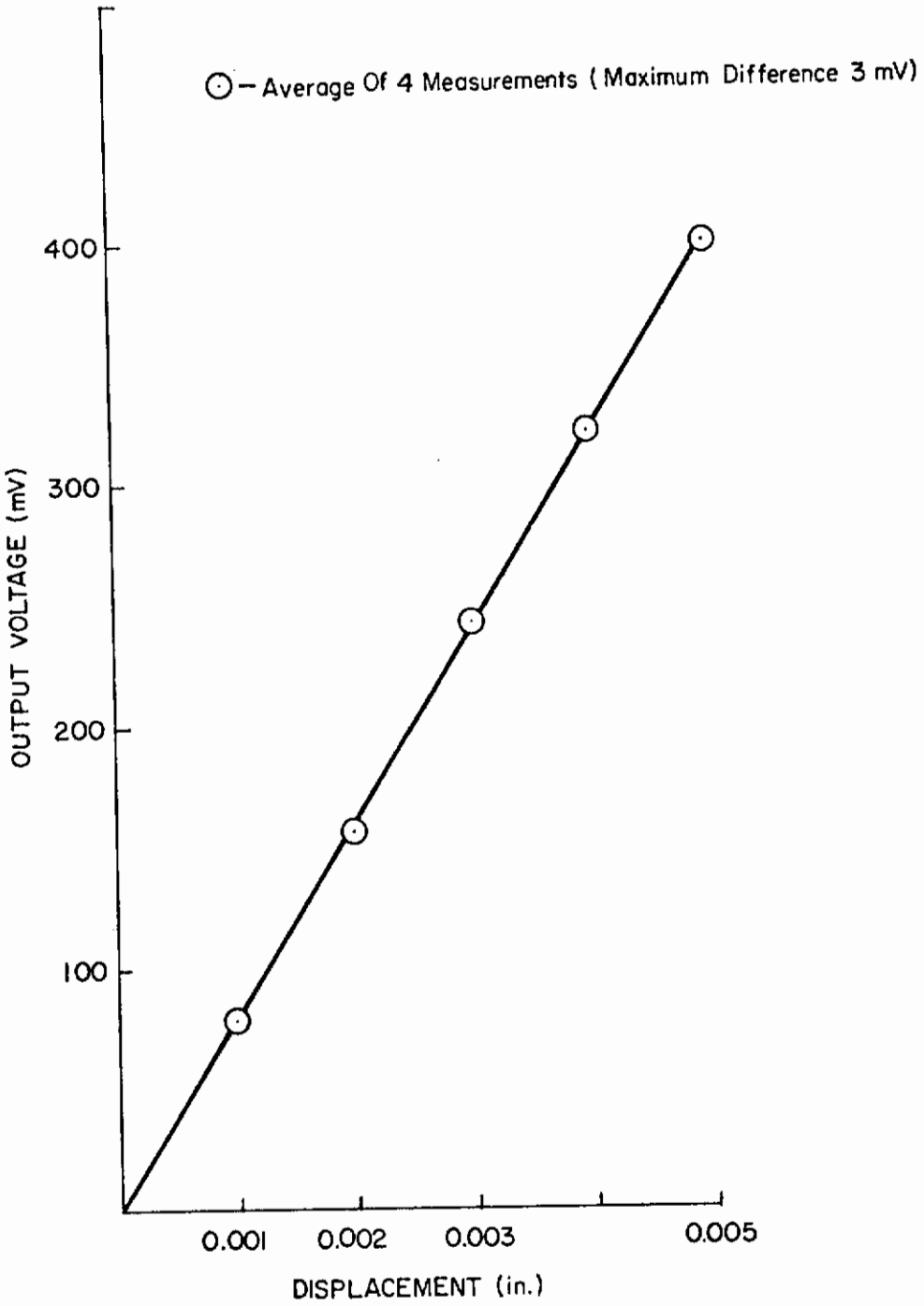

Fig. 156 - Output Voltage vs. Displacement for Schaevite Engr. PCD-121S-125 Linear Displacement Transducer

least squares analysis. All aqueous tests were performed in 3.5% NaCl solution adjusted to pH = 6.0 with NaOH or HCl solutions.

In the gaseous studies, the specimen chamber is evacuated to 2×10^{-6} torr. The vacuum pumps are then valved off, and the chamber is backfilled to a given pressure with purified hydrogen gas. Ultimate pressure and steady state outgassing rates are measured prior to each test with an NRC Type 507 ionization gauge. Outgassing rates are less than 5×10^{-5} torr/minute before backfilling. Two liquid nitrogen traps, one containing zeolite, are operated continually to trap oil vapor. The residual gases in the vacuum chamber were analyzed using an Aero-Vac Residual Gas Analyzer and found to be predominantly water vapor. The hydrogen gas (pre-purified grade) was further purified by passing through an Englehard Industries Deoxo-Unit, through indicating drierite, over heated copper turnings at 300°C, and finally through a liquid N_2 trap. Hydrogen pressures were measured with an NRC Model 820 Alphatron gauge. Prior to the removal of a specimen from the test chamber, the applied load is removed and the chamber is backfilled to 1 atmosphere with H_2 to check the Alphatron sensitivity for H_2 gas. Within the accuracy of the gauge, no sensitivity changes were observed. No vacuum greases were used in the system, and all components were cleaned in reagent grade acetone prior to their use.

The material used in the testing was AISI 4335 V steel. The chemical analysis, performed by Carpenter Technology Corporation, is given in Table XXI. All specimens were heat treated in neutral salt, polished to a 400-grit finish, and pre-fatigue cracked to within 1/8" of the constant K_I zone using a Krouse fatigue test machine. The fatigue apparatus is shown in Fig. 157. The side grooves in each specimen were sandblasted following heat treatment, and fatigue cracks were produced with loads less than 2500 lb. All specimens were ultrasonically cleaned in reagent grade acetone prior to fatiguing, and kept in plastic bags with indicating drierite. Fatigue cracks were examined for continuity and measured to within 0.001" with a travelling stage microscope. Following fatiguing, the specimens were lightly swabbed with acetone, and stored in air-tight dessicators with indicating drierite until testing.

Table XXI - Chemical Analysis of AISI 4335 V Steel

C	Mn	Si	P	S	Cr	Ni	Mo	V	Fe
0.36	0.75	0.30	0.009	0.009	0.78	1.74	0.39	0.17	balance

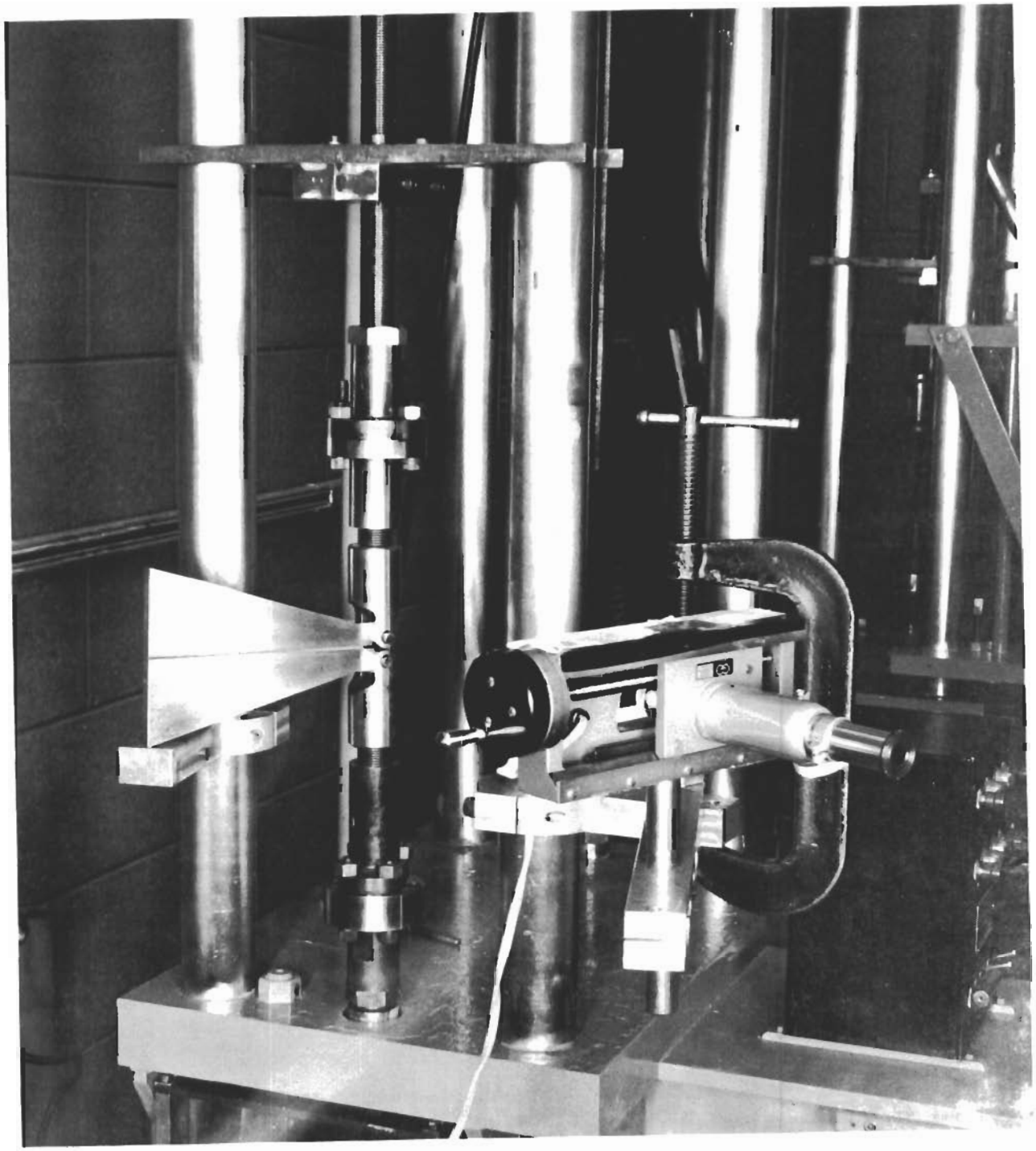

Fig. 157 - Krouse Fatigue Testing Apparatus

Heat treatment variables in this study were (1) austenitizing temperature, (2) austenitizing time, (3) tempering temperature, and (4) tempering time. Austenitizing temperatures were 1600 and 1700°V. Austenitizing time (at 1700°F) were 1 hr and 3 hr. Tempering temperatures were 400, 600, 800, and 1000°F. Tempering times (at 1000°F) were 1 hr and 3 hr. Normal austenitizing and tempering times were 1 hr. All heat treatment was done by the National Heat Treating Service Co.

All tensile tests were performed on an Instron tensile testing machine at a crosshead velocity of 0.1 cm/min. Tensile test specimens were std. 0.250" diam., 1.0" gauge length specimens. The reduced section of each specimen was polished to a 400-grit finish prior to testing. Three specimens were tested per heat treatment condition.

The variation of crack opening displacement rate with hydrogen pressure was determined at three different stress intensity values (three different specimens). The specimens had been austenitized for one hour at 1600°F, oil quenched, and tempered at 400°F for one hour. Crack opening displacement, at constant stress intensity, is directly proportional to crack velocity. Also the dependence of crack velocity on stress intensity (K_I) was determined in both H_2 gas and 3.5% NaCl solution for material tempered at 400°F (1 hr) and at 1000°F (3 hr). The austenitizing temperature was 1600°F.

c. Results

Ultimate tensile strength and 0.2% offset yield strength data are shown in Figs. 158 and 159, respectively. Figure 160 shows 500X photomicrographs of prior austenite grains after different austenitizing treatments. The specimens in Fig. 160 were tempered at 400°F or 600°F, as shown. The grain boundaries were etched using the method of Haruff and Underwood.[117] Severe matrix pitting occurred with this technique, as seen in the photomicrographs, and could not be avoided by variation of etchant concentration or etching time.

Figure 161 shows crack opening displacement rate as a function of hydrogen pressure, at constant stress intensity. Figure 162 shows crack velocity as a function of stress intensity factor for both gaseous (50 torr H_2) and aqueous (3.5% NaCl) environments. The material in Figs. 161 and 162 was tempered at 400°F. Figure 163 shows crack velocity vs. stress intensity factor (for material tempered at 400°F) in 100 torr H_2 and 3.5% NACl solution. All tests were conducted at room temperature.

Crack velocities were obtained using compliance data determined by Gallagher[118] for this specimen geometry. Slow growth zones of two specimens tested in hydrogen were measured, and the amount of propagation observed agreed within 15% to that predicted by crack opening displacement measurements and compliance data.

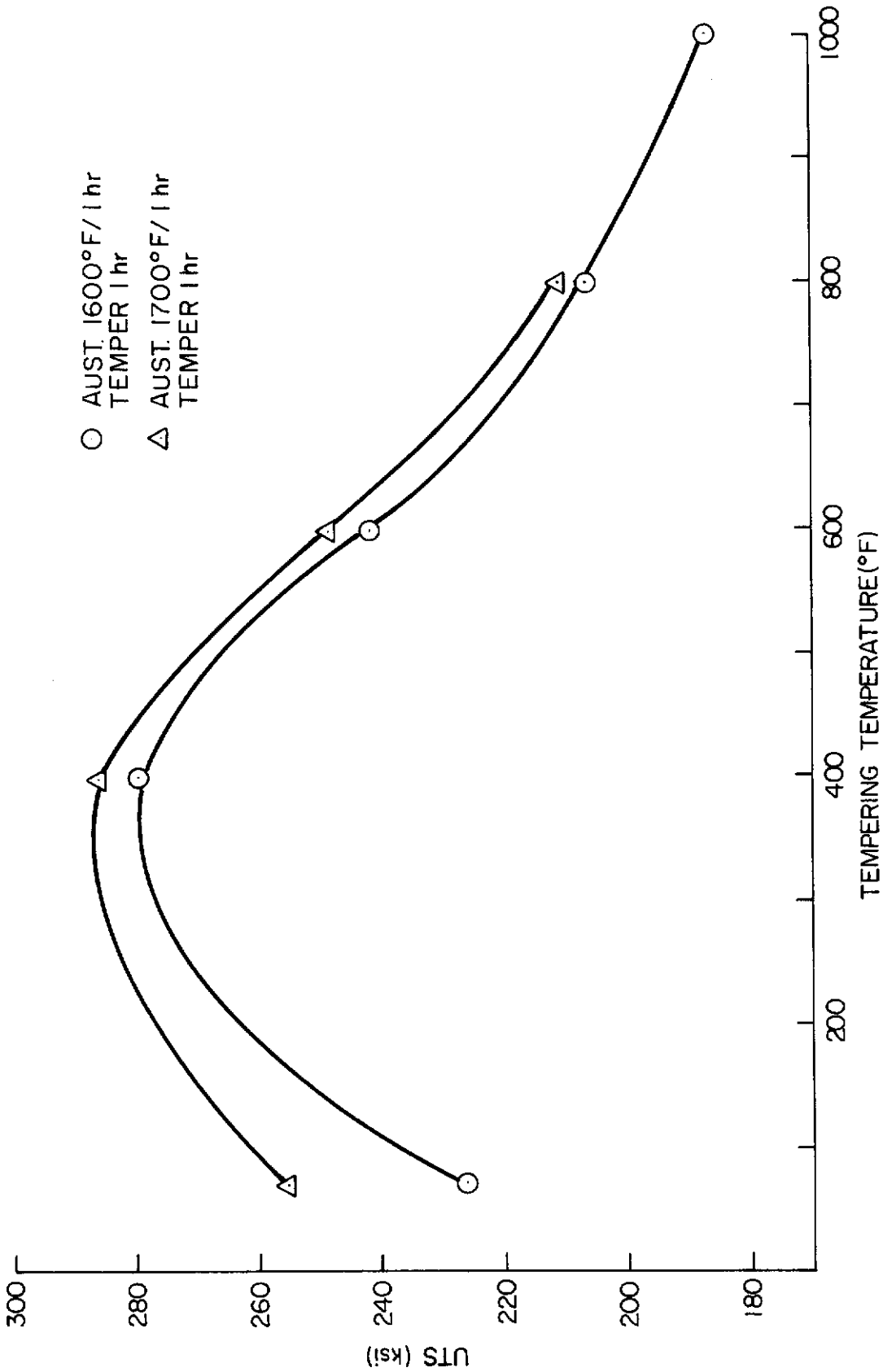

Fig. 158 - Ultimate Tensile Strength vs. Tempering Temperature for AISI 4335 V Steel

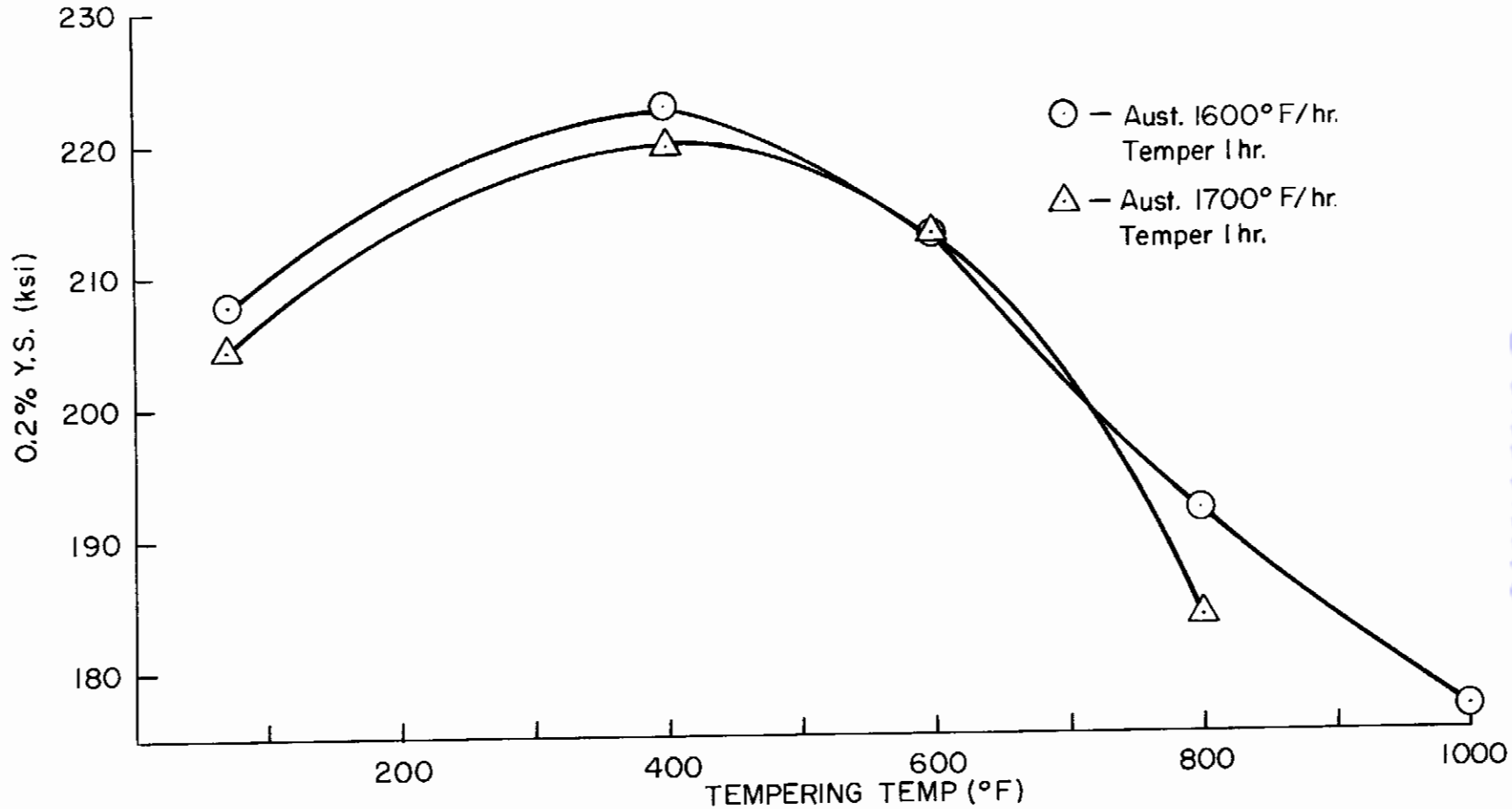

Fig. 159 - Yield Strength (0.2% offset) vs. Tempering Temperature for AISI 4335 V Steel

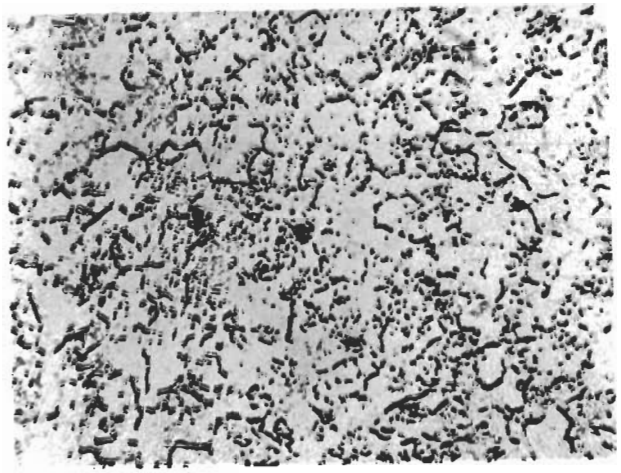

1600°F/1 Hr + O.Q. Tempered at 600°F/1 Hr

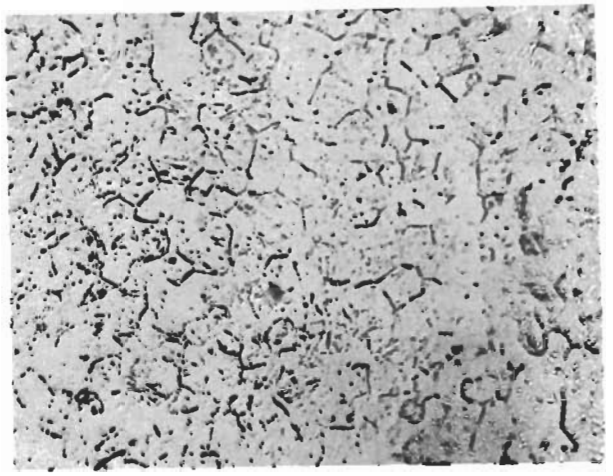

1700°F/1 Hr + O.Q. Tempered at 600°F/1 Hr

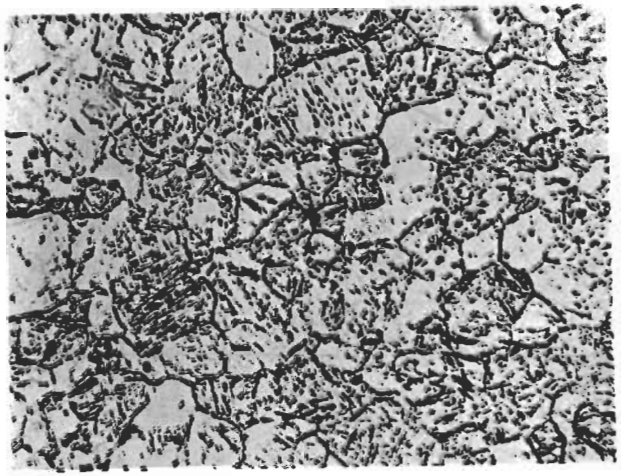

1700°F/3 Hrs, Furnace Cooled to 1600°F, O.Q. Tempered 400°F/1 Hr

Fig. 160 - Prior Austenite Grain Structure After Various Austenitizing Treatments (500X)

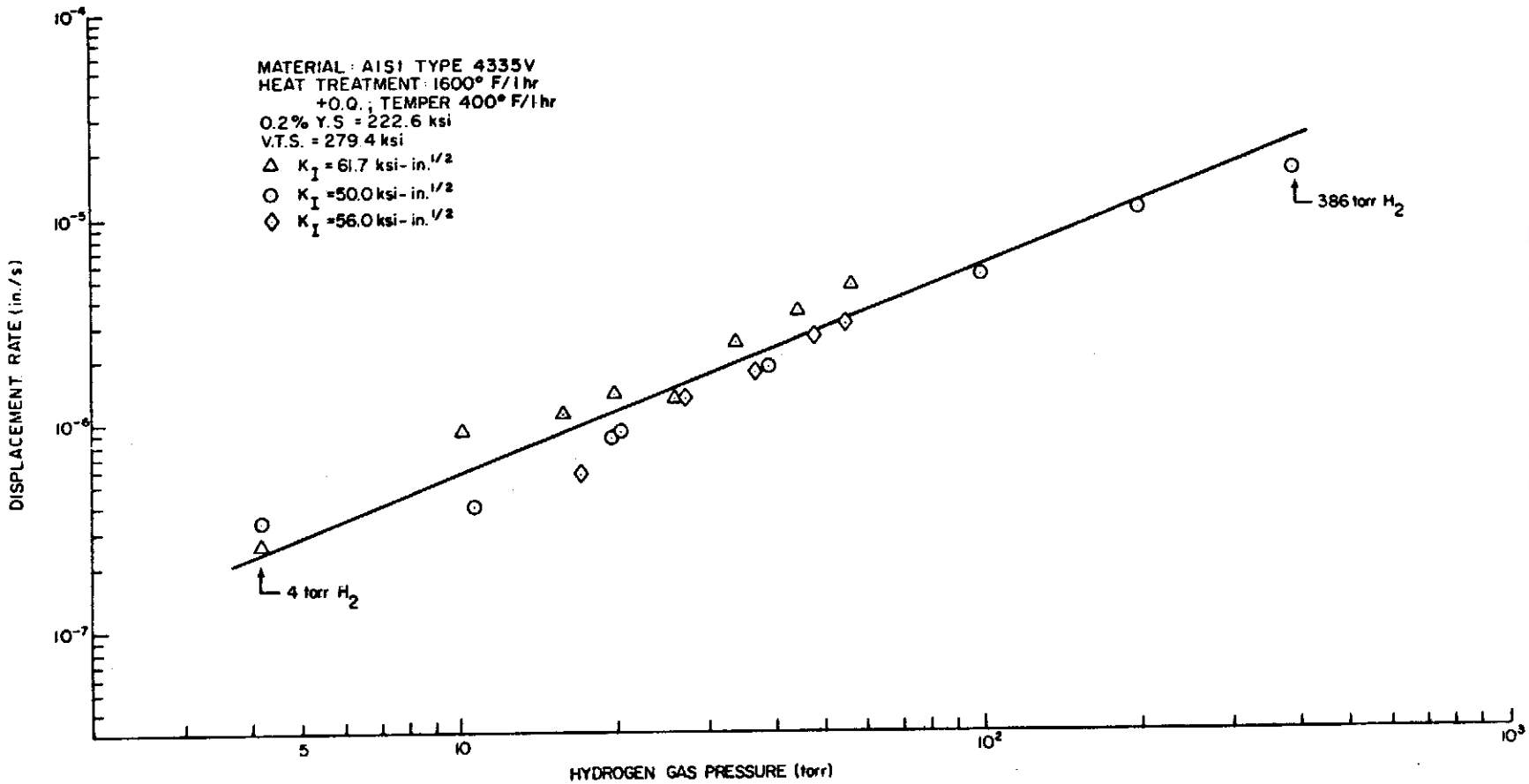

Fig. 161 - Crack Opening Displacement Rate vs. Hydrogen Gas Pressure at Constant Stress Intensity (K_I)

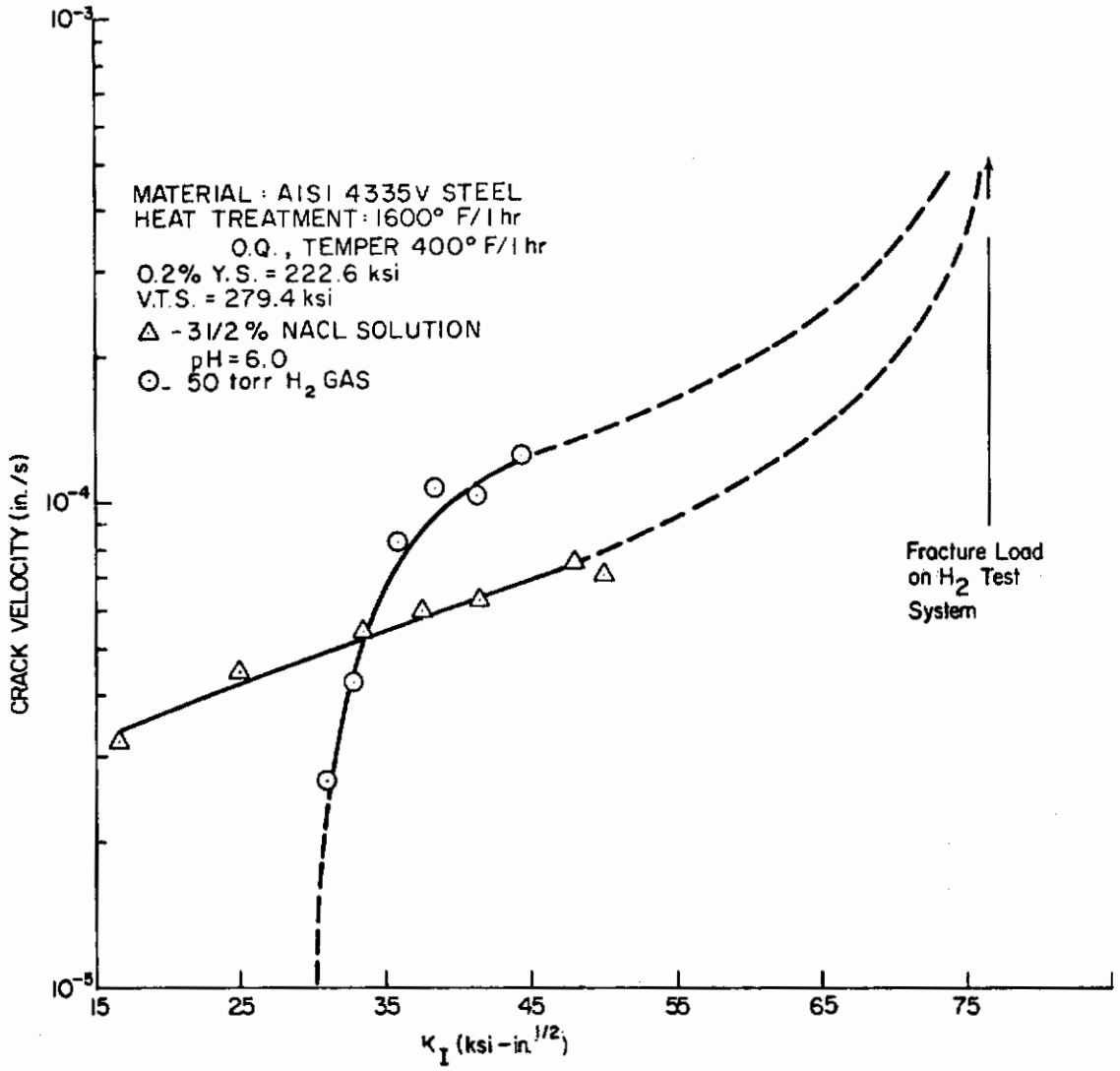

Fig. 162 - Crack Velocity vs. Stress Intensity Factor for Specimens Tempered at 400°F

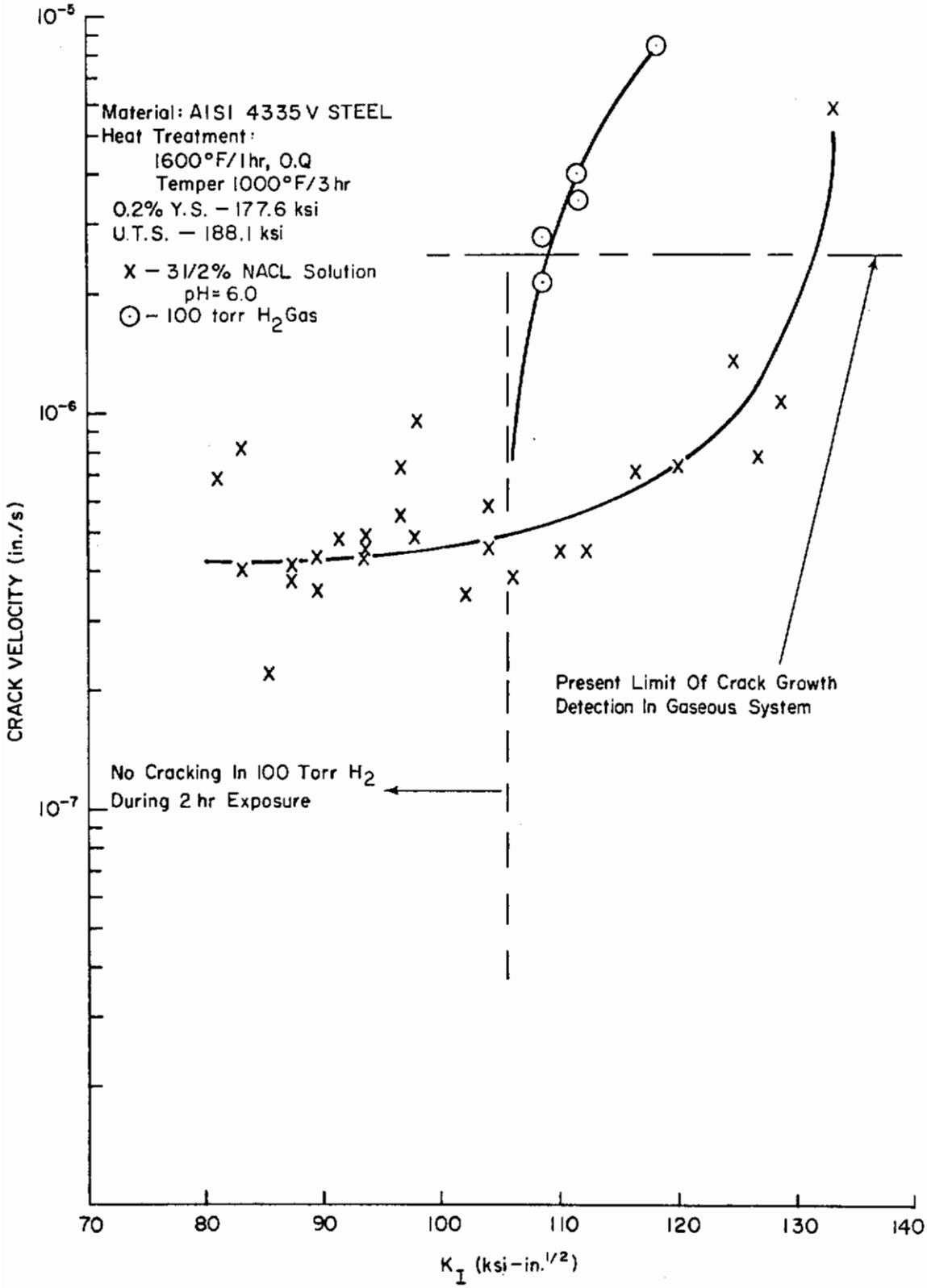

Fig. 163 - Crack Velocity vs. Stress Intensity Factor for Specimens Tempered at 1000°F

d. Discussion

The room temperature dependence of crack velocity on hydrogen pressure is consistent with results obtained by several other investigators.[112,114,115] Examination of the crack velocity vs. K_I plots shows distinctly different kinetics in H_2 gas and NaCl solution. At both strength levels, cracking begins at a rather well-defined K_I value (K_{ISCC}) in H_2 gas, approximately 30 ksi-in$^{1/2}$ for the 400°F tempered specimens, and 105 ksi-in$^{1/2}$ for the 1000°F/3 hr tempered specimens. Also the stress intensity dependence of crack velocity in dry H_2 is much different than in the aqueous environment over the same range of K_I values. Minimum exposure time in the hydrogen gas was 2 hr. If no cracking began, the test conditions were changed. Also, crack velocities upon initiation for the 400°F temper specimens is much greater than for the 1000°F temper specimens.

The 1000°F temper specimens often showed discontinuous cracking and crack arrest in gaseous H_2. The velocities given are the maximum velocities observed in the test. The behavior in NaCl solution shows cracking at much lower loads, and has been observed by prior investigators[119] only in material-environment combinations in which stress corrosion occurs. Data for each curve were obtained using one test specimen.

The loading devices used in these studies have not been calibrated with respect to one another. Therefore specimen loads (hence K_I values) may not be exact. However, slow growth zone measurement for the 400°F specimen tested in salt water was within 15% of the predicted value from fracture mechanics.

The stress corrosion processes in the test environments, although possibly quite different, are enhanced in both cases by lower tempering temperature (hence, higher strength level). Continuous cracking occurred in aqueous tests for both heat treatments. However, the 1000°F temper specimens in hydrogen gas showed a decrease in the time of crack growth with increasing stress intensity above the value for initiation (approximately 105 ksi-in$^{1/2}$). The duration of steady state crack growth was 3-3$\frac{1}{2}$ hrs at the lowest K_I value in Fig. 163, and 1/2 hr at the highest K_I value given. In all but one test, crack velocity decreased during the time of the test. Crack arrest due to preferential adsorption of contaminant species is unlikely, since (1) oxygen levels required to stop cracks are high (i.e., on the order of 0.1 - 1.0%);[120,121] (2) initiation of crack growth occurred in all 400°F tempered specimens within one minute; and (3) increasing the K_I value reduced the time of crack growth.

Possible explanations attributable to the lower material strength level and higher K_I values, are crack arrest due to bifurcation,[122] and the absence of electrochemical dissolution (as in aqueous testing) or fast fracture processes (linking up of arrested crack with

advance crack) seen in higher strength material in hydrogen gas.[123] However, metallographic examination of an arrested crack is required to substantiate this point.

In the reported tests, stability of the LVDT output voltage was checked for a minimum of $\frac{1}{2}$ hr before and after each test. However, in overnight testing, erroneous drift of output voltage occurred. This is believed to result from froom temperature changes (21.5 C to 24.5°C). Therefore, if the largest observed drift occurs over a typical test period (2 hr), the resulting apparent crack velocity would be 2.5×10^{-6} in./sec. Therefore data in this range must be suspect to a possible error due to such drifting.

e. Conclusions

1) Higher material strength level, as determined by tempering temperature, increases stress corrosion crack growth rates in both gaseous hydrogen (50-100 torr) and 3.5% NaCl aqueous solution.

2) In the range of stress intensity valves investigated, crack growth in hydrogen gas is more strongly dependent on this parameter than is crack growth in 3.5% NaCl solution.

3) Sustained crack growth in 100 torr H_2 gas does not occur in the investigated material tempered at 1000°F.

B. EFFECTS OF METALLURGICAL STRUCTURE (M. T. Wang)

1. Objectives

The objective of this study is to investigate the effects of metallurgical structure on the stress corrosion cracking of high-strength steels. The point of view here is that SCC crack propagation is a structure-sensitive, as well as an environment-sensitive process

The general approach here is to keep the continuum variable constant (strength level) and vary the microstructure (through heat treatment), alloy chemistry, state of stress, and environment. The two alloys to be used are AISI 4340 steel and 18% Ni 250 maraging steel. These provide two basically different structures and alloy chemistries.

2. Fracture Mechanics Consideration

In the crack propagation experiments, holding constant the state of stress and stress intensity at the crack tip (K_I) or its equivalent crack extension force (G_I) reduces the uncertainties. The SCC experiments were conducted by using tapered double-cantilever specimens which permit a constant stress intensity for constant load. The justification for this approach lies in the fracture mechanics analysis which is reviewed below.

From an energy consideration, it was first proposed by Irwin[124] that energy balance of the fracture process in a system can be expressed as

$$P \frac{d\ell}{da} + \frac{dE}{da} = \frac{dW}{da} + \frac{dK}{da} \quad , \tag{50}$$

where

a = crack length,
p = applied load,
E = strain energy,
K = kinetic energy
W = work done by fracture and plastic flow, and
ℓ = length between grips.

Two assumptions have been made in this analysis. First, the rate of kinetic energy change as a function of crack length is assumed to be zero. The slow growth of cracks in the SCC experiment satisfies this requirement because of the trivial kinetic energy produced from the slow crack velocity and the negligible mass removed from the crack tip. Second, the plastic flow capacity of the steel investigated is required to be small, such that the length between grip (ℓ) can remain constant and that the plastic zone size at the crack tip is small enough to meet the boundary condition in fracture mechanics analysis. To meet this requirement, the strength levels of the steels investigated were heat treated to a minimum of 200 ksi to produce a limited flow capacity. Evidences of limited flow capacity of the steels investigated are shown in the load extension curve of the 18% Ni maraging steel of Fig. 164 where the steels were heat treated to a minimum strength of 200 ksi through different aging treatments. Table XXII summarizes the mechanical properties of the 18% Ni maraging steel.

From linear elasticity, the strain energy release rate (dE/da), known as crack extension force (G_I) can be expressed as

$$\frac{dE}{da} = G_I = \tfrac{1}{2} P^2 \frac{\partial\left(\frac{1}{M}\right)}{\partial a} \quad , \tag{51}$$

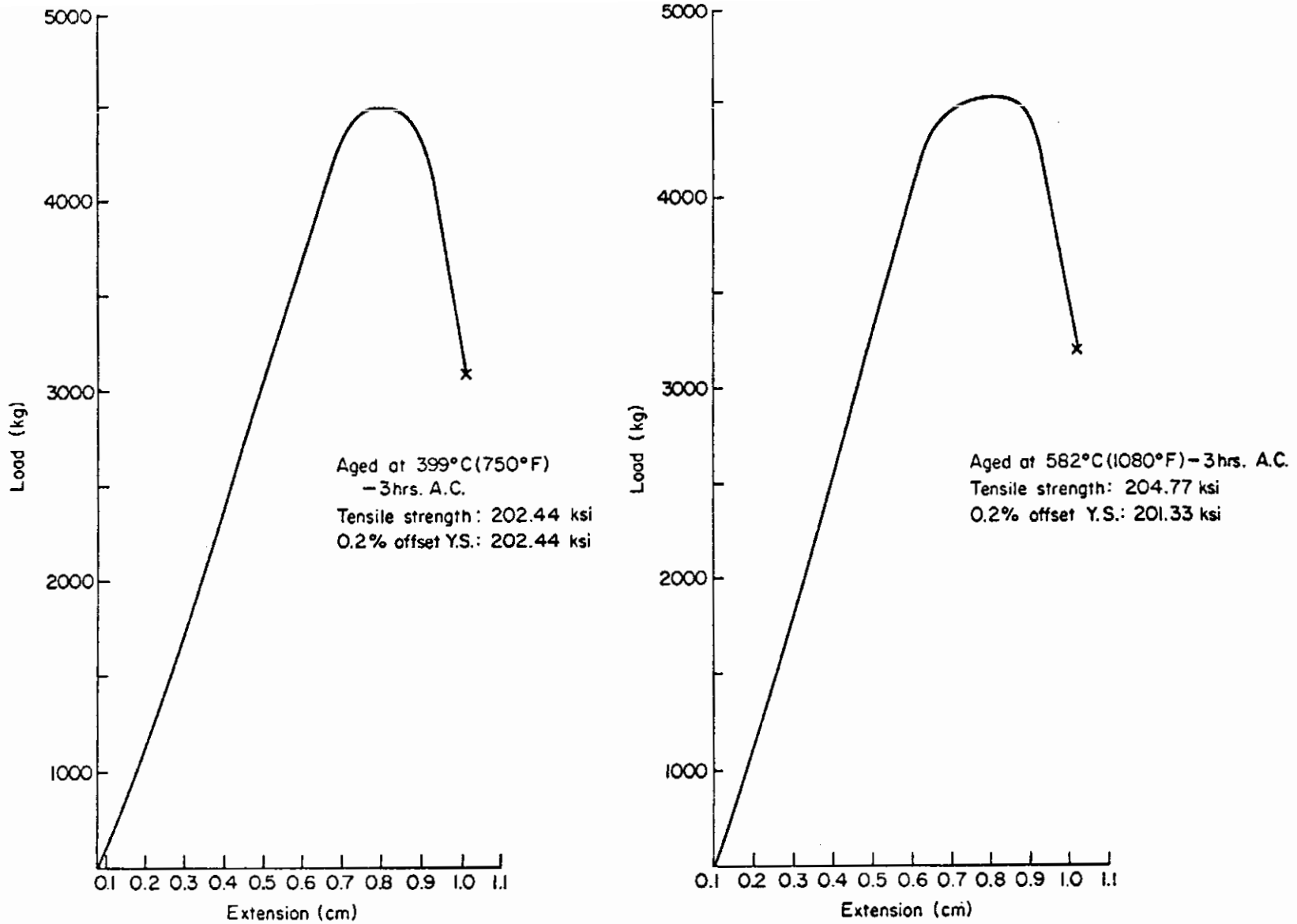

Fig. 164 - Load Extension Curve of Two Different Heat-Treatments of 18% Ni Maraging (RMS 250) Steel with Standard Round 0.250-Inch Diameter and 1.0-Inch Gage Length Specimen

Table XXII - Mechanical Properties* of 18% Ni Maraging Steel

Aging Treatment** 3 Hours Air-Cooled Temp. (°C)	Temp. (°F)	Tensile Strength (ksi)	Yield Strength 0.2% Offset (ksi)	Elongation (%)	Reduction Area (%)	Rockwell Hardness (R_c)
399	750	202.44	202.44	13.06	25.47	47.5
		198.59	198.59	15.73	28.43	47.0
		191.47	191.47	13.1	33.5	47.7
438	820	216.88	216.88			
		207.59	207.59	9.5	31.5	49.5
510	950	235.80	233.16	10.1	29.5	52.2
554	1030	210.13	205.70	11.1	30.2	49.6
582	1080	204.71	201.83	16.2	30.7	47.4
		195.88	192.55	16.4	28.9	47.3
593	1100	196.92	193.49	12.8	32.5	46.1

* Determined from standard, round 0.250-inch diameter tensile specimens with cross-head speed at 0.5 cm/min and rolling direction parallel to tensile axis.

**Prior to aging treatment, specimens were double austenitized at 899°C (1650°F) 1 hour air-cooled + reaustenitized at 843°C (1550°F) 1 hour air-cooled.

where

p = applied load per unit thickness,
M = spring constant per unit thickness, and
a = crack length.

The tapered double-cantilever specimen configuration, as shown in Fig. 165, is so designed[125] provide a constancy of the term $\partial(1/M)/\partial a$ such that a constant crack extension force (G_I) can be achieved under a given load over a certain crack length. The crack extension force also depends on the material properties under a given specimen geometrical condition. The crack extension force (G_I) can be related to the stress intensity factor at the crack tip (K_I) as

$$K_I^2 = EG_I \quad , \quad \text{for plane stress condition} \tag{52}$$

and

$$K_I^2 = \frac{EG_I}{1 - \nu^2} \quad , \quad \text{for plane strain condition,} \tag{53}$$

where

E = Young's modulus for the material, and
ν = Poisson's ratio.

The stress intensity factor at crack tip can be approximately related to the material property to account for the local plastic yielding as

$$K_I = \sigma_{y.s.}(2\pi r_y)^{1/2} \quad , \tag{54}$$

where

r_y = plastic zone size,

K_I = stress intensity factor at crack tip, and

$\sigma_{y.s.}$ = 0.2% offset yield strength.

From Eqs. (52)-(54) it can be seen that the crack extension force (G_I) is also a function of yield strength of the material. Thus, the study of the metallurgical structural effects on the SCC of high-strength steels becomes significant only if the steels investigated have identical strengths. Table XXII lists the strength and mechanical properties of 18% Ni (250) maraging steel used in this investigation.

The crack velocity (da/dt) can be obtained by differentiating Eq. (51) with respect to time (t). Under the conditions of constant

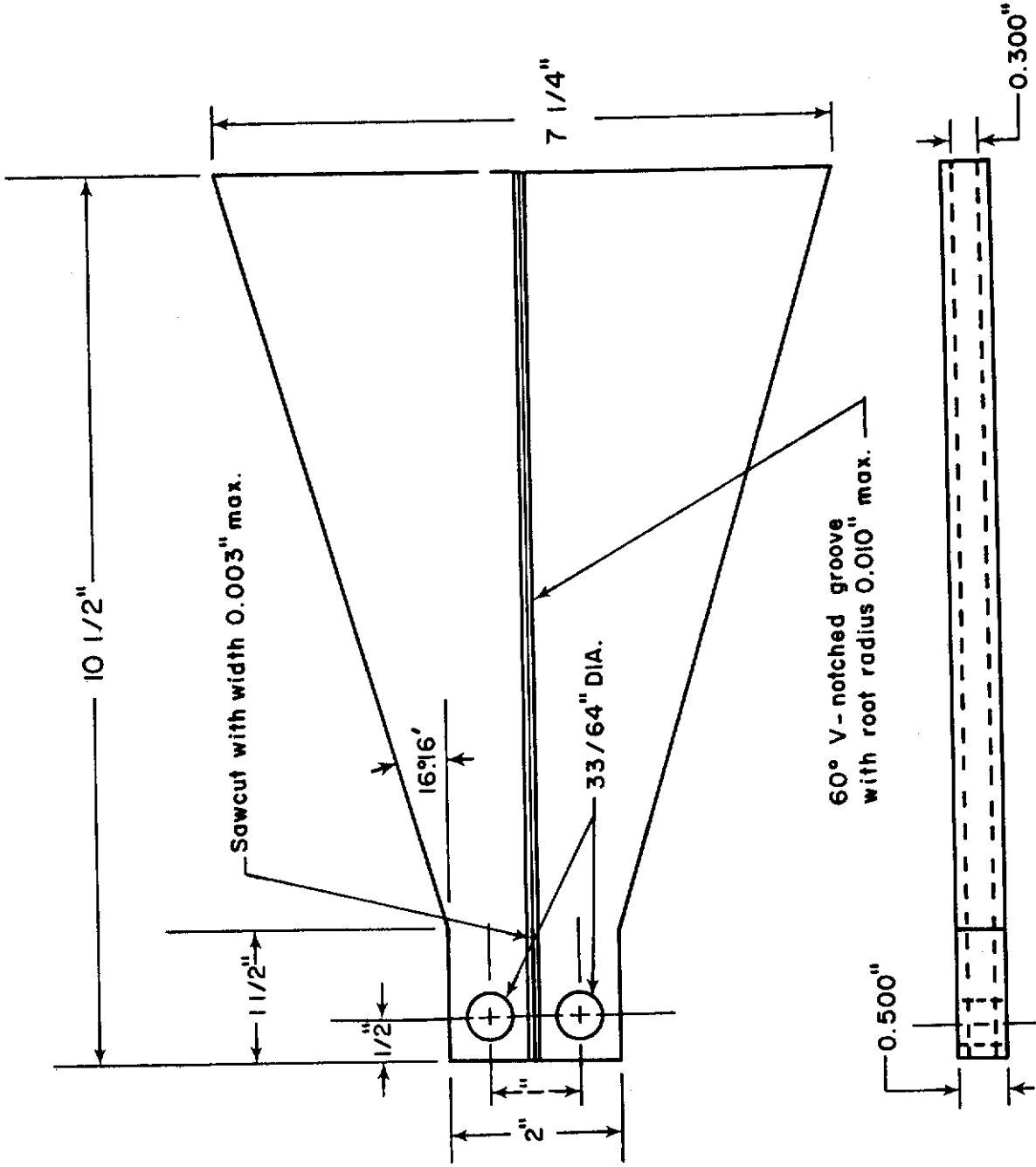

Fig. 165 - Tapered Double Cantilever Beam Specimen

load (P) and crack extension force (G_I), the crack propagation rate can be obtained as follows:

$$(da/dt) = [(C/P)(d\delta/dt)] , \tag{55}$$

where

$C = 1/[\partial(1/M)\partial a]$ = constant for a specific material with tapered double cantilever beam specimen,

M = spring constant, a = crack length, and

P = applied load.

The quantity $[\partial(1/M)/\partial a]$ for a given steel has been determined to be constant by Van Der Sluys[126] for the specific specimen geometry of the tapered, double-cantilever beam specimen used in this investigation. Since the spring constant (M) is the slope of load vs. deflection, the quantity $[\partial(1/M)/\partial a]$ is very sensitive to the elastic property of material, especially Young's Modulus (E) but independent of the alteration of microstructures for a given steel. Thus, under a given constant applied load (P), the deflection rate ($d\delta/dt$) can be used as a direct measure of crack velocity (da/dt).

For a constant $[\partial(1/M)/\partial a]$, the interrelationship between crack extension force (G_I), the stress intensity factor at crack tip (K_I), and applied load (P) can be expressed as

$$G_I \propto P^2 \propto K_I^2 . \tag{56}$$

Thus, the use of applied load (P) to express directly the stress intensity factor at crack tip (K_I) can be justified.

To the first approximation, the deflection at the load points of the specimen is considered to be proportional to the displacement at crack tip. This provides a good experimental technique to solve the dilemma in measuring the actual crack tip displacement. The utilization of Eq. (55) to obtain the crack propagation rate have been successfully carried out by Van Der Sluys[126] and others.

3. Crack Propagation Measurements

Crack propagation rates were measured from the tapered double-cantilever beam specimen at different heat treating conditions of the two steels by using Eq. (55) in terms of deflection rate of the specimen under a constant load. The specimens were precracked chemically with concentrated hydrochloric acid, and then baked at 176°C for one hour to

prevent any hydrogen uptake during the chemical cracking process. Constant loads were applied through a modified SATEC Mode D creep tester, and deflections of the specimen at the load points were measured from a Daytronic Model DS 100 linear variable differential transducer (LVDT). The 3.5% NaCl aqueous solution was adjusted to pH 6 and deaerated by bubbling prepurified nitrogen gas in a reservoir for 24 hours. An overall view of the experimental arrangement is shown in Fig. 166 and a close-up view of experimental cell and the location of LVDT is shown in Fig. 167. The deflections of the LVDT were calibrated by a mechanical displacement from a Starrett micrometer with an accuracy of 0.0001 inch. The calibration curve for the LVDT deflection with respect to mechanical displacement is shown in Fig. 168. The error in linearity of the LVDT deflection is about 0.25% within the range of calibration. Deflections were recorded by an Esterline Angus strip chart recorder at speeds from 0.5 inch/hr up to 1 inch/min at different load conditions. The deflection measured at each data point is in the range 0.002-0.005 inch which requires from 30 minutes to 24 hours for each determination. The crack propagation rates in terms of deflection rates at the load points were obtained from the recorded chart using least square analysis.

Crack propagation rates as a function of applied load have been measured on 18% Ni maraging steel with three aging treatments as shown in Fig. 169. The measurements of crack propagation rates as a function of applied load for AISI 4340 steel with tempered martensite and tempered bainite structures are presented in Section 7-c.

The resultant data of crack propagation rate as a function of applied loads on the 18% Ni maraging steel, shown in Fig. 169, clearly demonstrates that the metallurgical structure alters the crack propagation rates. It is noteworthy, from Table XXII, that the ductility parameters for the two similar strength conditions do not differ significantly. The comparison of crack propagation rates on the aged specimens at 438°C (820°F) and 554°C (1030°F) are fruitful because of their identical strength. The crack propagation rates for aged specimens at 510°C (1950°F) are not comparable to the other two specimens because of the difference in strength levels. However, it is of practical importance to document the crack propagation rates of this aging condition for reference because aging at 510°C (950°F) for three hours is a standard commercial heat treatment for 18% Ni (250) maraging steel.

Because of the high fracture toughness of 18% Ni maraging steel and the limited 120,000 lb loading capacity of the SATEC Model D creep tester, no crack propagation rates can be obtained at high stress intensity levels for the specimen of 554°C (1030°F) aged condition. To overcome this experimental difficulty, a reduced-size, tapered, double-cantilever specimen is designed for future investigation (see Fig. 170).

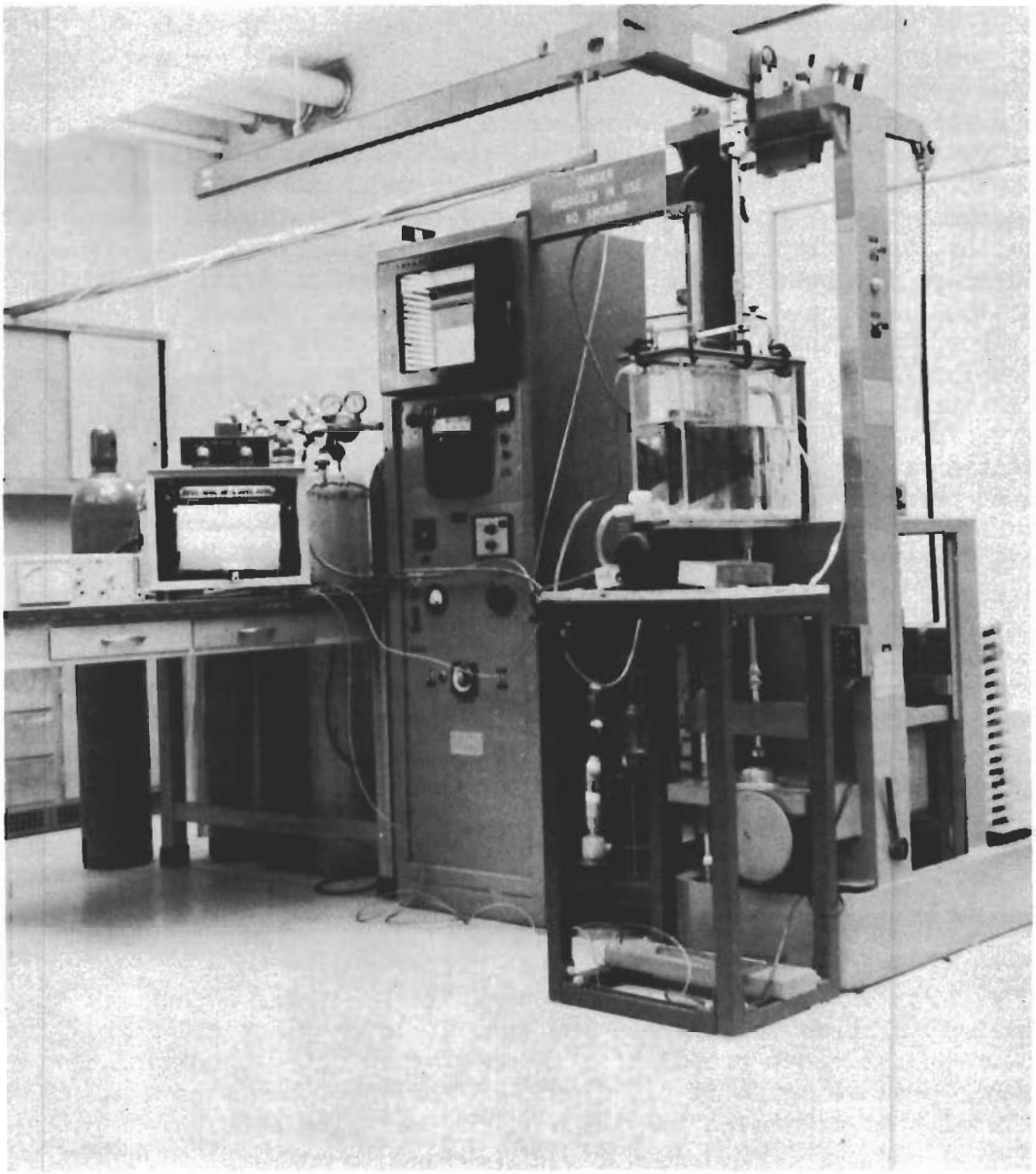

Fig. 166 - Apparatus for the Crack Propagation Test

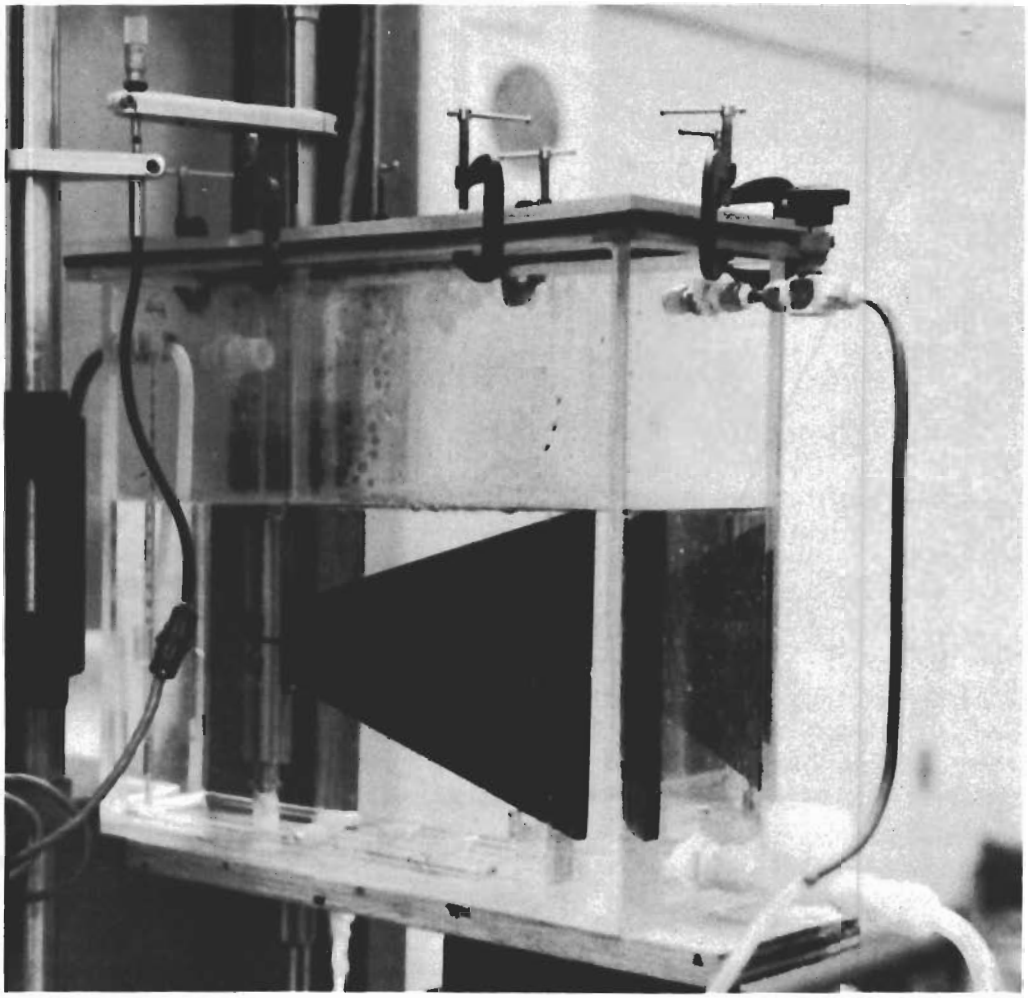

Fig. 167 - A Close-Up View of Environmental Cell and Location of LVDT

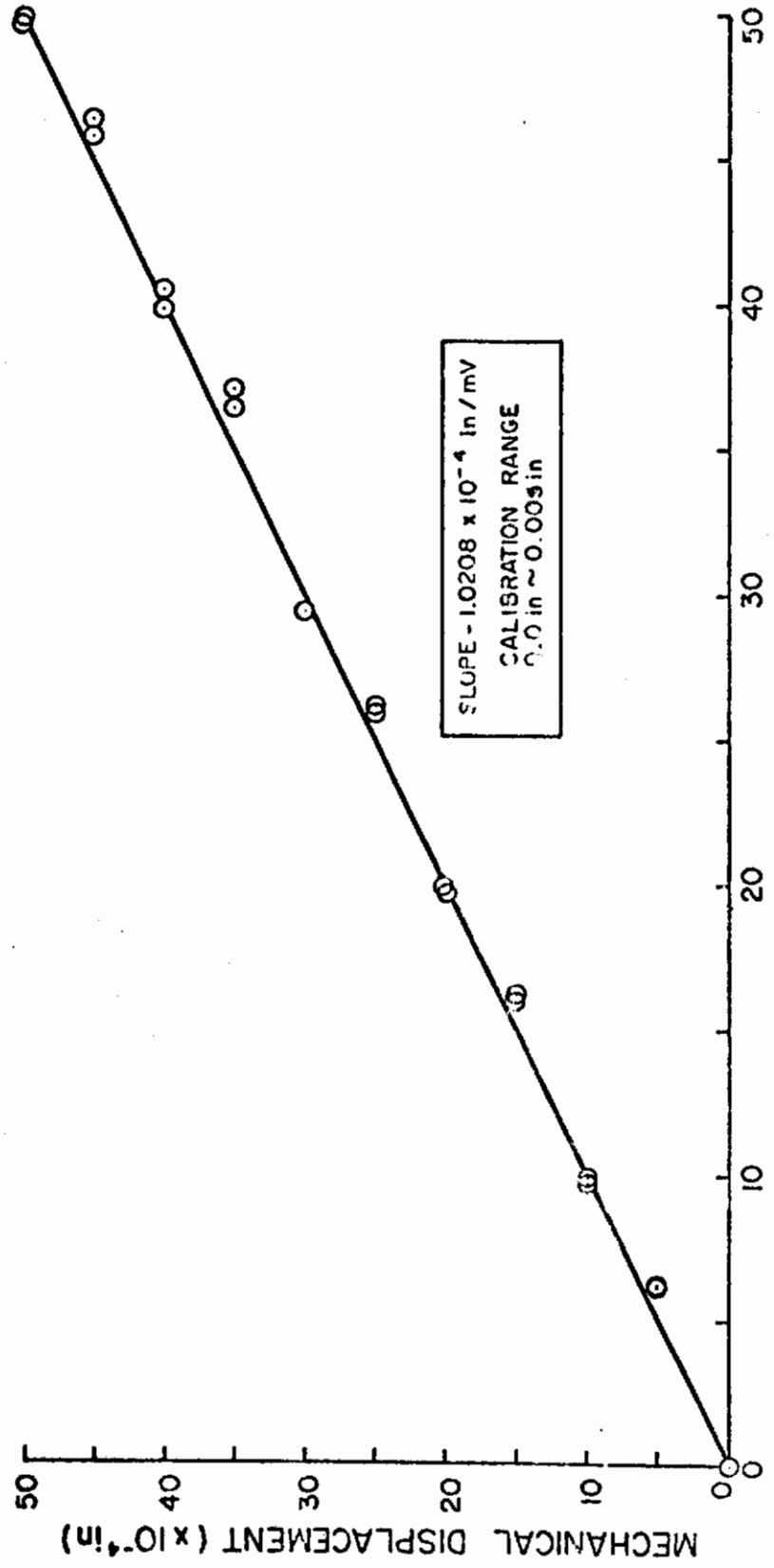

Fig. 168 - Calibration Curve for Linear Variable Differential Transducer

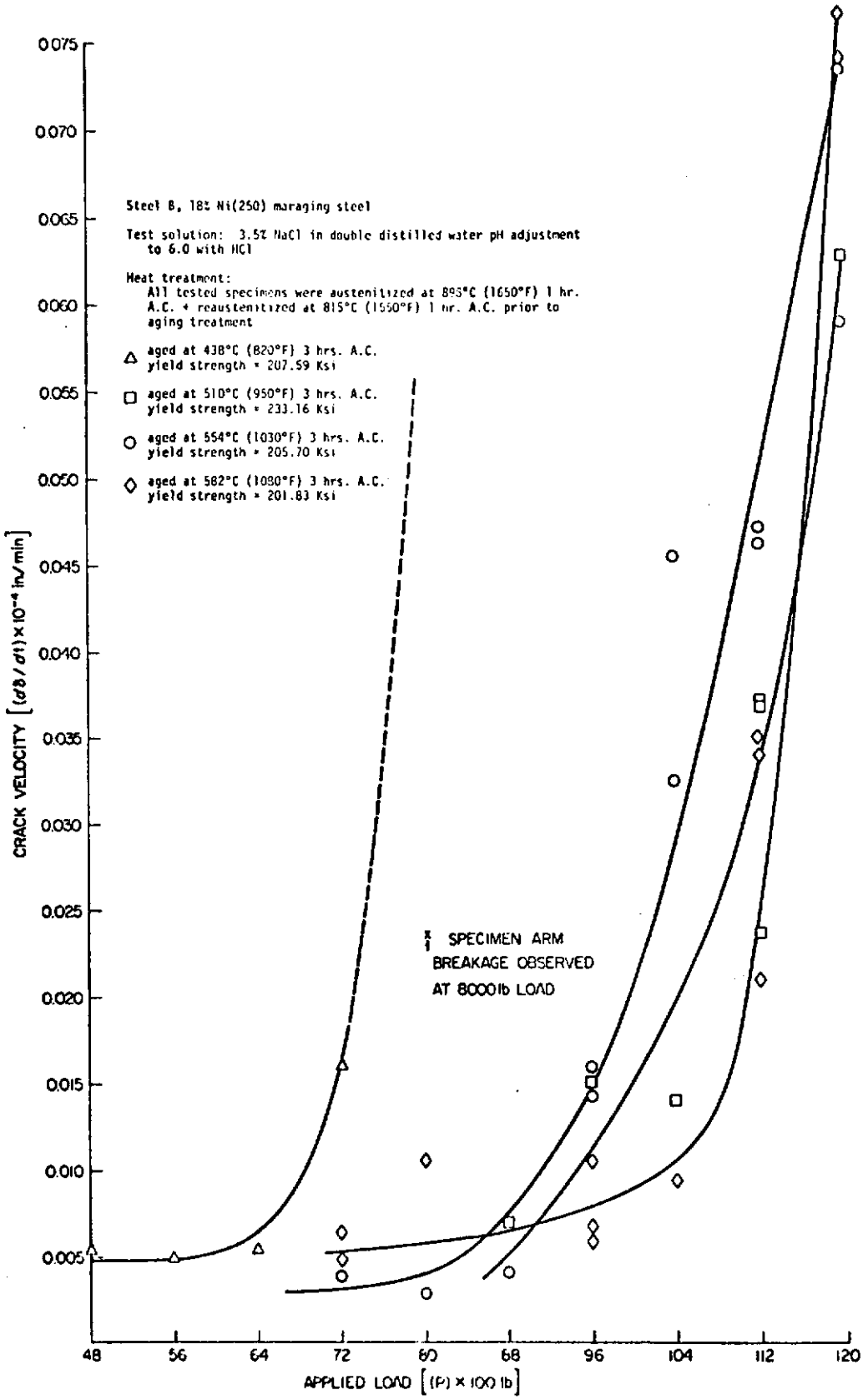

Fig. 169 - Subcritical Crack Growth of 18% Ni (250) Maraging Steel

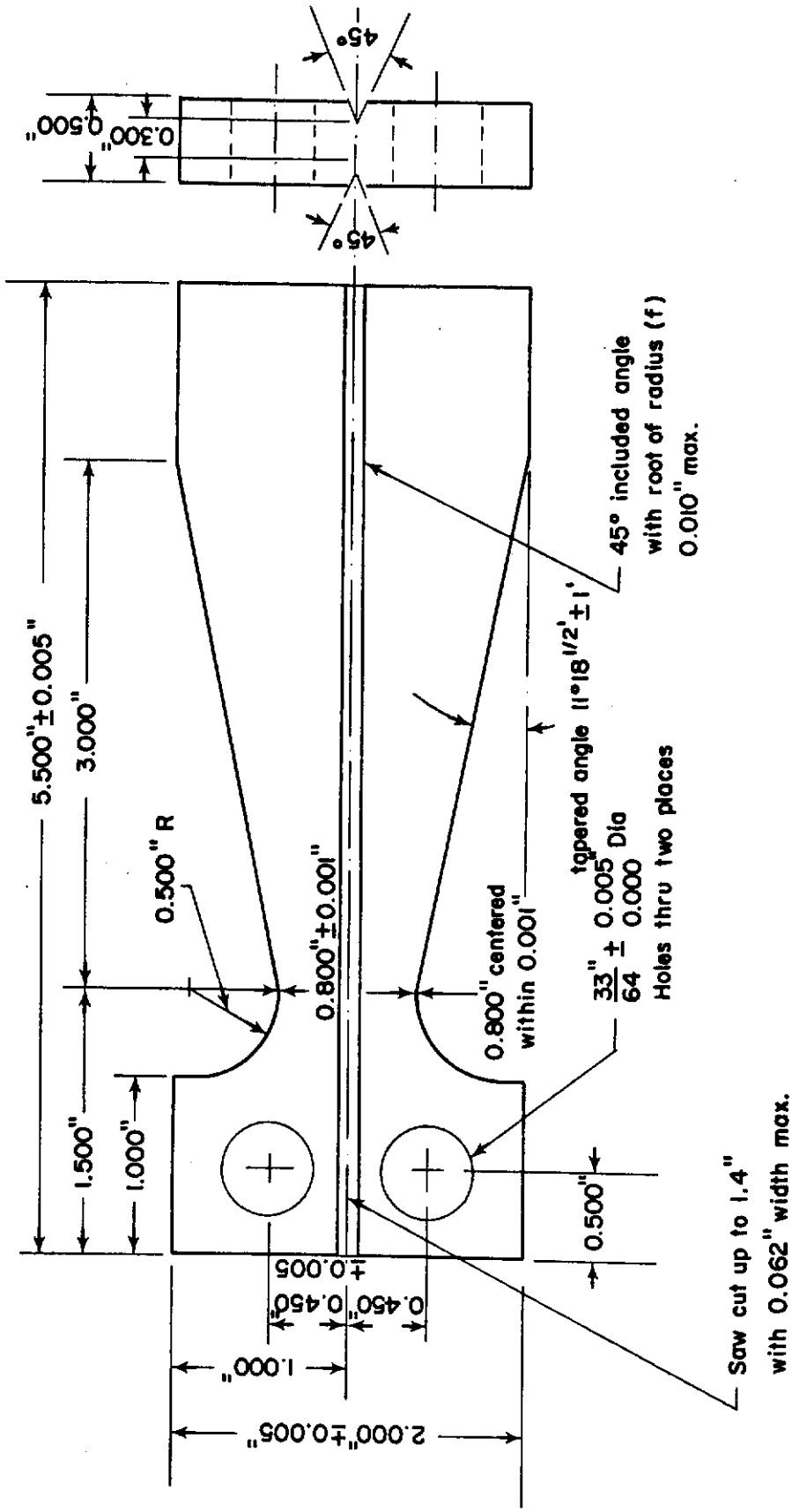

Fig. 170 - Tapered Double-Cantilever Beam Specimen

4. Metallurgical Structure Consideration

The high-strength steels used in this investigation exhibit two basically different structures and alloy chemistries. Two commercial heats of consumable electrode vacuum melt 18% Ni (RMS 250) maraging steel and AISI 4340 steel were purchased from Republic Steel Corporation in the form of hot-rolled 0.5-inch thick plates with a final mill-annealed condition. The certified chemical analysis of the two steels is tablulated in Table XXIII.

Table XXIII - Chemical Composition of High-Strength Steels*

Steel No.	Steel	C	Mn	P	S	Si	Ni	Co	Mo	Ti	Al	Zr	B	Ca	Cr
A	AISI 4340 Steel Heat No. 3952755	0.41	0.73	0.005	0.005	0.23	1.81		0.25						
B	18% Ni (RMS 250) Maraging Steel Heat No. 3951440	0.029	0.09	0.006	0.007	0.09	17.68	7.18	4.86	1.38	0.05	0.02	0.003	0.06	0.83

*Republic Steel Corp. certified analysis; chemical composition in weight percent

Maraging steel derives its high fracture toughness and strength by martensite transformation through slow cooling, and precipitation hardening through aging; whereas, the typical low alloy AISI 4340 steel yields an optimum combination of toughness and strength through quench-temper or austempering with tempered martensite and bainite structures, respectively. The susceptibility of SCC for these two steels in terms of time-to-failure has been observed by Steigerwald and Benjamin[127] to have two orders of magnitude difference at the same strength level of 236 ksi. From a microstructural viewpoint, the only structure of the two steels in common is grain size. Indeed, SCC has been, from time to time, reported to have intergranular fracture and grain size dependent in nature. The objective of this investigation is to determine the characteristic responses to SCC of the two high-strength steels, each with different structures. Various heat treatments are used in the steels to obtain identical strength and grain size with significant difference in microstructures.

The heat treatments for 18% Ni maraging steel are austenitized at 899°C for one hour and air-cooled, plus reaustenitized at 816°C for one hour and air-cooled prior to aging at different temperatures for maraging steel are shown in Fig. 171 and Table XXII. The use of double austenitized temperatures at 898°C (1650°F) and 815°C (1550°F) aims at minimizing the anisotropic mechanical properties and eliminating the

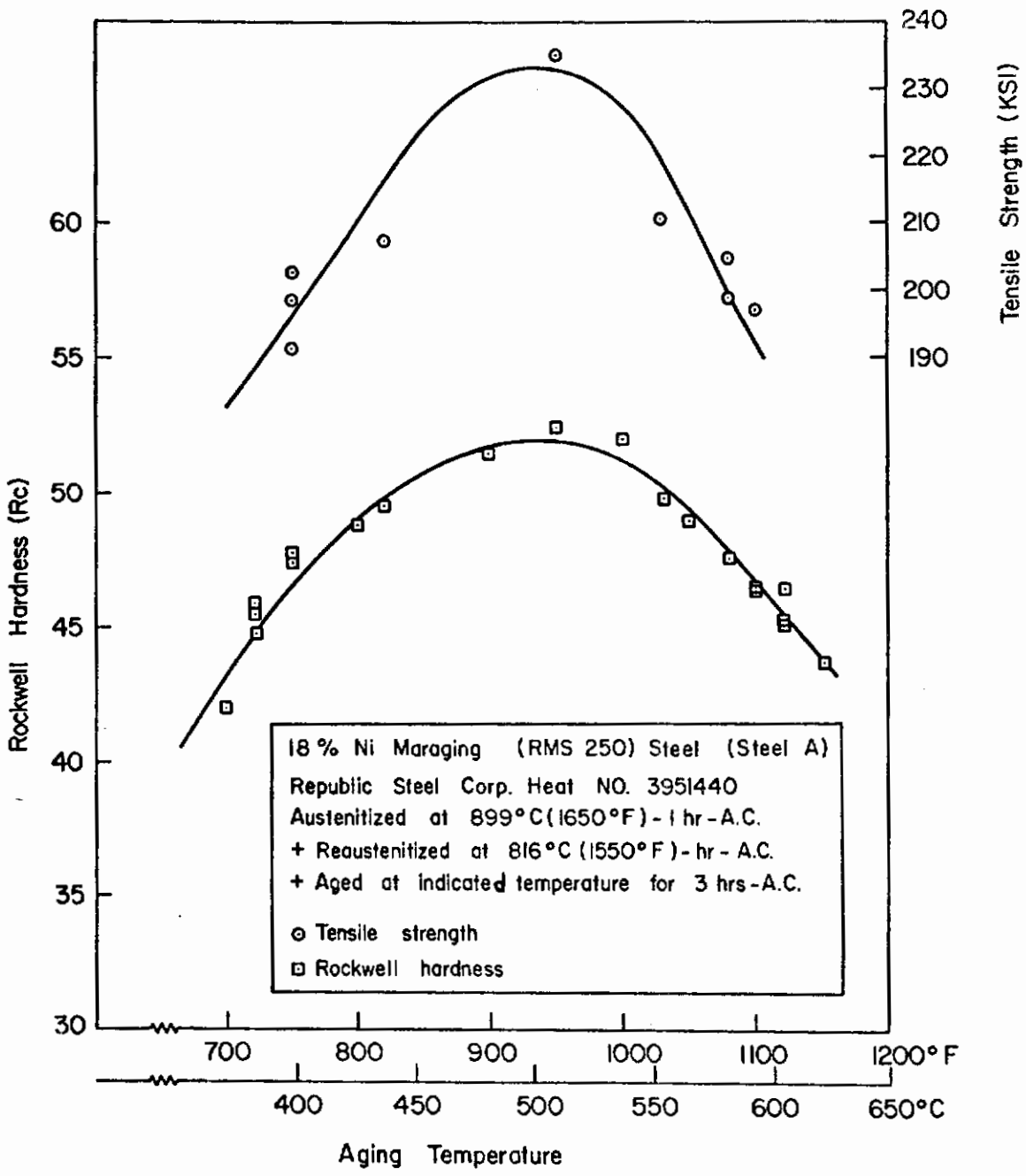

Fig. 171 - Hardness and Tensile Strength as a Function of Aging Temperature of 18% Ni Maraging (RMS 250) Steel

significant difference in grain size during the subsequent aging treatment at different temperatures. Moreover, the choice of temperatures in the double austenitizing treatment is intentional to avoid the grain boundary segregation to response for thermal embrittlement in maraging steel.

Recent publication on SCC of 18% Ni (300) maraging steel by Starvros and Paxton[128] show intergranular fractures for the steel with six different heat treatments and identical strengths. It appears that those heat treatments used in their investigations may have produced thermal embrittlement which enhanced SCC. Thermal embrittlements in maraging steel has been reported to produce intergranular fracture.

For practical purposes the grain sizes, which are duplex fine grains from all different aging treatments, are approximately in the range of ASTM No. 9 to 11. The microstructural constituents in this steel with various aging treatments are mainly cubic martensite, precipitation phases, and reversion austenite. Reversion austenite in maraging steel is a typical structure resulting from the hysteresis of the transformation in the iron-nickel system and from the partitioning of alloying elements upon precipitation. The enhancement of ductility and toughness by reversion austenite in 18% Ni maraging steel may give rise to beneficial effects on the resistance to crack propagations of SCC.

Two major structures have been produced in AISI 4340 steel through the following heat-treatment schedules:

a. Tempered martensite structure with quench-temper treatment

Normalized at 899°C (1650°F), 40 min A.C. + austenitized at 843°C (1550°F), 30 min, then oil quenched + tempered at 426°C (800°F) 1 hour A.C.

b. Temper bainite structure with austempering treatment

Normalized at 899°C (1650°F), 40 min A.C. + austenitized at 843°C (1550°F), 30 min + rapid quenched at 315°C (600 ± 10°F), 2 hours A.C. + tempered at 400°C (750°F), 1 hour A.C.

These treatments give the same strength of the steel for tempered martensite and bainite with Rockwell hardness between 44-46 R_C; these treatments produce the same grain size and carbide distribution and morphology in the structures being studied. It is worthwhile to mention that tempering at 400°C in AISI 4340 steel is in the third stage of tempering in which retained austenites are completely decomposed and ϵ carbides are completely transformed to cementite in an early stage of spheroidization.

5. Electron Metallographic Examination

Microstructures of the steel specimens were examined by electron transmission using thin foils.

a. Examination of Maraging Steel

Upon air cooking from the austenitizing temperature, a low-carbon cubic martensite matrix with high dislocation densities is anticipated in the 18% Ni maraging steels. The high dislocation density in the cubic martensite matrix is attributed to the metastable austenite-alpha prime (γ-α') transformations. Aging at 438°C (820°F) for three hours produces annihilation and intersection of dislocations to form dislocation cell structures. Figure 172 shows the dislocation cell structures in the cubic martensite matrix. Whether the dislocation cell structure is equivalent or related to the martensite laths remains to be verified. It is important to mention that precipitations of second phases (intermetallic compounds) have already formed at 438°C (820°F) aging; however, the tiny coherent precipitates are too small to be observed at this magnification with thin-foil techniques, as shown in Fig. 172. As the aging temperature increases to 510°C (950°F) for three hours, the dislocation density drastically decreases and a small amount of reversion austenite formed at the sub-boundaries can be observed, as shown in Fig. 173. Extensive examination of thin foils at hgiher magnification suggests that reversion austenites in 18% Ni maraging steel form by nucleation and growth at the sub-boundaries. The terminology of martensite laths used here is to distinguish the incoherent un-twinned cubic martensite from the twin plates of medium carbon martensite in AISI 4340 steel. The low-carbon cubic martensite in maraging steel is believed to be incoherent at the lath interfaces. The amount of reversion austenite increases as aging temperature increases. Figure 174 shows the increasing amount of reversion austenite aged at 554°C (1030°F). Positive identification of reversion austenite in maraging steel was carried out in succeeding work. Optical micrographs for the steel are shown in Figs. 175 and 176 to account for the significant difference in microstructures. Electron micrographs of a direct carbon replica are shown in Fig. 177.

b. Examination of AISI 4340 Steel

The purpose of this investigation is to compare the crack propagation characteristics of martensite and bainite structures. Figures 178 and 179 reveal the morphologies of tempered martensite and bainite, respectively. The third-stage tempering process is intentionally used here not only to avoid the tempered martensite embrittlement [i.e., 204°C (400°F), 371°C (700°F) tempering] and the reversible temper embrittlement (i.e., 482-593°C tempering), but also to attempt to obtain a similar morphology and distribution of carbides in both tempered martensite and bainite. No retained austenites were observed in either

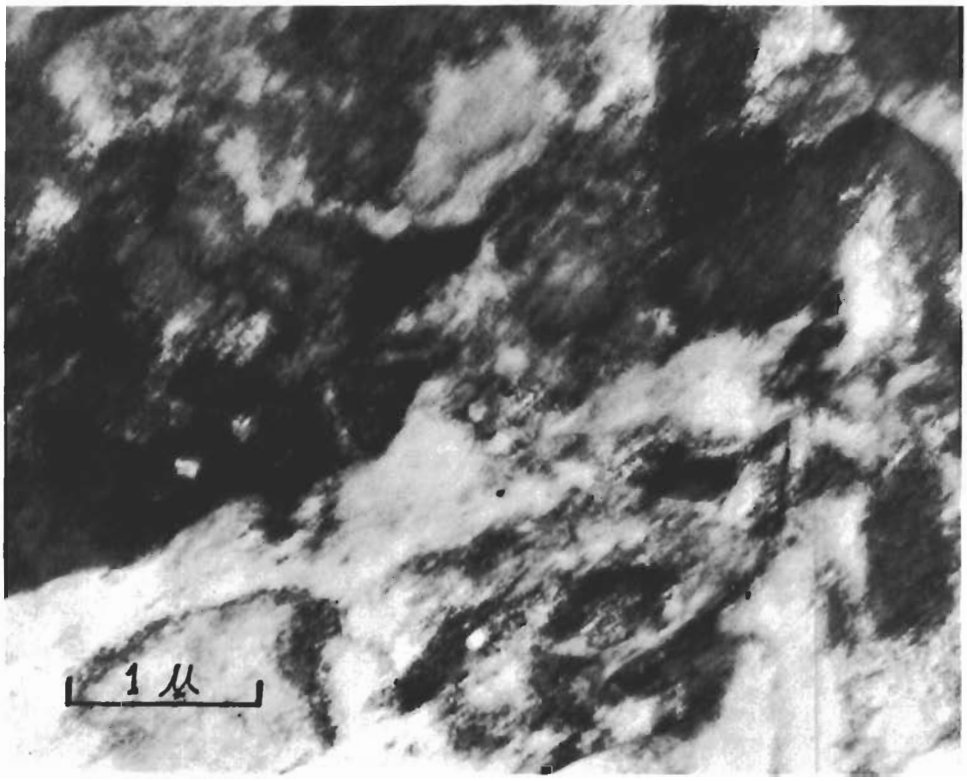

Fig. 172 - Microstructures of 18% Ni Maraging Steel

Heat treatment: 899°C (1650°F)-1 hr. A.C. + 815°C (1550°F) 1 hr. A.C. + 438°C (820°F)-3 hr. A.C.
Tensile strength: 235.80 ksi; yield strength: 233.16 ksi
Rockwell hardness, R_C: 52.2

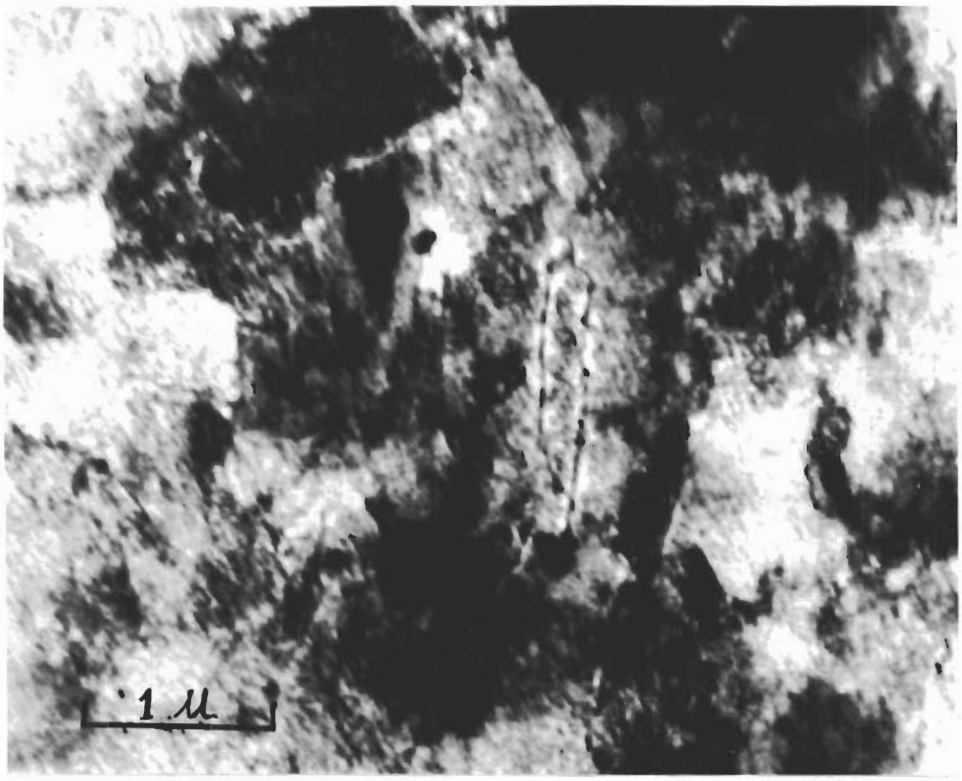

Fig. 173 - Microstructures of 18% Ni Maraging Steel

Heat treatment: 899°C (1650°F)-1 hr. A.C. + 816°C (1550°F)-1 hr. A.C. + 510°C (950°F)-3 hr. A.C.
Tensile strength: 235.80 ksi; yield strength: 233.16 ksi
Rockwell hardness, R_c: 52.2

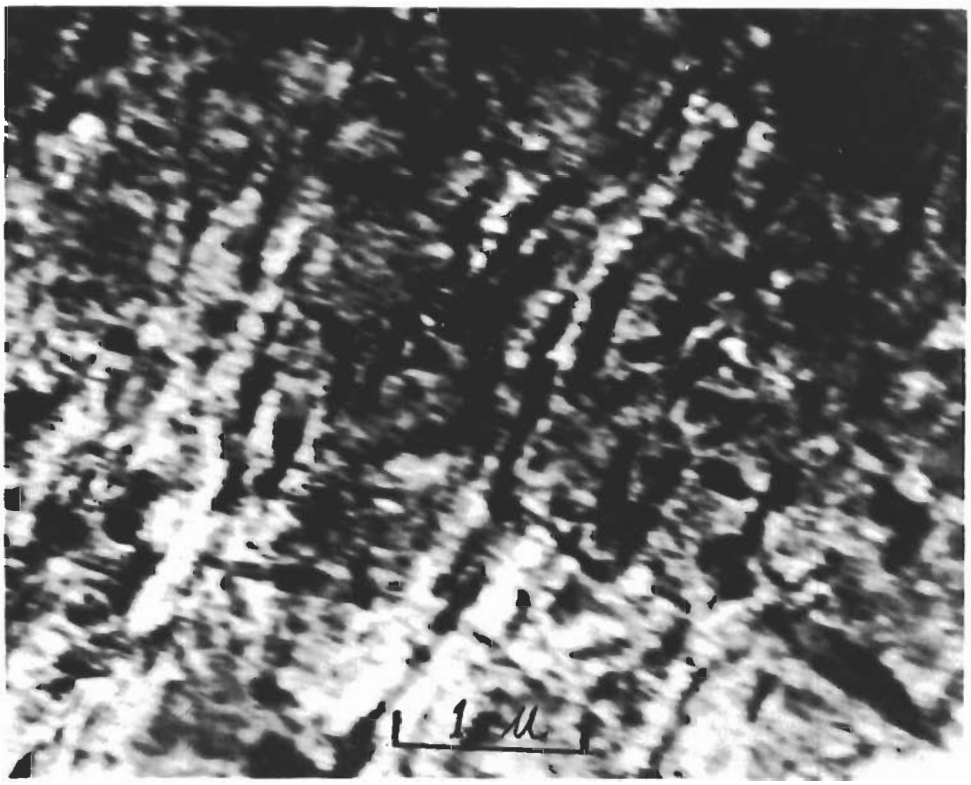

Fig. 174 - Microstructures of 18% Ni Maraging Steel

Heat treatment: 899°C (1650°F)-1 hr. A.C. + 815°C (1550°F)-1 hr. A.C. + 554°C (1030°F)-3 hr. A.C.
Tensile strength: 210.13 ksi; yield strength: 205.70 ksi
Rockwell hardness, R_c: 44.6

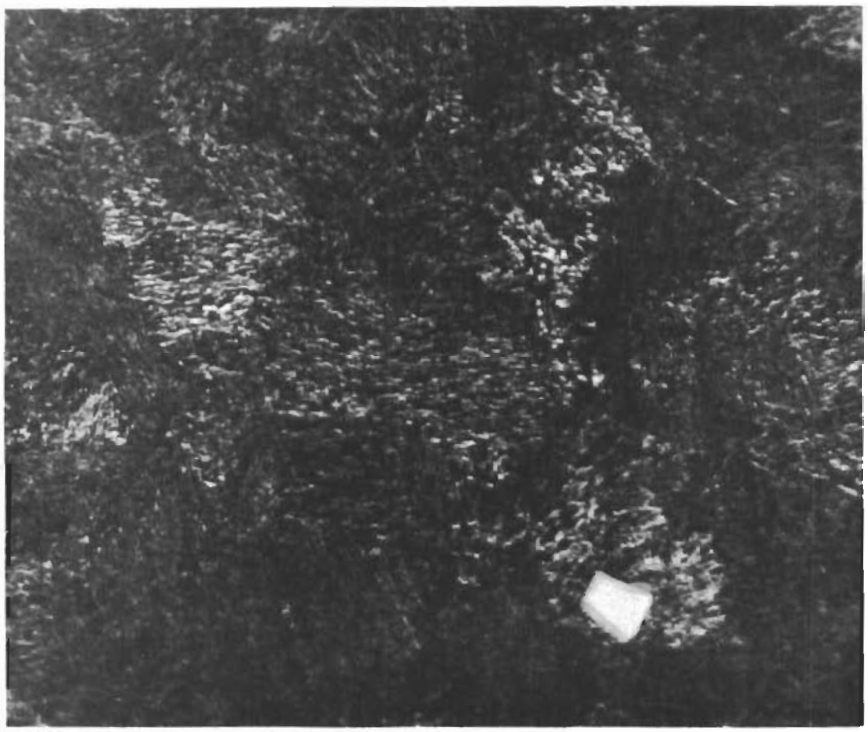

1200X

Fig. 175 - Optical Micrograph of 18% Ni Maraging (259) Steel

Heat Treatment: 898°C - 1 hr. A.C. + 815°C - 1 hr. A.C. + 582°C - 3 hr. A.C.
Tensile strength: 204.77 ksi; yield strength: 201.83 ksi
Rockwell Hardness, R_c: 47.3

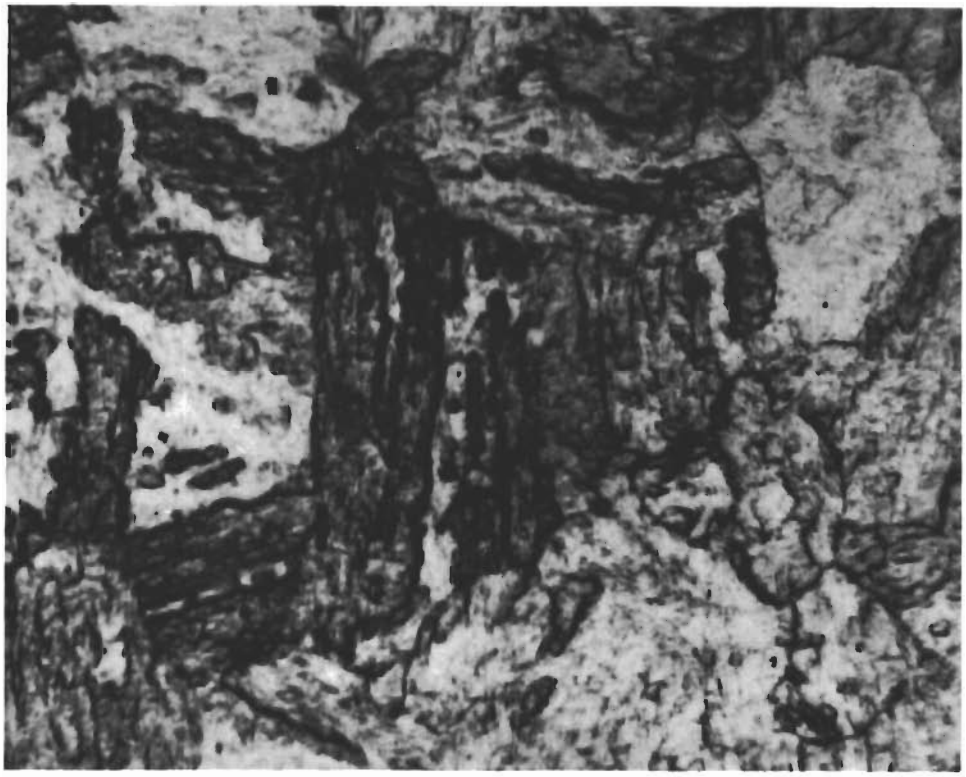

1200X

Fig. 176 - Optical Micrograph of 18% Ni Maraging (250) Steel

Heat treatment: 898°C - 1 hr. A.C. + 815°C - 1 hr. A.C. + 398°C - 3 hr. A.C.
Tensile strength: 202.44 ksi; yield strength: 202.44 ksi
Rockwell hardness, R_c: 47.5

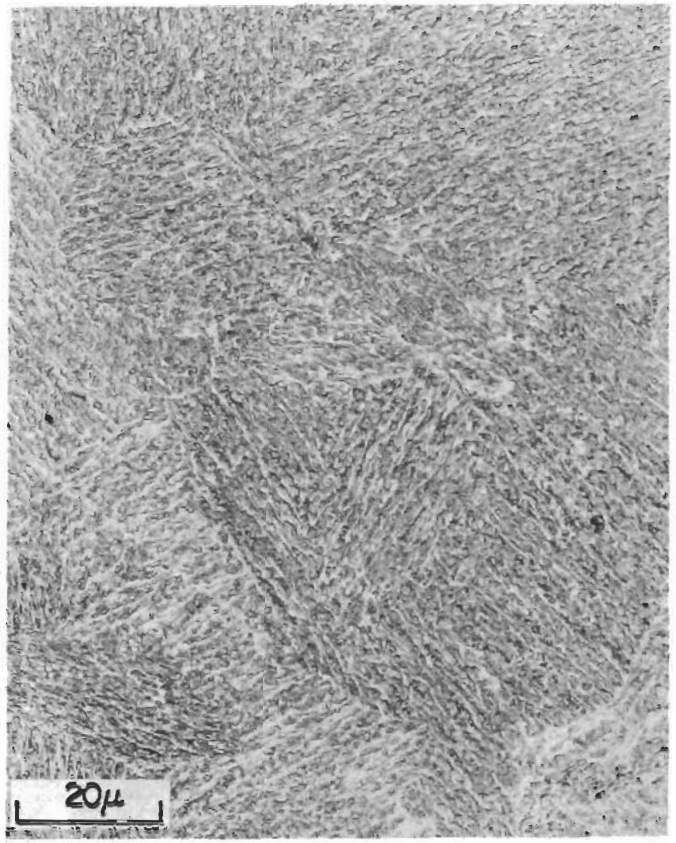

A. Magnification: 1000X

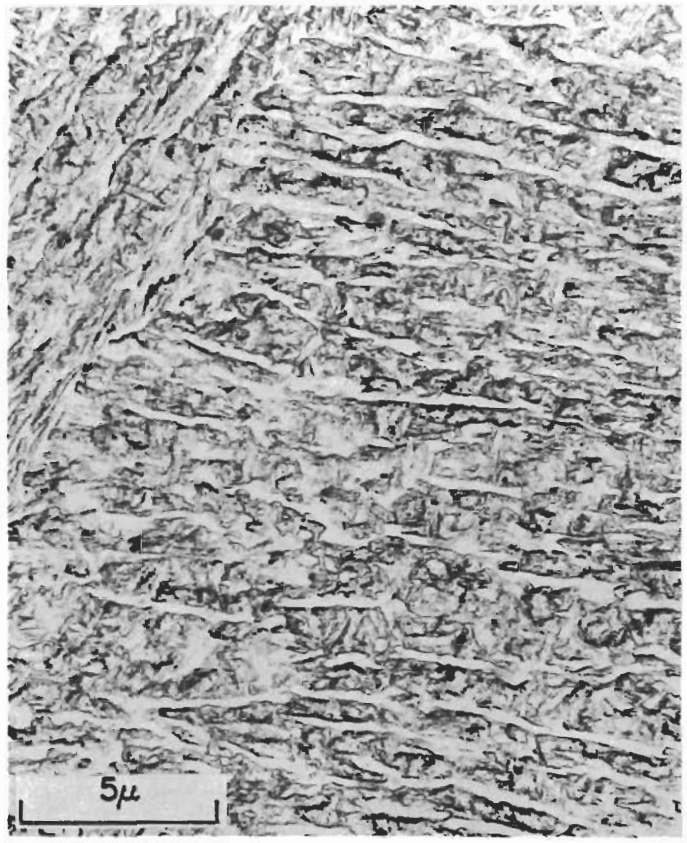

B. Magnification: 5000X

Fig. 177 - Electron Micrographs of Direct Carbon Replica of 582°C (1080°F) Overaged 18% Ni (250) Maraging Steel

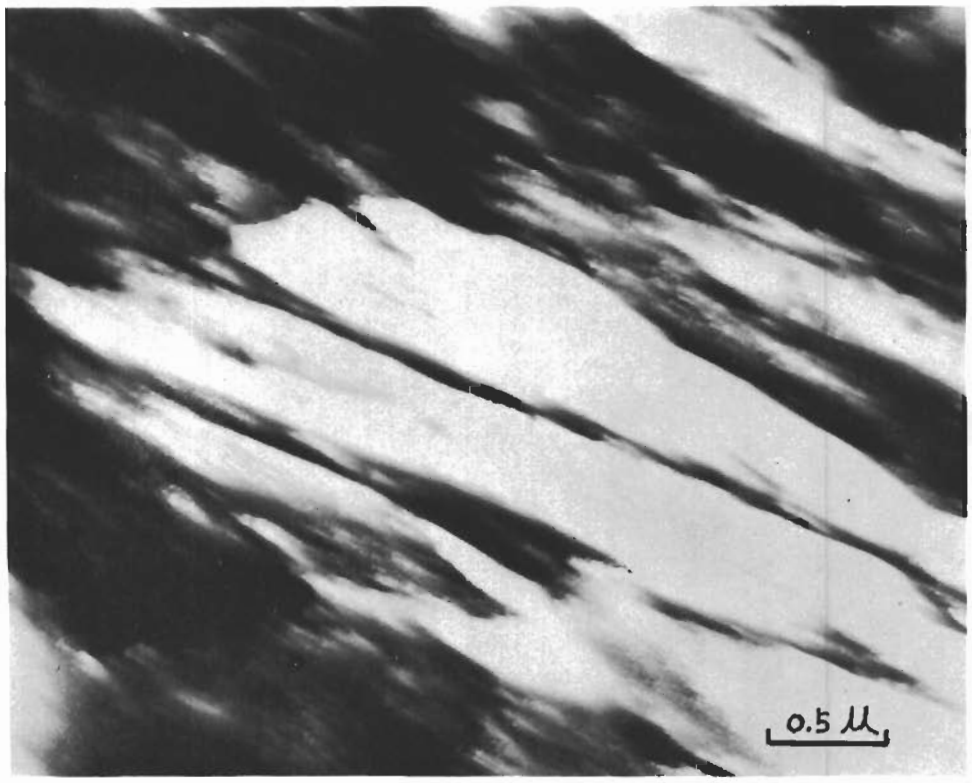

Fig. 178 - Morphology of Tempered Martensite in AISI 4340 Steel

Heat treatment: Oil quenched + tempering at 425°C (800°F) for one hour A.C.

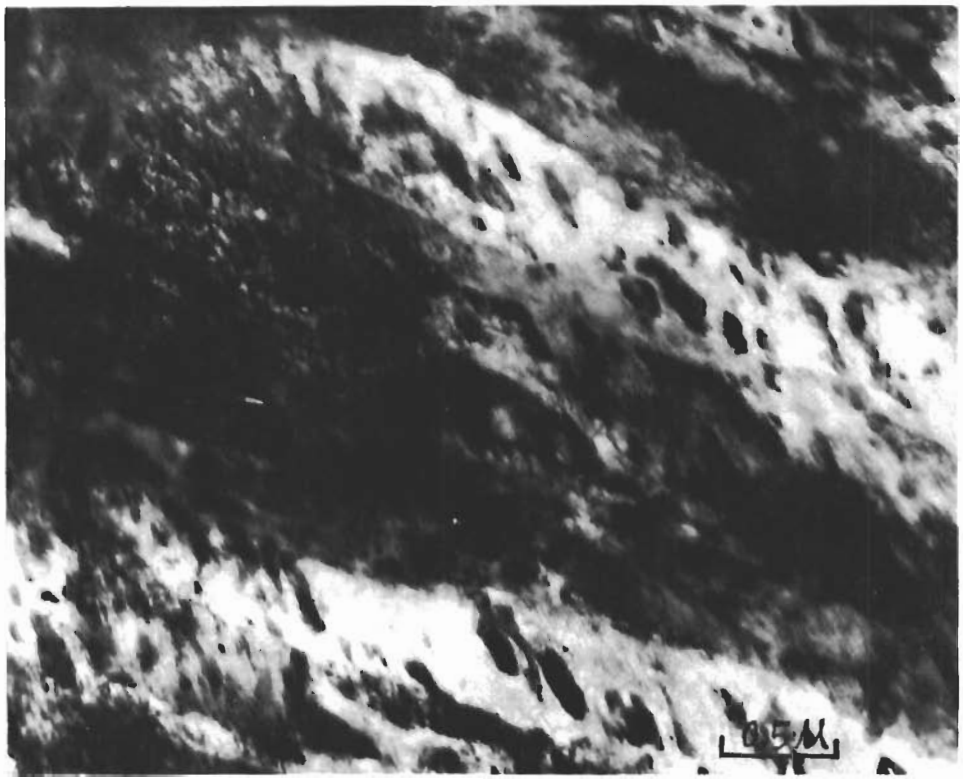

Fig. 179 - Morphology of Tempered Bainite in AISI 4340 Steel

Heat Tempering: Austempering at 315°C (600 ± 10°F) for 2 hr. A.C. + tempering at 400°C (750°F) for 1 hr A.C.

structure; this is in agreement with a review of literature showing that retained austenite is completely decomposed in the third stage of tempering. The carbides in both structures exhibit a similar morphology of the early stage of spheroidization. The amount of carbides appears to be more dense in tempered bainite than in tempered martensite. No further adjustments of the tempering temperatures have been made because of the identical strength requirement from a fracture mechanics consideration. The morphology and distribution of carbides are shown in Fig. 180. Intergranular fracture has been hypothesized to be related to the grain boundary precipitation of second phases; i.e., carbides. An extensive search of grain boundaries in the thin foils of both structures shows very clean grain boundaries without any carbide precipitation, as shown in Fig. 181.

c. Correlation of Crack Velocity to Microstructures

(1) AISI 4340 Steel--Two different types of microstructures (namely, quench and tempered martensite and quench and tempered lower bainite) have been produced in the test specimen of this steel. Both tempered martensite and tempered lower bainite test specimens were tempered for one hour at 426°C (750°F), respectively, to obtain an identical yield strength of 205 ksi with Rockwell hardness (R_c) ranging from 46.7 to 47.1. The resultant data of crack velocity (da/dt) as a function of applied load (P) for the two structures of the steel are shown in Fig. 182.

From the applied load vs. crack velocity of the tempered martensite and tempered lower bainite shown in Fig. 182, it can be seen that tempered martensite is more susceptible to the slow growth of subcritical cracks than tempered lower bainite at an identical strength, environment, and given applied stress intensity at crack tip. This shows that microstructure plays an important role for the slow growth of subcritical cracks in this steel.

From a metallurgical microstructural consideration, intergranular SCC of low-alloy, high-strength steel has been reported from time to time in the literature, and it is practically impossible to eliminate completely the intergranular SCC in both tempered martensite and tempered lower bainite of the AISI 4340 steel. To overcome this experimental dilemma, all test specimens have been subjected to identical normalizing and austenitizing treatments at 899°C (1650°F) and 843°C (1550°F), followed by tempering at 426°C (800°F) and 400°C (750°F) for the tempered martensitic and tempered lower bainitic specimens, respectively.

Identical normalizing and austenitizing treatments produce the same prior austenite grain size, while the tempering temperatures used in this investigation aim to avoid the possible tempered martensite embrittlement and the reversible tempered embrittlement, which is a typical intergranular embrittlement resulting from grain boundary impurity

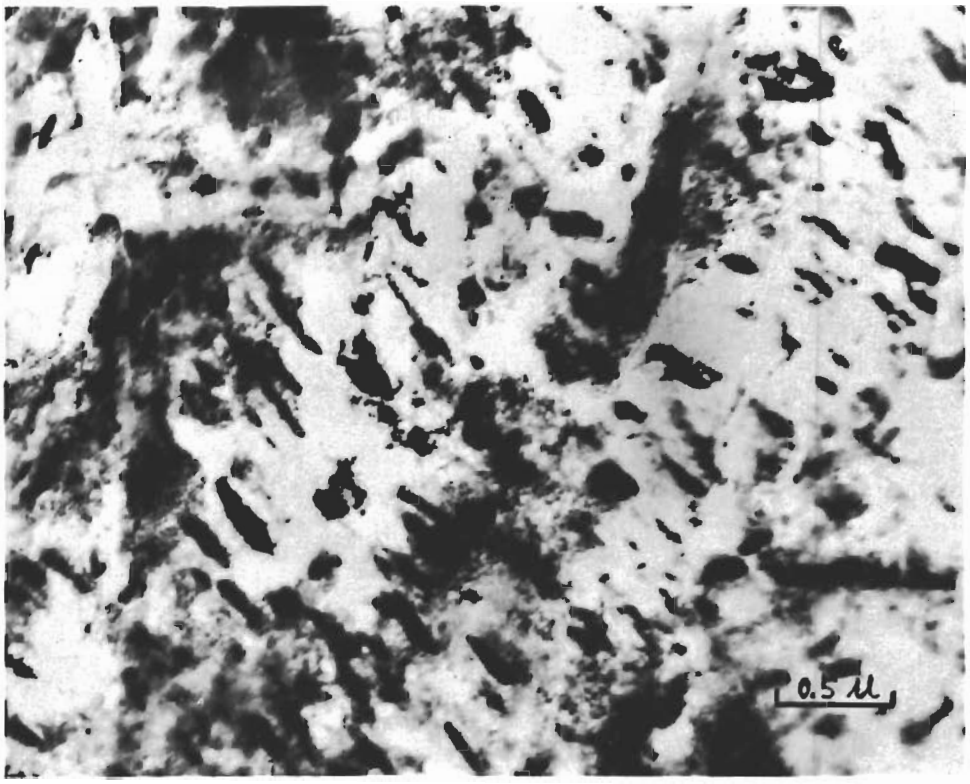

Fig. 180 - Morphology of Spheroidized Carbide in Tempered Bainite of AISI 4340 Steel

Heat Treatment: Austempering at 315°C (600 ± 10°F) for 2 hr. A.C. + tempering at 400°C (750°F) for 1 hr. A.C.

Fig. 181 - Grain Boundaries in AISI 4340 Steel of Tempered Bainite Structures Showing No Grain Boundary Precipitation of Carbides

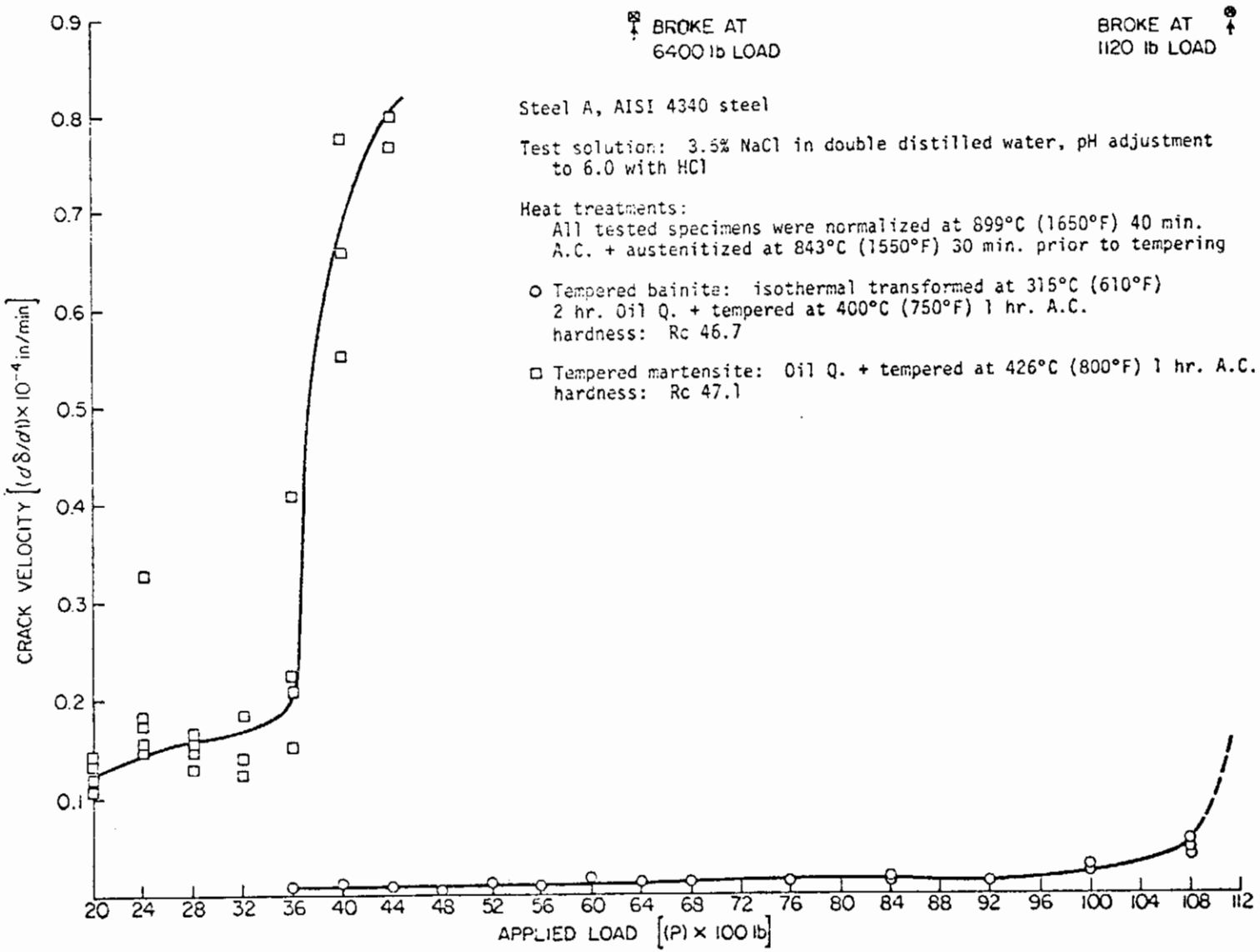

Fig. 182 - Subcritical Crack Growth of AISI 4340 Steel

segregation. Moreover, the tempering temperatures used in this investigation fall in the third stage of the tempering process, in which all the retained austenites are decomposed and all the coherent ϵ carbides in the early stage of tempering are transformed to noncoherent cementite (Fe_3C). Thus the heat treatments employed for both tempered martensite and tempered lower bainite yield similar grain size, morphology, and distribution of carbide phase. The significant difference in the crack velocity of the slow growth of subcritical cracks in tempered martensite and tempered lower bainite can be attributed to the inherent structural difference.

The significant differences in the substructures of martensite and lower bainite have been controversial for some time, especially tempered martensite and tempered bainite. The term lower bainite is defined as an isothermal transformation product of the bainite reaction just slightly above the martensite start (M_S) temperature whereas the upper bainite transformation reaction takes place at higher temperatures. Morphologically, upper bainite can be easily distinguished from lower bainite by its lamellar carbide characteristics. However, the internally precipitated carbide in the ferrite lath of lower bainite bears a morphology similar to martensite, especially when both are subjected to tempering treatment. Transmission electron microscopical examination of both tempered lower bainite and martensite morphology indicates that the fine spheroidized carbides tend to lie in a certain direction at an angle to the major axis of the ferritic lath, whereas the spheroidized carbides in martensite plates tend to be randomly distributed, and the interface between martensite plates are coherent interfaces which are essentially microtwins as identified from the selected area diffraction analysis and justified from the slight misorientation of twin plates through dark field technique, as shown in Figs. 183 and 184. The twin axis and plane were observed to be [110] and (110), respectively. Recent examination of the bainite lath interfaces through selected area diffraction analysis shows that the bainite laths are noncoherent with highly misoriented interfaces, as shown in Fig. 185. From this experimental evidence, it is conceivable that the essential microstructural differences between tempered martensite and tempered lower bainite are the coherent twin interfaces of martensite plate and the noncoherent interface of bainite laths. Correlation of the two structures with the crack velocity of the slow growth of subcritical cracks in AISI 4340 steel indicates that the coherent microtwins in tempered martensite are primarily responsible for the enhancement of SCC in AISI 4340 steel.

(2) 18% Ni (250) Maraging Steel--Five aging treatments have been carried out in the 18% Ni (250) maraging steel with two pairs of identical strength levels and one standard commercial aging at 510°C (950°F) for three hours which gives a maximum achievable strength of 235 ksi to this grade. In order to minimize the contribution from intergranular SCC, double austenitizing treatment at 898°C (1650°F) and 815°C (1500°F) for one hour was employed to prevent the change in grain size during subsequent aging and to avoid any possible thermal embrittlement resulting from grain boundary segregation. The experimental results of

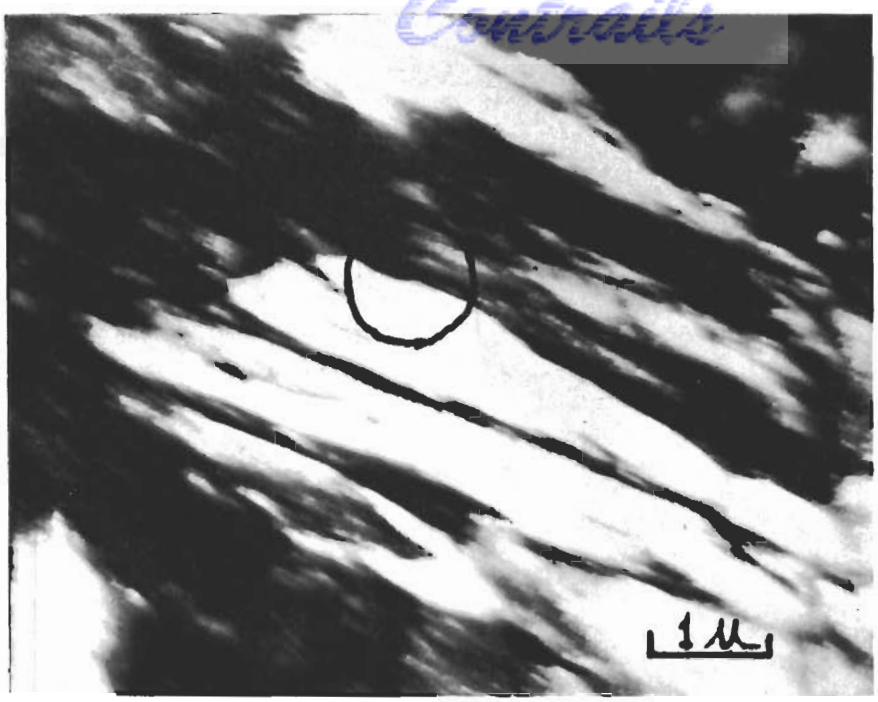

a. Martensite plate in tempered martensite of AISI 4340 steel. Circle indicates selected area.

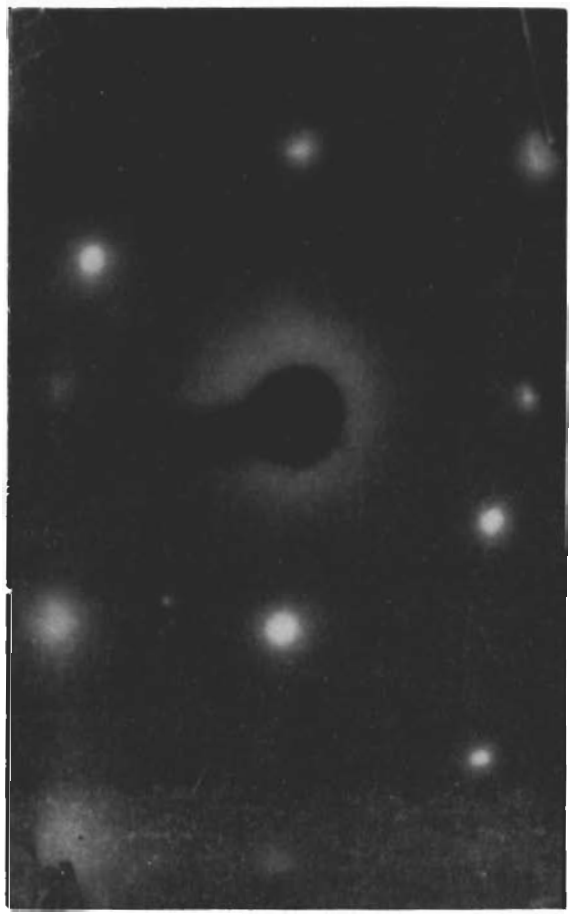

b. Selected area diffraction of encircled area

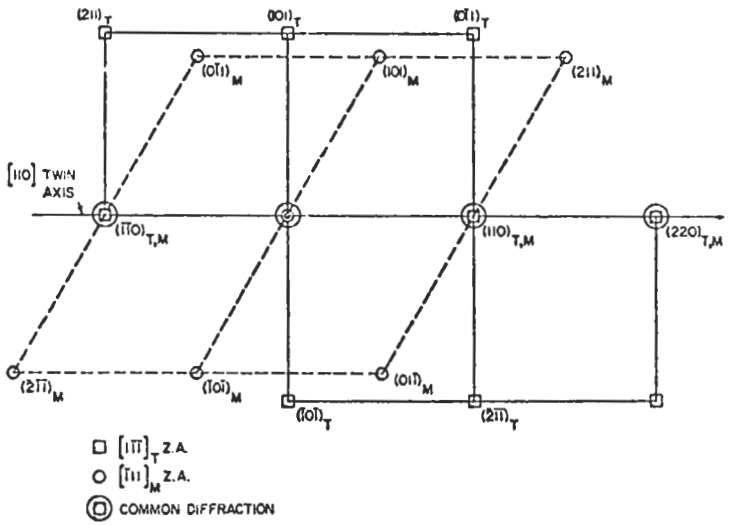

c. Analysis of diffraction pattern

Fig. 183 - Analysis of Selected Area Diffraction Patterns from a Pair of Twin Plates in Tempered Martensite of AISI 4340 Steel

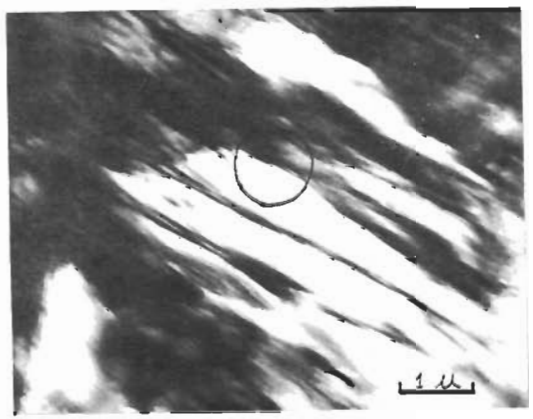

A. Bright field of tempered martensite plates. Circle indicates selected area

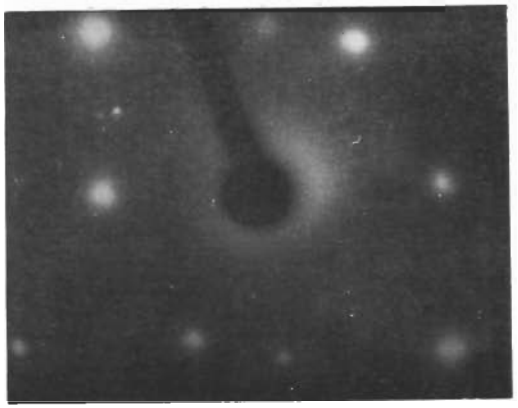

B. Selected area diffraction of encircled area

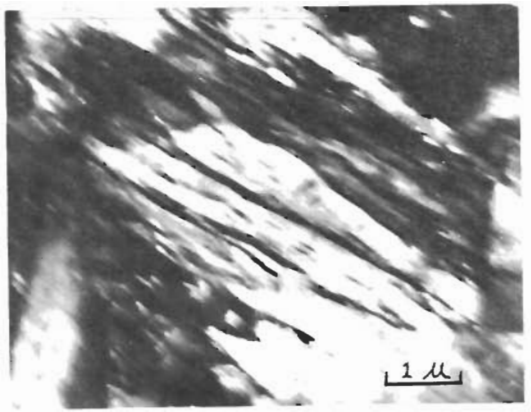

C. Dark field of spot A, the common diffraction of both twin and matrix at $[\bar{1}\ \bar{1}\ 0]$ direction

D. Dark field of spot C, $[0\ \bar{1}\ 1]_T$ direction of twin

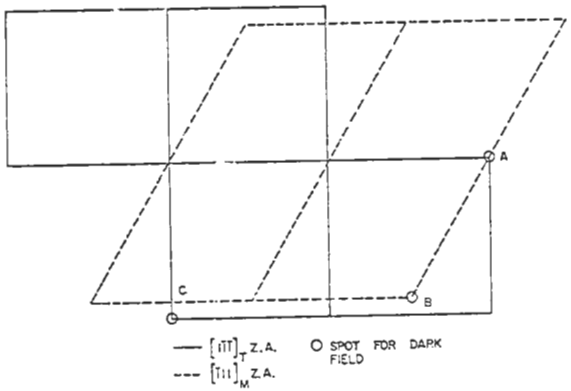

E. Trace of diffraction pattern from B.

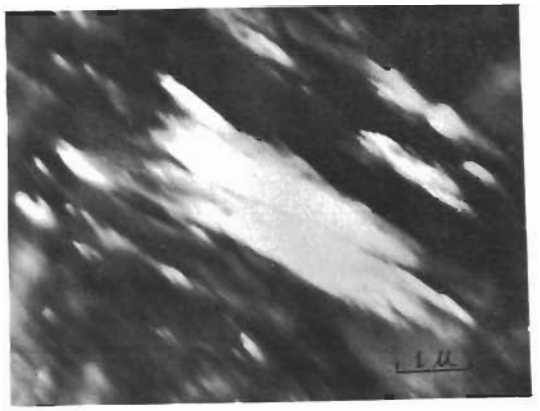

F. Dark field of spot B, $[0\ \bar{1}\ \bar{1}]_M$ direction of matrix.

Fig. 184 - Slight Misorientation of Tempered Martensite Plates in AISI 4340 Steel with Selected Area Diffraction and Dark Field Techniques (Index of diffraction patterns, see Fig. 183)

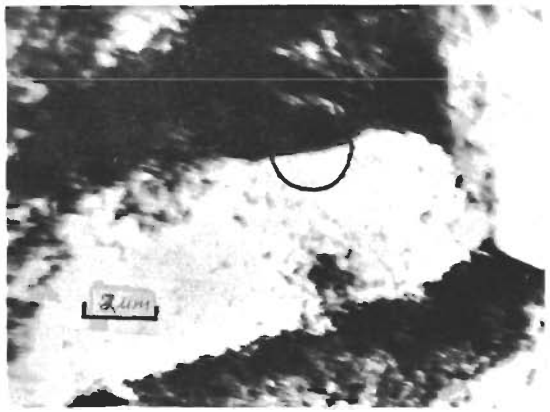

A. Bainite laths in tempered lower bainite. Circle indicates selected area.

B. Selected area diffraction of bainite laths interface in the encircled area.

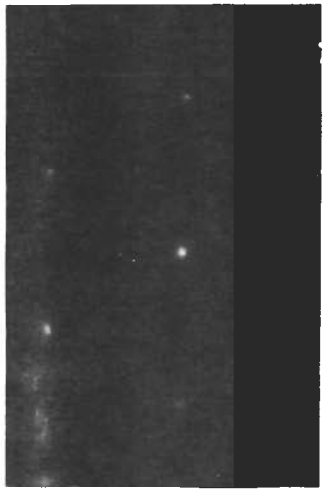

C. Diffraction from white area.

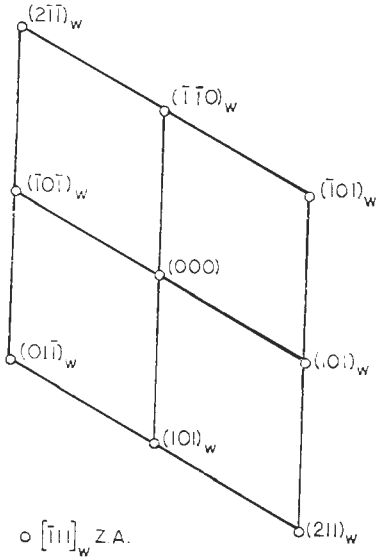

D. Diffraction analysis of white area from C.

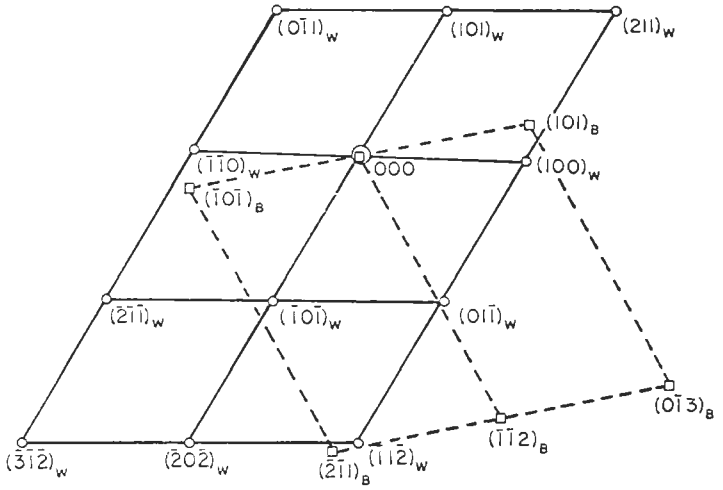

E. Diffraction analysis of bainite laths interface from B.

Fig. 185 - Analysis of Selected Area Diffraction Patterns from a Pair of Noncoherent Bainite Laths in Tempered Lower Bainite of AISI 4340 Steel

crack velocity (dδ/dt) as a function of applied load for the 18% Ni (250) maraging steel with various microstructural alterations, are shown in Fig. 169. It is worthwhile to note that the early stage aging [such as aged at 399°C (750°F) for 3 hours] of 18% Ni (250) maraging steel with highly coherent precipitates results in a strong susceptibility to SCC. As a result, no reliable crack velocity can be obtained from this aging condition in this investigation, and difficulties arise from the arm breakage of the tapered double-cantilever-beam specimens.

It can be readily seen from Fig. 169 that early stage aging results in a rapid crack propagation, in contrast to strength maximum or over-aging conditions of identical strength on the 18% Ni (250) maraging steel. This is attributed to the alteration of microstructures and can be rationalized from detailed microstructures. Detailed thin foil transmission electromicroscopic examinations of the steel with various heat treatments have been reported. The essence is that early-stage aging produces incoherent precipitates of intermetallic compounds with smaller dislocation cell substructures which are inherited from the massive transformation of the iron-nickel cubic martensite in the steel. Meanwhile the dislocation cell substructures increase in size as aging proceeded and vanished in the over-aged condition. The term over-aged condition is based on the strength maxima criteria and is defined as aging beyond the maximum strength condition; namely, the standard commercial aging at 510°C (950°F) for three hours. The microconstituents in over-aged condition are noncoherent intermetallic compound precipitates and reversion austenite embedded in the aged martensite matrix. An increased amount of reversion austenite has been observed in the over-aged condition as aging proceeds. It is of practical importance to mention the morphology of reversion austenite which is observed first in the strength maximum condition, and encircling the substructure boundaries. As aging proceeds the cell substructure disappears and the reversion austenite grows in a form of vein structures. Further aging leads to a lamellar structure embedded in the aged martensite matrix.

Correlation of crack propagation with the aging condition of this steel indicates that there exists a significant difference in crack velocities between the under-aged condition and over-aged condition, whereas the crack velocities between strength maximum and different over-aged conditions are small. From a microstructural point, reversion austenite is responsible for enhancement of ductility in the maraging steel and hence contributes somewhat to the resistance of crack propagation in SCC. However, the increase of a substantial amount of reversion austenite gains only slightly in the crack propagation resistances as observed from Fig. 184 for the three high-temperature aging conditions. Thus, it is logical to deduce that the small contribution of reversion austenite to the crack propagation resistance may be attributed primarily to the morphology rather than the amount present. Especially, the small amount of reversion austenite outlining the cell substructural boundaries, as observed in the strength maximum condition, may greatly improve the crack propagation resistance.

In the under-aged condition, the lowest-temperature-aged [i.e., 399°C (750°F)] condition which was exhibited, a severe SCC susceptibility led to difficulty in obtaining reliable crack velocity measurements. No comparison of crack velocity can be made at this aged condition to the other higher-temperature under-aged condition [i.e., 438°C (820°F)]. Nevertheless, there is no doubting the assertion that a higher-temperature under-aged condition produces a substantial crack propagation resistance. The important structural features in the under-aged conditions are coherent precipitates of intermetallic compounds and the dislocation cell substructures. Increased aging temperature in an under-aged condition leads to the reduction of both the dislocation cell size and the coherence of precipitates; these substructures are primarily responsible for the enhancement of crack propagation of the SCC in maraging steel.

(3) Summary of Microstructural Effects on SCC--Correlation of microstructures on the crack propagation of SCC for the two high-strength steels leads to the following conclusions:

a. The transgranular mode, as well as the intergranular mode, plays an important role in the SCC of both AISI 4340 and 18% Ni (250) maraging high-strength steels.

b. Tempered lower bainite exhibits a superior SCC resistance to that of tempered martensite in AISI 4340 steel. The major enhancement of SCC in tempered martensite is attributed to coherent twin boundaries of martensite.

c. The major responses for the enhancement of SCC in 18% Ni (250) maraging steel are the dislocation cell substructures and coherent precipitates of intermetallic compounds, whereas a small amount of reversion austenite encircling the dislocation cell substructures greatly improves the SCC resistance.

d. The common microstructure feature responsible for the enhancement of SCC in both high-strength steels is the coherent interface.

Since it is assumed that hydrogen embrittlement controls the mechanism of SCC of high-strength steel, it is logical to assume that hydrogen trapping at the coherent interface is the major factor in the SCC of high-strength steel. The hydrogen trapping results from the interaction of hydrogen and the high-strength steel, through strain energy reduction. To test this hypothesis, a new task was initiated recently on the study of hydrogen permeation behavior of high-strength steels. It is anticipated that a significant hydrogen trapping parameter may be obtained to assess the hydrogen trapping at the coherent interface.

6. Analysis of Stress Intensity Independency of Crack Velocity

A number of investigators[129,130] have recently observed the phenomenological fact that there exists a range of stress intensity independency of crack velocity in the high-strength steels and a number of high-strength alloys. Such a phenomenon can be observed when crack velocity (da/dt) is plotted logarithmically as a function of applied stress intensity (K_I), as shown in Fig. 186. The presence of stress intensity dependence of crack velocity (region II of Fig. 186 is not clearly understood. Speidel[130] in his crack velocity measurements on a group of high-strength aluminum alloys with untapered WOL double cantilever beam specimens, shows that the slopes of crack velocity versus applied stress intensity $d(da/dt)/dK_I$ for region II are essentially zero for a number of aluminum alloys, and the presence of region II is strongly dependent on environmental species and insensitive to material properties. Thus, Speidel suggests that the shift of the region II in V - K curve is attributed to the limitation of the mass transport process of the environmental species at crack tip. In order to assess the existence of such a behavior of the V - K curve on high-strength steels, plots of crack velocity versus applied stress intensity in terms of applied load (V - K curve) for all heat-treatment conditions of both AISI 4340 and 18% Ni (250) maraging steels are shown in Figs. 187-192. The validation for the expression of applied stress intensity (K) in terms of applied load (P) for the tapered double cantilever beam specimen has been justified in previous discussions.

It is clearly shown in Figs. 187-192 that, indeed, there does exist the stress intensity independency of crack velocity (region II) in the V - K curves for the two high-strength steels with all types of microstructures observed in this investigation. The absence from region I in the V - K curve of the two steels with different microstructures is attributed to the limitation of crack velocity measurements in the experimental set-up used for this investigation. The ranges of region II in the V - K curve depend on alloy chemistry [AISI 4340 steel versus 18% Ni (250) maraging steel] as well as on the alteration of microstructures.

It is important to point out that the slopes of crack velocity versus stress intensity $d(da/dt)/dK_I$ are not zero in the high-strength steels used in this investigation. This strongly suggests that microstructures play an important role in the shift of region II in V - K curve, as well as in the limitation of the mass transport process of environmental species at crack tip. Based on the present data obtained from the two high-strength steels, a trend can be deduced; i.e., that a steel with a high degree of susceptibility to SCC, region II in V - K curve, tends to have a narrower range and shift to higher crack velocity as evidenced from Figs. 188 and 189. On the other hand, region II tends to cover a wider range of applied stress intensity with a shift toward lower crack velocity for stronger SCC resistant steels as evidenced from

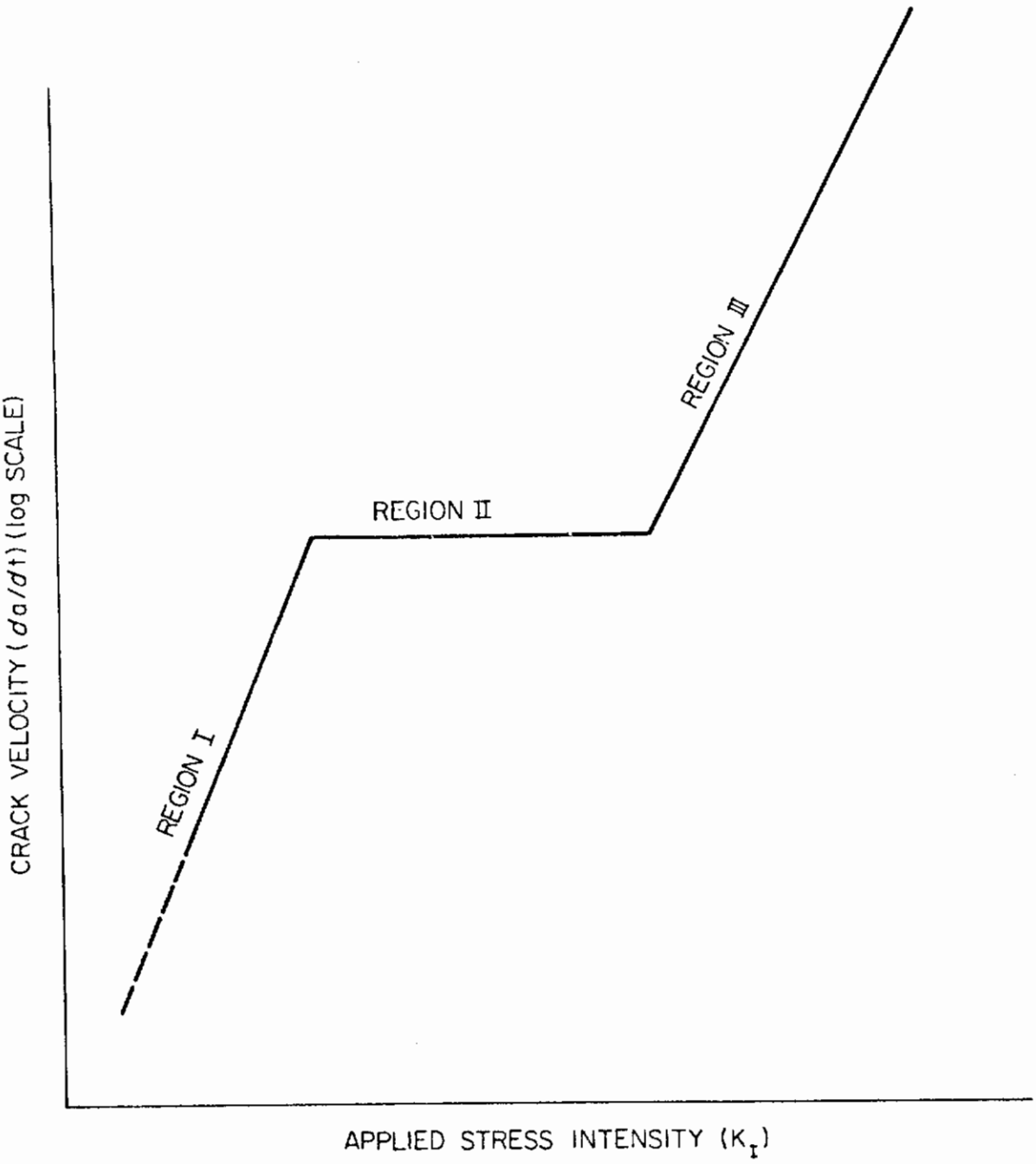

Fig. 186 - Schematic Curve of Logarithmic Crack Velocity versus Applied Stress Intensity on Stress Corrosion Cracking

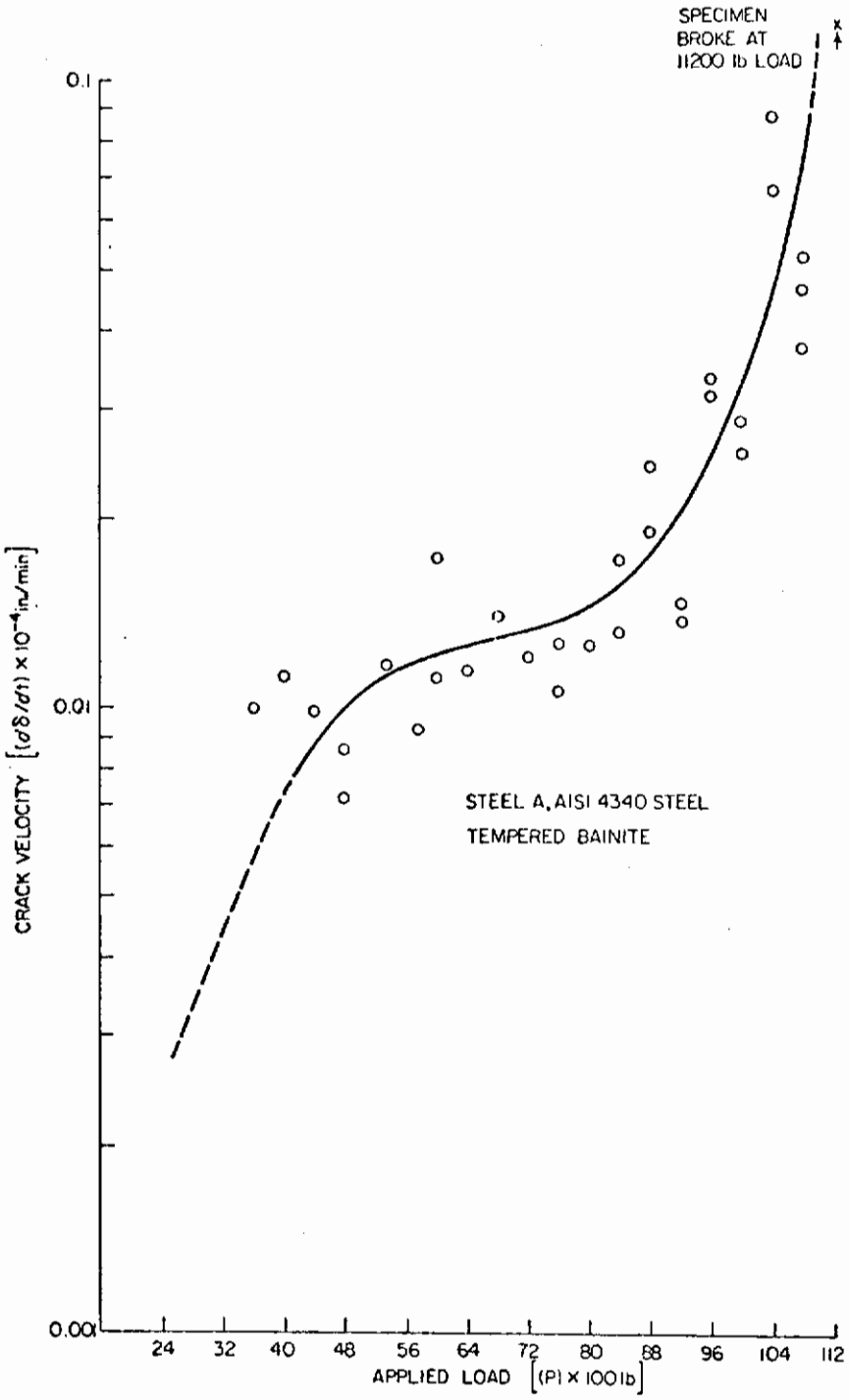

Fig. 187 - V-K Curve for Tempered Bainite in AISI 4340 Steel

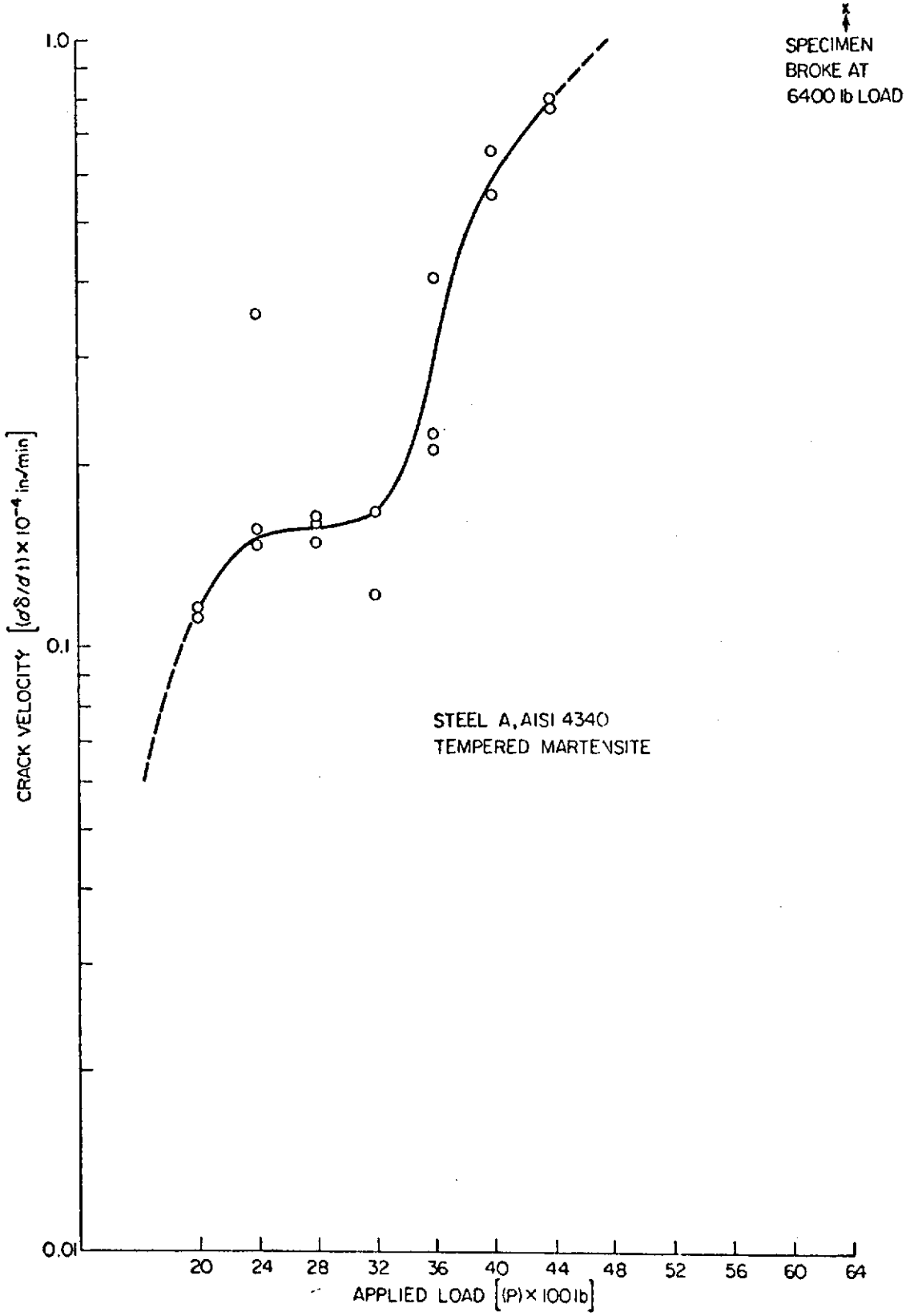

Fig. 188 - V-K Curve for Tempered Martensite in AISI 4340 Steel

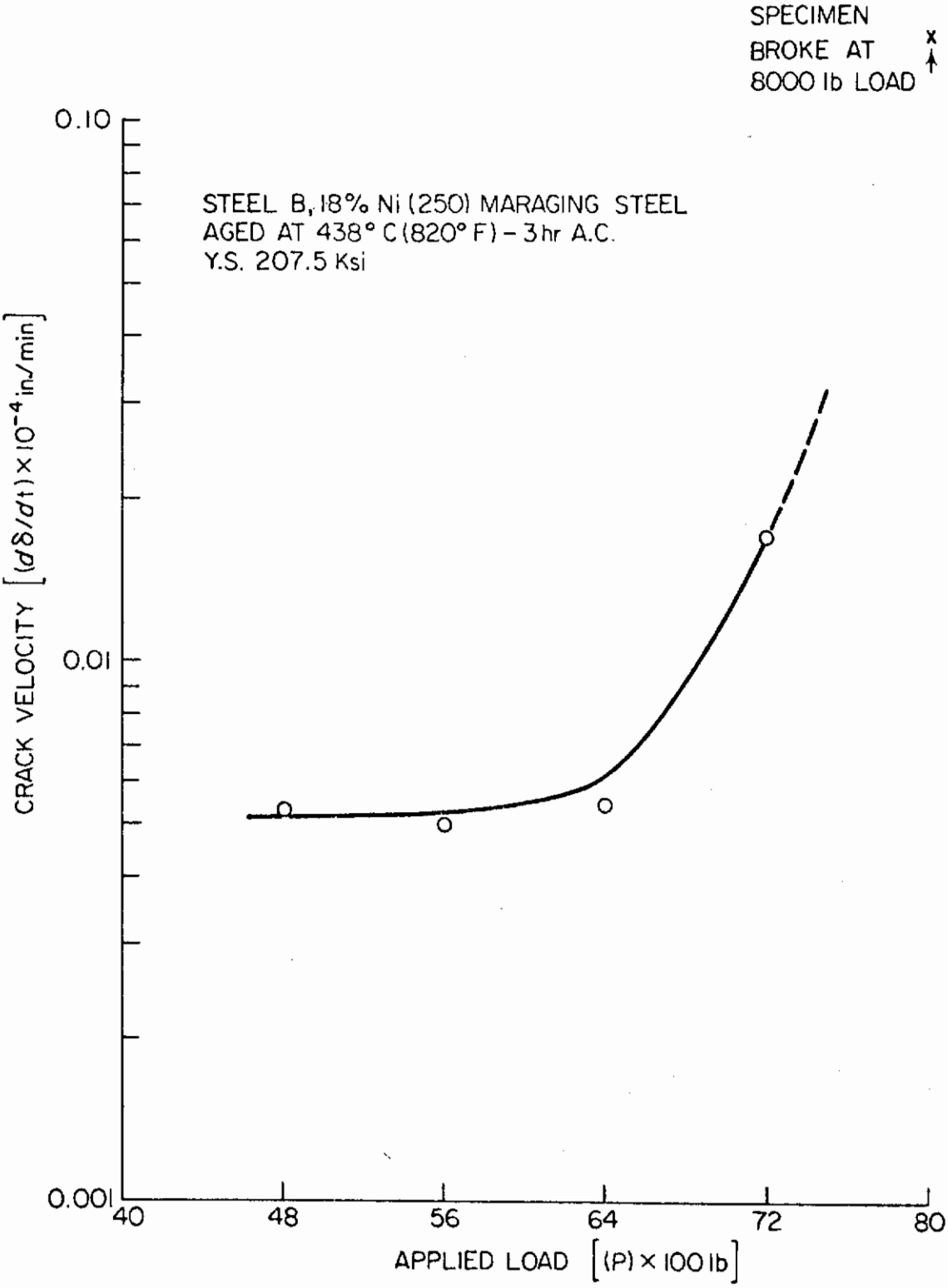

Fig. 189 - V-K Curve for 18% Ni(250) Maraging Steel Aged at 438°C (820°F) - 3 Hours A.C.

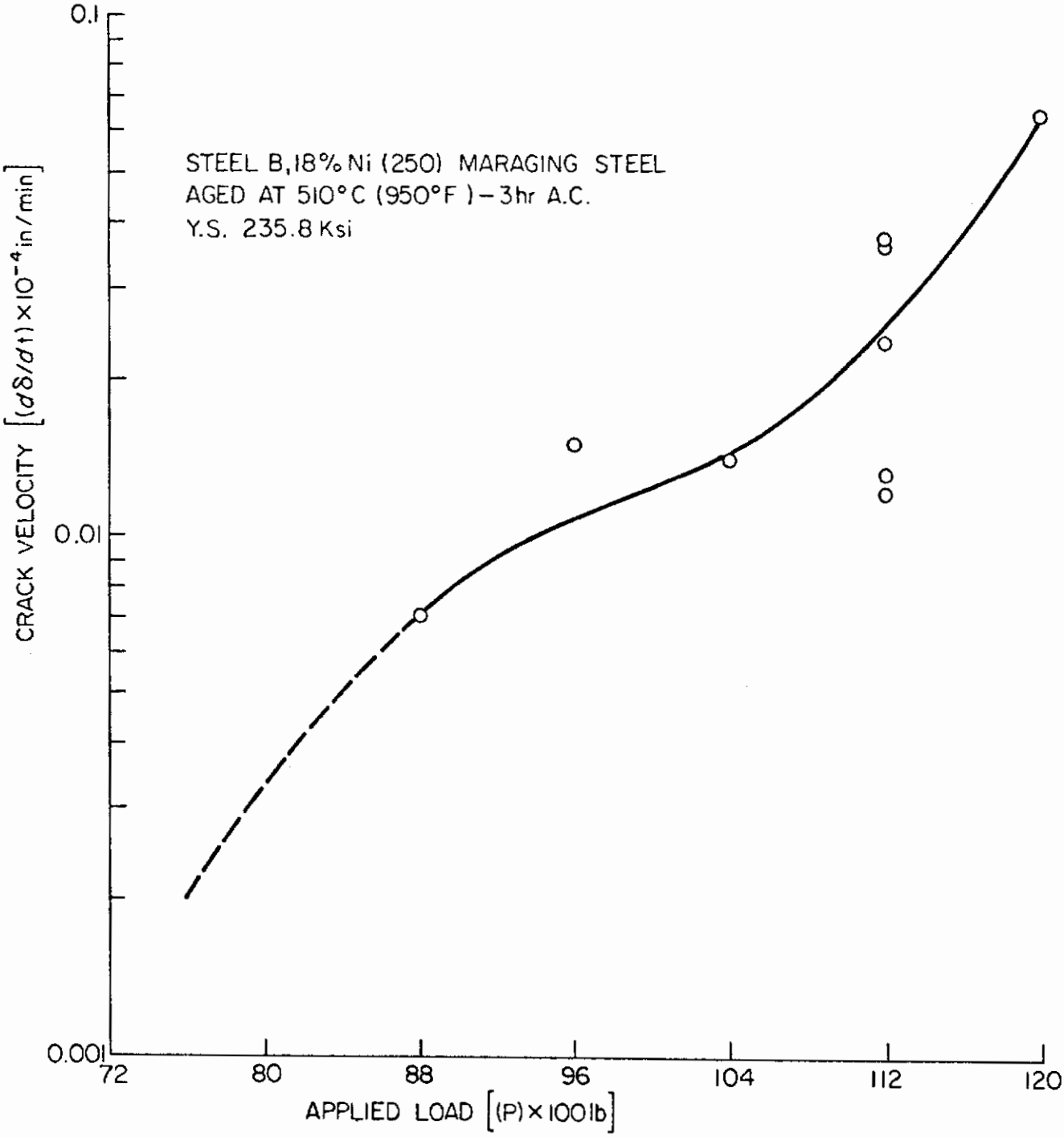

Fig. 190 - V-K Curve for 18% Ni(250) Maraging Steel Aged at 510°C (950°F) - 3 Hours A.C.

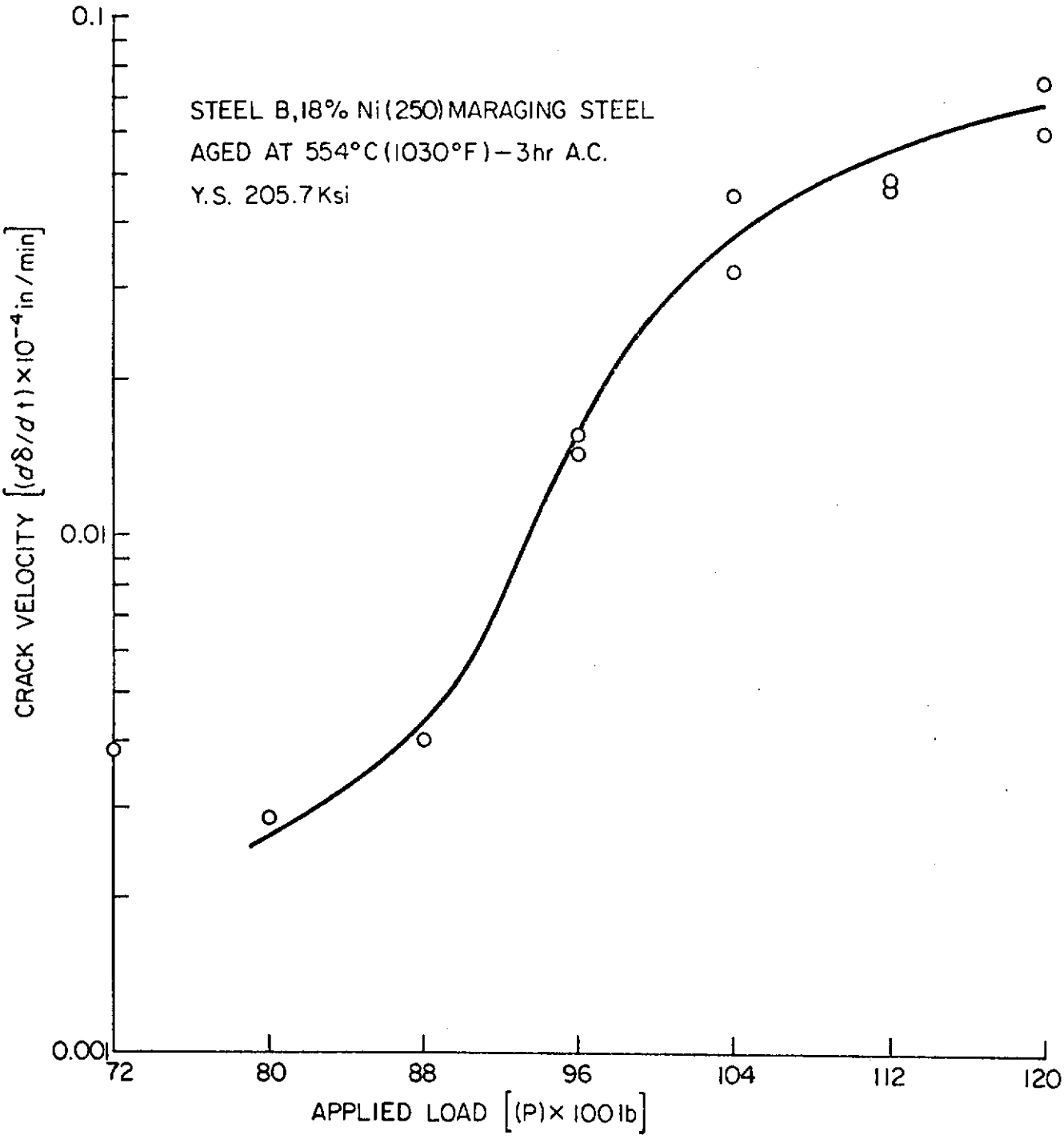

Fig. 191 - V-K Curve for 18% Ni(250) Maraging Steel Aged at 554°C (1030°F) - 3 Hours A.C.

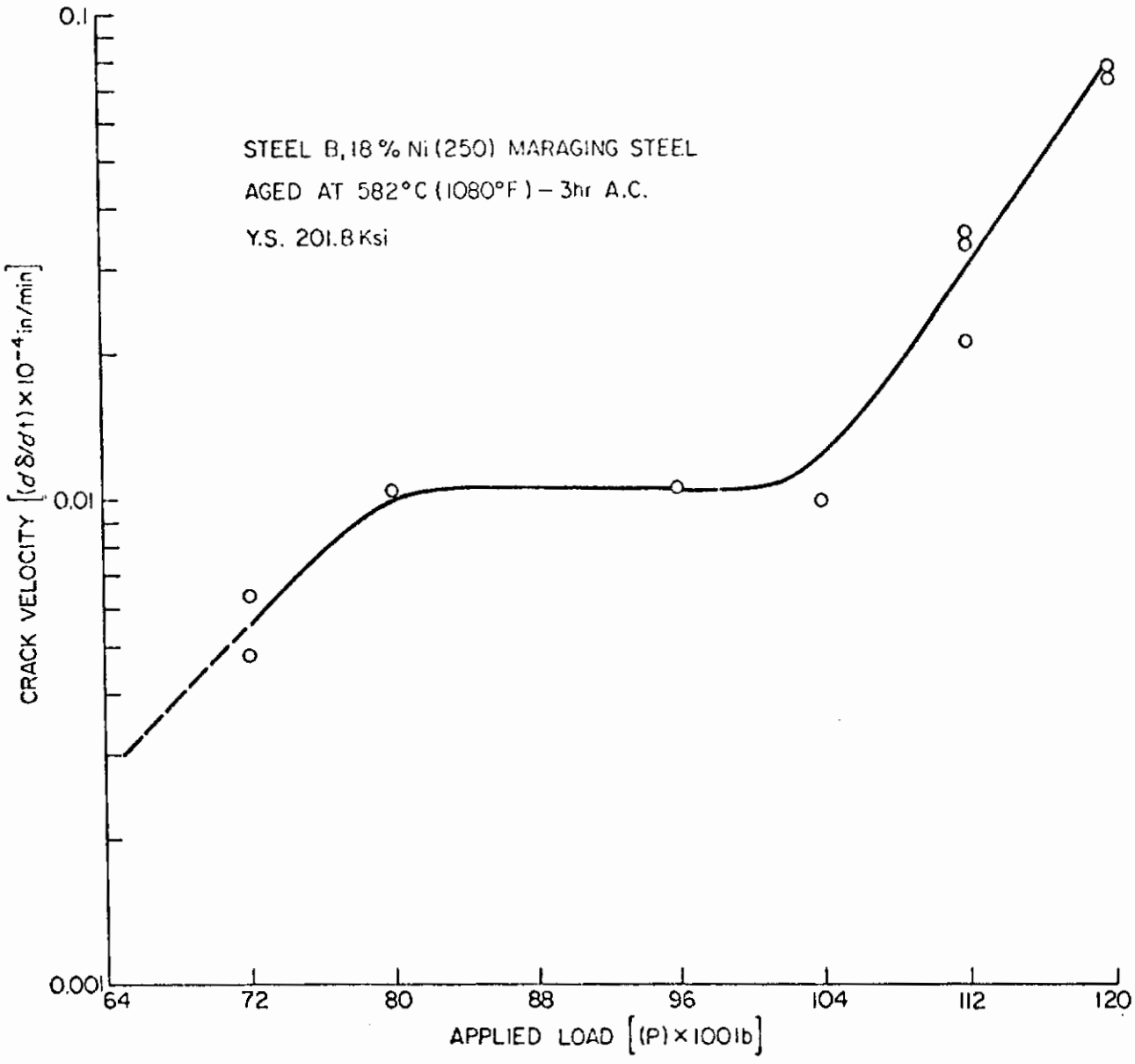

Fig. 192 - V-K Curve for 18% Ni(250) Maraging Steel Aged at 582°C (1080°F) - 3 Hours A.C.

the V - K curve of bainitic AISI 4340 steel and over-aging conditions of 18% Ni (250) maraging steel. However, theoretical models based on material properties have not been established to rationalize this phenomenon of stress intensity independency of crack velocity.

C. HYDROGEN PERMEATION BEHAVIOR OF HIGH-STRENGTH STEELS (M. T. Wang)

1. Aims and Significance

The objective of this study is to investigate the hydrogen permeation behavior of high-strength steels as affected by the alteration of metallurgical microstructures. Since there exist complexity and variety of alloy chemistry and microstructures in high-strength steels, theories and mathematical models developed for the diffusion and permeation of hydrogen through pure iron, or a simple binary alloy, may not be applicable to high-strength steels. It is anticipated that a significant parameter can be obtained through a systematic permeation study of a series of microstructures of high-strength steels to account for the abnormal diffusion characteristics and the variety of hydrogen permeation behaviors, especially the hydrogen trapping effects.

2. Background

Studies of the effect of metallurgical structure on stress corrosion cracking of high-strength steels suggest that a hydrogen-related mechanism controls the SCC. Since hydrogen is believed to be in solid solution in high-strength steel, direct evidence of hydrogen interaction in high-strength steel lattice and the trapping effects are difficult to assess. It is hoped that investigation of hydrogen permeation kinetics and transient behaviors will lead to a quantitative parameter for evaluating the hydrogen trapping effect in high-strength steel.

a. Material Experiments and Specimen Preparation

Two high-strength steels [i.e., 18% Ni (250) maraging steel and AISI 4340 steel] are used in this investigation. These steels were cold rolled from 1/4-inch thickness to a final thickness of 4 mils. After cold working, 18% Ni (250) maraging steel was softened by an intermediate step anneal in an evacuated quartz capsule. However, no intermediate step anneal has been done for AISI 4340 steel because of the decarburization problem. Heat treatments used for the steels investigated are identical to those used in the crack propagation studies. Detailed alloy chemistry and heat treatments for these steels have been reported previously. The identical heat treatments used in both crack propagation studies and hydrogen permeation experiments not only provide well-controlled microstructures but also yield vital information about hydrogen trapping effects for the evaluation of the hydrogen embrittlement mechanism controlling the slow growth of subcritical cracks of these

high-strength steels. Because of the thinness of the specimens used in this investigation, these specimens were sandwiched in thick plates of identical material and encapsuled in an evacuated quartz tube during heat treatment to prevent surface oxidation decarburization and warpage. All specimens were slightly electrolytically thinned to remove oxide film and subsequently activated by dipping into 3% H_2So_4 in methanol for five minutes prior to hydrogen permeation experiments.

b. Hydrogen Permeation Experiments

The hydrogen permeation arrangement used in this investigation is similar to that used by McCright,[131] with slight modification, as shown in Figs. 193 and 194. Constant current of 2.58 mA/cm^2 is used for cathodic charging to maintain a constant source of hydrogen absorption on the steel surface of the hydrogen entry side. In order to increase hydrogen permeation efficiency, a thin coating of palladium has been plated on the hydrogen exit side to increase the hydrogen exchange current density for the oxidation of exit hydrogen. A negative potential of -50 mV (SCE) is potentiostatically charged to the hydrogen exit side in a 0.2N NaOH solution such that a background current between 0.2 $\mu A/cm^2$ can be obtained in the hydrogen exit side within a relatively short time. The permeated hydrogen, in terms of anodic permeation currents, was monitored through a Weking Model 121 potentiostat, a Keithley 601 B electrometer, and an Esterline Augus 10-inch strip chart recorder.

In the hydrogen entry side (cathodic side) 0.1 N H_2SO_4 solutions with different amounts of $NaAsO_2$ additions have been used; poor permeation efficiency and abnormal permeation currents were obtained. However, an identical 0.2 N NaOH solution used in the hydrogen entry, as well as in the hydrogen exit, side is found to have a higher permeation efficiency and satisfactory permeation behavior. The contradiction of electrochemical principle may be attributed to the extremely low hydrogen permeability in high-strength steels and the crevice corrosion effects between the teflon washer and steel specimens. Thus, 0.2 N NaOH solutions were used in the hydrogen entry side in this investigation.

3. Results and Discussion

a. Hydrogen Permeability (J_∞)

Direct correlation of crack velocity to the hydrogen permeability (J_∞)(i.e., steady state hydrogen permeation) in high-strength steels appears to be rather difficult, as revealed from Tables XXIV and XXV, where crack velocities are shown in a descending order for various microstructures in the two steels investigated. For AISI 4340 steel, no direct correlations are exhibited between permeability and crack velocity among martensite and bainite under different tempering conditions, as delineated in Table XXVI; whereas, the permeabilities (J_∞) in 18% Ni (250) maraging steel decrease progressively as a function

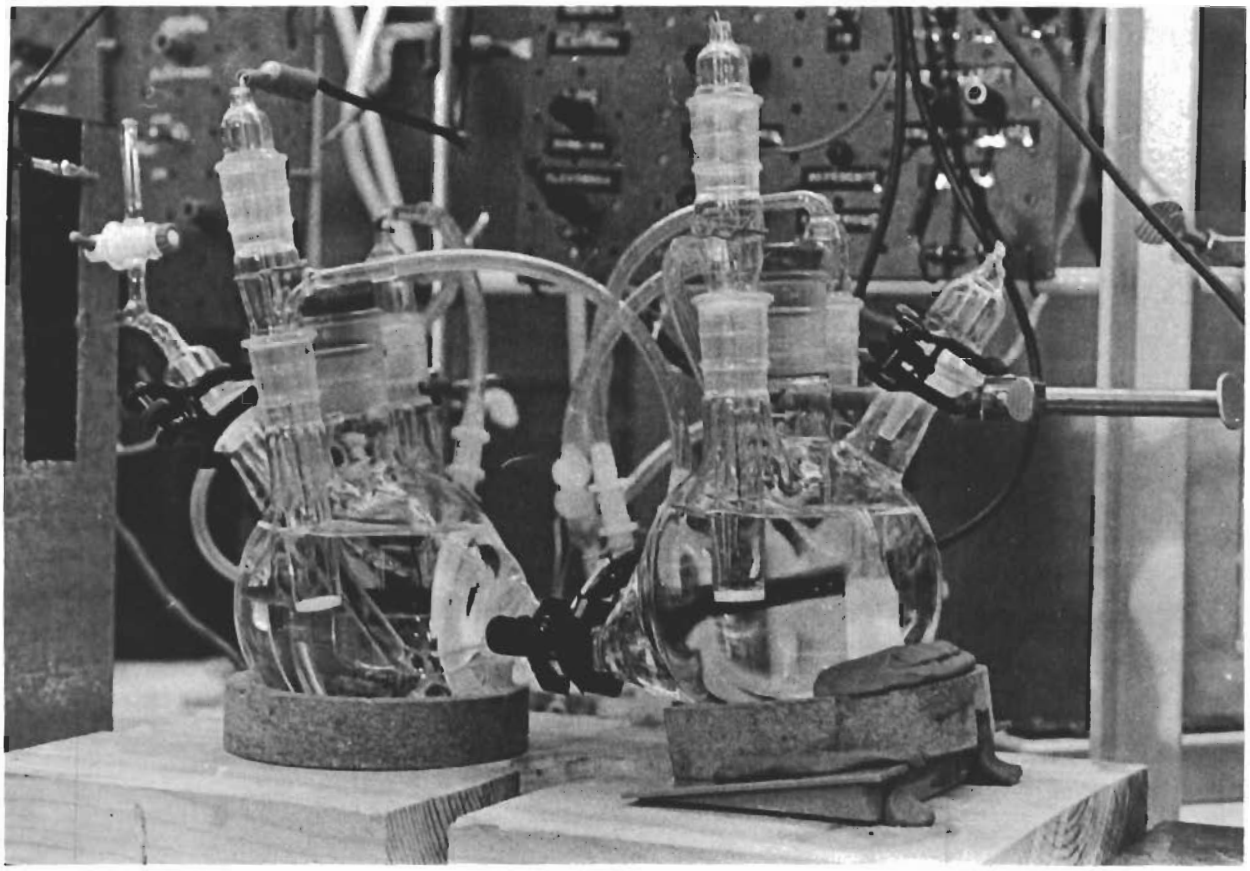

Fig. 193 - Close-Up View of the Electrolytic Hydrogen Permeation Cell

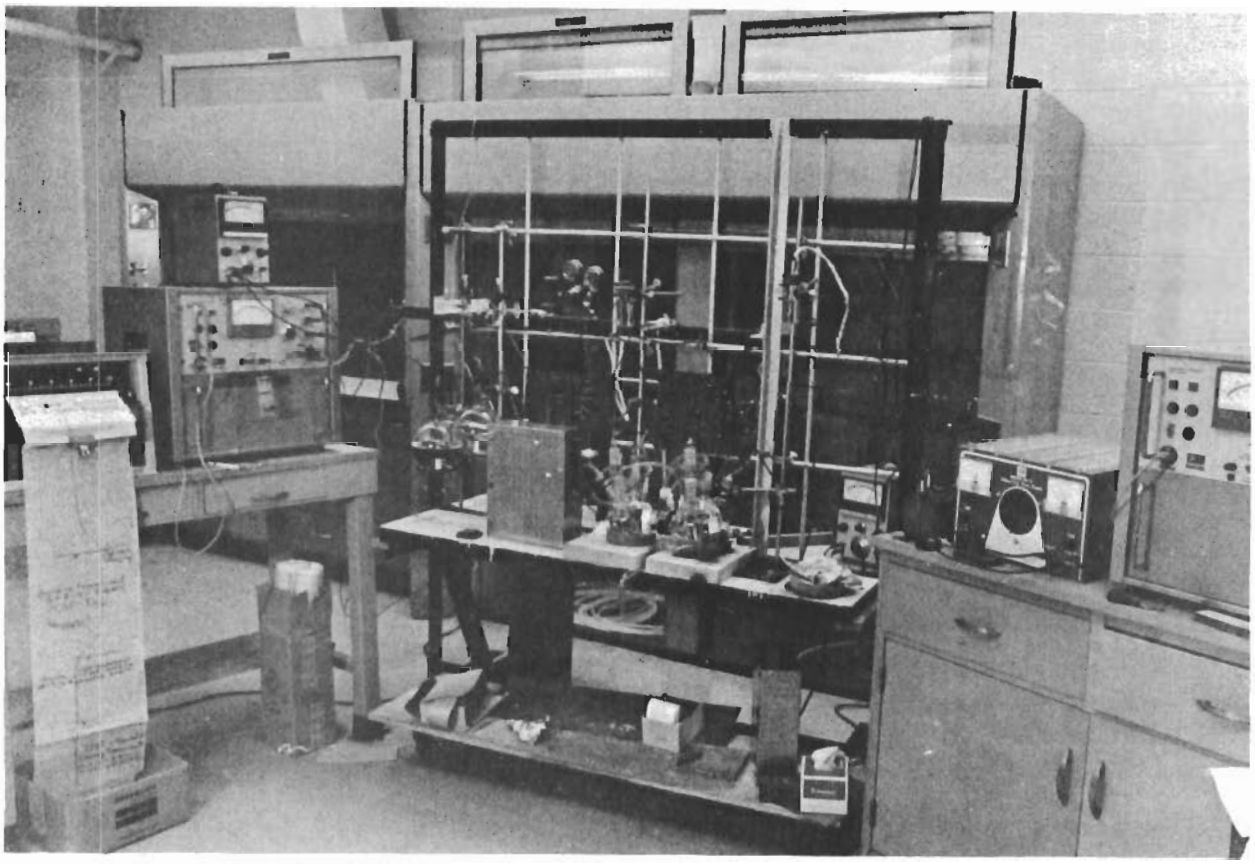

Fig. 194 - A Panoramic View of the Electrolytic Hydrogen Permeation Apparatus

Table XXIV - Hydrogen Permeation Results for AISI 4340 Steel

Heat Treatment[a]	J_∞ Steady State Permeation Current ($\mu A/cm^2$)	t_B Break-through Time (min)	$t_{1/2}$ Time to Reach $\frac{J_t}{J_\infty} = 0.5$ (sec)	D Diffusivity Based on $\frac{J_t}{J_\infty} = 0.5$ [$(cm^2/s) \times 10^{-7}$]	C_L^o Hydrogen Concentration at Cathodic Surface [(Mole H/cm^3) $\times 10^{-5}$]	Q_{ab} Hydrogen Absorbed at Steady State (Mole H $\times 10^{-7}$)
Untempered Martensite [as quenched]	1.9119	1.08	216	0.988	24.994	30.08
	1.9119	1.08	261	0.817	30.164	36.31
	1.9119	0.69	177	1.205	20.452	24.62
(Average)	1.9119	0.95	218	1.003	25.203	30.33
Tempered Martensite [tempered at 426°C(800°F)-1 hr.]	1.9119	0.70	130.2	1.639	15.036	18.09
	2.2219	0.70	114.0	1.872	15.299	18.41
	2.1444	0.70	153.0	1.395	19.814	23.84
(Average)	2.0927	0.70	132.4	1.635	16.716	20.12
Untempered Bainite [as isothermal transformed]	2.3252	0.34	63.0	3.387	8.849	10.65
	2.1702	0.30	72.0	2.764	9.438	11.36
	2.4028	0.32	81.0	2.634	11.758	14.15
(Average)	2.2994	0.32	72.0	2.995	10.015	12.05
Tempered Bainite [tempered at 400°C(750°F)-1 hr.]	1.6018	0.25	61.2	3.487	5.944	7.15
	1.6535	0.25	66.0	3.233	6.592	7.93
	1.6793	0.25	75.0	2.845	7.608	9.16
(Average)	1.645	0.25	67.4	3.188	6.714	8.08

[a]Prior to tempering treatment specimens were normalized at 899°C(1650°F), 40 minutes, air-cooled + austenitized at 843°C(1550°F), 30 minutes.

Table XXV - Hydrogen Permeation Results for 18 Ni (250) Maraging Steel

Aged[a] at Indicated Temperature for 3 Hours A.C.	J_∞ Steady State Permeation Current (μ A/cm^2)	t_B Break-through Time (min)	$t_{1/2}$ $\frac{J_t}{J_\infty} = 0.5$ (sec)	D Diffusivity Based on $\frac{J_t}{J_\infty} = 0.5$ [(cm^2/s) x 10^{-9}]	C_L^o Hydrogen Concentration at Cathodic Surface [(Mole H/cm^3) x 10^{-5}]	Q_{ab} Hydrogen Absorbed at Steady State (Mole H x 10^{-7})
As annealed	(steady state not achieved)	0.15				
399°C(750°F)	1.7310	0.25	1395	7.376	2.100	1.754
438°C(820°F)	1.5501	15.0	1800	5.717	2.427	2.028
510°C(950°F)	1.3176	32.0	4140	2.485	4.745	3.965
	1.3693	27.5	4020	2.559	4.789	4.001
(Average)	1.3434	29.75	4080	2.522	4.767	3.983
554°C(1030°F)	0.8784	24	3120	3.298	2.384	1.992
	0.8784	28.25	3375	3.049	2.578	2.154
(Average)	0.8784	26.12	3247	3.173	2.481	2.073
582°C(1080°F)	0.5942	20.5	4050	2.541	2.093	1.749
	0.6459	21.5	4410	2.333	2.478	2.070
(Average)	0.6200	21.0	4230	2.437	2.285	1.909

[a]Prior to aging treatment, specimens were double austenitized at 899°C (1650°F) 1 hour air-cooled + reaustenitized at 816°C(1500°F) 1 hour air-cooled.

of aging temperatures, in which crack propagations in the steel behave in a similar manner. A correlation between the hydrogen permeation parameters and the mechanical properties of the 18% Ni (250) maraging steel as a function of aging temperatures is shown in Fig. 195.

Basically hydrogen permeability (J_∞) is a product of diffusivity (D) and solubility (S) at a steady state condition. The presence of hydrogen trapping at energetic favorable sites, and the change of internal substructures result in an abnormal hydrogen diffusion behavior, and, consequently, make the direct correlation of permeability (J_∞) and crack propagations in the steel difficult. This can be rationalized from the abnormal diffusivities (D), listed in Tables XXIV and XXV, from a microstructural consideration, where the lowest SCC resistance in untempered martensite exhibits a lowest diffusivity in contrast to the other microstructures in AISI 4340 steel; however, lowest SCC resistance in the lowest underaged condition shows a highest diffusivity in contrast to the other aging conditions in 18% Ni (250) maraging steel.

b. Apparent Diffusivity (D)

For a given microstructure in a steel, the hydrogen permeability (J_∞) and solubility (Q_{ab}) may vary from experiment to experiment because of different cathodic charging conditions and specimen thickness used in the electrolytic hydrogen permeation. The apparent diffusivity (D) is independent of experimental conditions, and is an inherent property to microstructures. The experimental apparent hydrogen diffusivities of AISI 4340 steel in this investigation are comparable to the results of previous investigators[132] on 0.4 percent carbon low-alloy steels with a quench and tempered martensitic structure. On the other hand, no experimental data were found in the literature for 18% Ni (250) maraging steel. The best information available is the complete diffusivity data for the iron-nickel alloy system.[133] For a rough comparison, taking the diffusivity of HCP cobalt equal to the FCC nickel and the BCC molybdenum equal to BCC iron, the composition of the 18 Ni-9Co-5Mo maraging steel used in this investigation is considered to be equivalent to that of 27 Ni-Fe in the iron-nickel system, in which the diffusivity was found to be 8×10^{-9} cm^2/s at ambient temperature. Surprisingly, the experimental diffusivity of the under-aged 18% Ni (250) maraging steel is also found to be 7×10^{-9} cm^2/s, as delineated in Table XXV, and iron-nickel cubic martensite structure was reported in both systems.[134,135] This striking coincidence strongly suggests that the excellent SCC resistance of maraging steel in comparison with low-alloy martensitic steel is primarily attributed to the slow diffusion of hydrogen in maraging steel. Since there exists a great variation in the microstructures of AISI 4340 and 18% Ni (250) maraging steels, discussions and correlations of the diffusivity of microstructure and crack propagation of the two steels are separated as shown in the sections below.

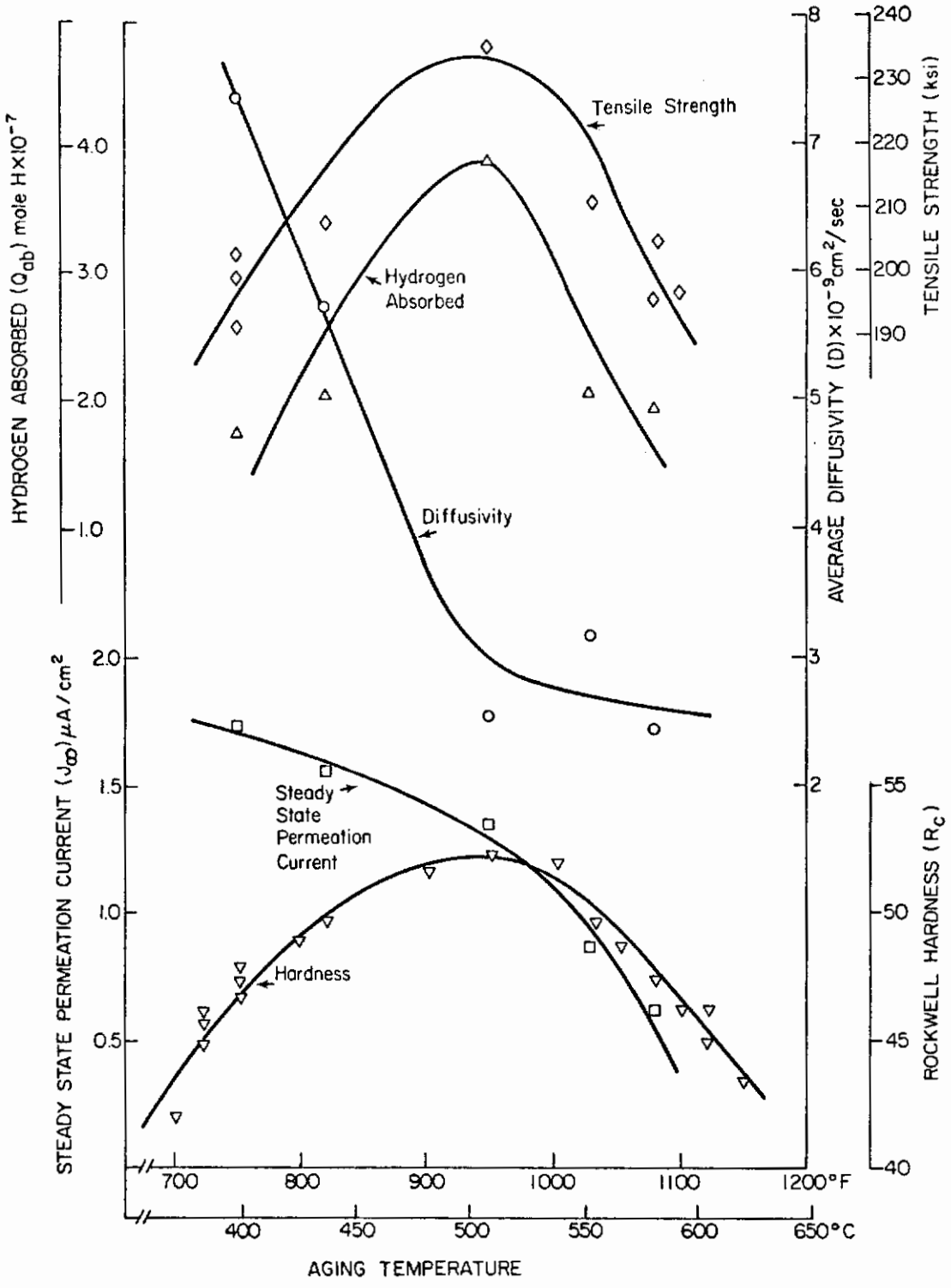

Fig. 195 - Mechanical Properties and Hydrogen Permeation Parameters as a Function of Aging Temperatures of 18 Ni(250) Maraging Steel

(1) AISI 4340 Steel--It was suggested by Nanis[136] that there exists a strong concentration dependency of the hydrogen diffusivity in AISI 4340 steel, and this concentration dependence is in the form of negative deviation; i.e., the concentration profile is convex when D increases with concentration. This led him to assume that no hydrogen trapping effect existed. On the contrary, the resultant diffusivity as a function of hydrogen concentration of the AISI 4340 steel in this investigation (shown in Figs. 196-199) reveals that the concentration dependence is in the form of positive deviation; i.e., the concentration is concave upward when D decreases with concentration, as schematically shown in line 3 of Fig. 200 and D can be expressed[137] as

$$D = D_o (1-bx)$$

$$\text{for } 0 < \chi < L \ , \qquad (57)$$

where D_o is the diffusivity at $C = 0$ near $\chi = L$. The physical meaning of this negative deviation of concentration dependency of hydrogen diffusivity in AISI 4340 steel is not clearly understood, especially for the pronounced effect on the tempered martensite and tempered bainite heat treatment conditions. This may result from lowering the activity coefficient or from the local equilibrium of the hydrogen atom at the trapping site. Comparisons between the rise and decay transients of hydrogen permeation indicate that the flux of hydrogen absorption (rise transient) is always greater than that of hydrogen evolution (decay transient), hence, D (absorption) is also greater than D (evolution). This can be further proved from Figs. 196-199 where the apparent diffusivities of rise transient; i.e., D (absorption) are always larger than those of decay transient; i.e., D (evolution). Thus it is certain that hydrogen trapping at energetic favorable sites in the high-strength steel does exist. In fact, this phenomenological observation led Oriani[138] to create the local equilibrium model of hydrogen trapping where he found that interfaces of microconstituents are the energetically most favorable sites for trapping.

From a local segregation consideration, the equilibrium distribution of hydrogen solute atoms at interface can be described in terms of a Boltzman distribution function which has been utilized by Troiano[139] to analyze solute segregation for dilute solutions as

$$C = C_o \exp(-U/KT) \ , \qquad (58)$$

where

C = interstitial hydrogen concentration segregated at interface,
C_o = average interstitial content in matrix,
K = Boltzman's constant,
T = absolute temperature, and
U = interaction energy between the hydrogen and the strain field.

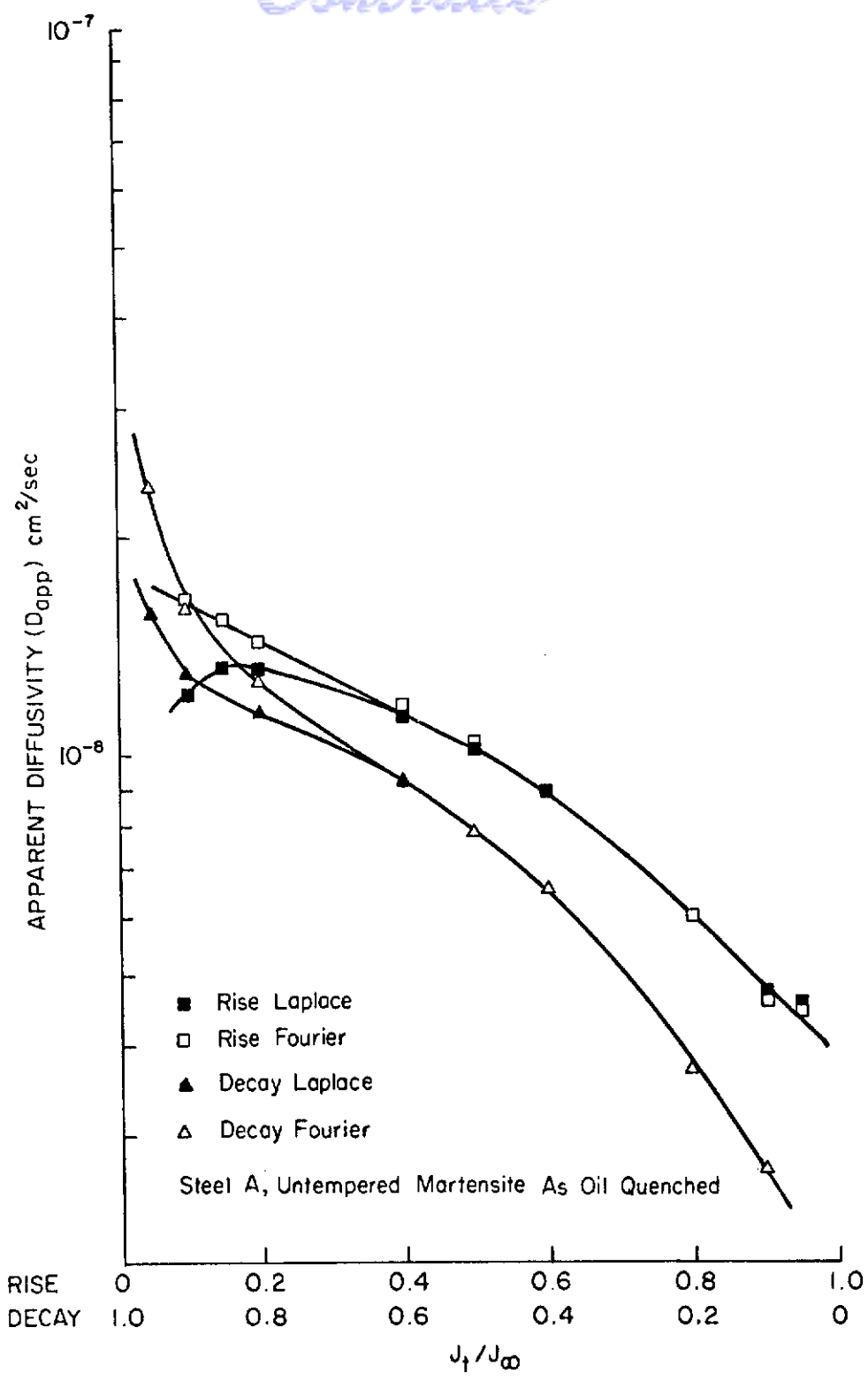

Fig. 196 - Apparent Diffusivity as a Function of (Jt/J_∞) for Rise and Decay Transients of As-Quenched, Untempered Martensite in AISI 4340 Steel

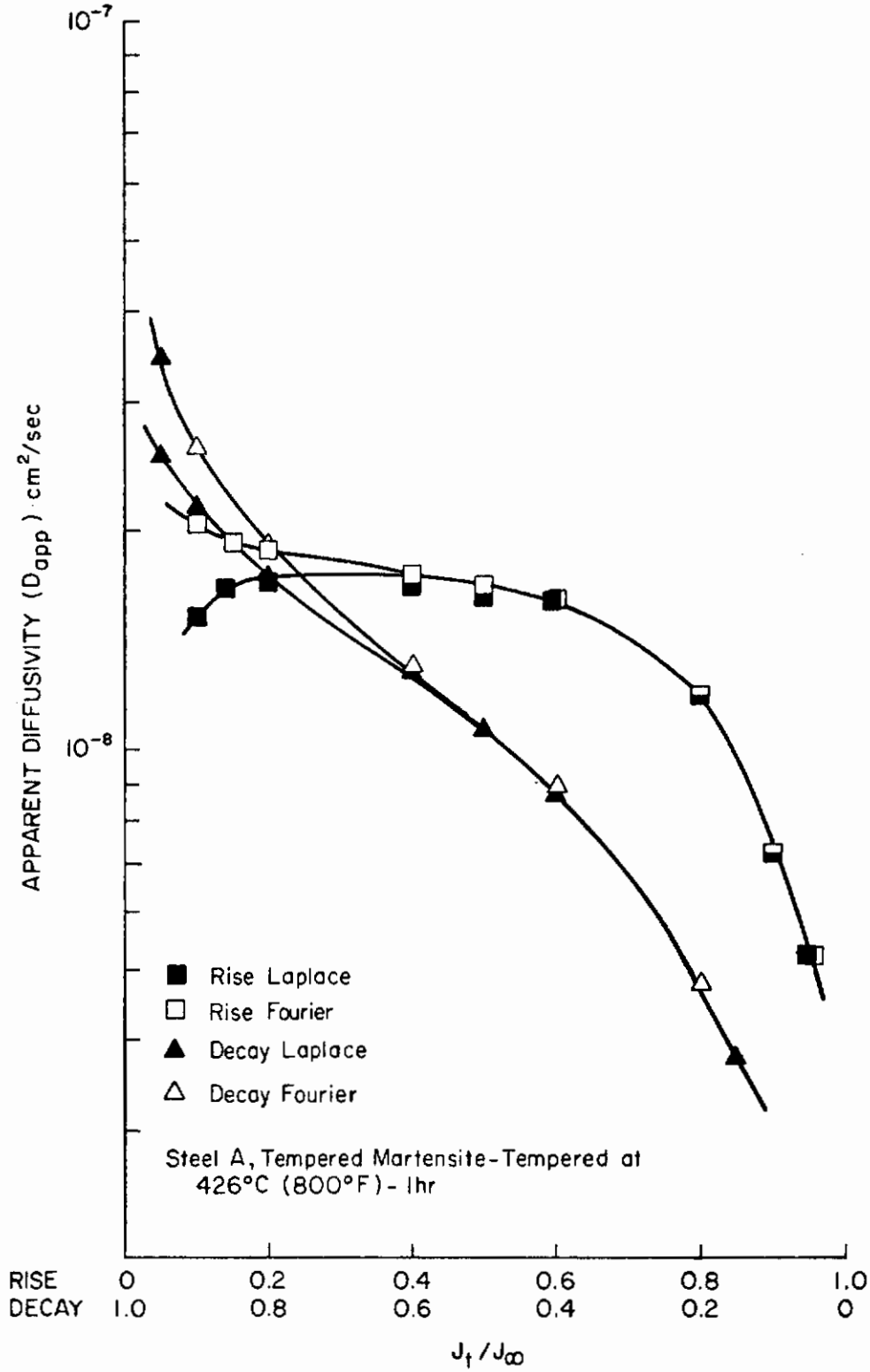

Fig. 197 - Apparent Diffusivity as a Function of (Jt/J_∞) for Rise and Decay Transients of Tempered Martensite in AISI 4340 Steel

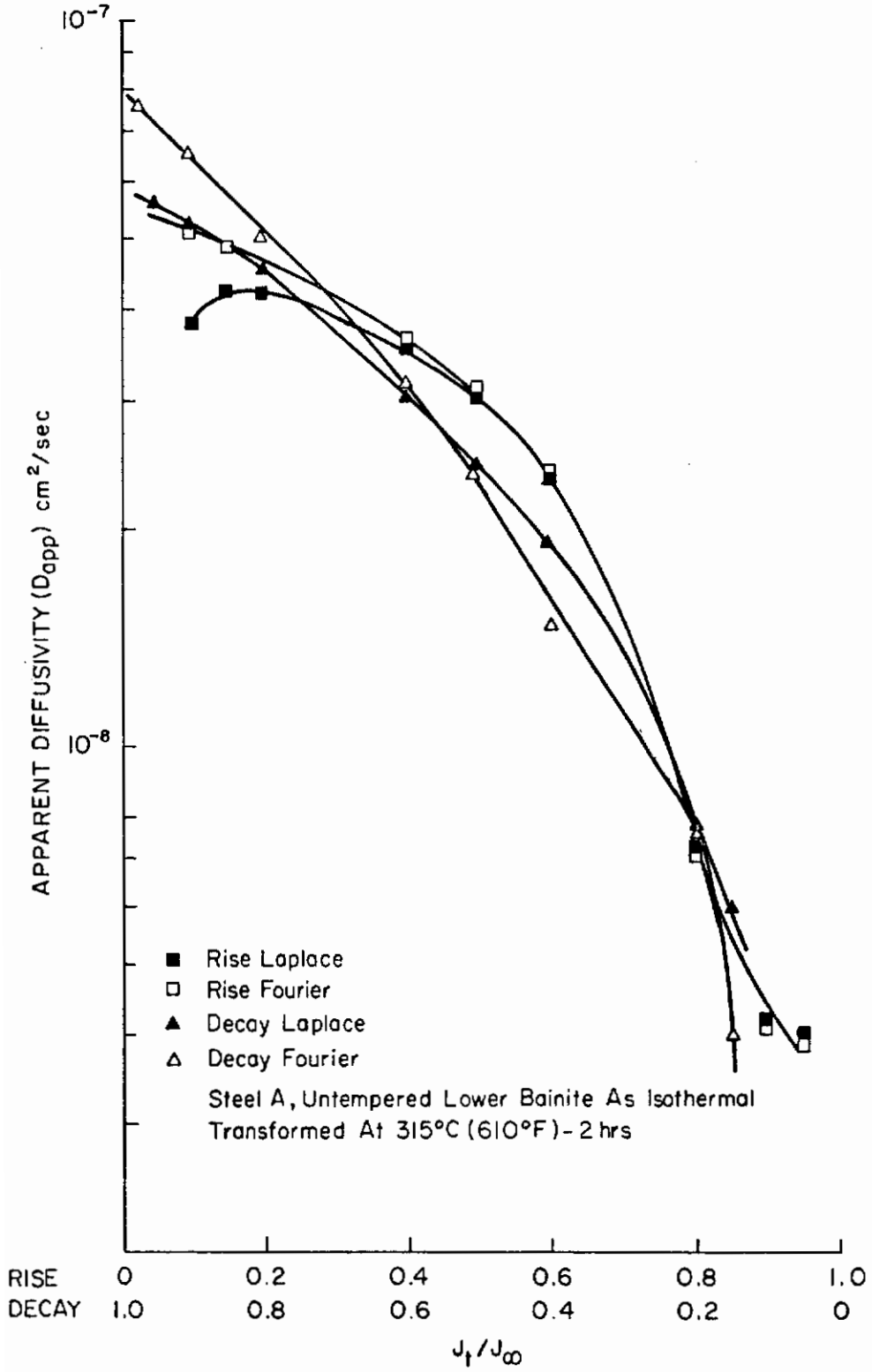

Fig. 198 - Apparent Diffusivity as a Function of (Jt/J_∞) for Rise and Decay Transients of As-Transformed, Untempered Lower Bainite in AISI 4340 Steel

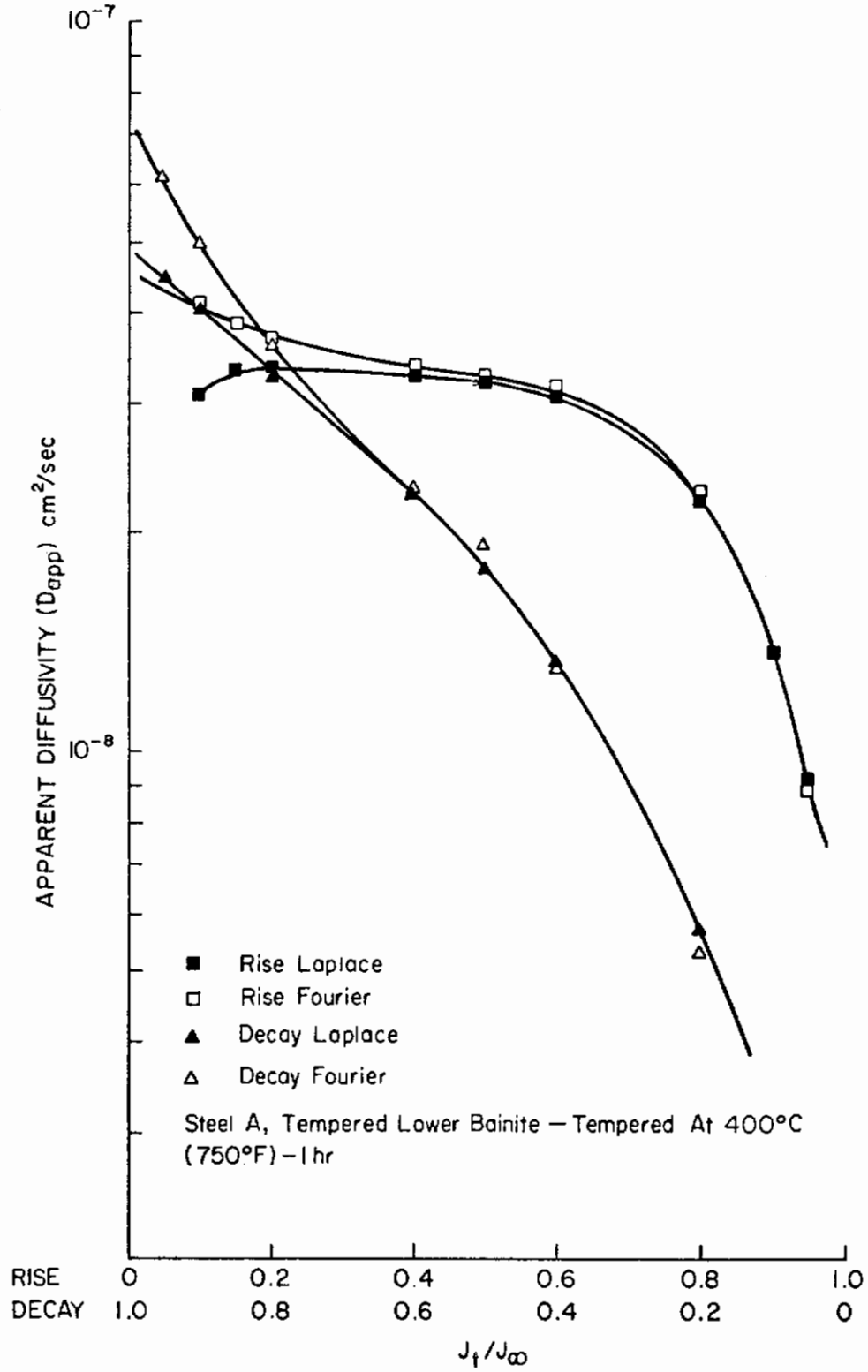

Fig. 199 - Apparent Diffusivity as a Function of (Jt/J_∞) for Rise and Decay Transients of Tempered Lower Bainite in AISI 4340 Steel

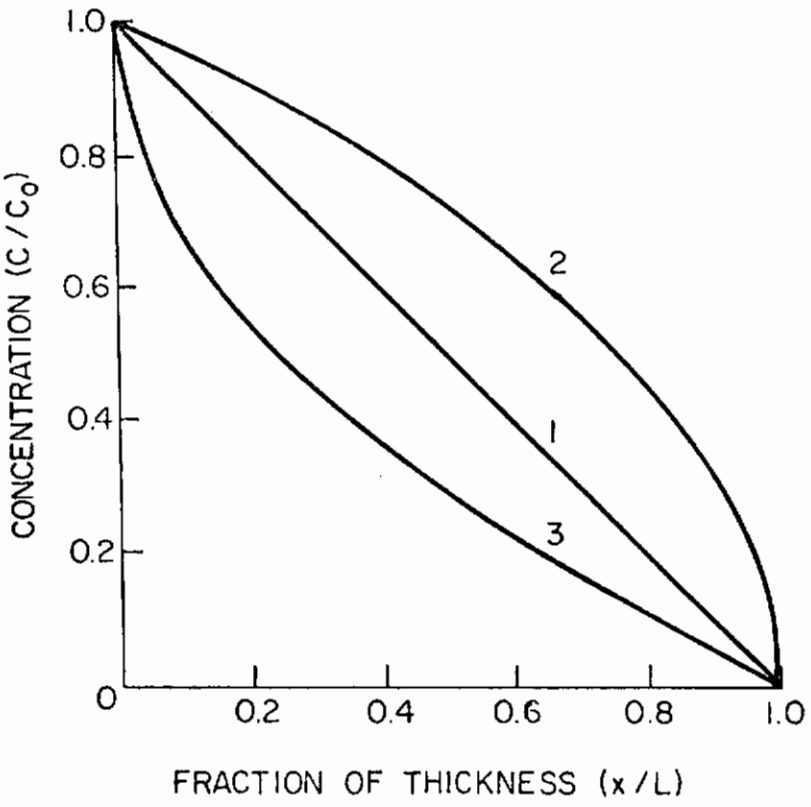

CURVE 1: D = CONSTANT
CURVE 2: $D = D_0(1+ax)$
CURVE 3: $D = D_0(1-bx)$

Fig. 200 - Steady-State Concentration Profile (Reference 137)

The strain fields for the interaction energy can be the coherent strain field from completely matched twin interfaces; or from the elastic misfit interaction of second phases (such as carbide, and intermetallic compounds) embedded in the matrix; or from two completely incoherent interfaces.

Upon examining the hydrogen solubility (Q_{ab}) and diffusivity (D) in AISI 4340 steel shown in Table XXIV, it is found that both the hydrogen solubility and diffusivity in the steel have changed by a factor of three as a result of microstructural alteration from untempered martensite to tempered lower bainite. Considering first tempered martensite and tempered lower bainite structures of the steel with identical strength, the most significant differences among these interfaces are the coherent twinned-plate martensite and noncoherent lath lower banite interfaces as discussed previously.[140] The noncoherent carbides in both structures bear a similar morphology and distribution, hence, the trapping sites of carbide interfaces for the two structures can be considered to be identical. In order to gain a realistic physical picture, the coherent twinned-plate martensite interfaces were treated as completely matched lattices with superimposition of a strong coherent strain field, rather than partial dislocations of stacking fault. Meanwhile, tempered lower bainite interfaces are incoherently mismatched. Under the conditions of identical strength, and hydrogen input flux, the average hydrogen solubility of the bulk tempered martensite is about a factor of two higher than that of tempered lower bainite; whereas, there is an opposite relationship for the diffusivities of the two structures. This can be further demonstrated from Fig. 201 where diffusivities were obtained from both rise and decay transients across a wide range of hydrogen fluxes. The decreases in diffusivities as a function of the ratio (J_t/J_∞) are attributed to the dragging effect of hydrogen-strain field interaction together with local segregation, as predicted from Eq. (58). Based on the above discussion, it can be deduced logically that local segregation of hydrogen at the twinned-plate martensite interfaces is attributed primarily to the coherent strain field, therefore, coherent interfaces make an important contribution to hydrogen trapping. Further confirmation of this deduction can be asserted from the comparisons of the hydrogen solubility (Q_{ab}) and diffusivity (D) between untempered as-quenched martensite and tempered martensite, where additional coherent strain fields arise from the coherent interfaces between ϵ transition carbide and martensite. Indeed, the hydrogen solubility in as-quenched martensite is higher than that of tempered martensite by a factor of almost 1.5, whereas the diffusivity decreases by a factor of 1.5, as revealed from Table XXIV and Fig. 202.

In short, the above correlations are positive proof of the postulation that the rapid crack propagation of tempered martensite in mild aqueous environments is a result of the absorption of hydrogen at crack tip, and of further segregation of hydrogen at the coherent twinned-plate martensite interfaces through hydrogen-strain field interactions.

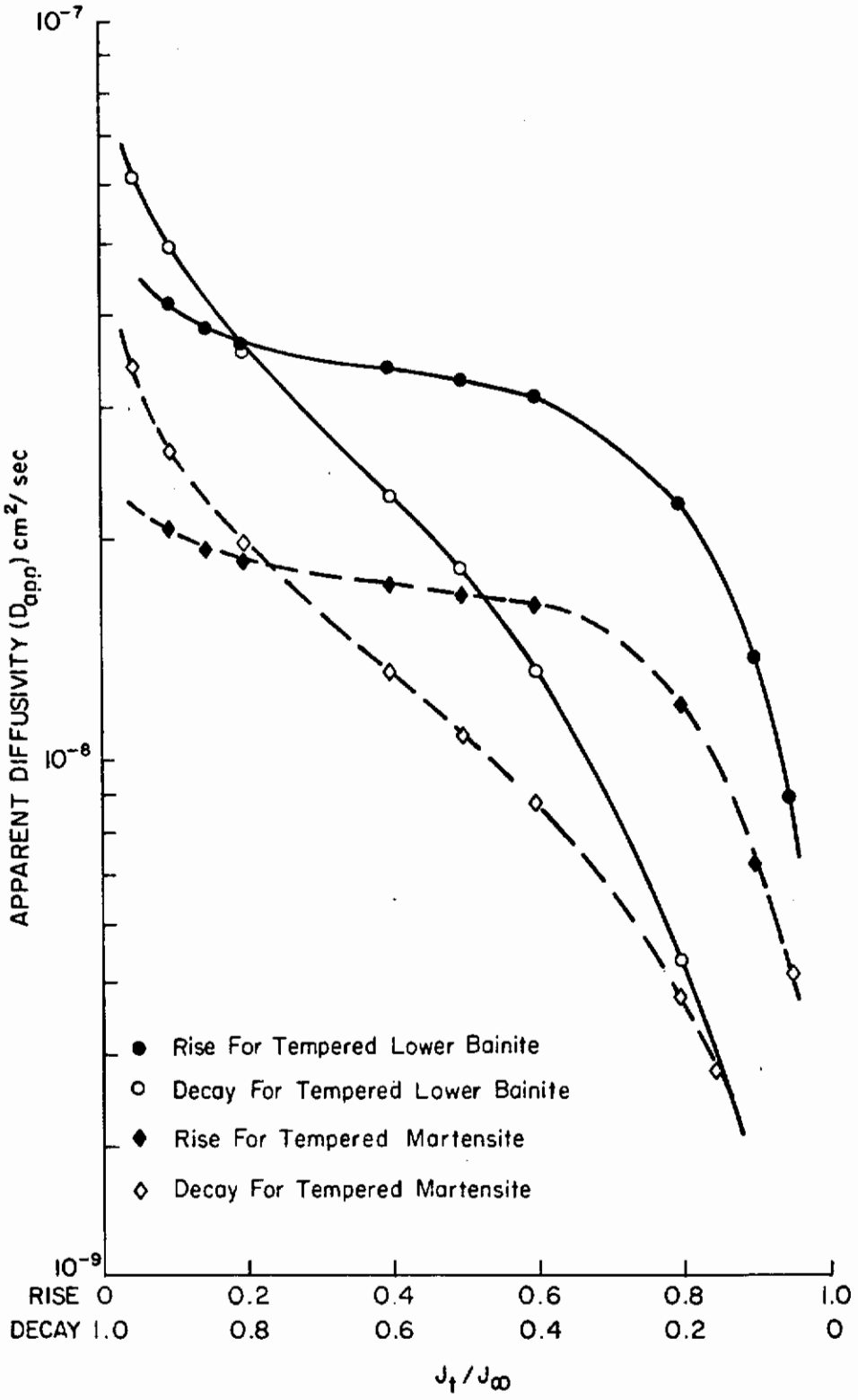

Fig. 201 - Comparison of Apparent Diffusivity of Tempered Lower Bainite and Tempered Martensite in AISI 4340 Steel

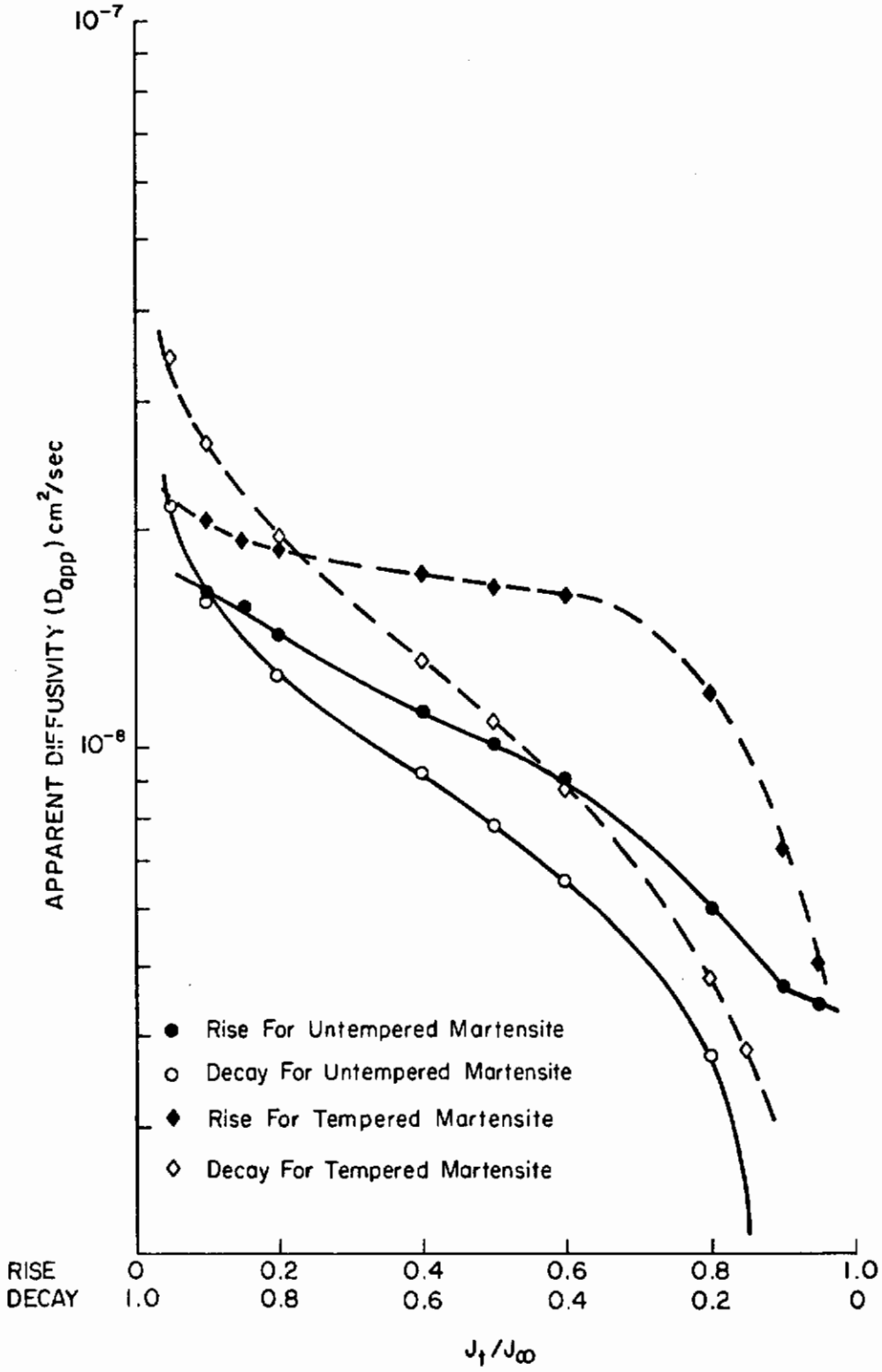

Fig. 202 - Comparison of Apparent Diffusivity of As-Quenched, Untempered Martensite and Tempered Martensite in AISI 4340 Steel

(2) 18% Ni (250) Maraging Steel--The analysis of concentration dependency of hydrogen diffusivities in 18% Ni (250) maraging steels is rather difficult because of the intricacy of substructures, intermetallic compound precipitation, and the coexistence of the two phases in which the diffusion behaviors are erratic, as shown in Figs. 203-207.

Comparison of diffusivities of the two under-aged conditions shown in Table XXV and Fig. 208 indicate that the diffusivities at 399°C (750°F) are lower than that at 438°C (820°F), whereas the solubilities (Q_{ab}) for the two under-aged conditions are considered to have practically no difference. This abnormality is attributed to the compensation effect of dislocation densities in the cubic martensite laths and the coherent strain from the early stage of intermetallic compound precipitation.

In 18% Ni (250) maraging steel, increasing aging temperatures in the under-aged conditions results in reduction of the martensite transformation-induced dislocations as well as promotion of the precipitation of coherent intermetallic compounds and its associate precipitation coherency at the interfaces. Therefore, the overall trapping effect in the two under-aged conditions results in a small difference in the hydrogen solubilities (Q_{ab}). Judging from the lower diffusivity and highest solubility (Q_{ab}) of the 510°C (950°F) aged condition from Table XXV, it is suggested that the coherent interface trapping effect may extend to this strength-maximum condition in view of the very small amount of reversion austenite, and the highest precipitation coherency at this aging condition as suggested by Miller et al.[135] However, it is necessary to mention that even at the severe hydrogen trapping situation, the slower crack propagation rates in this strength-maximum condition, in contrast to those of the under-aged conditions, are attributed to the morphology and distribution of the very small amount of reversion austenite for which the dislocation cells of martensite laths are continuously encircled to blockade the crack propagation.

In the over-aged conditions, the coexistence of BCC aged martensite and FCC reversion austenite leads to the lowering of diffusivities. This is attributed to the lower hydrogen diffusivity in austenite, and can be assessed from law of mixtures as

$$D_{exp} = N_{\alpha}D_{\alpha} + N_{\gamma}D_{\gamma} \ , \qquad (59)$$

where

D_{exp} = experimentally determined apparent diffusivity,
D_{α} = diffusivity of aged martensite,
D_{γ} = diffusivity of reversion austenite,

and N_{α} and N_{γ} are the volume fraction of aged martensite and reversion austenite in maraging steels, respectively. However, both diffusivity

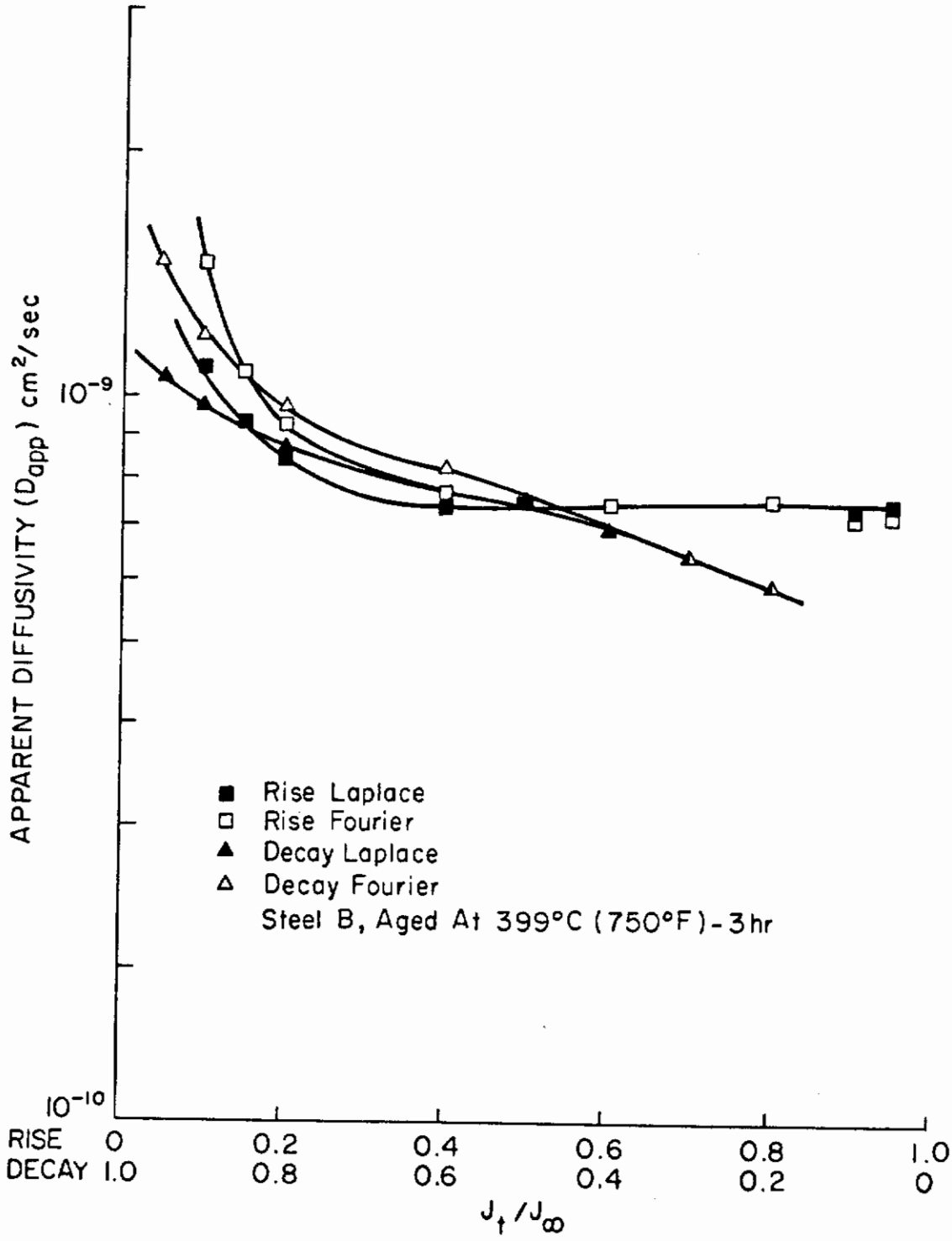

Fig. 203 - Apparent Diffusivity as a Function of (Jt/J_∞) for Rise and Decay Transients in 399°C (750°F) Aged 18 Ni (250) Maraging Steel

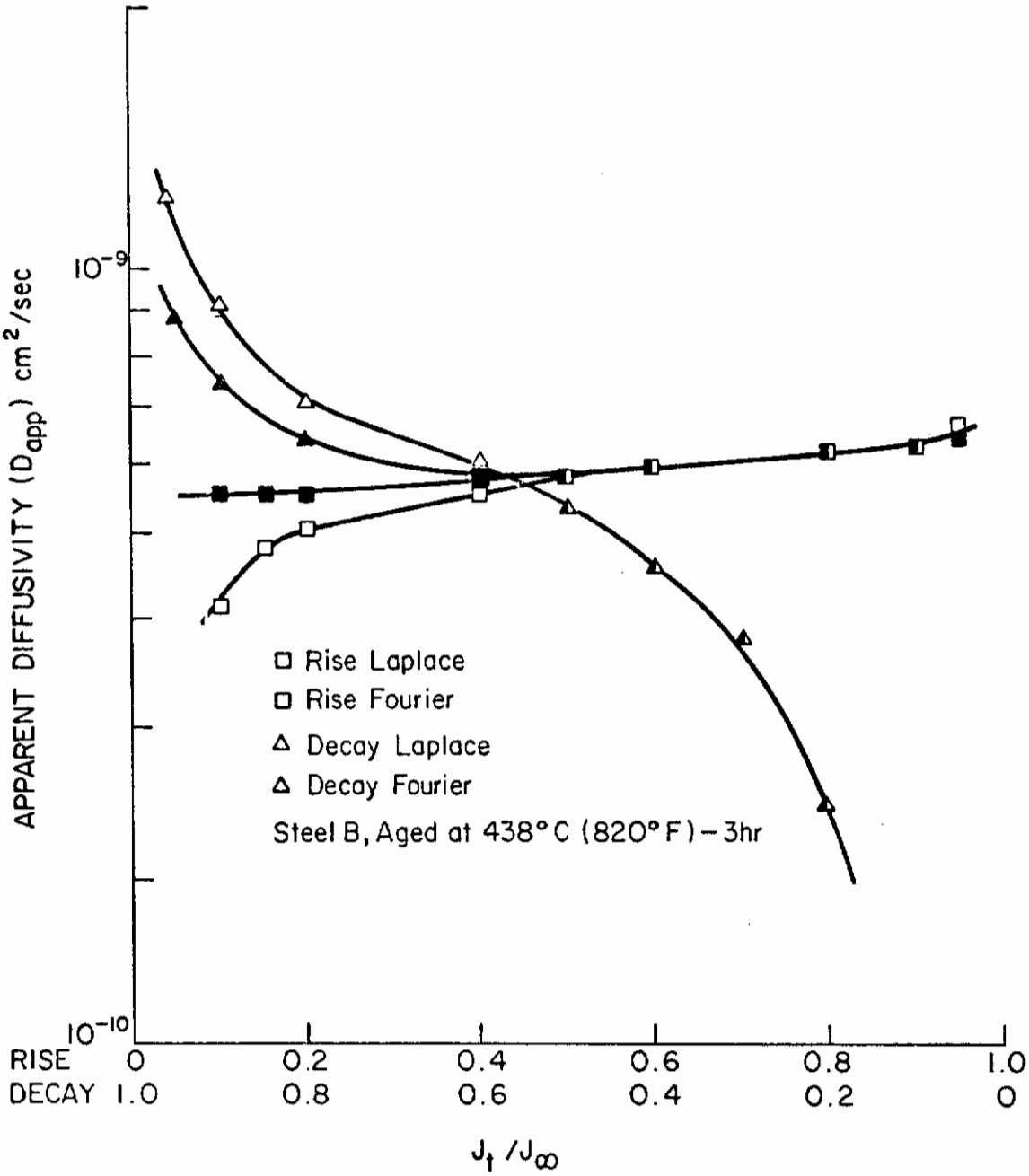

Fig. 204 - Apparent Diffusivity as a Function of (Jt/J_∞) for Rise and Decay Transients in 438°C (820°F) Aged 18 Ni (250) Maraging Steel

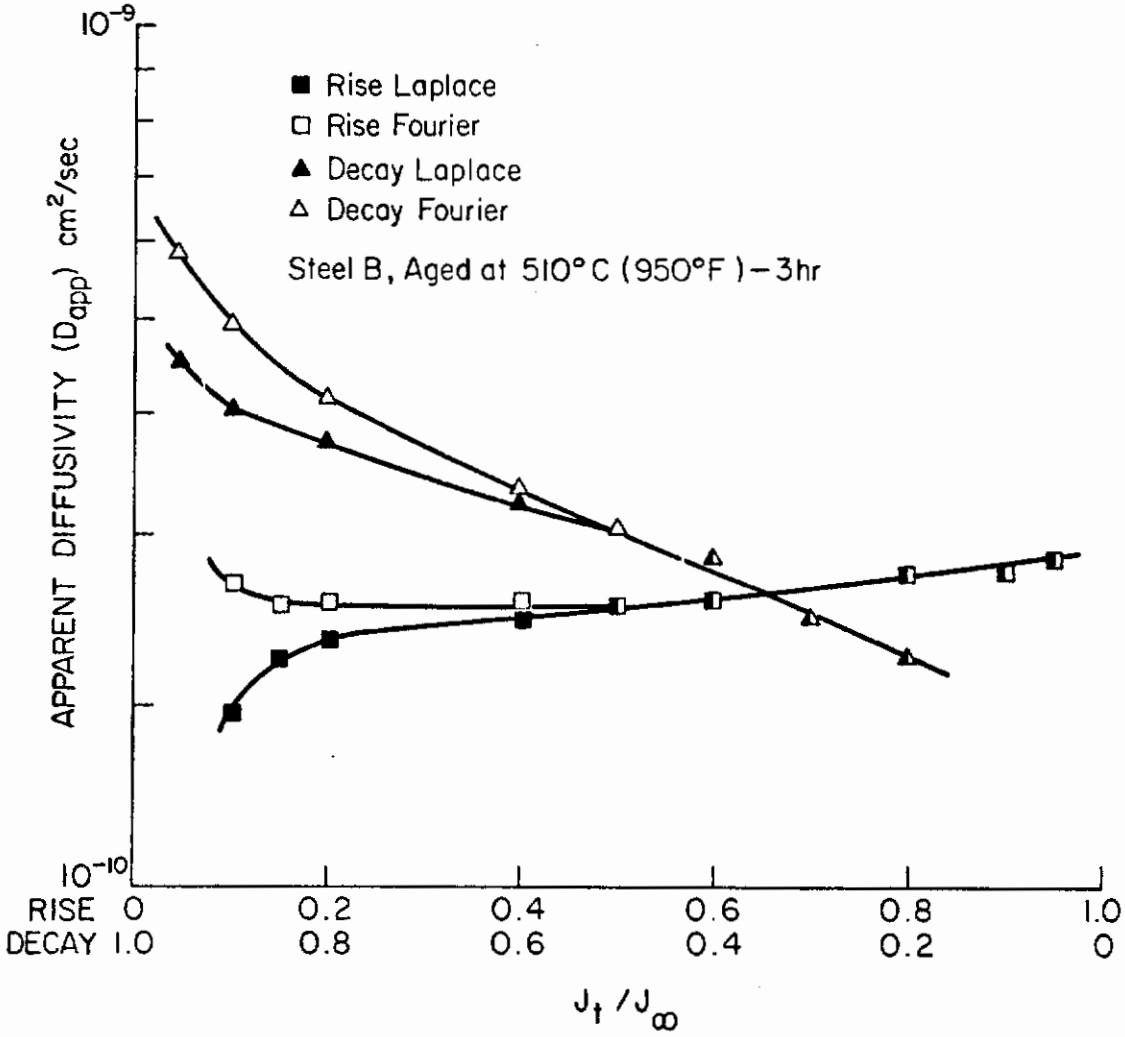

Fig. 205 - Apparent Diffusivity as a Function of (Jt/J_∞) for Rise and Decay Transients in 510°C (950°F) Aged 18 Ni (250) Maraging Steel

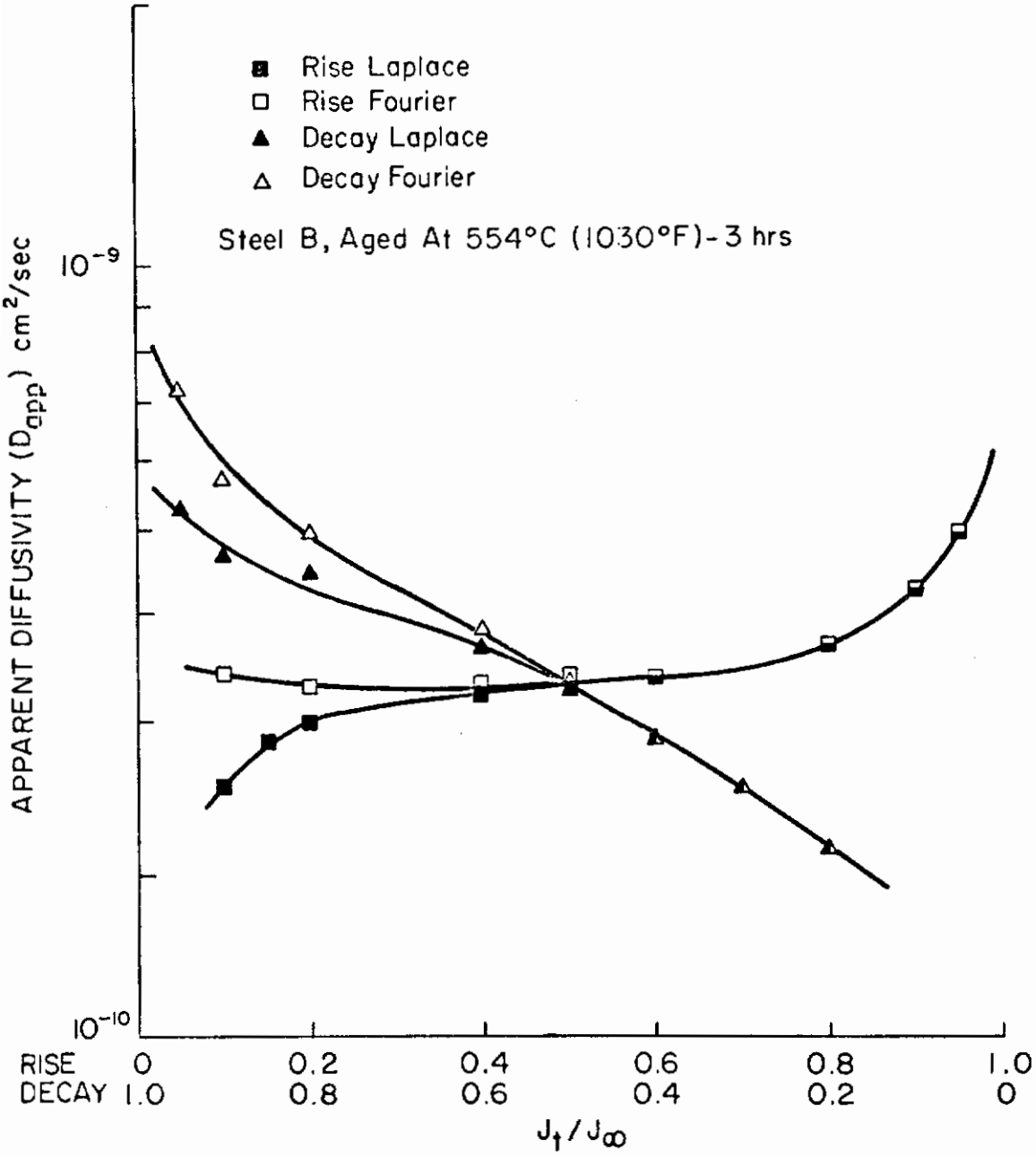

Fig. 206 - Apparent Diffusivity as a Function of (Jt/J_∞) for Rise and Decay Transients in 554°C (1030°F) Aged 18 Ni (250) Maraging Steel

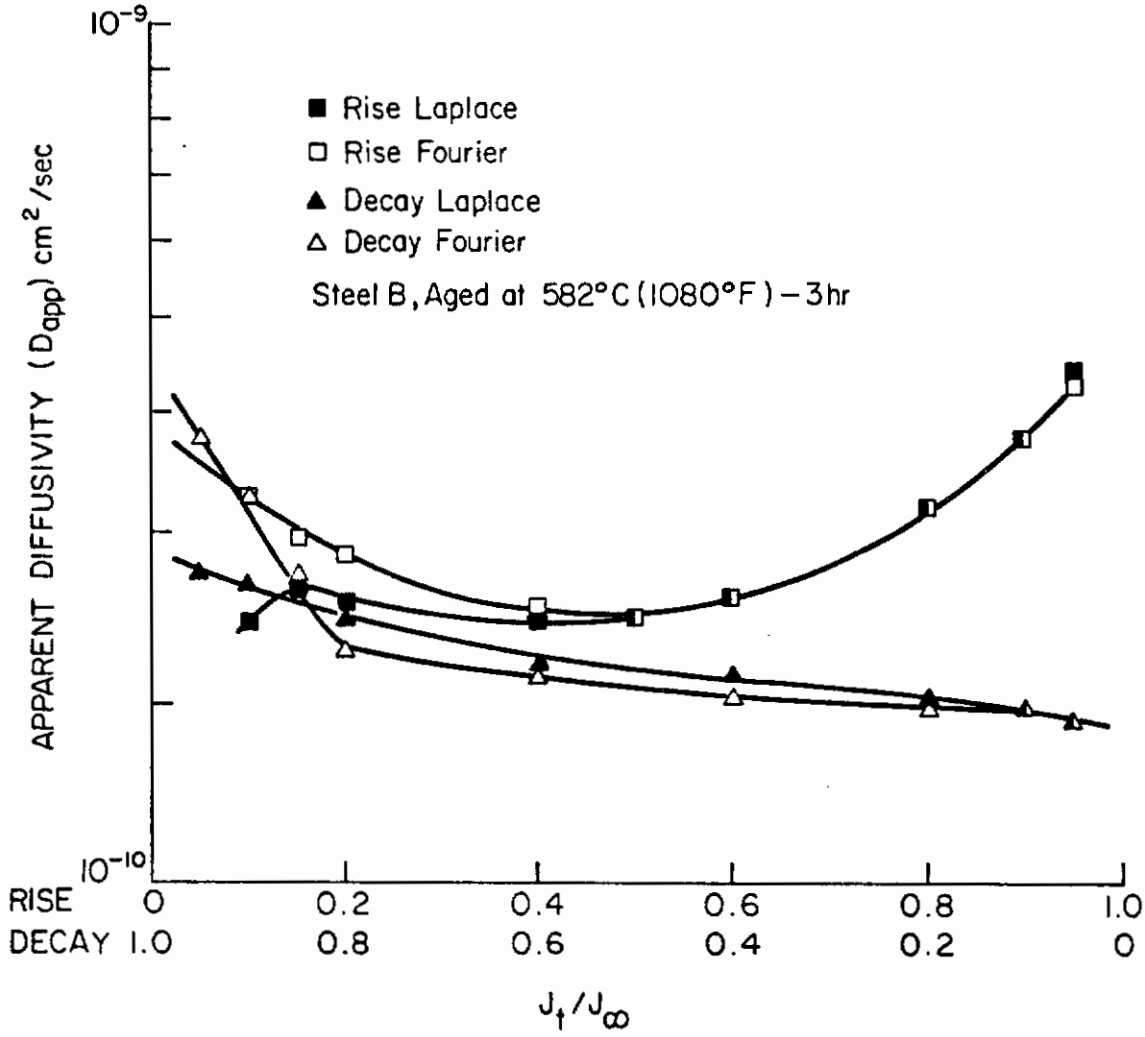

Fig. 207 - Apparent Diffusivity as a Function of (Jt/J_∞) for Rise and Decay Transients in 582°C (1080°F) Aged 18 Ni (250) Maraging Steel

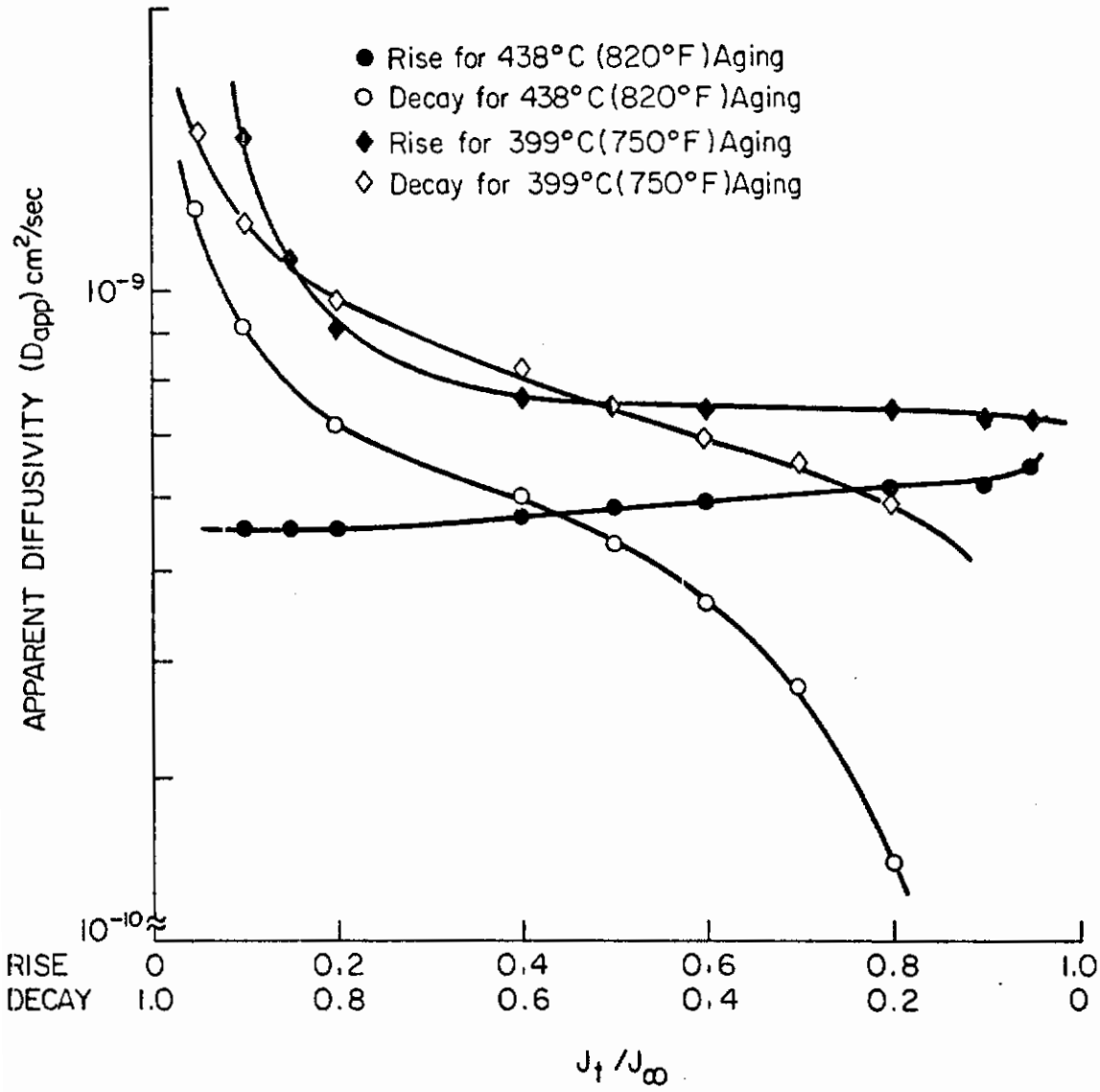

Fig. 208 - Comparison of Apparent Diffusivity of the Two Under-aged Conditions of 18 Ni (250) Maraging Steel

and solubility data in Table XXV reveal no significant difference between these over-aged conditions. This is attributed to the experimental difficulties in controlling the hydrogen absorption kinetics for a long-time immersion of the steel specimens in the electrolytic solution, before or during hydrogen permeation. For comparison of diffusivities between the under- and over-aged conditions in the maraging steel, these data in Table XXV are still valuable.

Comparisions of diffusivity data between the under- and over-aged conditions of the maraging steel under identical strength levels (shown in Table XXV, and Figs. 209 and 210), suggest that, indeed, slow hydrogen diffusivities in the over-aged conditions are the major contributions to reduction of crack propagations for the promotion of SCC resistance in over-aged maraging steel.

Based on the hydrogen diffusion behaviors in AISI 4340 as well as 18% Ni (250) maraging steels, certain generalizations can be made as follows:

(1) In the presence of hydrogen trapping at energetically favorable sites, slow diffusion of hydrogen through high-strength steels enhances the crack propagations as demonstrated in martensite structures of AISI 4340 steel, whereas, slow diffusion of hydrogen promotes SCC resistance in the case of two phases with large differences in diffusivities (such as BCC martensite and FCC reversion austenite).

(2) Apparent transient hydrogen diffusivities were observed to be faster than those at steady state for all heat treatments of AISI 4340 steel. The slower steady state hydrogen diffusivities in the steel are attributed to the lagging of hydrogen motion as a consequence of hydrogen-strain field interactions. Nevertheless, there exists a similar trend on the use of the two diffusivities to correlate to the crack propagation behaviors.

D. KINETICS OF GROWTH OF PASSIVE FILMS
(K. N. Goswami)

1. Objective and Background

The objective of this study is to determine the kinetics of growth of passive films on iron alloy surfaces. This work is directly relevant to the state of affairs immediately following the formation of fresh surfaces at a crack tip. The rate of formation of passive films affects the quantity of ions going into solution and also provides a barrier to the subsequent entry of hydrogen into the metal.

2. Experimental

The specimens of Fe, Fe-10Cr, Fe-10Ni, and Fe-10Cr-10Ni were mechanically polished (final polish with 1μm diamond abrasive) and

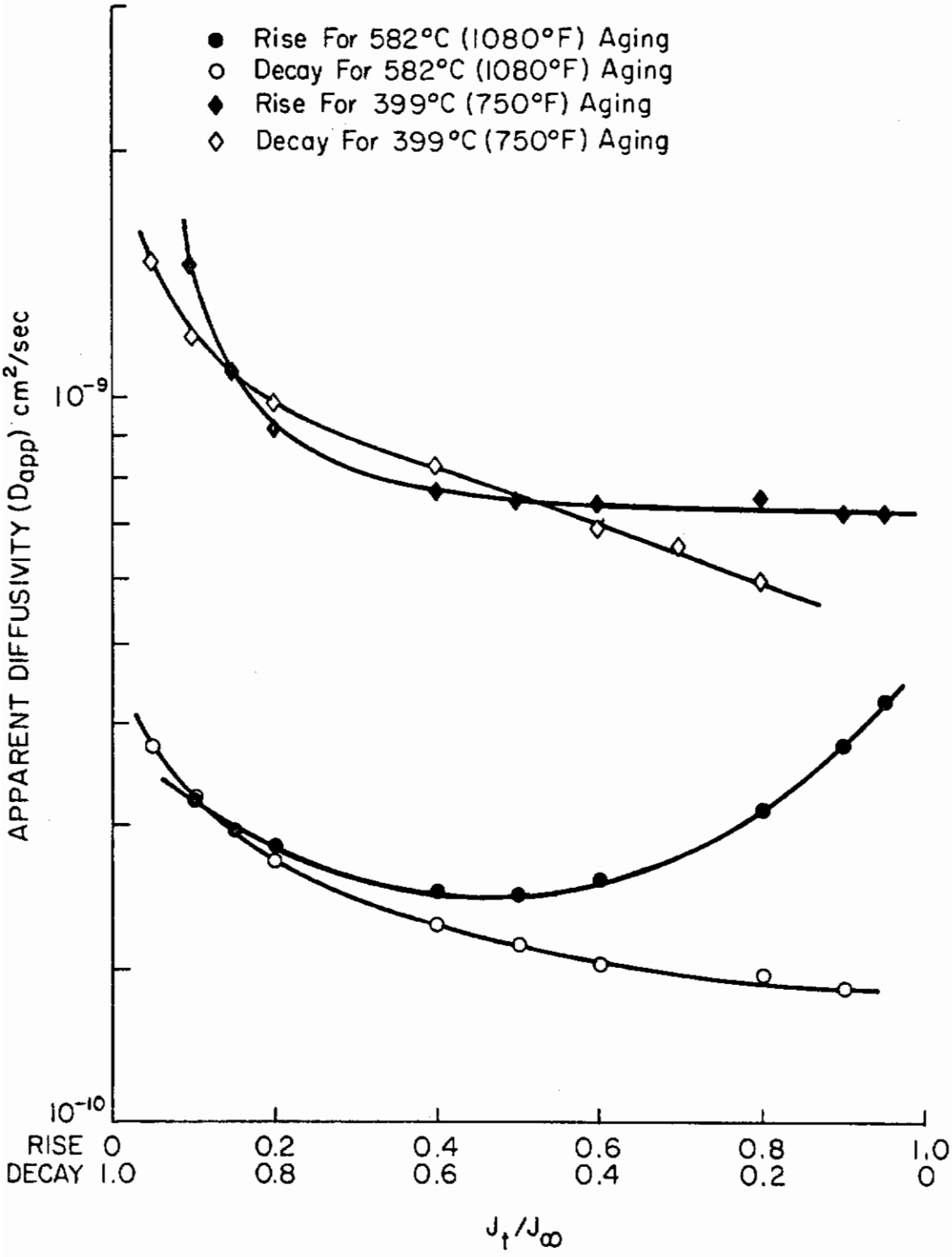

Fig. 209 - Comparison of Apparent Diffusivity of 399°C (750°F) and 582°C (1080°F) Aged Conditions of 18 Ni (250) Maraging Steel

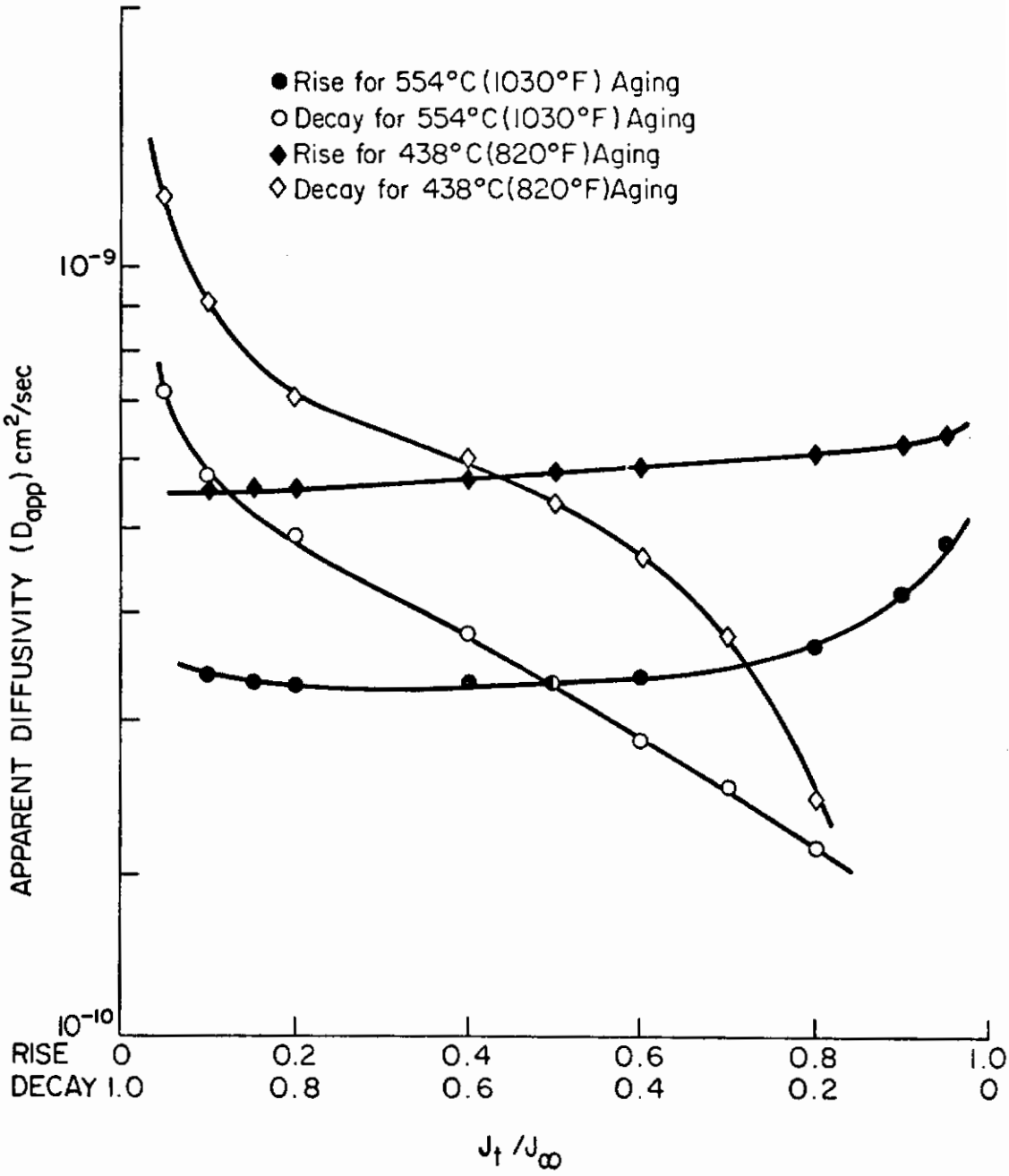

Fig. 210 - Comparison of Apparent Diffusivity of 438°C (820°F) and 554°C (1030°F) Aged Conditions of 18 Ni (250) Maraging Steel

finally washed in the spectrographic grade methanol, dried quickly by absorbing the methanol with lens paper, and placed in the cell. The existing air-formed oxide films on the specimen surfaces were reduced galvanostatically at 10-20 $\mu A/cm^2$ cathodic current. After cathodic reduction, the solution was completely replaced by fresh solution with the metal surface maintained at the reduction potential. When the surface was so reduced, optical readings were made and the surface was then brought rapidly by the potentiostat to an anodic potential where films start to form.

Experiments were carried out at PH 4, 6, 8.4 and 10. The region of potential in which film growth was studied varied, depending on the pH. Solutions used for the various pH's were as follows: pH 4 and pH 6, 0.5M H_2SO_4 + 0.5N Na_2SO_4 + NaOH; pH 8.4, sodium borate + boric acid; pH 10, same as pH 6 with different NaOH.

3. Results and Discussion

Optical constants were determined and are reported in Table XXVI. There appears to be a significant change from pH 4 to 8.4; the variation among alloys appears to be not quite so prominent. An explanation for these changes is not so clear at this time.

The growth rates of films were determined over the possible range of potentials and kinetic measurements were performed from 1 to 100 minutes. Typical of the thickness-time plots is Fig. 211 for Fe-10Ni at pH 4. These data plot equally well and linearly in an inverse logarithmic plot as shown for Fig. 212 at pH 8 for pure Fe.

The effect of potential on film thickness is summarized in Figs. 213-215. The effect of pH at 600 mV is summarized in Fig. 217.

The linear dependence of film thickness on potential is an expected result according to the already well-known patterns for field effects on film growth.

The effect of pH on film thickness is an entirely acceptable result but by no means an easily rationalized one. The basis for this result needs further illucidation.

Table XXVI - Optical Constants of $\eta(1-ik)$ of Films Formed at pH 4, 6, 8.4 for Fe-base Alloys ; λ=5461Å

pH 4

Potential,	Fe-10Ni		Fe-10Cr		Fe-10Cr-10Ni	
mV	n	k	n	k	n	k
100	--	--	2.00	0.14	--	--
200	--	--	--	--	2.20	0.12
400	2.10	0.12	2.00	0.14	2.20	0.12
600	2.10	0.12	2.00	0.14	2.20	0.12
800	2.10	0.12	2.00	0.14	2.30	0.14
1000	2.20	0.14	2.00	0.14	2.30	0.14
1200	2.20	0.14	2.00	0.14	--	--

pH 6

Potential,	Fe-10Ni		Fe-10Cr		Fe-10Cr-10Ni	
mV	n	k	n	k	n	k
0	--	--	2.30	0.08	2.20	0.10
200	--	--	2.30	0.08	2.20	0.10
250	2.40	0.12	--	--	--	--
400	2.40	0.12	2.30	0.08	2.20	0.10
600	2.40	0.12	2.30	0.08	2.20	0.10
800	2.60	0.12	3.00	0.10	2.30	0.10
1000	2.60	0.12	3.00	0.10	--	--

pH 8.4

	Substrate		Anodic Oxide Film	
	n	k	n	k
Fe	2.833	1.190	2.480	0.11
Fe-10Ni	2.875	1.255	2.300	0.12
Fe-10Cr	2.727	1.307	2.300	0.100
Fe-10Cr-10Ni	2.757	1.343	2.300	0.12

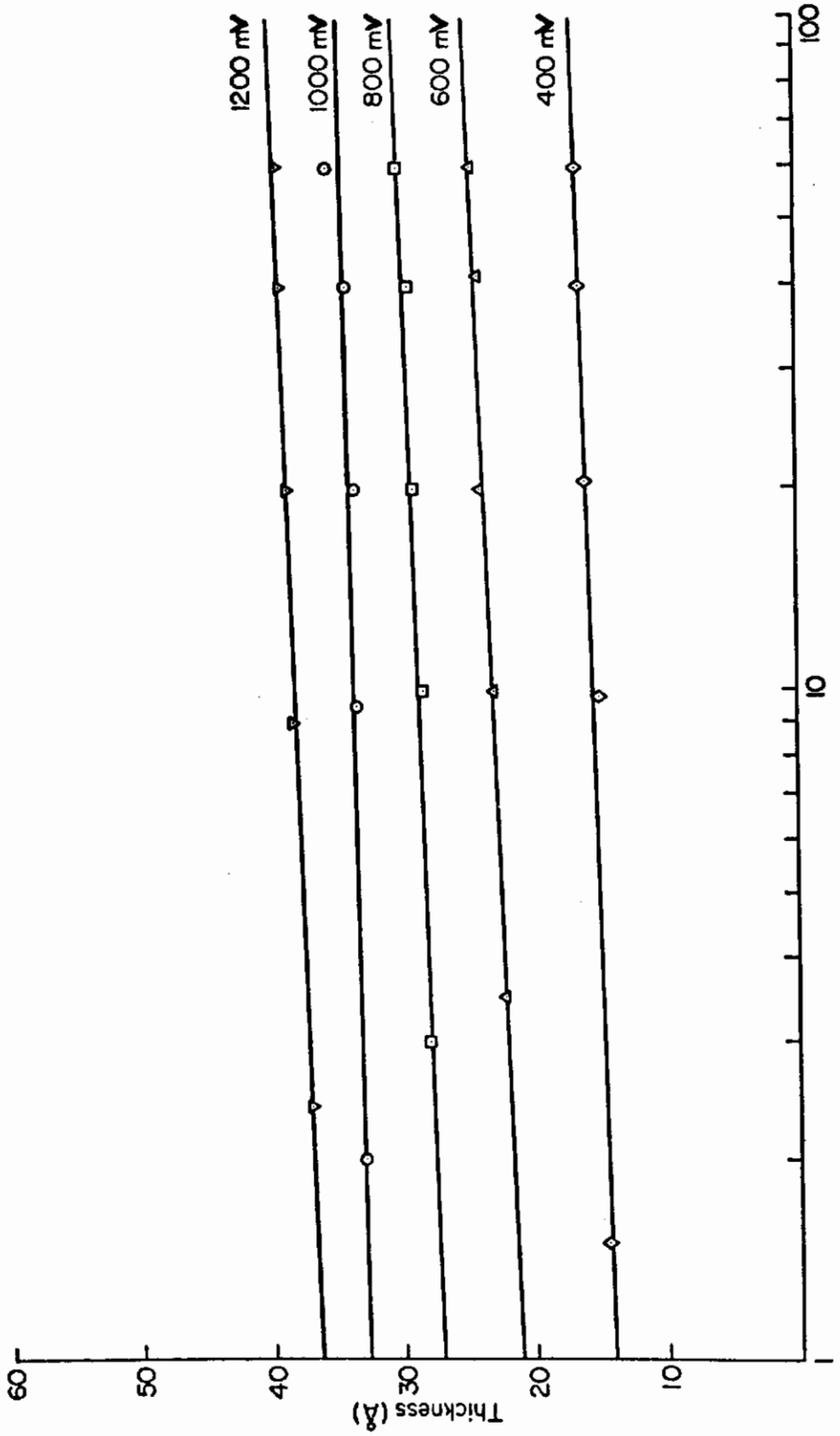

Fig. 211 - Growth of Passive Film on Fe-10Ni in Electrolyte of pH 4

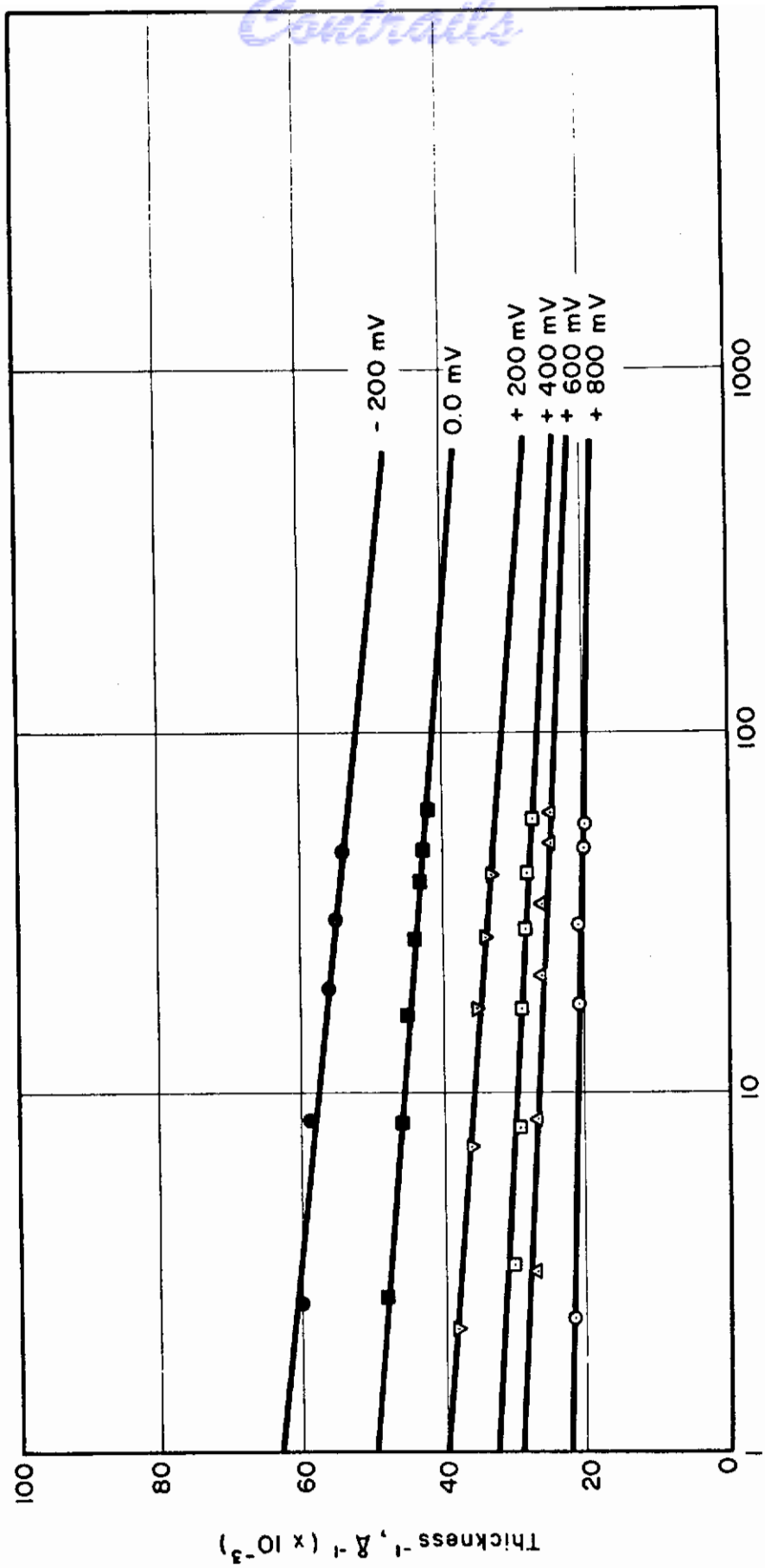

Fig. 212 - Plot of Reciprocal of Film Thickness vs. Time for Fe in Solution pH 8.41

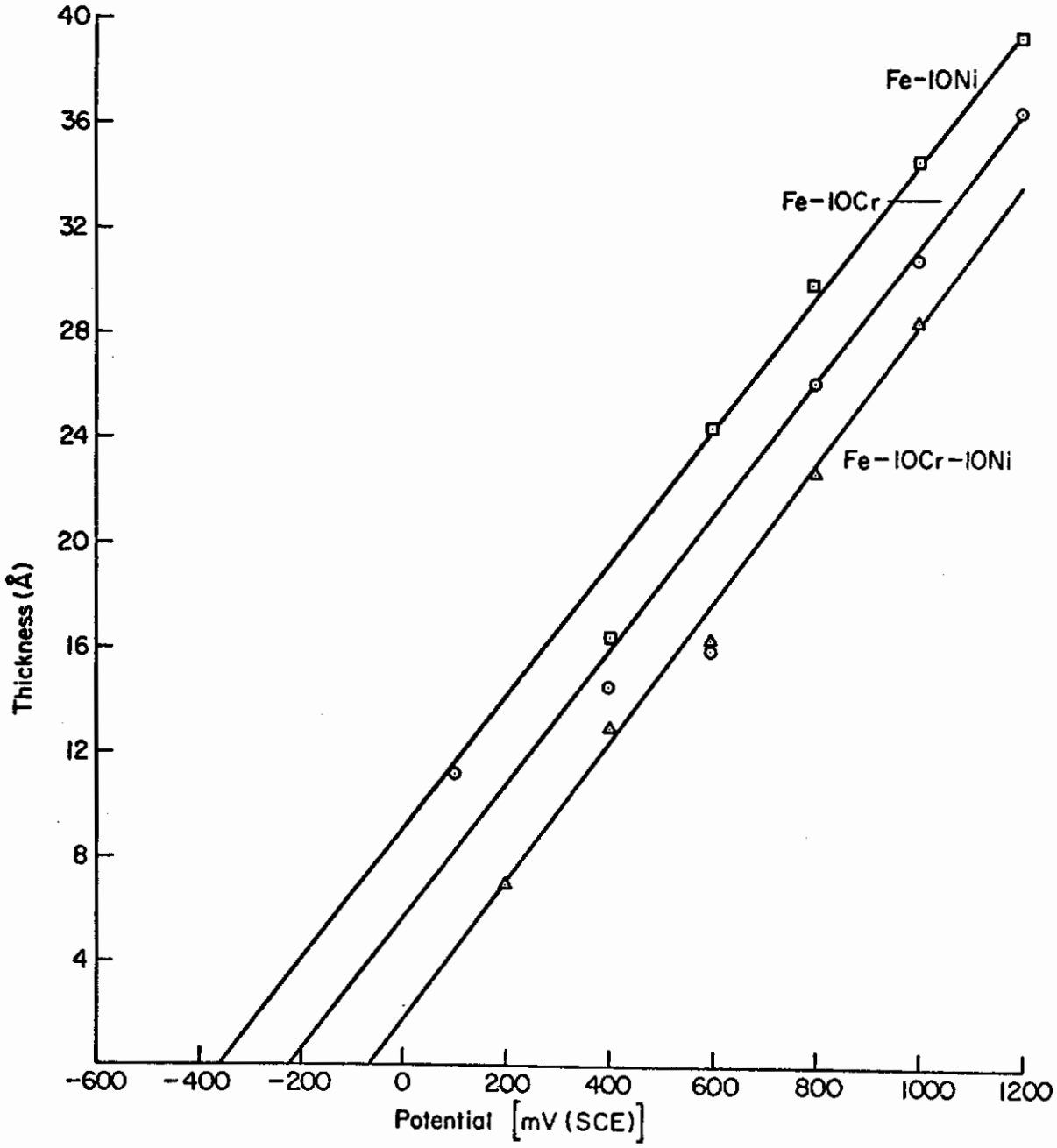

Fig. 213 - Film Thickness vs. Passivation Potential for One Hour of Passivation in Electrolyte of pH 4

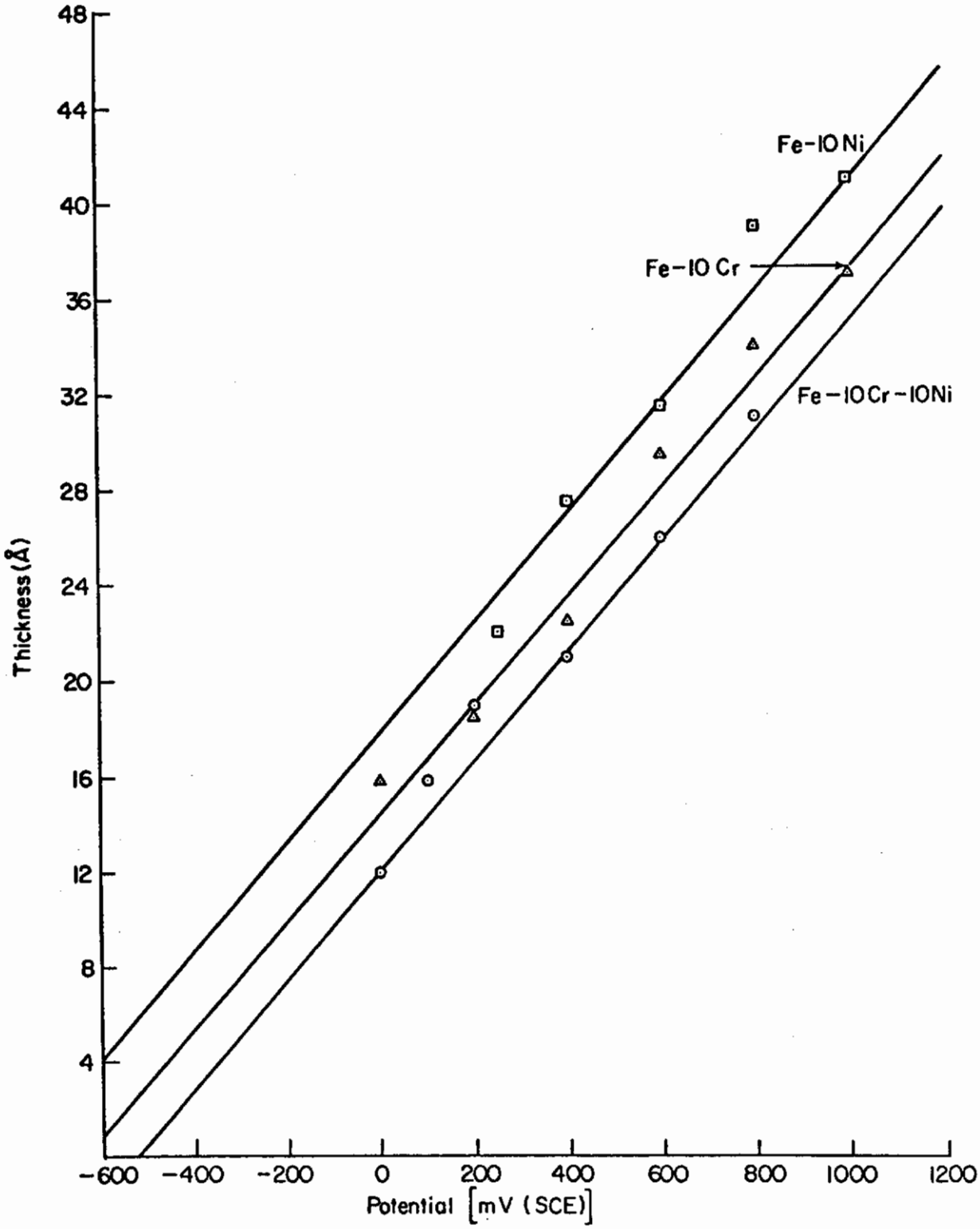

Fig. 214 - Film Thickness vs. Passivation Potentials for One Hour of Passivation in Electrolyte of pH 6

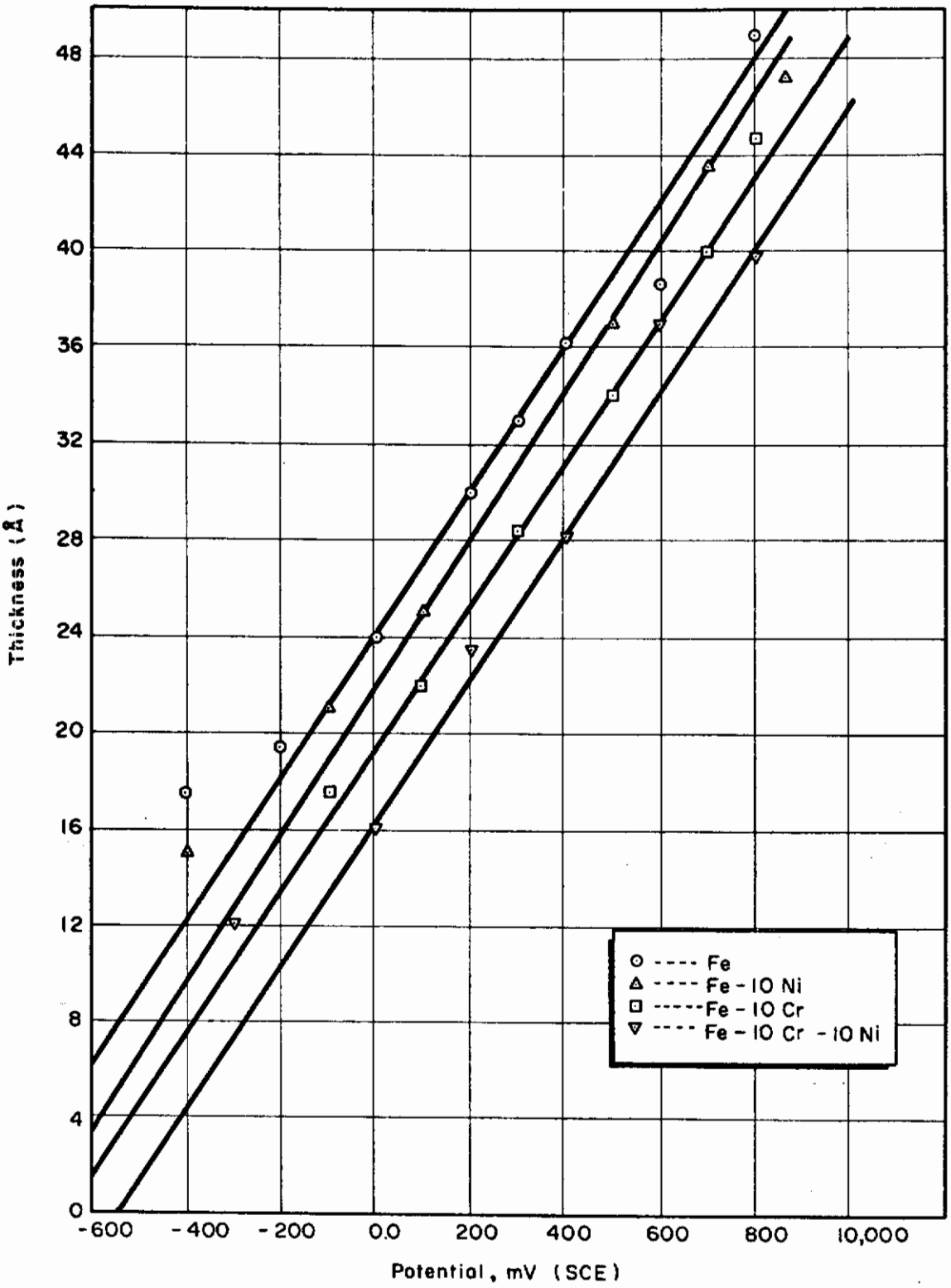

Fig. 215 - Film Thickness vs. Potential for One Hour Polarization

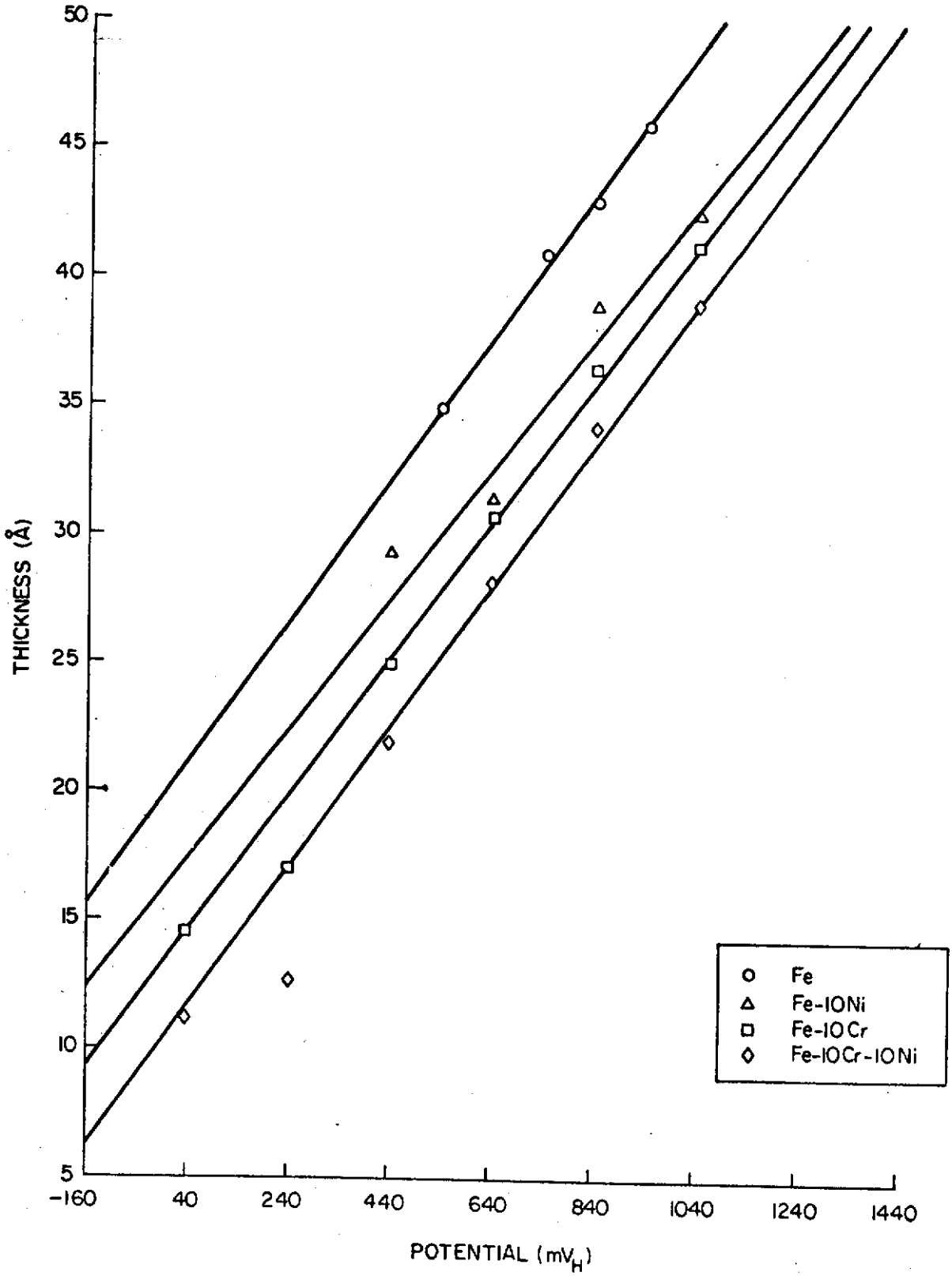

Fig. 216 - Film Thickness vs. Passivation Potential for One Hour of Passivation in Solution of pH 10

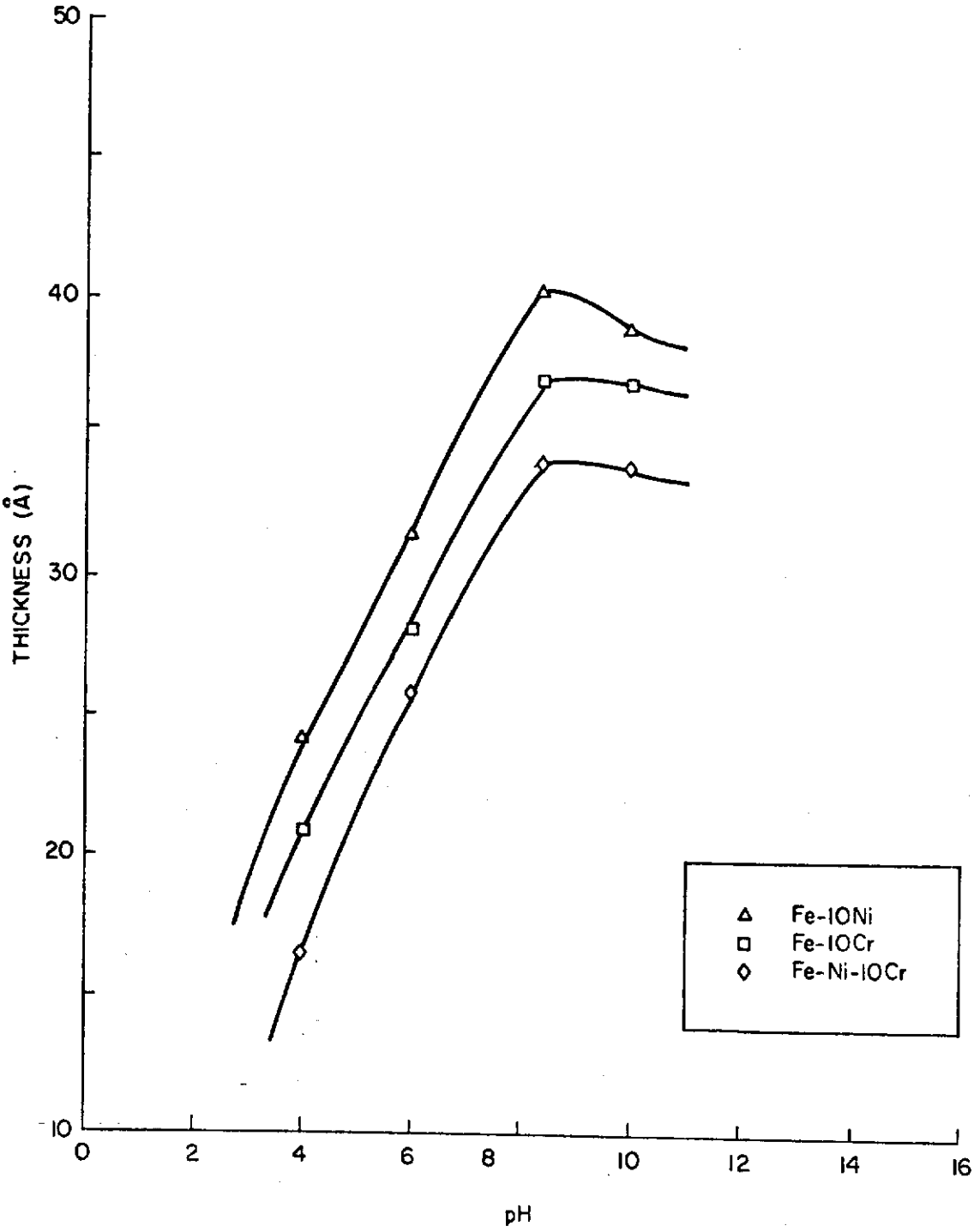

Fig. 217 - Film Thickness vs. pH of Solution for One Hour of Passivation at 600 mV

E. DISSOLUTION OF FERRITE-CARBIDE HETEROGENEOUS STRUCTURE (C. Cron and J. Payer)

1. Objectives

High-strength steels are complex materials containing a number of chemically and structurally different phases. This work is aimed at elucidating the detailed nature of the local dissolution processes in these materials. In order to obtain a less ambiguous understanding, a pure Fe-C (1045 nominal) alloy is being used where there is less uncertainty about the Fe_3C and ferrite compositions and structures than would be the case of the high-strength steel.

2. Experimental

Specimens are prepared by first thinning to the thickness required for transmission electron microscopy. The specimens are then mounted in an electrochemical cell with the salt bridge probe adjacent at various values of pH (0, 4, 10, 14). Figure 218 shows these potentials and pH's relative to schematic figures of the potential-pH diagrams for iron-H_2O and carbon-H_2O. In addition, the effect of various anions was examined at pH 4 and pH 14. All experiments are performed at 25°C. All potentials are reported on the standard hydrogen scale.

3. Results and Discussion

After exposing the specimens at specified potentials and pH's, they are examined in the transmission electron microscope. Figure 219 shows the specimens prior to exposure at constant potential to the environments. Examples of the various types of attack observed are shown in Fig. 220. Clearly, there are four modes of attack. First, the carbide can be dissolved without attack on the ferrite as shown in Fig. 220, a,b. Secondly, the ferrite can be dissolved without dissolving the carbide as shown in Fig. 220, c,d. Thirdly, the interface between ferrite and carbide can be preferentially dissolved as shown in Fig. 220, g,h. Finally, a general attack is possible as shown in Fig. 220, e.f.

The effects of applied potential, pH, and Cl solution composition are summarized in Fig. 221.

Results in Fig. 221 suggest that answers should first be sought by considering the thermodynamic stability of the carbide relative to iron. Tables XXVII and XXVIII summarize relevant equilibria for the Fe-C-H_2O and Cr-C-H_2O systems and the thermodynamic data. Figures 222-225 are plots of the Fe-H_2O, C-H_2O, Fe_3C-H_2O, and Cr_7C_3 equilibria, respectively. Clearly, the Fe_3C and Cr_7C_3 compounds are sufficiently unstable to dissolve over a wide range of potentials. In these diagrams, Figs. 222-225, only the question of stability, but not kinetics, is considered. In view of the inherently unstable nature of the carbides, as well as carbon itself, one must turn to kinetic consideration for

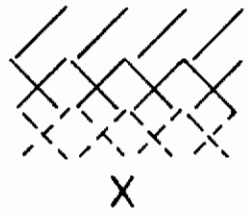

REGION OF PASSIVATION
REGION OF STABILITY FOR Fe
REGION OF STABILITY FOR C
X TEST CONDITIONS FOR VARIOUS SPECIMENS

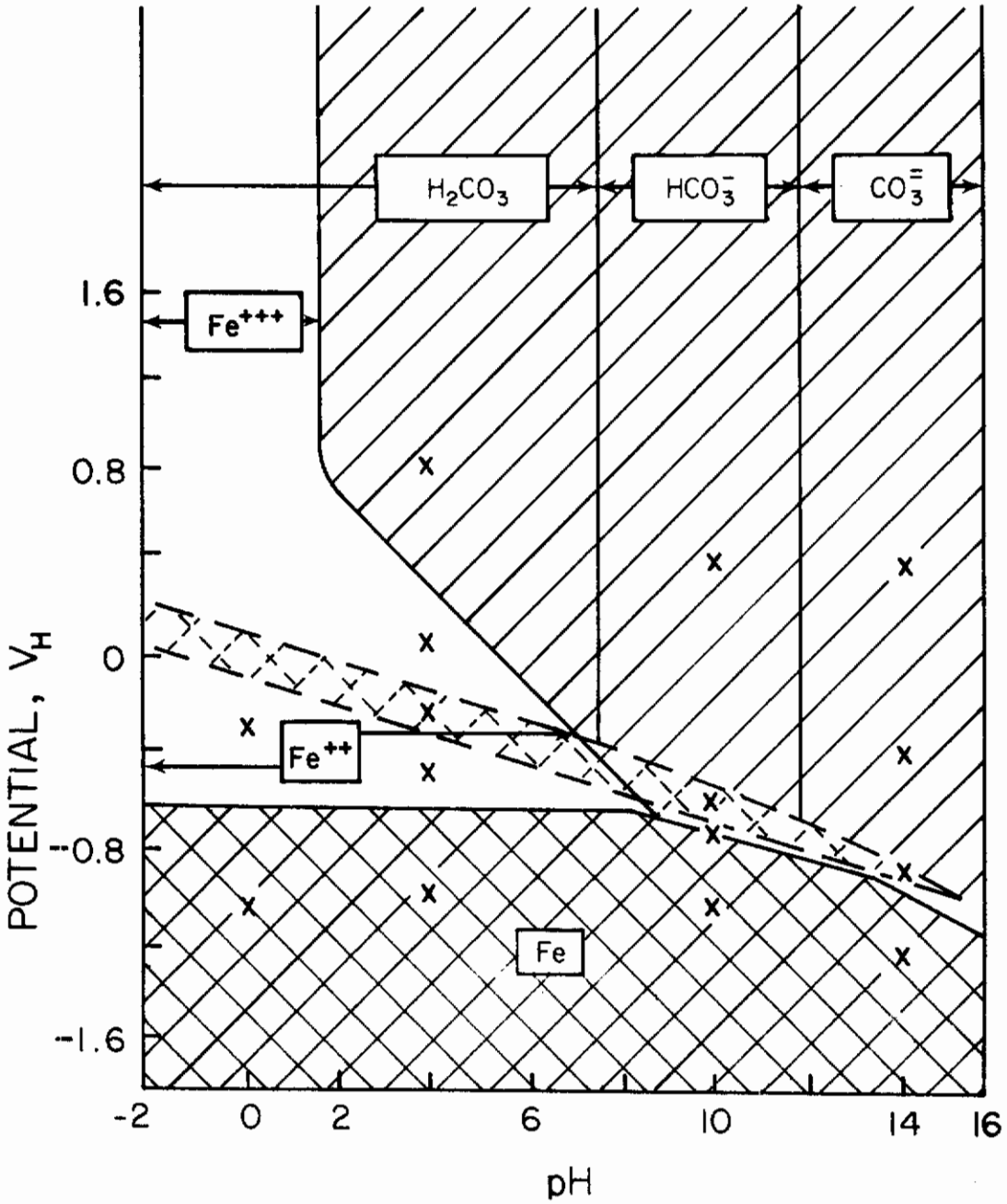

Fig. 218 - Schematic Potential-pH Diagram for Fe-H_2O at 25°C Showing the Potentials at Which Specimens Were Examined in the Electron Microscope

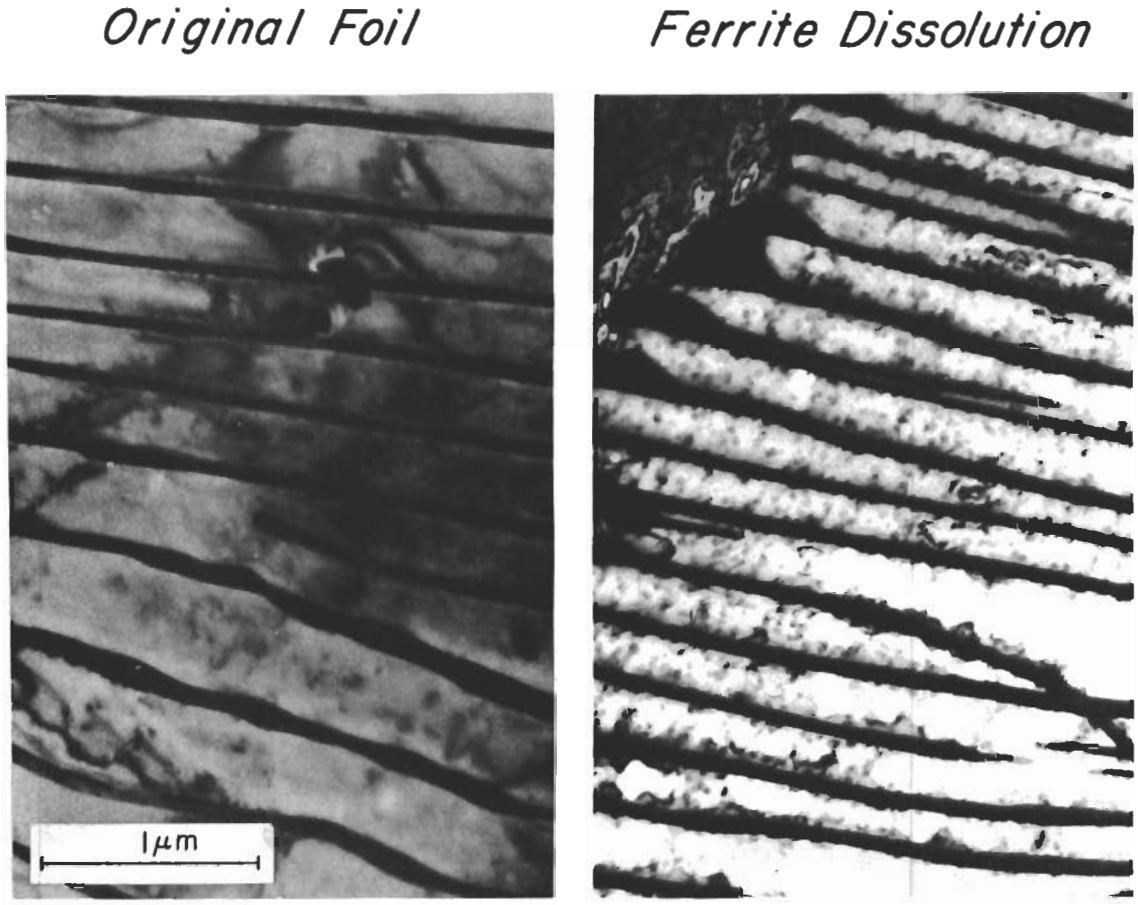

Fig. 219 - Electron Micrographs of the 1045 Carbon Steel Used in These Investigations (as-received)

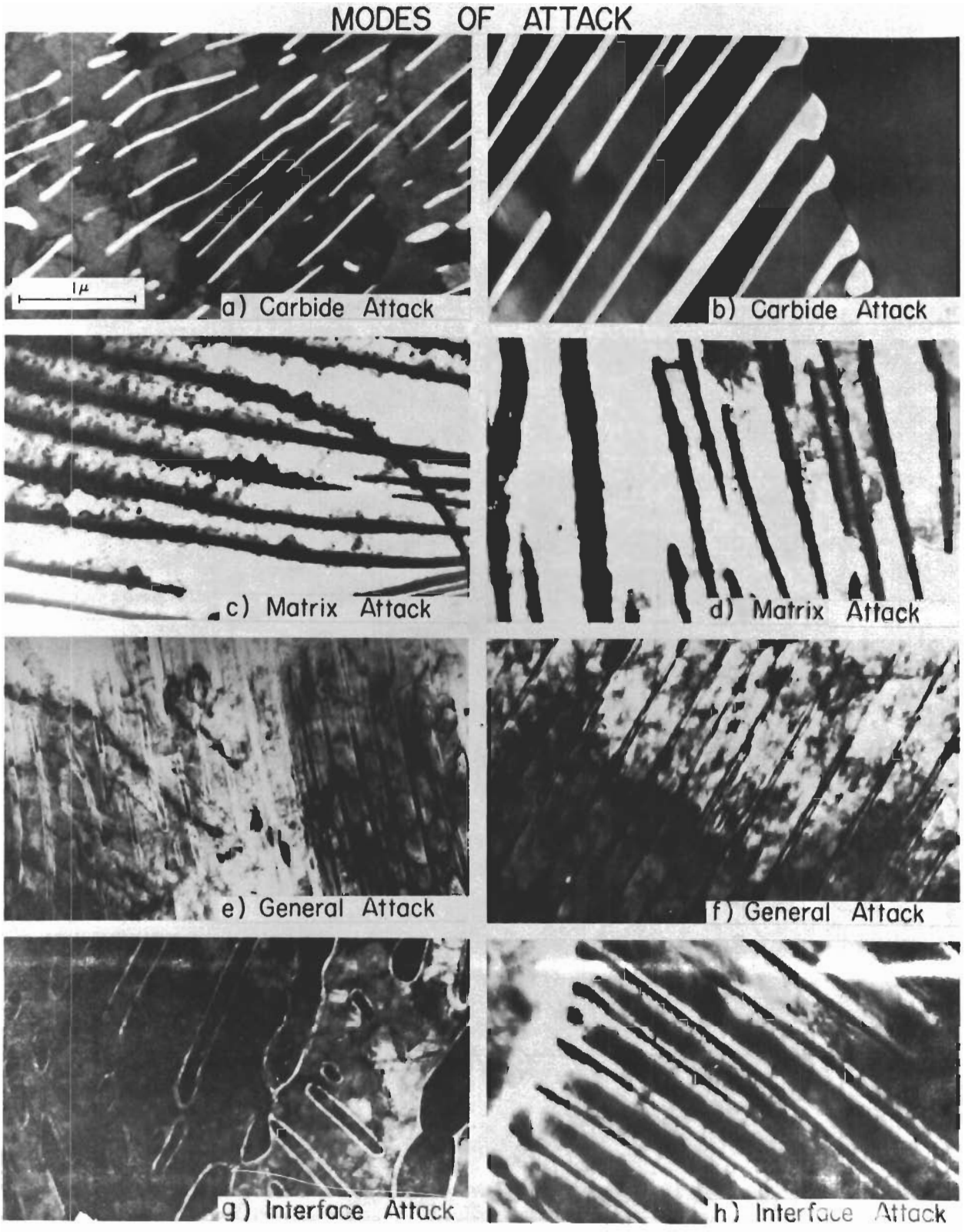

Fig. 220 - Electron Micrographs Showing Various Modes of Attack

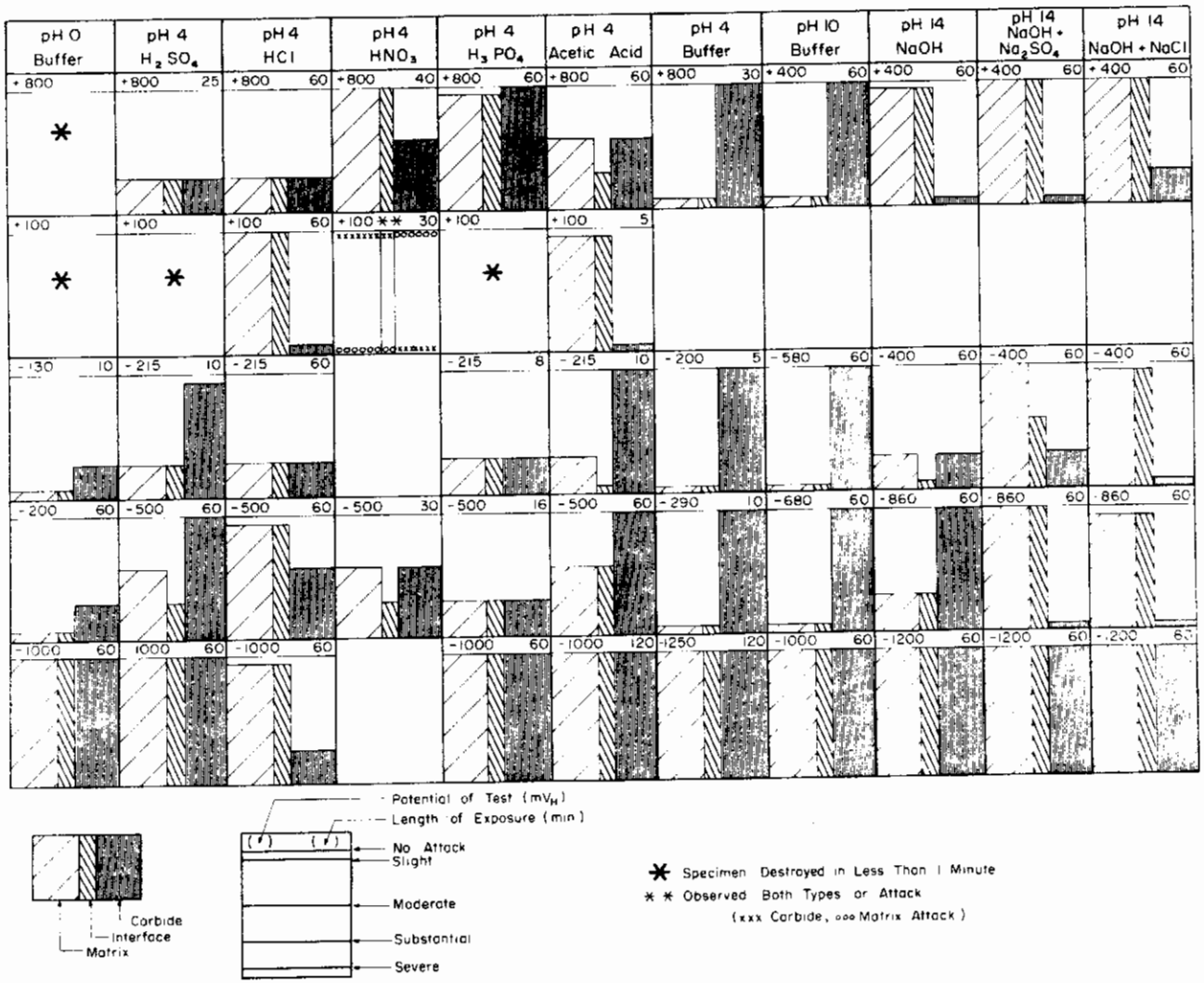

Fig. 221 - Degree of Attack as a Function of Potential and Environment

Table XXVII - Free Energy of Formation of Species Considered

Species	ΔG° (cal/mol)
H_2O	
Fe^{++}	- 20,300
Fe^{+++}	- 2,530
FeO (hydro)	- 58,880
Fe_3C	+ 4,760
CH_3OH	- 41,700
CH_4	- 12,140
H_2CO_3	-149,000
HCO_3^-	-140,310
$CO_3^=$	-126,220
CO_2	- 94,260
Cr_7C_3	- 43,840
Cr^{++}	- 42,100
Cr_2O_3 (hydro)	-250,200
CrO_2^-	-128,090
CrO_3^{-3}	-144,220
CrO (hydro)	- 83,810

Table XXVIII - Reactions and Equilibrium Formulae

Iron-Water System

1. $Fe \rightarrow Fe^{++} + 2e^-$

   $E = - 0.440 + 0.0295 \log [Fe^{++}]$

2. $Fe + H_2O \rightarrow FeO + 2H^+ + 2e^-$

   $E = - 0.047 - 0.059\ pH$

3. $Fe + 2H_2O \rightarrow HFeO_2^- + 3H^+ + 2e^-$

   $E = - 0.493 - 0.087\ pH + 0.0295 \log [HFeO_2^-]$

4. $Fe^{++} + H_2O \rightarrow FeO + 2H^+$

   $\log [Fe^{++}] = 13.29 - 2\ pH$

5. $2Fe^{++} + 3H_2O \rightarrow Fe_2O_3 + 6H^+ + 2e^-$

   $E = 1.057 - 0.177\ pH - 0.0591 \log [Fe^{++}]$

6. $2Fe^{+++} + 3H_2O \rightarrow Fe_2O_3 + 6H^+$

   $\log [Fe^{+++}] = 4.84 - 3\ pH$

7. $2FeO + H_2O \rightarrow Fe_2O_3 + 2H^+ + 2e^-$

   $E = 0.271 - 0.059\ pH$

8. $2HFeO_2^- \rightarrow Fe_2O_3 + H_2O + 2e^-$

   $E = - 0.810 - 0.059 \log [HFeO_2^-]$

Carbon-Water System

1. $CH_3OH \rightleftarrows C + H_2O + 2H^+ + 2e^-$

   $E = - 0.325 - 0.0591\ pH - 0.0295 \log [CH_3OH]$

2. $CH_4 \rightarrow C(s) + 4H^+ + 4e^-$

   $E = 0.132 - 0.0591\ pH - 0.0148 \log [PCH_4]$

Table XXVIII - Continued

3. $C + 3H_2O \rightarrow H_2CO_3 + 4H^+ + 4e^-$

$E = 0.228 - 0.0591\ pH + 0.0148 \log [H_2CO_3]$

4. $C + 3H_2O \rightarrow HCO_3^- + 5H^+ + 4e^-$

$E = 0.323 - 0.0739\ pH + 0.0148 \log [HCO_3^-]$

5. $C + 3H_2O \rightarrow CO_3^= + 6H^+ + 4e^-$

$E = 0.475 - 0.0887\ pH + 0.0148 \log [CO_3^=]$

6. $CO_2 + 4H^+ + 4e^- \rightarrow C + 2H_2O$

$E = 0.207 - 0.0591\ pH + 0.0148 \log [P_{CO_2}]$

7. $H_2CO_3 \rightarrow HCO_3^- + H^+$

$[H_2CO_3] = [HCO_3^-]$ @ pH 6.38

8. $HCO_3^- \rightarrow CO_3^= + H^+$

$[HCO_3^-] = [CO_3^=]$ @ pH 10.34

Iron Carbide-Water System

1. $Fe_3C \rightarrow 3Fe^{++} + C(s) + 6e^-$

$E = - 0.475 + 0.0295 \log [Fe^{++}]$

2. $Fe_3C + H_2O + 2H^+ + 2e^- \rightarrow 3Fe(s) + CH_3OH$

$E = 0\ 0.222 - 0.0591\ pH - 0.0295 \log [CH_3OH]$

3. $Fe_3C + H_2O + 2H^+ \rightarrow 3Fe^{++} + CH_3OH + 4e^-$

$E = - 0.549 + 0.0295\ pH + 0.0148 \log [Fe^{++}]^3\ [CH_3OH]$

4. $Fe_3C + 4H^+ + 4e^- \rightarrow 3Fe(s) + CH_4(g)$

$E = 0.183 - 0.0591\ pH - 0.0148 \log [P_{CH_4}]$

5. $Fe_3C + 4H^+ \rightarrow 3Fe^{++} + CH_4 + 2e^-$

$E = - 1.687 + 0.1182\ pH + 0.0886 \log [Fe^{++}] + 0.0295 \log [P_{CH_4}]$

Table XXVIII - Continued

6. $Fe_3C + 3H_2O \rightarrow 3Fe(s) + H\,CO_3 + 4H^+ + 4e^-$

$E = 0.177 - 0.0591\ pH + 0.0148 \log [H_2CO_3]$

7. $Fe_3C + 3H_2O \rightarrow 3Fe^{++} + H_2CO_3 + 4H^+ + 10e^-$

$E = -0.194 - 0.0236\ pH - 0.0059 \log [H_2CO_3] + 0.0177 \log [Fe^{++}]$

8. $Fe_3C + 3H_2O \rightarrow 3Fe(s) + HCO_3^- + 5H^+ + 4e^-$

$E = 0.271 - 0.0739\ pH + 0.0148 \log [HCO_2^-]$

9. $Fe_3C + 3H_2O \rightarrow 3Fe^{++} + HCO_3^- + 5H^+ + 103^-$

$E = -0.156 - 0.0295\ pH + 0.0177 \log [Fe^{++}] + 0.0059 \log [HCO_3^-]$

10. $Fe_3C + 3H_2O \rightarrow 3Fe(s) + CO_3^= + 6H^+ + 4e^-$

$E = 0.424 - 0.0886\ pH + 0.0148 \log [CO_3^=]$

11. $Fe_3C + 3H_2O \rightarrow 3Fe^{++} + CO_3^= + 6H^+ + 10e^-$

$E = -0.095 - 0.0354\ pH + 0.0177 \log [Fe^{++}] + 0.0059 \log [CO_2^=]$

12. $Fe_3C + 2H_2O \rightarrow 3Fe(s) + CO_2 + 4H^+ + 4e^-$

$E = 0\ 0.156 - 0.059\ pH + 0.0148 \log [P_{CO_2}]$

13. $Fe_3C + 2H_2O \rightarrow 3Fe^{++} + CO_2 + 4H^+ + 10e^-$

$E = 0\ 0.202 - 0.024\ pH + 0.018 \log [Fe^{++}] + 0.006 \log [P_{CO_2}]$

14. $Fe_3C + 3H_2O \rightarrow 3FeO(s) + C(s) + 6H^+ + 6e^-$

$E = -0.082 - 0.059\ pH$

15. $Fe_3C + 4H_2O \rightarrow 3FeO + CH_3OH + 4H^3 + 4e^-$

$E = -0.040 - 0.059\ pH + 0.0148 \log [CH_3OH]$

16. $Fe_3C + 3H_2O \rightarrow 3FeO + CH_4 + 2H^+ + 2e^-$

$E = -0.509 - 0.059\ pH + 0.0296 \log [P_{CH_4}]$

17. $Fe_3C + 6H_2O \rightarrow 3FeO + H_2CO_3 + 10H^+ + 10e^-$

$E = -0.042 - 0.059\ pH + 0.006 \log [H_2CO_3]$

Table XXVIII - Continued

18. $Fe_3C + 6H_2O \rightarrow 3FeO + HCO_3^- + 11H^+ + 10e^-$

$E = + 0.080 - 0.065\ pH + 0.006 \log [HCO_3^-]$

19. $Fe_3C + 6H_2O \rightarrow 3FeO + CO_3^= + 12H^+ + 10e^-$

$E = + 0.141 - 0.071\ pH + 0.006 \log [CO_3^=]$

20. $Fe_3C + 5H_2O \rightarrow 3FeO + CO_2 + 10H^+ + 10e^-$

$E = + 0.034 - 0.059\ pH + 0.006 \log [P_{CO_2}]$

Chromium Carbide-Water System

1. $Cr_7C_3 \rightarrow 7Cr^{++} + 3C(s) + 14e^-$

$E = - 0.775 + 0.0295 \log [Cr^{++}]$

2. $Cr_7C_3 + 3H_2O + 6H^+ + 6e^- \rightarrow 7Cr(s) + 3CH_3OH$

$E = - 0.641 - 0.0591\ pH - 0.0295 \log [CH_3OH]$

3. $Cr_7C_3 + 3H_2O + 6H^+ \rightarrow 7Cr^{++} + 3CH_3OH + 8e^-$

$E = - 1.09 + 0.044\ pH + 0.049 \log [Cr^{++}] + 0.021 \log [CH_3OH]$

4. $Cr_7C_3 + 12H^+ + 12e^- \rightarrow 7Cr(s) + 3CH_4$

$E = 0.025 - 0.0591\ pH - 0.0148 \log [P_{CH_4}]$

5. $Cr_7C_3 + 12H^+ \rightarrow 7Cr^{++} + 3CH_4 + 2e^-$

$E = - 6.23 + 0.354\ pH + 0.203 \log [Cr^{++}] + 0.089 \log [P_{CH_4}]$

6. $Cr_7C_3 + 9H\ O \rightarrow 7Cr(s) + 3H_2CO_3 + 12H^+\ 12e^-$

$E = 0.387 - 0.0591\ pH + 0.0148 \log [H_2CO_3]$

7. $Cr_7C_3 + 9H_2O \rightarrow 7Cr^{++} + 3H_2CO_3 + 12H^+ + 26e^-$

$E = - 0.313 - 0.027\ pH + 0.016 \log [Cr^{++}] + 0.007 \log [H_2CO_3]$

8. $Cr_7C_3 + 9H_2O \rightarrow 7Cr(s) + 3HCO_3 + 15H^+ + 12e^-$

$E = 0.481 - 0.074\ pH + 0.0148 \log [HCO_3^-]$

Table XXVIII - Continued

9. $Cr_7C_3 + 9H_2O \rightarrow 7Cr^{++} + 3HCO_3^- + 15H^+ + 26e^-$

$E = - 0.269 - 0.0341\ pH + 0.0159 \log [Cr^{++}] + 0.0068 \log [HCO_3^-]$

10. $Cr_7C_3 + 9H_2O \rightarrow 7Cr(s) + 3CO_3^= + 18H^+ + 12e^-$

$E = 0.634 - 0.0887\ pH + 0.0148 \log [CO_2^=]$

11. $Cr\ C_3 + 9H_2O \rightarrow 7Cr^{++} + 3CO_3^= + 18H^+ + 26e^-$

$E = - 0.199 - 0.0409\ pH + 0.0159 \log [Cr^{++}] + 0.0068 \log [CO_3^=]$

12. $2Cr_7C_3 + 21H_2O \rightarrow 7Cr_2O_3 + 6C + 42H^+ + 42e^-$

$E = - 0.489 - 0.0591\ pH$

13. $2Cr_7C_3 + 39H_2O \rightarrow 7Cr_2O_3 + 6H_2CO_3 + 66H^+ + 66e^-$

$E = - 0.228 - 0.0591\ pH + 0.0054 \log [H_2CO_3]$

14. $2Cr_7C_3 + 39H_2O \rightarrow 7Cr_2O_3 + 6HCO_3^- + 72H^+ + 66e^-$

$E = - 0.194 - 0.0645\ pH + 0.0054 \log [HCO_3^-]$

15. $2Cr_7C_3 + 39H_2O \rightarrow 7Cr_2O_3 + 6CO_3^= + 78H^+ + 66e^-$

$E = - 0.138 - 0.0698\ pH + 0.0054 \log [CO_3^=]$

16. $Cr_7C_3 + 23H_2O \rightarrow 7CrO_2^- + 3CO_3^= + 46H^+ + 33e^-$

$E = 0.095 - 0.824\ pH + 0.0054 \log [CO_2^=] + 0.0125 \log [CrO_2^-]$

17. $Cr_7C_3 + 14H_2O \rightarrow 7CrO_2^- + 3C + 28H^+ + 21e^-$

$E = - 0.122 - 0.0788\ pH + 0.0197 \log [CrO_2^-]$

18. $Cr_7C_3 + 30H_2O \rightarrow 7CrO^{\equiv} + 3CO_2^= + 60H^+ + 33e^-$

$E = 0.468 - 0.1075\ pH + 0.0125 \log [CrO_3^{\equiv}] + 0.0054 \log [CO_3^=]$

19. $Cr_7C_3 + 21H_2O \rightarrow 7CrO_3^{\equiv} + 3C + 42H^+ + 21e^-$

$E = 0.464 - 0.1182\ pH + 0.0197 \log [Cr_2O^{\equiv}]$

20. $Cr_7C_3 + 7H_2O \rightarrow 7CrO + 3C + 14H^+ + 14e^-$

$E = - 0.452 - 0.0591\ pH$

Table XXVIII - Continued

21. $Cr_7C_3 + 16H_2O \rightarrow 7CrO + 3H_2CO_3 + 26H^+ + 26e^-$

$E = - 0.138 - 0.0591\ pH + 0.0068 \log [H_2CO_3]$

22. $Cr_7C_3 + 16H_2O \rightarrow 7CrO + 3HCO_3^- + 29H^+ + 26e^-$

$E = - 0.0946 - 0.0659\ pH + 0.0068 \log [HCO_3^-]$

23. $Cr_7C_3 + 16H_2O \rightarrow 7CrO + 7CrO + 3CO_3^= + 32H^+ + 26e^-$

$E = - 0.024 - 0.0727\ pH + 0.0068 \log [CO_3^=]$

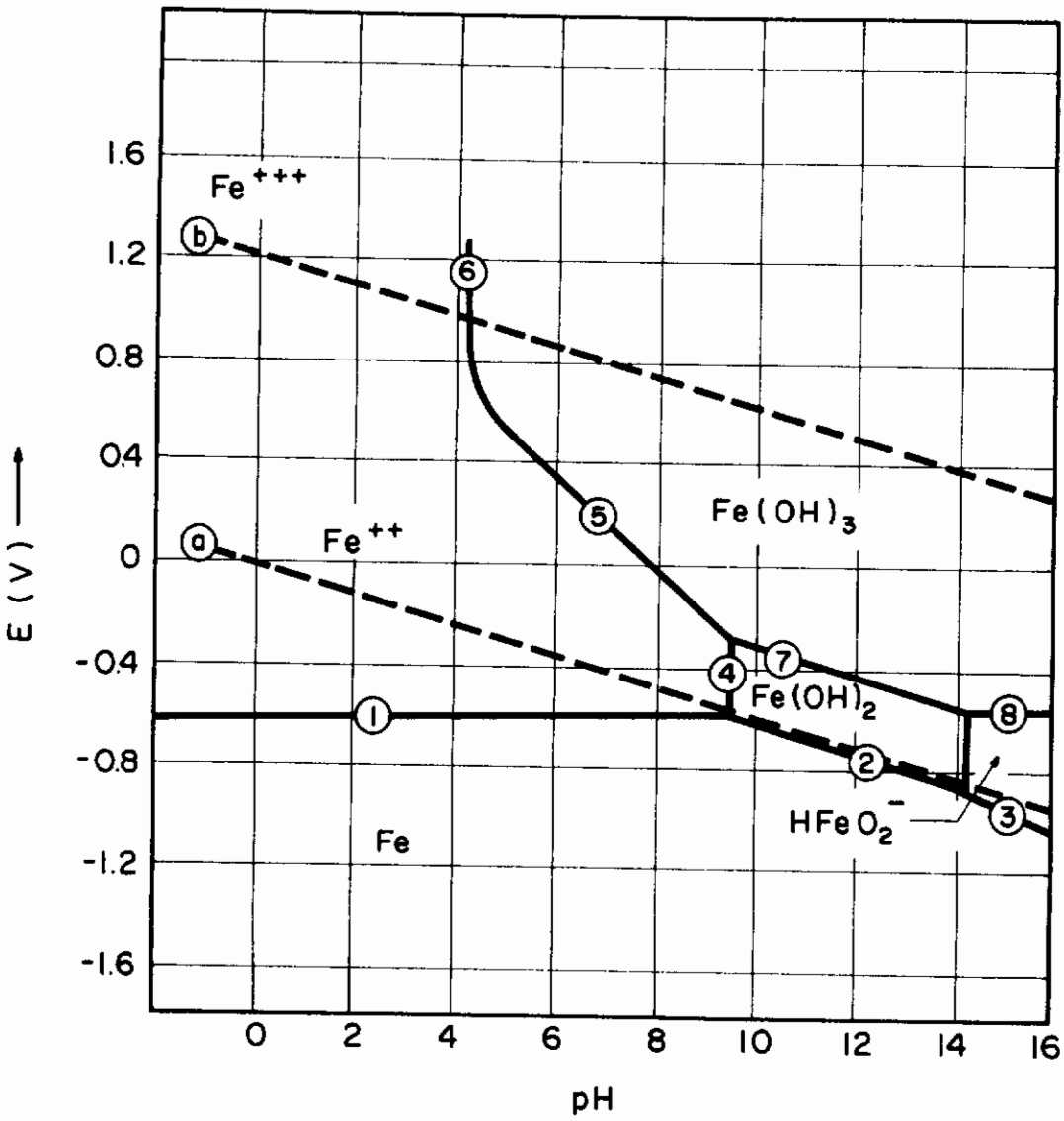

Fig. 222 - Potential-pH Diagram for the Iron-Water System at 25°C

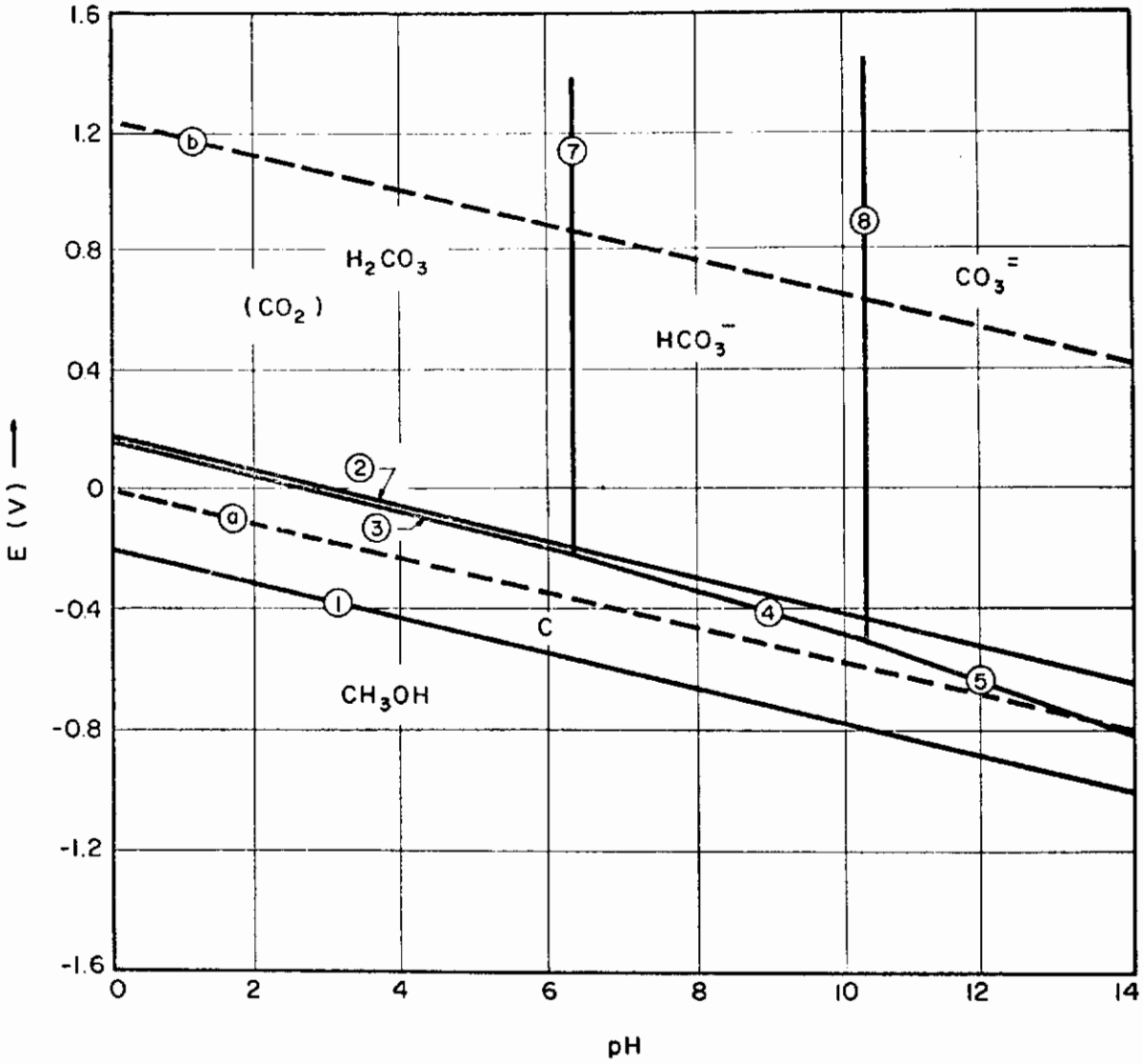

Fig. 223 - Potential-pH Diagram for the Carbon-Water System at 25°C

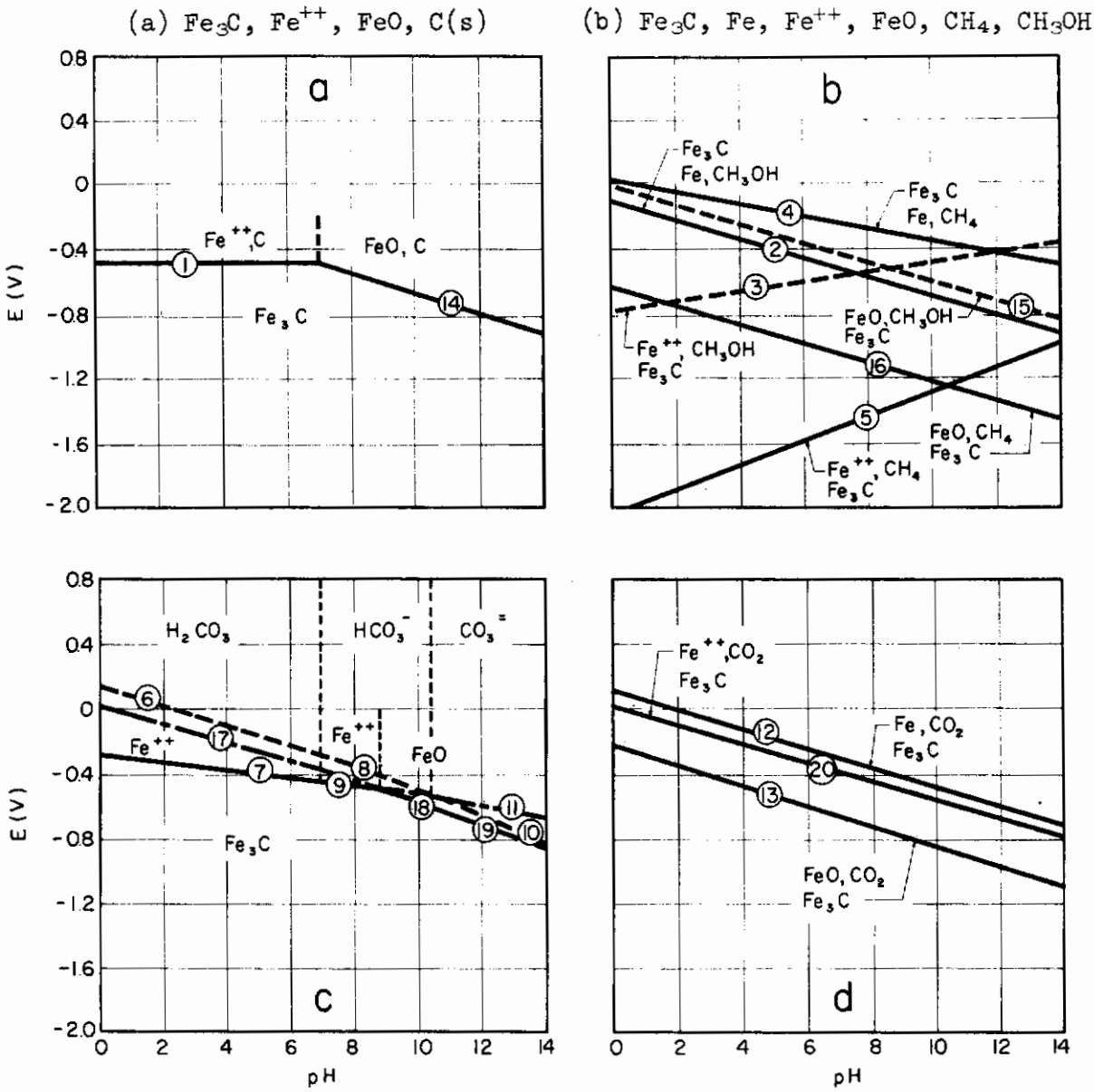

Fig. 224 - Potential-pH Diagrams for Fe_3C in H_2O Considering Species Shown

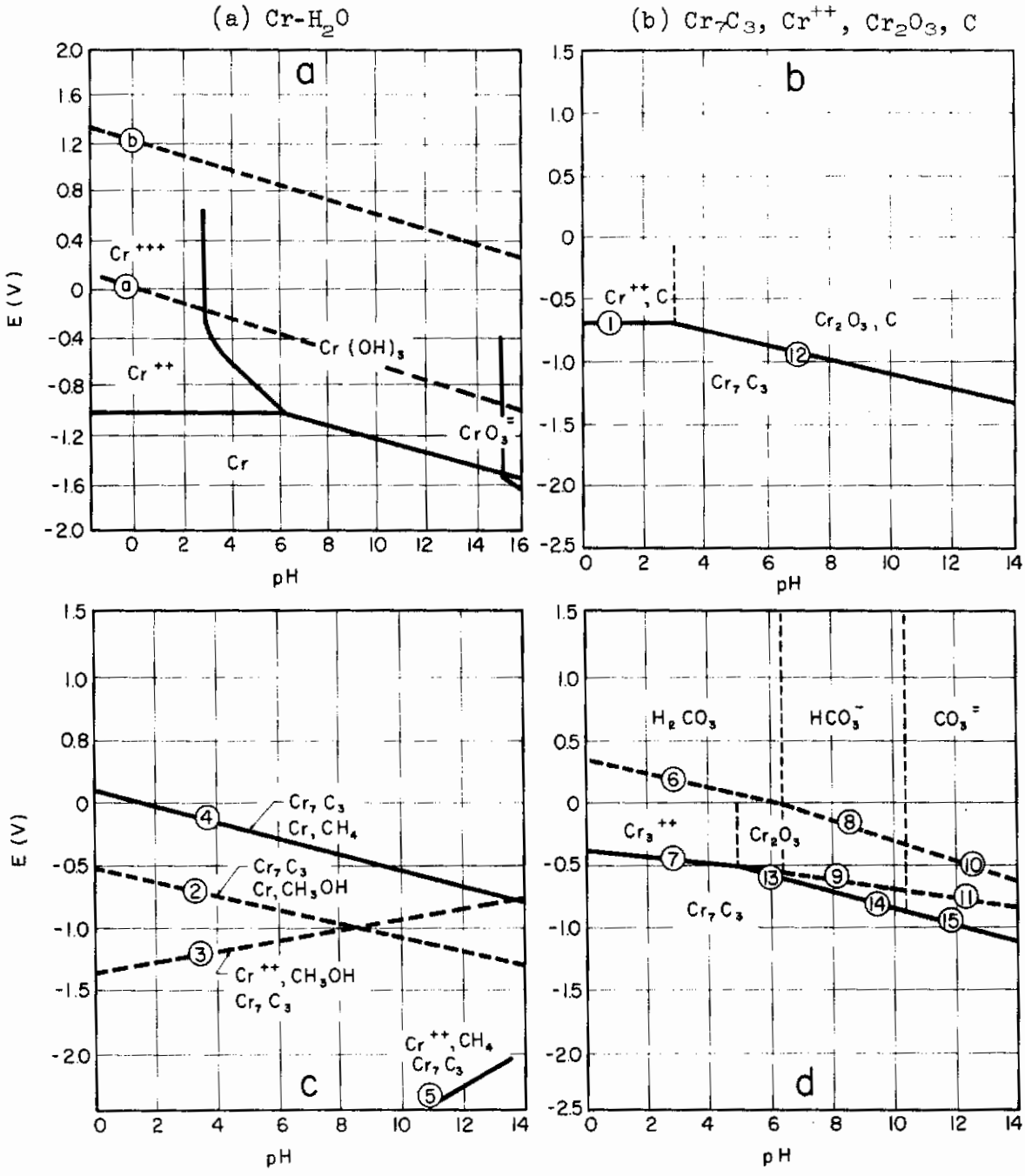

Fig. 225 - Potential-pH Diagrams for Cr_7C_3 Considering Species Shown

understanding the patterns of Fig. 221. Specific considerations of these thermodynamic diagrams are listed below.

(1) Iron Stability

The equilibrium diagram for Fe-H_2O, shown in Fig. 222, has been taken from Pourbaix. The species considered for the diagram are Fe, Fe^{++}, Fe^{+++}, $Fe(OH)_2$, $Fe(OH)_3$, and $HFeO_2^-$. The equilibrium formulae are given in Table XXVIII. The region below lines 1, 2, and 3 is the region in which iron is thermodynamically stable in water at 25°C. Iron is unstable and will corrode in regions where the product of oxidation is soluble; i.e., in regions of Fe^{++} and $HFeO_2^-$. In regions where the corrosion product is a solid, iron can passivate; i.e., in regions of $Fe(OH)_2$ and $Fe(OH)_3$. Lines a and b define the region of stability of water with respect to hydrogen gas and oxygen gas, respectively.

(2) Carbon Stability

The equilibrium diagram for C-H_2O is shown in Fig. 223. The species considered are C, CH_3OH, CH_4, H_2CO_3, HCO_3^-, $CO_3^=$, and CO_2. Above lines 3, 4, and 5 carbon can be oxidized to H_2CO_3, HCO_3^-, and $CO_3^=$, respectively. Lines 7 and 8 define the regions of predominance of H_2CO_3, HCO_3^-, and $CO_3^=$. Below lines 2 and 4 carbon can be reduced to CH_4 and CH_3OH, respectively. It is of interest to note that carbon has no region of thermodynamic stability in aqueous solution. However, the strength of the carbon-carbon bond makes the system react irreversibly, thus graphite finds use as anodes in cathodic protection. The equilibria involved are listed in Table XXVIII.

(3) Iron Carbide Stability

The species considered are Fe, C, Fe_3C, Fe^{++}, $Fe(OH)_2$, CH_3OH, CH_4, H_2CO_3, HCO_3^-, $CO_3^=$, and CO_2. The equilibria involved are listed in Table XXVIII. Figure 224 a-d shows the potential-pH plots of the equilibria. In Fig. 224b lines 2 and 4 show the potential required to reduce Fe_3C to methanol and methane, respectively. The iron carbide is less stable with respect to methane. The oxidation of iron carbide to carbonic acid, bicarbonate ion, and carbonate ion is considered in Fig. 224c. The dashed lines are metastable with respect to solid lines 7, 9, 18, and 19. Figure 224d shows lines for oxidation of Fe_3C to carbon dioxide.

(4) Chromium Carbide (Cr_7C_3) Stability

The stability of chromium carbide is of interest because of its presence in any alloy of practical significance. Sensitization of stainless steels is but one example in which the electrochemical behavior of chromium carbide is important. Figure 225 shows plots of the equilibria are listed in Table XXVIII. The species considered are Cr_7C_3, Cr^{++}, Cr_2O_3, CrO_2^-, CrO_3^{-3}, CrO (hydr), C, CH_3OH, CH_4, H_2CO_3, HCO_3^-, and $CO_3^=$.

Figure 225a is the potential-pH diagram for the chromium-water system. Chromium, like iron, corrodes in acid solutions and passivates as pH increases. The chromium passive region is larger than that of iron.

(5) Complex Species Solubility

The formation of complexes between ions in solution may affect the kinetics of dissolution. If a soluble complex is stable, the dissolution kinetics can be accelerated. Conversely, if an insoluble compound is stable, the dissolution kinetics can be retarded. It is thought that the presence of complexes will prove to be the reason for the different behavior observed in the presence of different anions. A study was thus undertaken to define the region of stability of the various complexes which are possible in an iron-water-carbon system. Some of the results of this study are given below.

(a). Iron Carbonate ($FeCO_3$). The solubility product for this complex as given by Latimer is 2.11×10^{-11} ferrous carbonate will be precipitated. Higher ferrous ion concentration is favored by low pH whereas higher carbonate ion concentration is favored by high pH. The carbonate ion concentration falls off much more rapidly than the ferrous ion concentration increases as pH is lowered. Thus, precipitation of iron carbonate is favored by high pH.

(b). Carbon Tetrachloride (CCl_4). In solutions containing chloride ions, carbon tetrachloride could be present. The free energy of formation of CCl_4 is small and hence the reaction, $C + 4Cl^- \leftrightarrows CCl_4 +$ has a high reversible potential ($E^\circ = 1.18$). The tendency to form CCl_4 is small.

(c). Ferric Tartrate - $Fe_2(C_4H_4O_6)_3$. The pH 4 buffer solution contained 0.1M $KHC_8H_4O_4$. Ferric tartrate is a soluble complex and may possibly explain why the specimens at +800 mV in the pH 4 buffer solution exhibited very rapid matrix attack.

4. Conclusions

The significance of the above results is still not completely clear but a number of important ideas should be emphasized as follows:

(a). The behavior of ferrite and iron carbide varies drastically over the range of potential and pH.

(b). The effect of the anion present is substantial in some instances.

(c). The consideration of complexes formed in the system is of great importance and further work in this area should prove fruitful.

(d). In several cases, the carbide-ferrite interface was attacked more vigorously than the rest of the specimen. It is possible that this is the result of segregation of other elements to this interface. Manganese is suspected because it would be rejected from the carbide during carbide growth and it accelerates the anodic dissolution kinetics of iron.

(e). The dissolution of carbides and slight attack of the matrix at -1000 mV in the pH 4 HCl solution is unexpected but is in accord with the prediction of Fig. 224b.

F. STABILITY OF METALLIC CARBIDES (J. Payer)

1. Objectives and Background

The purpose of this work is to characterize the dissolution behavior of carbides, and relate their behavior to that of the engineering materials in which they commonly occur. The dissolution of Fe-C alloys with carbon contents of 0.8, 2.0, and 4.3 wt % are determined electrochemically, and the products of carbon oxidation or reduction are identified by gas chromatography. The electrochemical behavior chromium carbide ($Cr_{23}C_6$), titanium carbide (TiC), vanadium carbide (VC), and uranium carbide (UC) was examined in several environments.

Carbides are common constituents of engineering materials and can greatly affect the corrosion behavior of these materials. The sensitization of stainless steel alloys is directly related to the presence of chromium carbides at the grain boundaries. "Ring worm" corrosion, common in the petroleum industry, occurs because of the decreased corrosion resistance of steel when carbides form a spheroidized structure as opposed to a pearlite (lamellar) structure.

The morphology of local dissolution of an Fe-C alloy as a function of potential, pH, and environment is reported. It has been shown that the dissolution of the ferrite matrix and the iron carbide is a function of these three variables and that the mode of attack observed can be altered by changing either the potential, the pH, or the anion present.

The processes determining the dissolution behavior of compounds are not well understood. The aim of this work is to elucidate these processes and to define their controlling parameters.

2. Materials

a. Iron-Carbon Alloys

Three Fe-C alloys were cast; i.e., a 0.8 wt% C (eutectoid) alloy, a 2.0 wt%C alloy, and a 4.3 wt%C (eutectic) alloy. The as-cast

0.8 wt % C and 2.0 wt % C alloys were solution-treated at 815°C for 25 minutes and then held at 650°C for 50 hours. The 4.3 wt % C alloy was solution-treated at 815° for 20 minutes and then held at 650° for 20 hours. A molten salt bath was used during heat treating in order to avoid oxidation of the specimens. Figures 226a and b are metallographs of the 0.8 wt % C alloy after heat treatment. In the structure the carbides are evenly distributed and roughly spherical in shape. Figures 227a and b are metallographs of the 2.0 wt % C alloy after heat treatment. The carbides in this structure are elongated as spherodization of the cementite lamellae is not complete. Figures 228a and b are metallographs of the 4.3 wt % C alloy after heat treatment. Cementite is the continuous phase in this alloy.

X-ray diffractometer scans of all the heat-treated alloys showed strong lines for both α-Fe and Fe_3C. No peaks for γ-Fe, Fe_2C, or graphite were observed.

b. $Cr_{23}C_6$, VC, and TiC

The chromium carbide ($Cr_{23}C_6$) sample was prepared by induction melting, using conventional practices.* X-ray diffraction analyses indicate it to be stoichiometric and no other carbides, nor elemental Cr, are present.

Single crystal samples of TiC and VC were prepared from sintered powder rods of 80-90% density by the floating zone technique.** The samples were subsequently annealed at 1800°C for 5 hours and furnace cooled. Chemical analyses indicate that the crystals contained approximately 0.01 w/o each of oxygen and nitrogen, and traces ($< 0.1\%$) of metallic impurities such as Cr and Fe. The stoichiometry of the vanadium carbide is $VC_{0.85}$. The approximate size of each sample is 6 mm x 2 mm x 2 mm.

3. Description of Gas Chromatographic Technique to Analyze Gaseous Products of Carbide Dissolution

The products of reaction of the carbides are primarily CO_2 and CH_4. Thus, a gas chromatographic technique is particularly useful. Details of these analytical efforts are described below:

a. Theory of Operation

Figure 229 is a schematic diagram of a gas chromatograph. A gas sample to be analyzed is inserted into the carrier gas stream.

---

*$Cr_{23}C_6$ provided by Dr. C. S. Tedmon of the General Electric Company Research & Development Center; Schenectady, N. Y.

**TiC and VC supplied by Dr. G. E. Hollox of Brown, Boveri and Company; Baden, Switzerland.

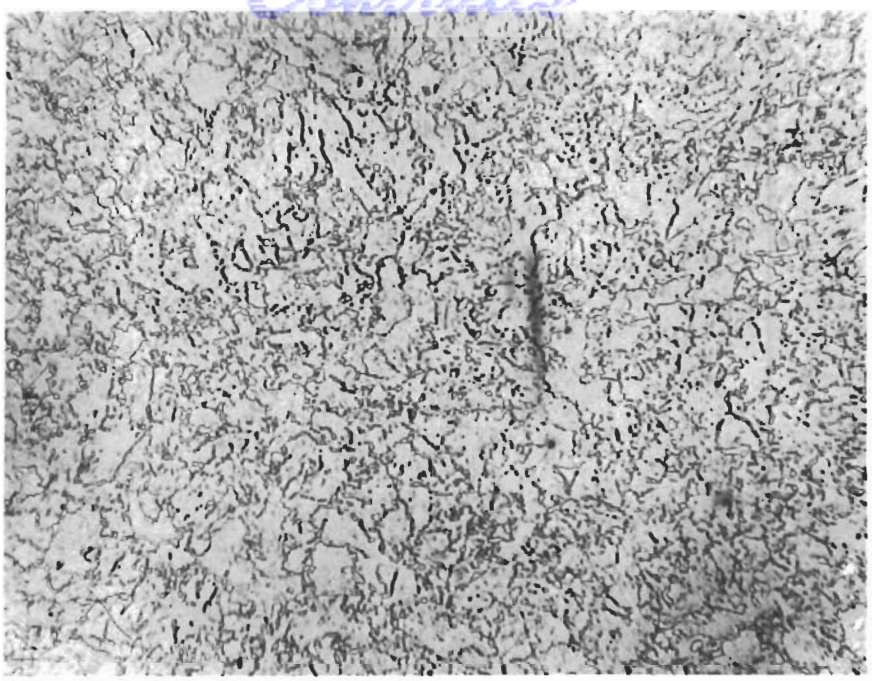

(a) 150X

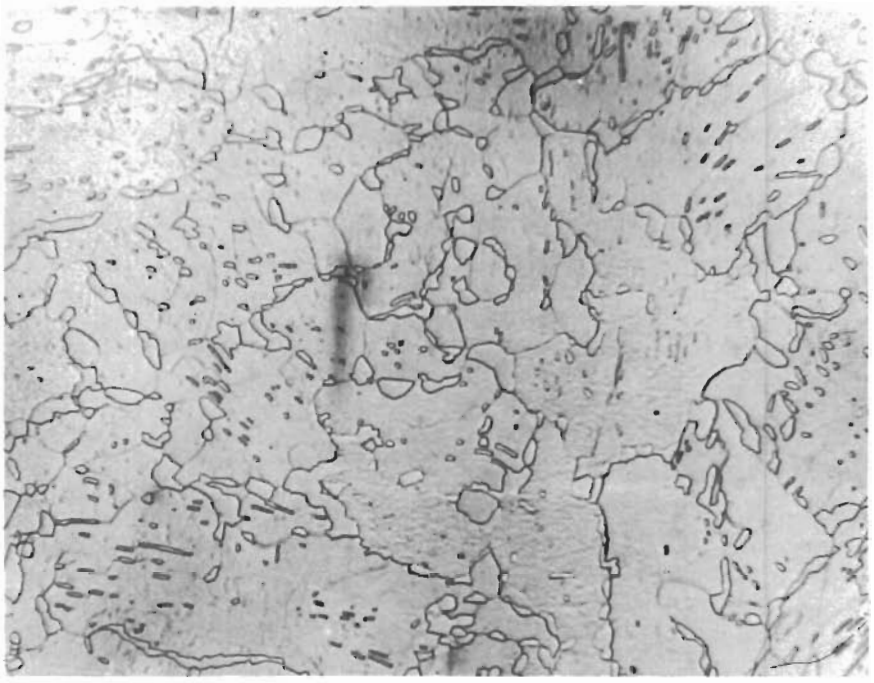

(b) 1000X

Fig. 226 - Carbide Morphology and Distribution in 0.8 w/o C Iron-Carbon Alloy (Heat treatment - 815°C, 25 min and 650°C, 50 hr) 3% Nital Etch

(a) 150X

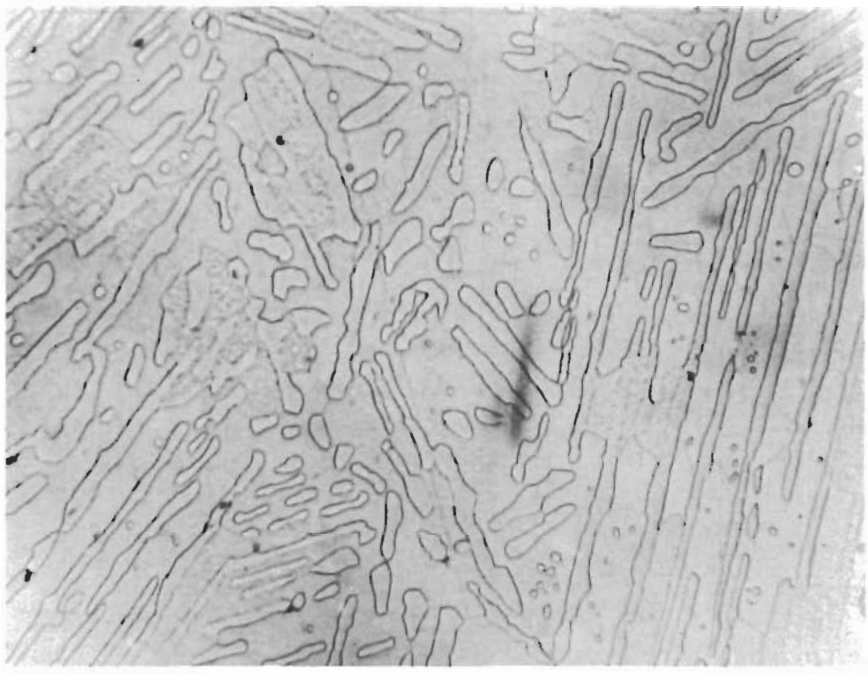

(b) 1000X

Fig. 227 - Carbide Morphology and Distribution in 2.0 w/o C Iron-Carbon Alloy (Heat treatment - 815°C, 25 min and 650°C, 50 hr) 3% Nital Etch

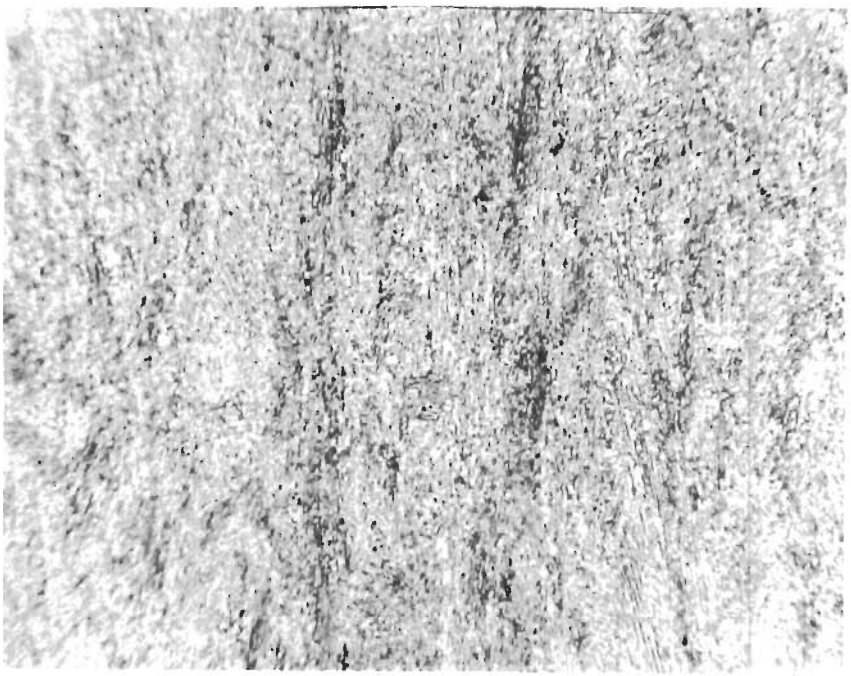

(a) 150X

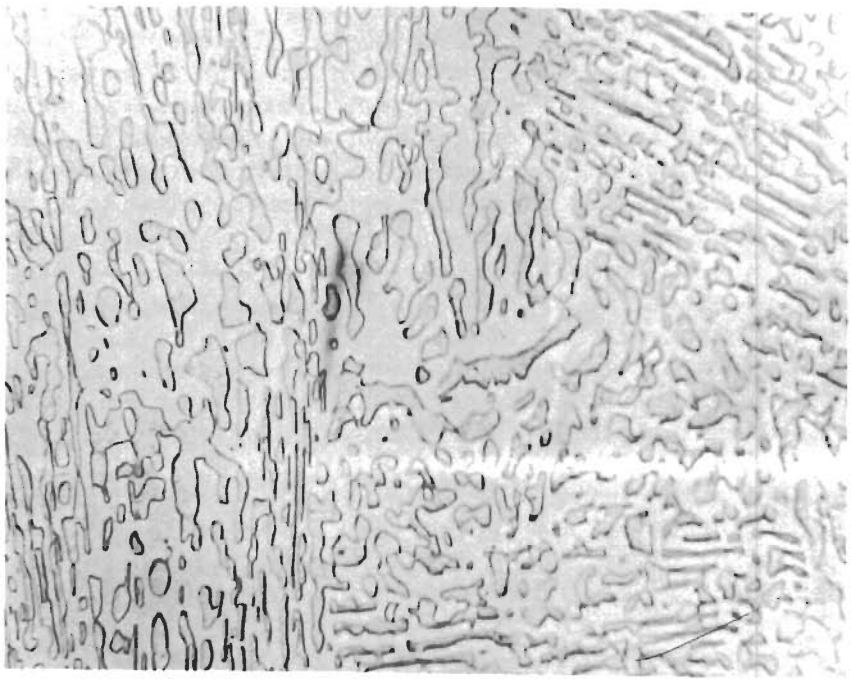

(b) 1000X

Fig. 228 - Carbide Morphology and Distribution in 4.3 w/o C Iron-Carbon Alloy (Heat treatment - 815°C, 20 min and 650°C, 20 hr) 3% Nital Etch

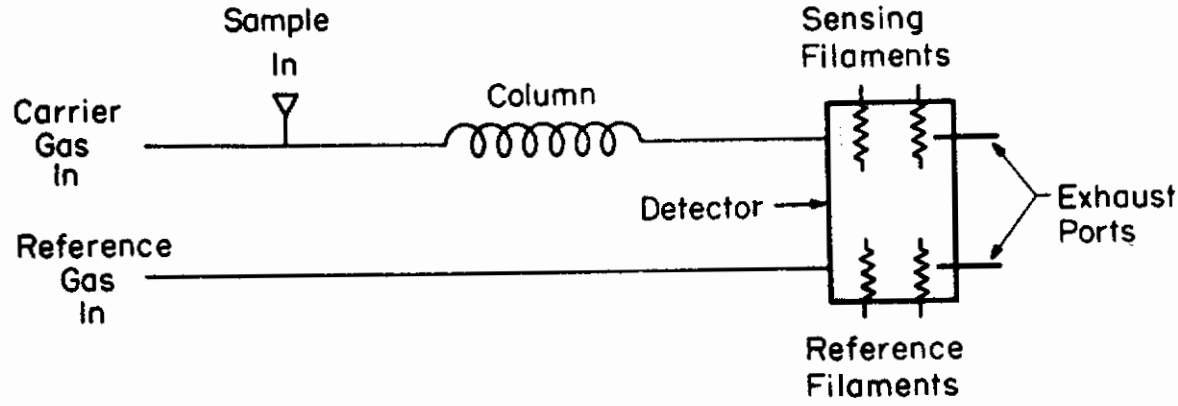

Fig. 229 - Schematic of Gas Chromatograph

Separation of the sample into its constituents occurs as they progress at different rates along the column. If the temperature, carrier gas flow rate, and column substrate are correctly selected, each constituent occupies a space containing only carrier gas. Therefore the effluent from the column consists of a sequence of vapor pockets, each pocket consisting of a different constituent. The effluent passes through the sensing filaments of the detector, while the erference gas passes through the reference filaments.

Detectors may be of several types; i.e., thermal conductivity, flame ionization, or electron capture. The operation of a thermal conductivity detector will be discussed here. The detector bridge circuits control the signal to the recorder. This signal is proportional to the difference in thermal conductivity of the gases in the sensing and reference chambers. The output is adjusted to give zero output when pure carrier gas is present in both compartments. The sensing and reference filaments form the four legs of the detector bridge. The presence of vapor, other than the carrier gas, in the sensing chamber alters the sensing filament electrical resistance, thus unbalancing the bridge and producing a difference in potential at the output terminals. For any concentration of vapor, the unbalance voltage is constant. The resulting chromatogram is interpreted quantitatively by comparing it with chromatograms of known samples. The constituents are identified by their characteristic retention times, while the amount present is determined by comparing the given area under a peak on the unknown to the area for a known quantity. A typical chromatogram is shown in Fig. 230, where the potential difference between the sensing and reference filaments of the detector is plotted versus time after sample injection.

b. Analysis of Carbon-Containing Species

This investigation requires analysis of the following constituents which may be products of carbide dissolution: H_2, O_2, CO, CO_2, CH_4, plus several higher hydrocarbons. The gases from hydrogen through methane are analyzed by using two columns in series. A Por-A-Pak Q column is attached to the sensing side of the detector and a 5 A

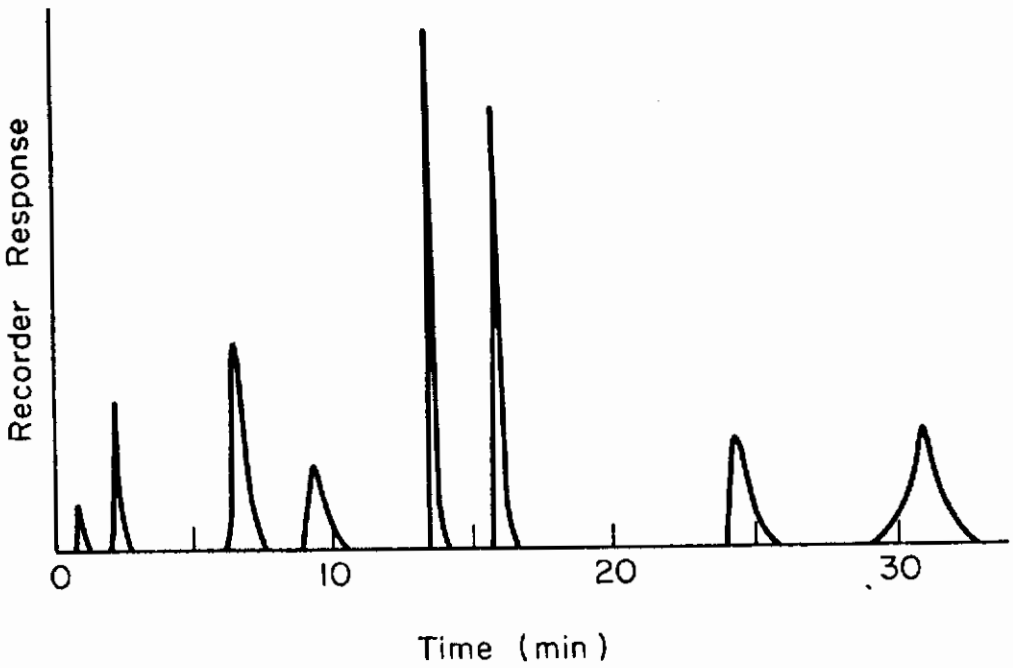

Fig. 230 - Typical Gas Chromatograph

Molecular Sieve column is attached between the sensing and reference sides of the detector. After sample injection all the gases except carbon dioxide are eluted through the Por-A-Pak and show up as a single composite peak on the recorder. The CO_2 is held up and appears as the next peak. Meanwhile, the other gases, such as O_2, CO, CH_4, are being separated in the Molecular Sieve column. As they are eluted into the detector they are sensed by the reference filaments and subsequently exhausted. The column lengths and operating parameters are chosen so that no peaks overlap. The carrier gas flows through the injector, into the Por-A-Pak column, then into the sensing side of the detector, through the molecular sieve, into the reference side of the detector, and finally, into the atmosphere.

The hydrocarbons higher than methane are analyzed using a 3% Squalane-97% Burell medium-activity silica gel column. This column will separate the following constituents: ethane, ethylene, n-propane, actelylene, n-butane, propylene, isopentane, n-pentane, and butene-1.

4. Experimental

Polarization curves have been determined by a potentiodynamic technique. A Wenking model TS-3 potentiostat and Wenking SMP-66 STEP motor potentiometer were used to control the potential. Currents were recorded with an Esterline Angus model E1101S speed servo recorder. All tests were run at a sweep rate of 300 mV/min unless otherwise specified.

The electrochemical cell consisted of a 500 ml flask with ports for the sample, counter electrode compartment, Luggin probe assembly, and inert gas ports. All potentials were measured vs. a saturated calomel electrode and subsequently converted to the hydrogen scale by adding +242 mV. The solutions were magnetically stirred during tests to minimize local changes in solution chemistry at the specimen surface. The tests were run at room temperature unless otherwise specified. The cell was wrapped with heating tape for the tests with boiling solutions.

All solutions were prepared from triple-distilled water and reagent grade chemicals. The solutions were deaerated by bubbling argon through them prior to the experiments. During the tests argon was passed over the surface of the solutions.

5. Results and Discussion

a. Fe-C Alloys

The polarization behavior of Fe, Fe-0.8 wt % C, Fe-2.0 wt % C, and Fe-4.3 wt % C was determined in deaerated 0.3M H_2SO_4-K_2SO_4 solutions at pH 2, 4, and 6. The Fe-C alloys were heat treated to obtain a spheroidized carbide structure. The details of the alloy preparation, heat treatment, and microstructure have been reported. The environments, pH 2, pH 4, and pH 6 are chosen to investigate the effect of increasing tendency for passivation of the ferrite matrix upon the dissolution behavior of the carbides.

The anodic polarization curves for Fe and the Fe-C alloys in pH 2, 0.3M H_2SO_4-K_2SO_4 are presented in Fig. 231. All of the materials exhibit active-passive behavior. The anodic current maximum decreases with increasing carbide content and passivation occurs more readily. The current density in the passive region increases with increasing carbide content. The transpassive region occurs at approximately 1.5 V and is independent of the carbide content. The corrosion potential of the alloys increases linearly with the amount of carbide present, see Fig. 232.

The cathodic polarization curves for Fe and the Fe-C alloys in pH 2, 0.3M H_2SO_4-K_2SO_4 are present in Fig. 233. The current increases with increasing amount of carbide, until the onset of concentration polarization where the cathodic current is independent of the alloy composition.

The anodic polarization curves for Fe and the Fe-C alloys in pH 4, 0.3M H_2SO_4-K_2SO_4 are shown in Fig. 234. The tendency for passivation again increases with increasing carbide content. The passive current densities are higher for the higher wt % C alloys but not as noticeably as in the pH 2 solution. The magnitudes of the passive current densities are approximately the same in pH 2 and pH 4, whereas the active dissolution current densities are lower at pH 4. The presence of an active peak at about -0.3 V is observed for all materials, but decreases with increasing carbide content.

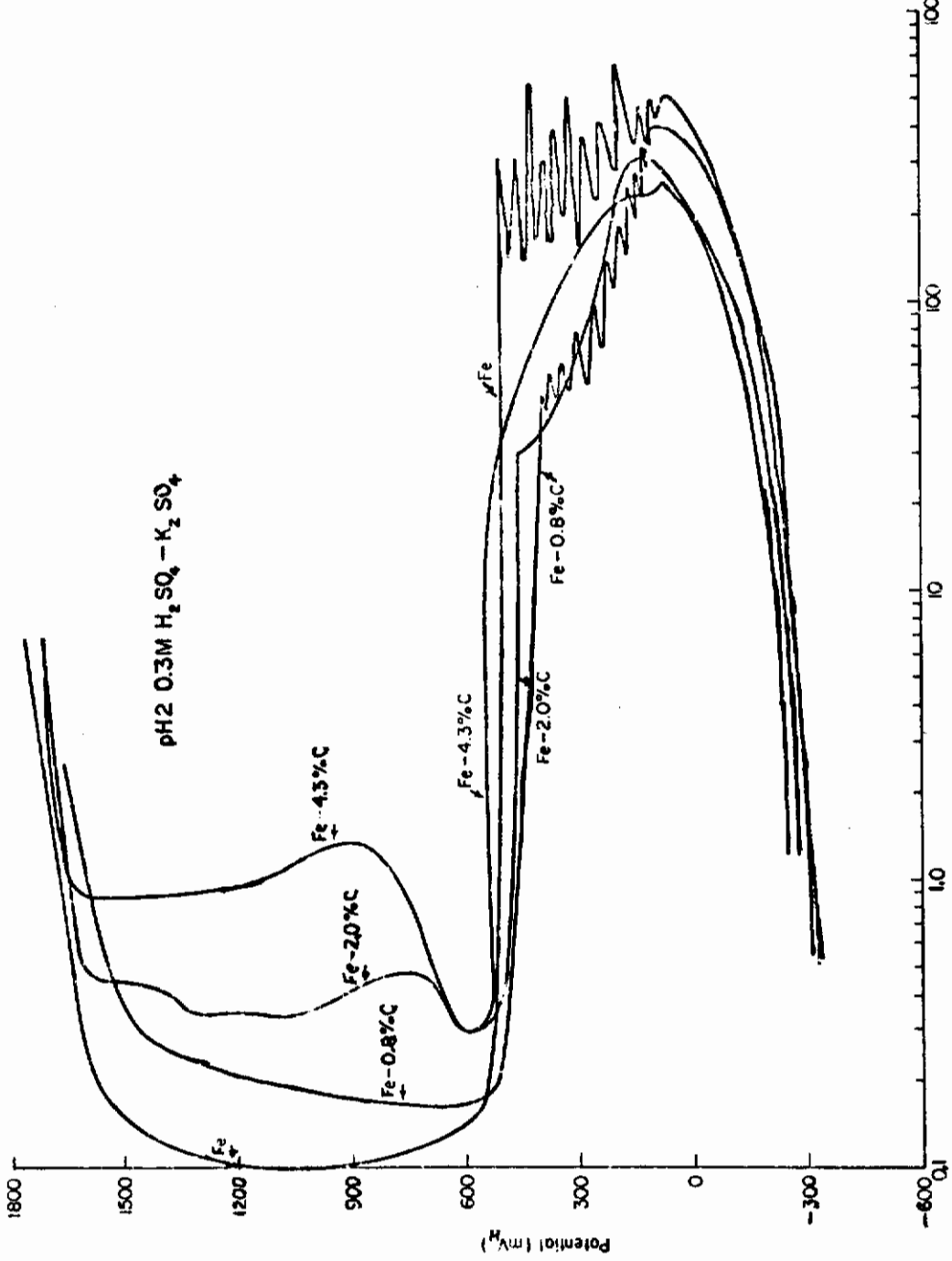

Fig. 231 - Anodic Polarization Curves of Fe, Fe-0.8 Wt% C, Fe-2.0 Wt% C, and Fe-4.3 Wt% C in pH 2 (0.3M H_2SO_4-K_2SO_4)

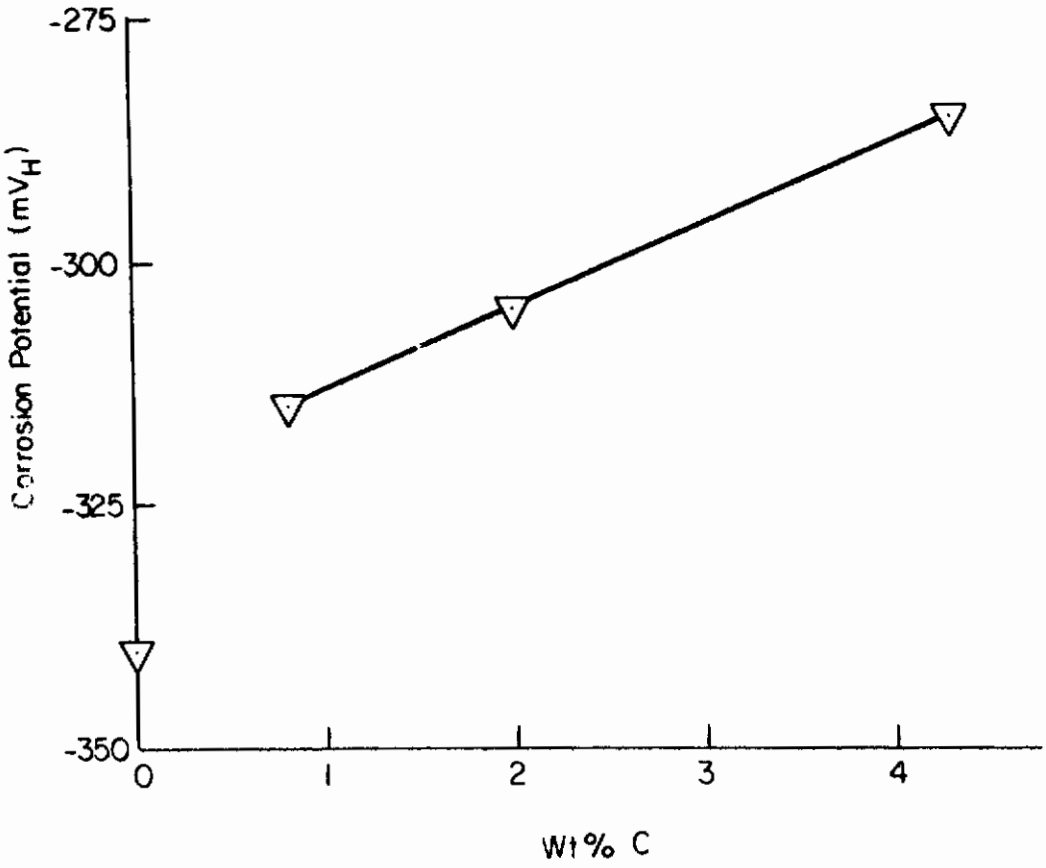

Fig. 232 - Corrosion Potential vs. Wt% C in pH2 (0.3M H_2SO_4-K_2SO_4)

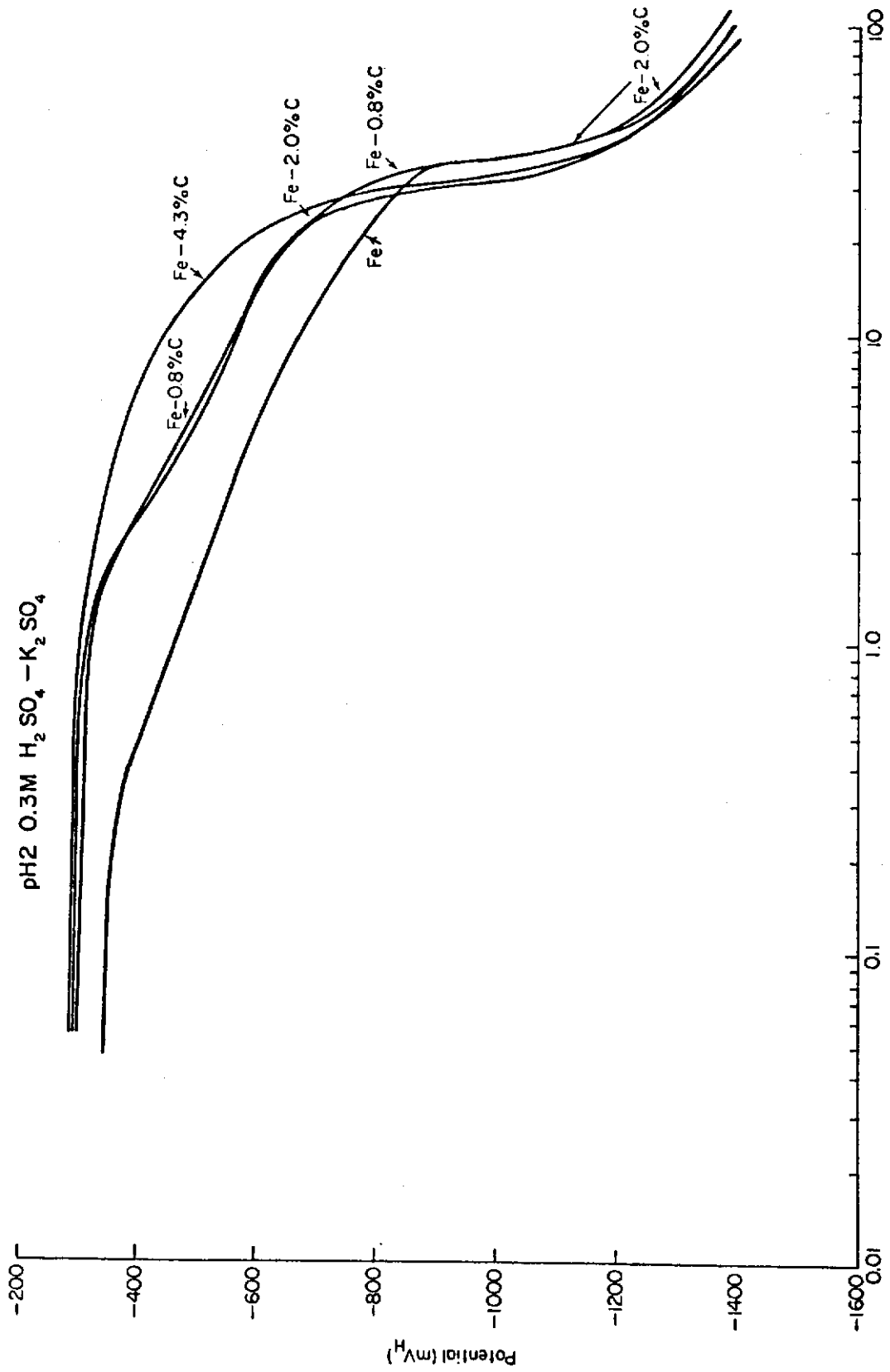

Fig. 233 - Cathodic Polarization Curves of Fe, Fe-0.8 Wt% C, Fe-2.0 Wt% C, and Fe-4.3 Wt% C in pH 2 (0.3M H_2SO_4-K_2SO_4)

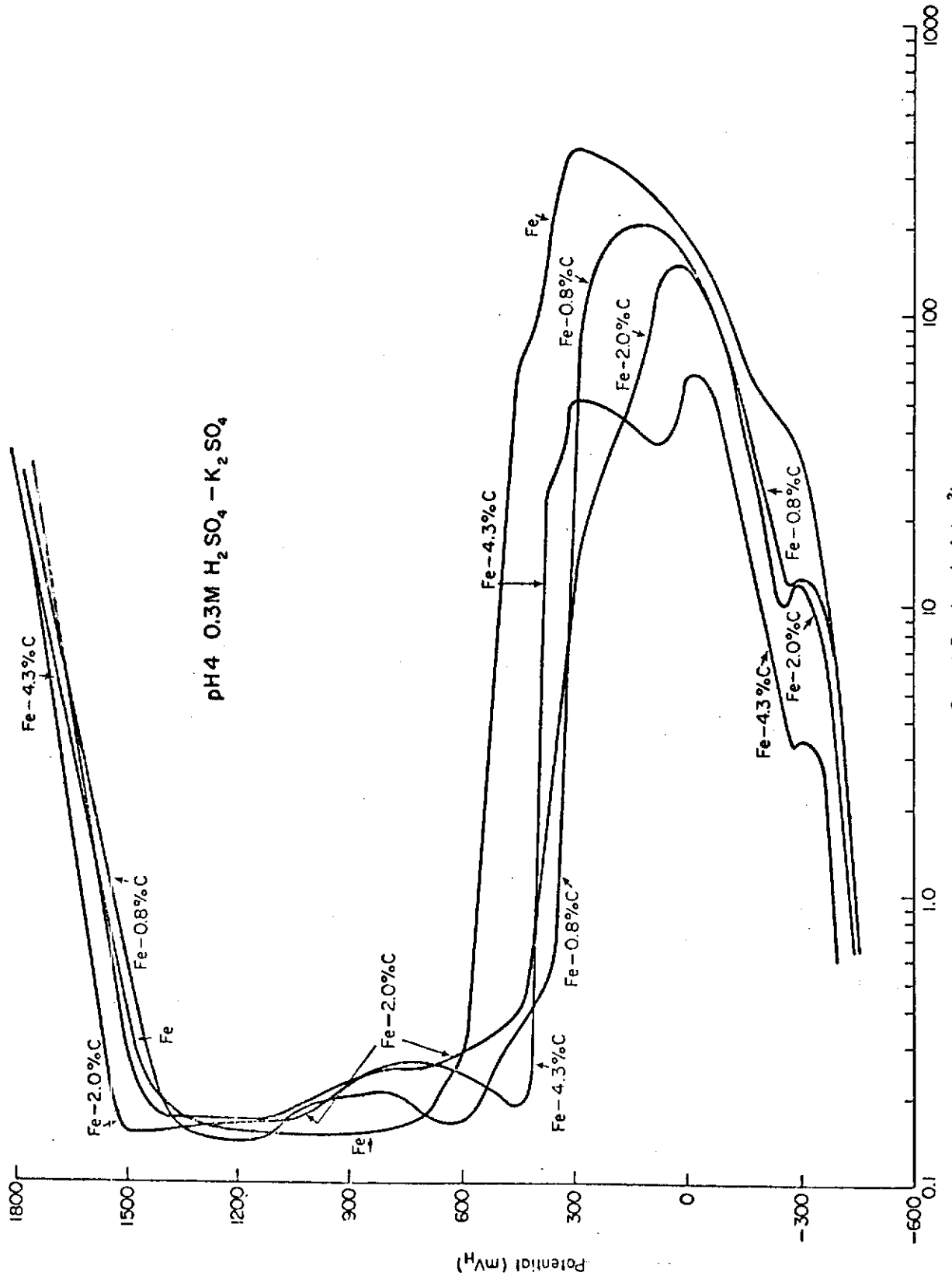

Fig. 234 - Anodic Polarization Curves of Fe, Fe-0.8 Wt% C, Fe-2.0 Wt% C, Fe-4.3 Wt% C in pH 4 (0.3M H_2SO_4-K_2SO_4

The cathodic polarization curves for the pH 4 solution are shown in Fig. 235. The curves all exhibit a potential independent portion between 3 and 5 μA current density. The cathodic polarization behavior is quite insensitive to carbide content at pH 4.

The presence of iron carbide in the iron matrix affects the polarization behavior in a number of ways; e.g., (1) increased tendency to passivate, (2) increase in passive current density, (3) increase of corrosion potential to more noble values, and (4) increased reduction kinetics in the pH 2 environment. The presence of iron carbide has no effect upon the transpassive behavior of the alloys.

The reasons for a lower anodic current maximum and enhancement of passivity with higher carbon content are not clear. The increased passive current with higher carbide content is rationalized by the presence of a more heterogeneous structure giving rise to more flaws in the passive film and more sites where film breakdown may occur. At pH 4, where passivity is more easily achieved and film repair can occur more readily, the presence of carbides does not have as great an effect as at pH 2 where passivity is not as stable.

The increase in reduction kinetics, evident in the pH 2 environment, indicates that the reduction of hydrogen ions upon the carbide surface occurs more readily than on the iron surface. This increase in reduction kinetics is consistent with the fact that the corrosion potential increases with carbide content. The step in the cathodic curves results from the onset of concentration polarization in the reduction of hydrogen ions. The limiting current decreases with increasing pH; i.e., 35 mA at pH 2, and 3 μA at pH 4. The cathodic current remains independent of potential until another reaction occurs. In this system the direct reduction of water occurs, about -0.8 V in pH 4 (see Fig. 235) with a corresponding increase in current with overpotential. The direct reduction of water is not influenced by the presence of carbides.

b. Dissolution of $Cr_{23}C_6$ and TiC in 2N H_2SO_4

Chromium carbide ($Cr_{23}C_6$) and titanium carbide (TiC) are important constituents in stainless steel. This study was undertaken to ascertain the corrosion behavior of these carbides and relate it to the stainless steels in which they occur. In order to compare the results with the broad range of literature on intergranular corrosion, boiling 2N H_2SO_4, which is the base solution for the Strauss test, was chosen as the environment.

Chromium carbide exhibits active-passive behavior in boiling 2N H_2SO_4, see Fig. 236. The corrosion potential is -190 mV. The anodic peak occurs at -150 mV, with the passive region extending from +100 to +1050 mV, and the onset of transpassivity at +1150 mV.

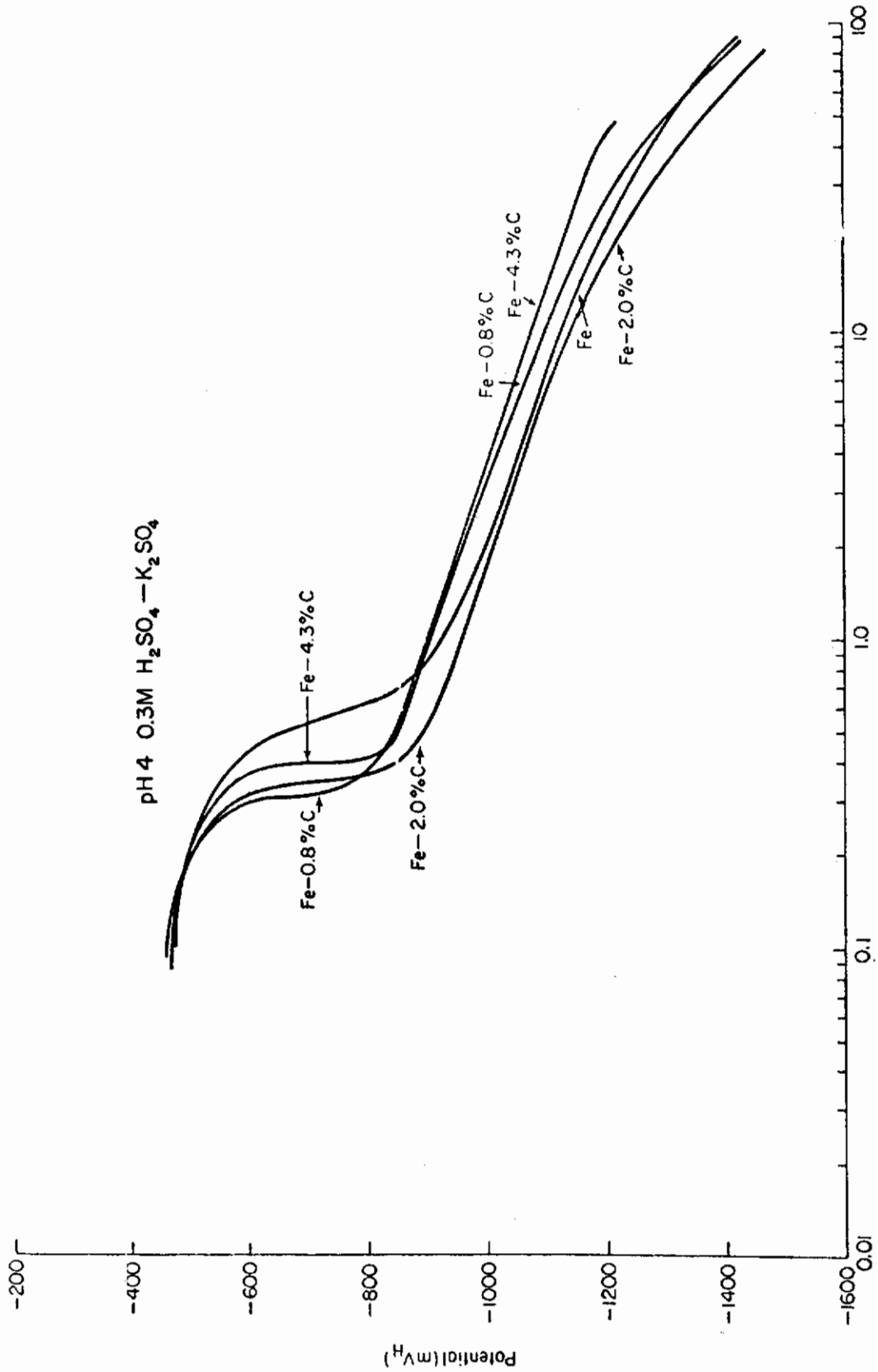

Fig. 235 - Cathodic Polarization Curves of Fe, Fe-0.8 Wt% C, Fe-2.0 Wt% C, Fe-4.3 Wt% C in pH 4 (0.3M H_2SO_4-K_2SO_4)

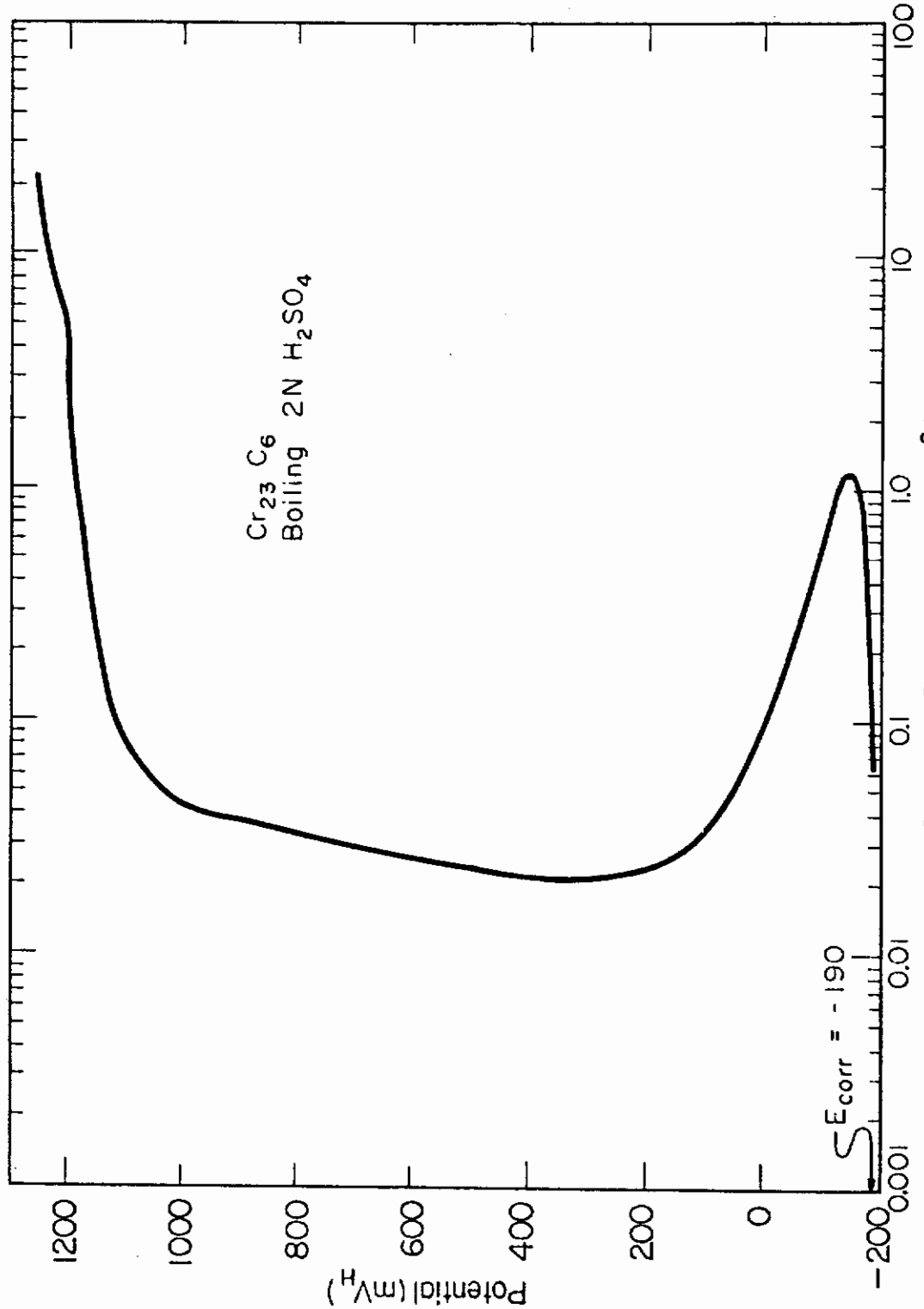

Fig. 236 - Anodic Polarization Curve $Cr_{23}C_6$, Boiling 2N H_2SO_4

The anodic polarization behavior of TiC is shown in Fig. 237. Upon immersion, the open-circuit potential rises from approximately +200 mV to a value of +350 mV after 15 minutes, and continues to drift in the noble direction at an ever-decreasing rate. A polarization curve starting at 350 mV is presented here. The current density increases to a maximum at +1040 mV, decreases with increasing potential up to +1400 mV, and then rapidly increases again.

6. Conclusions

The active-passive behavior shown in Figs. 236 and 237 confirms the unusual behavior of the carbides shown in Fig. 221. Carbides, like metals, exhibit active-passive behavior; thus, even though the carbides are unstable, they are protected by their protective film. One needs therefore to study this behavior to predict the behavior of carbide-enriched grain boundaries.

G. EFFECT OF ENVIRONMENTAL ADDITIVES--HYDRAZINE

(R. D. McCright, P. L. Carter, and J. S. Snerry)

1. Objectives and Background

The objective of this work is to assess the behavior of certain environmental species known to interact with surface processes. By using various additives in environments in which cracks are propagating it should be possible to obtain additional information on critical processes occurring at the crack tip. The work described herein was performed using hydrazine additives to aqueous solutions. In order to understand the cracking behavior, polarization and hydrogen permeation experiments were conducted.

2. Results and Discussion

a. SCC Experiments

The cantilever beam experiment was used for studying crack propagation. The base solution was 3.5% NaCl; hydrazine was added in the range 0 to 2.0%. The crack propagation data are summarized in Fig. 238. Additives of hydrazine are shown clearly to exert a slowing effect on crack propagation. The total time-to-cracking is increased by a factor of about 10 and the crack propagation rate in the early stages is substantially slowed.

b. Polarization Experiments

Potentiokinetic polarization curves were run on AISI 1010 steel. A small specimen (area = 0.504 cm^2) was cut from a coupon and ground with 600-grit paper. The specimen was polarized in 3.5% NaCl solution, with and without hydrazine (NH_2NH_2) additions. Solutions were

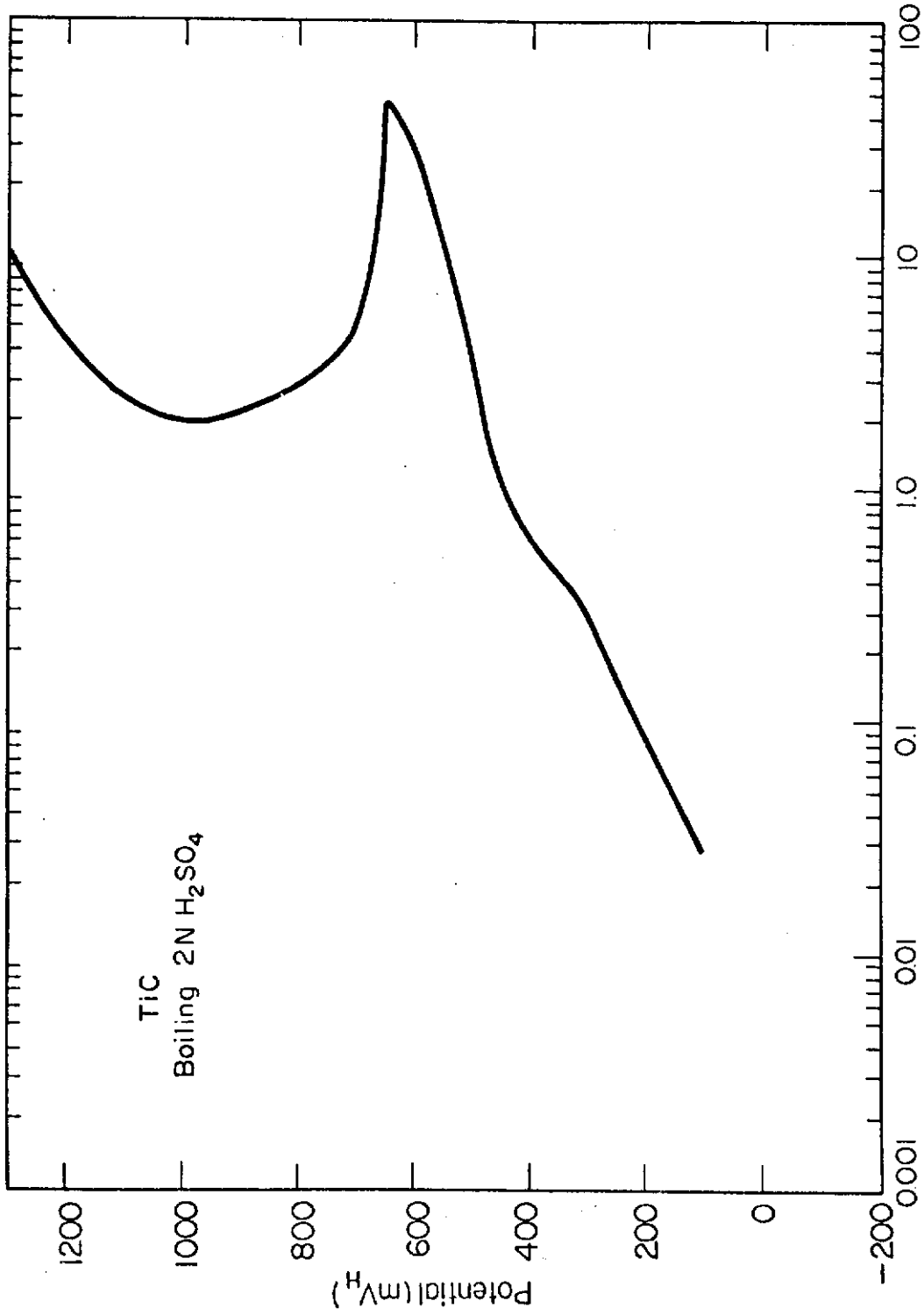

Fig. 237 - Anodic Polarization Curve TiC, Boiling 2N H_2SO_4

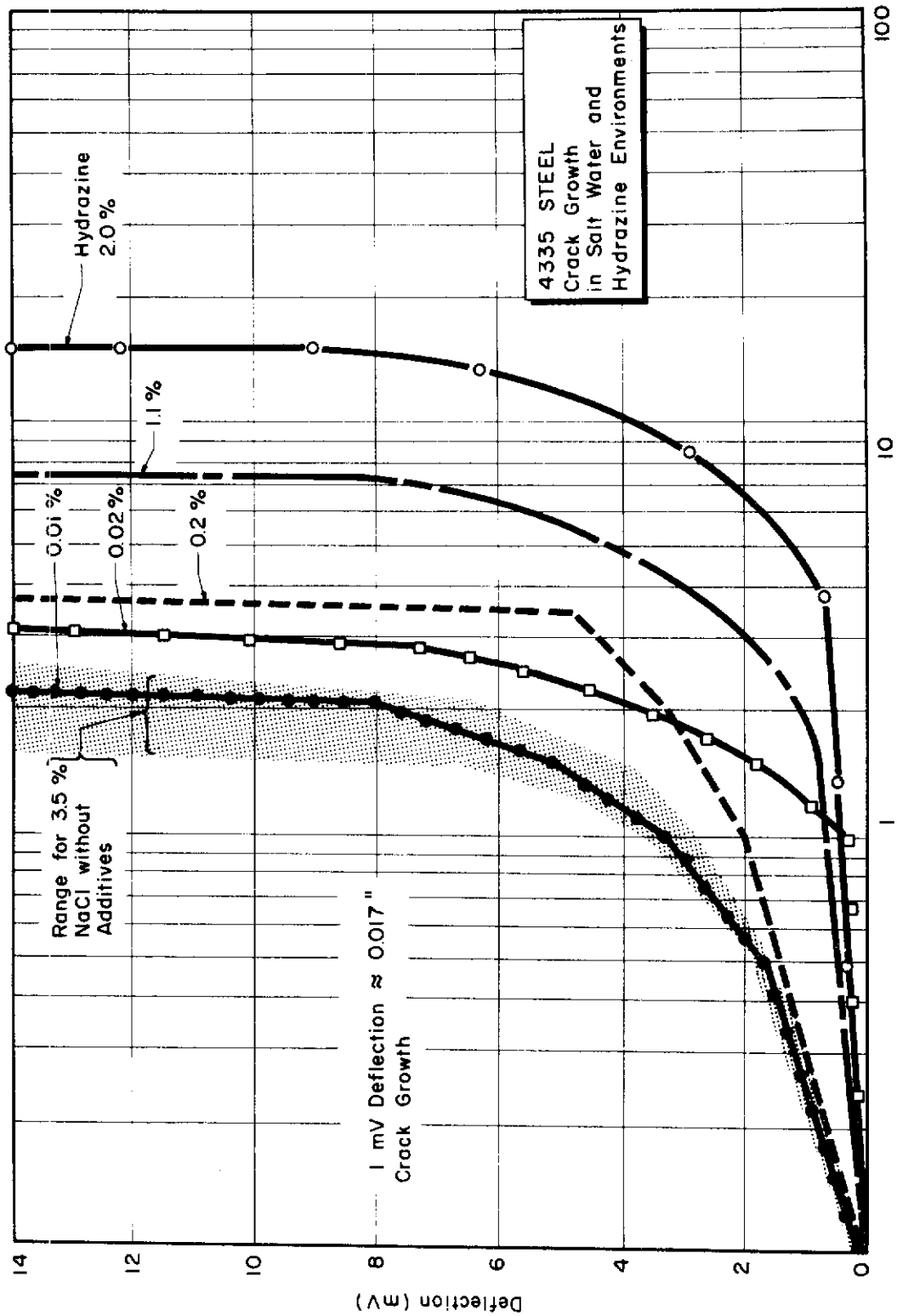

Fig. 238 - 4335 Steel Crack Growth in Salt Water and Hydrazine Environments

deaerated for at least two hours before the test and during the test by bubbling high-purity tank nitrogen through the system. In the tests in which hydrazine was used, this compound was added shortly before the test was started because of its volatility. The bubbling nitrogen thoroughly mixed the liquid hydrazine with the salt solution. The potential was scanned at 5000 mV/hr beginning at -1600 mV(SCE) which is on the cathodic side of the rest potential. Figure 239 shows the result of polarization curves. Addition of the hydrazine clearly retards the oxidation kinetics. This may be a more significant factor than its oxygen-gathering behavior.

The tendency for this hydrazine to inhibit the oxidation reaction may be the controlling factor in retarding the crack velocity. Thus, the retarded oxidation reaction reduces the rate of hydrogen ion reduction.

H. INTERACTION OF HYDROGEN WITH STEEL
(R. D. McCright)

1. Objectives

The purpose of this work is to determine how hydrogen enters and interacts with the metal structure. The work involves two types of experiment; one involves hydrogen entry studies and the other hydrogen trapping.

2. Experimental

The hydrogen entry work was conducted primarily using an electrochemical system in which hydrogen was charged from one side of a membrane and monitored from another. Figure 240 shows the overall system. The cathodic polarization circuit produces hydrogen from the $e + H^+ \rightarrow H$ reaction. The amount passing through is determined by oxidizing the hydrogen according to the $H \rightarrow H^+ e$ reaction. Figure 241 shows the schematic arrangement of the membrane.

3. Preliminary Studies

a. Alternate Charging and Discharging

A test was run on an AISI 1010 steel sample in which the cathodic charging current at the entry side (see Fig. 241) was alternately turned on and off, during which time an oxidation potential was kept constantly on the hydrogen exit side. Thus, permeation currents of rise and decay transients were recorded. The diffusivity can be calculated from these transients, as explained in a previous report,[141] by approximating suitable equations to the transient. These[142] are, for the rise transient,

$$i_{p_\infty} - i_{p_\infty} = 2\, i_{p_\infty} \exp\left[-\frac{D\pi^2}{L^2}\, t\right], \qquad (60)$$

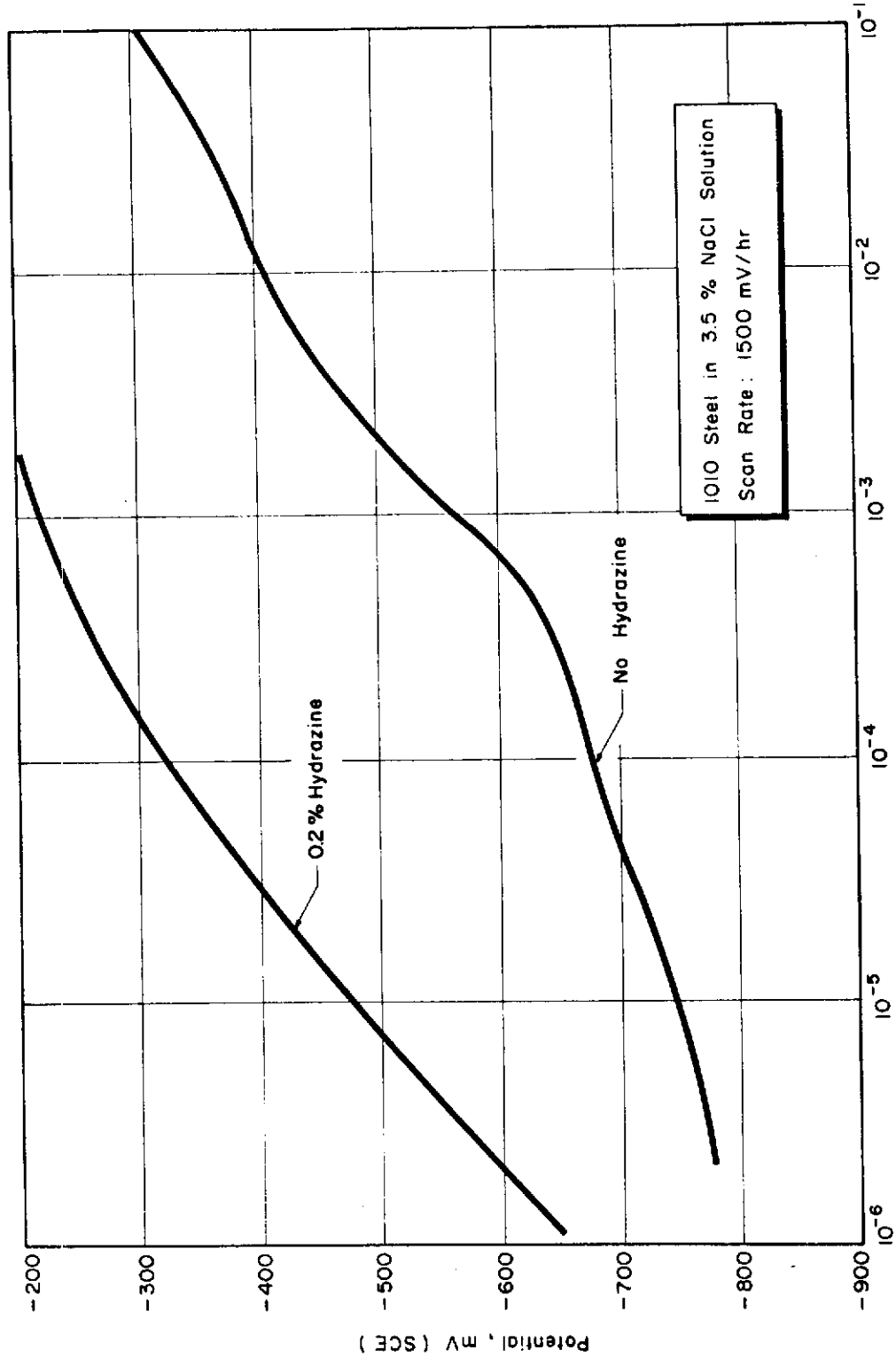

Fig. 239 - Anodic Scans Comparing Effects With and Without Hydrazine for 1010 Steel

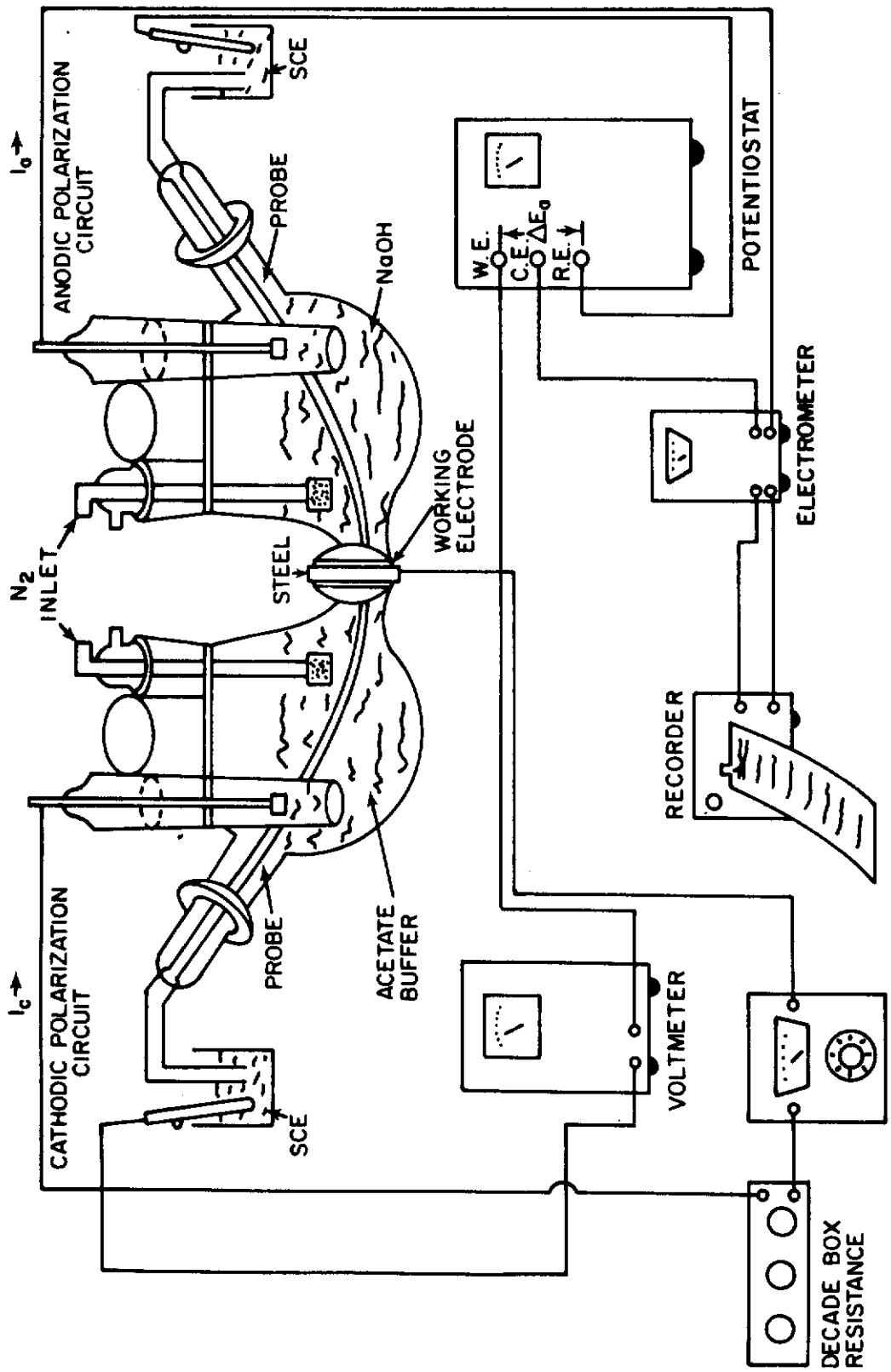

Fig. 240 - Schematic Arrangement of Apparatus Used for Measuring Hydrogen Permeation

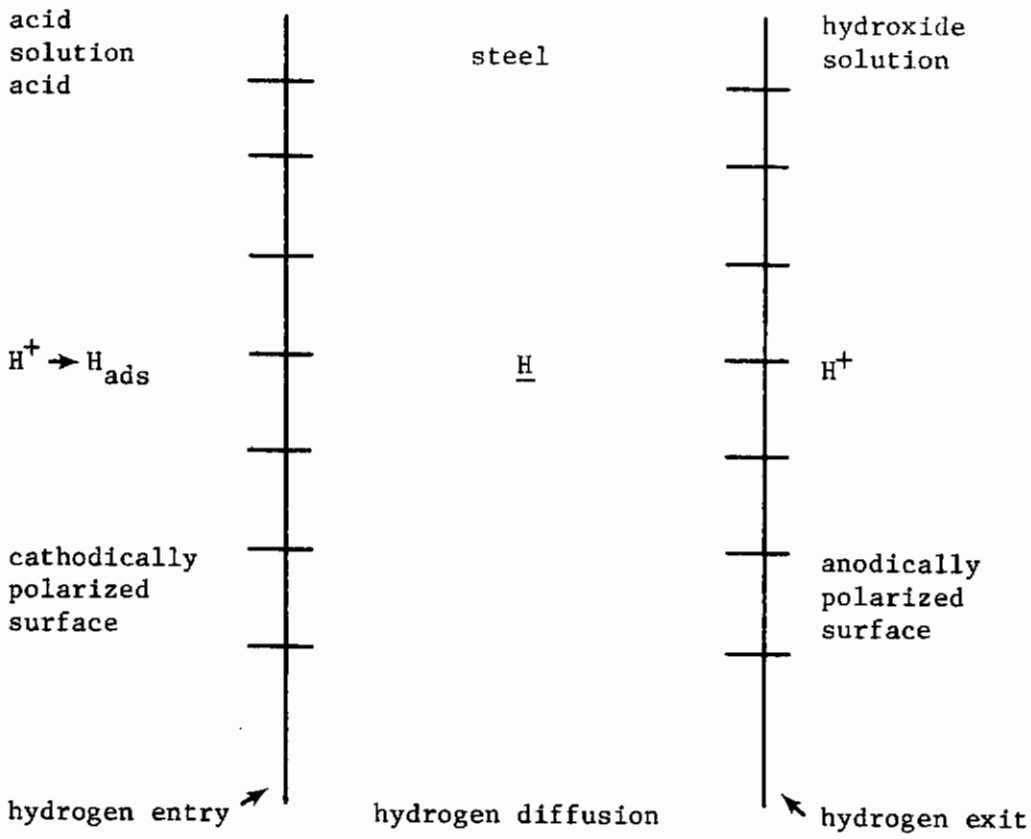

Fig. 241 - Schematic Model for Permeation of Hydrogen Through a Membrane

where

i_p = value of the permeation current at time, t,
i_{p_∞} = steady state value of permeation current,
D = hydrogen diffusivity,
L = sample thickness, and
t = time from when cathodic current turned on (rise) and or off (decay);

and, for the decay transient,

$$i_p = i_{p_\infty} \exp\left[-\frac{D\pi^2}{L^2} t\right], \tag{61}$$

Therefore, D can be found from the slopes of the respective plots,

$$\log\left(\frac{i_p - i_{p_\infty}}{i_{p_\infty}}\right) \text{ vs } t \text{ and } \log\left(\frac{i_p}{i_{p_\infty}}\right) \text{ vs } t. \tag{62}$$

The specimen was 10 mils thick and was vacuum annealed at 650°C for an hour. The surface was ground lightly with emery paper and cleaned with acetone. The charging solution was acetate buffer (pH 4.3) with an addition of 1 g/l of thiourea. The solution on the anodically polarized side was 0.1N NaOH (pH 12.8). The test temperature was 24°C. A galvanostatic system was set up for this test since it was felt that, because of the long time between hydrogen entry and exit, a potentiostatic charg- system would not allow the exit condition to reflect the conditions at the entering surface because of the change of the cathodic current with time.

The charging current density was 45 mA/cm^2; the potential at the exit side was kept at +100 mV (SCE). The results of this test are shown below.

Transient Type	Diffusivity (cm^2/s)
First rise	7.9×10^{-8}
First decay	8.2×10^{-8}
Second rise	7.0×10^{-7}
Second decay	1.7×10^{-7}
Subsequent rises and decays	10^{-7}

The steady-state permeation current for the first rise was 7.1μA/cm^2; that for the second and third rises was 2.8 μA/cm^2.

The increase of diffusivity upon continued charging seems to substantiate the theory[143] that the mobile hydrogen atoms inside the metal first seek to lodge at or near structural defects. Since the mean time of stay for an atom in these sites is greater than in an interstitial

lattice site, the apparent diffusivity is low (all of these experimentally determined diffusivities are apparent). This network of "rifts" is unconnected[144] and this should slow diffusion.

After these sites are filled, diffusion should be slower, and additional hydrogen atoms can locate only on interstitial lattice sites where their mean time of stay is shorter. Hence, the diffusivity increases. These tests were run with the rise transients being spaced about 3/4 to 2 hours apart (longer at the beginning since it took longer to come to steady state). When a decay transient is run for a longer time, as in some of the other experiments, (overnight or longer) the behavior of the subsequent rise transient is usually the same as the initial rise transient (no hydrogen in the steel). This would indicate that the first hydrogen discharged from the steel is the interstitial lattice hydrogen and after prolonged hydrogen discharge of the steel the hydrogen associated with structural defects diffuses out.

For shorter time intervals between rise transients, the value of the permeation current decreases from run to run, as it did in this experiment. When the sample is allowed to discharge overnight, the permeability is restored to its initial value and often exceeds it (see next section). Again, this is consistent with the supposition that the permeation should be highest when there is the largest number of accommodating sites (interstitials and rifts vs. interstitials alone).

b. Effect of Oxidizing Potential at the Exit Side

A significant amount of hydrogen discharged from the steel at the anodically polarized side undergoes the recombination reaction to form molecular hydrogen instead of the oxidation reaction of atomic hydrogen to hydrogen ion. Since the former reaction does not contribute to the current, the true permeability is higher than the apparent one. The higher (more noble) the potential at this surface, the less thermodynamic tendency for the recombination reaction. At all the potentials considered molecular hydrogen is unstable, but its presence apparently results from the high bond energy in molecular hydrogen. Since this loss of hydrogen flux cannot be measured by permeation current, many investigators plate palladium on this side of the specimen.

The initial rise transients for 2-mil-thick, AISI 1010 steel samples held at different anodic potentials on the exit side exposed to 0.1N NaOH are shown in Fig. 242. The conditions at the cathodically polarized side were the same in all cases; i.e., acetate buffer (pH 4.3) plus 5 x 10^{-4}M $NaAsO_2$ (375 μg As/ml), cathodic current density of 10 mA/cm^2 galvanostatically controlled, specimen surface lightly ground. The steady-state permeation current (plateau of transient) increases as the potential increases in the noble direction.

Shown in Fig. 243 are permeation transients for the same specimens and conditions but after the charged specimen was allowed to

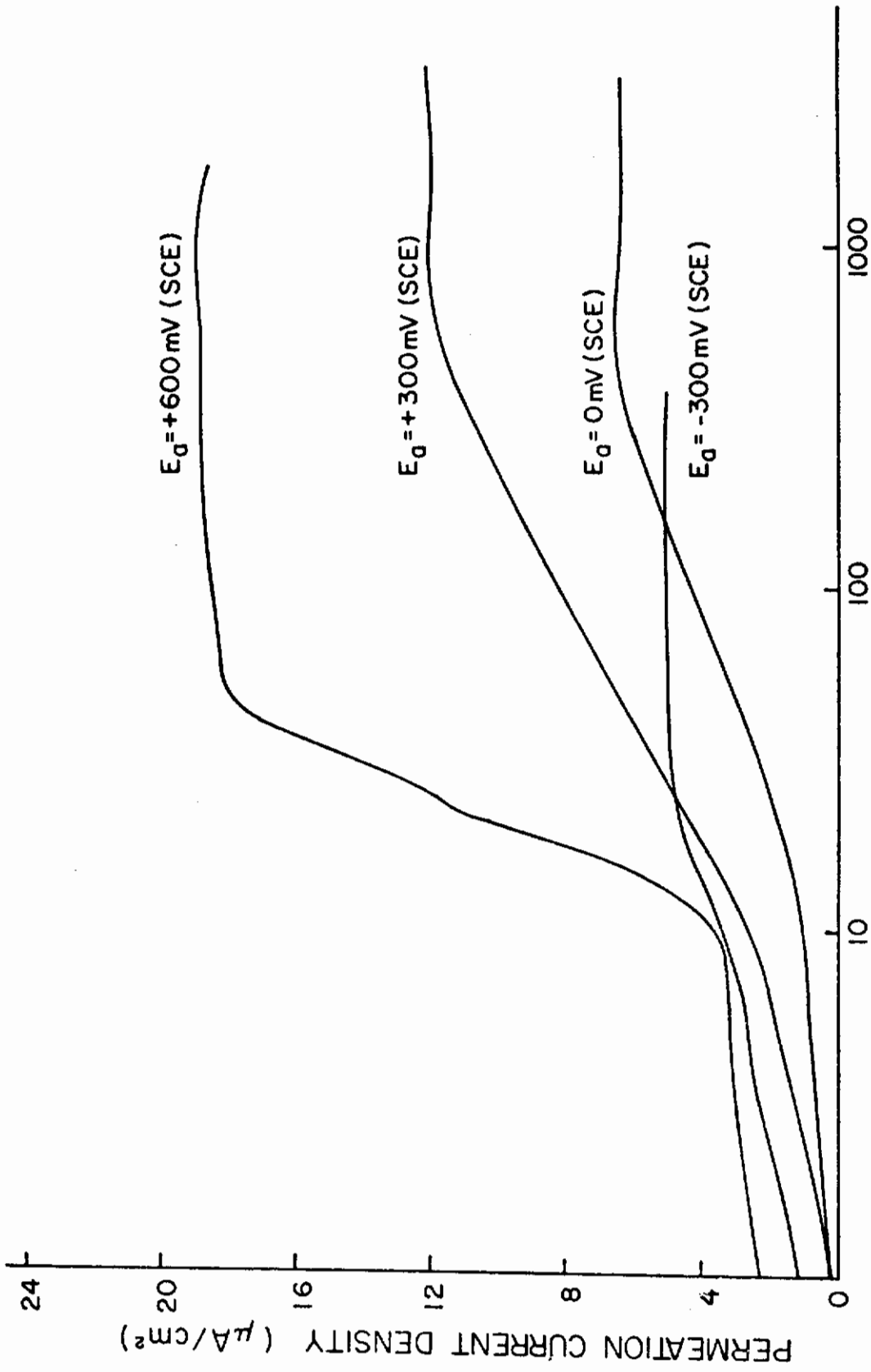

Fig. 242 - Initial Transients for Hydrogen Permeation

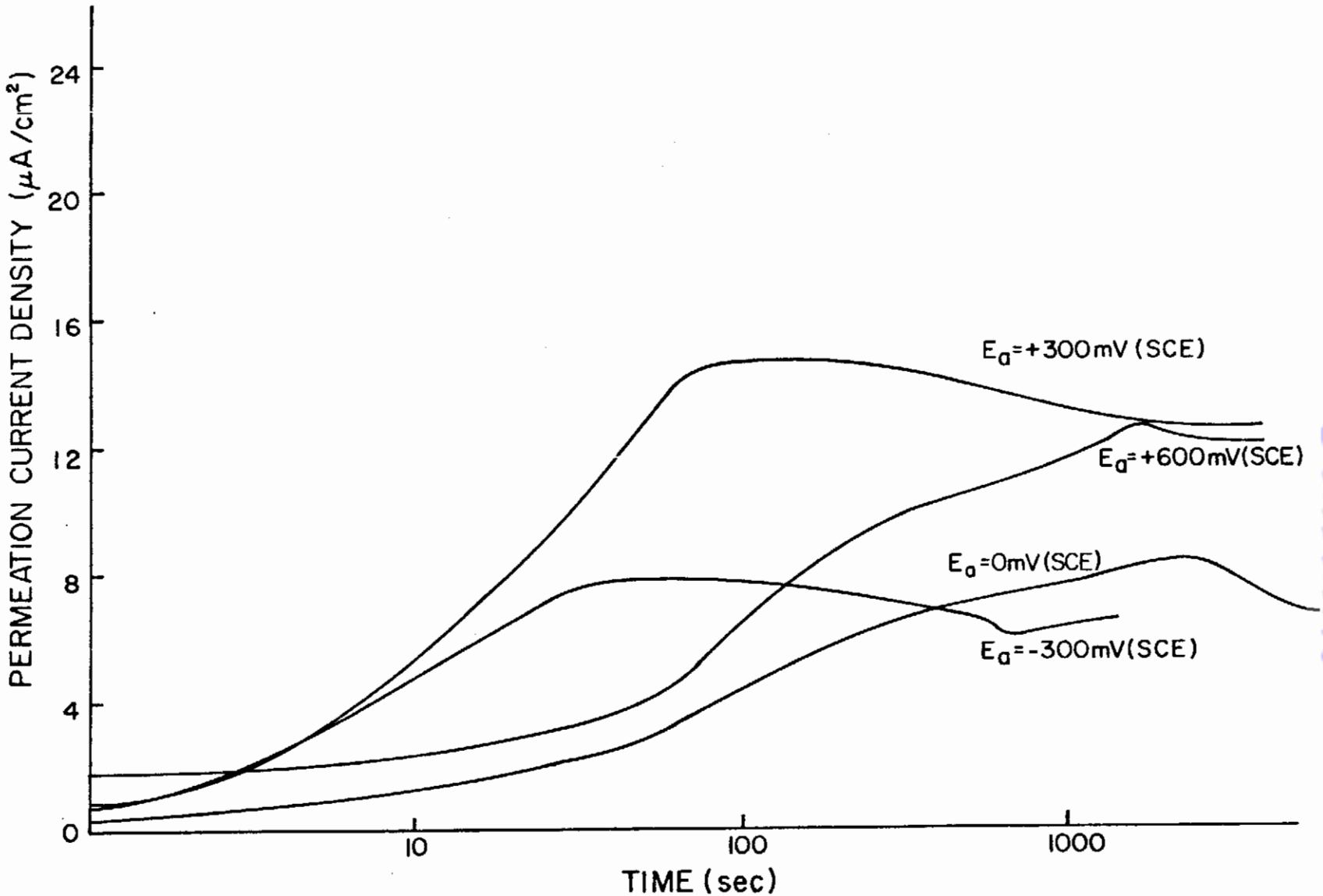

Fig. 243 - Rise Transients for Experiment Conducted on Subsequent Day

expel hydrogen overnight. In all but one case the next-day transients were higher than the initial ones. In some cases these next-day transients show an anomalous permeation maximum and decrease of permeability with time.

c. Effect of Palladium Plating

A thin coating of palladium was electrolytically plated on the hydrogen exit side. This is the surface which is exposed to NaOH solution, as shown in Fig. 241. The effect of the palladium was to show a large increase in the hydrogen permeation for a given set of boundary conditions (charging and discharging parameters). Figure 244 illustrates the enormous increase in the permeation current when the exit surface is palladized. It is believed that the emerging hydrogen atom is more rapidly oxidized to hydrogen ion or water on the palladium surface because of the high exchange current (10^{-3} A/cm^2 for hydrogen on palladium compared to 10^{-7} A/cm^2 on iron). As a result, the permeation current through a palladized sample is a measure of the true permeability of hydrogen. The diffusivity[145] of hydrogen in palladium is $\sim 10^{-7}$ cm^2/s comparable to that of the steel; and the palladium plate is much thinner than the thinnest steel specimen used (Pd plate about 6×10^{-6} cm thick and the thinnest steel specimen, 5×10^{-3} cm thick). Thus, the hydrogen diffusion through the steel is the slowest reaction in the permeation series and the time lag to reach steady state in the permeation current transient is inversely proportional to the hydrogen diffusivity in the steel. Permeation is the overall process of reducing the hydrogen ion at the cathodically polarized surface, transporting the hydrogen across the metallic phases, and oxidizing it at the anodically polarized surface. Diffusion, then, is associated only with the transport through the metalalic phases (steel, and palladium in some cases).

Unless otherwise stated, the specimens used in the tests reported in this text were 2 mils thick (5×10^{-3} cm).

d. Effect of Arsenite Additions to the Charging Solution

The presence of species such as sodium arsenite (hydrolyzed to arsenious acid) generally increases the hydrogen entry rate into the steel. The data in Table XXIX show this effect. The charging solution was acetate buffer, pH 4.5.

When sodium arsenite is added to the acetate buffer, the rest potential of the steel electrode moves in the noble direction, as shown in Fig. 245. The arsenite arsenic couple is more noble than the hydrogen ion/hydrogen gas couple. The pH of the solution is unchanged until large amounts of the arsenite (a weak base) are added. This is also shown in Fig. 245.

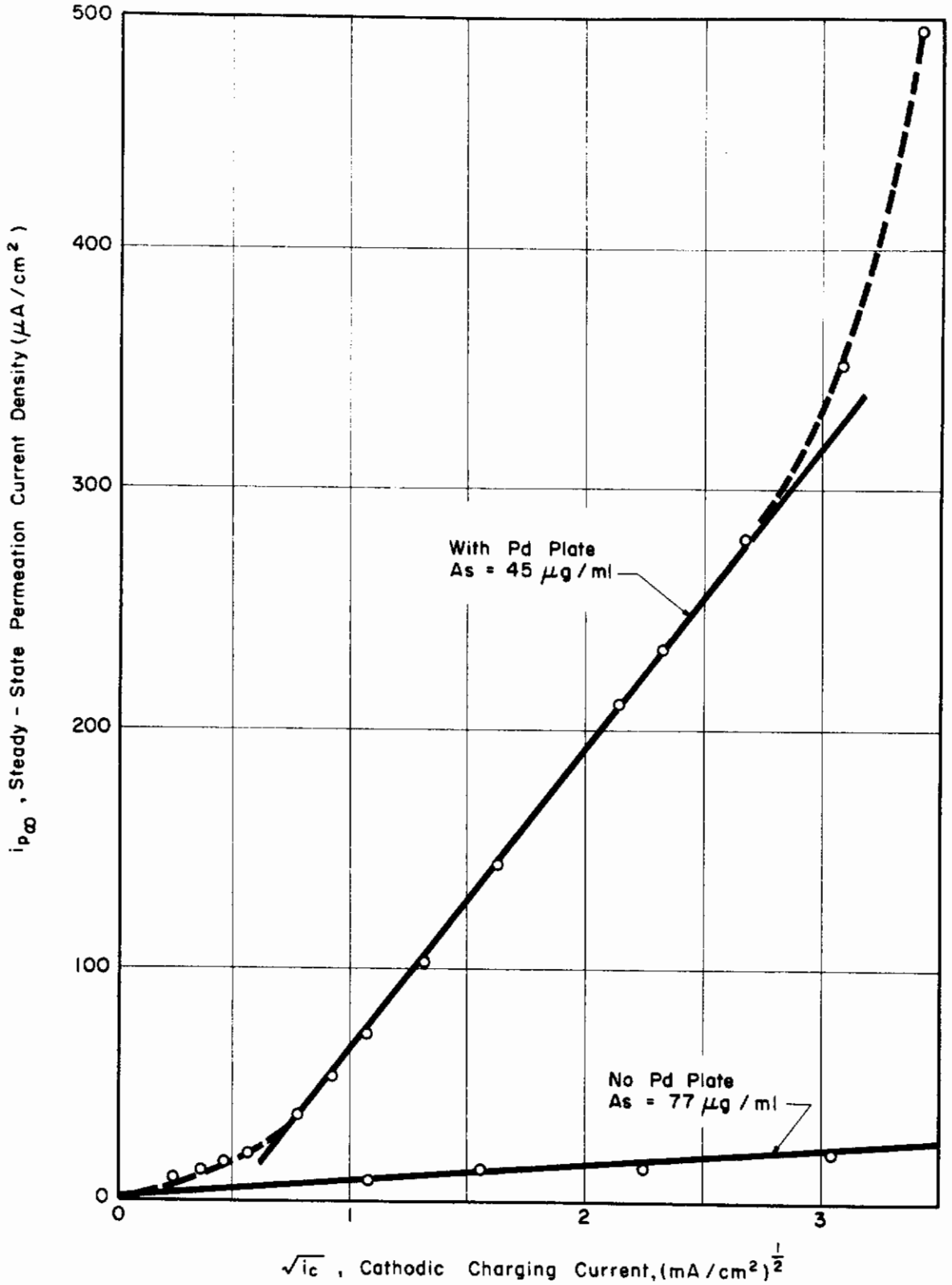

Fig. 244 - Effect of Palladium Plating of the Exit Surface on the Hydrogen Permeability in AISI 1010 Steel

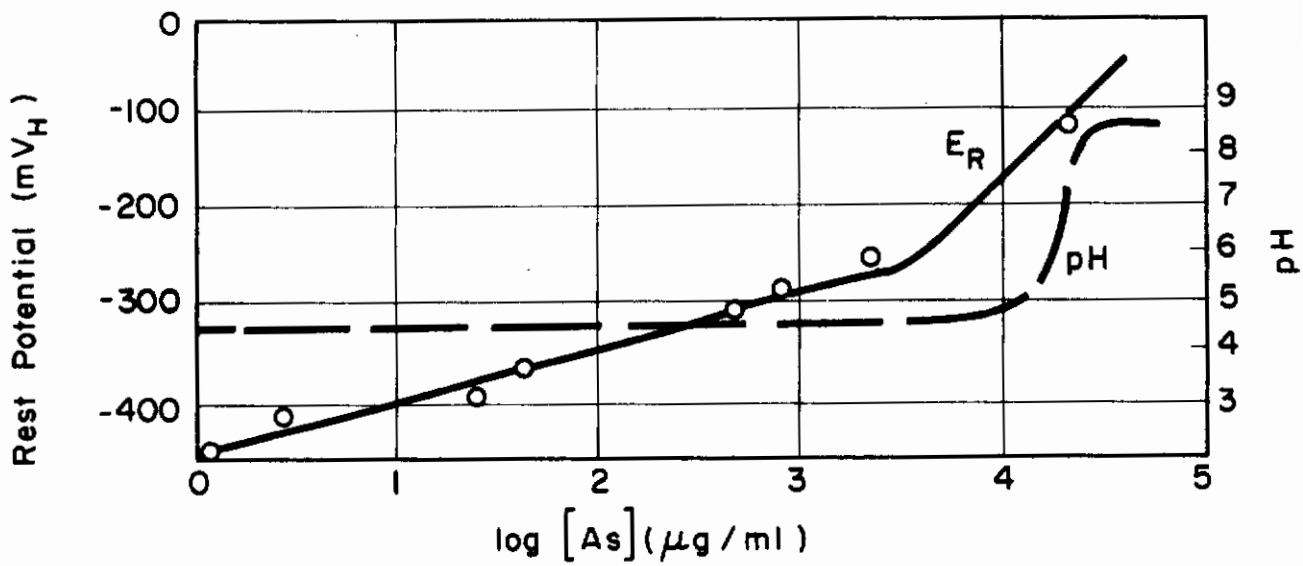

Fig. 245 - Effect of Arsenite Additions to Acetate on Solution pH and Rest Potential of 1010 Steel

Table XXIX - Effect of Arsenite Additions on the Hydrogen Permeability of Unpalladized AISI-1010 Steel at Room Temperature

Concentration, Wxpressed as μg Elemental As/ml solution	Charging Current Density (mA/cm^2)	Potential at Exit Surface mV (SHE)	Permeation Current Density ($\mu A/cm^2$)
0	20	+540	0.75
3.9	20	+540	19.3
77.0	20	+540	20.8
394.0	20	+540	19.0
768.0	20	+540	16.3

The cathodic polarization behavior of the acetate and acetate-arsenite solutions is shown in Fig. 246 for a wide range of arsenite concentrations, expressed in terms of elemental arsenic. At small arsenic concentrations (up to about 6 μg/ml typified by the curve for 4.1 μg/ml) the arsenic increases the cathodic kinetics. Thus arsenic deposition occurs simultaneously with hydrogen deposition. As the potential becomes more active, the ratio of the partial currents for arsenic deposition to hydrogen deposition becomes smaller as the polarization curve for the dilute arsenite-acetate solution approaches that of the solution without arsenite. At higher concentrations of arsenic the curves show a "two hump" behavior. The first corresponds

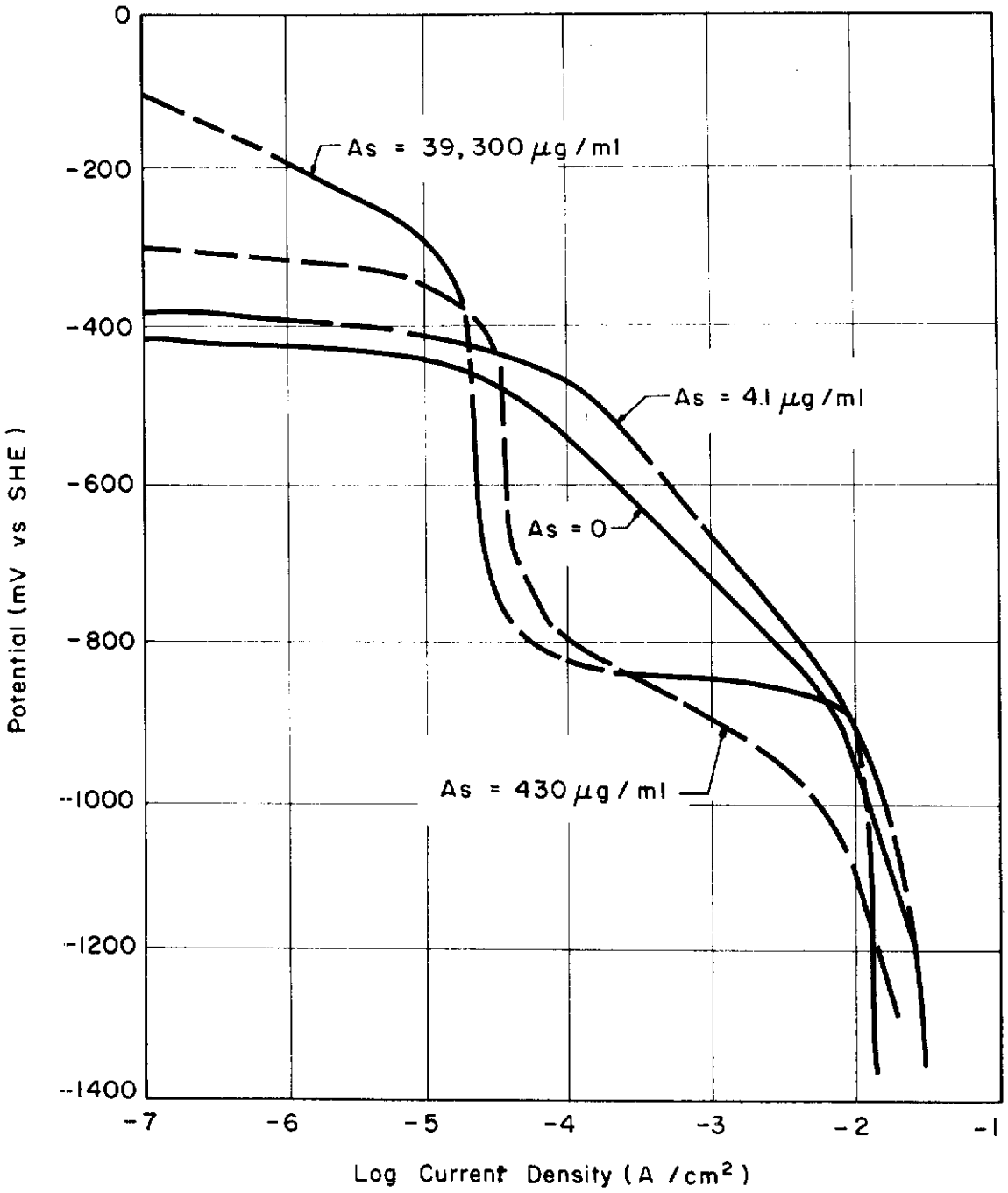

Fig. 246 - Cathodic Polarization of 1010 Steel in Acetate Buffer With Arsenite Additions

to As deposition and the second, at more active potentials, to H^+ reduction. The depression of the hydrogen evolution region may be caused by changes in the local pH brought on by a very high arsenite concentration. The apparent limiting current obtained in the arsenic reduction region does not correspond to the bulk solution. Thus, if the reduction rate of arsenite were controlled by mass transfer from the solution, the limiting currents would be directly proportional to the concentration of arsenite in solution. This is not the case and it must be concluded that the critical step is some sort of surface diffusion.

Hydrogen permeation experiments were conducted by charging from arsenite-containing solutions into AISI-1010 steel palladized at the exit surface. This method gave high permeabilities, even at low charging current densities. In Fig. 247, the permeation rise transients are shown for hydrogen charging from acetate alone, and acetate plus small and large additions of arsenite. The boundary conditions were a charging current of 125 $\mu A/cm^2$ and a potential at the exit side of 0 mV(SCE) [240 mV (SHE)]. The highest permeability was from the solution with the small As concentration. These data are tabulated in Table XXX.

The highest permeation occurred when there was simultaneous deposition of the arsenic and the hydrogen (3.9 μg As/ml). Chronopotentiometric measurements during the charging showed that the potential decreased from an initial value of -450 mV (SHE) to -620 mV at 180 seconds (onset of steady-state diffusion). At the higher arsenite concentrations there was an initial deposition of arsenic followed by co-deposition of arsenic and hydrogen, with hydrogen predominating as illustrated in the polarization diagram, Fig. 246. In these cases the potential at steady-state hydrogen diffusion was -700 mV and lower. These latter solutions had permeation behavior characteristics of pure acetate as tabulated in Table XXX.

Table XXX - Effect of Arsenite Additions on the Hydrogen Permeability of Palladized AISI 1010 Steel at Room Temperature

Concentration, Expressed as μg Elemental As/ml Solution	Charging Current Density (mA/cm^2)	Potential at Exit Surface mV (SHE)	Permeation Current Density ($\mu A/cm^2$)
0	0.125	+540	42
3.9	0.125	+240	61.5
7.8	0.125	+240	48.0
19.7	0.125	+240	39.5
39.4	0.125	+240	44.0

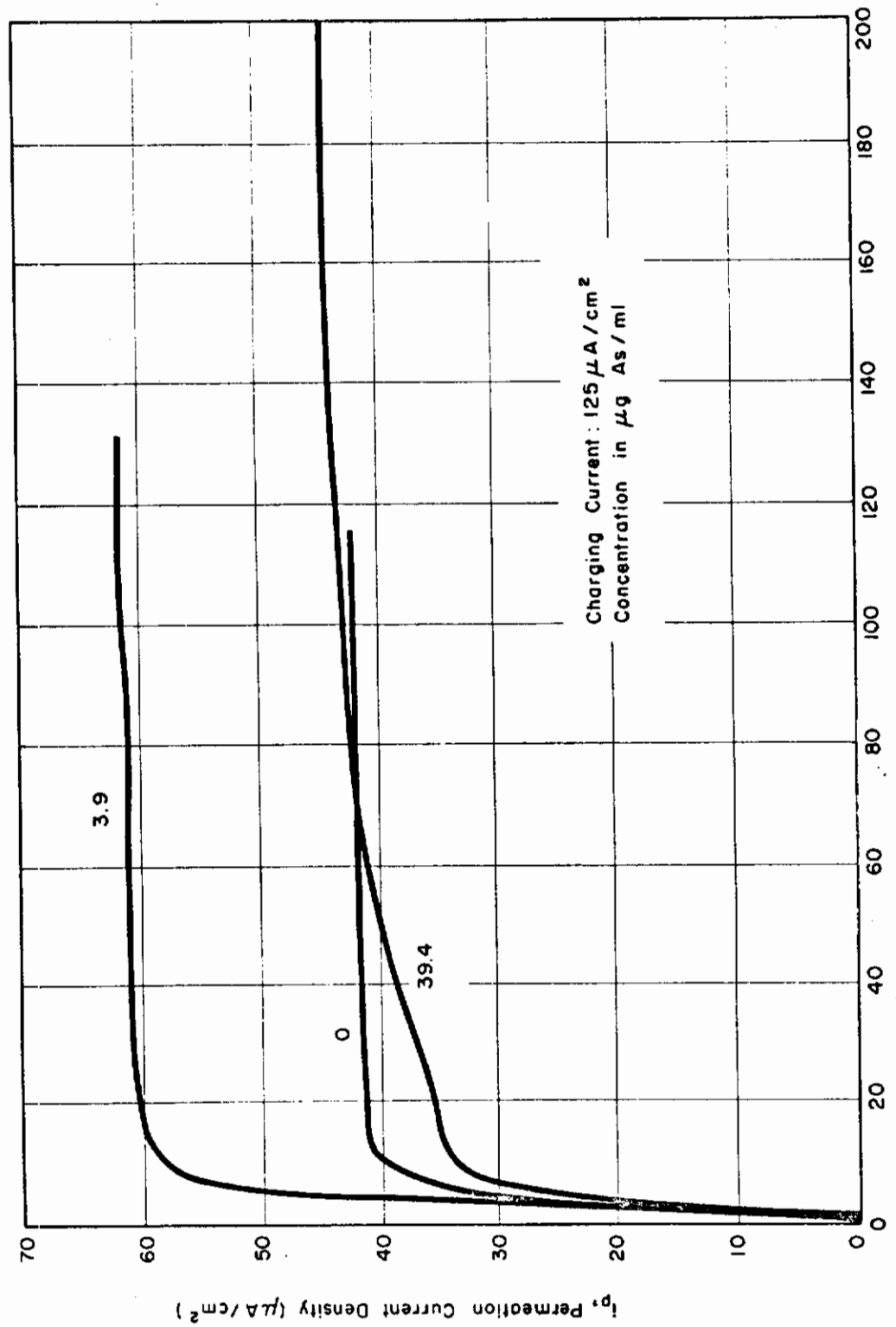

Fig. 247 - Rise Transients for Hydrogen Permeation in Palladized AISI 1000 Steel

However, as the charging current was increased, the permeation current increased. At high charging currents, the permeation current for all As-containing solutions greatly exceeded that of the acetate-only solution.

In Fig. 248, the permeation current at steady-state (the plateau current in Fig. 247) is plotted against the square root of the charging current. This relationship has been developed in the literature[146] and applies when recombination of the freshly deposited nascent hydrogen atoms on the metal surface is the rate-controlling step in the cathodic reduction process. The constant of proportionality involves the diffusivity of hydrogen, the thickness of the specimen, and the specific rate constants for the recombination and absorption reactions. When recombination is hindered, the competitive absorption reaction, H (absorbed, surface) $\rightarrow$ H (absorbed, lattice), is promoted. The deposited arsenic can hinder recombination in a purely geometric way or by a chemical coordination with the hydrogen. Presumably the chemical compound can break down and release hydrogen to the steel. Qualitative tests for compound AsH_3 in the charging solution showed none present.

Figure 249 shows an anomalous effect. At low charging currents a higher permeability obtains from the solution containing no arsenic. Up to a charging current of 0.31 mA/cm^2, the transients show the "plateau behavior" for this solution. Above this charging current value, steady-state does not occur and the permeation falls off with time. Since the permeability is proportional to the product of the diffusivity and the solubility, either or both of these must decrease. When the same experiment was run, charging from an arsenited solution, the series of plateaus for charging current increases was observed up to 20 mA/cm^2. Beyond this value, the "saw-tooth" shape response was noted. Thus the presence of arsenite in the solution would not affect the hydrogen diffusivity, but the arsenic deposits on the surface have a great influence on the fugacity of the adsorbed hydrogen and, therefore, on the hydrogen solubility just inside the steel. Therefore, the appearance of this "saw-tooth" behavior is not a criterion for detecting hydrogen trapping (decreased diffusivity due to preferential hydrogen migration to structural defects where the mean time of stay is longer and the migration away is a slow process).

e. Effect of Co-deposition

In order to show that arsenic and hydrogen co-deposition (i.e., as opposed to As on the surface) was a necessary condition for enhanced permeation rates, a steel sample was deliberately plated with 50 mC of arsenic which was an amount of arsenic estimated to be deposited during a hydrogen permeation test for the conditions corresponding to the maximum permeation rate in Fig. 250. This sample was then placed in an acetate solution with no arsenite present, and a hydrogen permeation transient was obtained. This permeation behavior of this arsenic-plated

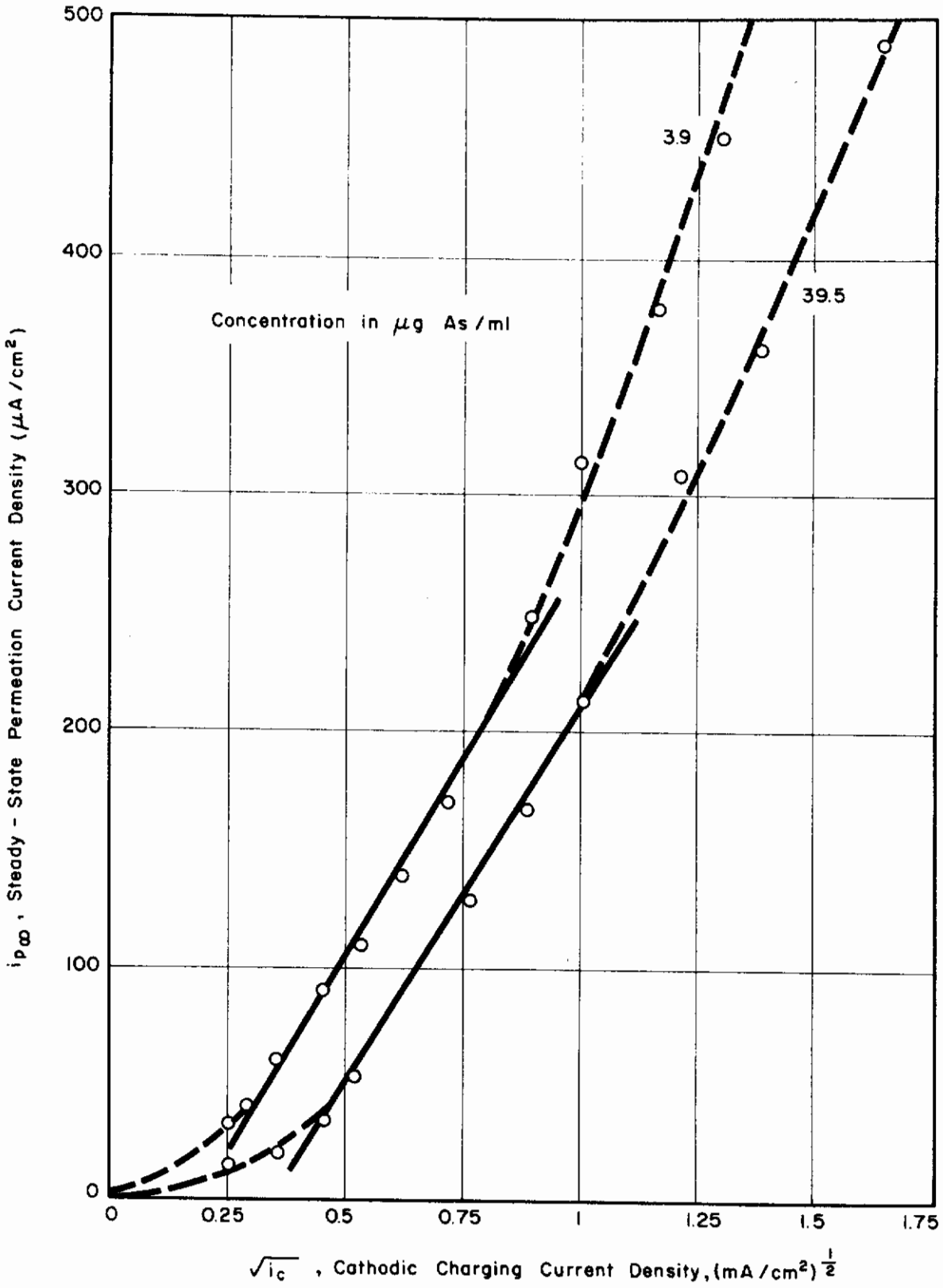

Fig. 248 - Relationship of Permeation Current to Charging Current

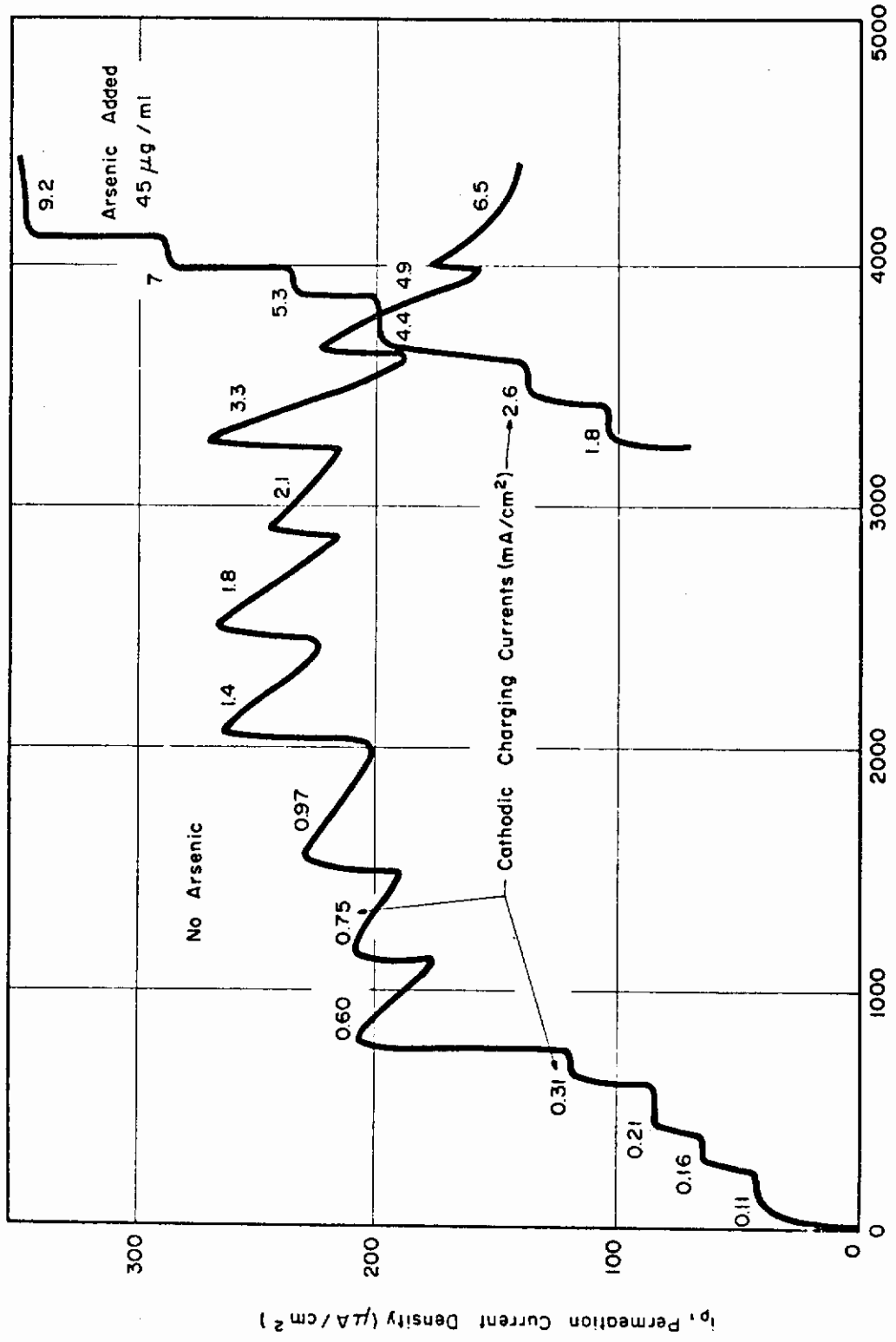

Fig. 249 - Nonsteady-State Behavior Permeation Transients

specimen is compared to that of a sample charged from a solution containing no arsenite and the one containing arsenite. Figure 250 shows the highest permeation for the case of simultaneous arsenic and hydrogen deposition and about the same rates for (arsenic plated specimen) hydrogen deposition only. The thickness of these specimens was 3 mils.

f. Calculation of Diffusivity

The analytical bases for diffusivity calculations is described in a previous section.

The results of experiments on hydrogen diffusivity are tabulated below.

Table XXXI - Diffusivity of Hydrogen in Palladized AISI-1010 Steel. Hydrogen Charged from Arsenite-Acetate Solutions. Units: cm^2/s.

Method of Calculation	Arsenic Concentrations (μg/ml)			
	3.9	7.8	19.7	39.4
Lag Time	4.98×10^{-8}	0.378×10^{-8}	2.73×10^{-8}	2.32×10^{-8}
Time Rise Constant	12.5×10^{-8}	0.426×10^{-8}	4.73×10^{-8}	1.76×10^{-8}
Decay Transient	4.65×10^{-8}	2.39×10^{-8}	1.63×10^{-8}	2.17×10^{-8}

Table XXXII - Diffusivity of Hydrogen in Palladized AISI-1010 Steel for Various Thicknesses

Method of Calculation	Sample Thickness (mils x 10^{-8})			
	2	3	5	10
Time Lag	0.378	1.57	3.02	2.32
Time Rise Constant	0.426	3.35	1.67	7.36
Decay Transient	2.39	1.20	1.92	2.87

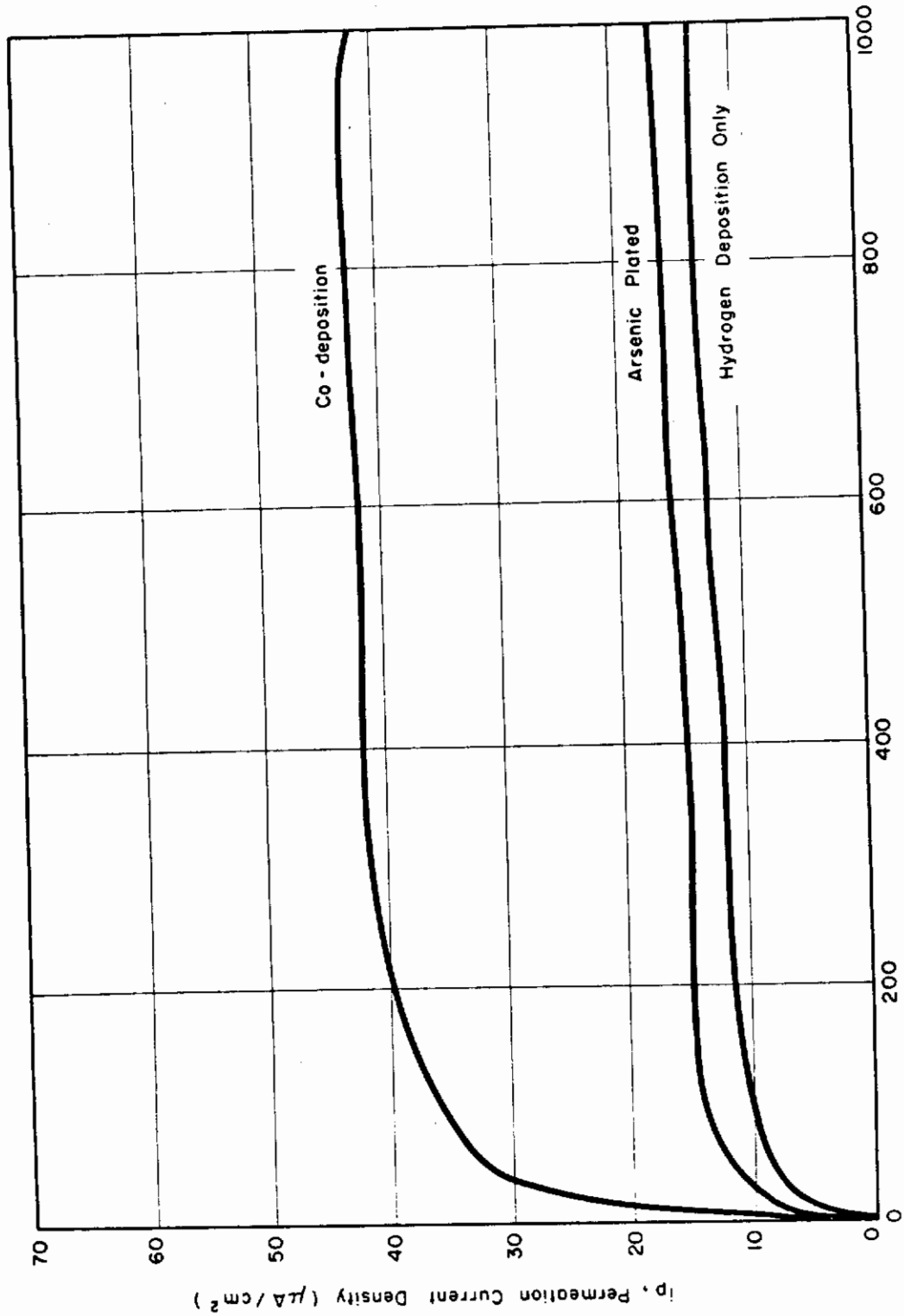

Fig. 250 - Effect of Deposition Processes on Hydrogen Permeation

The decay transients give the most consistent values since neither the thickness nor the charging solution should affect the diffusivity. The diffusivity can therefore be taken as approximately 2×10^{-8} cm^2/s.

g. Morphology of the Arsenic Deposits

It was established that elemental arsenic was deposited on the charging surface during permeation tests by electron diffraction of this surface. In addition, there was agreement of gravimetric and coulometric determinations of the amount of arsenic deposited at constant potential [-1000 mV (SHE)] and from a high concentration of arsenite in acetate solution. Scanning electron photomicrographs were taken of the arsenic-deposited surface, as shown in Figs. 251 and 252. In Fig. 251, the steel substrate can be seen since the preparation scratches are visible. The arsenic plate is not uniform. In Fig. 252, the cracks show the plate is brittle, and the arsenic appears to adhere poorly to the substrate. It appears that an initial thick plate is formed on top of this. The plate thickness was estimated to be 8000Å.

Most of the above work is aimed at establishing parameters for subsequent experiments. The work on arsenic co-deposition sheds new light on the mechanism for the absorption of hydrogen. It would appear that the absorption is influenced by the ionic form of arsenic rather than noncharged arsenic.

4. Experimental Results and Discussion - Promoter Effects

a. Galvanostatic and Potentiostatic Control

The establishment of defined boundary conditions for the iron or steel foil is of paramount importance for the mathematical models needed to solve the diffusion equation. Most of the work reported in the literature has described a galvanostatically controlled system where the control of the input hydrogen is by a constant current; this control can also be obtained by applying a constant potential to the entry side.

b. Effect of Arsenite as a Cathodic Promoter

Sodium arsenite greatly increases the hydrogen permeability. At potentials at which hydrogen is deposited, arsenite is reduced, according to Fig. 253, which is the equilibrium pH-potential diagram. The specific equilibria for the concentrations of arsenite and pH's of solutions used in this investigation are shown. The rest potentials for sulfuric acid and acetate solutions containing arsenite additions (expressed as μg As/ml are shown in Fig. 254. The concentration dependence of these varies approximately according to the Nernst equation for the arsenite/arsenic equilibrium.

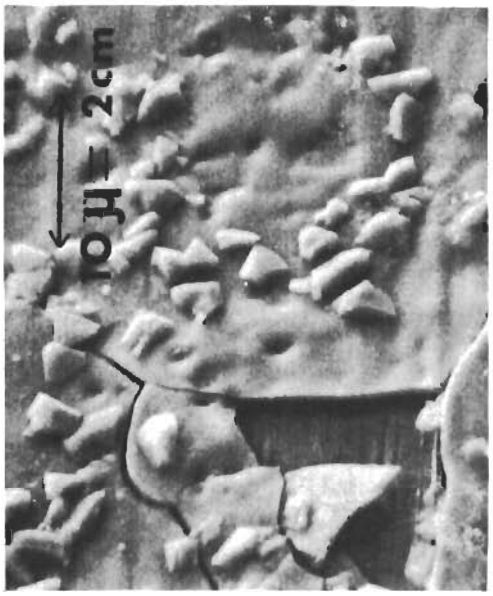

Fig. 252 - Arsenic Deposits on Steel Substrate 2000X

Fig. 251 - Arsenic Deposits on Steel Substrate 500X

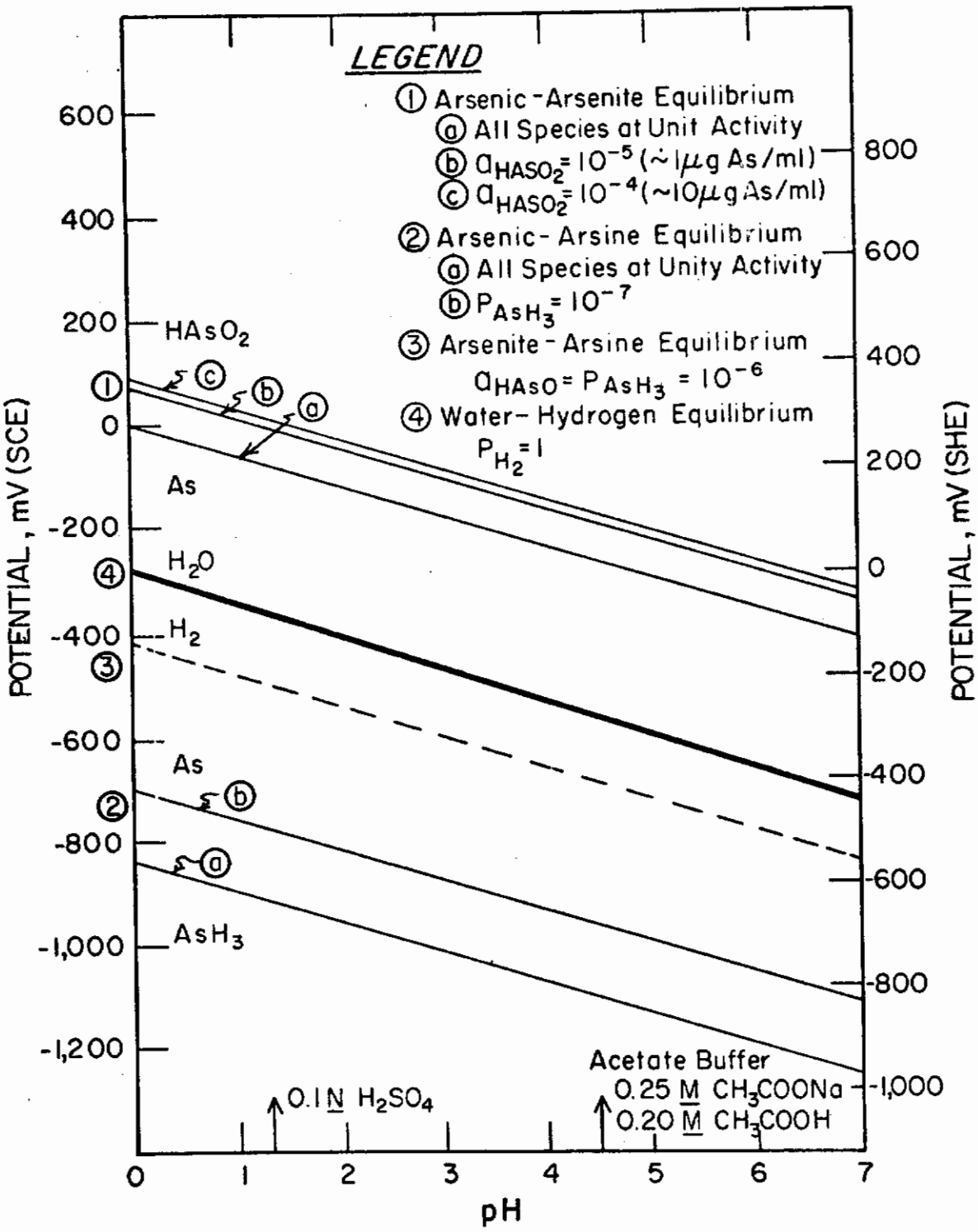

Fig. 253 - Equilibrium Potential-pH Diagram for the System Arsenic-Water at 25°C

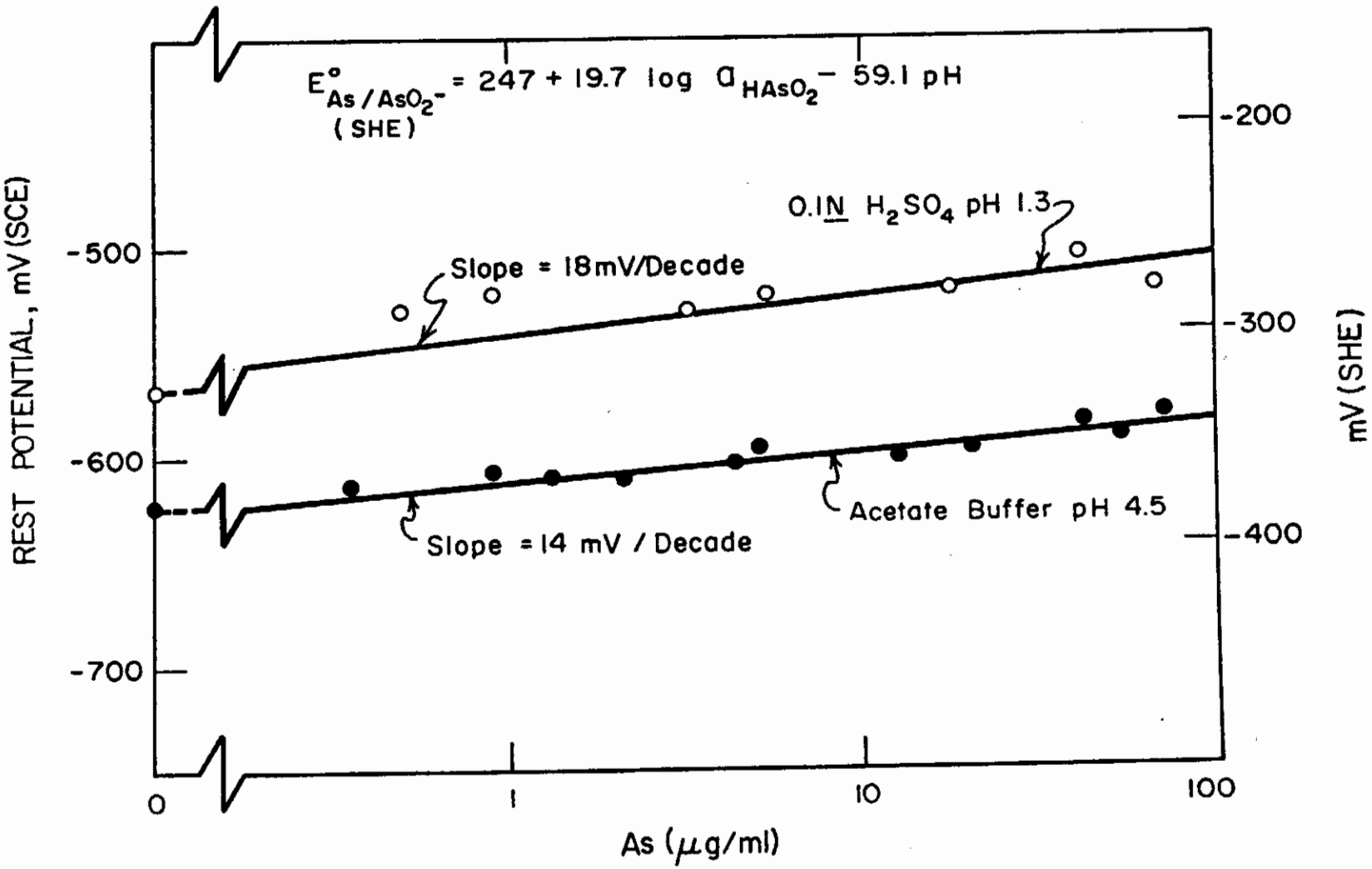

Fig. 254 - Rest Potential of Steel Electrodes as a Function of the Arsenite Concentration

Permeation transients of 1010 steel galvanostatically charged with hydrogen from the acetate buffer containing arsenite are shown in Fig. 255. The transients for the different charging currents show an increase of permeation current with the increase in charging current density and also illustrate the different behaviors, reflecting hydrogen interaction with the metal structure. The initial transient often shows a long time to come to steady state, while subsequent ones at relatively low current densities show the "normal" behavior, a sharp rise to a constant permeation current. Upon increasing the charging current density there can be a slight decline of the permeation current after the system appeared to reach steady state. Finally, at high charging current densities, the permeation current reaches a maximum and declines rather sharply, the "sharpness" usually increasing with the charging current densities.

In the next set of experiments described, the hydrogen was charged into the steel potentiostatically or galvanostatically and the steady state permeation current measured. These results are plotted in Figs. 256-259. The graphs show points where the anomalous behavior described in Fig. 255 occurred. One notes from these that in sulfuric acid (Figs. 256 and 257);

1. Arsenite additions are more effective in increasing the permeation current as the potential becomes more active or the charging current becomes larger.

2. The onset of the anomalous behavior--sharp maximum in the permeation current transient--occurs at more active potentials or higher charging currents when arsenite is present.

These same conclusions hold for the specimens charged with hydrogen from the acetate buffer (Figs. 258 and 259). In addition, some of the specimens were pre-deposited with a thin coating of arsenic (about 50 μC). These curves have the same general shape as those in which the charging solution contained arsenite, but the magnitude of the permeation is not as great. Generally, the pre-deposit arsenic specimen behave similar to specimens charged from more concentrated arsenite-containing solutions (> 30 μg As/ml).

In galvanostatic charging the expected relationship between i_p and i_c is $i_p \propto i_c^{1/2}$ if the recombination step is the rate-controlling one. The exponent of proportionality is 0.6 - 0.9 for these experiments. Similarly, there is an exponential relationship between the permeation current and the cathodic potential, which seems to hold at the less active potentials.

Another way of plotting these data is to show the relationship between the permeation efficiency and either the applied potential or charging current density. The permeation efficiency is the ratio of

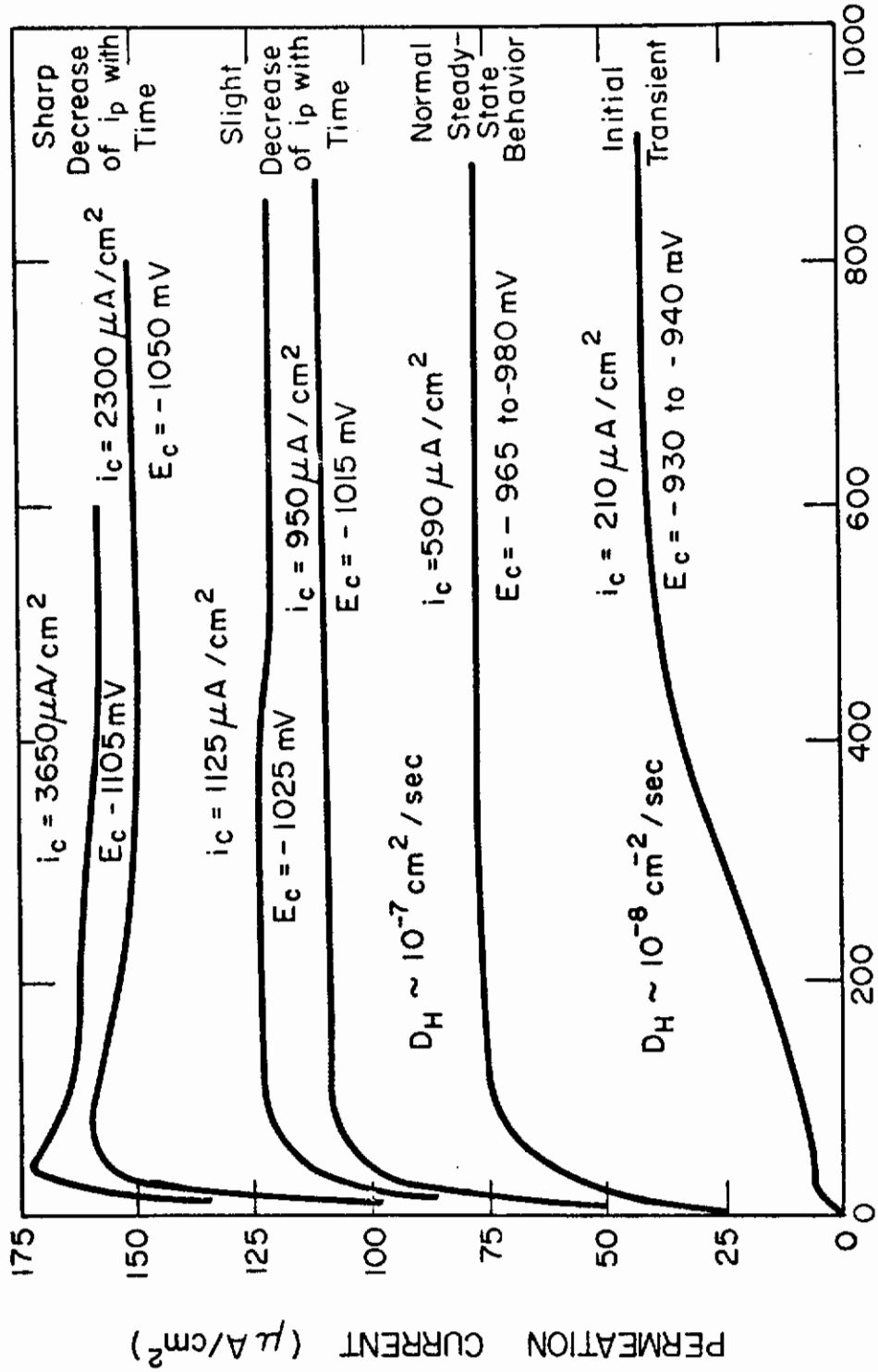

Fig. 255 - Examples of Hydrogen Permeation Rise Transients. Conditions: Charging solution, acetate buffer pH 4.5 with arsenite additions (0.9 μg As/ml); membrane, 2-mil thick 1010 steel, vacuum annealed at 650°C for 2 hours, palladized on exit surface; exit solution, 0.1N NaOH

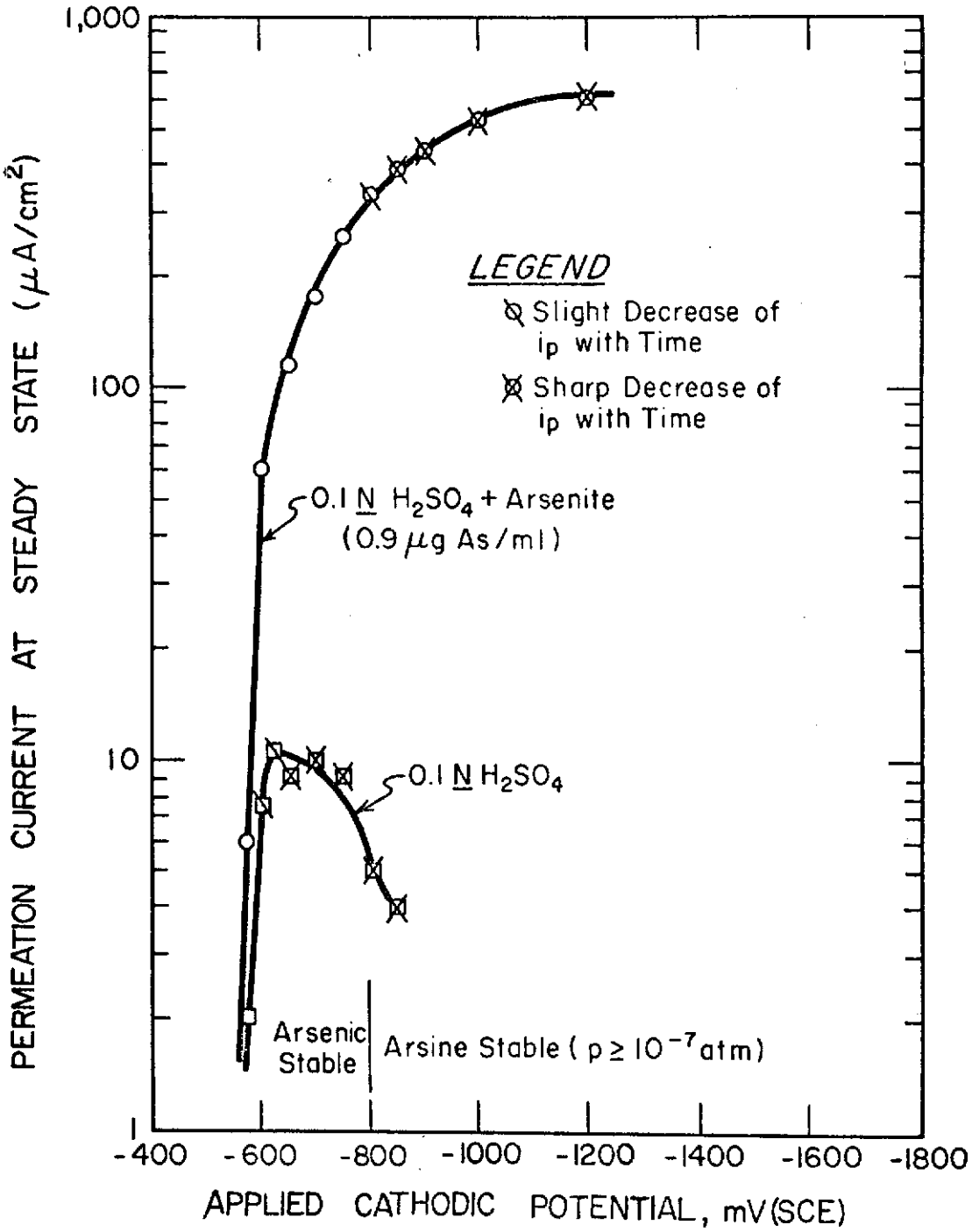

Fig. 256 - Steady State Hydrogen Permeation of 1010 Steel as a Function of the Cathodic Potential (sulfuric acid solutions)

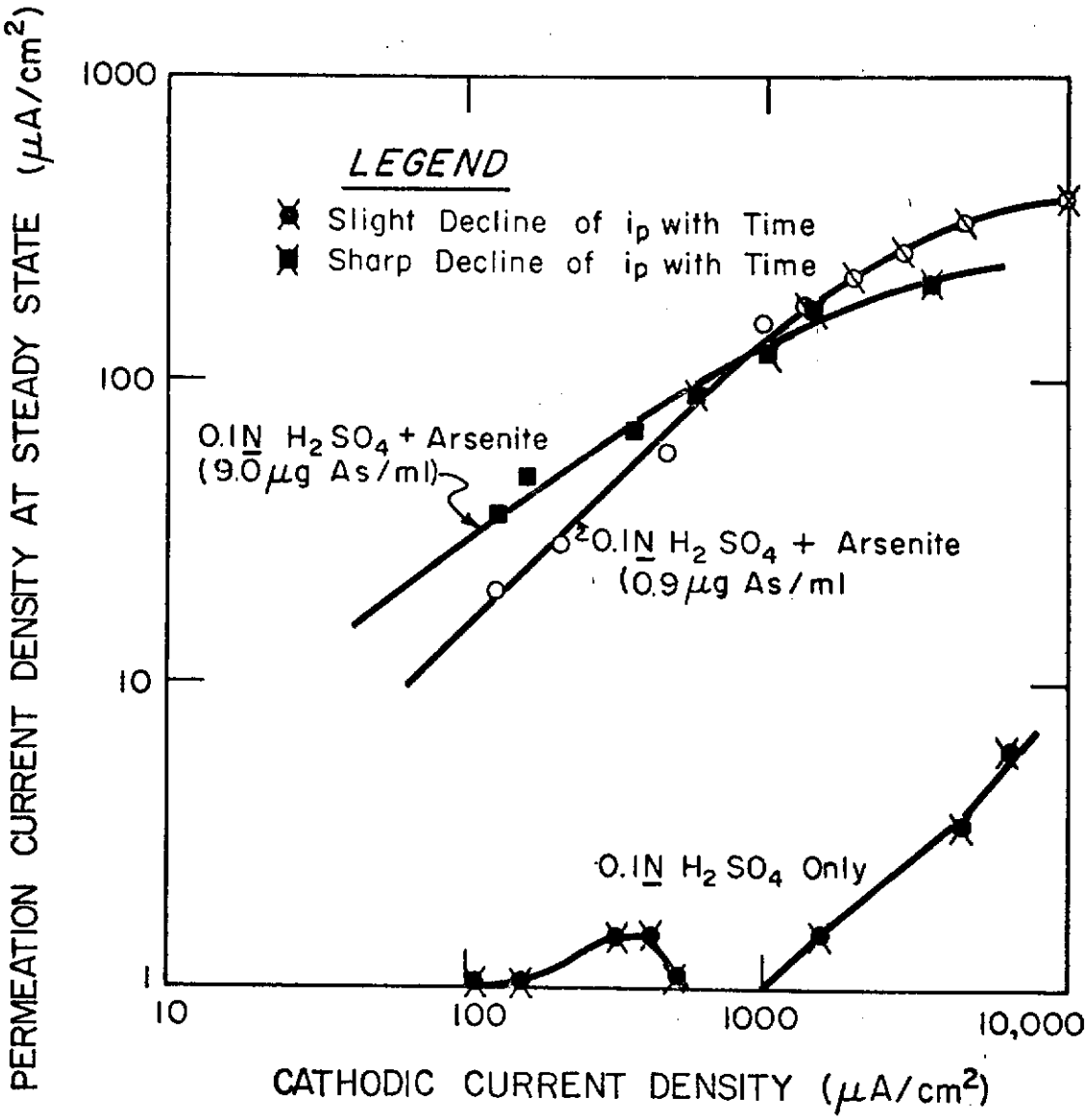

Fig. 257 - Steady State Hydrogen Permeation of 1010 Steel as a Function of the Cathodic Current Density

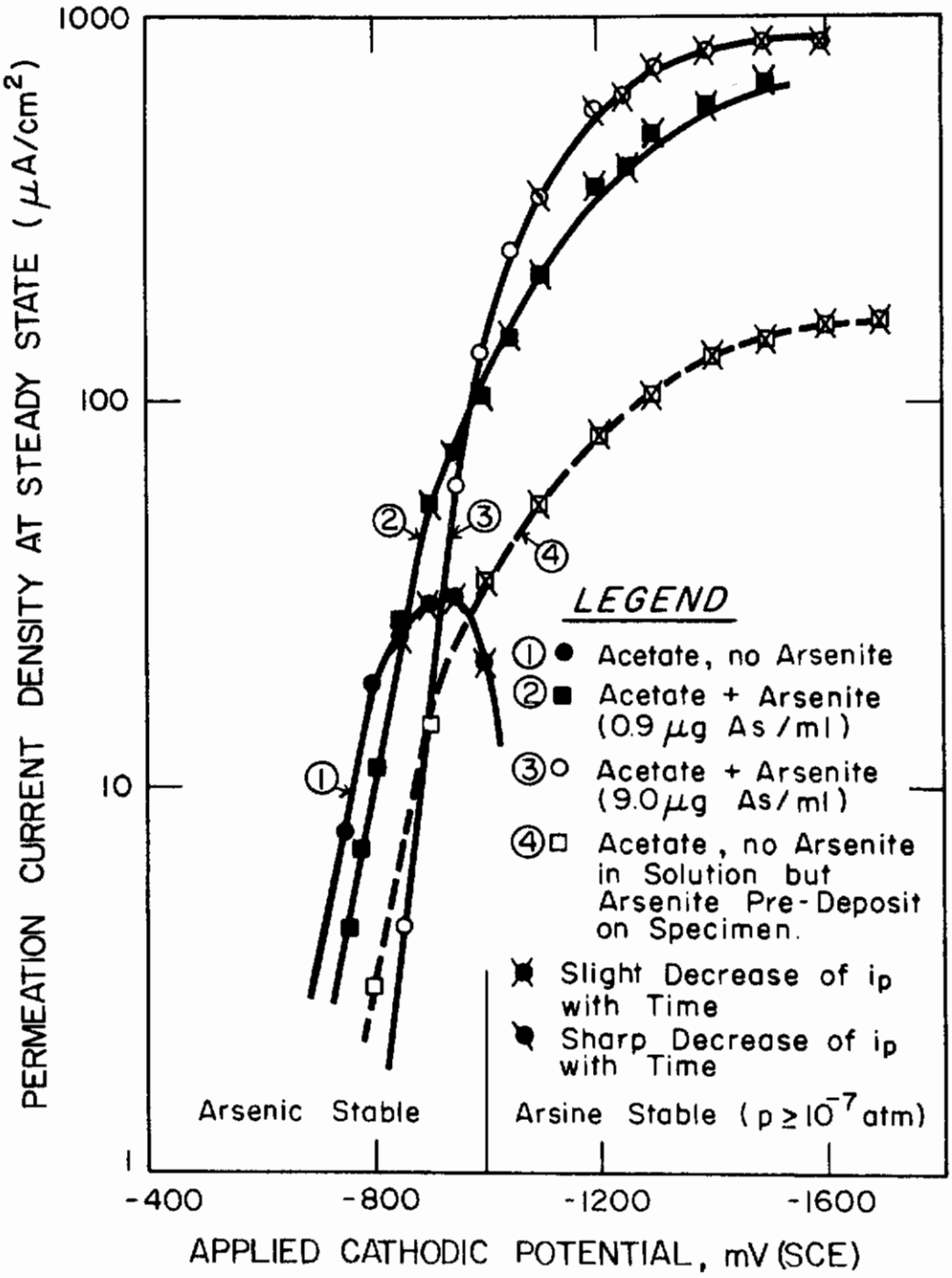

Fig. 258 - Steady State Hydrogen Permeation of 1010 Steel as a Function of the Cathodic Potential (acetate solutions)

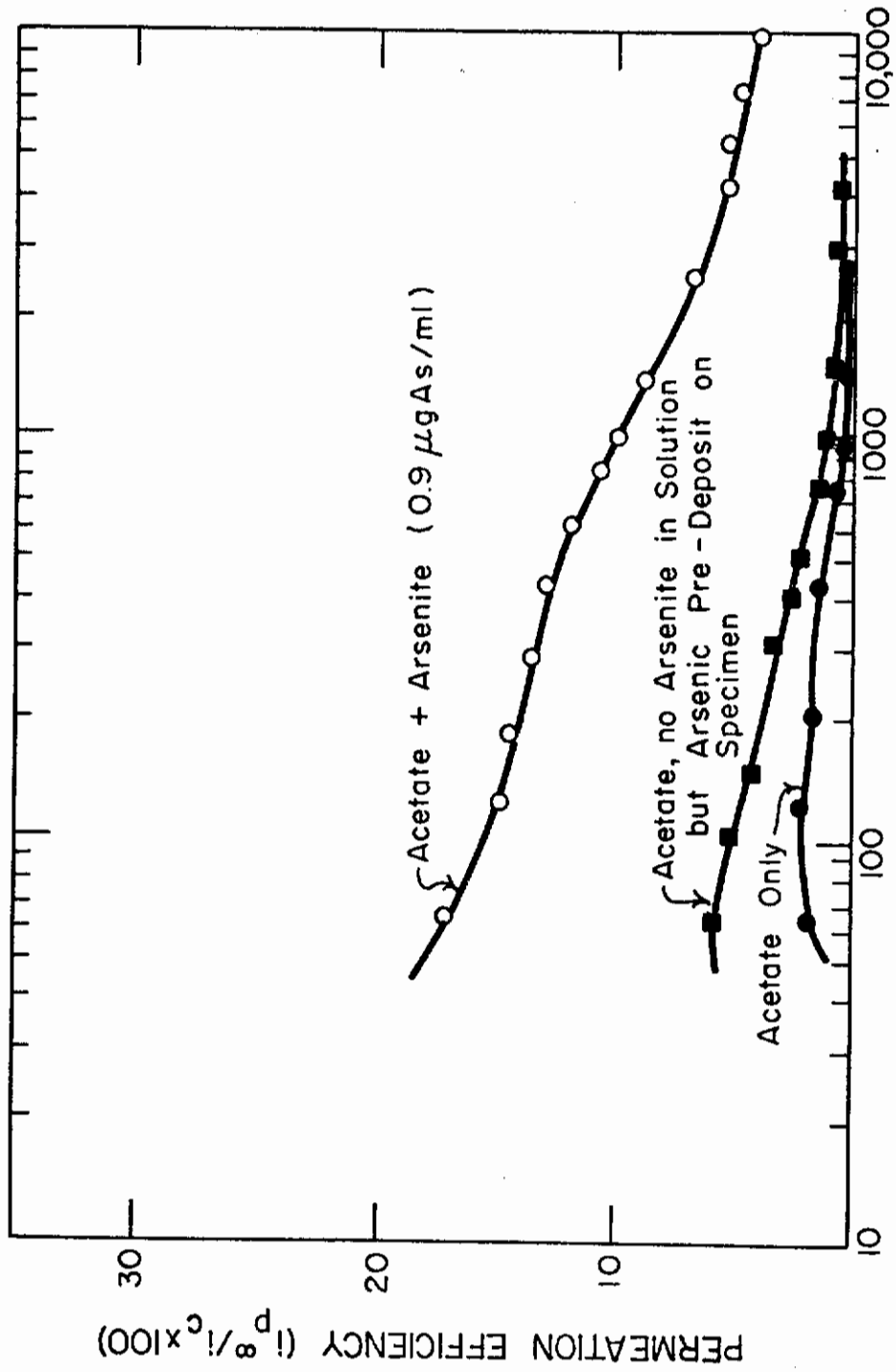

Fig. 259 - Permeation Efficiency of 1010 Steel Membranes as a Function of the Cathodic Current Density (acetate solutions)

the permeation current density (at steady state, or at the maximum if anomalous behavior obtains) to the charging current density. This gives the percent of hydrogen entering the metal and diffusing through it, assuming that all of the cathodic current is utilized for hydrogen ion reduction.

Figures 260 and 261 illustrate the relationship between permeation efficiency and the applied potential. At potentials slightly cathodic with respect to the rest potential, say, less than -600 mV (SCE) in the absolute sense for the 0.1N H_2SO_4 and less than -750 mV (SCE) for the acetate buffer, the permeation efficiency of the pure acid is either higher or about the same value as the acid containing arsenite. However, the permeation efficiency of the former decreases rather drastically above these values while that of the latter increases. The case where arsenic was pre-deposited shows behavior like that of the pure acid case except that the permeation efficiency is higher for the arsenic predeposit at all potentials. In some of the early work[147] in which the arsenite additions to the acid enhanced the permeation, but not until some critical potential was exceeded, it was concluded that the formation of the promoter hydride (here, arsine, AsH_3) was a necessary condition for the increase in permeation current. The critical potentials in this cited work corresponded to an arsine fugacity (partial pressure) of about 10^{-7} atmospheres. In the present work the equilibrium potential for the arsenic (arsine, $P_{AsH_3} = 10^{-7}$) is shown. This potential is more active than the permeation efficiency maxima which would correspond to much lower arsine fugacity ($de/d \log P_{AsH_3} = -19$ mV/decade). Of course, this vanishingly small amount of arsine may be significant, although it appears that the species enhancing the permeability is arsenic.

Permeation efficiency vs. cathodic charging current density is plotted in Fig. 262 for the galvanostatic-controlled case with charging from acetate solution. There does not appear to be a maximum, but the smallest charging current attainable with the experimental apparatus was 60 $\mu A/cm^2$ which corresponds to a potential more active than the potential at which the maximum occurred for the corresponding potentiostatic charging and the value of i_c when i_p reached steady state is the one used for the calculation of permeation efficiency. In Fig. 263, the potentiostatic control gives higher efficiencies than galvanostatic control.

c. Discussion of Arsenic Effects

The metals with the greatest tendency to form solid solutions with hydrogen are those with the largest number of "d" electrons. While these metals have a rather large exothermic heat of hydrogen adsorption (25-40 kcal/mole), the solubility of hydrogen increases with the decrease in bond energy of the metal-hydrogen bond for the transition metals. This probably indicates the need for a more unsaturated bonding arrangement to promote hydrogen entry. An adatom-like elemental arsenic deposited on the surface along with adsorbed hydrogen can promote

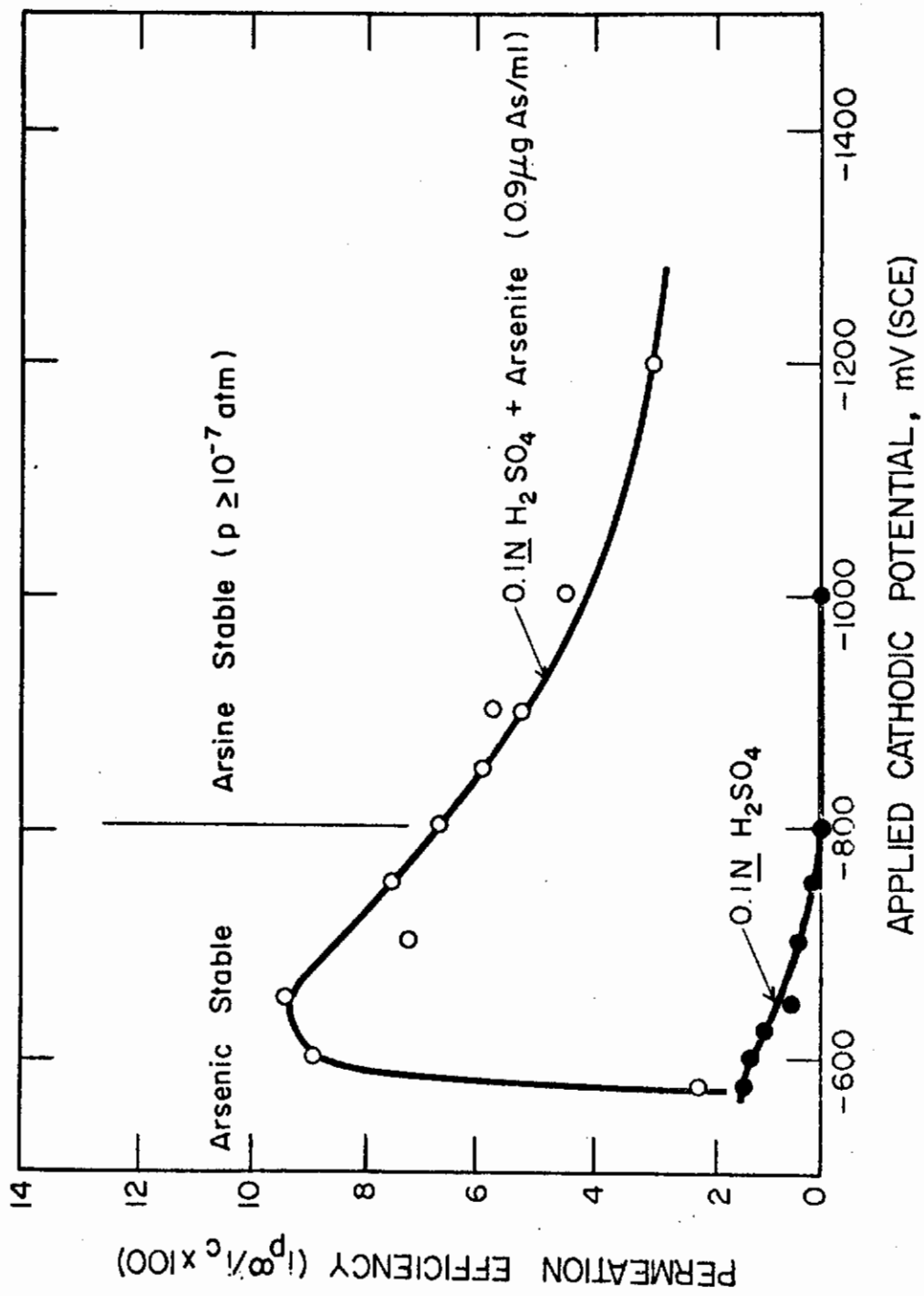

Fig. 260 - Permeation Efficiencies of 1010 Steel Membranes as a Function of the Cathodic Potential (sulfuric acid solutions)

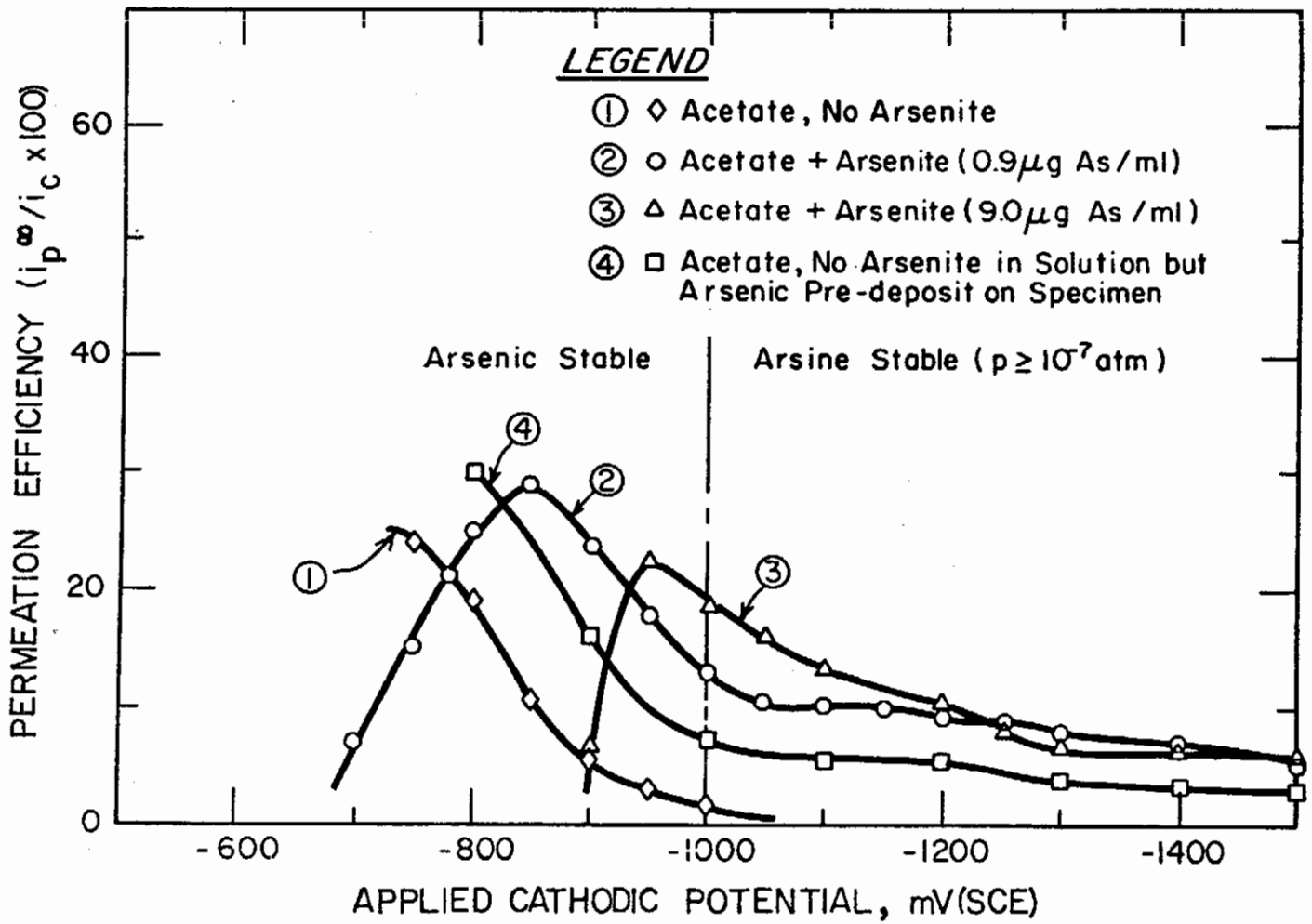

Fig. 261 - Permeation Efficiencies of 1010 Steel Membranes as a Function of the Cathodic Potential (acetate solutions)

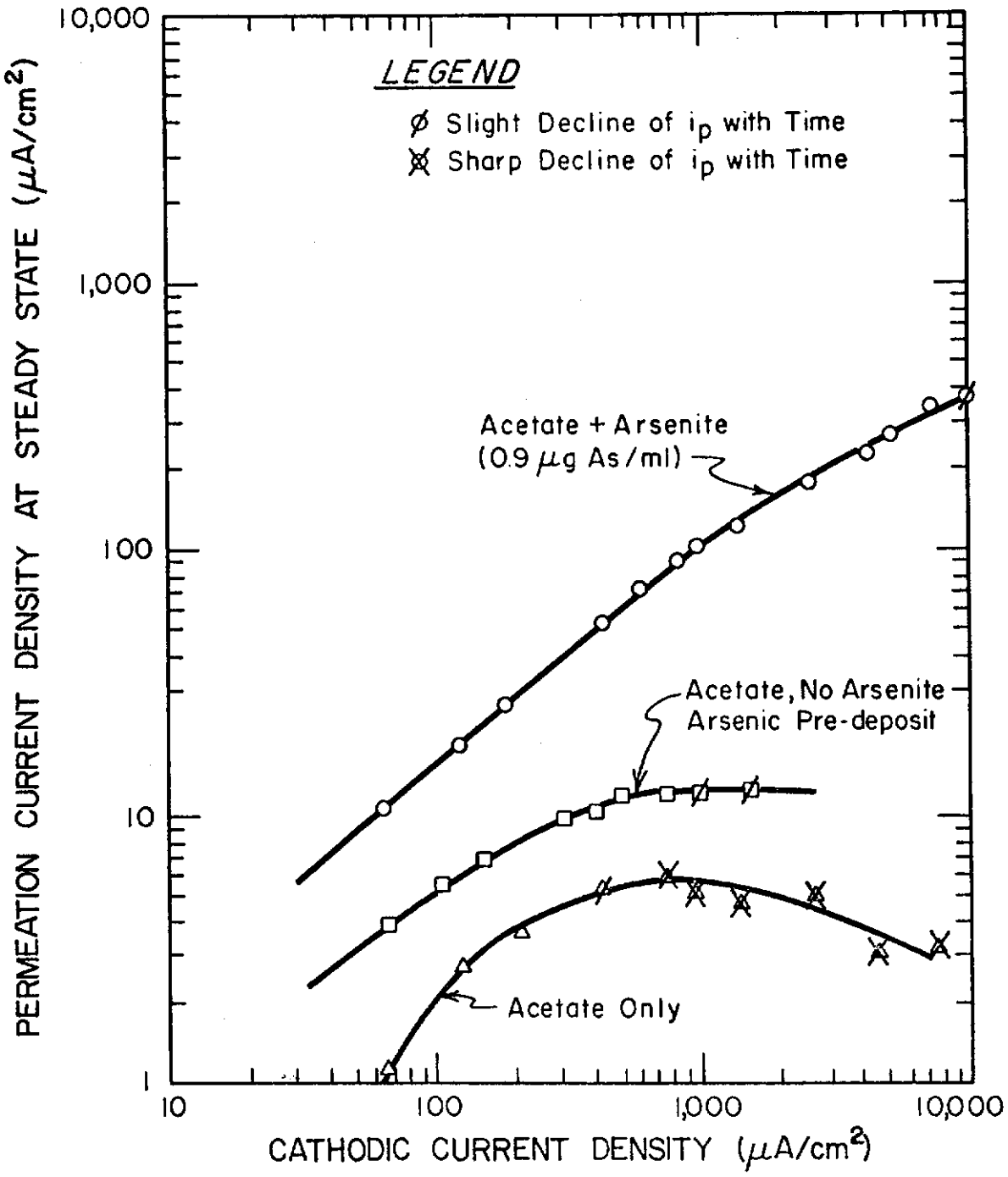

Fig. 262 - Permeation Efficiencies of 1010 Steel Membranes as a Function of the Cathodic Charging Current (acetate solutions)

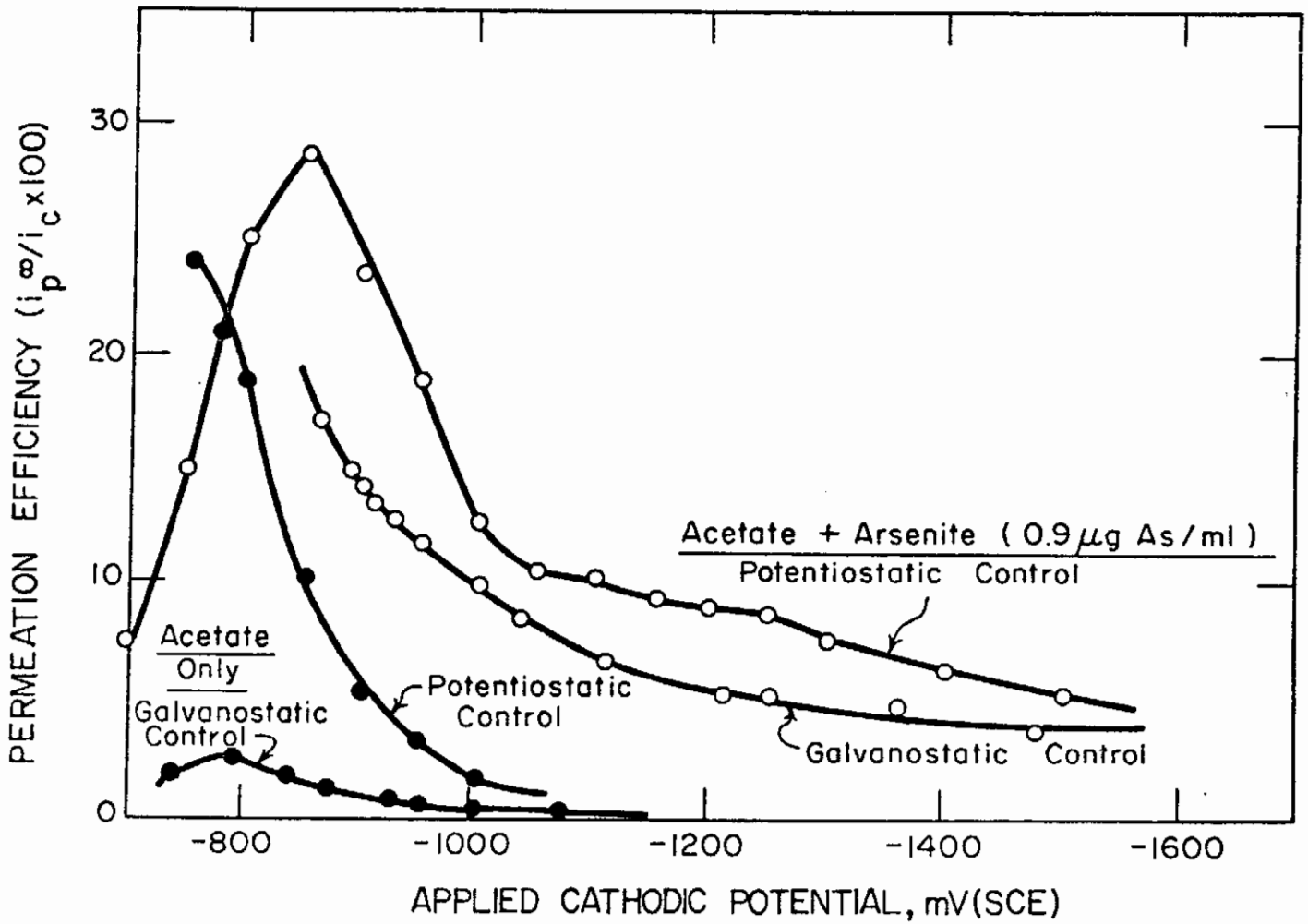

Fig. 263 - Permeation Efficiences of 1010 Steel Membranes as a Function of the Cathodic Potential for Galvanostatically and Potentiostatically Controlled Charging from Acetate Solutions

the entry of the latter in either or both of two ways; i.e., by supplying additional electrons to the metal or by decreasing the heat of hydrogen adsorption by lateral interaction between co-deposited arsenic and hydrogen. At the same time these interactions of the hydrogen with the metal and the arsenic slow down the kinetics of hydrogen atom recombination.

Cathodic promoters have electrons that can be given to or shared with the substrate, thus raising the "d" electron density of the metal. Examples of promoters are S^{2-}, P^{2-}, CN^{-}, Cl^{-}, Se^{o}, As^{o}, and As^{3-}, to list a few. Some of these are adsorbed on the surface (Cl^{-}, CN^{-}, H_2S), some are deposited electrochemically (Se from H_2SeO_2, As from $HAsO_2$). Elemental arsenic has five valence electrons which could be shared with the substrate if it is plated. Arsenic in the form of arsine would have a pair of unshared electrons that would be shared with the substrate if it were strongly adsorbed. The electron density of the iron atoms is thereby increased by the presence of these compounds or elements and, thus, the iron should form a more unsaturated bond with the hydrogen. Because of the open BCC structure of the iron, it requires little energy for movement of a strongly adsorbed hydrogen into the metal lattice. Therefore, a high concentration of hydrogen adatoms is tantamount to a high permeation rate.

Therefore, the maxima in the permeation efficiency vs. potential plots (Figs. 261-263) occur in the arsenic stable region because arsenic is a better supplier of electrons to the "d" shell of the iron than is arsine. As the potential becomes more active, arsine is formed from the arsenic (although there is experimental evidence that this reaction is not efficient)[128] and permeation efficiency falls. Another contributing factor, and perhaps a more important one, is that the permeation reaction depends on the concentration (surface coverage) of hydrogen adatoms, θ, while the competing recombination reaction of the hydrogen adatoms depends on θ^2. Increasing the cathodic current or moving the cathodic potential in the active direction will increase θ, so that at these more severe charging conditions, the permeation efficiency would be expected to fall off even if arsenic were stable over this entire potential range.

d. Polarization Work

Some additional polarization curves were run on the 1010 steel in the environments selected for the permeation studies. Figure 264 shows the results for 0.1N H_2SO_4 and Fig. 265 for the acetate buffer with various amounts of sodium arsenite added (always expressed as µg As/ml. At all potentials in the sulfuric acid solution and at potentials less active than about -1050 mV(SCE) in the acetate, the presence of the arsenite is to reduce the overall cathodic kinetics. The curves for the arsenite-containing solutions have a shape that is characteristic of two reduction reactions, each predominating in a different potential

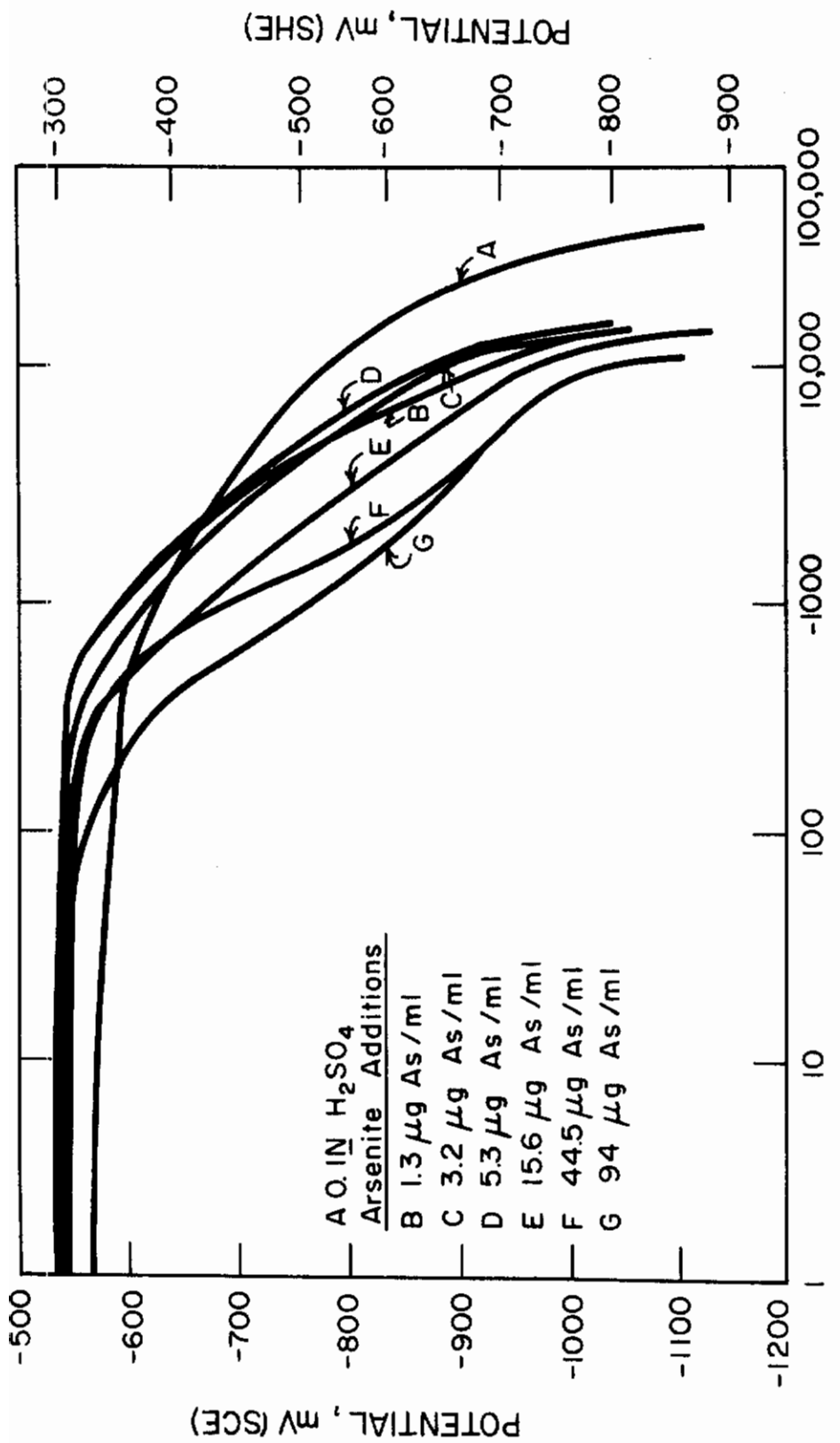

Fig. 264 - Potentiokinetic Polarization Curves for 1010 Steel in 0.1N H_2SO_4 With Arsenite Additions. Scan rate: 15,000 mV/hr

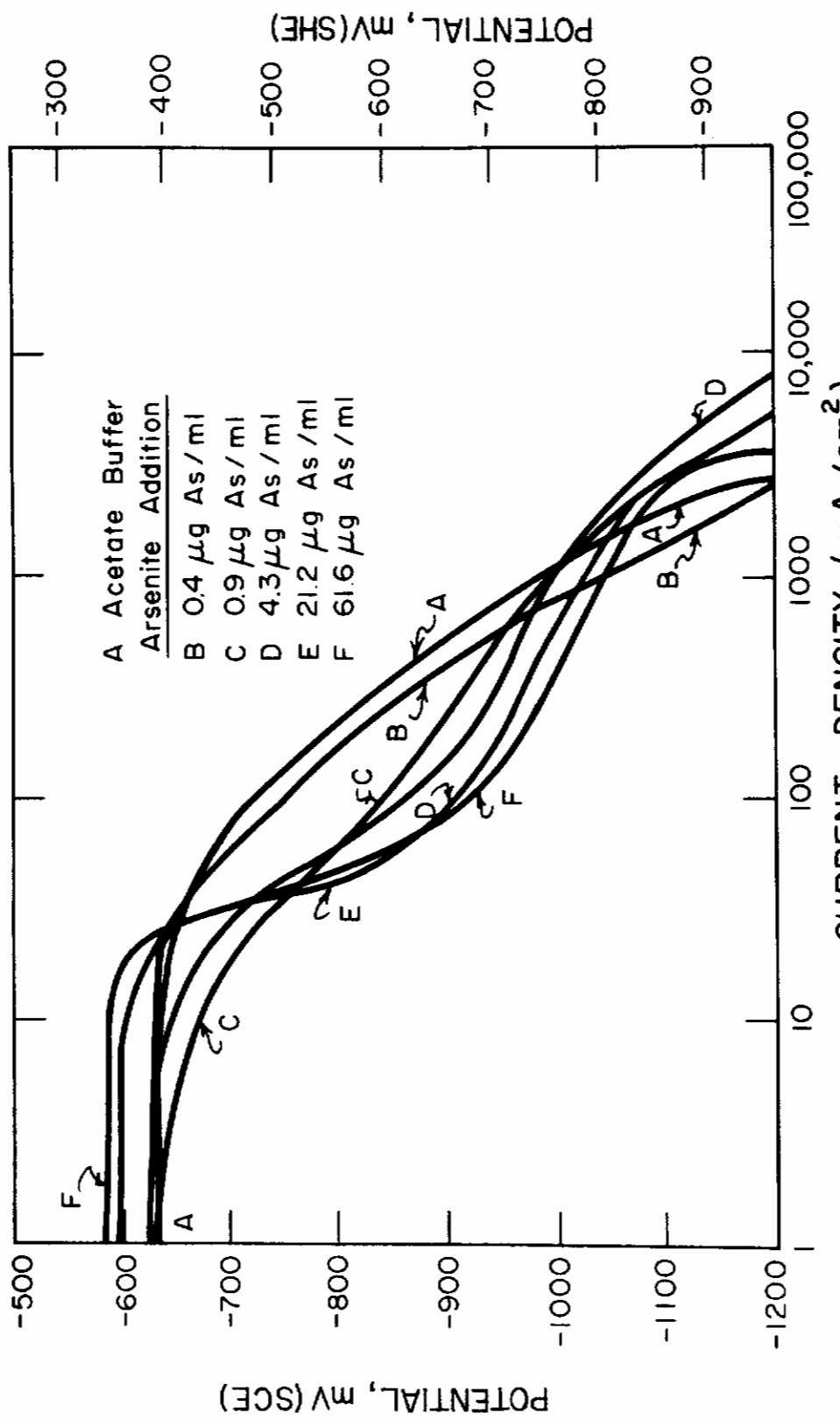

Fig. 265 - Potentiokinetic Polarization Curves for 1010 Steel in Acetate Buffer Solutions (pH 4.5) With Arsenite Additions

region. In other words, these curves are like those used for polarographic analysis. The first wave (the one at the less active potential) corresponds to arsenite reduction to elemental arsenic, and the second wave to hydrogen ion reduction on the arsenated steel surface. A possible and probable additional reaction to the second wave is the further reduction of arsenic to arsine or another hydride, this occurring at the most active potentials.

The relationship between the arsenite concentration and the apparent limiting current density that obtains in the potential region where arsenite-to-arsenic reduction predominates is not the one observed for concentration polarization; that is, the limiting current density is proportional to the concentration (activity) of the species in question. In this investigation the higher the arsenite concentration, the lower the apparent limiting current density and the more sharply defined it is.

Arsenic, as it is initially deposited, has an amorphous, vitreous structure with a high resistivity that partially insulates the metal underneath; the resistivity of this deposit was estimated at 10^8 Ω-cm. By continued electrolysis this arsenic deposit takes on a crystalline character. Electron diffraction patterns (extraction replicas) confirmed the presence of amorphous and crystalline As.

The hydrogen evolution reaction on the now arsenated surface is suppressed and the slope (de/d log i) is lower than that for hydrogen evolution in acid alone. Comparison with Figs. 260 and 261 show that the permeation efficiency maximum occurs at more active potentials as the arsenite concentration increases. The hydrogen reaction is suppressed until the arsenite-to-arsenic reaction occurs, which is the case of the acetate solution (Fig. 261) containing 9 μg As/ml in the region -700 to -900 mV (SCE). Once the potential is achieved at which hydrogen-ion reduction predominates, the kinetics of the hydrogen reaction are changed by comparison with the acid-only case. The smaller slope (Fig. 265) in the Tafel region of hydrogen ion reduction in arsenite-containing solutions is characteristic of a system where the recombination is the overall rate controlling step. At room temperature and assuming a symmetry coefficient of 0.5, the slope of the hydrogen ion reduction polarization curve is 30 mV/decade if the recombination step controls and 120 mV/decade if the discharge step controls. These slopes are for activation kinetics only. In this investigation it was not possible to eliminate concentration and resistance polarization effects because a static electrode with solution agitation was used and the pH of the acetate solutions was high (4.5). The suppression of the hydrogen reaction to more active potentials is explained by noting that the exchange current density for the reaction on an iron surface is of the order 10^{-7} A/cm^2 while on an arsenic surface it is of the order 10^{-12} A/cm^2 in very acid solutions.[148]

A further example of the suppression of the overall kinetics in arsenite-acetate solutions is shown in Fig. 266. The steel sample

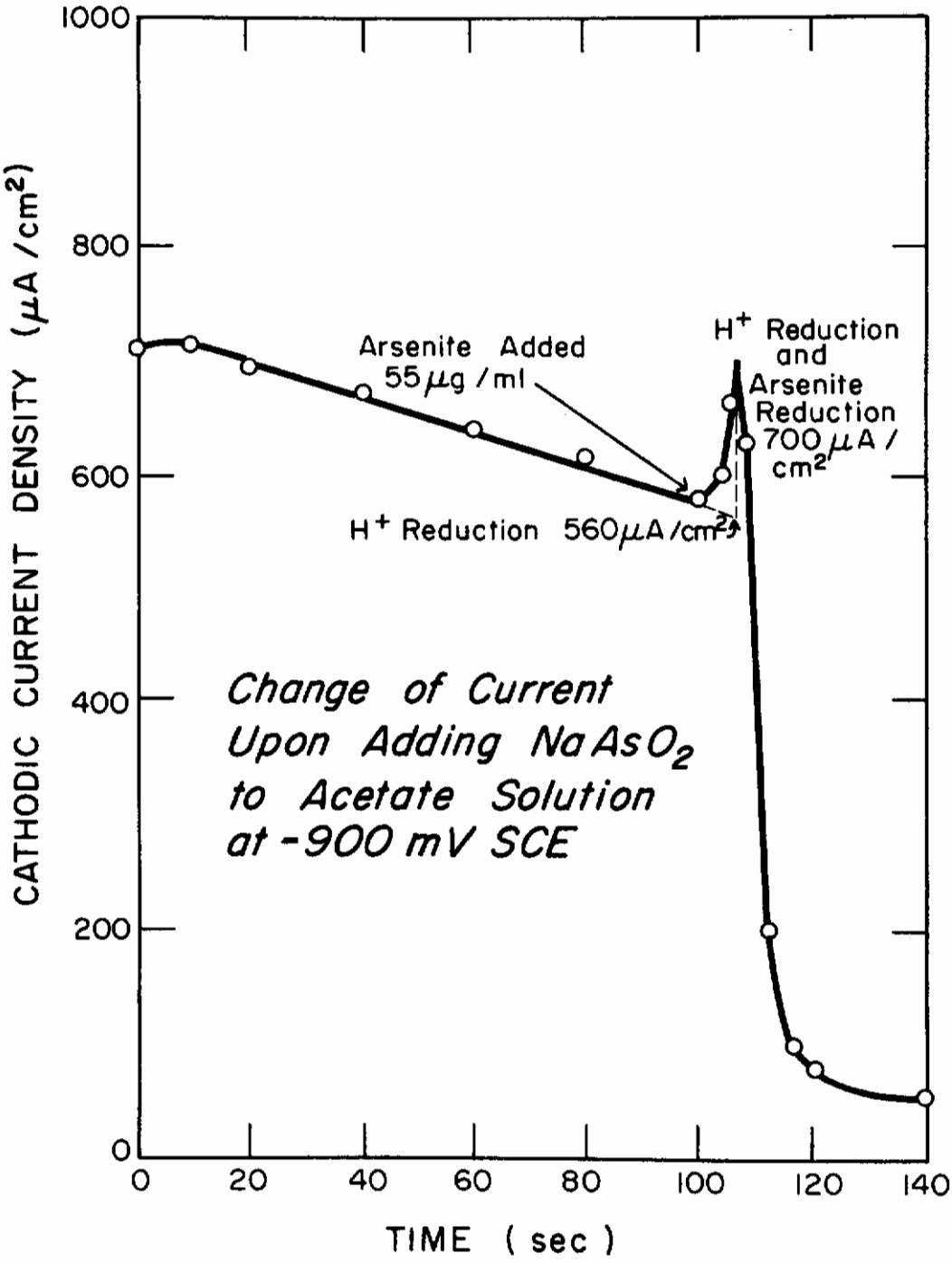

Fig. 266 - Change of Current Upon Adding Arsenite to Acetate Solution at Constant Potential

was held at -900 mV (SCE) in acetate solution and the current density decreased with time. When sodium arsenite was added at t = 100s, there was a sharp increase in the current followed by an even sharper decrease in the current. The current maximum is the super positioning of the arsenic reaction on the hydrogen reaction. However, the very limited amount of arsenite in the solution causes the onset of concentration polarization, and the arsenic deposits themselves on the surface impede the hydrogen reaction; thus there is the sharp decrease in the current. The result shown in Fig. 266 is the same as going from Curve A to Curve F in Fig. 265 at -900 mV (SCE).

The oxygen content of the solutions was determined by the Winkler method (thiosulfate titration, determination of end point with iodine). This was found to be 0.43 ppm O_2.

e. Significance of Polarization and Permeation Work

The significance of this argument is that potentiostatic and galvanostatic control of the hydrogen reaction can lead to quite different conclusions. Many investigators[147,149,150,151] have charged their specimens galvanostatically and have measured either the hydrogen permeability by the permeation current technique, determined the hydrogen content analytically, or have measured some physical property while charging, as the expansion of the sample due to hydrogen absorption. All of these methods have shown the hydrogen uptake in the metal increasing with arsenite concentration in the charging solution until some critical concentration is reached, beyond which the hydrogen uptake is constant despite an increasing arsenite concentration. This critical concentration is of the order 1-5 μg As/ml.

By potentiostatic control of the charging reaction the permeation can be increased or discreased by arsenite additions. Referring again to Fig. 258 at -700 mV (SCE) the permeation is decreased by adding arsenite (compare curve 1 with curves 2 and 3). At -800 mV (SCE) the permeation can be decreased by adding arsenite at a concentration of 9 μg As/ml. At -850 mV (SCE) the permeation is increased by adding arsenite at a concentration of 0.9 μg As/ml, but is decreased by adding the arsenite at a concentration of 9 μg As/ml etc. The plot of permeation efficiency vs. potential, shown in Fig. 261 illustrates this point even more effectively.

f. Separation of Rate Processes Associated with Hydrogen Entry

In the hydrogen entry studies there has been a traditional problem having to do with galvanostatic or potentiostatic control of hydrogen entry. In this program we elected to use potentiostatic control because of the better established relationship of the electrochemical potential with thermodynamically significant variables. The current associated with these potentials can be monitored.

In order to establish a general correlation between the galvanostatic and potentiostatic experiments, the data in Figs. 263, 267, and 268 were obtained.

Figures 267 and 268 give potential vs. time at constant current and current vs. time at constant potential. In general, it may be seen that either the current or time is time-independent for periods of direct interest to these experimental studies. Figure 263 shows that the permeation efficiency obtained from either approach is generally the same. The basis for the slight difference is not clear at this time.

A detailed analysis of cathodic kinetics in solutions with and without sodium arsenite is important in order to clarify the overall kinetic processes for hydrogen entry. A priori, one may expect these three reductions (i.e., As^{+3} to As^{0}, H to H^{0}, and As^{0} to As^{-3}) to occur in polarographic wave form; that is, an initial rise in the current as the potential is made more active until a plateau corresponding to a limiting current density for the As^{+3} to As^{0} reduction. Since the limiting current density in this case is the result of concentration polarization, the height of the polarographic wave is proportional to the concentration of the reducing species. This technique has wide use in analytical chemistry. Similarly, as the first limiting current is reached and the potential is continuously shifted to more active values, second and third waves are obtained, corresponding to the other reduction processes. There are several indications from the literature[146,152] that the first wave (As^{+3} to As^{0}) is not obtained, at least not with the expected concentration dependence. In fact, the higher the arsenite concentration the lower the apparent limiting current for this reduction step (Figs. 264 and 269).

At very active potentials the total current for the arsenite-containing solutions becomes greater than that for acetate alone, but it is less than that for the sulfuric acid alone. As expected from the lower pH of the latter, the current densities are generally higher for the sulfuric acid solution than for the acetate solution.

This determination is made in light of the theory of consecutive and alternative processes. Two experimentally determined polarization curves are depicted in Fig. 270; the first (solid line) one shows the case of polarization in acid solution alone and the second one (dotted line) shows the case in acid solution plus arsenite. When hydrogenation occurs in the latter solution, there appears to be a change in mechanism because of the slope change. Figure 271 is a schematic drawing designed to elucidate the processes which may be occurring, and shows the experimental curves (solid lines) as being the sum of partial currents (dashed lines). The justification for drawing the lines representing these partial currents is as follows:

(1) Hydrogen evolution on an iron electrode with discharge of hydrogen ions as the rate-determining step, followed by chemical desorption (recombination) of the hydrogen adatoms,

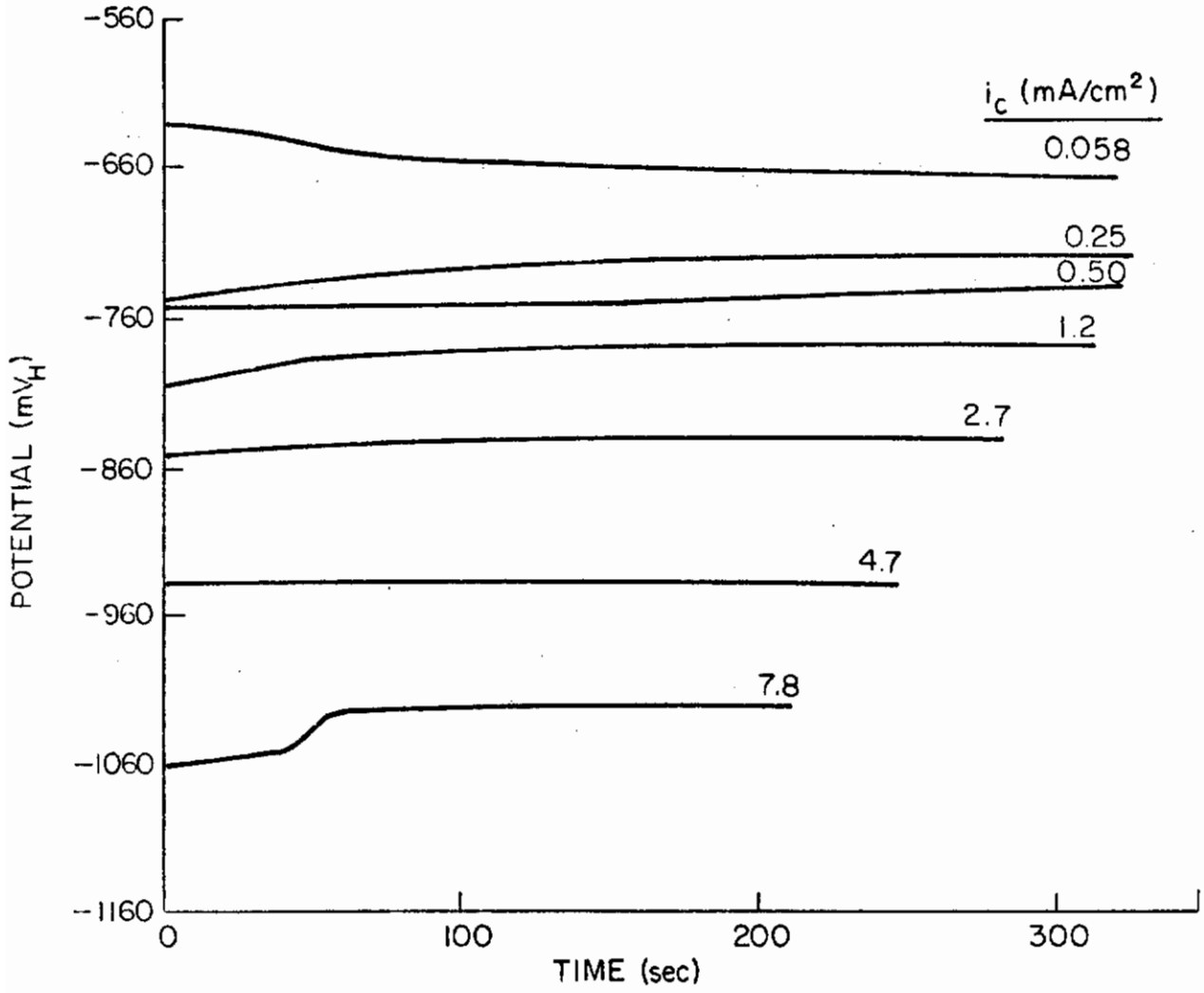

Fig. 267 - Variation of Potential With Time at Constant Current
(1010 Steel in acetate solution + arsenite)

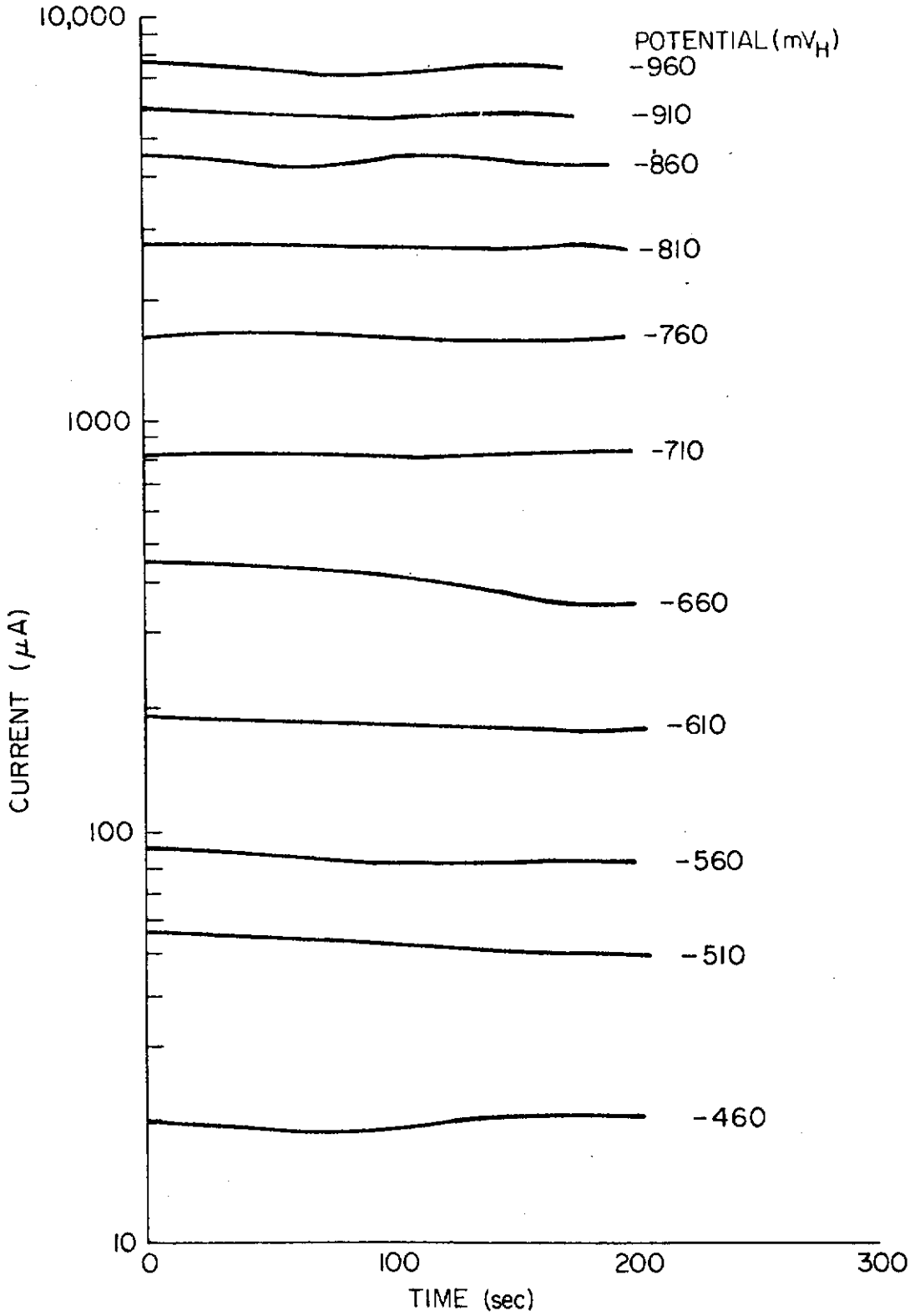

Fig. 268 - Variation of Current With Time at Constant Applied Potential (1010 Steel in acetate solution + arsenite)

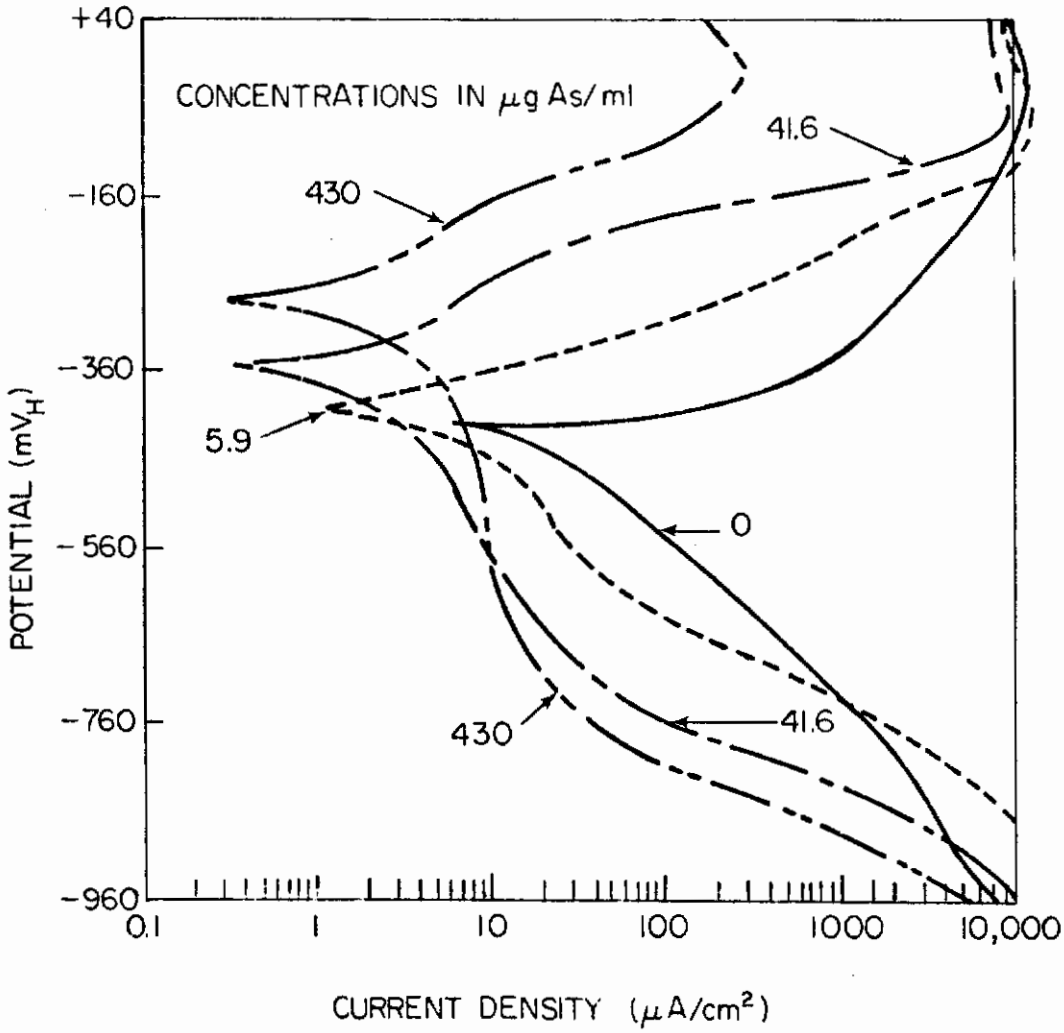

Fig. 269 - Anodic and Cathodic Polarization Curves of 1010 Steel in Acetate With and Without Additions of Sodium Arsenite. Scan rate: 6000 mV/hr

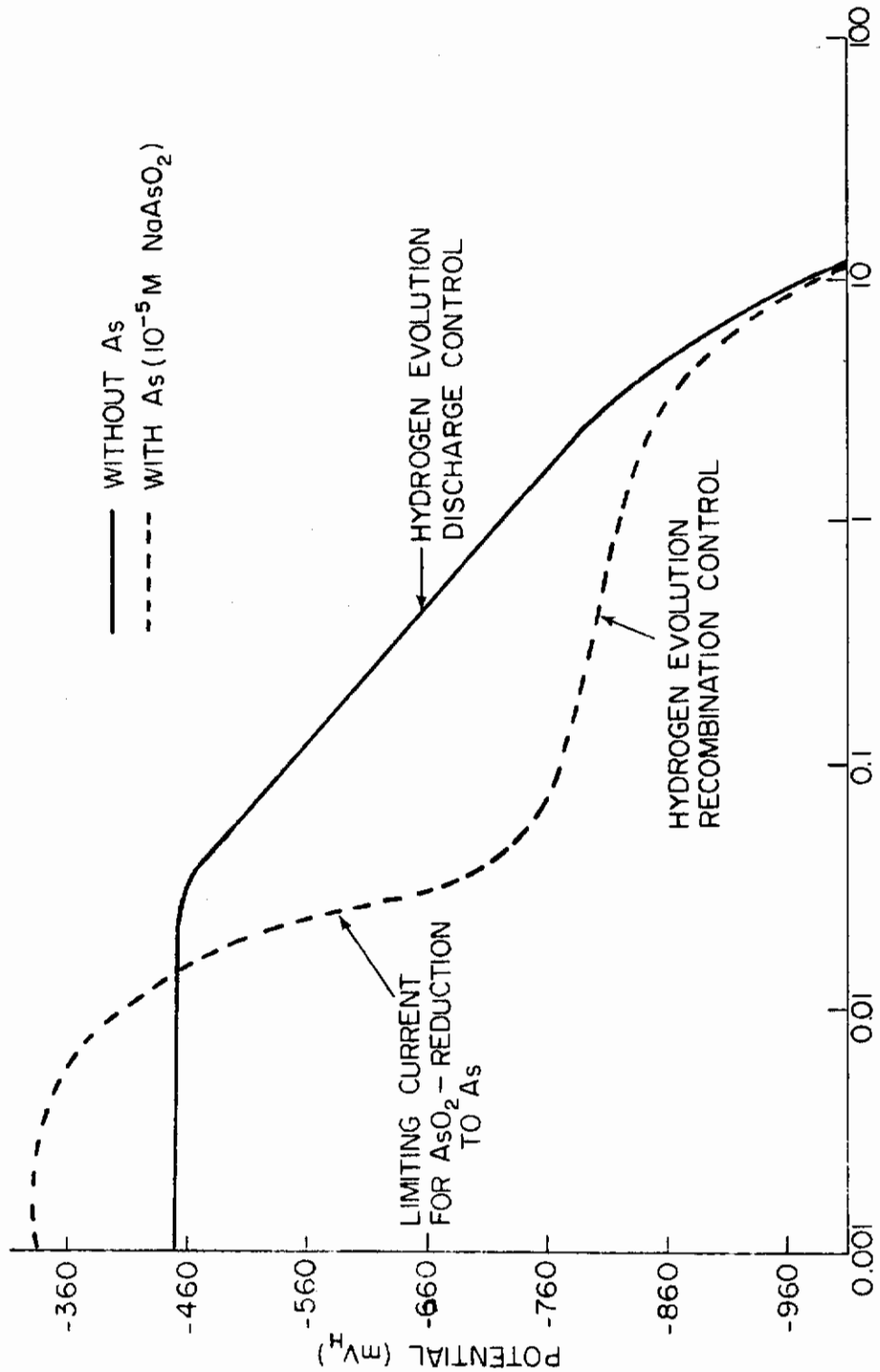

Fig. 270 - Comparison of Polarization Curves of 1010 Steel in Acetate Solutions (pH 4.5) With and Without Arsenite Additions

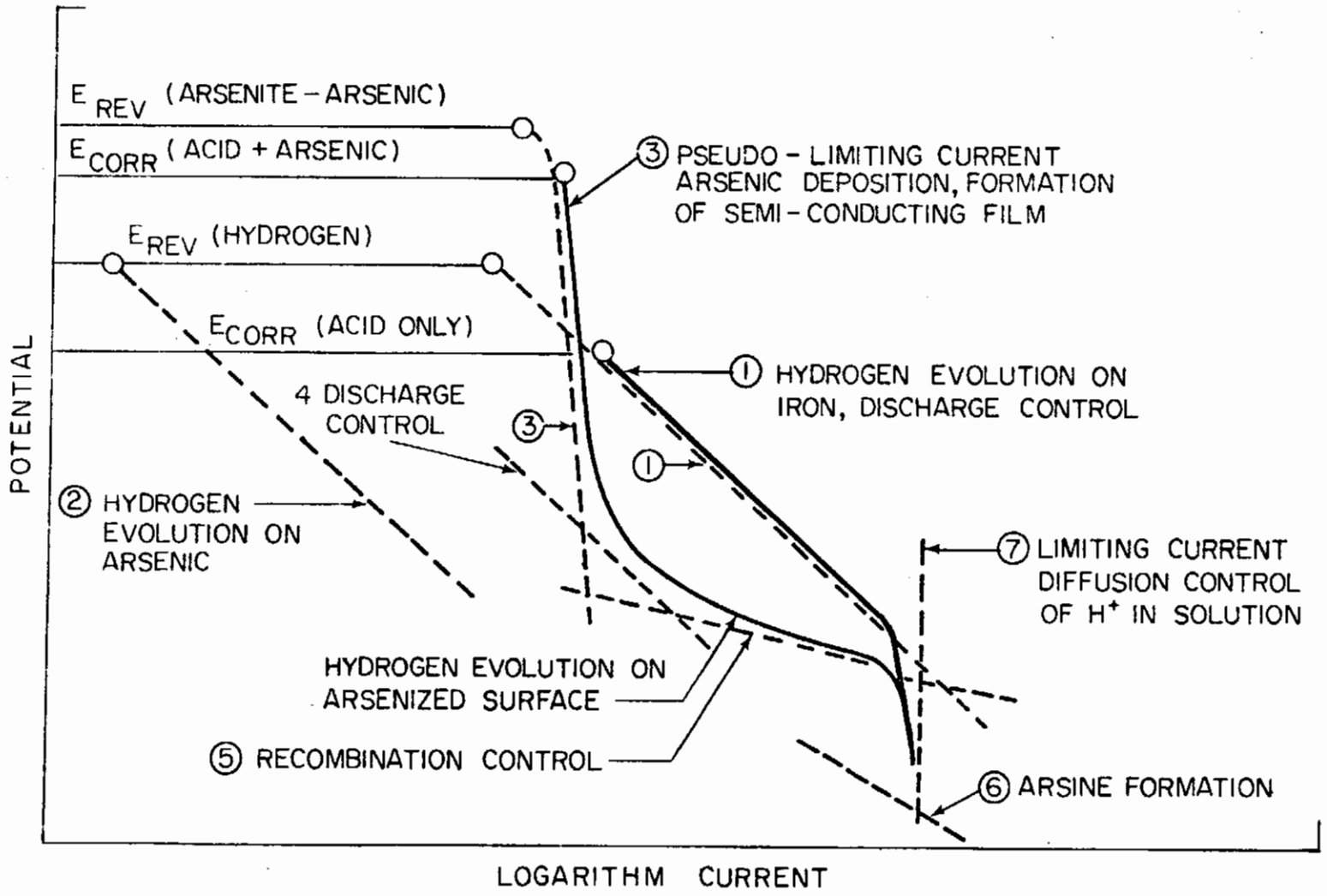

Fig. 271 - Analysis of Cathodic Polarization Curve in Acetate Solutions Containing Sodium Arsenite

has a slope of 2RT/F according to the data presented in Table XXXIII. This same slope obtains whether the adsorbed step follows Langmuir or Temkin kinetics. If the actual mechanism of the iron is the coupled discharge-chemical desorption mechanism as postulated by Devanathan and Stachurski,[153] the 2RT/F slope obtains for Langmuir adsorption and steepens to 3RT/F or 5RT/2F for Temkin adsorption (depending on whether the desorption step itself is activated). For simplicity the slope is taken here at 2RT/F (120 mV/decade).

(2) The very low value of the exchange current density of hydrogen on arsenic (10^{-12} A/cm^2) suggests that the controlling step is the discharge of hydrogen ions. Therefore, the slope of this line is taken to be 2RT/F.[154]

(3) The electrodeposition of arsenic has an exchange current density of about 10^{-6} A/cm^2 since it is classed as an intermediate metal by Piontelli and Poli[155] and behaves similarly to bismuth and antimony, about which some deposition data are known. The reversible potential is calculated from the Nernst equation. If the deposition of arsenic were controlled by electron transfer, the slope would be on the order of 39 mV/decade, as given by West[156] for Sb deposition. As observed by Menzies and Owen[157] and by Wranglen,[158] deposition of arsenic appears to be governed by the formation of a film of amorphous arsenic that stifles the deposition of more arsenic because of the high resistivity of the deposited film. This is in accord with our observation that the higher the arsenite concentration in the solution the lower the current in the potential region, -600 to -1000 mV (SCE).

(4) Hydrogen evolution of the arsenized surface (as deposit on Fe) occurs with discharge control; the slope is equal to 2RT/F. This is justified by the low coverages of adsorbed hydrogen.

(5) If recombination of the hydrogen atoms becomes the rate-controlling step, there is a change to a less steep slope. Among the possibilities given in Table XXXIII are the slopes RT/F for Temkin adsorption (desorption step having an

Table XXXIII - Kinetic Derivatives for Mechanisms of the HER, Evaluated for $\beta = 1/2$

Mechanism	Tafel Slope $-(\partial\eta/\partial \ell n\, i_c)_{pH}$				Reaction Order $-(\partial \ell n\, i_c/\partial pH)_\eta$			
	Langmuir		Temkin		Langmuir		Temkin	
	$\theta \to 0$	$\theta \to 0$	Activated Desorption	Nonactivated Desorption	$\theta \to 0$	$\theta \to 1$	Activated Desorption	Nonactivated Desorption
Rate determining discharge followed by chemical desorption	$\frac{2RT}{F}$	$\frac{2RT}{F}$	$\frac{2RT}{F}$	$\frac{2RT}{F}$	1	1	1	1
Discharge followed by rate determining chemical desorption	$\frac{RT}{2F}$	0	$\frac{RT}{F}$	$\frac{RT}{2F}$	2	0	1	2
Coupled discharge-chemical desorption	$\frac{2RT}{F}$	0	$\frac{3RT}{F}$	$\frac{5RT}{2F}$	1	0	2/3	4/5
Rate determining discharge followed by electrodic desorption	$\frac{2RT}{F}$	$\frac{2RT}{3F}$	$\frac{RT}{F}$	$\frac{2RT}{3F}$	1	2	3/2	2
Discharge followed by rate determining electrodic desorption	$\frac{2RT}{3F}$	$\frac{2RT}{F}$	$\frac{RT}{F}$	$\frac{2RT}{3F}$	2	1	3/2	2
Coupled discharge-electrodic desorption	$\frac{2RT}{F}$	$\frac{2RT}{F}$	$\frac{2RT}{F}$	$\frac{2RT}{F}$	1	1	1	1

activation energy) and RT/2F for either Langmuir adsorption or Temkin adsorption with no activation energy for desorption.

(6) Arsine formation, according to Salzberg and Goldschmidt,[159] is by a disproportionation scheme involving a one-election transfer step. The possible location of this line is shown in Fig. 271.

(7) Eventually diffusion of hydrogen ions to the electrode surface dominates over all the other steps and a limiting current is reached.

For the acid-only case the experimental line representing the total cathodic current (solid line in Fig. 271, extrapolated to the corrosion potential) follows the line for the hydrogen evolution on iron with discharge control (line 1) until its intersection with line 7, the limiting current. This is an example of a consecutive reaction with the slowest step (diffusion of H^+) controlling.

For the acid + arsenite case, the total current is the sum of the partial currents for arsenic deposition with resistance control (line 3), hydrogen deposition on the arsenized surface with discharge control (line 4), and hydrogen deposition with recombination control (line 5). These are examples of alternative (competing) reactions.

A few additional remarks are needed at this point to elaborate on some of the complexities of the analysis.

It can be shown that the control of As deposition is indeed resistance. The slope of line 3 is proportional to i, the total current, in the potential region in which this step dominates. This is shown in Fig. 272. From the figure,

$$\frac{\Delta\eta}{\Delta i} = ki \ ; \qquad (63)$$

and by Ohm's Law,

$$\frac{\Delta\eta}{\Delta i} = \rho i \ , \qquad (64)$$

since i is the current density, the resistivity (ρ) of the film can be estimated if the thickness is known.

The change in mechanism for hydrogen production on the arsenized surface is in accord with the observation by Menzies and Owen[157] that the "hydrogen overpotential was lowered" during the plating of As (loss of current efficiency with respect to As because of increased hydrogen evolution). Arsenic is interacting with hydrogen at the surface, allowing an increase in coverage of the latter. The

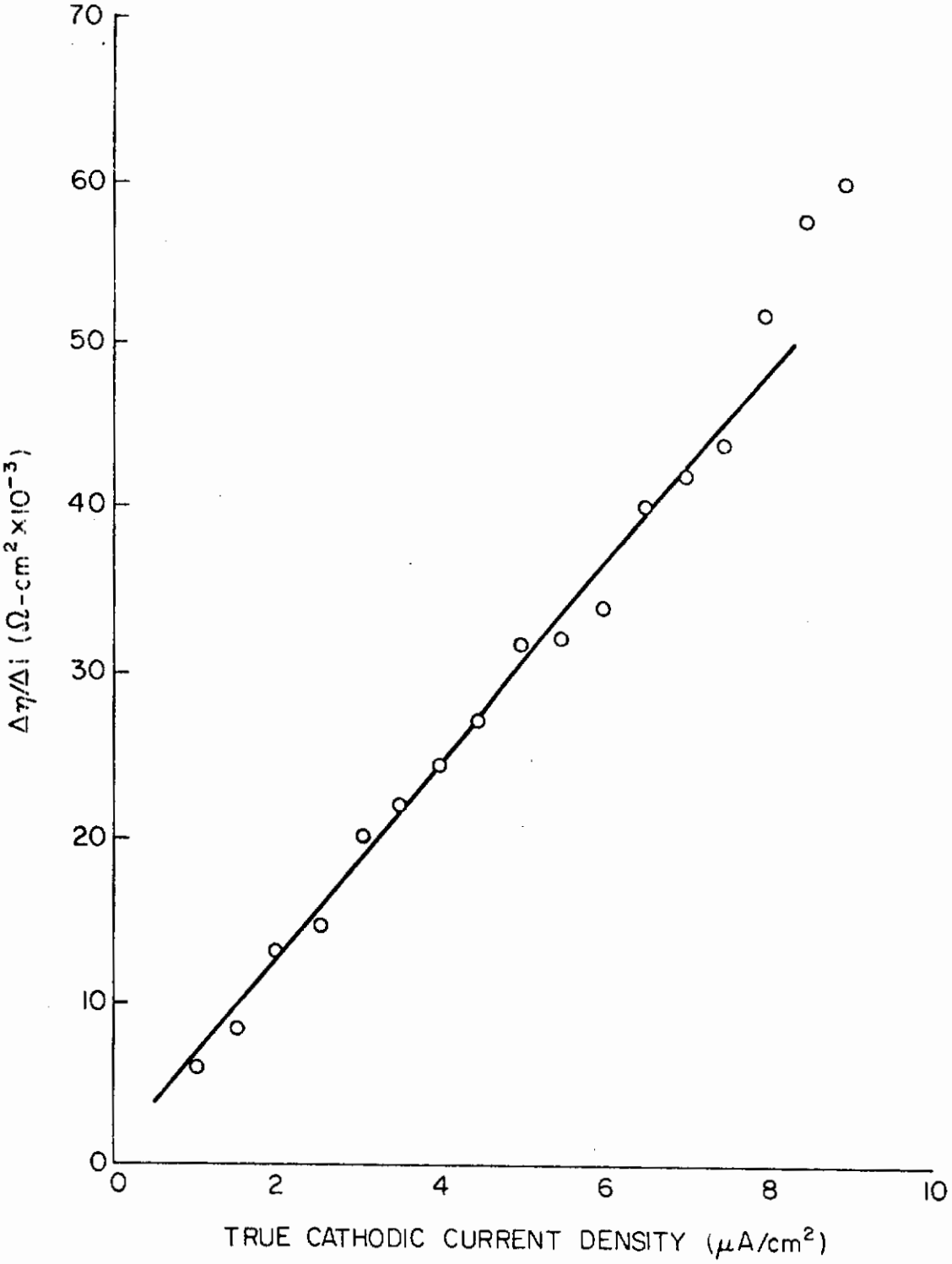

Fig. 272 - Resistivity Control of Arsenic Deposition from Acetate + Arsenite Solutions

interaction (which is a manifestation of Temkin adsorption kinetics) between hydrogen atoms and arsenic atoms discourages recombination of the hydrogen.

It should not be construed that this "arsenized surface" is an intact layer of As over the steel. Even in thin sections the As plate cracks and spalls; therefore, some iron surface is exposed to the solution and/or to chemisorbed hydrogen so that a very heterogenous situation exists.

Further support for the shift to recombination control is the fact that the observed dependence of the permeation current on cathodic current (slope of log i_ρ^∞ vs i_c was 0.6-0.9; Fig. 262) and of the permeation current on cathodic overpotential (90-140 mV/decade; Fig. 258) is tenable with the mechanism discharge followed by rds chemical desorption in Tables XXXIV and XXXV, respectively. Similar behavior was observed in the sulfuric acid solutions and on the specimens where As was predeposited.

The formation of arsine has not been considered in the above analysis because no AsH_3 was observed during the course of the permeation or polarization experiments. The highest cathodic potential usually encountered in these tests was about -1400 mV (SCE) which is about 400 mV more active than the As/AsH equilibrium for $P_{AsH_3} = 10^{-7}$ atm in pH 4.5 solution. Menzies and Owen[157] reported only a trace of arsine (at a current density of 10 mA/cm^2, which is probably in this potential range) and Salzberg and Goldschmidt,[159] in their studies of AsH_3 formation kinetics, determined that the current efficiency is only 1-2% in acid solution. In our work some solutions were tested for AsH_3 by addition of H_2O_2. If AsH_3 were present the peroxide would oxidize it to a fine black suspension of arsenic. This was not observed. The characteristic garlic-like odor of arsine was not detected, which is fortuitous since the gas is highly toxic.

The increased current for the arsenite-containing acetate solutions in the very active potential range is probably more correctly attributed to an indeterminable area effect (due to the As plating and surface roughness) rather than arsine formation, because the latter would be forming at the rate of milliamperes which is completely incongruous with observation. If any arsine formed, it was present only in trace amounts. Less saturated hydrides of arsenic (e.g., As_2H) are possibly formed since these are solid materials.[160]

Another factor which complicates the analysis in the same potential region as the above is the onset of resistance control by the solution. The modulating voltage of the potentiostat is 12 V and a possible cell and circuit impedance of 500 Ω permits a maximum current of about 60 mA. This completely overrides any other factor, such as the limiting current density attributable to mass transport in the solution, and may lead to a misinterpretation of what appears to be a diffusion-limiting current density. This is a good reason for confining most of

Table XXXIV - Relationship of Permeation Current (Steady State) to the Charging Current

Mechanism	$\left[(\partial \ln i_p^\infty)/(\partial \ln i_c)\right]_{pH}$			
	Langmuir Adsorption		Temkin Adsorption	
	$\theta \to 0$	$\theta \to 1$	Activated Desorption	Nonactivated Desorption
Discharge RDS, Chemical Desorption	0	0	0	0
Discharge, Chemical Desorption RDS	1/2	0	1	1/2
Coupled Discharge Chemical Desorption	1/2	0	1	2
Discharge RDS Electrodic Desorption	-2	-2/3	-1	-2
Discharge, Electrodic Desorption RDS	2/3	2	1	2/3
Coupled Discharge, Electrodic Desorption	0	0	0	0

Table XXXV - Relationship of Permeation Current (Steady State) to the Overpotential

Mechanism	$-(\partial\eta)/(\partial \ln i_p^{\infty})_{pH}$			
	Langmuir Adsorption		Temkin Adsorption	
	$\theta \to 0$	$\theta \to 1$	Activated Desorption	Nonactivated Desorption
Discharge RDS Chemical Desorption	--	--	--	--
Discharge, Chemical Desorption RDS	$\frac{RT}{F}$	$\frac{RT}{F}$	$\frac{RT}{F}$	$\frac{RT}{F}$
Coupled Discharge, Chemical Desorption	$\frac{4RT}{F}$	$\frac{4RT}{F}$	$\frac{3RT}{2F}$	$\frac{5RT}{2F}$
Discharge RDS, Electrodic Desorption	$\frac{RT}{F}$	$\frac{RT}{F}$	$\frac{RT}{2F}$	$\frac{2RT}{3F}$
Discharge, Electrodic Desorption RDS	$\frac{RT}{F}$	$\frac{RT}{F}$	$\frac{RT}{F}$	$\frac{RT}{F}$
Coupled Discharge Electrodic Desorption	--	--	--	--

the analysis to the region of current densities well below the limiting current. In a pH 4.5 solution, incidentally, the limiting current densities for diffusion control range from 0.6 to 32 mA/cm^2, the higher ones occurring in well-agitated solutions. Therefore, it is believed that in the above analysis a true limiting current for mass transport was reached.

The correlation between the hydrogen permeation and polarization behavior of steel in acetate solution with small additions $NaAsO_2$ shows that the permeation efficiency maximum, based on the total cathodic current, falls in the potential region, in which the hydrogen evolution reactions begin to dominate the arsenic deposition reaction. In Fig. 273 a plot of the partial currents, extracted from Fig. 265, shows the potential range of domination for the arsenic and hydrogen reduction reactions. The hydrogen reaction is itself the sum of the partial currents for discharge and recombination control, since it is believed that the first hydrogen evolution on the arsenized surface is controlled by the discharge step while the coverage of adsorbed hydrogen is low. Arsenic deposition continues in this region so that the situation is one of co-deposition.

Figure 273 shows that the potential at which the hydrogen deposition begins to dominate over the arsenic deposition (50% of the total current) occurs (for this concentration 4.31 μg/ml) between the respective permeation efficiency maxima for 0.9 and 9.0 μg As/ml. What this means is that the hydrogen reaction is suppressed at small cathodic overpotentials in arsenite solutions, although the permeation efficiency of the very small amount of hydrogen is high. As the potential becomes more active the rate of hydrogen deposition becomes greater while the rate of arsenic deposition remains relatively constant. Thus, the hydrogen reaction accounts for a larger portion of the current at the more active potentials, regardless of the particular mechanism controlling its reaction rate.

The polarization behavior predicts that the higher the arsenite concentration, the more active the potential needed for specimen hydrogenation.

The results are in qualitative accord with the observation by Hudson and Stragand[161] that in a mild steel pickling bath in 2N H_2SO_4 at 38°C, an addition of 1 μg As/ml (added as As_2O_3) doubled the pickling rate over the As-free acid, an addition of more than 4 μg As/ml inhibited pickling and promoted hydrogenation, and an addition of more than 8 μg As/ml inhibited the absorption of hydrogen. These experiments were performed without applied potential. In other words, at the low concentration of As the two reduction processes (As and H) are independent and additive, causing an increase in the corrosion rate of the metal. This effect is also shown in Fig. 264. Where the first small additions of arsenite tend to increase the corrosion rate in H_2SO_4. (In acetate, on the other hand, the very small additions of arsenite tend to decrease

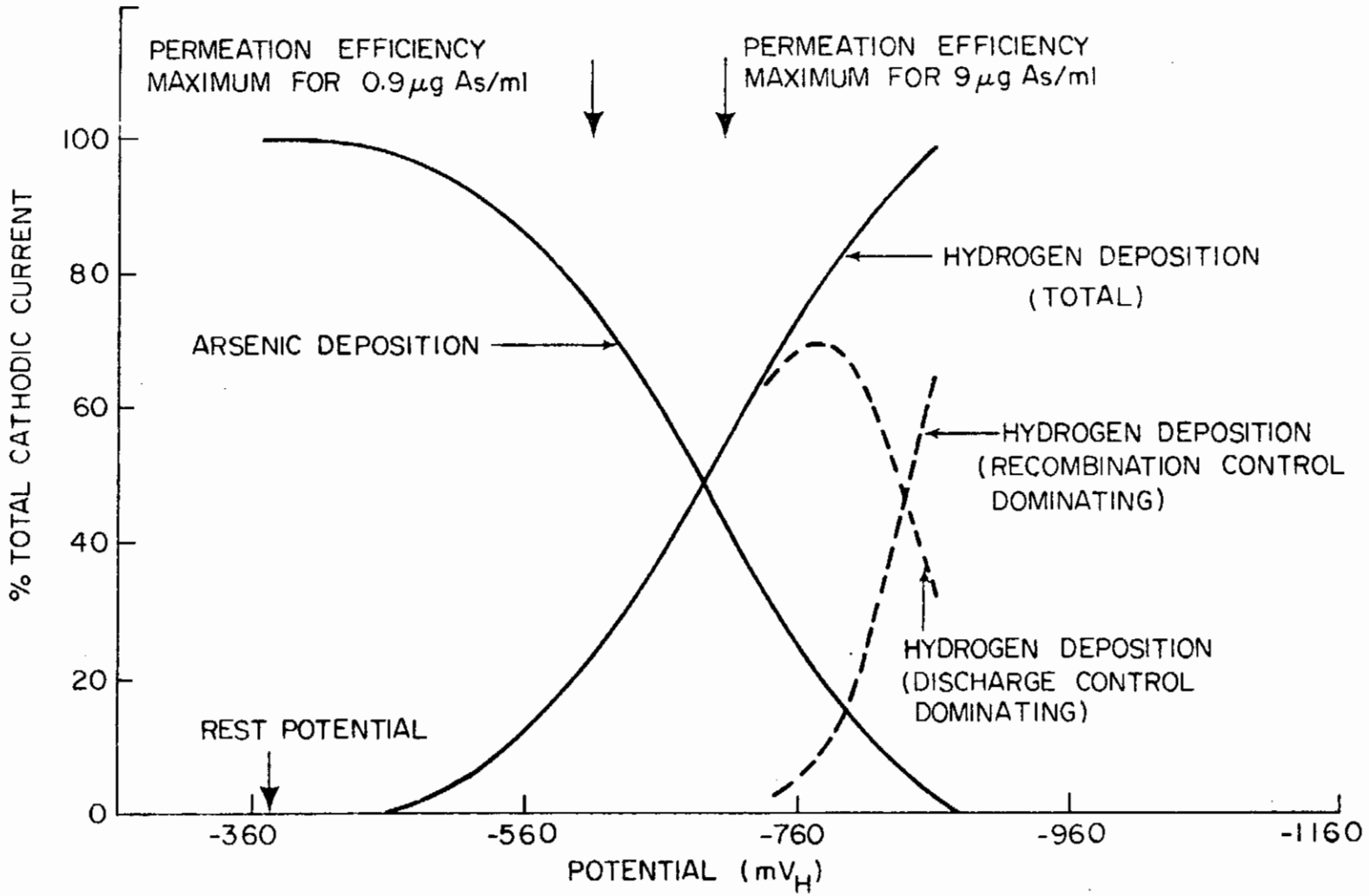

Fig. 273 - Contribution of Partial Currents to Total Currents for Arsenic and Hydrogen CoβDeposition. Correlation With Permeation Behavior

corrosion.) In the intermediate concentrations, hydrogenation of the specimen occurs at the rest potential, although the total cathodic current, and hence pickling rate, is rather small because the permeation efficiency of this hydrogen is high. At the higher concentrations of As in the solution, the permeation efficiency at the rest potential is still high, but the partial current due to hydrogen reduction is so small that for all practical purposes hydrogenation is inhibited. Thus, the product of the permeation efficiency and the hydrogen reduction partial current is the criterion for specimen hydrogenation.

Difficulties in carrying out the analysis of the polarization behavior in conjunction with the permeation behavior for low As concentrations are that the polarization curves are not readily separable from the As-free solutions and the 0.43 ppm oxygen content of the solution adds another reduction process to complicate the analysis. By coincidence a concentration of 1 μg As/ml is about 1 ppm As. At higher As concentrations the effect of oxygen is negligible.

Some interesting data obtained in our laboratories concerns the subject of specimen hydrogenation in arsenic-containing solutions. Using a 0.1N NCl solution, Kerns and Sneary[162] found that the time to failure for a pre-notched loaded 4335 steel cantilever beam specimen was reduced when the first addition of arsenite was made but was increased when a higher arsenite concentration was used. Their data are tabulated below.

Table XXXVI - Effect of Sodium Arsenite Additions to the Time Failure for a Loaded High-Strength Steel Specimen

Concentration of Sodium Arsenite	Time to Failure (hours) At -300 mV (SCE)	At -1000 mV (SCE)
0	1.2	1.5
0.01 M	0.3	1.3
0.1 M	no failure	6

The initial film thickness of the arsenic co-deposit can also be estimated. Figure 266 shows that a sample was held at -900 mV (SCE) in acetate buffer and the current recorded as a function of time. After 100 seconds arsenite was added. There was a sharp rise in the current, then an even sharper decrease. The area within the cusp can be taken as the initial film thickness that would have been formed at the rest potential had the sample been exposed to arsenite solution before polarization. This area is found to be proportional to 3200 $\mu C/cm^2$.

By Faraday's Law this corresponds to a deposition of

$$(q/ZF) = (D\ell A/M) \quad , \tag{65}$$

which rearranges to

$$\ell = \quad (q/A) \cdot M \quad /ZFD \ , \tag{66}$$

where M is the atomic weight of arsenic and D is its density, and the other symbols have their usual meanings.

$$\ell \simeq \frac{3200 \times 10^{-6} \ (C/cm^2) \times (75g/mole)}{3 \times 10 \ (C/mole) \times 47 \ (g/cm_3)} = 17 \text{ Å} \ , \tag{67}$$

which would correspond to about six monolayers if the plate is uniform.

Using the value of the slope in Fig. 272, $\Delta\eta/\Delta i$, an estimate of the film resistivity is made knowing the thickness. From the equation below,

$$\rho = Ki/\ell \ , \tag{68}$$

and using the value of i and ℓ at the rest potential

$$\rho = \frac{4.8 \times 10^7 [(\Omega\text{-cm}^4)/A](A/cm^2)}{17 \times 10^{-8} \text{ cm}} = 2 \times 10^8 \ \Omega\text{-cm}. \tag{69}$$

Wranglen[158] measured the resistivity of vitreous arsenic films and estimated it to be 10^{12} times that of metallic arsenic. This would give a value for ρ of $\simeq 3 \times 10^8$ Ω-cm. The existence of this vitreous arsenic film explains why many investigators have been able to get only thin electrodeposits in acid solution and poor current efficiencies.

Arsenic was intentionally deposited from solution in order to accomplish the following:

(1) Obtain a relatively thick As plate which could be examined for morphology and extracted for determining a diffraction pattern. These samples would serve as bases for comparison.

(2) Obtain a thin As plate which approximated the amount of arsenic deposited during a typical permeation determination experiment. This specimen would, itself, be used in a permeation experiment to determine if there was a difference in behavior between the case where

hydrogen and arsenic were co-deposited (the usual case in the permeation experiment) and this case where hydrogen would be deposited on the arsenic pre-deposit.

In order to deposit the arsenic, solutions of higher pH were used. This was accomplished by adding $NaAsO_2$ to the acetate buffer. Because sodium arsenite acts as a base it raises the solution pH when it is added to the acetate. The equivalence point was found to be about 2,000 μg As/ml. Adding more arsenite than this raised the pH to about 9.

The reason for using the concentrated arsenite, and therefore high pH, solution was to be able to calculate the amount of As deposited coulometrically. The depositions were obtained in the potential range -800 to -1200 mV (SCE)[-560 to -960 mV (SHE)] which is below the reversible potential for hydrogen evolution at this pH [-530 mV (SHE)]. The solutions used contained 46,000 μg As/ml. This choice of potential was made so that the rate of hydrogen deposition was negligible while the arsenic deposition was sufficiently high to be measurable. Once the surface becomes arsenized the kinetics of hydrogen reduction on the electrode surface becomes so small that it contributes a negligible amount to the total current. This was verified by weighing the steel specimens before and after arsenic deposition. The current efficiencies were near 100% within the potential range used. The specimens which were held at the less active potentials yielded arsenic mirrors which were blackish, and silvery if a bit thicker. The weight gain of these coatings was too small to be detected gravimetrically. Those specimens held at the most active potentials gave much thicker deposits because of the higher currents. These coatings were silvery and lustrous but tended to flake away from the substrate. A photomicrograph of the thick deposit is shown in Fig. 251. The picture was taken on the scanning electron microscope. The deposit was found to be crystalline As by replication and electron diffraction. The arsenic plate appears to be very brittle, and a section of it has broken away in the picture revealing the steel substrate. Adherence to the substrate was poor for these thick deposits. The thickness of this plate was estimated at 0.8 μm (some 3200 layers).

The production of thinner, adherent, and coherent deposits for hydrogen permeation work were done at less active potentials and shorter times. In all cases there was a fairly sharp drop of current with time at constant potential. The amount of arsenic deposited was equivalent to 50 mC (25 mc/cm^2 over the 2 cm^2 area surface). This corresponds to about 50 layers of arsenic, an amount that is attainable during the course of a permeation test $i_{As} \simeq$ 10-40 μA/cm^2, t ≃ 500-2000 sec, plus the 6 layers in the usual time between immersion and beginning of cathodic charging). These deposits were mirror-like; an example of the surface is shown in Fig. 251. The deposit had a vitreous appearance, shows evidence of cracking, and had a non-crystallographic electron diffraction pattern.

During the course of a permeation experiment the characteristics of the arsenic deposits are unlike either of these. Because very dilute solutions are used in the permeation experiments, the arsenic is deposited over a long period of time instead of in the few seconds for making these pre-deposits. There is significant co-deposition of hydrogen at most of the potentials. There is a period of corrosion of the electrode when the applied cathodic current (or potential) is shut off, as in the beginning of the experiment when establishing the residual current and during the decay transient when the metal has previously been hydrogen charged. A scanning photomicrograph of a sample which has been hydrogen permeated is shown in Fig. 251. The sample was exposed only to small hydrogen charging currents and no visible evidence of blistering was seen. The picture shows, however, the corrosion damage to the metal. At the rest potential arsenic deposition is the principal reduction reaction, which must be balanced by an equivalent amount of metal dissolution. The photomicrograph shows pitted regions where the dissolution has taken place and areas on which arsenic deposition has occurred. The crystals, which are electronic nonconductors, were not identified.

Electron diffraction patterns of the surface revealed As, but no As_2O_3, FeAs, or $FeAs_2$. The crystals appear to be impregnated in the arsenic "cement" which, at least in the 100 kV beam, tended to crystallize. The electron diffraction patterns often appeared after a few seconds delay when the arsenic was in this form. Thick As films gave electron diffraction patterns immediately. Upon prolonged exposure there was some evaporation of the arsenic. Table XXXVII summarizes the indexing. The ASTM X-ray data card file was consulted for verification and the values for α-As (rhombohedral structure) given in the file are also shown in the table. The camera constant for the particular microscope and pole piece used was 3.9796, so that the d spacing can be found by the formula $d_{hkl} = \frac{3.9796}{D}$, where d_{hkl} is the distance (in Å) between planes with a particular set of hkl Miller indices and D is the diameter (in cm) of the ring measured on the patterns.

The electron diffraction pattern for the thick deposit confirms very well to the ASTM X-ray standard, although the intensities for the two methods do not necessarily match. The electron diffraction pattern for the sample exposed to hydrogen permeation conditions from an arsenite-containing solution (acetate buffer) lacks many of the lines observed in the thick As deposit but most of the intense lines of the latter are apparent in the former. The former had a spotted ring pattern, indicating that not all orientations were present. This may explain why so many lines are not visible on the second sample. No extraneous lines were seen on it, however,

A mechanism for the hydrogenation promotion effects due to the presence of arsenic must account for the following important observations:

Table XXXVII - Electron Diffraction Indexing of Arsenic Deposits

ASTM X-Ray Data Card File			Electron Diffraction Thick Predeposit			Electron Diffraction, Specimen Exposed to Permeation Conditions		
hkl	d_{hkl} (Å)	I/I°	D (cm)	d_{hkl} (Å)	Qualitative Intensity	D (cm)	d_{hkl} (Å)	Qualitative Intensity
003	3.52	26	1.12	3.56	lt			
011	3.112	6	1.27	3.11	ltmed			
102	2.771	100	1.42	2.80	med			
014	2.050	24	1.91	2.08	med-dk	1.92	2.07	dark
110	1.879	26	2.10	1.89	dk			
105	1.768	10	2.20	1.81	lt	2.23	1.785	med-dk
006	1.757	7	2.35	1.69	ltmed			
113	1.658	6	2.44	1.63	lt			
022	1.556	11	2.53	1.57	med			
204	1.386	6	2.84	1.45	ltmed			
017	1.367	4			missing			
025	1.289	5	3.06	1.30	lt			
116	1.284	5			missing			
121,108	1.222	1	3.27	1.22	very lt			
212	1.1987	7	3.31	1.20	med-dk	3.36	1.183	med-dk
009	1.1727	1			missing			
124	1.1158	4	3.54	1.12	lt			
207	1.1062	2			missing			
300	1.0857	3	3.65	1.09	med			
215	1.0631	3	3.72	1.07	very lt			
303	1.0374	2	3.82	1.04	very lt	3.88	1.030	lt
127	0.9948	2	3.96	1.005	very lt			
220	0.9297	1	4.18	0.95	very lt			
101	0.9198	3	4.22	0.945	lt			
218	0.8995	1	3.20	0.92	lt			
132	0.8903	2	4.47	0.89	med	4.45	0.894	med

(1) Hydrogenation of the specimen is promoted to the greatest extent (maximum permeation efficiency) in the potential region where co-deposition of H and As takes place.

(2) Although the permeation efficiency decreases as the potential becomes more active, the permeation rate and efficiency are higher for the As-containing solutions than the As-free solutions.

(3) At the rest potential, addition of excess arsenite appears to inhibit hydrogenation; however at overpotentials greater than about 300 mV, hydrogenation occurs regardless of the arsenite concentration.

(4) The promoter effects of As appear to operate at all values of pH. The work here considered only two values, but the work of Newman and Shreir[163] showed hydrogenation over a wide range of pH.

(5) The theory should apply, in part at least, to the other elements and compounds which promote hydrogen entry.

There have been a number of explanations regarding the phenomenon of the sharply increased entry rate. The general conclusion is that the metal-to-hydrogen bond is reduced in the presence of the promoting species. Reduction of this bond energy creates a more flexible, less directional bond so that the transition from adsorbed hydrogen to absorbed hydrogen is facilitated with less activation energy. This hypothesis is based partly on the observed phenomenology that the heat of adsorption (and hence the metal-hydrogen bond energy) decreases as the metal becomes more "catalytically active." Catalytically active metals (so-called because of their ability to hydrogenate organic reactions) have a higher inherent solubility of hydrogen (Pd > Ni > Pt > Fe). The disagreements or controversies range over what causes the decrease in the metal-hydrogen bond energy.

McBreen and Genshaw[164] showed that a decreased metal-hydrogen bond energy has the kinetic effect of lowering the activation energy for the absorption process relative to the barrier for the recombination process. Since these processes compete for the adsorbed hydrogen, this lowering favors absorption.

The question is, then, how can the metal-hydrogen bond be lowered? There have been at least three proposals to account for this.

(1) The adsorbed species forms a dipole oriented the same way as the M-H dipole with the H side negative according to Frumkin and Slygin.[165]

(2) The electronic interaction of the promoter species with the metal lowers the bond between metal and hydrogen. In general promoter species are electron-rich and adsorb readily. The metals are transition metals with unfilled d-band electrons. The general observation again is the metals with the most "d-band character" (Pd, Pt) have the greatest propensity for hydrogenation.[166,167]

(3) The competitive adsorption between promoter and hydrogen results in the promoter lodging at the most energetic surface sites and the hydrogen at less energetic sites, since it is presumed that the promoter species is more "surface active" than hydrogen.

McBreen and Genshaw[164] considered the above explanations and concluded that they are not mutually exclusive and all could operate simultaneously. We shall return to this matter and their kinetic model based on the lowering of M-H bond energy after considering some additional points.

Recent work by Kim and Wilde[168] has established that the surface coverage of hydrogen adatoms is low in basic solutions. Kim[169] has shown this low coverage exists in acid solutions. He has found by a double-pulse galvanostatic technique that the coverage is about 5-12% at the corrosion potential; whereas, heretofore, it was believed to be much higher. Although the coverage increases with applied cathodic potential, it is conceivable that the presence of arsenic or another species increases the surface coverage of hydrogen on iron by crowding the hydrogen onto adjacent available iron surfaces since the discharge process on As has high kinetic barriers. Increasing the surface activity of adsorbed hydrogen (in the thermodynamic sense) increases the entry rate. Permeation rates in the presence of arsenic are on the order of 2, 3, or 4 times the rate from As-free solutions, so that the increased adatom concentration has to increase by a corresponding amount.

On a bcc metal, such as iron, the surface is "atomically rough" compared to an fcc metal. Oriani[170] has estimated that the surface diffusivity of hydrogen is smaller for the bcc metals than the fcc. Hence, hydrogen atoms are more likely to stick where they are discharged and the likelihood of their absorption is increased because of the increased lifetime as H (ads).

Comparing the solubilities of fcc Ni and bcc Fe, one finds the hydrogen to be about a 1000 times more soluble in nickel. To make the comparison more valid by considering fcc Fe, extrapolation of high-temperature solubility data to room temperature only accounts for an increase in solubility of a factor of 2-3 over bcc Fe. Thus, it seems that the effect of crystal structure, and the previous argument based on it, is of secondary importance.

The bonding between H and As should be considered. According to the Pauling theory the energy of this bond is 57 kcal mole. This compares to a value of 60-70 kcal/mole for the H-Fe bond[171]. There is also interaction between iron and arsenic. At room temperature the solubility of As in Fe is about 5% and arsenic forms arsenides FeAs and $FeAs_2$ at higher concentrations. The diffusion of As into Fe is probably negligible at room temperature from the plate at the surface. However, Besnard[172,173] has considered that As is itself absorbed preferentially at the grain boundaries because of its lowering of the surface tension in addition to the chemical effects. He believed this absorption was responsible for premature cracking of the iron specimens, but it is conceivable that this addition of surface could further enhance the hydrogen permeation since there would be greater opportunity for the electronic interaction between Fe and As which is indicated by the chemical affinity.

The above makes tenable the model of Fe-H and Fe-As dipoles that are mutually repulsive. The Fe-H bond energy would be lowered by the addition of electrons to the d-shell of Fe by the As and the repulsive forces among the dipoles themselves.

Explaining the adsorption of hydrogen as affected by arsenic, reference is made to the "d-band character" of metals.

This played an important role in determining the interaction of the metal with hydrogen. A short digression may help the reader to grasp this significance. According to Pauling's theory[174] the necessary condition for metallic bonding is a reasonating covalent bond. In order to accommodate the resonance there must be vacant atomic orbitals. Then electrons from neighboring atoms can jump into this unused orbital and make the bond. The same reasoning applies to bonds between like atoms and unlike atoms if the tendency is to form solid solutions. This is the chief distinction between metallic and covalent bonding, because in the latter there are only half-filled orbitals (to match up with other half-filled orbitals from adjacent atoms) while in the former there are half-filled orbitals and resonance states (empty orbitals).

The electronic configurations are written for iron and nickel. The symbol x represents a filled orbital, an electron with "spin up" and one with "spin down." The symbol o represents a half-filled orbital,

while - represents an empty orbital. For Fe and Ni the normally occupied orbitals are in the 3d and 4s sub-shells, but hybridization to the 4p states is possible because of overlap of electron energy bands from the close proximity of other atoms in the crystal. For iron there are eight outer electrons; for nickel, ten.

	Configuration	3d	4s	4p	Bohr Magnetons
	A	x x x x -	-	- - -	0
	B	x x x o o	-	- - -	2
Fe	C	x x o o o	o	- - -	3
	D	x o o o o	o	o - -	4
	E	o o o o o	o	o o -	5
			***		
	A	x x x x x	-	- - -	0
	B	x x x x o	o	- - -	1
Ni	C	x x x o o	o	o - -	2
	D	x x o o o	o	o o -	3
	E	x o o o o	o	o o o	4

The number of Bohr magnetons (half-filled d orbitals) is experimentally known from the ferromagnetic properties of these elements. For Fe this is 2.2 Bohr magnetons and 0.6 Bohr magneton for Ni.[175] Thus, for Fe the dominant configurations are B and C, while those for Ni are A and B. The higher number of filled d electron orbitals for Ni tend to constrict with width of the d-shell and to draw the higher 4s and 4p energy levels toward the d-shell. This makes the resonance states more accessible for electrons from adjacent atoms.

Therefore, more hydrogen can be accommodated in the nickel lattice because of the closer energy levels. The usual role of hydrogen is to decrease the magnetic susceptibility (as it does for palladium) which would slightly increase the probability of the A configuration in Ni. If a promoter substance, like arsenic, is present it should tend to decrease the magnetic susceptibility and thereby constrict the d sub-shell, opening up the higher sub-shells to electrons from As and H atoms. Thus, more hydrogen is accommodated in the Fe or Ni lattice when the promoter is present.

An extremely useful, but apparently lacking, piece of information is an analytical determination effect of arsenic on the solubility of hydrogen in iron. If As raises the solubility significantly, then a high concentration of hydrogen at the plated surface would drive a greater flux into and through the metal.

The electron interaction between the promoter substance and the metal also explains nicely the effects of various strongly adsorbed anions such as the halides, cyanide, and certain organic compounds at naphthalene.[176]

It therefore becomes more and more clear why the greatest promotion effects occur in the co-deposition potential range and why the formation of arsine would tend not to promote permeation. The isolated As atom has up to five electrons which it could share or donate to the iron; AsH_3 has only an unshared electron pair that can be used for bonding to the substrate. Solid intermediate unsaturated hydrides have numbers of unshared electrons in between.

5. Experiments and Discussion Associated with Hydrogen Trapping in Fe and Fe-Cu Alloys

Hydrogen moving through interstitial sites in the lattice has a high diffusivity even at room temperature because the activation energy for this movement is about 2 kcal/mole. Defects in the lattice decrease the hydrogen diffusivity, whereas these defects are usually regarded as high diffusivity paths for substitutional species. These defects are called "traps." Comparison of high- and low-temperature diffusion data show that the mode of transport is through the lattice at high temperatures (above about 200°C) but that the hydrogen tends to associate itself with defects at lower temperatures. The activation energy for the movement through the defects is 6-9 kcal/mole. Because of the high fugacity of electrolytically discharged atomic hydrogen, all accommodating lattice sites are filled and excess hydrogen lodges in the vicinity of defects (vacancies, stacking faults, dislocations, interfaces). The extrapolated lattice diffusion coefficient for α-Fe at room temperature is of the magnitude 10^{-5} cm^2/s; this value has been corroborated by room temperature internal friction measurements and by electrolytic-charging permeation methods under certain circumstances. The diffusivity which is often calculated from room temperature permeation studies is, therefore, an "apparent diffusivity" when there is trapping in a defected region. The "apparent diffusivity" is always less than the "true diffusivity" associated only with movement through the perfect lattice.

There are at least two kinds of trap.[177] The first kind does not retain the hydrogen permanently but slows down its passage. The second kind causes molecularization of the atomic hydrogen and this hydrogen is extremely slow at room temperatures. The activation energy of the first kind of trapped hydrogen is perhaps approximately 16 kcal/mole.[178]

In Fig. 255 the initial transient shows a lower apparent diffusivity than subsequent ones. (The time to reach steady state is inversely proportional to the diffusivity.) This is an example of the first kind of trapping effects. At several charging conditions in which the permeation current reaches a maximum and then drops off sharply with time is regarded as the second, or permanent, type of trapping.[179]

A recent paper[178] has shown that interfaces are the most important sites for trapping hydrogen. This trapped hydrogen need not be held permanently in the metal; it is more likely that the hydrogen atom is slowed down in its passage through the defects. The apparent diffusivity calculated from permeation transients is of the order 10^{-6} cm^2/s for single-pass zone-refined iron (80 ppm total impurities) and 10^{-8} cm^2/s for 1010 steel. Both materials had the same grain size (annealed at 650°C for two hours before the permeation test) so that the only major difference was the carbide precipitation (pearlite colonies) in the steel. This second phase is, therefore, responsible for the lower diffusivity. The iron-copper system was selected for study[151,180] because the system is precipitation-hardenable and the particles can be grown by aging. At room temperature the terminal solubilities of copper in iron and iron in copper are very small. The iron and copper atoms are of comparable size but the metals are of different crystal structures. Because of this mismatch the precipitates tend to be incoherent with the matrix.

This work has been conducted using a precipitation-hardening Fe-Cu system described in previous reports. The purpose of using such a system was to control the nature of interfaces present since an extensive study by Hornbogen and Glenn[180] had already defined the system.

In all of the experiments performed on the Fe-Cu alloy, 10-mil thick specimens were utilized. This choice was an optimization between too-thin specimens (low D values) and too-thick specimens (long time to come to steady state and its concomitant problems of crevice attack). These specimens were charged from acetate solution containing arsenite (0.9 μg As/ml) at potentials in the range -800 to -1000 mV (SCE) because these are conditions where a significant portion of the electrolytically discharged hydrogen is absorbed by the metal. In this range, the cathodic currents are small enough to avoid the problem of excessive hydrogen bubbles preventing access of the charging solution to the surface.

Microhardness data for the various aging conditions employed are shown in Fig. 274. These results are in good agreement with those of Hornbogen and Glenn.[180] They were able to observe the Cu precipitates after about 24 hours aging at 500°C and concluded that this was due to the creation of an incoherent interface between the phases since the similar electron scattering factors for Fe and Cu make detection of the clustering stage difficult.

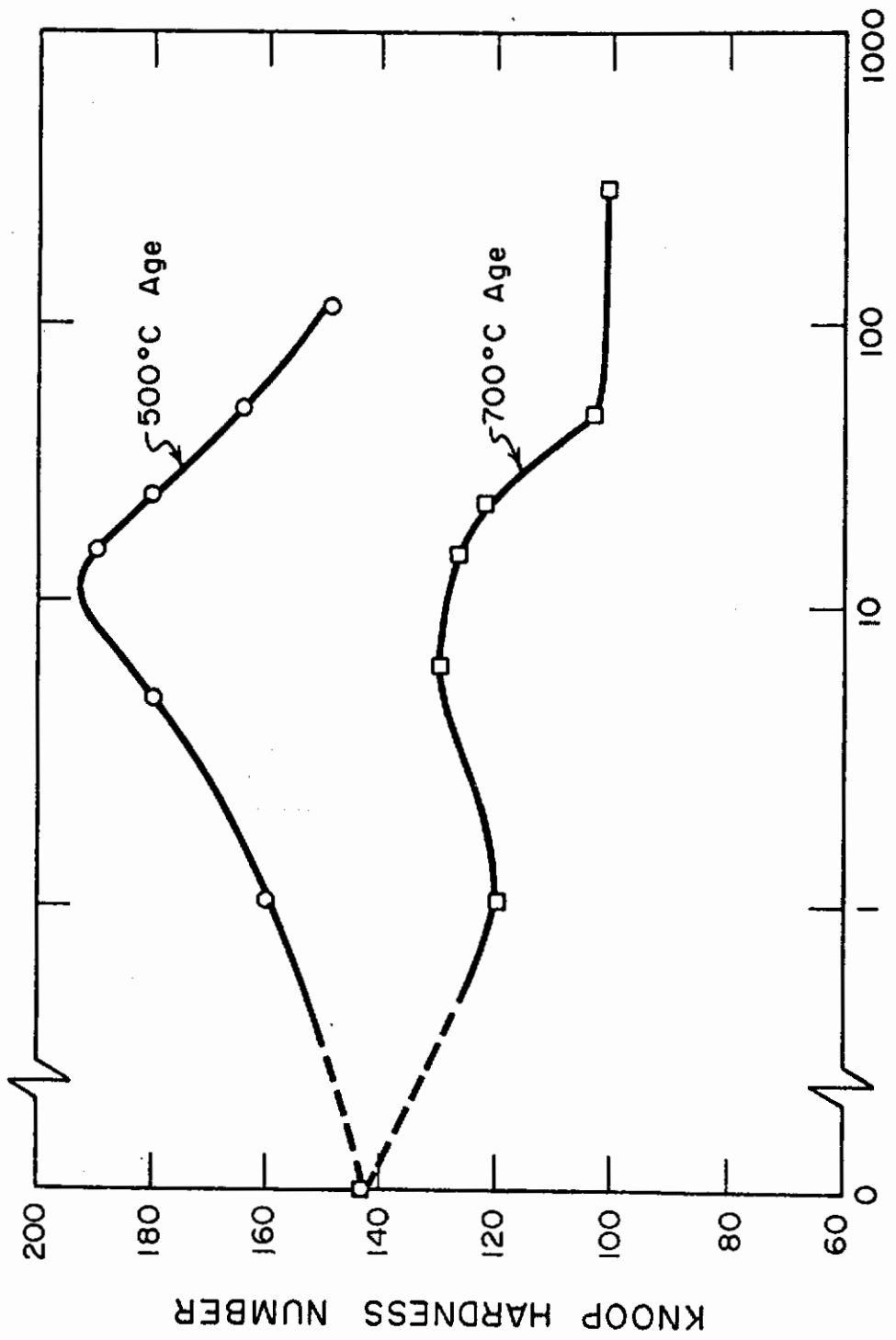

Fig. 274 - Microhardness of Aged Iron-1% Copper Alloy Specimens

For this investigation the Fe-1% Cu alloy was solution treated at 840°C for 93 hours for homogenization. This temperature is above the solvus line but below the $\alpha \rightarrow \gamma$ transformation temperature. The alloy samples encapsulated in argon-filled quartz cylinders to minimize oxidation were quenched in water, then aged at 500 and 700°C to precipitate the copper phase. Sample thickness was 10 mils.

The specimens were hydrogen charged from acetate buffer solutions (pH 4.5) containing arsenite (0.9 μg As/ml. The permeation transients of some of the specimens charged at -900 mV (SCE) and -1000 mV, (SCE) are shown in Figs. 275 and 276, respectively. These results are summarized in Table XXXVIII along with some others.

These data show that the tendency for trapping occurs as the aging time increases and as the charging conditions become more severe (more active charging potential). In addition, the type of trapping changes from temporary to permanent (tendency toward anomalous behavior) as the aging time increases for a given charging potential. The apparent diffusivity decreases generally with the aging time as shown in Table XL. In all cases, some degree of trapping is presumed because single-pass zone-refined iron charged under the conditions of -800 mV (SCE) yielded an apparent diffusivity of 3×10^{-6} cm^2/s, well below the 10^{-5} cm^2/s value for lattice diffusion. Permeation measurements alone are not sufficient evidence that hydrogen entry is responsible for susceptibility to embrittlement. Either solubility or diffusivity must be determined in addition to the permeability. Although the susceptibility to hydrogen cracking in a Ni-Cr-Mo high-strength steel increases with the yield strength, the steady state hydrogen permeability is nearly the same regardless of the heat treatment. The time required to come to steady state increases as the yield strength increases. Since the diffusivity is inversely proportional to the lag time, it decreases with increasing yield strength. Since the deviation of the apparent diffusivity from the true lattice diffusivity is a measure of the extent of trapping, it is the degree of trapping that is the critical diagnosis.

The most significant change occurs upon initial aging of the solution-treated metal. For moderate charging conditions (-800 and -900 mV) the solution-treated metal has high permeability and diffusivity. The diffusivity decreases generally with aging time. At more severe charging conditions the permeation response generally shows a sharp maximum followed by a decrease. The diffusivity cannot be determined for this type of behavior since there is no steady state region. The rise and fall is believed to be caused by recombination of trapped hydrogen atoms on internal surfaces. These specimens showed blistered and plastically deformed areas.

Although there is scatter of the diffusivity and solubility data, the solubility of hydrogen in the metal in the aged condition is larger than in the solution-treated condition. It would appear that the interface around the copper precipitates and the precipitates themselves dissolve considerable hydrogen. Metallographic examination

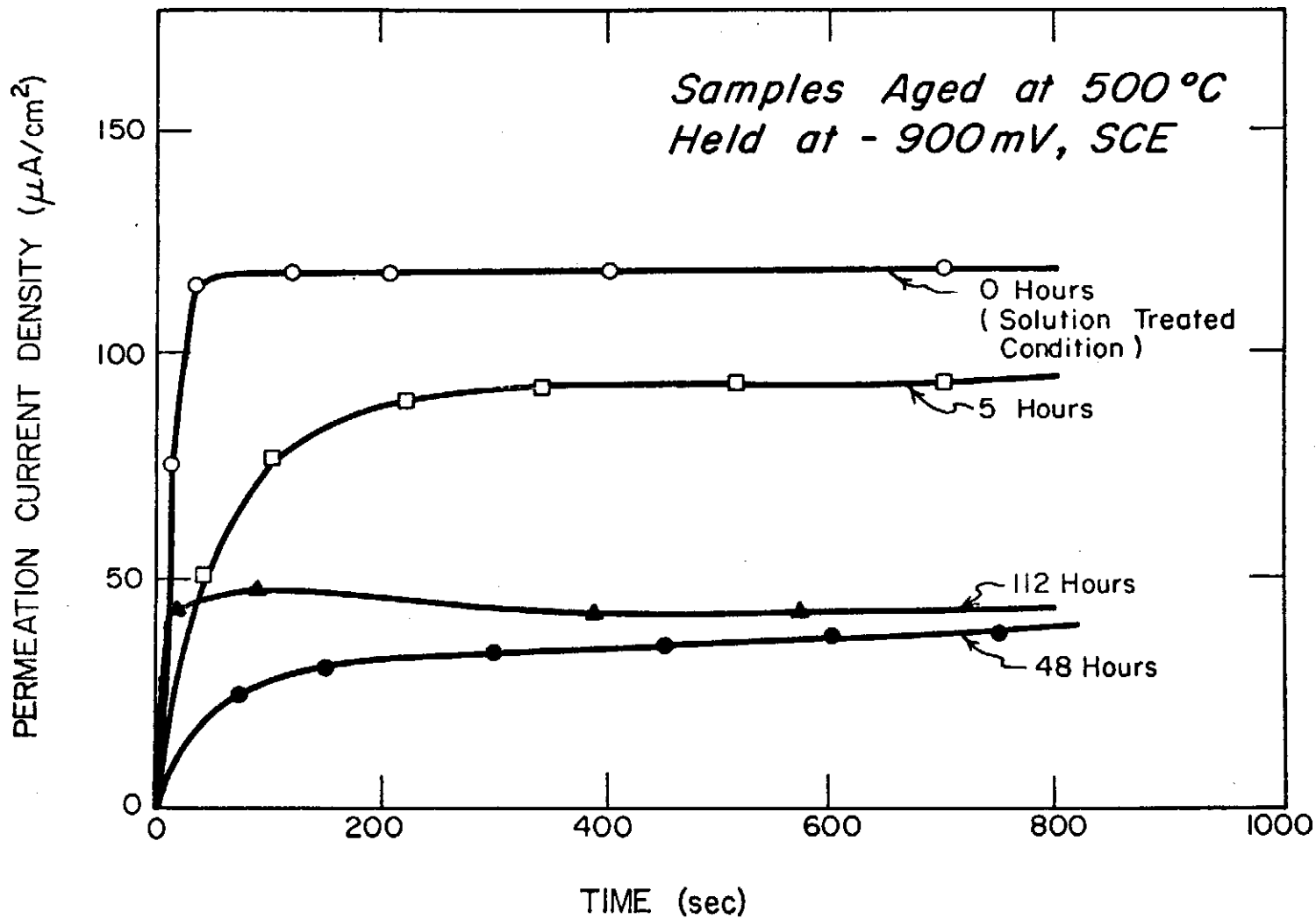

Fig. 275 - Hydrogen Permeation Rise Transients for Fe-1% Cu Alloy Specimens Aged at 500°C for Various Times. Conditions: charging potential, -900 mV SCE; charging solution, acetate buffer plus arsenite (0.9 μg As/ml); specimen thickness, 10 mils, palladized at exit surface; exit solution, 0.1N NaOH

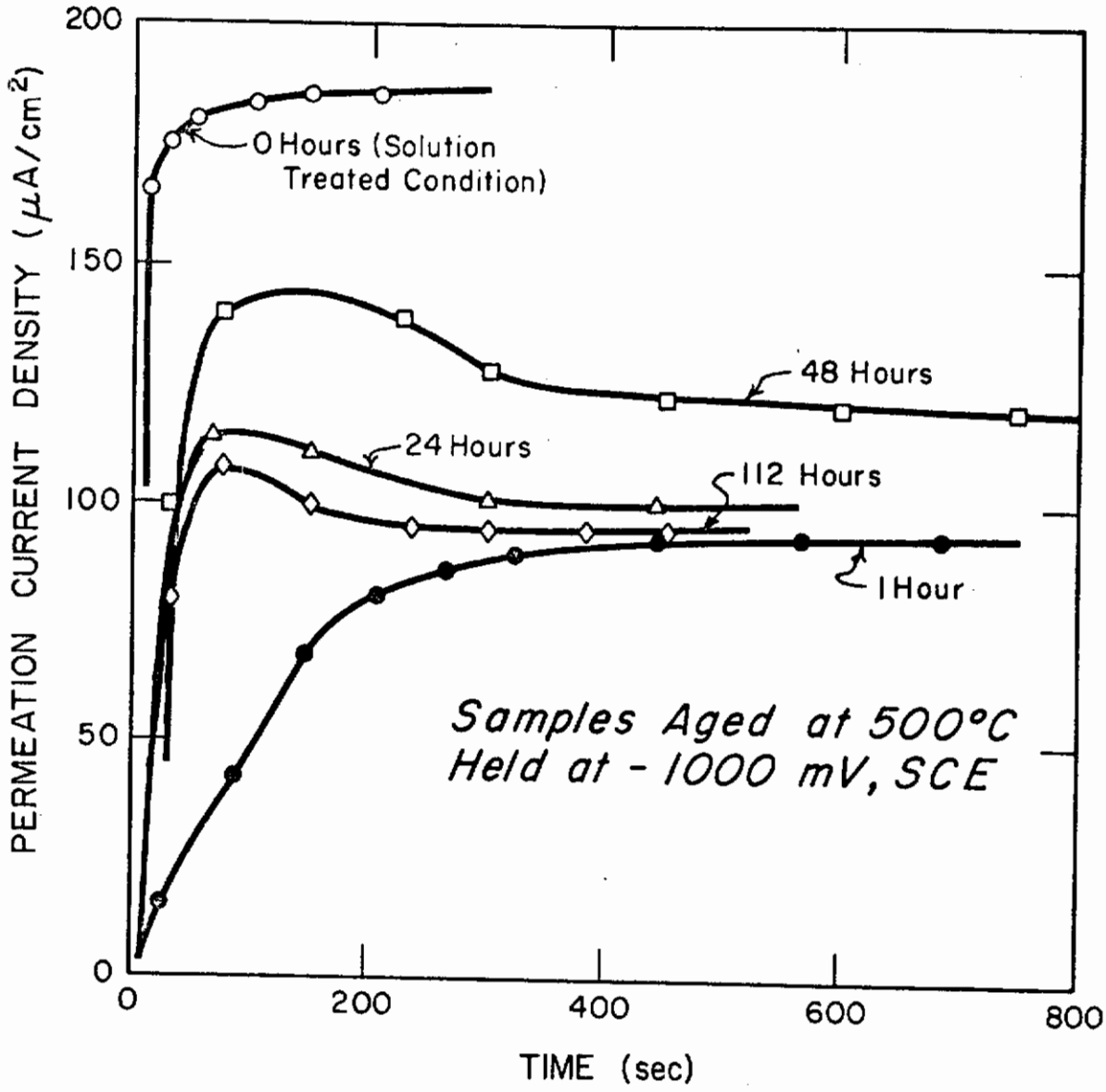

Fig. 276 - Hydrogen Permeation Rise Transients for Fe-1% Cu Alloy Specimens Aged at 500°C for Various Times. Conditions: charging potential, -1000 mV SCE; charging solution, acetate buffer plus arsenite (0.9 μg As/ml); specimen thickness, 10 mils, palladized at exit surface; exit solution, 0.1N NaOH

Table XXXVIII - Calculation of Hydrogen Diffusivities and Saturation Solubilities for Fe-Cu Alloy Aged for Different Times

Aging Condition (°C)	Time (hr)	Changing Condition mV(SCE)	Steady State Permeation Current Density ($\mu A/cm^2$)	Calculated Diffusivity ($cm^2/s \times 10^{-7}$)	Saturation of Hydrogen ($mole/cm^3 \times 10^{-6}$)	Changing Condition mV(SCE)	Steady State Permeation Current Density ($\mu A/cm^2$)	Calculated Diffusivity ($cm^2/s \times 10^{-7}$)	Saturation of Hydrogen ($mole/cm^3 \times 10^{-6}$)
Solution treated		-800	34	8.75	9.9	-900	132	19.4	176
500	1	-800	7	6.7	26				
500	5	-800	10.5	5.48	49	-900	92	5.65	45
500	16	-800	2.5	5.0	12.7				
500	24	-800	9	4.27	53.6				
500	48	-800	4.5	3.9	29.4	-900	36	2.92	314
500	112	-800	9.5	6.0	15.8	-900	47	1.46	820
700	1	-800	16.5	25	16.7				
700	5	-800	8	5.3	38.2				
700	16	-800	1	5.84	4.0	-900	23	1.84	318
700	24	-800	2	5.47	9.1	-900	95	1.75	1370
700	50	-800	6	5.0	32.	-900	91	4.86	475
700	100	-800	12	3.14	97.	-900	79	5.0	400
700	280	-800	16	3.5	115.	-900	86	1.17	1870

(transmission electron microscopy) showed that copper precipitates were visible after one hour aging at 500°C and that there was some growth and clustering of these precipitates at longer times and higher temperatures. As with the permeation data, the most noticeable change occurred between the solution-treated condition and the first aged condition.

Permeation rise transients for the various conditions of the alloy are shown in Figs. 277 (at a charging potential of -800 mV, SCE), 278 (-900 mV, SCE), and 279 (-1000 mV, SCE). Similar permeation behavior is shown for pure iron at -800 mV (SCE) for comparison. The solution treated condition generally gives the highest permeation rate, which decreases with aging and then increases again for the overaged alloy. At -1000 mV blistering starts to occur at the surface. This happens as the permeation transient reaches a maximum and decreases.[164]

It is believed that the permeation effects are due to the hydrogen interaction with the copper particles in the bulk rather than a surface effect. Polarization curves run on pure iron and the overaged iron-copper alloys showed exactly the same shape although the corrosion current extrapolated from the Tafel region was higher for the alloy. This is expected because of the great difference in dissolution between Fe and Cu, however the hydrogen evolution characteristics are similar on the two metals. The value of the exchange current density is about an order of magnitude lower for the Cu than Fe. The mechanism for hydrogen evolution on a pure Cu surface is slow discharge - fast chemical desorption (similar to iron).[164]

Diffusivity calculations made from these experiments are shown in Fig. 280. These were calculated from the decay curves after charging at -900 mV (SCE). All of the conditions show high diffusivity in the initial steady state condition (traps filled). When the permeation current falls to about 50% of its initial value the diffusivity starts to decrease. This first hydrogen to effuse out is interstitial hydrogen and the quantity of it contained in the specimens is small because the drop of i_p to 50% of its initial value is very rapid (characteristically about 10 seconds). The quantity of hydrogen is the integration of i_p and time. In recovering the trapped hydrogen much longer times are required (at least an hour). It should be emphasized that this hydrogen is not trapped in the sense of formation of H_2; it is atomic hydrogen that is less mobile because of its affinity for dislocations and the dislocation structure at the incoherent boundary.

The lowest apparent diffusivities are recorded for the fully hardened condition and the slightly overaged condition (500°C, 16 and 48 hours, respectively). The diffusivity recovers as the growth process continues. It is apparent that the interfacial area is playing an important role in determining the trap population. This area is maximal just beyond the hardness peak when the particle size and, particularly, the particle density (number per volume) are large.

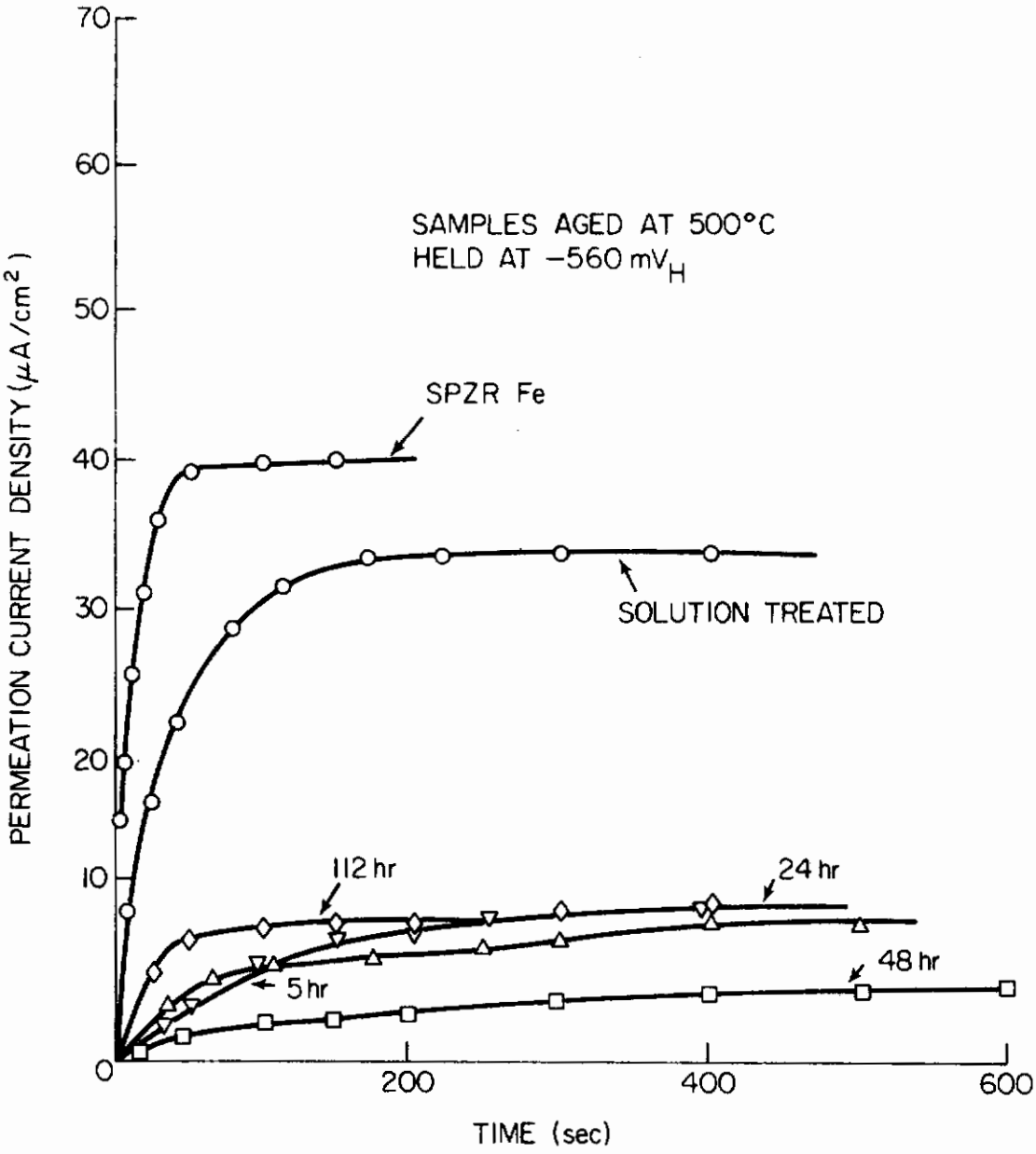

Fig. 277 - Hydrogen Permeation Rise Transients for Fe-Cu Charged at -800 mV SCE

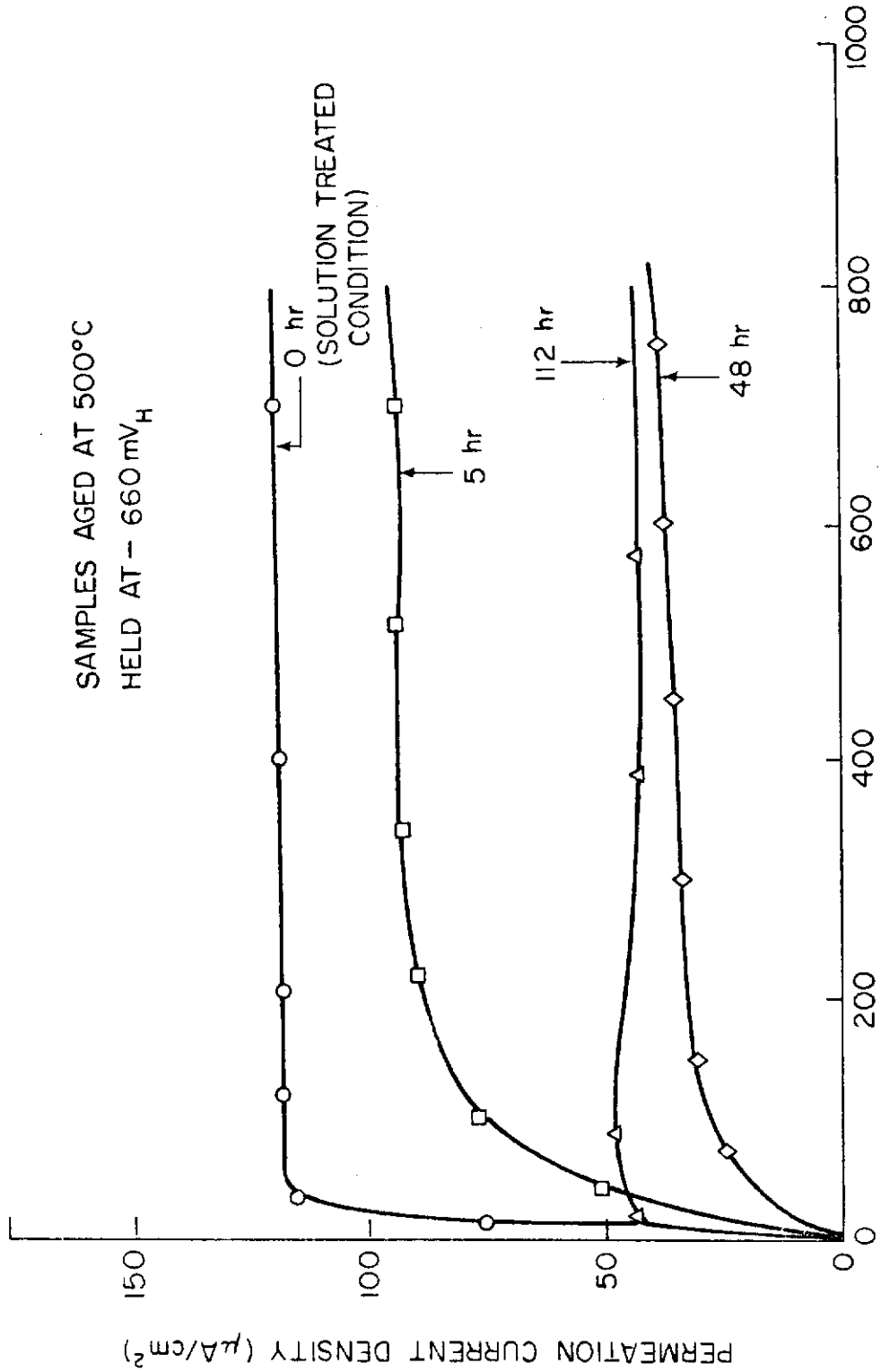

Fig. 278 - Hydrogen Permeation Rise Transients for Fe-Cu Charged at -900 mV SCE

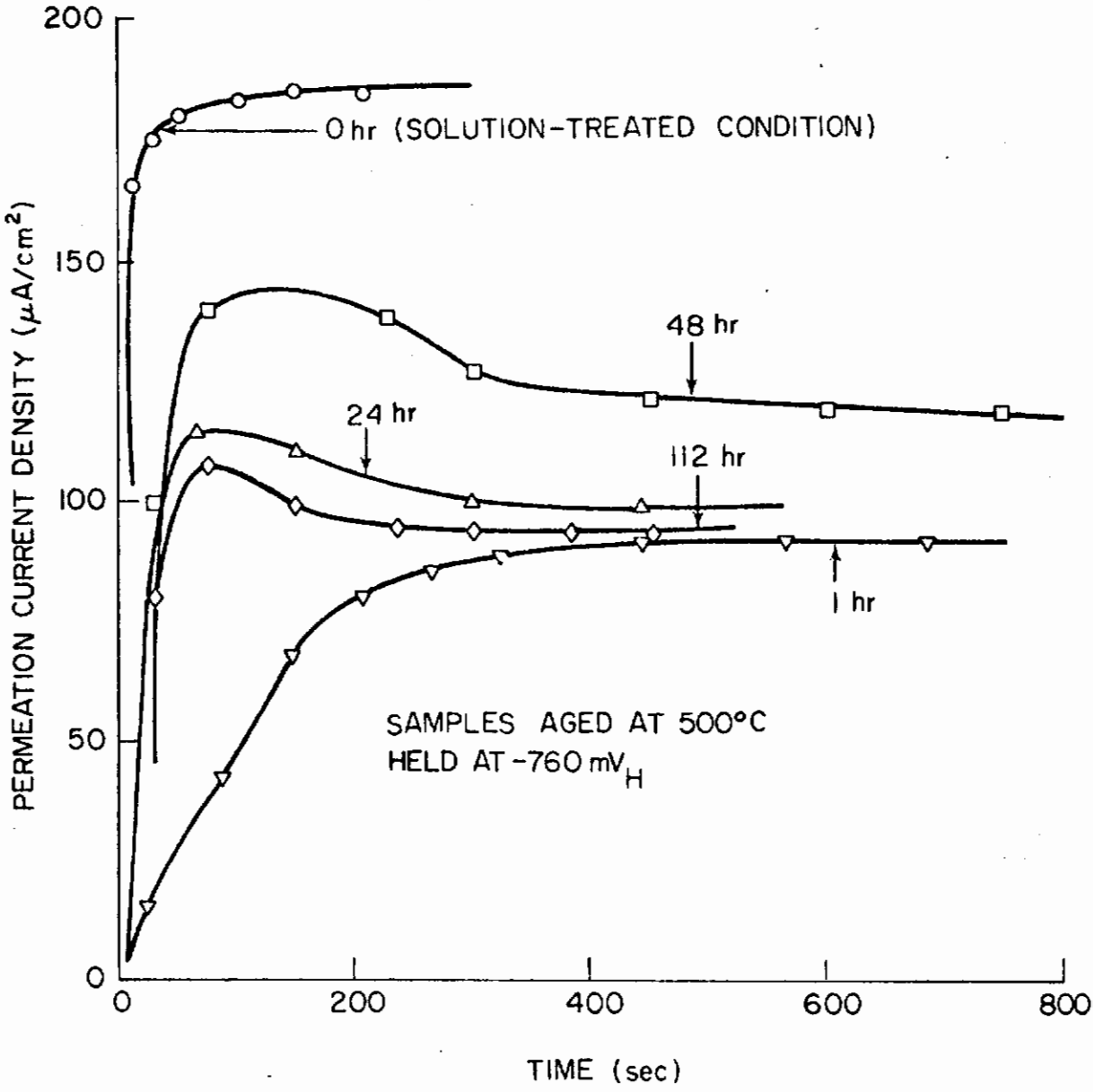

Fig. 279 - Hydrogen Permeation Rise Transients for Fe-Cu Charged at -1000 mV SCE

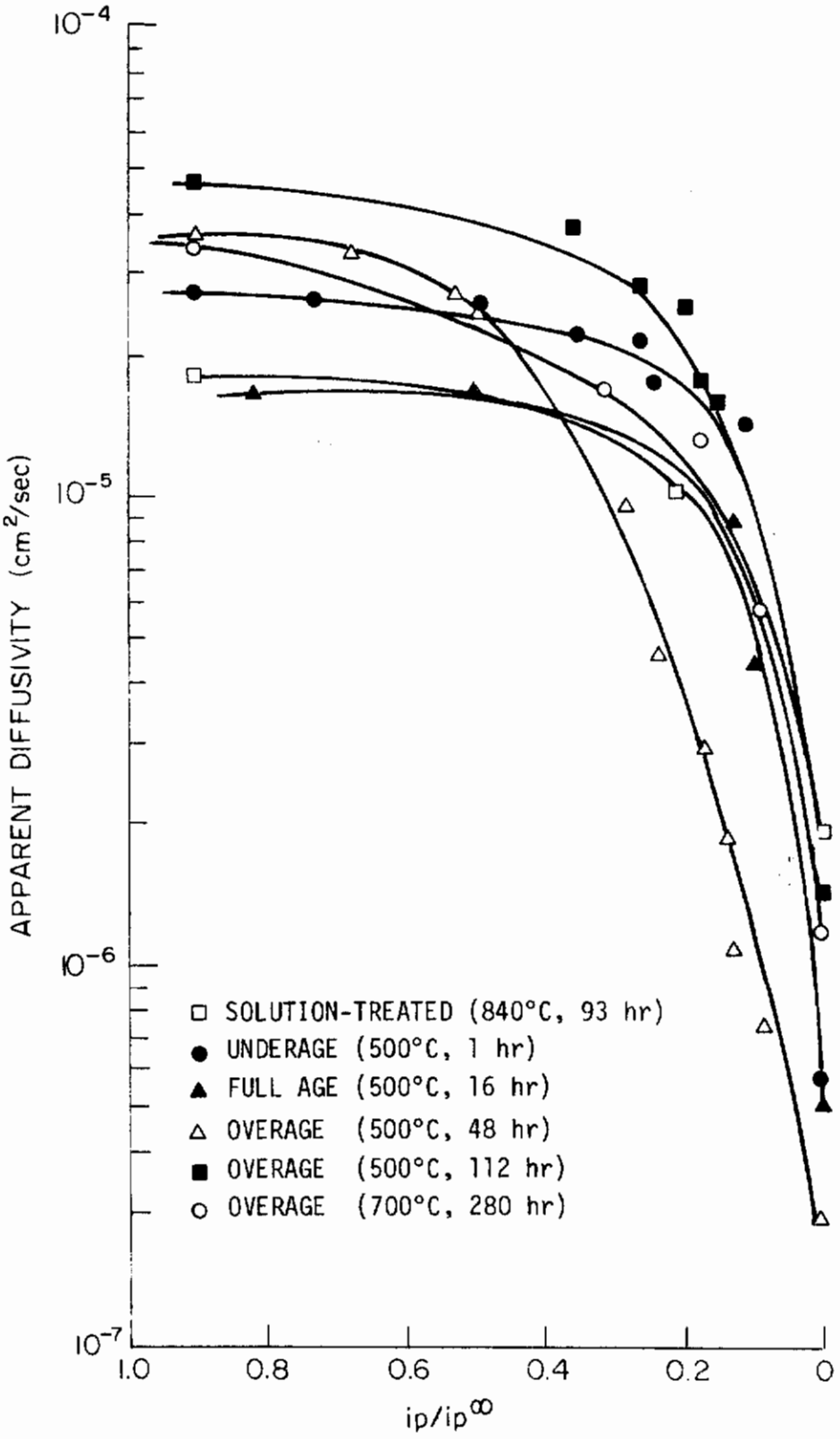

Fig. 280 - Apparent Diffusivity of Hydrogen in Fe, 1% Cu Alloy Aged at Various Conditions

When the copper transforms from a bcc lattice coherent with the iron lattice to its own fcc lattice, there is a decrease in the volume occupied by the copper clusters if one assumes that the radius of the Cu atom is the same in both coordinations. The decrease in volume creates vacancies at the interface or induces a tensile strain in the matrix surrounding the particle. Either or both of these would enhance the hydrogen solubility in the vicinity of the interface. The highest hydrogen contents were calculated when the metal was still underaged (coherent particles) but the solubility remained high at the coherent to incoherent transition. The volume decrease of the particles would be on the order of 6% (74% packing factor in fcc; 68% in bcc).

The true hydrogen diffusivity occurs when i_p/i_p^∞ approaches unity (Fig. 280) and the apparent diffusivity (with trapping effects) is seen as this ratio approaches zero. Again it should be reiterated that the reproducibility problems make the order of magnitude of D the important consideration.

In Table XXXIX are summarized the results of diffusion calculations of the Fe-1% Cu alloy.

Table XXXIX - Diffusion of Hydrogen in Fe-1% Cu Alloy

Aging Condition	With Trapping (time lag) ($\times 10^{-7}$ cm^2/s)	Without Trapping (decay, t = 0) ($\times 10^{-5}$ cm^2/s)
Solution treated (840°C, 93 hr)	19.4	2.71
Underage (500°C, 5 hr)	5.65	3.36
Full age (500°C, 16 hr)	5.0	1.63
Slight overage (500°C, 48 hr)	2.92	3.52
Average (500°C, 112 hr)	14.6	4.77
Much overage (700°C, 280 hr)	11.7	1.82

For the Fe-1% Cu the largest $D_{apparent}/D_{true}$ ratio is about 10^{-2}

A schematic plot of the various quantities measured or calculated from the experiments with iron-copper is shown in Fig. 281. Permeability, diffusivity, solubility at the entry surface, hardness, and the interfacial area are shown on a relative basis.

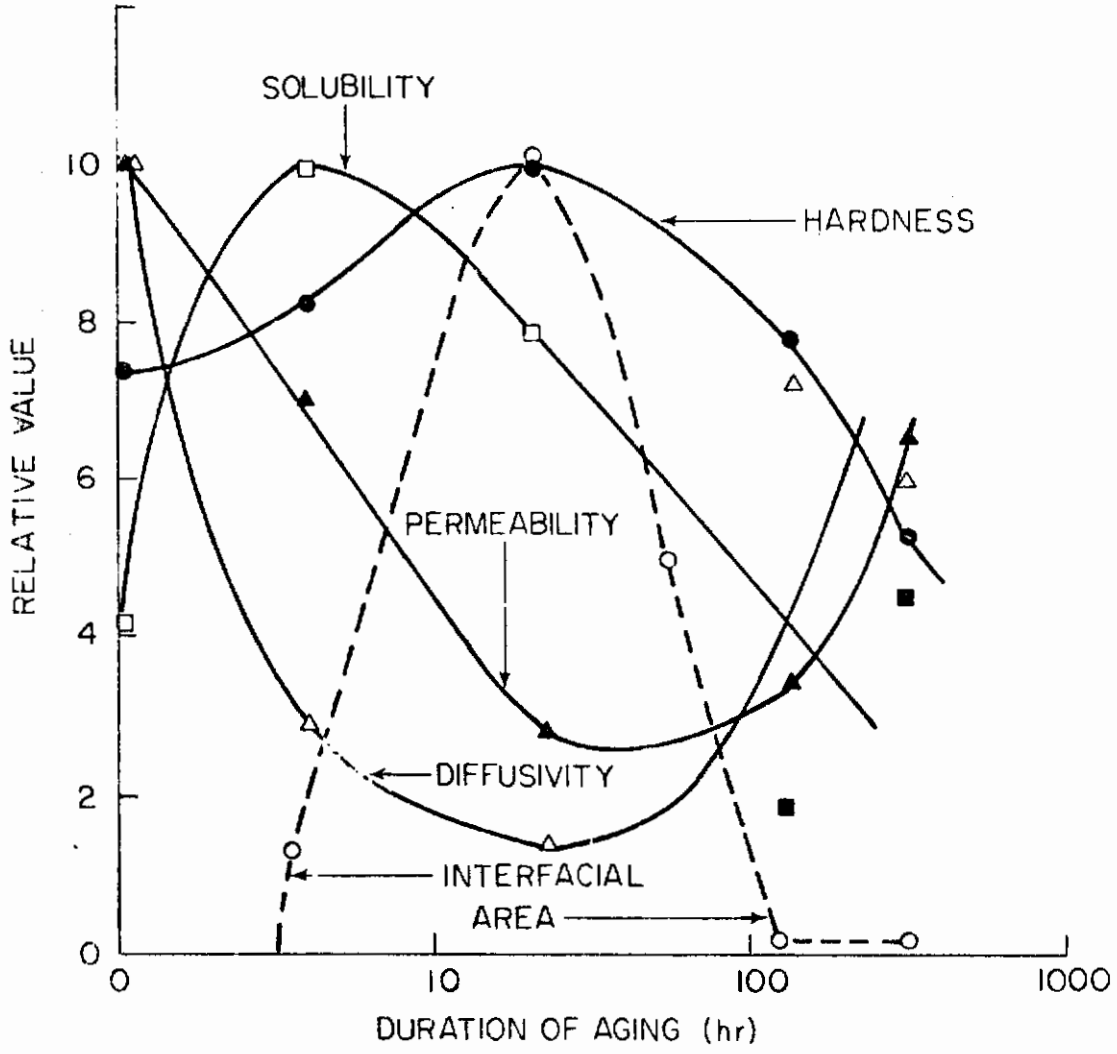

Fig. 281 - Relative Values of Permeability, Diffusivity, Hardness, Hydrogen Solubility, and Interfacial Area in Fe-Cu

It is necessary to know the interfacial area between the copper particles and the ferrite matrix for a population estimate of the trap sites on which the hydrogen atoms can lodge. The important quantities to calculate are the particle diameter (from which the area is calculable) and the particle density (the number of particles in a unit volume).

A montage of photomicrographs (Fig. 282) shows the appearance of a few small particles after about 5 hours of aging at 500°C. These particles retain coherency because of the strain halos.[181] In general, copper clusters are not visible in transmission electron microscopy because the scattering factors for Fe and Cu are very similar. What appears to be a doublet of particles is probably a single particle with the strain halos taking on a rounded appearance. In the aging condition of 16 hours at 500°C, which corresponds to the hardness maximum (Fig. 276), the copper is apparent as the particles lose coherency and the copper is on an fcc lattice. These particles appear larger in the next photomicrographs of Fig. 282 (48-hr age, 112-hr age at 500°C; and 1-hr and 16-hr age at 700°C). At the last condition shown, 280 hours at 700°C, the particles tend to grow in a rod shape. The number of particles decreases in the overaged conditions.

The average caliper diameter of the particles and the mean free path between particles was determined for each of the aging conditions. These data are given in Table XL.

Table XL - Particle Size and Spacing in Aged Iron-Copper Alloy

Aging Condition	L, Mean Free Path (x 10^{-4} cm)	D, Particle Diameter (Å)	D^2/L^3 (relative scale)
500°C, 16 hr	2.58	505	1.5
500°C, 48 hr	2.18	860	7.2
500°C, 112 hr	16.10	1100	0.03
700°C, 1 hr	5.76	674	0.24
700°C, 16 hr	13.20	1460	0.10
700°C, 280 hr	34.8	1000	0.02

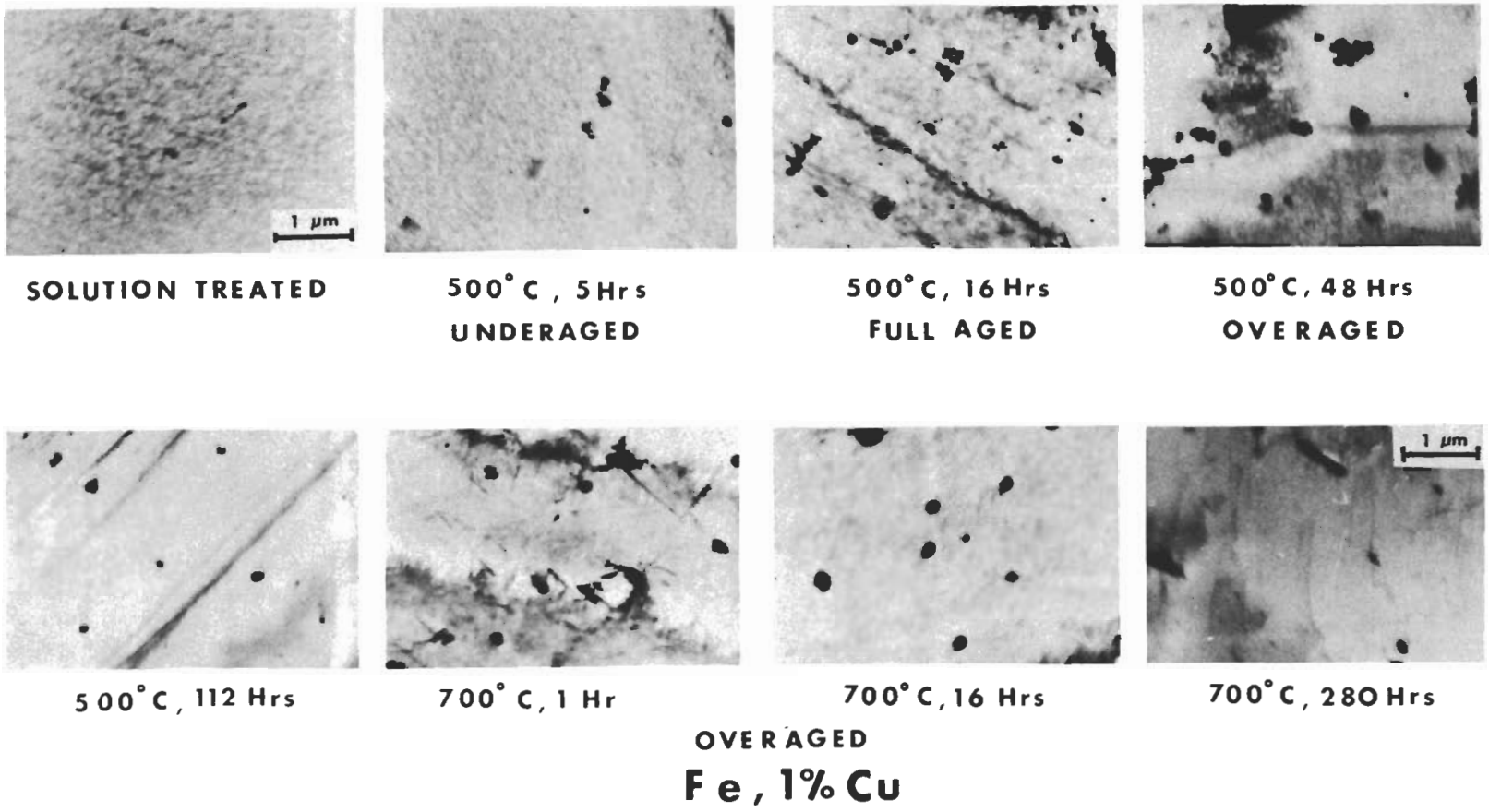

Fig. 282 - Montage of Photomicrographs of Fe-Cu Showing Particle Appearance and Growth. Transmission Electron Microscopy

The particle diameters in the above table are probably too large since they do not take into account the various factors used by Hornbogen.[182] He found that a 500°C age for 24 hours gave particles 40 Å in diameter with a minimum interparticle spacing of 940 Å. At 100 hours age at this temperature the particles were 75 Å in diameter with 530 Å spacing. At 240 hours at 500°C the particles grew to 125 Å and were spaced 630 Å. At 700°C age for 96 hours the particles attained 800 Å diameters and a spacing of 10,000 Å.

It is possible to calculate the hydrogen concentration at the entry surface from the steady permeation current and the diffusivity. The diffusivity used for this calculation is the one which prevails at long times. This calculation is based on the equation

$$C_o = (i_p^\infty/ZF)(L/D_{app}) \quad . \qquad (70)$$

These calculations are summarized in Table XLI.

Table XLI - Calculation of Saturation Hydrogen Content in Fe-1% Cu

Aging Condition	I_p^∞ ($\mu A/cm^2$)	D_{app} (cm^2/s)	C_o ($moles/cm^3$)	C_o (ppm)
Solution treat (840°C, 93 hr)	132	19.4×10^{-7}	17.7×10^{-6}	2.27
Underage (500°C, 5 hr)	92	5.65	42.9	5.49
Full harden (500°C, 24 hr)	37	2.92	33.4	4.27
Overage (500°C, 112 hr)	45	14.6	8.1	1.04
Much overage (700°C, 280 hr)	86	11.7	19.3	2.47

The maximum hydrogen content occurs before the hardness maximum although the diffusion minimum occurs close to the hardness maximum.

Although it would be well to have an analytical determination of the hydrogen content of these samples as an independent check, none was attempted because of the problems of reliability of the analysis and difficulty in removing the specimen from the charging apparatus to a location where it could be stored before analysis (example, liquid nitrogen flask).

According to Oriani[178] the trap depth should be about 8-9 kcal/mole H for the ratios of D encountered in this experiment. The interaction energy between hydrogen and dislocations is about 6 kcal/mole H according to Gibala.[183] It was shown earlier that a dislocation density of about 10^{11} cm/cm^3 is necessary to attain the trap population of 10^{19} sites/cm^3. Thus, interaction of hydrogen with dislocations in annealed metals is not a likely source of traps but the interfacial area of an incoherent boundary (which is, of course, an array of dislocations) is a likely source of trapping.

One factor, that under certain conditions may be overriding all of the above, is hydrogen interaction with free surfaces inside the metal; that is, with microcracks and microvoids. The interaction energy of these is some 20 kcal/mole H.[178] The number of these voids is generally indeterminable but is the probable explanation for the blistering observed in Bernstein's experiments.[184] He charged high-purity iron but under very severe conditions (high currents, prolonged electrolysis) which were purposely avoided here. The ratio of the apparent to the diffusivity is related to the trap population by

$$D_{true}/D_{app} \simeq 3N_x/C_L \ , \qquad (71)$$

where N_x is the number of trap sites (not all necessarily filled) and C_L the concentration of interstitial (lattice) hydrogen. Since C_L has been shown to be 0.1 ppm maximum by Gibala,[183] experimental determination of the ratio of diffusivities gives an order of magnitude value to N_x.

(1) Mild Steel

In the case of the mild steel the D ratio was 10^3 which requires $N_x \simeq 10^{20}$. According to Kramer, et al.[185] the interfacial area of an all pearlitic (0.8%C) is 10^4cm^2/g and if the supposition is true that a 0.1% C steel has 1/8 this area:

$$N_x \simeq 10^4(\text{cm}^2/\text{g}) \times (1/8) \times [(3 \text{ sites on 100 plane})/(2.86 \times 10^{-8})^2\text{cm}^2] \times 7.8\text{g/cm}^3 = 4 \times 10^{19} \text{ sites/cm}^2.$$

(This model assumes 100 planes parallel to the interface)

(2) Iron-Copper

For the iron-copper alloy consider two of the overaged conditions:

(a) At 500°C for 48 hours, $D_{true}/D_{app} = 10^2$
Therefore $N_x \simeq 10^{19}$. The number of sites per volume can be found by

particle area x (no. particles/volume) x (no. sites/interfacial area) = sites/volume.

For this condition the particle size is about 100 Å diameter and the mean spacing about 600 Å. If two sites are assigned to each lattice parameter unit for the mismatch at the interface, one obtains

particle area: 3.14×10^{-12} cm^2/particle, and

particle density: 4.6×10^{15} particle/cm^3; and using the lattice parameter of iron, the product of these yields a calculated trap population on the order 3.5×10^{19} sites/cm^3.

(b) At 700°C age, 280 hours, the ratio of the D values is 15. At this condition the particle size has grown to 800 Å, and the spacing to 10,000 Å. A similar calculation gives particle area: 200×10^{-12} cm^2/particle, particle density: 10^{13} particles/cm^3, and trap population: 5.5×10^{18} sites/cm^3.

This compares very favorably with the 2×10^{18} predicted by the D ratio.

Therefore it is concluded that the incoherent interface is the source of the trap population in both mild steel and iron-copper.

Thus, there is reasonably good agreement between phenomenological predictions and the physical predictions.

A specimen showing a blistered surface is shown in the photomicrograph (Fig. 283). The specimen is overaged iron-copper and was hydrogen charged at -1400 mV (SCE) in acetate solution containing a small amount of arsenite. In general, specimens held at potentials more active than about -1000 mV (SCE) in this environment blistered. The permeation transients under these conditions showed a peak, which was followed by a sharp drop in the permeation rate.

It was anticipated that the structural damage might show up as an increase in the dislocation density or as the formation of small cracks. A series of steel specimens charged under conditions leading to surface blistering and anomalous permeation transients was examined in transmission electron microscopy. A montage of photomicrographs is shown in Fig. 284.

Although there appears to be a slight increase in the number of dislocations in the specimens which had been hydrogen permeated, it appears that there is no structural damage done to the permeated specimens so far as crack formation goes.

Fig. 283 - Blistered Surface of Fe-Cu Specimen Held at -1400 mV SCE in Acetate + Arsenite Solution. Scanning Electron Microscopy 1000X

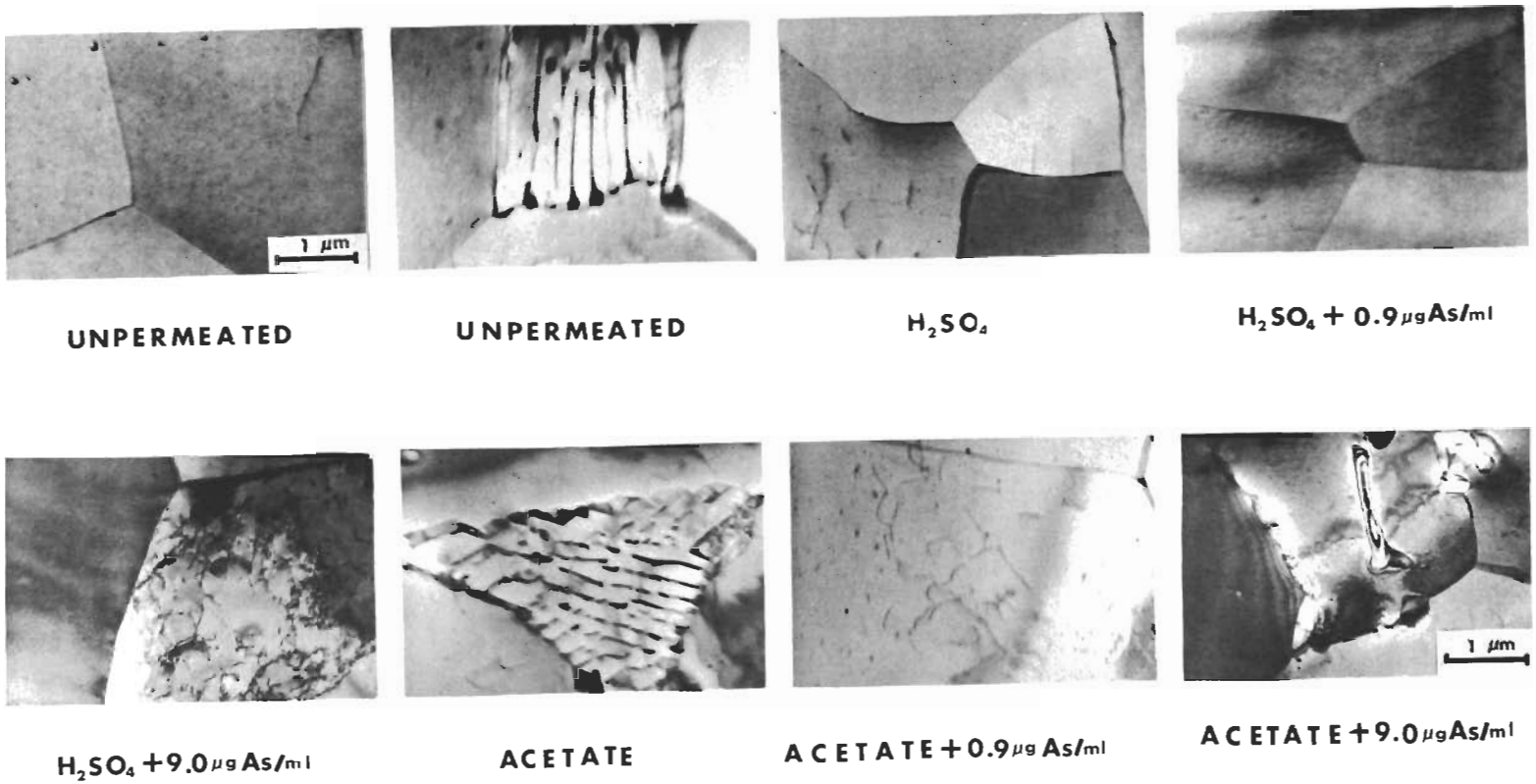

HYDROGEN PERMEATION IN MILD STEEL

Fig. 284 - Montage of Photomicrographs of Mild Steel Specimens Unpermeated and Permeated from the Indicated Environments. Transmission Electron Microscopy

SECTION V

HYDROGEN-INDUCED DELAYED FAILURE IN ULTRAHIGH-STRENGTH STEELS

A. INTRODUCTION

The problem of hydrogen-induced delayed failure was encountered toward the end of World War II when the aircraft industry requested steel parts having higher strength-to-weight ratios and then cadmiun-plated them for corrosion protection. More recently it has been encountered during the hydrostatic testing of rocket motor casings made from high-strength steel. With the increased demand for materials with increased strength-to-weight ratios and more precise design practices has come the ever-growing need for increased reliability. This investigation demonstrates a microstructural dependence of susceptibility to hydrogen-induced delayed failure as well as material reliability in ultrahigh-strength steel wire.

The feasibility of a study of static fatigue behavior of two ultrahigh-strength steel wires was demonstrated by a simple test; i.e., a static bend, in situ charging test. A static bend test jig was designed and constructed such that the wire was threaded back and forth through a series of equally spaced, parallel holes one-quarter inch apart and perpendicular to the long axis of the jig. The maximum stress level in each loop is inversely proportional to the distance of the bend from the jig. The qualitative effects of varying the potential across the charging cell, specimen diameter, specimen strength level, and bending stress on the time-to-failure were investigated.

In the first test on high strength level material, several bends of nominally the same stress level were tested and found to fail in 5 to 10 seconds. In the second test the potential was decreased to decrease the charging rate and thereby increase the time-to-failure. To check the effect of bending stress with a minimum number of specimens, bends of increasing severity were located at increasing separation from the power source so that when the most highly stressed bend broke, the remaining bends would not be affected by that break in the circuit. The time-to-failure for a comparable stress level was greater than that in the first test because of the decreased charging rate; the time-to-failure was inversely proportional to the bend stress level. In the third test, a specimen of comparable strength but increased diameter was used to detect whether there was a size effect. The result in that case was an increased time-to-failure, other conditions being the same. A fourth test was performed using a material (280 ksi strength level) of much different strength level. In this case, even with the potential across the cell increased to the value in the first test, the specimen did not fail in a time interval two orders of magnitude greater than those required for failure of the higher-strength material.

The results indicated that: (1) at higher strength levels, AISI 4140 steel wire is susceptible to delayed failure and that (2) increased potential across the cell, (3) decreased wire diameter, and (4) increased bending stress will decrease the time-to-failure under *in situ* charging conditions.

A considerable amount of scatter in the data was observed in the literature, especially for unnotched, smooth test specimens.[186] To maximize reproducibility of the test results, the system was defined in a reasonable manner. A technique for cleaning and storing the specimens prior to testing was developed such that it resulted in no degradation of the specimen and provided a reproducible initial condition of the specimen. Polarization curves were determined to define the electrochemical behavior of the specimens. An intriguing hysteresis phenomenon was observed with the cathodic polarization curves. An investigation of the hysteresis effect indicated, however, that it did not occur under *in situ* cathodic charging test conditions. A test technique was developed using a high-strength music wire because the amount of test material (i.e., AISI 4140 and HY-TUF, especially) was limited. The music wire exhibited the characteristics found in a static fatigue (S-F) curve; e.g., upper critical stress (UCS), a range of time-to-failure relatively insensitive to applied stress, and a lower critical stress (LCS). The static fatigue curve shifted to longer time-to-failure with an increasing LCS when the charging current density (c.d.) was decreased. A satisfactory testing technique was established and a study of the 4140 material initiated. A check on the reproducibility of the S-F curve using AISI 4140 material having a strength level of 408 ksi and a diameter of 15.8 mils $\left[\left(\frac{408}{158}\right)\text{AISI 4140}\right]$ was determined because of the importance of the resistance to delayed failure that it exhibited. Subsequent testing demonstrated the reversibility of the crack incubation period in $\left(\frac{408}{158}\right)$ AISI 4140 as well as in $\left(\frac{300}{267}\right)$T (tempered) HY-TUF. Finally, some SEM fractography on selected specimens indicates that there are some fractographic features found in hydrogenated specimens which are not found in specimens pulled to fracture in the air. The most pertinent survey of hydrogen-induced delayed failure as well as the best testing format for characterizing material behavior with respect to susceptibility to hydrogen-induced delayed failure in applied situations was found in an article by Sachs and Morgan.[187] The format of the preceding investigation is very broad in scope. Its main value lies in clearly defining the system, thereby minimizing spurious data, so that analysis of the test results will be more meaningful.

B. EXPERIMENTAL

AISI 4140 wires used in this investigation were cathodically charged *in situ* with hydrogen, galvanostatically controlled under isothermal ($37 \pm 1°F$) conditions. The tests were run using a constant-load lever-arm stress-rupture machine designed to accurately apply a known

tensile load axially to the specimen. Three different testing machines were used during the investigation. The composition of the wires is given in Table XLII. All the 4140 wires and the 42.2 mil HY-TUF wires were tested in the as-drawn condition. The other HY-TUF wires had been tempered at 450°F for one hour after drawing. Prior to the final cold drawing the 4140 wires were strand austenitized, interrupted quenched into a lead bath, cooled in air to room temperature with no isothermal transformations, and tempered at the appropriate temperature for subsequent processing to the desired strength level. The HY-TUF wires were similarily pretreated but depended on combinations of cold reduction and tempering for the ultimate strength level attained (see Table XLIII for this information).

Table XLII

Composition	C	Mn	P	S	Si	Ni	Cr	Mo
AISI 4140	0.425	0.94	0.015	0.019	0.34	--	1.04	0.19
HY-TUF	0.25	1.30	--	--	1.50	1.80	0.35	0.40

Table XLIII

Material	AISI 4140						HY-TUF		
Tensile Strength of Wire (ksi)	400		350		280		300	300	425
Starting Wire Size (mil)	52	80	52	80	52	--	62.7	82.7	82.7
Finishing Wire Size (mil)	15	20	15	20	15	--	42.2	26.7	15.5
Austenitizing Temp.(°F)	1600	--	--	--	--	1600	1530	1530	1530
Tempering Temp.(°F)	700	700	800	800	1000	1000	A	B	C

Interrupted Quench Temp. - HY-TUF 730°F

A. 450°F for 1 hr.
B. A plus intermediate 450°F temper for 1 hr.
C. B plus intermediate 450°F temper for 1 hr.

For removing the draining lubricant and oxide from the wire surface with as little damage as possible to the underlying metal, the wires were wiped with acetone, placed in a hot (180° ± 10°F) neutralized (pH 7.5 to 8.0) citric acid solution for 30 minutes, rinsed with distilled water followed by acetone for 10 minutes each in an ultrasonic cleaner, wiped again with acetone and stored in a vacuum desiccator until ready for use. At any other time the wires were stored in a conventional desiccator. Prior to testing, the cleaned specimen was baked-out (215° ± 2°F) for at least 1 hour. Immediately before the test the specimen was taken from the drying oven and wiped with acetone followed by methanol. The specimen surface around the two-inch test length was coated with Microstop. After allowing the Microstop about

10 minutes to dry, the specimen was placed in the test cell, the load applied, the electrical circuit completed, the electrolyte added, and the time-to-fail recorded. The above preparation method produced a specimen having a reproducible initial condition for testing.

The incubation study was conducted in the same manner as the above except that the load and electrolyte were removed after a predetermined charging period and there was no additional baking out of the specimen. The cell was filled and drained four times with distilled water within 60 seconds) followed by several rinsings. To accelerate drying, the final rinse was with methanol. A jet of ambient temperature air was used to dry the cell and specimen. The specimen was then aged at room temperature.

The electrolyte was IN H_2SO_4 to which 1 g/l thiourea had been added. It was aged at least 6 hours prior to a test. The oxygen content of the electrolyte was kept low by holding it in a 5 l pyrex reservoir and bubbling prepurified N_2 through it by means of a gas dispersion tube for at least 12 hours prior to a test. The electrolyte was chilled before adding it to the test cell so that the isothermal conditions of the test could be more easily maintained.

The test cell consists of a double-walled vessel constructed completely of non-metallic commercially available components to eliminate corrosion and the possibility of spurious cations from entering the electrolyte from the apparatus, as well as eliminating the problem of breakage encountered with glass cells. Because of its chemical stability in a wide range of environments, a mesh platinum anode was used rather than a stainless steel one. A high anode-to-cathode area ratio was maintained to achieve a more uniform current density over the specimen. Initially, a conventional galvanostatic set-up consisting of a resistance several orders of magnitude greater than that of the cell resistance in series with the cell was used with a filtered dc power supply. However, a solid-state, constant-current source relying on feedback control to maintain galvanostatic conditions was assembled and replaced the conventional control. In preliminary testing, the solid-state device (designed by Mr. Joseph Dryer) provided constant current even with rapid changes in supply voltage and in simulated cell resistance. The instrumentation in the cell circuitry had at least ± 1% accuracy.

Under the various loading conditions, three types of wire grips were required to secure the specimen. A wedge-type grip worked best with larger wires. A cam-type grip was developed because of the problem of slippage and wire failure at notches caused by the serrated gripping surfaces of the wedge-type grips. To maintain concentric axial loading with the cam-type grip, the wire enters the grip seated in a round-bottomed groove. The groove is helically cut around a disk having a radius large with respect to that of the wire. Seated in the groove, the wire completes one turn about the disk and passes under the securing cam. The snubbing action of wrapping around the disk in a groove combined with the self-tightening action of the cam secures the wire with

a minimum of concentrated stress, thereby decreasing the possibility of plastically deforming the specimen by the gripping action alone. During testing, difficulties with specimen fracture at the grips became evident. This fracture was probably due to torque introduced into the specimen during mounting in the cell. Suitable adapters were made so that pin-vises could be substituted for the cam-type grips. The design of the test cell was slightly modified to accommodate the introduction and removal of the specimen/pim-vise assembly in toto. With a more accessible assembly, retightening the specimen in the grips becomes much simpler, should slippage occur. This feature enables many tests to be performed that formerly may have been scrapped. The pin-vise used a shorter specimen length, thereby saving material. Another advantage to the pin-vise arrangement is that the wire is subjected to minimal torque on loading.

Polarization studies were made on the wire in situ in the charging set-up using a Luggin probe-salt bridge assembly, a saturated calomel reference electrode (SCE), a suitable high quality potentiostat, a motorpotentiometer, milliammeter, and a recorder. The potential scanning rate was controlled using a motorpotentiometer at either 1500 or 15,000 mV/hr.

Optical metallography was completed on all the 4140 material and the HY-TUB material prior to the final drawing sequence. Some SEM fractography results have been obtained for the 4140.

C. RESULTS AND DISCUSSION

Since a fundamental portion of this investigation, (i.e., cathodic changing of the specimen) is electrochemical in nature, a description of the electrochemical properties [e.g., corrosion potential (E_{corr}) and the range of Tafel behavior] should be included if the system is to be well-defined. Several E_{corr} determinations as well as polarization curves were run on both materials. The 4140 specimens were prepared for testing as described in the experimental section.

Evidence as to the susceptibility of $\left(\frac{400}{202}\right)$ AISI 4140 to hydrogen-induced delayed failure came to light when several specimens fractured after a time when subjected to in situ cathodic charging while bearing no external load or only that load required to straighten the wire and hold it in place. Because of its pronounced susceptibility, $\left(\frac{400}{202}\right)$ was replaced with $\left(\frac{356}{202}\right)$ AISI 4140 in the investigation of the effects of varying loads and/or impressed cathodic currents or the cathodic cell potential. A continuous test was made at a constant load (0.94 lv) during which the applied cathodic currents of 0.50, 5.00, and 24.8 mA were applied for varying lengths of time in a varying sequence (see Fig. 285). The points on the graph represent the time and potential at which the

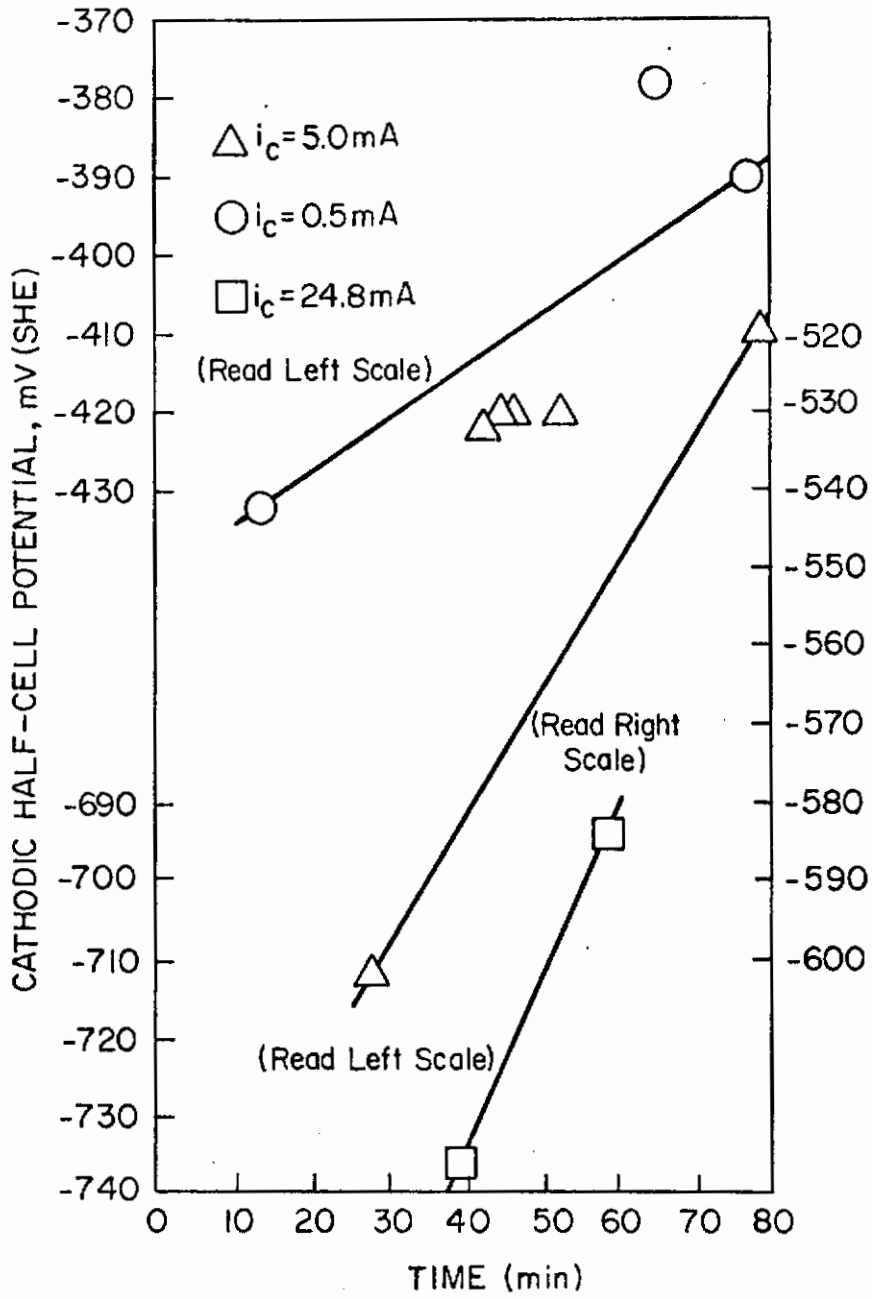

Fig. 285 - The Effect of Prior Applied Cathodic Currents on the Cathodic Half-Cell Potential When Different Currents Are Subsequently Applied During a Continuous, Constant Load Test of a 2-Inch Length of 356/202 Wire in 1N H_2SO_4 + 1g/ℓ $CS(NH_2)_2$

application of current was terminated. These results indicate that if a high cathodic current is applied, subsequently applied cathodic currents will yield more positive cathodic cell potentials; i.e., the cathode surface is more easily activated. This effect is more pronounced with increasing current. From the results of single tests (i.e., a new specimen and fresh electrolyte for each load/current combination, see Fig. 286) it was observed that the cathodic cell potential increases with increasing tensile load while under galvanostatic conditions. This correlates with the increased current from a strained electrode subjected to increased tensile load while under potentiostatic conditions.

Because $\left(\frac{356}{202}\right)$ AISI 4140 also failed when subjected to the more severe cathodic charging conditions encountered while determining a cathodic polarization curve, it was replaced by $\left(\frac{280}{155}\right)$ AISI 4140. This material showed itself to be least susceptible of all the 4140 material tested for delayed failure. It remained intact after several cathodic polarization scans to current densities greater than 800 mA/cm^2. The anodic polarization curve was quite reproducible (see Fig. 287a for AISI 4140 and Fig. 287b for $\left(\frac{300}{257}\right)$T HY-TUF). A reversed direction of potential scan was not attempted for the anodic curve because of the drastic change in the specimen surface after being exposed to high anodic overpotentials (η). The cathodic polarization curves, however, were determined by scanning over the same potential range in negative and positive directions. Large hysteresis behavior appeared related to the prepolarization effect on electrode potential values determined in earlier tests (see Figs. 285 and 286). Consequently, cathodic polarization curves were determined with prepolarizing treatments. One test was run as soon as 90% of the E_{corr} value had been reached (i.e., 120 seconds) to see if time in solution prior to the cathodic polarization determination had any effect on the subsequent polarization behavior. The specimen is usually left in solution for 1 hour so that steady-state conditions are established prior to the cathodic polarization determination. For the results of this investigation see Fig. 289.

The series of curves depicted in Fig. 288 duplicate the results of a similar series of tests run earlier. In each series, the initial polarization curves are practically identical, indicating good reproducibility and are represented in Fig. 289 by curve A. The most important area of the curve for the purpose of this investigation is the Tafel region. Curve G from Fig. 288 represents the limiting hysteresis condition in Fig. 289 (i.e., the uppermost curve). After completing the determination of curve G, the specimen was cathodically protected by application of 0.5 mA current for a period of 12 hours. The subsequent polarization behavior of this specimen is represented by the curve immediately below G, indicating that some recovery has occurred. Another specimen was exposed to solution for 18 hours under a cathodic current of 0.5 mA. Its polarization behavior is represented by the curve just above A in Fig. 289. The displacement of the curves to higher potentials

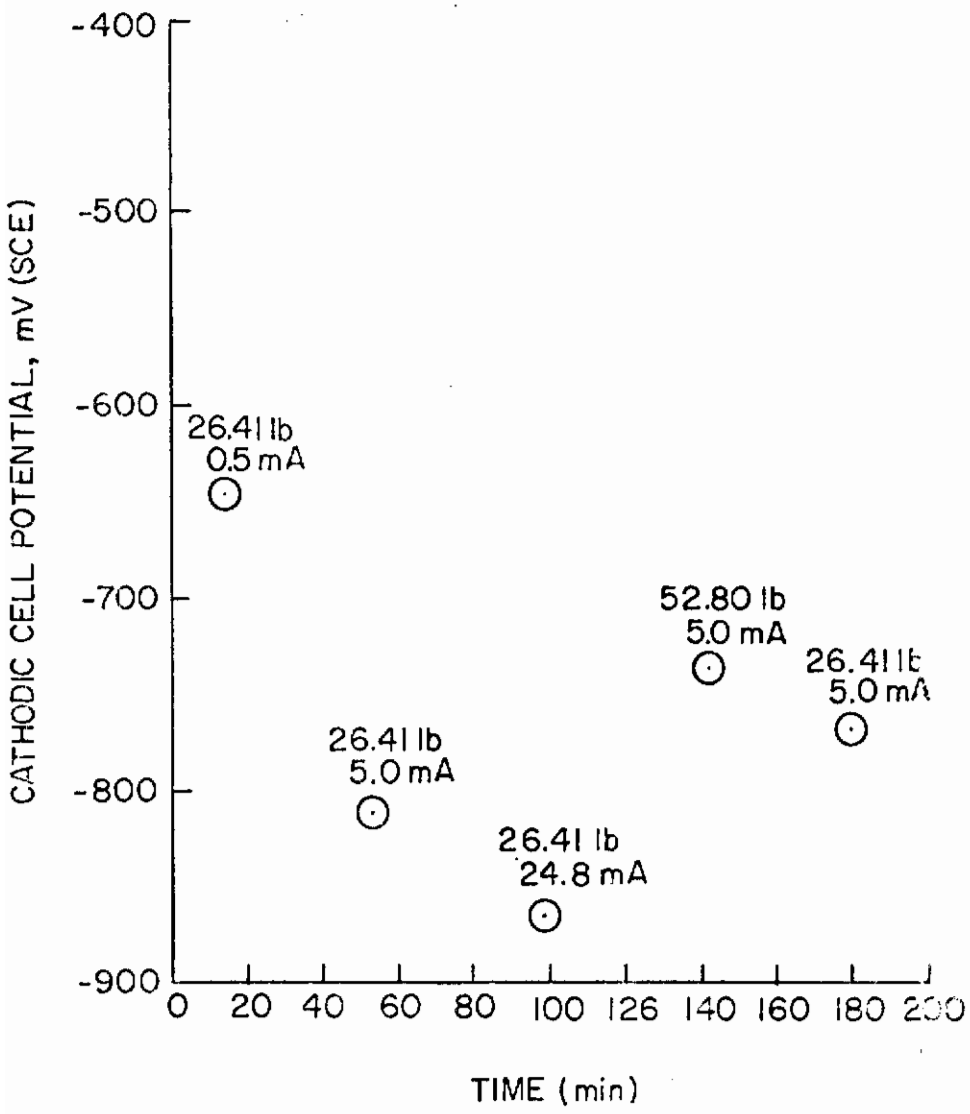

Fig. 286 - Cathodic Half-Cell Potentials for Various Load/Current Combinations for 356/202 AISI 4140 Wire Specimens in 1N H_2SO_4 + 1 g/ℓ CS $(NH_2)_2$

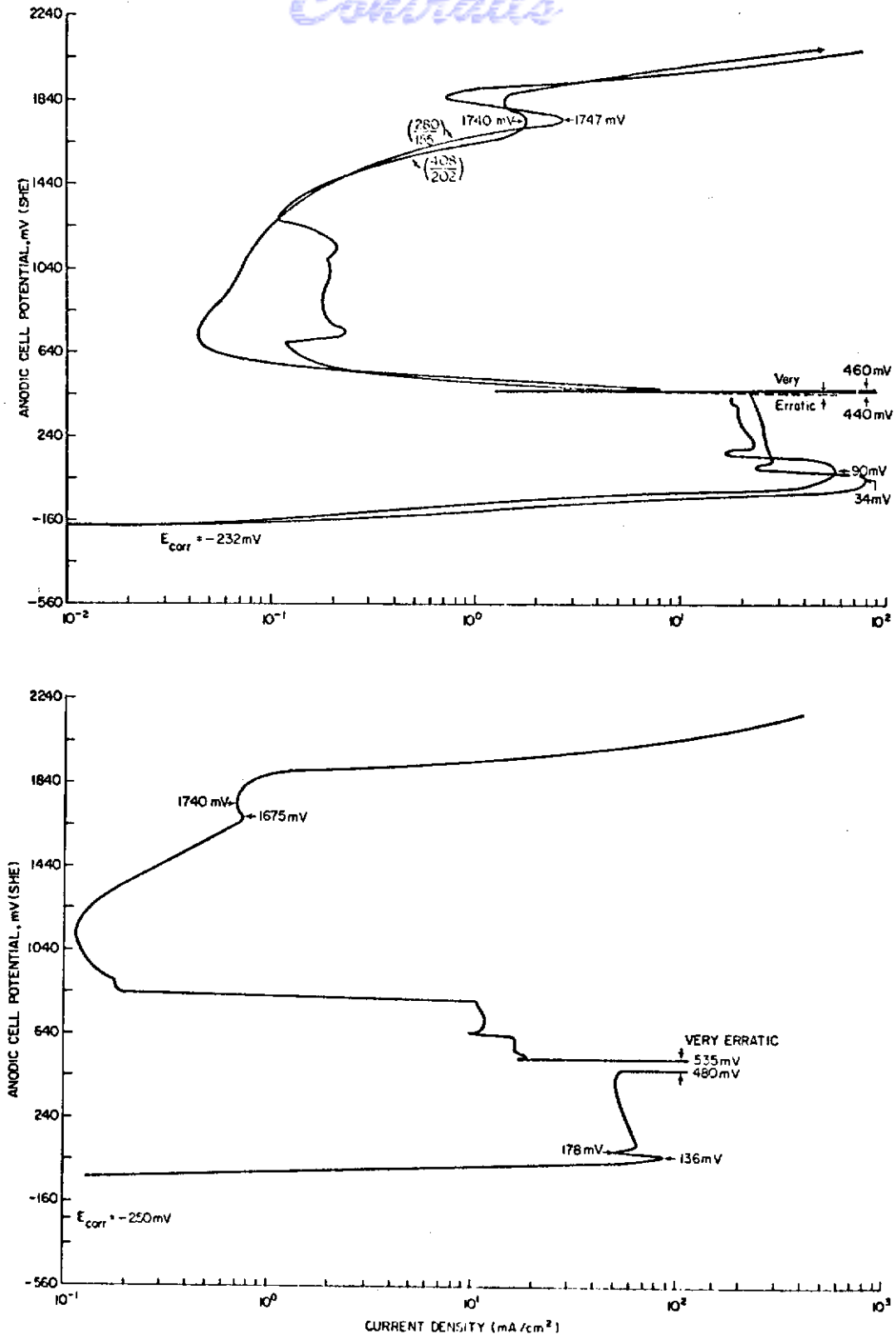

Fig. 287 - Anodic Polarization Behavior of AISI 4140 and HY-TUF Materials

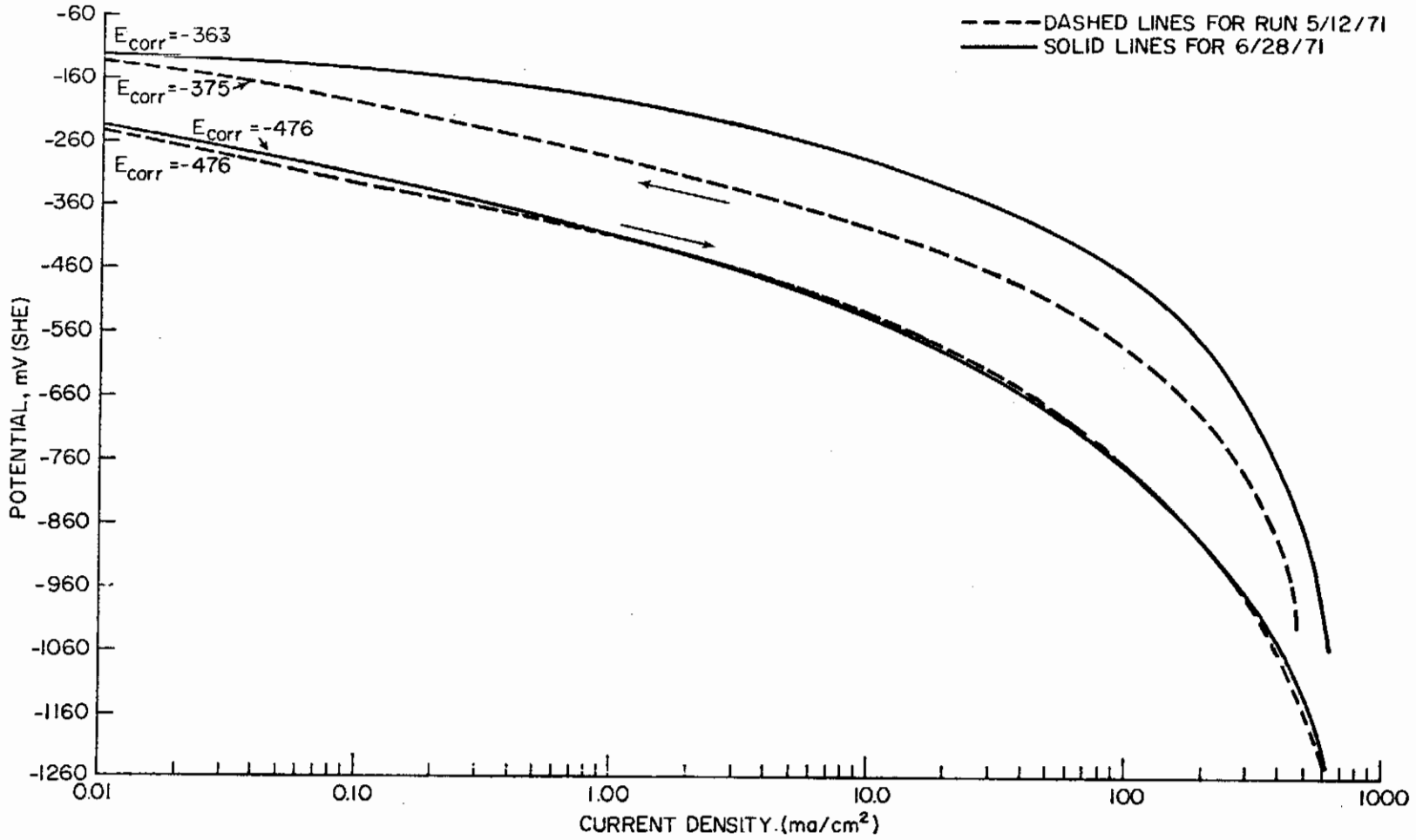

Fig. 288 - Cathodic Polarization Behavior of $\left(\frac{280}{155}\right)$ AISI 4140 C.D. Wire in 1N H_2SO_4 + 1 g/ℓ CS $(NH_2)_2$ (37° ± 1°F N_2 (saturated)

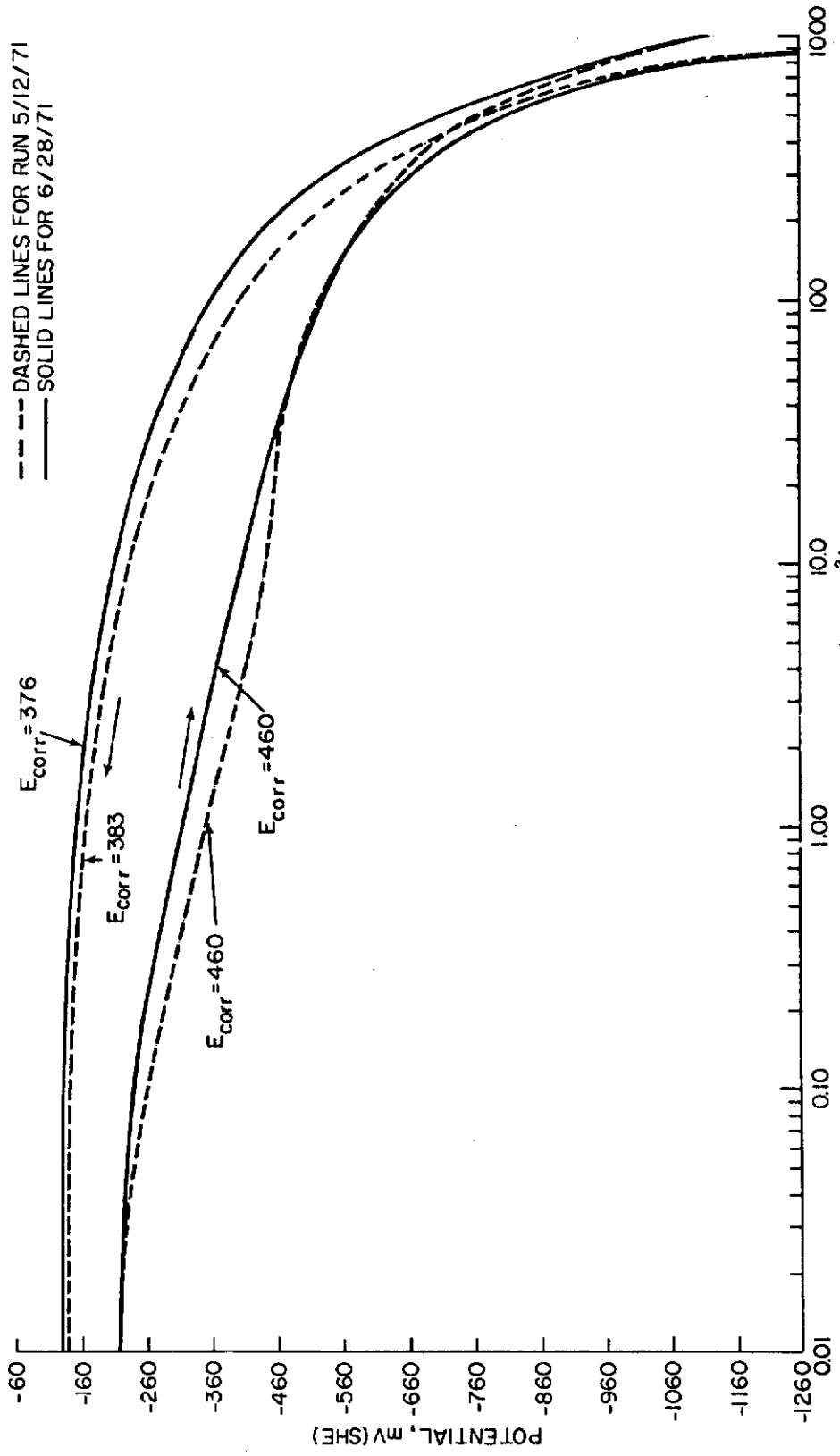

Fig. 288 - Continued

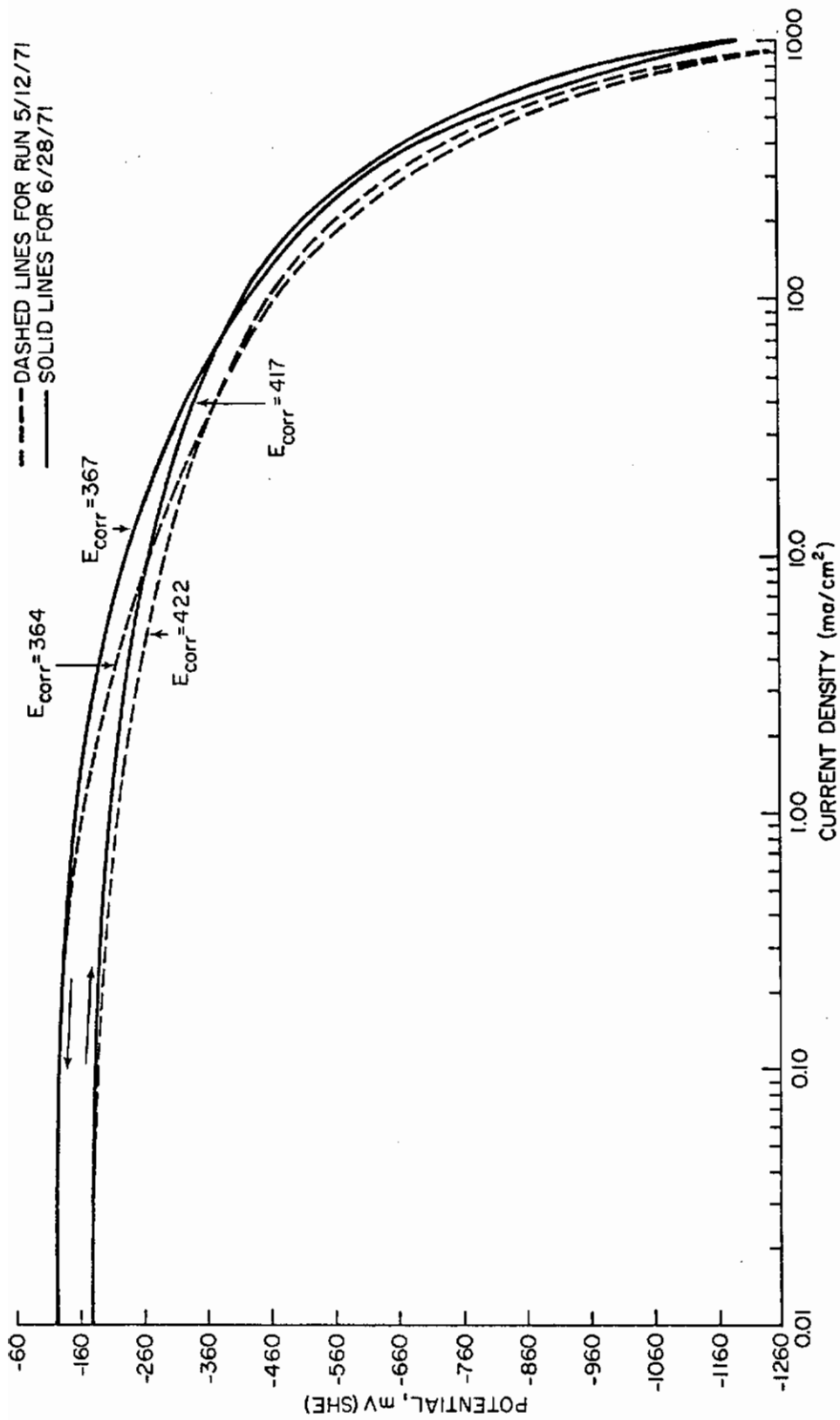

Fig. 288 - Continued

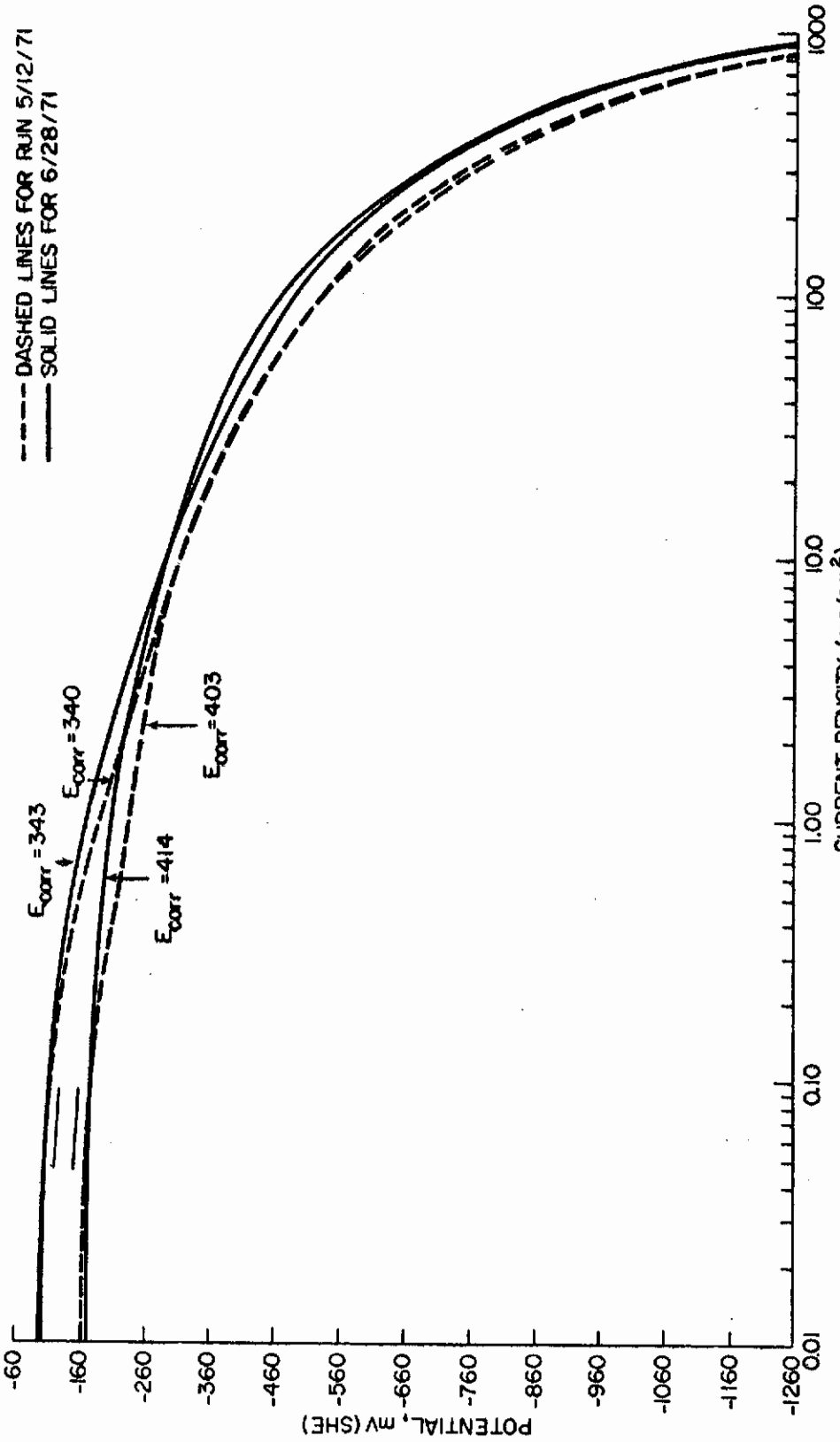

Fig. 288 - Continued

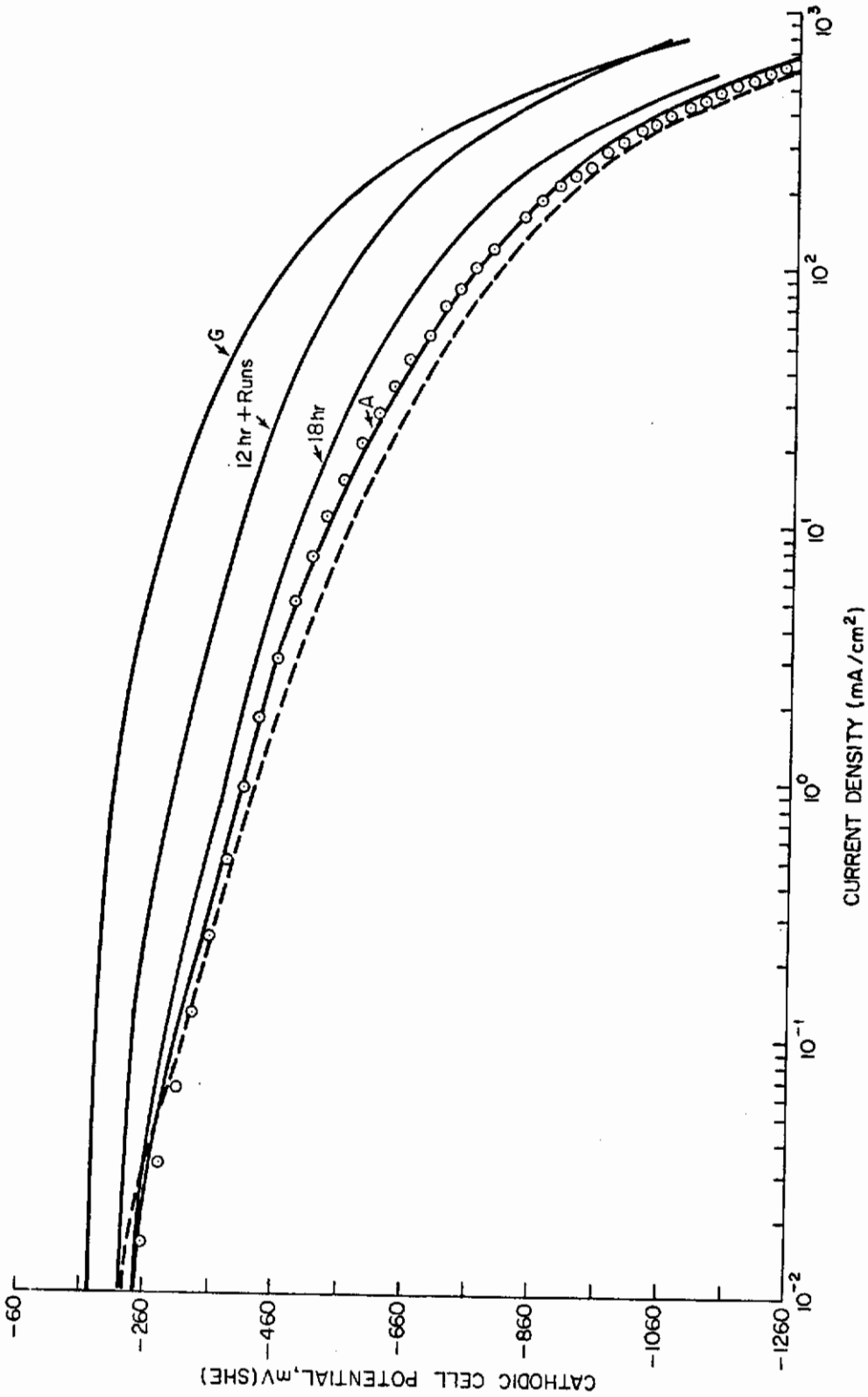

Fig. 289 - Results of the Investigation of Hysteresis Behavior in Cathodic Polarization of AISI 4140 C.D. Wire

with increased surface coverage by hydrogen correlates well with the effects seen in Figs. 285 and 286. The fact that G represents a limiting condition for the hysteresis effect is reasonable considering the current limiting behavior (hence, limiting surface coverage by hydrogen) observed in cathodic polarization curves. The polarization curve of the specimen exposed to the solution for only a short time to determine the effect of time in solution was located just below curve A, the normal polarization curve. This displacement could be reasoned on a basis of surface coverage by hydrogen also. However, it is more likely that specimens in solution undergo some surface roughening as a function of time as well as charging condition. Surface roughening would tend to increase the potential at a constant apparent current density and would be an irreversible effect under these conditions. Without conducting an in-depth investigation and considering the more elegant mechanisms such as described by G. C. Soltz,[188] it appears that the hysteresis effect observed in the cathodic polarization behavior of $\left(\frac{280}{155}\right)$ AISI 4140 wires is due to the irreversible effect of surface roughening and the reversible effect of surface coverage by hydrogen. The cathodic polarization behavior of $\left(\frac{300}{267}\right)_T$ HY-TUF wires in the same solution is depicted in Fig. 290. Once the cathodic behavior of the materials was determined, limiting experimental conditions could be chosen. It is beneficial to perform in situ charging tests at currents within the Tafel region because the hydrogen evolution reaction is the predominant reaction occurring then, thereby minimizing the experimental variables. The minimum cathodic charging current density was determined by determining the lower current limit of the Tafel region (i.e., the point at which the effect of the anodic current begins to appear in the polarization curve as it deviates from a straight line, see Fig. 291). Below this minimum current value cathodic protection is not guaranteed, and the specimen may be anodically attacked. The effects of the double layer also contribute to this deviation. The polarization current deviates from linearity at higher current densities because of concentration polarization. In addition, severe hydrogen evolution occurs at the specimen surface making reproducible charging conditions impossible to obtain. Cathodically charging the specimens in situ at current densities within the Tafel range should eliminate some spurious data, enhance the reproducibility of the test, and make interpretation of the results more meaningful. Transient measurements of the open circuit potential made when the electrolyte was added to the cell indicated that the transient E_{corr} obtained 90% of its final value in about 30 seconds. Transient E_{corr} measurements made with an applied cathodic current under the above conditions indicated that 90% of the final cathodic potential value was obtained in less than 30 seconds. These, as well as long-term measurements, indicated that there was no film on the specimen surface which would be removed in time with the specimen immersed in the electrolyte either at open circuit or under an impressed cathodic current. Therefore, we can say that during a static fatigue test the cathodic cell potential remained constant within a few millivolts after the initial 25 seconds and that the charging current was constant throughout.

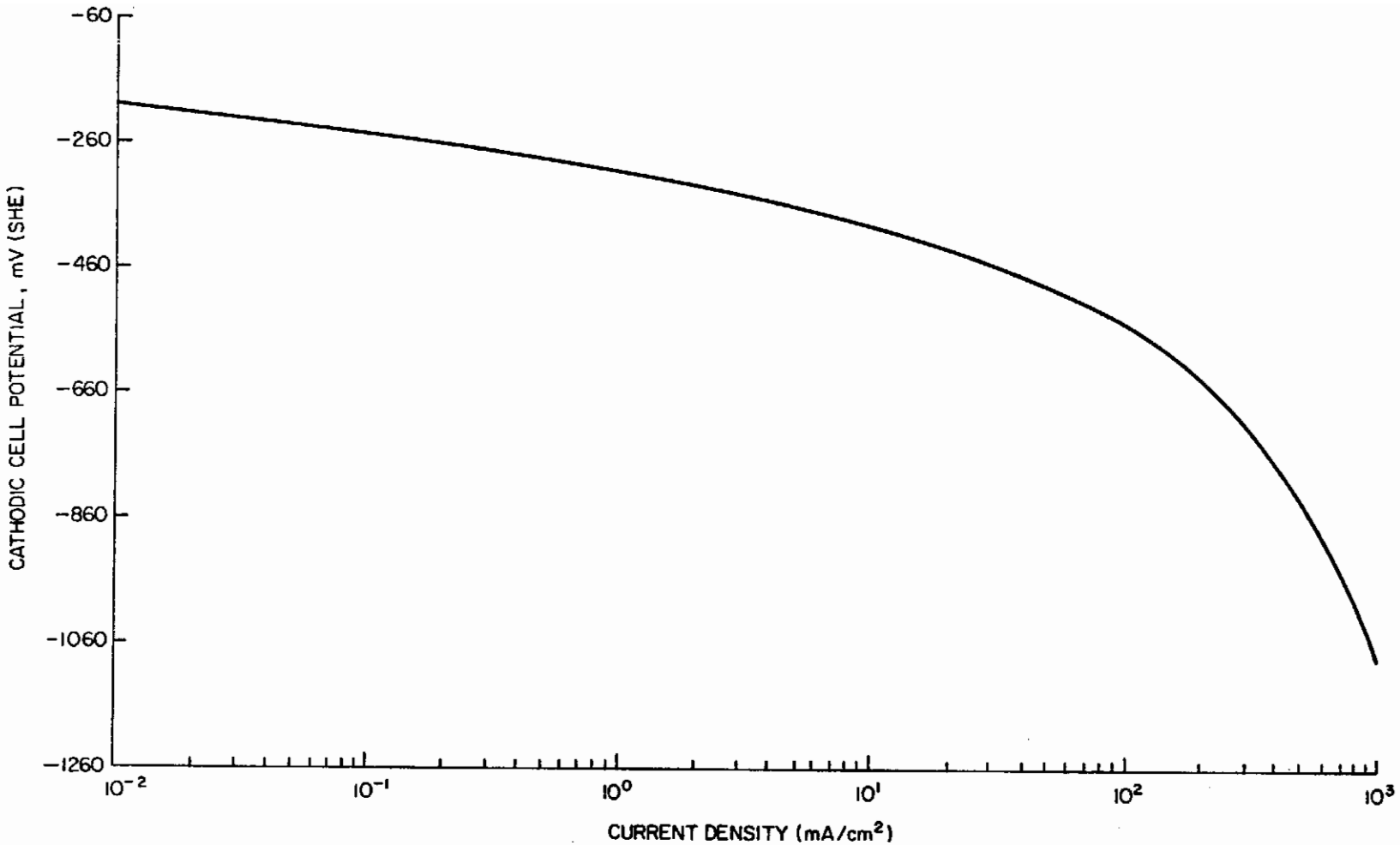

Fig. 290 - Cathodic Polarization Curve of a Hy-TUF C.D. Wire $\left(\frac{300}{267}\right)_T$ in 1N H_2SO_4 with 1 g/ℓ Thiourea Added (37° + 1°F N_2 saturated)

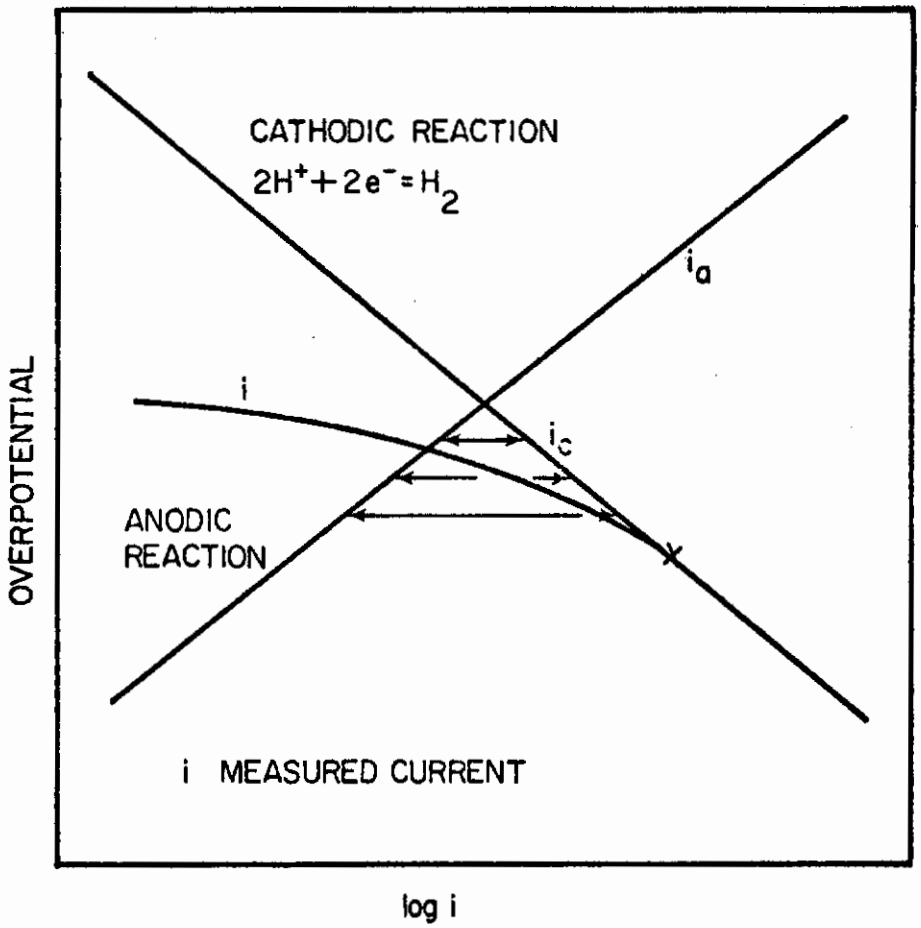

Fig. 291 - The Measured Current Represents the Difference Between the Cathodic and Anodic Reaction Currents

The static fatigue characteristics of the materials are represented in Figs. 292-294. An investigation of the reproducibility of the S-F curves was conducted by making a series of 12 test runs using $\left(\frac{408}{158}\right)$ AISI 4140 material at a charging current density of 1.0 mA/cm^2. The results appear in Table XLIV and Fig. 295. The variance was determined using the expression

$$V = \frac{\Sigma\ (\log t - \overline{\log t}\ )^2}{N-1}\ , \qquad (72)$$

where V = variance ,

t = time-to-fail,

$\overline{\log t}$ = average value of log (time-to-fail), and

N = number of values of t.

The standard deviation (σ) was taken as

$$\sigma = \sqrt{V}\ .$$

The resulting best curve was located between the static fatigue curves determined at current densities of 1.56 mA/cm^2 and 0.78 mA/cm^2.

The static fatigue curve is affected by the hydrogen content of the specimen (in this case the charging current density), the strength level of the material, and the size of the specimen. The expected effects of these variables on the static of fatigue curves have been as expected. Decreasing the charging current density increases the time-to-fail for a specimen and may result in the specimen exhibiting a lower critical stress (LCS) below a certain current density (hydrogen content). Increasing the size of the specimen leads to longer time-to-fail but will never prevent failure altogether. Decreasing the strength level will lead to longer time-to-fail and increasing values for the LCS. The appearance of an LCS indicates that the material is not susceptible to delayed failure under the existing charging conditions (i.e., hydrogen content) when loaded to levels below the LCS value. The S-F curves for the smaller diameter wires show the LCS more clearly. Correspondence of characteristic curve shapes between specimens of the same diameter is better than between those of different size.

The HY-TUF results show a general increase in time-to-fail when compared to the 4140 results. A size effect on time-to-fail is observed between the two specimens at the 300 ksi strength level, the larger specimen having the longer time-to-fail. It is also noted that the smaller of the two is less susceptible, according to the LCS criteria.

A study was initiated to determine if the embrittlement observed was reversible. Several other studies have been conducted which indicate that the embrittlement effects occurring during the incubation period

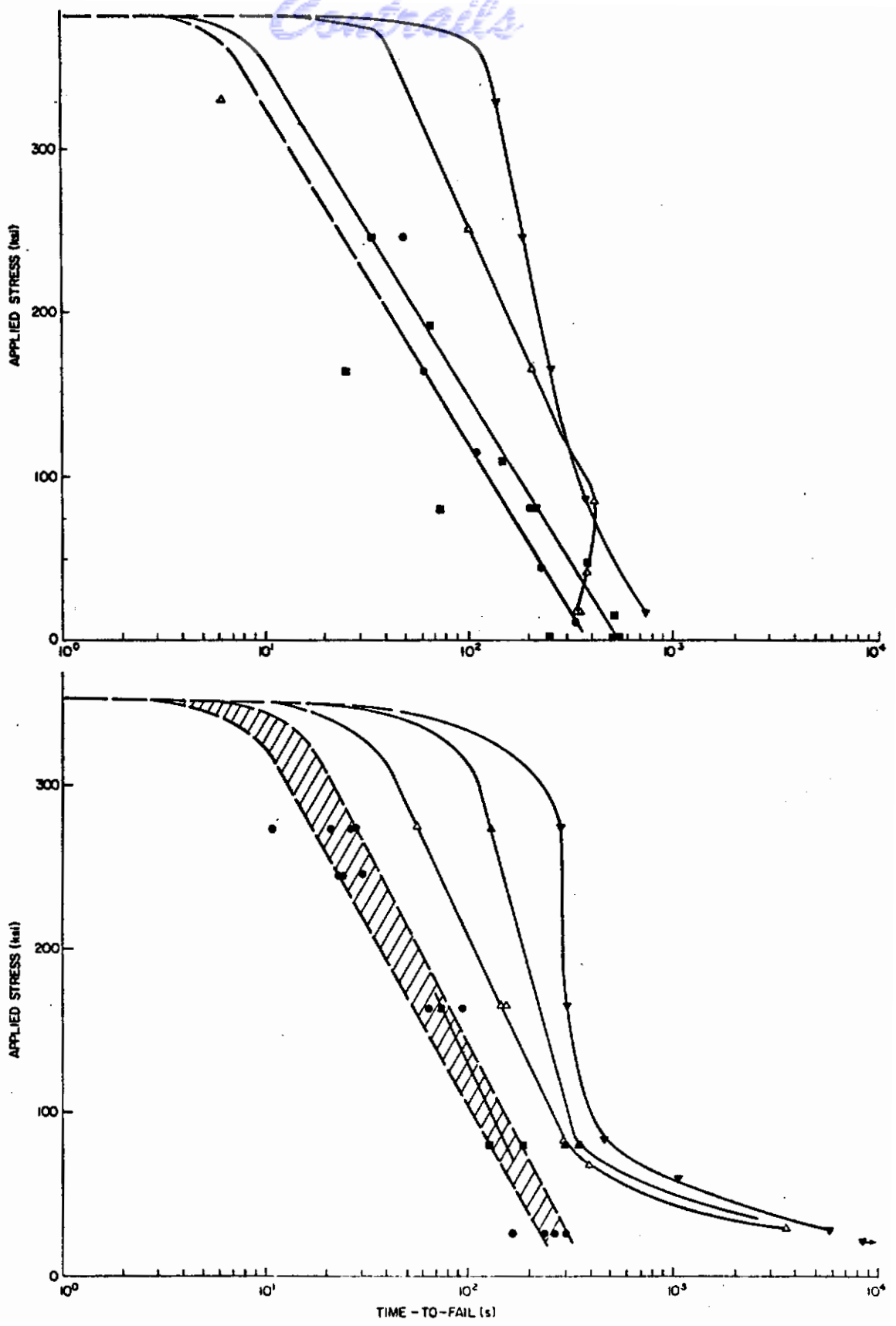

Fig. 292 - Static Fatigue Curves for 20.2 mil AISI 4140 C.D. Wire

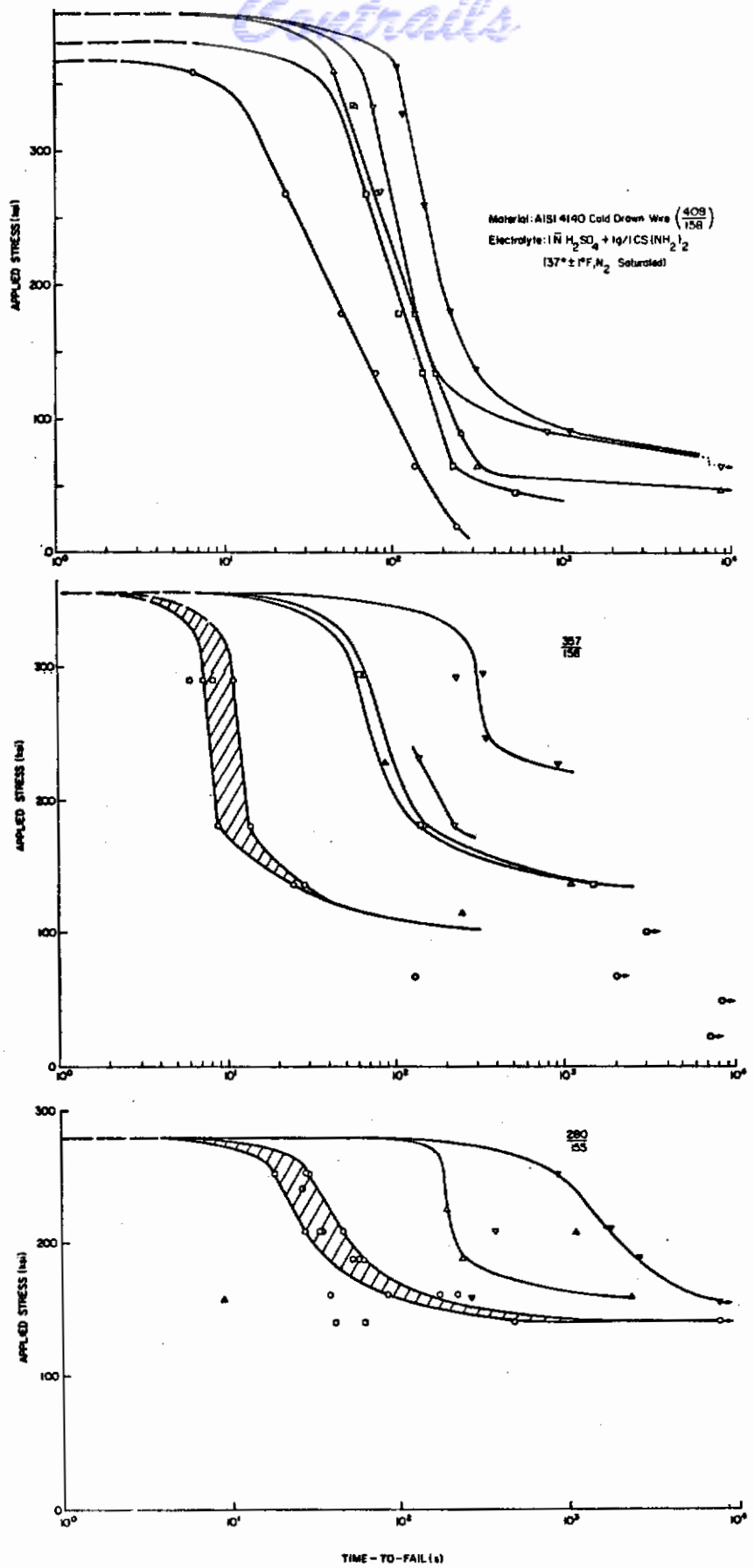

Fig. 293 - Static Fatigue Curves for 15.8 mil AISI 4140 C.D. Wire

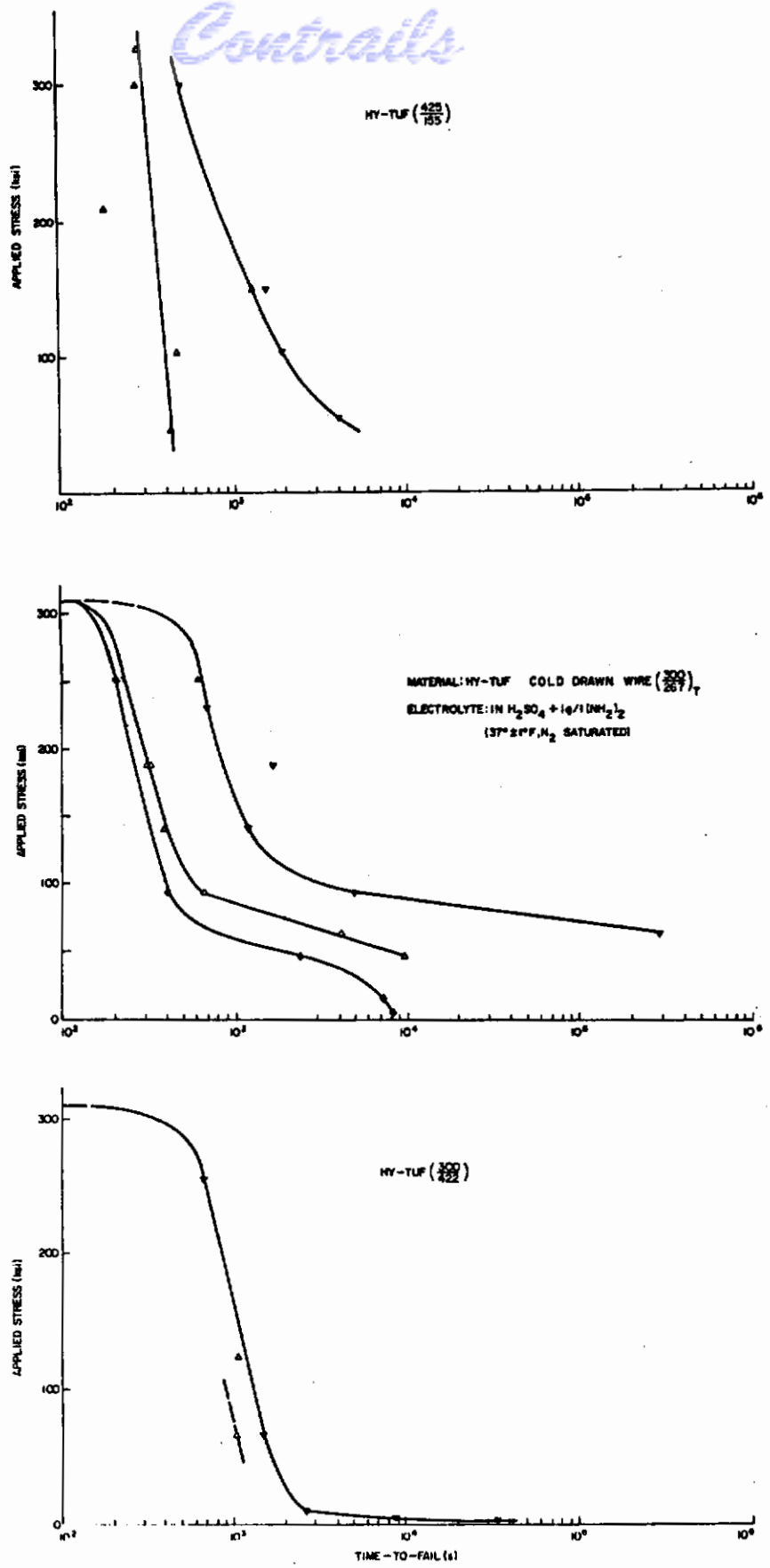

Fig. 294 - Static Fatigue Curves for All HY-TUF Wires

Table XLIV - Time-To-Failure for AISI 4140 C.D. Wire $\left(\frac{408}{158}\right)$ in 1 $\overline{N}$ H_2SO_4 + 1 g/ℓ $CS(NH_2)_2$ at 37.5 ± 1.5°F.

[A 2-inch length of specimen is exposed to the electrolyte. The hydrogen is electrolytically introduced into the specimen using a galvanostatically controlled, cathodic current (i_c = 1.0 mA/cm²)]

0.5 mA 4/13/71	1.0 mA 4/14/71	Test No / Load (Lb)	1 7/13/71	2 7/14/71	3 7/15/71	4 7/16/71	5 7/16/71	6 7/17/71	7 7/17/71	8 7/18/71	9 7/18/71	10 7/23/71	11 7/24/71	12 7/24/71
Fraction Loading	--	70.78	--	--	--		--	45.3	--	47.4	--	--	47.9	--
80.1	60.0	65.58	86.0	84.0	57.6	66.6	58.0	50.2	52.4	59.8	45.0	63.4	65.5	61.6
88.5	73.0	52.80	80.0	87.4	85.1	79.0	87.2	72.0	80.8	80.5	83.0	89.1	72.8	96.0
137.0	111.0	35.35	108.9	136.8	161.3	150.7	153.3	145.4	115.6	160.2	165.6	128.6	96.8	116.6
186.6	150.4	26.41	162.2	218.5	145.5	200.4		183.0		191.2	176.4	167.7	180.0	
837.0	--	17.92	--	271.6	257.9	278.4	250.0	258.2	284.3	240.7	248.2	233.0	215.6	
15,066.0	231.0	12.82	6 Inch Specimen Too Short	319.6	271.6	549.8	317.5	337.5	269.3	325.0	265.0	305.2	314.0	Stopped At 1500.0
--	538.0	8.94	Stopped At 57,060.0	Stopped At 30,240.0	3198.0	--	5556.0	--	375.0	--	117,384.0	2084.0	--	355.0

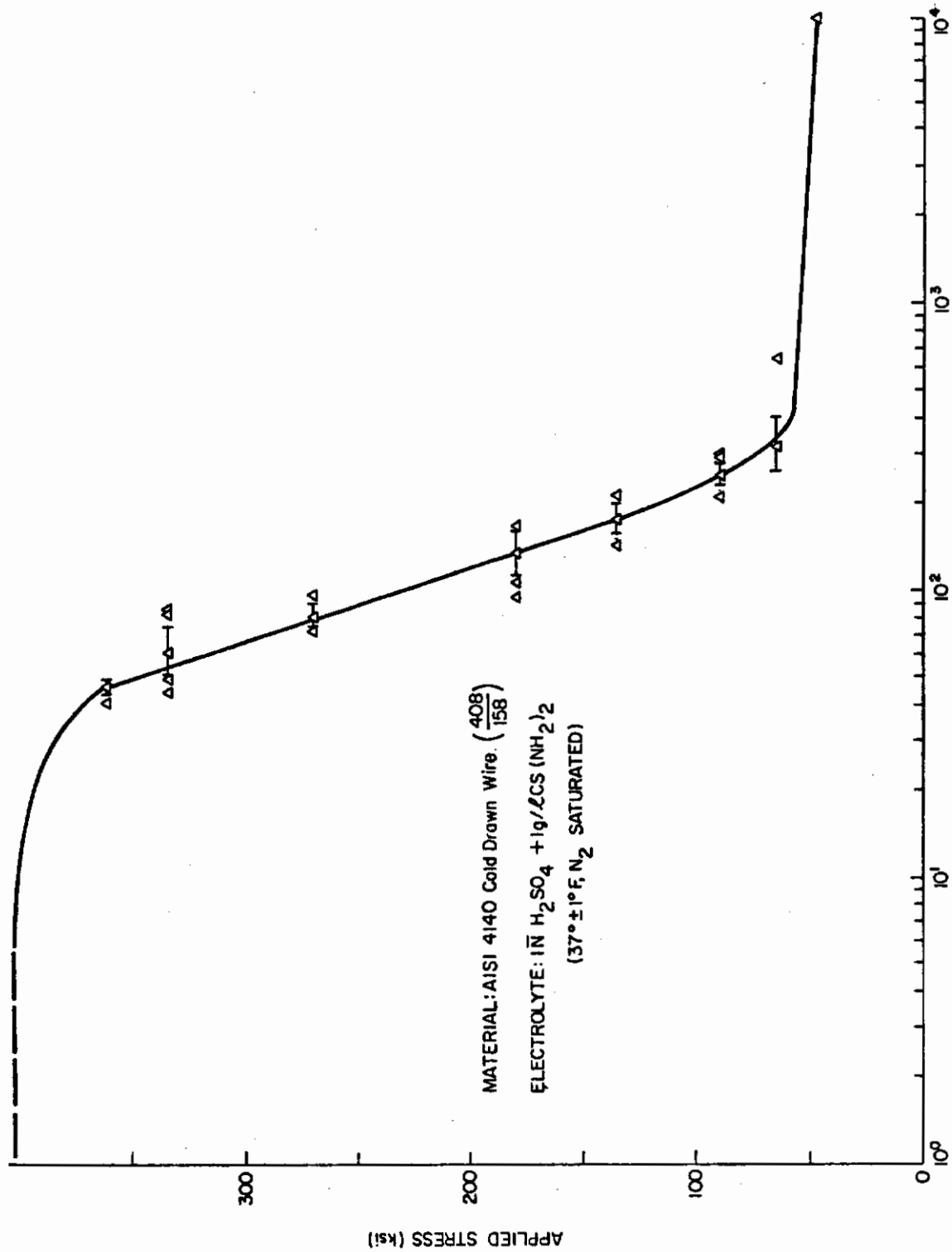

Fig. 295 - Static Fatigue Curve Obtained During Reliability Study for AISI 4140 C.D. Wire $\left(\frac{408}{158}\right)$

preceding crack initiation in a specimen showing susceptibility to delayed failure are reversible.

Considering the specimen to be primarily under a state of uniaxial longitudinal stress, one would expect that hydrogen introduced by maintaining the surface at a constant hydrogen chemical potential could be removed by simply lowering the surface chemical potential of hydrogen to some low value (e.g., 0.5 ppm H_2, the concentration in dry air) without actually having to unload the specimen. Considering the heterogeneous nature of the specimen and the complex microstress distributions within, the general lowering of the lattice hydrogen content by diffusion would be enhanced by unloading the specimen during the aging period, which was done. The specimen should be aged *in situ* since the investigation is for damage to the specimen accomplished during hydrogen charging under load. Removal of the specimen for any purpose raises the possibility of introducing extraneous and variable amounts of damage to the specimen. The material selected for the first investigation was $\left(\frac{408}{155}\right)$ AISI 4140. The initial charging period was 0.5 x (time-to-fail) as determined in the reproducibility study. A "bracketing" technique was used to determine an interval for a charging period during which failure would occur. A constant charging period of shorter duration was then used for the next series of tests. A test series was run for five charging periods or until failure occurred. If fracture occurred in the second interval of the test (i.e., the specimen was irreversibly damaged during the first interval), the charging period was shortened and the test series repeated using a new specimen. During this testing program it was evident that when the hydrogen content of the specimen increased above a certain value, accumulation would occur if the aging period was not long enough. This factor complicated interpretation of the test results. Eventually, a sufficiently long aging period was determined. After aging the specimen for 200,000 seconds, specimen failure could be attributed to permanent damage done to the specimen during charging and not to the complicating effect of hydrogen accumulated in addition to that introduced during the present charging period. Using the diffusion calculations of Crank[189] and $D = 0.79 \times 10^{-7}$ (cm^2/sec) determined by Steigerwald and Barth[190] for AISI 4340 at 32°F, it should take about 4400 seconds for the center of a 15.8 mil specimen to reach 90% of the surface concentration of hydrogen. Considering the ultrafine-grained nature of the material in this investigation as well as the indications of a uniform distribution of very fine carbides at grain and dislocation cell boundaries, it is not surprising that the time required for hydrogen effusion was more than an order of magnitude larger than that calculated for larger-grained microstructures and coarser precipitate particle distributions.[191,192] The results of the incubation study (Figs. 296 and 297) clearly show that the incubation period is reversible in materials exhibiting resistance to delayed failure.

The metallographic investigation of all the 4140 material and the starting HY-TUF material at magnifications of up to 2000X indicates that the material does contain inclusions and that the carbide size is

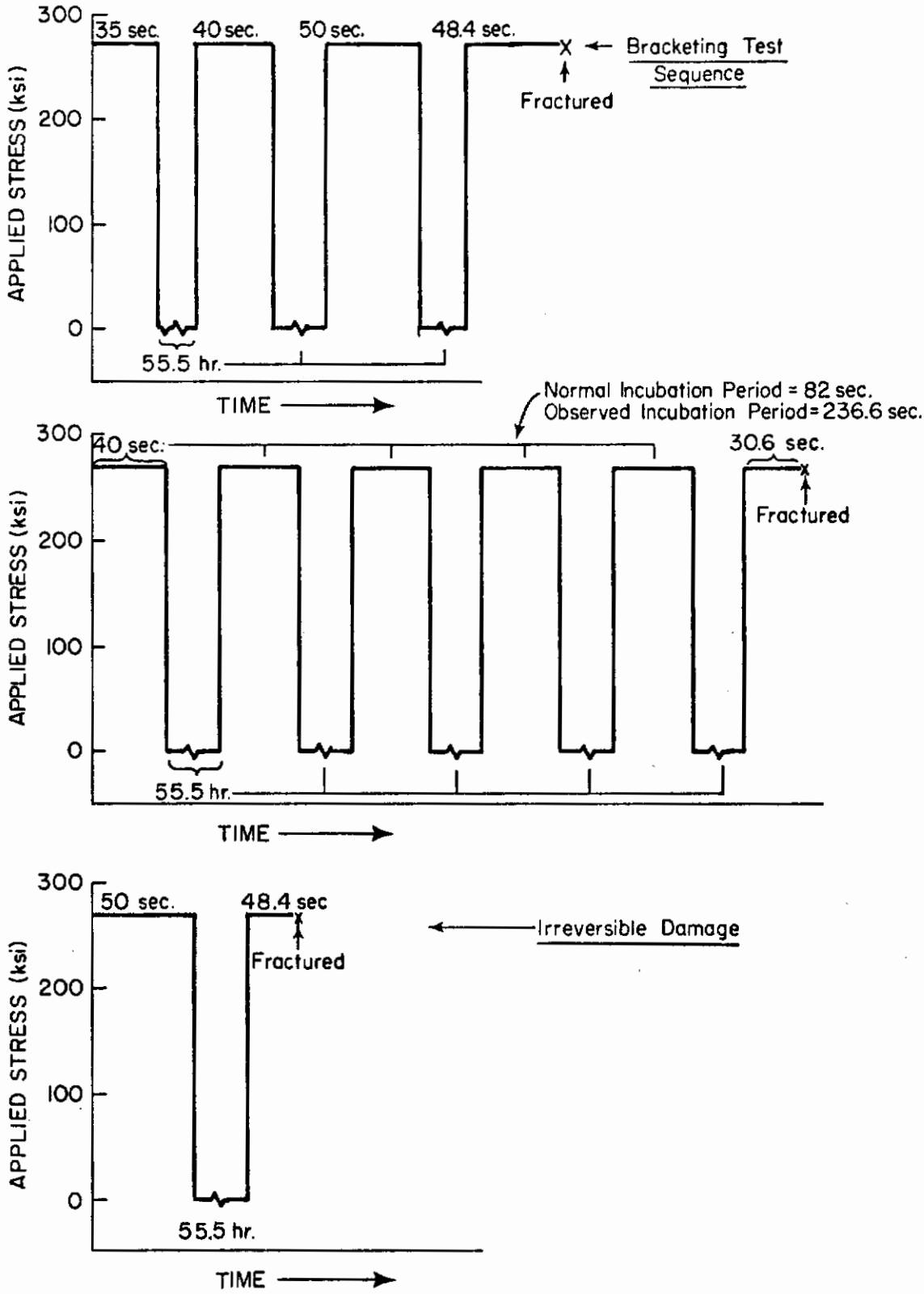

Fig. 296 - Schematic Diagram of Loading and Aging Treatments Used in Incubation Period Study of AISI 4140 C.D. Wire

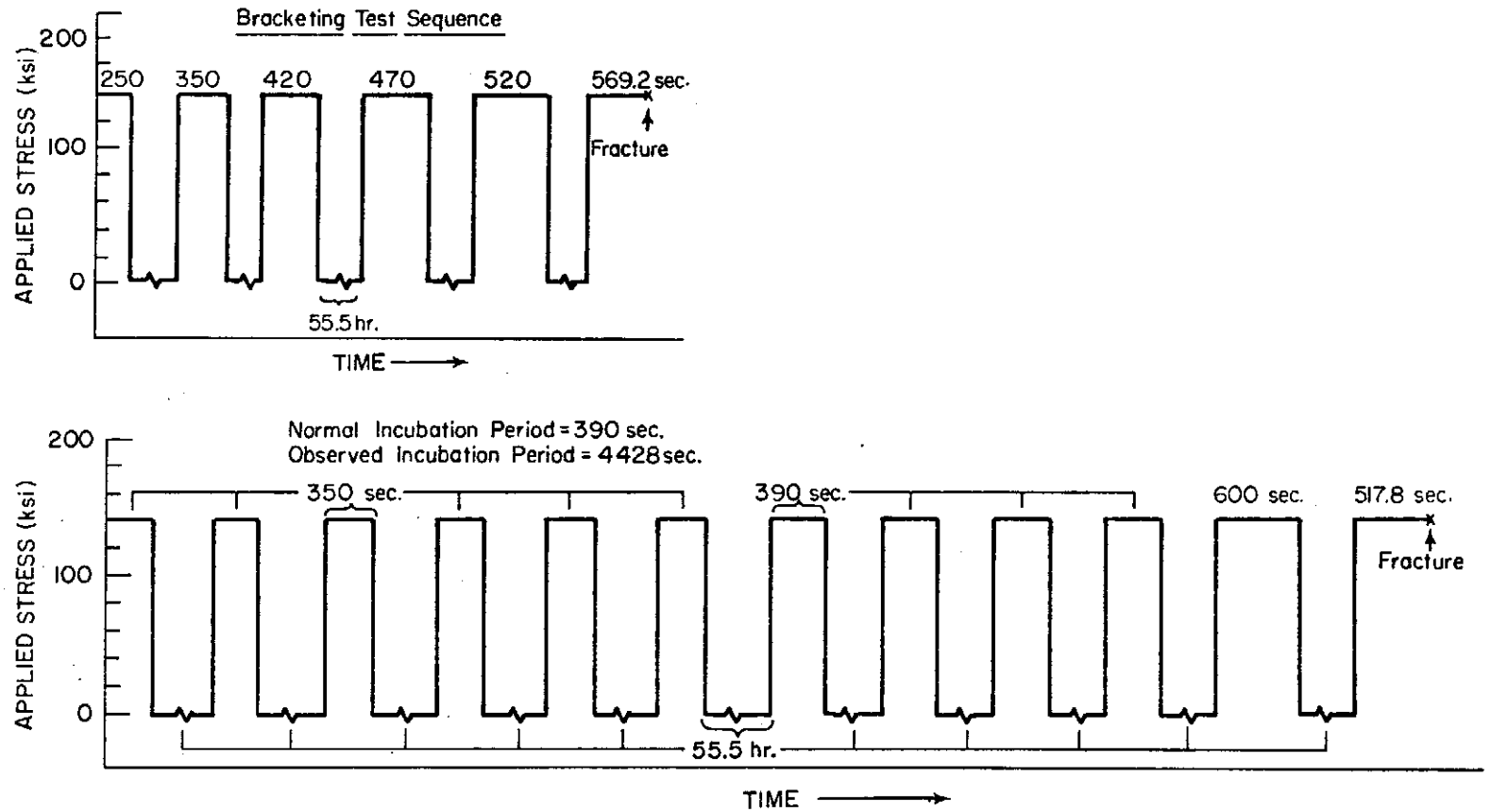

Fig. 297 - Schematic Diagram of Loading and Aging Treatment Used in Incubation Period Study of AISI 4140 C.D. Wire

fine and its distribution uniform. The grain boundaries were not resolved although texturing was quite evident.

The SEM fractography work showed the embrittling effect of hydrogen in terms of reduced necking most graphically in the case of $\left(\frac{280}{155}\right)$AISI 4140. The fracture surface was covered with dimples ranging in size from fine to very fine; i.e., the fracture occurred as a result of microvoid coalescence. Considering the nature of the fracture surface and that, in general, no single fracture initiation point was detected, the final fracture probably occurred as a result of multiple fracture nucleation. When the fracture nucleation density became high enough a crack opened and the rest of the failure resulted from material overload. The very fine and uniform nature of the dimples is consistent with the carbide distribution.

In some of the uncharged material, small equiaxed fragments of material (about 3 μm in diameter) appeared nearly to have been separated from the surrounding material by microvoid coalescence occurring on all surfaces. The surface of the fragments was covered uniformly with small ductile dimples. This may actually have been a subcell separating from the matrix as described above because of coalescence of voids nucleated at fine carbides which had precipitated on the subcell boundary.

A fracture feature observed in hydrogen-charged specimens which was not observed in uncharged specimens was an area more or less parallel to the specimen axis having a "fibrous" appearance. In Fig. 298 the formation of this type of surface can be seen. Areas of very fine dimple formation on the curved surfaces and fine dimple formation on the surface normal to the specimen axis can also be seen in the same picture. The picture shows necking down of the material between microvoids which are very much elongated parallel to the specimen axis. So even this "fibrous" surface which might be attributed to intergranular separation is formed in a ductile manner.

Considering the prior history of the material and the metallographic and fractographic results, one would expect the microstructure to consist of very small dislocation subcells together with very closely spaced fine carbide precipitates. The decrease in susceptibility to failure of the smaller wire can be attributed to the size of the microstructural features and the interaction of hydrogen with the high density of dislocations in cell walls in the heavily drawn wires.

D. SUMMARY

The feasibility of studying the susceptibility of ultrahigh-strength steel wires to hydrogen-induced delayed failure was determined using a simple qualitative test. The experimental variables were defined as clearly as possible to minimize spurious results. During polarization

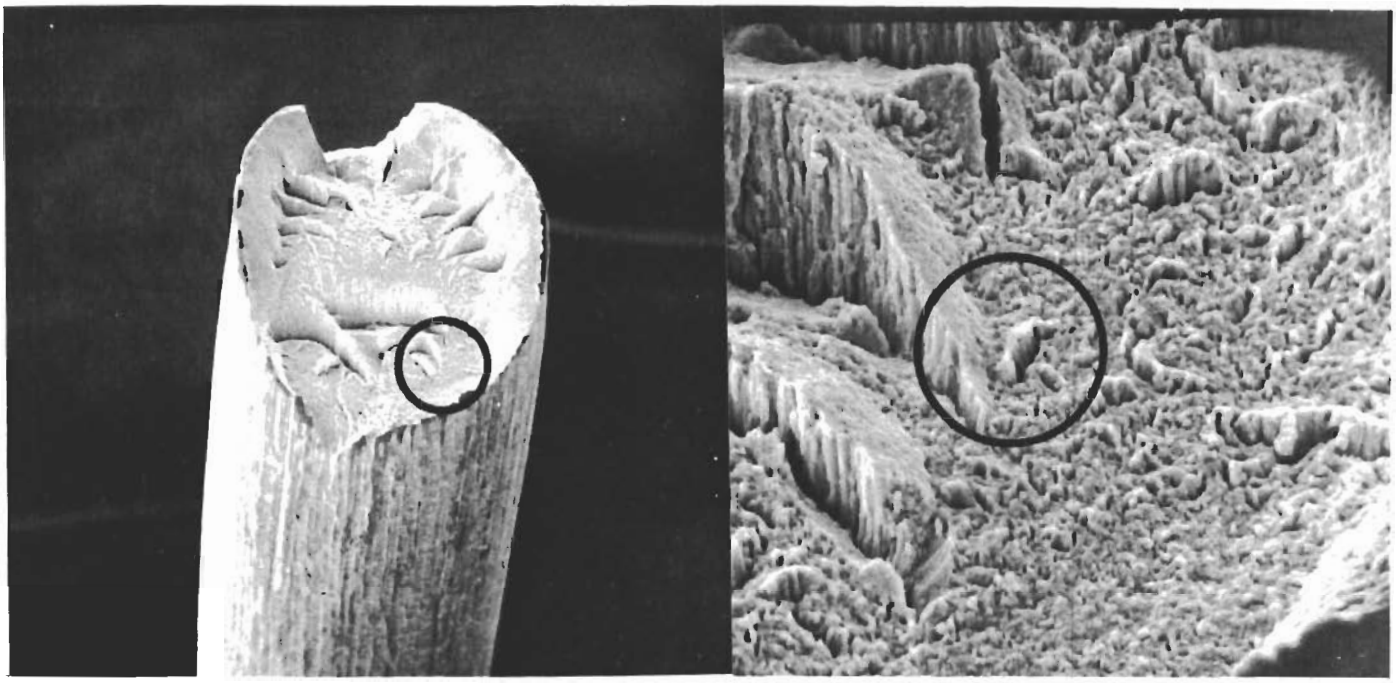

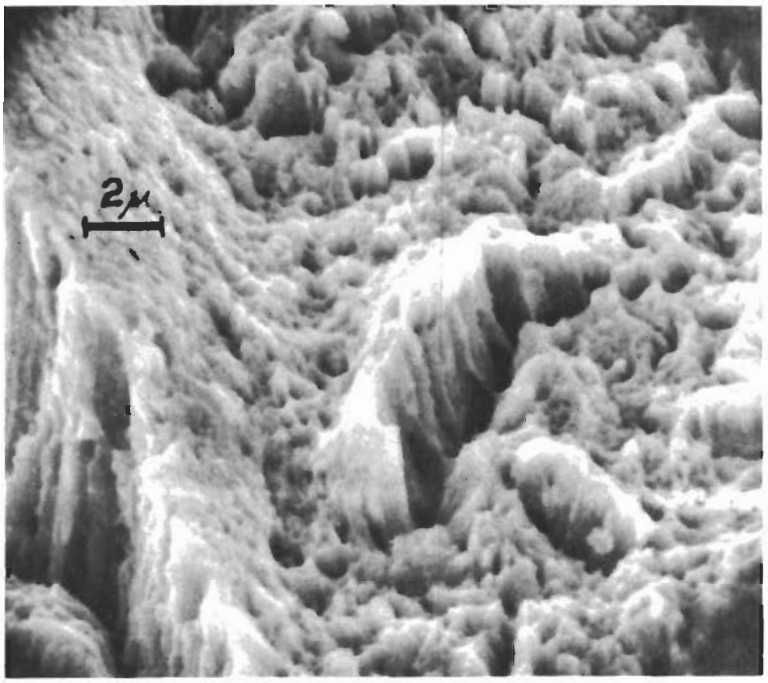

Fig. 298a - Formation of Fibrous Appearing Surface by Microvoid Coalescence

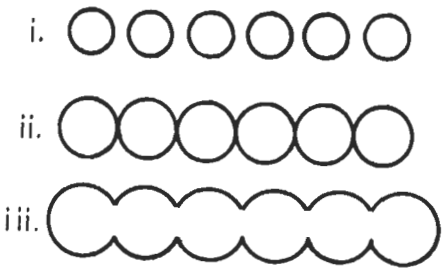

Fig. 298b - Microvoid Coalescence Model

studies an hysteresis effect was observed and investigated. It does not occur under the conditions of the experiment. Standard static-fatigue curves were determined for the materials while cathodically charging hydrogen in situ as a function of charging current density (i.e., hydrogen content), specimen strength level, and size. An incubation period study indicated that the embrittling effect due to hydrogen was reversible during the incubation period prior to crack initiation. A low apparent diffusivity of hydrogen in the material was also observed during the incubation tests. SEM examination of the specimen fracture surface indicated that all the fracture surface was formed by microvoid coalescence.

E. CONCLUSIONS

1. Surface roughening and surface coverage by hydrogen are factors in the hysteresis behavior observed during polarization studies of AISI 4140 and HY-TUF heavily cold-drawn wires.

2. The small dislocation subcell size and small intercarbide spacing are responsible for the high strength of the materials being investigated.

3. The trapping character of the microstructure is conducive to a low apparent diffusivity of hydrogen in the material.

4. The specimen fracture surfaces were all formed by microvoid coalescence.

5. A reversible incubation period is exhibited by the AISI 4140 and HY-TUF cold-drawn wires studied.

6. Decreased susceptibility to hydrogen-induced delayed failure is due to the fine size of the microstructural features and the interaction of hydrogen with the high density of dislocations in the cell walls of the drawn wire.

REFERENCES

1. C. Edeleanu, Metallurgica, 50 (1954), 113.

2. J. D. Sudbury, O. L. Riggs, Jr. and D. A. Shock, Corrosion, 16 (1960), 47t and 55t.

3. O. L. Riggs, Jr., M. Hutchison, and N. L. Conger, Corrosion, 16 (1960), 58t.

4. A. O. Fisher and J. F. Bradly, Corrosion, 19 (1963), 37t.

5. M. G. Fontana and N. D. Greene, Corrosion Engineering, McGraw-Hill (1967).

6. W. D. France and N. D. Greene, "Passivation of Crevices During Anodic Protection," Corrosion, 24 (1968), 247-51.

7. M. N. Fokin and V. A. Timonin, Doklady Akademic Nauk SSSR 164, (1965), 50.

8. C. M. Chen, F. H. Beck, and M. G. Fontana, Corrosion, 27 (1971), 77-83.

9. C. M. Chen, F. H. Beck, and M. G. Fontana, Corrosion, 26 (1970), 135-140.

10. E. J. Timmer, Master's Thesis, The Ohio State University, (1969) (see also Section II F).

11. R. J. Wasilewski and G. L. Kehl, "Diffusion of Hydrogen in Titanium," Metallurgia XL, 50 (November, 1954), 301.

12. N. J. Petch, J. Iron and Steel Institute, 173 (1953), 25.

13. J. D. Eshelby, F. C. Frank, and F. R. N. Nabarro, Phil. Mag., 42 (1951), 351.

14. A. N. Stroh, Proc. Roy. Soc., 223 (1954), 404-14.

15. W. B. Robertson and A. S. Tetelman, Strengthening Mechanisms in Solids, ASM, (1960).

16. D. N. Fager and W. F. Spurr, Transaction of ASM, 61 (1968), 283.

17. D. A. Mauney and E. A. Starke, Jr., Corrosion, 25 (1969), 177.

18. H. L. Gegel, H. B. Kirkpatrick, and C. M. Swinning, Corrosion, 25 (1969), 215.

19. H. L. Gegel and S. Fujishiro, J. Less-Common Metals, 17 (1969), 305.

20. J. R. Ambrose and J. Kruger, Corrosion Science, 8 (1969), 119.

21. L. R. Leith, Joe W. Hightower and C. G. Harkins, Corrosion (To be published).

22. S. Kishimoto, J. Phys. Chem., 66 (1962), 2694.

23. I. Uhara, S. Yanagimoto, G. A. Adachi, and S. Teratani, J. Phys. Chem., 66 (1962), 2691.

24. T. R. Beck and M. J. Blackburn, AIAA Journal, 6 (1968), 326.

25. K. E. Weber, J. S. Fritzen, D. S. Cowgill, and W. C. Gillchriest, "Accelerated Crack Propagation of Titanium by Methanol, Halogenated Hydrocarbons, and Other Solution," DMIC Memorandum 228, 6 March 1967, p.39.

26. W. S. Deforest, paper presented at the Western Regional Meeting of N.A.C.E. San Diego, California, Sept. 1968.

27. R. L. Horst, Jr., E. H. Hollingsworth, and W. King, Corrosion, 25 (1969), 199.

28. F. H. Cocks, J. F. Russo, and S. B. Brummer, Corrosion, 24 (1968), 206.

29. A. J. Sedriks, J. A. Green, and R. W. Slattery, "S.C.C. and Corrosion Behavior of Ti-Al Alloys in Methanol Ildine Solutions," Corrosion, 24:6, (1968), 172.

30. E. G. Haney, "Investigation of S.C.C. of Ti Alloys," Mellon Institute, Semi-Annual Progress Report No. 1, (November 30, 1966).

31. R. Wenk, Master's Thesis, The Ohio State University, (1968).

32. R. Cocks, J. Russo, and S. Brumner, "The Separation of Corrosion and Stress Effects in Stress Corrosion: Ti-Al-4V in Bromine-Methanol Solutions," J. Electrochem. Soc., (May, 1968).

33. R. Cochran, Master's Thesis, The Ohio State University, (1966).

34. R. Green and J. Myers, "Effect of Grain Size on Incubation and Propagation of S.C.C. in Type 302 Steel," Corrosion, 24 (1968), 5.

35. I. A. Menzies and A. F. Averill, "The Anodic Behavior of Ti in HCl-Methanol Solutions," Electrochemica Acta, 13 (1968), 801.

36. F. W. Fink and R. S. Peoples, "The S.C.C. of Ti and Ti Alloys," TML Report No. 84, (September 15, 1957).

37. J. R. Aylward and E. Whitener, "Dissolution of Zr in HCl-Methanol," J. Electrochem. Soc., (February, 1962).

38. T. R. Beck, "S.C.C. of Ti Alloys," Quarterly Progress Report, Boeing Corp., (June 30, 1967).

39. Ming Chen, private communication.

40. J. C. Scully, "S.C.C. of Alpha Titanium Alloys at Room Temperature," Corrosion, 24:6, (1968).

41. L. W. Berger, D. N. Williams, "Hydrogen in Ti-Al Alloys," Trans AIME, (August, 1958).

42. H. A. Robinson, P. D. Frost, and W. M. Paris, "Effect of Hydrogen on Some Mechanical Properties of Ti Alloy Heat Treated to High Stress," Trans AIME, (August, 1958).

43. J. C. Scully, Corrosion Science, 7 (1967), 197.

44. P. J. Fopiano, M. G. Bever, and B. L. Averback, "Phase Transformations and Strengthening Mechanisms in the Alloy Ti-6Al-4V," Trans. Quarterly A.S.M., 62 (June, 1969), 324.

45. E. G. Haney, W. R. Wearmouth, G. Goldberg, R. F. Ernsberger, and W. T. Brehm, "Investigation of Stress Corrosion Cracking of Titanium Alloys," Mellon Institute Progress Report No. 3, NGR-39-008-014, (November, 1967).

46. E. G. Coleman, D. Weinstein and W. Rostoker, "On A Surface Energy Mechanism for Stress-Corrosion Cracking," Acta Met, 9 (1961), 491.

47. D. T. Powell and J. C. Scully, "Stress Corrosion Cracking of Alpha Titanium Alloys at Room Temperature," Corrosion, 24 (1968), 151.

48. V. L. Barnwell, J. R. Myers, and R. K. Saxer, "Effect of Grain Size on Stress Corrosion of Type 302 Austenitic Stainless Steel," Corrosion, 22 (1966), 261.

49. G. Sanderson, D. T. Powell, and J. C. Scully, "Metallographic Studies of Stress Corrosion Cracking of Titanium Alloys in Aqueous Chloride Solutions," Proceedings of the International Conference on Fundamental Aspects of SCC, The Ohio State University, (September, 1967).

50. Discussion, "Chemical and Environmental Behavior," The Science, Technology and Application of Titanium, edited by Jaffee and Promisel, Pergamon Press, (1970), 324.

51. N. D. Tomashov, R. M. Altovskiy, and V. B. Vladimirov, Ref. 49.

52. A. J. Sedriks, P. W. Slattery, and J. A. S. Green, "Failure of Alpha Titanium in Methanol-Hydrochloric Acid-Water Solutions," Trans. A.S.M., 61 (1968), 625.

53. A. J. Sedriks and J. A. S. Green, "Stress Corrosion Cracking of Titanium in Organic Liquids," RIAS Technical Report 69-11, (August, 1969).

54. I. R. Lane and J. L. Cavallaro, "Applications of Related Phenomena in Titanium Alloys," ASTM STP 432, American Society for Testing and Materials, Philadelphia, Pa., (1967), 147.

55. R. E. Johnson, "NASA Experiences with Ti-6Al-4V in Methanol," DMIC Memorandum 228, Battelle Memorial Institute, (March, 1967), 2.

56. J. C. Williams, " Some Observations on the Stress-Corrosion Cracking of Three Commercial Titanium Alloys," Trans. A.S.M., 60 (1967), 646.

57. J. C. Scully, "Kinetic Features of Stress-Corrosion Cracking," Corrosion Science, 7 (1967), 197.

58. M. J. Blackburn and J. C. Williams, "Metallurgical Aspects of the Stress Corrosion Cracking of Titanium Alloys," Proceedings of the Conference on Fundamental Aspects of SCC, The Ohio State University, NACE, Houston, Texas (1967), 620.

59. G. Sanderson and J. C. Scully, "Hydride Formation in Corroded Titanium Alloys," Corrosion Science, 6 (1966), 541.

60. T. R. Beck, M. J. Blackburn, and M. O. Speidel, Quarterly Progress Report No. 11, NAS 7-489, (March, 1969).

61. T. R. Beck, "Electrochemical Mechanism in the Stress Corrosion Cracking of Titanium Alloys," The Science, Technology and Application of Titanium, edited by Jaffee and Promisel, Pergamon Press, (1970), 239.

62. F. Mazza, Werkstaffe und Korrosion, 3 (1969), 199.

63. E. G. Haney and R. W. Wearmauth, Corrosion, 25 (1969), 87.

64. H. Herrigel, "Titanium U-Bends in Organic Liquids and the Effect of Inhibitors," DMIC Memorandum No. 228, Battelle Memorial Institute, Columbus, Ohio (March 6, 1967).

65. H. Lund and J. Bjerrum, Berichte der Chemischem Gesellshaft, 64 (1931), 210.

66. K. Fischer, Angew. Chem., 48 (1935), 394.

67. J. Mitchell and D. M. Smith, Aquametry, Interscience Publishers, Inc., New York, (1948), p. 86.

68. G. Charlot and B. Tremillon, Chemical Reactions in Solvents and Melts, Pergammon Press, (1969), 280.

69. J. R. Myers, E. G. Gruenler, and L. A. Smulczenski, Corrosion, 24 (1968), 352.

70. I. J. Loomba, Master's Thesis, The Ohio State University, 1971 (see also Section II G).

71. N. D. Tomashov, Passivity of Metals.

72. M. Stern and H. Wissenberg, J. Electrochem. Soc., 106 (1959), 755.

73. D. Schlain and J. S. Smatko, J. Electrochem. Soc., 99 (1952), 417.

*74. A. P. Brynza and V. P. Fedash, Zashchita Metallov, 4 (1968), 228.

75. V. A. Larionov and N. M. Pultsin, Zashichita Metallov, 4 (1968), 513.

76. A. M. Sukhotin and L. I. Tungusova, Zashchita Metallov, 4 (1968), 5.

77. R. Otsuka, J. Metals, 9 (Trans. A.I.M.E.) (1957), 75.

78. R. Otsuka, Corrosion Engineering (Japan), 15 (1966), 491.

79. Von D. Franz and H. Göhr, Ber. Bunsengesell. Phisik. Chemie., 67 (1963), 680.

80. R. D. Armstrong, J. A. Harrison, H. R. Thirsk, and R. Whitfield, J. Electrochem. Soc., 117 (1970), 1003.

81. N. T. Thomas and Ken Nobe, J. Electochem. Soc., 117 (1970), 622.

82. F. F. Faizullin and D. A. Baitalov, Zashchita Metallov, 4 (1968), 8.

83. A. J. E. Pourbaix, M. Marek, and R. F. Hochman; Proc. Stress Corrosion Cracking Mechanism of Ti and Its Alloys. Atlanta, Georgia, (January, 1971).

84. T. R. Beck, J. Electrochem. Soc., 116 (1969), 177.

85. M. Levy and G. N. Sklover, J. Electrochem. Soc., 116 (1969), 323.

86. F. Mansfeld, J. Electrochem. Soc., 118 (1971), 1412.

87. J. W. Olver and J. W. Ross, Jr., J. Am. Chem. Soc., 85 (1963), 2565.

88. M. Pourbaix, Atlas of Electrochemical Equilibria, Pergamon Press, New York (1966).

*English translation of Zashchita Metallov is available as a periodical under the title Protection of Metals.

89. M. Pourbaix, paper presented at CITLE meeting, Istanbul, Turkey, (September, 1967).

90. A. J. Sedriks, Corrosion, 25 (1969), 207.

91. A. J. Sedriks and J. A. Green, Corrosion, 25 (1969), 324.

92. T. R. Beck, J. Electrochem. Soc., 116 (1967), 551.

93. T. R. Beck and E. A. Grens, J. Electrochem. Soc., 116 (1969), 177.

94. R. Otsuka, Z. Metallk, 47 (1951), 714.

95. G. S. Forbes and I. P. Hall, J. Am. Chem. Soc., 46 (1924), 385.

96. M. J. Blackburn, J. A. Feeney, and T. R. Beck, State of the Art of Stress Corrosion Cracking of Titanium Alloys, Boeing, Seattle, Washington, (June, 1970).

97. J. O'M. Bockris, D. Drazic, and A. R. Despic, Electrochem. Acta, 4 (1961), 325.

98. J. O'M. Bockris, A. K. N. Reddy, and B. Rao, J. Electrochem. Soc., 113 (1966), 1133.

99. L. D. Jaffee, J. Metals, 8 (1956), 861.

100. B. Stalinski and Z. Buganski, Bull. Acad. Polom. Sci. Ser. Chim., 10 (1962), 247.

101. T. R. Beck, J. Electrochem. Soc., 115 (1968), 890.

102. G. A. Griffis, Ph. D. Dissertation, The Ohio State University, (1968).

103. J. W. Spretnak and C. A. Griffis, "Research on Notch Plasticity May Contribute to the Understanding of Stress Corrosion Cracking," Corrosion, 25:5 (May, 1969), 193.

104. W. F. Brown, Jr. and J. E. Strawley, "Plane Strain Crack Toughness Testing of High Strength Metallic Materials," ASTM Tech. Publ. No. 410, (1966), 33-38.

105. W. F. Brown, Jr., private communication with Brown.

106. L. E. Kinsler and A. R. Frey, Fundamentals of Acoustics, John Wiley & Sons, New York (1962), 2nd Ed.

107. H. H. Johnson and G. G. Hancock, "Hydrogen, Oxygen, and Subcritical Crack Growth in High Strength Steel," Trans. AIME, 236 (April 1966), 513-516.

108. Clevite Corp., Modern Piezoelectric Ceramics, Publ. No. PD-9247.

109. W. P. Mason, Physical Acoustics and the Properties of Solids, D. VanNostrand, Inc., Princeton, New Jersey, (1958) p. 17.

110. H. L. Dunegan and A. T. Green, "Factors Affecting Acoustic Emission Response from Materials," Mat'ls. Research and Standards, MTRSA, Vol. 11, No. 3, p. 21.

111. N. L. Haruff and C. R. Underwood, "A New Etchant for Low Alloy Steel," Met. Prog. 89 (1), (January 1966) 101.

112. D. P. Williams and H. G. Nelson, "Embrittlement of 4130 Steel by Low-Pressure Gaseous Hydrogen," Metallurgical Transactions, 1, (Jan. 1970) 63-68.

113. R. A. Oriani, "Discussion of Embrittlement of 4130 Steel by Low-Pressure Gaseous Hydrogen," Metallurgical Transactions, 1, (August 1970) 2346-2347.

114. V. Sawicki and H. H. Johnson, "The Effective Area Concept, Permeation, and Hydrogen Gas Crack Growth Kinetics," Metallurgical Transactions, 2 (Dec. 1971).

115. H. L. Marcus and P. J. Stocker, "An Ultra-High Vacuum System for Studying the Effects of Gaseous Environments on Fatigue and Fracture Properties of Metals," North American Rockwell Science Center, Thousand Oaks, California (to be published).

116. T. P. Radhakrishnan and L. L. Shreir, "Permeation of Hydrogen through Steel by Electrochemical Transfer - I. Influence of Catalytic Poisons," Electrochimica Acta, 11 (1966) 1007-1021.

117. N. L. Harull and C. R. Underwood, "A New Etchant for Low Alloy Steel," Metal Progress, 89 (1) (January 1966) 101.

118. J. P. Gallagher, "Environmentally Assisted Fatigue Crack Growth Rates in SAE 4340 Steel," Ph. D. Dissertation, University of Illinois, Feb. 1968.

119. M. O. Speidel, M. J. Blackburn, T. R. Beck and J. A. Feeney, "Corrosion Fatigue and Stress Corrosion Crack Growth in High Strength Aluminum Alloys, Magnesium Alloys, and Titanium Alloys, Exposed to Aqueous Solutions," presented at the International Conference on Corrosion Fatigue, University of Connecticut, June 14-18, 1971.

120. H. H. Johnson, "On Hydrogen Brittleness in High Strength Steels," Proc. Conference on Fundamental Aspects of Stress Corrosion Cracking, The Ohio State University, (1969) 439-445.

121. D. P. Williams, personal communication.

122. C. S. Carter, "Stress Corrosion Crack Branching in High Strength Steels," ARPA Report D6-23871 (March 1969) 1-9.

123. "Stress Corrosion Cracking of Metallic Materials," Third Technical Management Report, Contract No. F33615-69-C-1258 (May 1971) 36-59.

124. G. R. Irwin, "Cricical Energy Rate Analysis of Fracture Strength," Welding Research Supplement 33 (1954) 193S-198S.

125. W. A. Van der Sluys, Babcock and Wilcox Co., Alliance Research Center, Alliance, Ohio, private communication, December 1, 1969.

126. W. A. Van der Sluys, "Mechanism of Environment Induced Subcritical Flow Growth in AISI 4340 Steel," Engineering Fracture Mechanics, 1 (1969) 447.

127. E. A. Steigerwald and W. D. Benjamin, "Environmentally Induced Delayed Failures in Martensitic High Strength Steels," Report AFML-TR-68-80, TRW Inc., Contract AF 33(615)-3651 (April 1968).

128. A. J. Stavros and H. W. Paxton, "Stress Corrosion Cracking Behavior of an 18% Ni Maraging Steel," Metallurgical Trans. 1 (1970) 3049.

129. B. F. Brown, "Stress Corrosion Cracking of High Strength Steel," presented at the Conference on Theories of Stress Corrosion Cracking in Alloys, sponsored by Science Committee, NATO, April 2, 1971.

130. M. O. Speidel, "Current Understanding of Stress Corrosion Crack Growth in Aluminum Alloys,"presented at the Conference on Theories of Stress Corrosion Cracking in Alloys, sponsored by Science Committee, NATO, April 2, 1971.

131. D. McCright, Ph.D. Dissertation, The Ohio State University (1971).

132. T. P. Radhakrishnan and L. L. Shrier, "Hydrogen Permeation through Iron and Steel by Electrochemical Transfer - II. Influence of Metallurgical Factors on Hydrogen Permeation," Electrochemica Acta 12 (1967) 889.

133. W. Beck, J. O'M. Bockris, M. A. Gensaw, and P. K. Subramanyan, "Diffusivity and Solubility of Hydrogen as a Function of Composition in Fe-Ni Alloys," Metallurgical Trans., 2 (1971) 883.

134. A. Gilbert, W. S. Owen, "Diffusionless Transformation in Iron, Nickel, Iron Chromium and Iron Silicon Alloys," Acta Met. 10, (1962) 45.

135. G. P. Miller and W. I. Mitchell, "Structure and Hardening Mechanisms of 18% Ni-Co-Mo Maraging Steel," JISI, 203 (1965) 899.

136. L. Nanis, "Hydrogen Embrittlement," Tech. Report UPH2-002, University of Pennsylvania, Dec. 1970.

137. J. Crank, The Mathematics of Diffusion, Oxford Univ. Press (1964) 261.

138. R. A. Oriani, " The Diffusion and Trapping of Hydrogen in Steel," Acta Metallurgica, 18 (1970) 147.

139. A. R. Troiano, "The Role of Hydrogen and Other Interstitial in Mechanical Behavior of Metals," Trans. ASM, 52 (1960) 54.

140. "Corrosion Cracking of Metallic Materials," AFML-TR-71-58.

141. Technical Report, AFML 69-16 (Feb. 1969).

142. E. G. Haney, "Investigation of SCC of Ti Alloys," Mellon Institute, Semiannual Progress Report No. 1, November 30, 1966.

143. R. A. Oriani, "Hydrogen in Metals," SCC Conference, The Ohio State University, Sept. 1967.

144. E. E. Fletcher and A. R. Elsea, "Hydrogen Movement in Steel Entry, Diffusion and Elimination," DMIC Report 219, Battelle Memorial Institute (June 30, 1965).

145. E. G. Haney, "Investigation of SCC of Ti Alloys," Mellon Institute, Semiannual Progress Report No. 1, November 30, 1966.

146. M. Tsümka and T, Kawase, Gifu Diagaku Nôgakubu Kenkyû Hôkoku, 10 (1960) 26.

147. M. Smialowski, and Z. Szlarska-Smialowski, Bull. Acad. Pol. Sci. 2, (1954) 73.

148. J. M. West, Electrodeposition and Corrosion Processes, D. Van Nostrand (1965).

149. T. P. Radhakrishnan and L. L. Shreir, Electrochem. Acta 11, (1966) 1007.

150. J. F. Newman and L. L. Shreir, Corrosion Science 9 (1969) 631.

151. K. Farrell, Corrosion 26 (1970) 105.

152. D. A. Everest and G. W. Finch, J. Chem. Soc. (1955) 704.

153. M. A. V. Devanathan and Z. Stachurski, J. Electrochem. Soc. (1964) 111.

154. E. A. Efimov and I. G. Erusalimchik, Elektrkhimiya 1 (1965) 1133.

155. I. R. Piontelli and G. Poli, Gazz. Chim. Ital, 79 (1949) 214.

156. K. M. West, Electrodeposition and Corrosion Processes, D. van Nostrand Co. Ltd., London (1965), Chap. 2 and 3.

157. I. A. Menzies and L. W. Owen, Electrochimica Acta, 11 (1966) 251.

158. G. Wranglen, J. Electrochem. Soc., 108 (1961) 1069.

159. H. W. Salzberg and B. Goldschmidt, J. Electrochem. Soc., 107 (1960)348.

160. W. L. Jolly, L. B. Anderson and R. T. Betrami, J. Amer. Chem. Soc., (1957) 2443.

161. R. M. Hudson and G. L. Stragand, Corrosion, 18 (1962) 259t.

162. G. Kerns and J. Sneary, The Ohio State University, unpublished results.

163. J. F. Newman and L. L. Shreir, Corrosion Science, 9 (1969) 631.

164. J. McBreen and M. A. Genshaw, Proc. of Conference: Fundamental Aspects of Stress Corrosion Cracking, Ohio State University, (1967), eds. R. W. Staehle, A. J. Forty, D. van Rooyen, Natl. Assoc. of Corrosion Engineers, Houston (1969) 51.

165. A. N. Frumkin and A. Slygin, Physiochim. Acta, URSS 5 (1936) 819.

166. B. E. Conway and J. O'M. Bockris, J. Chem. Phys. 26 (1957) 532.

167. B. E. Conway, Theory and Principles of Electrode Processes, Ronald Press, New York (1965) Chap. 8.

168. C. D. Kim and B. Wilde, J. Electrochem. Soc., 118 (1971) 202.

169. C. D. Kim, U. S. Steel Corp. Applied Research Lab., private communication.

170. R. A. Oriani, Proc. Conference: Fundamental Aspects of Stress Corrosion Cracking, The Ohio State University (1967) Eds. R. W. Staehle, A. J. Forty, D. van Rooyen, Natl. Assoc. of Corrosion Engineers, Houston (1969) 32.

171. H. A. Skinner, Trans. Faraday Soc. 41 (1945) 645.

172. S. Besnard, Corrosion Anti-Corrosion 10 (1962) 182.

173. S. Besnard and J. Talbot, Comptus Rendus, 144 (1957) 1193.

174. L. S. Darken and R. W. Gurry, Physical Chemistry of Metals, McGraw-Hill Book Co., New York (1953) 37.

175. A. H. Cottrell, Theoretical Structural Metallurgy, 2nd Edition, Edward Arnold Ltd., London (1955) 80.

176. J. O'M. Brockis, J. McBreen and L. Nanis, J. Electrochem. Soc. 112 (1965) 1025.

177. A. McNabb and D. K. Foster, TAIME 227 (1963) 618.

178. R. A. Oriani, Acta Met., 18 (1970) 147.

179. M. A. Genshaw and J. McBreen, Proc. of Conference: Fundamental Aspects of Stress Corrosion Cracking , The Ohio State University) (Sept. 1967) 51.

180. E. Hornbogen and R. C. Glenn, TAIME 218 (1960) 1064.

181. R. E. Smallman and K. H. G. Ashbee, Modern Metallography, Pergamon Press, Oxford (1966) Chaps. 7, 8, 9.

182. E. Hornbogen, Trans. Am. Soc. Metals, 57 (1964) 120.

183. R. Gibala, Trans. Met. Soc. AIME 239 (1967) 1574.

184. I. M. Bernstein, Metallurgical Trans. 1 (1970) 3143.

185. S. S. Kramer, G. M. Pound, and R. F. Mehl, Acta Met., 6 (1958) 763.

186. E. Strecker, D. A. Ryder and T. J. Davies, "An Investigation of Hydrogen-Induced Delayed Failure in Unnotched Specimens of 0.9% C Steel Strip," JISI, 207 (12) (1969) 1639-1641.

187. K. Sachs and A. Morgan, "Susceptibility to Delayed Failure," JISI, 206 (4) (1968) 357-362.

188. G. C. Wood and G. C. Soltz, "Influence of Prepolarization on the Electrochemical Behavior of Iron-Carbon Alloys," Corrosion 24 (6) (1968) 163-171.

189. J. Crank, Mathematics of Diffusion, Clarendon Press (1956) 67.

UNCLASSIFIED

Security Classification

DOCUMENT CONTROL DATA - R & D

(Security classification of title, body of abstract and indexing annotation must be entered when the overall report is classified)

1. ORIGINATING ACTIVITY (Corporate author) The Ohio State University Research Foundation Columbus, Ohio 43212	2a. REPORT SECURITY CLASSIFICATION Unclassified 2b. GROUP N/A

3. REPORT TITLE

CORROSION CRACKING OF METALLIC MATERIALS - Part I. SUMMARY

4. DESCRIPTIVE NOTES (Type of report and inclusive dates)

Final Report December 15, 1968 through December 31, 1971

5. AUTHOR(S) (First name, middle initial, last name)

Mars G. Fontana

6. REPORT DATE August 1972	7a. TOTAL NO. OF PAGES 516	7b. NO. OF REFS 189
8a. CONTRACT OR GRANT NO. F33615-69-C-1258 b. PROJECT NO. 7312 c. Task No. 731202 d.	9a. ORIGINATOR'S REPORT NUMBER(S) 9b. OTHER REPORT NO(S) (Any other numbers that may be assigned this report) AFML-TR-72- 102	

10. DISTRIBUTION STATEMENT

Approved for public release; distribution unlimited.

11. SUPPLEMENTARY NOTES	12. SPONSORING MILITARY ACTIVITY Air Force Materials Laboratory (LL) Wright-Patterson Air Force Base, Ohio

13. ABSTRACT

Studies on the stress corrosion cracking of titanium and its alloys involved the initiation and propagation of cracks in aqueous and organic environments, combined effects of stress and potential, corrosion processes within crevices, and alloy composition. Straining electrode studies are reported.

In Ti-6Al-4V specimens, crack initiation was associated with local anodic disintegration at α-β interfaces and at β grains. Crack velocity studies in titanium alloys show that crack velocity was independent of applied potential but directly dependent on stress. Studies within titanium crevices show that the corrosion inside a crevice is accentuated when the IR drop is large; procedures for minimizing this effect are discussed.

Activation energies of 6~7 kcal for stress corrosion cracking were determined for unalloyed titanium and titanium alloys Ti-6Al-4V, Ti-8Al-1V-1Mo, and βIII in CH_3OH + HCl + H_2O and CH_3OH + Br_2 solutions, suggesting that either halide ion attack or titanium hydride formation describe the cracking mechanism.

Chemical methods, to reduce the water content of methanol to low levels and to accurately determine these levels, have been developed to examine the effect of these small water concentrations on the stress corrosion cracking behavior of titanium in methanol environments.

Unalloyed titanium failed by stress corrosion cracking in distilled methanol containing chloride as low as 10 ppb. Stress corrosion susceptibility of unalloyed titanium and titanium alloys Ti-8Al-1V-1Mo, Ti-6Al-4V, and βIII increased when CaO was added to absolute methanol to reduce the water content of the methanol from the initial 0.015% level. A further increase in susceptibility was observed in dry methanol vapor. It is believed that the primary reaction of methanol with titanium involves the production of titanium methoxide and hydrogen. Mixtures of carbon tetrachloride and methanol are more reactive to titanium than are either of the pure solvents. Small amounts of bromine added to benzene, carbon tetrachloride, and diethyl ether increased greatly the susceptibility of Ti-8Al-1V-1Mo to cracking. This effect was most pronounced for diethyl ether.

Studies on the effect of grain size of Ti-6Al-4V on stress corrosion cracking in CH_3OH + H_2O + NaCl solution show that increased resistance with decreasing grain size is due primarily to increased crack initiation time.

DD FORM 1 NOV 65 1473

Unclassified

Security Classification

14. KEY WORDS	LINK A		LINK B		LINK C	
	ROLE	WT	ROLE	WT	ROLE	WT
Stress corrosion Propagation Ti-8Al-1V-1Mo Ti-6Al-4V Titanium						